Project No. 09-808

A Distributed Fiber Optic Sensor Network for Online 3-D Temperature and Neutron Fluence Mapping in a VHTR Environment

Reactor Concepts RD&D

Dr. Pavel Tsvetkov
Texas A&M University

In collaboration with:
General Atomics
Idaho National Laboratory
Luna Innovations

Suibel Schuppner, Federal POC
Abderrafi Ougouag, Technical POC

NEUP Nuclear Energy University Programs
U.S. Department of Energy

Final Report

A DISTRIBUTED FIBER OPTIC SENSOR NETWORK FOR ONLINE 3D TEMPERATURE AND NEUTRON FLUENCE MAPPING IN A VHTR ENVIRONMENT

Award: DE-AC07-05ID14517,

Project: 09-808

Contract: 00090311

2009 – 2012 (no-cost extension through 2013)

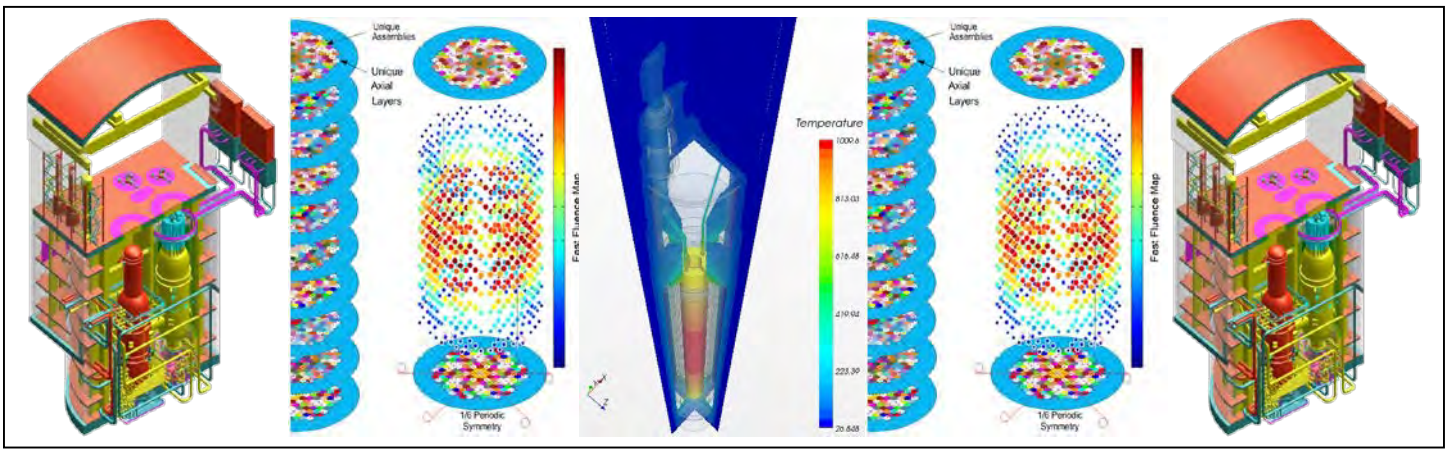

Texas A&M University, Department of Nuclear Engineering

Tel 979-845-7078
Fax 979-845-6443

337 Zachry Engineering Center,
MS3133, College Station, TX, 77843

http://engineering.tamu.edu/nuclear
tsvetkov@tamu.edu

Page intentionally blank

Table of Contents

A Distributed Fiber Optic Sensor Network for Online 3-D Temperature and Neutron Fluence Mapping in a VHTR Environment

Recipient:	Texas A&M University College Station, Texas, 77843	
Contract:	00090311	
Project:	09-808	
Principal Investigator:	Pavel Tsvetkov*,	979-845-7078, tsvetkov@tamu.edu
Co-Principal Investigator:	Shannon Bragg-Sitton*,	sitton@tamu.edu Shannon.Bragg-Sitton@inl.gov
Collaborators:	Bryan Dickerson, Joseph French, Donald McEachern, Abderrafi Ougouag,	dickersonb@lunainnovations.com frenchj@lunainnovations.com Donald.McEachern@ga.com (project advisor) Abderrafi.Ougouag@inl.gov (project advisor)
TPOCs:	Abderrafi Ougouag,	208-526-7659, Abderrafi.Ougouag@inl.gov
Federal POC:	Suibel Schuppner,	301-903-1652 SUIBEL.SCHUPPNER@nuclear.energy.gov

The work enables development of a highly reliable, distributed fiber optic temperature and fluence sensor network operable under high temperature/neutron fluence conditions and located throughout the reactor core (axial and transverse dimensions). The project scope encompasses fabrication of the sensor hardware, test article design and fabrication to support in-core testing, sensor hardware demonstration at the Texas A&M University TRIGA research reactor, 3D modeling of the NGNP/VHTR configuration and scaling from the TRIGA test environment to the anticipated VHTR operating conditions. The corresponding temperature/neutron field map reconstruction and optimization of in-core detector positioning to minimize uncertainties are also be performed. The advantages of real-time in-core monitoring are illustrated

*Dr. Bragg-Sitton is the original PI of the NEUP proposal and the awarded project in Year 1. Dr. Tsvetkov is the co-PI of the NEUP proposal and the awarded project in Year 1. The management roles were changed in Year 2 following Dr. Bragg-Sitton departure from Texas A&M University and joining Idaho National Laboratory. At that time, Dr. Tsvetkov took over as the project PI while Dr. Bragg-Sitton remained as Co-PI for the duration of the effort.

Page intentionally blank

Disclaimer

This report was prepared as an account of work sponsored by an agency of the United States Government. Neither the United States Government nor any agency thereof, nor any of their employees, makes any warranty, express or implied, or assumes any legal liability or responsibility for the accuracy, completeness, or usefulness of any information disclosed. The views and opinions of authors expressed herein do not necessarily state or reflect those of the United States Government or any agency thereof.

Page intentionally blank

Table of Contents

NEUP 09-0808

A Distributed Fiber Optic Sensor Network for Online 3-D Temperature and Neutron Fluence Mapping in a VHTR Environment

Battelle Energy Alliance — U.S. Department of Energy Project No. CFP-09-0808

FINAL TECHNICAL REPORT

Original release date – August 1, 2013, updated and revised – April 28, 2014, final release – August 4, 2014

Participating Institutions: Texas A&M University (through TEES), Luna Innovations, General Atomics, Idaho National Laboratory

Contact: Dr. Pavel V. Tsvetkov, Associate Professor, Department of Nuclear Engineering, Texas A&M University, MS3133 TAMU, 337 Zachry Engineering Center, College Station, TX, 77843-3133, tsvetkov@tamu.edu, 979-845-7078, fax: 979-845-6443

Page intentionally blank

Table of Contents

Principal Researchers

Jesse Johns	– Experimental Program
Matthew Johnson	– Distributed Sensor Network Modeling

Page intentionally blank

Contents

1. Abstract 1
2. Nomenclature 3
3. Executive Summary 5
   3.1. Fiberoptics-Based Sensing for Real-Time 3D In-Core Monitoring in NGNP/VHTRs 5
      3.1.1. Introduction 5
      3.1.2. High Temperature Furnace 5
      3.1.3. Fiberoptics vs. STAR-CCM+ Predictions 7
      3.1.4. Fiberoptics Lifetime Measurements 8
      3.1.5. In-Core Sensor Positioning and Data Processing 10
      3.1.6. Conclusions 11
      3.1.7. References 12
   3.2. 3D Mapping and Reconstruction for In-Core Monitoring in Advanced Reactors 12
      3.2.1. Introduction 12
      3.2.2. High-Fidelity Reactor Model 13
      3.2.3. Performance Analysis 13
      3.2.4. Reconstruction Approach 14
      3.2.5. Conclusions 16
      3.2.6. References 17
4. Introduction 18
   4.1. Objective 19
   4.2. Background 19
      4.2.1. VHTR In-Core Environment 19
      4.2.2. Candidate Sensors for VHTR In-Core Flux and Temperature 20
      4.2.3. Fiber Optic Temperature/Neutron/Gamma Mapping for VHTRs 21
      4.2.4. References 23
5. High Fidelity Modeling Approach 25
   5.1. 3D VHTR/NGNP Configuration Model 25

5.2. Image Reconstruction Applied to 3D Flux Data 28
5.2.1. Test Problems 28
5.2.2. Performance of the Applied Reconstruction Methods in the Test Problems 29
5.3. Application of 3D Flux Reconstruction by Interpolation to Fine-Mesh Flux Data 34
5.3.1. Test Problems 34
5.3.2. Sensor Arrangement 34
5.3.3. Reconstruction Results 36
5.3.4. Sensor failures 38
5.4. Emulation of VHTR Conditions in TRIGA 39
5.5. Safety Evaluations and Validation Program 44
5.5.1. Thermal Conditions 45
5.5.2. Heater Stress Testing 48
5.5.3. Physical Tests 48
5.5.4. Radiation Model Validation 50
5.6. Conclusions 50
5.7. References 51
6. Distributed Fiberoptics-Based Measurement System 52
6.1. Distributed Fiberoptic Characterization of In-Core Nuclear Radiation Fields 52
6.1.1. Introduction 52
6.1.2. Background 52
6.1.3. Distributed Fiberoptic Probe Development 53
6.1.4. Data Processing Software 55
6.1.5. Demonstration 56
6.2. Preliminary Design of the Test Probe Housing 58
6.3. Fiberoptics Probe Design for Distributed Measurements 59
6.4. Fiberoptics Performance Monitoring 63
6.5. Fiberoptics Data Processing 63
6.5.1. Data Acquisition Software 63

6.5.2. Temperature Correction 64
6.6. Fiberoptics Sensor Hardware Manufacturing 66
6.7. Fiberoptics Sensor Hardware Testing 71
6.7.1. Preface 71
6.7.2. Introduction 72
6.7.3. Reference Data 72
6.7.4. Obtained Data and Analysis 74
6.7.5. Conclusions 80
6.8. Vibration Testing 80
6.8.1. Summary 80
6.8.2. Introduction 80
6.8.3. Vibration Effects on Fiberoptics Temperature Measurements 81
6.8.4. Conclusions 93
7. High Temperature Test Assembly 94
7.1. Experimental Approach 94
7.2. Description of the System 94
7.3. Conceptual Design 95
7.4. Component Fabrication 97
7.4.1. Furnace Structure 97
7.4.2. Void Tube 104
7.4.3. Pressurization System 107
7.5. Acceptance Testing 108
7.6. Experimental Program 116
7.6.1. Fiberoptics Probe 116
7.6.2. Expected Fiberoptics Behavior 116
7.6.3. Irradiation 117
7.7. Conclusions 128
7.8. References 128

8. Sensor Networks and Data Processing Algorithms for Future Nuclear Systems 129
8.1. Introduction 129
8.1.1. Characterization of In-Core Conditions 129
8.1.2. Potential In-Core Neutron Sensors 130
8.1.3. Objectives 131
8.2. VHTR System Model 131
8.2.1. Introduction 131
8.2.2. Applied Codes and Models 132
8.2.3. Performance Analysis 140
8.3. Flux Reconstruction Theory 145
8.3.1. Overview 145
8.3.2. Interpolation-based Methods 146
8.3.3. POD-Based Methods 151
8.4. Flux Reconstruction Implementation and Performance 153
8.4.1. Introduction 153
8.4.2. Interpolation 155
8.4.3. POD 159
8.5. Conclusions 170
8.6. References 173
9. Conclusions 176
9.1. Outcomes of the Experimental Program 176
9.2. Fiberoptics Engineering Challenges 177
9.3. Development of the 3D In-core Reconstruction Method 178
10. Publications 180
11. Presentations 181
12. Participating Students 182
13. Appendix 183
13.1. Procurement and Fabrication Process 183
13.2. Fiberoptics Testing 185

13.3. Acceptance Testing 189
13.4. VHTR Control Rod Modeling 191
13.4.1. Design Details 191
13.4.2. References 191
13.5. Presentations 192
13.5.1. 3D High-Fidelity VHTR Modeling for Performance Optimization 192
13.5.2. Distributed Sensor Networks for Online 3D In-Core Monitoring 200
13.5.3. Emulation of VHTR Operating Conditions in TRIGA Reactors 210
13.5.4. In-Core Testing of Distributed Fiber Optic Sensors 225
13.5.5. TRIGA-Based Experimental Device for Fiber Optics Testing 243
13.5.6. 3D In-Core Monitoring in Advanced Reactor Environments 259
13.5.7. Fiberoptics-Based Sensing for Real-Time 3D In-Core Monitoring 272
13.5.8. 3D Mapping and Reconstruction for In-Core Monitoring 292
13.6. Safety Analysis for In-Core TRIGA Furnace 311
13.7. Experimental Setup In/By the Pool Wall 351
13.8. High Temperature Test Assembly (Furnace) Operation 353
Contact Information 368
University Information 368

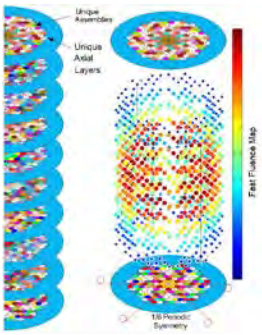

1. Abstract

Advanced instrumentation capable of operating in high-temperature/high-radiation environments is required to fully map the temperature and neutron fluence distributions in the proposed very high-temperature reactor (VHTR) cores. This project will develop a highly reliable, distributed fiber optic temperature and fluence sensor network operable under high-temperature/high-neutron fluence conditions and located throughout the reactor core. The project scope encompasses fabrication of the sensor hardware, test article design and fabrication to support in-core testing, sensor hardware demonstration at a university TRIGA research reactor, 3D modeling in a VHTR configuration, and scaling from the TRIGA test environment to the anticipated VHTR operating conditions. The project will also perform corresponding temperature/neutron field map reconstruction techniques and optimization of in-core detector positioning to minimize uncertainties. The proposed in-core monitoring is expected to reliably perform under extreme conditions that allow on-demand positioning in the reactor vessel. This results in direct in-core monitoring in prismatic core configurations and an opportunity to position detectors at innermost outer reflector locations or inside the central graphite column of the pebble bed system.

Online temperature and fluence mapping provides real-time assessment of reactor performance, benchmarks simulation and analysis codes used in core design and modeling, and allows optimization of operating margins. Existing instrumentation either fails prematurely due to combined effects of high temperatures and radiation and cannot perform reliably for the entire 18-month refueling cycle, or does not provide sufficient real-time information. The current near-term VHTR design has a projected coolant outlet temperature ranging from 750°C to 950°C, with nominal fuel temperatures ranging from 700°C to a maximum of 1,250°C. These conditions, combined with the high-radiation environment, create extremely harsh operational conditions that pose tremendous challenges for in-core monitoring system design. These challenges are currently mitigated by providing out-of-core monitoring capabilities and applying corresponding reconstruction techniques to determine temperature and neutron fluence rate profiles across the reactor core. These techniques cannot predict local phenomena due to significant uncertainties and, hence, result in higher safety margins.

Original project number designator: 09-241.

Original PI: S. Bragg-Sitton, Texas A&M University.

Collaborators: T. Bertch - General Atomics, B. Dickerson - Luna Innovations, R. Fielder - Luna Innovations, and D. McEachern - General Atomics, A. Ougouag - Idaho National Laboratory, A. Sang - Luna Innovations, P. Tsvetkov - Texas A&M University.

Page intentionally blank

2. Nomenclature

- BOL - beginning of life
- EOL - end of life
- FOM - figure of merit
- HTR - high temperature reactor
- INL - Idaho National Laboratory
- NGNP - next-generation nuclear plant
- OBR - Optical Backscatter Reflectometer
- PNNL - Pacific Northwest National Laboratory
- POD - proper orthogonal decomposition
- SPND - self-powered neutron detector
- SVD - Singular Value Decomposition
- TRISO - tri-structural isotropic
- VHTR - very high temperature reactor

Page intentionally blank

3. Executive Summary

3.1. Fiberoptics-Based Sensing for Real-Time 3D In-Core Monitoring in NGNP/VHTRs

3.1.1. Introduction

Robust sensing technologies allowing for 3D in-core performance monitoring in real time are of paramount importance for already established LWRs to enhance their reliability and availability per year, and therefore, to further facilitate their economic competitiveness via predictive assessment of the in-core conditions. This is even more so the case for emerging advanced reactor technologies, such as Next Generation Nuclear Plants (NGNPs), Very High Temperature Reactors (VHTRs). The NGNP/VHTR will be a full-sized demonstration of the Generation IV VHTR for a range of potential applications from electricity to process heat.[1] The novel VHTRs are characterized by very hostile in-core conditions of high temperatures and hardened neutron spectra, in which traditional sensors may operate reliably only for a limited amount of time failing prematurely due to combined effects of high temperatures and radiation.[2,3] In existing prototypes, like HTTR, this challenge is mitigated by providing out-of-core monitoring capabilities together with reconstruction of in-core values as well as by allowing for sensor insertion/withdrawal on demand thus extending their useful lifetime.[4]

In the present project, the 3-year effort is focused on enabling development efforts to yield a highly reliable, distributed fiber optic temperature and fluence sensor network operable under high temperature/neutron fluence conditions and located throughout the reactor core (axial and transverse dimensions).[5] The project scope encompasses fabrication of the sensor hardware, test article design and fabrication to support in-core testing, sensor hardware demonstration at the Texas A&M University TRIGA (Training, Research, Isotope Production, General Atomics) Mark I 1MW research reactor, 3D modeling of the NGNP/VHTR configuration and scaling of the results from the TRIGA test environment to the anticipated VHTR operating conditions. The corresponding temperature/neutron field map reconstruction techniques and optimization of in-core detector positioning to minimize uncertainties and enhance sensing reliability are also performed. The project is funded by the DOE Nuclear Energy University Program.

This paper discusses the project efforts and outcomes, hardware, and gained operational experience. Notably, advanced in-core test assembly has been developed and deployed for experimental confirmation of fiberoptics sensor performance characteristics in VHTRs via emulation of VHTR in-core conditions in TRIGA reactor cores. [5, 6]

3.1.2. High Temperature Furnace

Emulation of the VHTR conditions in the TRIGA requires three criteria to be met: spectrum, temperature, and environment. The sensor test assembly is required to be irradiated to a fluence of $2x10^{19}$ n/cm^2 and operate at 1000°C. A high temperature test furnace has been designed, manufactured and deployed in the TRIGA core to achieve this objective. The developed furnace design originates from the General Atomics furnace developed in the 1970s for high temperature reactor (HTR) fuel testing in TRIGA reactors. [6]

Figure 1 shows the overall layout of the high temperature test assembly (left) and the experimental setup in the TRIGA pool (right) during acceptance testing procedures confirming its operational readiness prior to installing in the allocated position within the TRIGA core and commencing the experimental program. This furnace assembly is a successful culmination of several years of design, construction and testing efforts within the project. The furnace was designed and fabricated with the guidance of analytical and numerical tools, the STAR-CCM+ package, in particular.

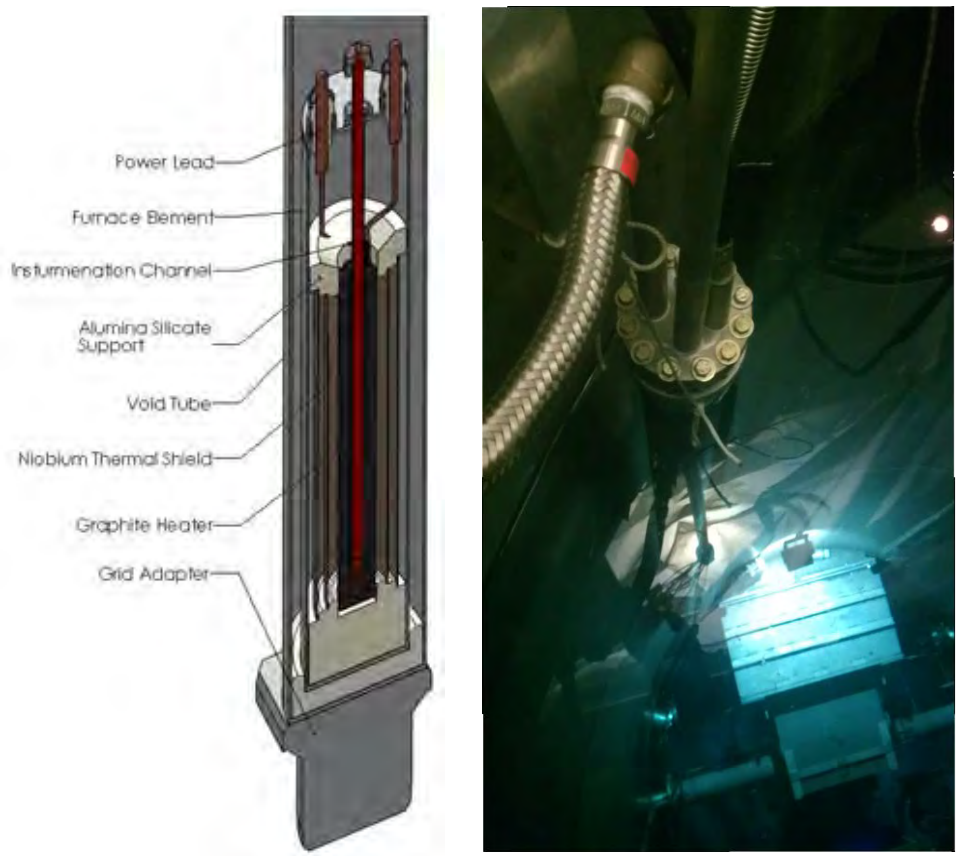

Fig. 1. High temperature test assembly design (left) and the experimental setup during the TRIGA in-pool acceptance testing (right).

The high temperature furnace is capable of an automatic startup triggered by a user input followed by a swap to a PID controller. Fig. 2 shows the transition during the startup to the PID controller. The transition limits the temperature gradient from exceeding 0.2 ^{o}C/s and prevents temperature overshoot to less than a degree. The PID controller was optimized at the acceptance testing stage of the experimental program and further improved following operation in the reactor environment.

During operation, the reactor undergoes various transients of known power. These are normally to accommodate sample movements or experiments and vary between 100 kW and 1 MW. With the PID controller active, the furnace temperature is maintained.

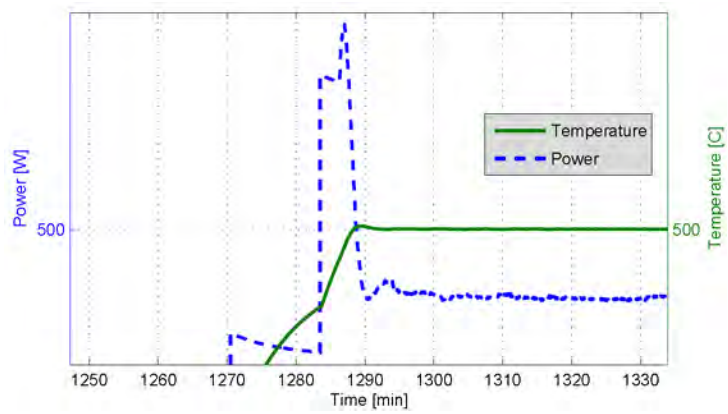

Fig. 2. Automatic swap to PID controller via LabView.

Figure 3 shows the operation of the high temperature furnace throughout a day, completely unattended where the depression in power between 500 and 1000 minutes corresponds to the reactor operation at 1MW.

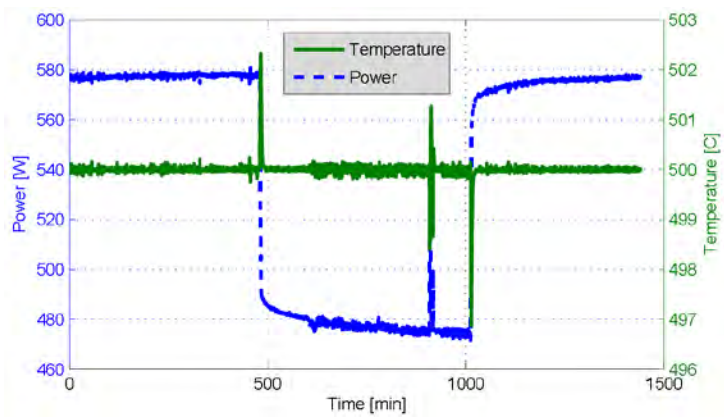

Fig. 3. Full day operation of the high temperature furnace showing ohmic power and temperature.

The high temperature furnace operation has been smooth and stable. It is expected to maintain operational integrity throughout the experimental program of the project and in follow-on experimental efforts with minimal maintenance. The process of installation and data acquisition has occurred without major problems. The automatic PID controller works well with the parameters that were set manually.

3.1.3. Fiberoptics vs. STAR-CCM+ Predictions

Figure 4 illustrates a comparison of the thermal distribution from fiber optic measurements to the spatial gradient from the STAR-CCM+ simulation. The largest discrepancies are at the axial ends of the graphite since there are significant assumptions on the contact resistances with the alumina supports. This will affect the heat transfer from the ends. It was assumed, in the

modeling, that there would be about 20% contact (only allowed 20% of the mesh volume to transfer heat between surfaces).

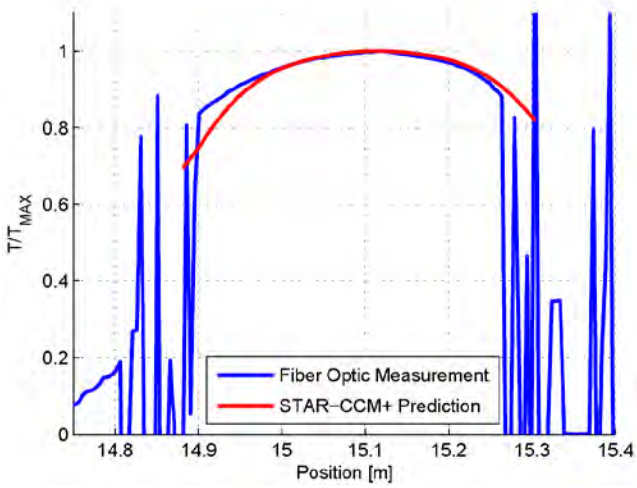

Fig. 4. Normalized temperature distributions from fiberoptics measurements and the STAR-CCM+ model.

It has been observed that fiberoptics measurements are severely affected by vibrations due to natural circulation cooling of the reactor while operating. The affected regions are typically at the fiber end (15.25+ meters) and at the feedthrough into the furnace (14.8 – 14.9 meters). It does appear that the vibration induced noise affects the measurement only locally and that the rest of the measurement is not impacted. The shape of the temperature distributions do closely match with the peak being predicted within a centimeter. As expected, the temperature gradients near the edges of the graphite heating element (the end of the STAR-CCM+ data plot corresponds with the end of the graphite heater) are steeper.

During operation of the furnace at an average temperature of 500oC, the fiberoptics measures an average temperature of 720.2oC; compared to the thermocouple readings this poses a challenge for the fiberoptics. The observed differences appear to be due to internal fiberoptics material effects and their interpretation by the fiberoptics data acquisition and processing software package.

At the present state of the question, there appear to be significant dependencies of the fiberoptics sensing on the software data package performance, especially on calibration and built-in material effects models. These dependencies jeopardize contemporary uses of fiberoptics-based sensing architecture. However, these observations do not exclude future potential applications as software packages mature.

3.1.4. Fiberoptics Lifetime Measurements

Twelve fiberoptics sensors were available for irradiation within the fiber optic instrumentation probe. This probe contains four of each of the temperature, gamma, and neutron detecting sensors, of which three fibers had failed prior to arrival of the probe at Texas A&M University. An average fluence of 1.0×10^{19} n/cm^2 was reached for each fiberoptics sensor type during the

available operational time. The results of this irradiation are summarized in Table 1. Two fibers failed to initial thermal stressing and the two remaining gamma fibers failed as a result of the irradiation, as shown in see Fig. 5.

Table 1. Fiberoptics 3-month-irradiaiton survivability

Fiberoptics Sensor Type	Final Condition	Comment
Gamma 1	Failed – DOA*	
Temperature 2	Failed	Failed immediately at startup.
Neutron 3	Survived	
Gamma 4	Failed – DOA*	
Temperature 5	Survived	
Neutron 6	Failed – DOA*	
Gamma 7	Failed	Failed at 4.5e18 n/cm^2 fluence.
Temperature 8	Survived	
Neutron 9	Survived	
Gamma 10	Failed	Failed at 5.8e18 n/cm^2 fluence.
Temperature 11	Failed	Failed immediately at startup.
Neutron 12	Survived	

DOA – dead on arrival.

It is likely that the failures of gamma-sensing fibers were resulting from material swelling. Both fibers failed with the same characteristics of increased return loss at point between support ferrule interfaces within the instrument probe. This assertion has not been physically confirmed in the present analysis.

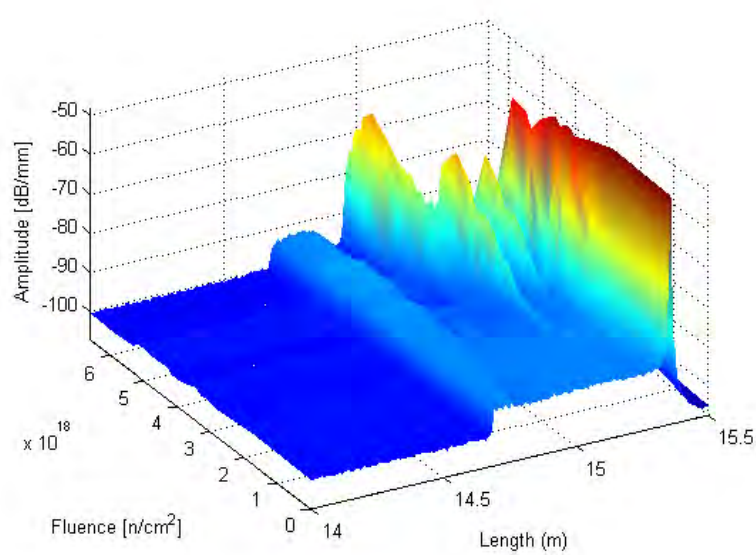

Fig. 5. Gamma fiber return loss over probe length during irradiation.

3.1.5. In-Core Sensor Positioning and Data Processing

A 3D whole-core exact-geometry model of a VHTR hexagonal-block configuration with a detailed component representation has been developed and implemented for calculations with MCNP/MCNPX and Serpent. The model is based on the NGNP pre-conceptual design features. [1]

The modeling approach allows for development and applications of in-core 3D performance map reconstruction techniques accounting for novel direct 3D in-core measurement approaches for extreme environments of HTRs such as would be eventually offered by fiberoptics sensing once this instrumentation technology matures to the level of reactor applications. Figure 6 summarizes six considered potential sensor arrangements within the VHTR including active core and reflector regions.

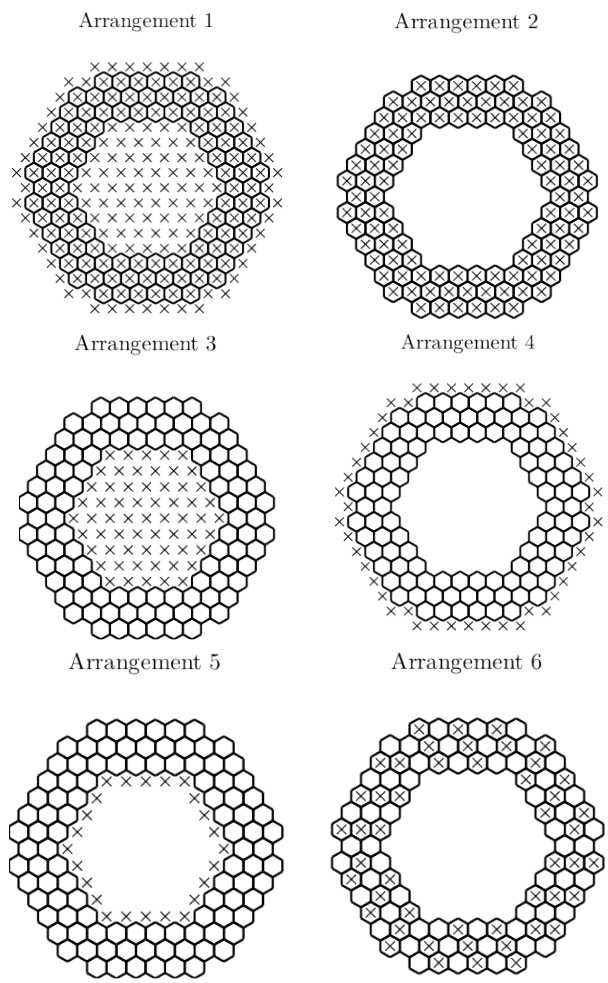

Fig. 6. Sensor arrangements within a VHTR, instrumented blocks are marked with "X".

Figure 7 shows the average reconstruction relative errors for each of the arrangements depicted in Fig. 6. It is interesting to note that while arrangement 1 contains the most sensors, it does not always perform the best.

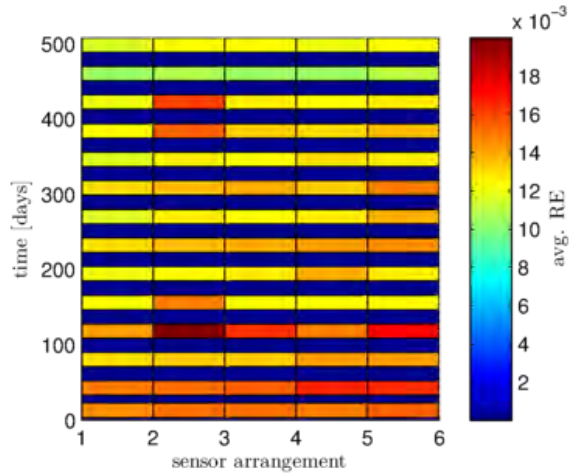

Fig. 7. Average reconstruction relative errors (avg. RE) for six sensor arrangement configurations.

3.1.6. Conclusions

This report presented the results and observations obtained in the course of the 3-year program. The gained practical experience with fiberoptics sensors and computational evaluations of distributed sensing networks for reactor in-core applications indicate potential opportunities for future applications, especially in the environments which would be either physically hostile or geometrically challenging for traditional sensing technologies. Furthermore, as indicated above, distributed sensing allows gathering more robust data during reactor operation which is essential not only for predictive safety monitoring but also for competitive reliability and economics. The project was focused on NGNP/VHTR environments but the analyzed fiberoptics sensing and 3D in-core monitoring via distributed sensing are of paramount value for LWRs, emerging SMRs and all advanced nuclear reactors.

Although fundamental feasibility and potential applications for fiberoptics sensors have been established, the technology, by far, is not ready for near-term practical in-core implementations. The noted challenges include excessive dependencies of sensing system performance characteristics on vibrations due to thermo-mechanical core characteristics, resulting noise effects, internal fiberoptics material effects and their interpretation by the fiberoptics data acquisition and processing, and overall inherent dependencies of fiberoptics sensing technologies on accompanying software components to recover and interpret measured performance characteristics, and frequent calibration needs for the system to operate meaningfully.

These observations strongly suggest the need for further research efforts to systematically resolve these challenges, thus allowing taking a full advantage of the existing fiberoptics and distributed sensing capabilities for next generation in-core instrumentation solutions for current LWRs as well as SMRs and advanced reactor systems.

3.1.7. References

1. "Next Generation Nuclear Plant Pre-Conceptual Design Report," INL/EXT-07-12967, (2007).

2. "Design Features and Technology Uncertainties for the Next Generation Nuclear Plant," Independent Technology Review Group, INEEL/EXT-04-01816, Idaho National Engineering and Environmental Laboratory (2004).

3. S. J. Ball, S. E. Fisher, "Next Generation Nuclear Plant Phenomena Identification and Ranking Tables," NUREG/CR-6944, ORNL/TM-2007/147 (2008).

4. K. Saito, H. Sawahata, F. Homma, M. Kondo, T. Mizushima, "HTTR: Instrumentation and Control System Design," *Nucl. Eng. Design*, **233**, pp. 125-133 (2004).

5. B. Dickerson, J. Farmer, J. French, M. Palmer, R. Fielder, "Fiber Optic Sensors Measuring Gamma Flux and Neutron Fluence," *Trans. Amer. Nucl. Soc.*, **99**, pp. 289-290 (2008).

6. E. E. Anderson, S. Langer, N. L. Baldwin and F. E. Vanslager, "An In-Core Furnace for the High-Temperature Irradiation Testing of Reactor Fuels," *Nucl. Tech.*, **11**, pp. 259-265 (1971).

3.2. 3D Mapping and Reconstruction for In-Core Monitoring in Advanced Reactors

3.2.1. Introduction

Advanced sensor networks and data processing algorithms are needed for future generation nuclear reactors and energy systems. In many cases, detector systems designed for current generation LWRs cannot survive in advanced reactors. Reactor safety margins for these advanced systems must account for uncertainties in reactor operating conditions.

Accurate on-line reconstruction approaches would significantly reduce the uncertainties present in predictive capabilities for core-wide distributions thus enhancing system reliability and availability per year, and therefore, facilitating economic competitiveness via predictive assessments of the in-core conditions.

This paper is focused on reconstruction techniques for the very high temperature reactor (VHTR), one of several next-generation designs supported by the Generation IV International Forum (GIF). [1]

The novel VHTRs are characterized by very hostile in-core conditions of high temperatures and hardened neutron spectra, in which traditional sensors may operate reliably only for a limited amount of time failing prematurely due to combined effects of high temperatures and radiation. [2, 3]

In existing prototypes, like HTTR, this challenge is mitigated by providing out-of-core monitoring capabilities together with reconstruction of in-core values as well as by allowing for sensor insertion/withdrawal on demand thus extending their useful lifetime. [4]

The goal of the ongoing effort is to develop an advanced 3D in-core mapping and reconstruction via distributed sensor networks.

3.2.2. High-Fidelity Reactor Model

A 3D whole-core exact-geometry model of a VHTR hexagonal-block configuration with a detailed component representation has been developed and implemented for calculations with MCNP/MCNPX and Serpent. The model is based on the NGNP pre-conceptual design features.[1] The modeling approach allows for development and applications of in-core 3D performance map reconstruction techniques accounting for novel direct 3D in-core measurement approaches for extreme environments of HTRs.

Earlier benchmark studies validated applicability of the modeling approach to correctly represent design features and performance characteristics of HTRs. [5, 6] Figure 1 illustrates details of this model. The model color scheme demonstrates the ability to quantify physics characteristics while varying properties per block. It allows for tracking environments in fuel and coolant channels.

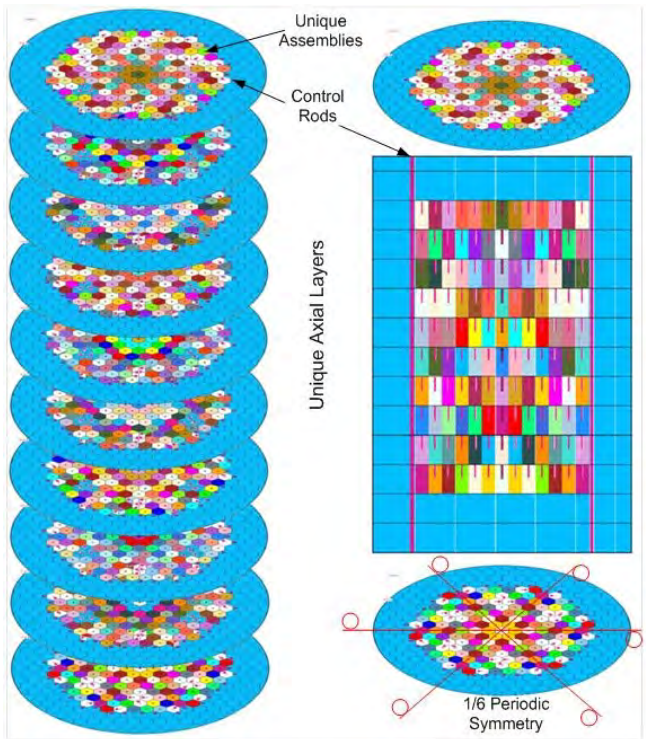

Fig. 1. High fidelity whole-core VHTR model.

3.2.3. Performance Analysis

This work is particularly concerned with the location in the core where neutron flux was at a maximum. The location of the hot spot is a complex function of time.

Figure 2 shows how the neutron flux hot spot moved up and down the core as a function of time. This complex behavior shows the need for a robust sensor network capable of providing sufficient information to reconstruct the in-core flux distribution. The corresponding Fig. 3 shows the flux distributions in the reactor at several different times during operation.

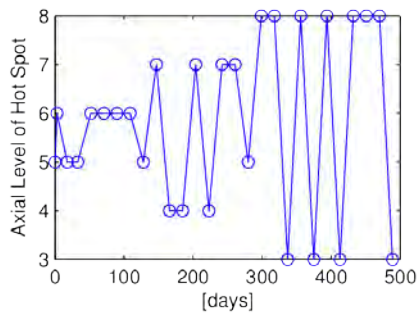

Fig. 2. Axial fluctuations of neutron flux hot spots as a function of time during reactor operation at full power.

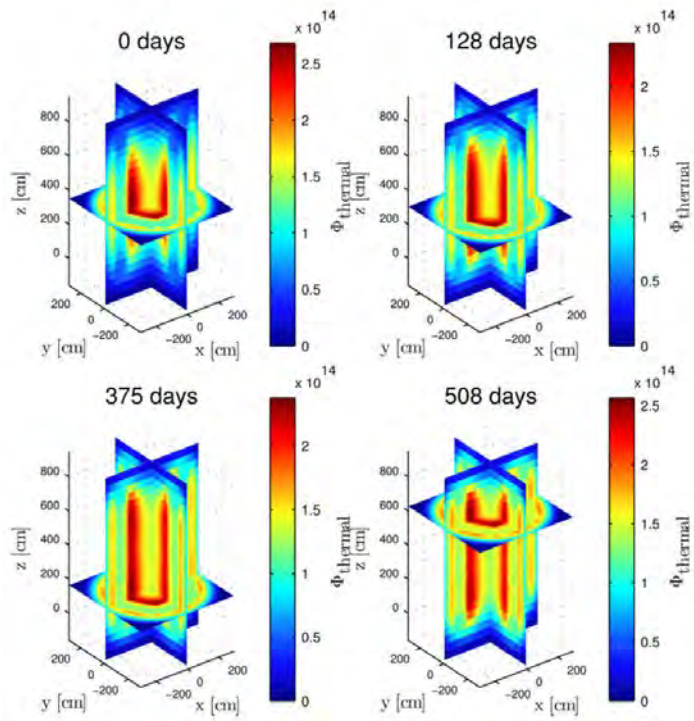

Fig. 3. Snapshots of the neutron flux distributions at several times during reactor operation at full power.

3.2.4. Reconstruction Approach

The conceptually simplest flux reconstruction methods are those based on pure interpolation. An algorithm that could linearly interpolate on an unstructured grid was used in order to accommodate any possible sensor configuration.

Using this method, a tetrahedral mesh is constructed whose vertices correspond to locations where the neutron flux is measured by a sensor. Mathematical techniques were then used to

linearly interpolate the neutron flux across the reactor core. The single-block sensor arrangement used to test the interpolation-based reconstruction algorithms is shown in Fig. 4.

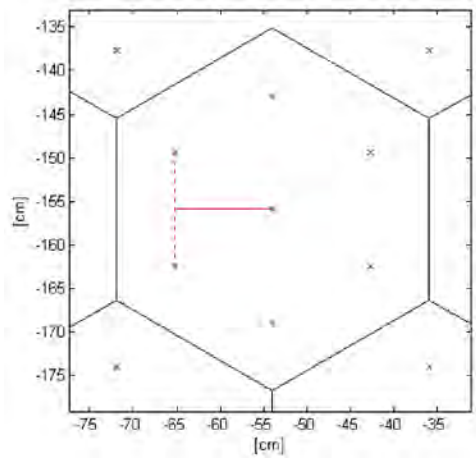

Fig. 4. Sensor layout used within a single block structure.

Figure 5 summarizes six considered potential sensor arrangements within the VHTR including active core and reflector regions.

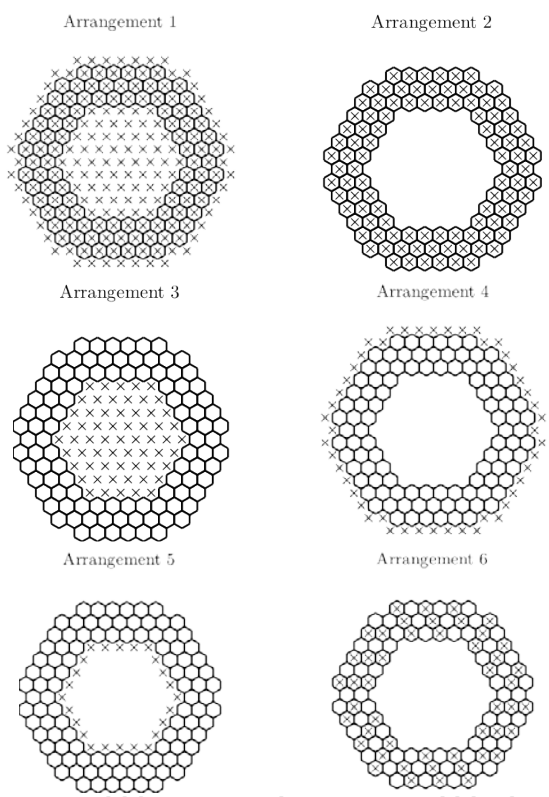

Fig. 5. Sensor arrangements within a VHTR, instrumented blocks are marked with "X".

The proper orthogonal decomposition (POD) is a data analysis tool that can be used to create low-dimensional representations of high-dimensional data. POD has been used in a variety of fields including image compression, signal processing, turbulence analysis, and design optimization. In this work we focused on its use with time-series data. Given an ensemble of time-series data, POD can be used to create spatial modes, sometimes called empirical eigenfunctions, that can be used to reconstruct the data.

The POD-based method performs well, and better than the interpolation-based method, in the reconstruction relative error and percent error in true hotspot magnitudes. Figure 6 shows a detailed view of the algorithm's performance in predicting the z coordinate of the hotspot. Except for a few spikes, the error is modest for lower levels of noise, but degrades to unacceptable levels as the noise amount increases.

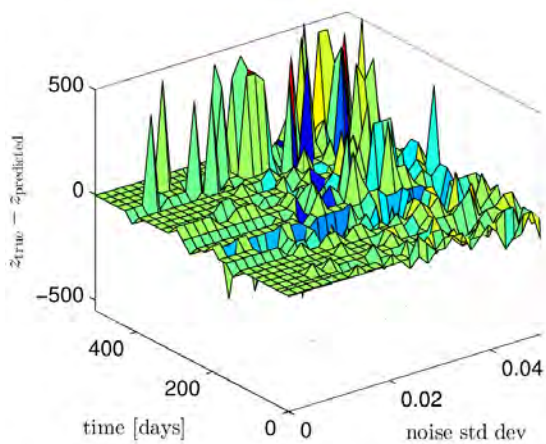

Fig. 6. Error in z coordinate of POD algorithm's predicted hotspot location when signal is noisy.

Sensor failure was modeled by deterministically failing the closest sensors to the core-wide hot spot. The reconstruction algorithm was run testing the effects of failing up 5 five sensors for each sensor arrangement. All cases used all modes from the POD basis generated from the odd-numbered snapshots. Sensor failure has the largest effect on arrangements 4 and 5; however, these two arrangements had the fewest sensors to begin with.

3.2.5. Conclusions

This paper presented the results and observations obtained in the course of the 3-year program. The computational evaluations of distributed sensing networks for reactor in-core applications indicate potential opportunities for future applications.

The project was focused on NGNP/VHTR environments but the analyzed sensing and 3D in-core monitoring via distributed sensing are of paramount value for LWRs, emerging SMRs and all advanced nuclear reactors.

The interpolation-based algorithm is conceptually straightforward and performs well provided enough sensors are placed in the core. It is doubtful that it would be economically feasible to remove fuel pins from the core just to insert more sensors.

The POD-based reconstruction method is recommended over the interpolation-based method because it yields more accurate reconstructions with fewer sensors. The POD-based method was able to reconstruct the in-core flux with 24 sensors more accurately than the interpolation-based algorithm could with 211 sensors. The POD method was also better at handling signal noise and sensor failure.

The chief disadvantage of the POD-based method is that its behavior is not as predictable as the interpolation-based method. The snapshots fed into the algorithm must span the operating conditions experienced by the reactor.

3.2.6. References

1. "Next Generation Nuclear Plant Pre-Conceptual Design Report," INL/EXT-07-12967, INL (2007).

2. "Design Features and Technology Uncertainties for the Next Generation Nuclear Plant," Independent Technology Review Group, INEEL/EXT-04-01816, Idaho National Engineering and Environmental Laboratory (2004).

3. S. J. Ball, S. E. Fisher, "Next Generation Nuclear Plant Phenomena Identification and Ranking Tables," NUREG/CR-6944, ORNL/TM-2007/147 (2008).

4. K. Saito, H. Sawahata, F. Homma, M. Kondo, T. Mizushima, "HTTR: Instrumentation and Control System Design," *Nucl. Eng. Design*, **233**, pp. 125-133 (2004).

5. D. E. Ames II, P. V. Tsvetkov, "Benchmark Efforts to Support Studies of Advanced VHTRs," *Proc. 4th Intern. Conf. HTRs*, HTR2008-58206, ASME (2008).

6. P. V. Tsvetkov, "Coupled Hybrid Monte Carlo - Deterministic Analysis of VHTR Configurations with Advanced Actinide Fuels," *Proc. ICAPP'06*, pp. 1984 - 1990 (2006).

4. Introduction

Generation IV very high temperature reactors (VHTR) constitute one of the near-term advanced reactor design groups that have a potential for early deployment. The VHTR designs stem from historical high temperature gas-cooled reactors which have been in operation since the 1950s.

Generation IV VHTRs offer a broad spectrum of potential applications ranging from electricity generation to industrial heat applications to nuclear waste management. The next generation nuclear plant (NGNP) will be a full-sized demonstration VHTR targeting industrial heat applications and electricity.[1]

However, the current near-term VHTRs have projected helium outlet temperatures ranging from 750°C to 950°C, with nominal fuel temperatures being as high as 1250°C.[1] These high temperatures expected in VHTRs, combined with the high radiation environment, create extremely harsh operating conditions for in-core monitoring systems, limiting accessibility of the core and longevity of the instruments. This challenge is currently mitigated by providing out-of-core monitoring capabilities together with reconstruction of in-core values.

Advanced instrumentation capable of operating in high temperature/radiation environments can be used to fully map the temperature and neutron fluence distributions in advanced reactor cores. Online, distributed measurements provide real-time assessment of reactor performance and can be used to benchmark simulation and analysis codes.

However, the harsh operational conditions pose tremendous challenges for in-core monitoring system design. A distributed fiber optic temperature and fluence sensor network operable under extreme conditions and which may be located throughout a reactor core (axial and transverse dimensions) is currently being developed.

Online direct 3D in-core temperature and fluence mapping via a distributed sensor network provides real-time assessments of reactor performance characteristics facilitating safe and reliable operation of VHTRs with optimized operational margins and potentially minimal needs for operator/maintenance interventions.

This report discusses the ongoing effort to develop an advanced 3D in-core mapping via a distributed sensor network that would be capable of reliable performance in high temperature/high radiation environments for prolonged periods comparable at least to the fuel loading lifecycles. The project is funded by the DOE Nuclear Energy University Program and is focused on testing of a distributed fiber optic sensor network for online 3D temperature and neutron fluence mapping in the VHTR in-core environment.[2]

Supported by a DOE Nuclear Energy University Programs award, the project scope encompasses fabrication of sensor hardware, test article design and fabrication to support in-core testing, sensor hardware demonstration at the Texas A&M University (TAMU) TRIGA research reactor, 3D modeling of the NGNP/VHTR configuration and scaling from the TRIGA test environment to the anticipated VHTR operating conditions. A test configuration that allows for simultaneous exposure of the fiber optic sensors to high temperature and high radiation fields has been designed, and fabrication is currently under way.

The high temperature test device is adapted from in-core furnace equipment licensed for use in TRIGA research reactor facilities in the early 1970s (Nuclear Regulatory Commission licenses

R-38 and R-67). Device irradiations and post-test analysis will be performed at the TRIGA facility. Although the TRIGA environment can vary significantly from that expected in the proposed VHTR and other advanced reactor designs, the flexibility of operation, ease of startup, and sample accessibility make it ideal for initial component testing.

4.1. Objective

The proposed work will enable development of a highly reliable, distributed fiber optic temperature and fluence sensor network operable under high temperature/neutron fluence conditions and located throughout the reactor core (axial and transverse dimensions).

The project scope encompasses fabrication of the sensor hardware, test article design and fabrication to support in-core testing, sensor hardware demonstration at a university TRIGA research reactor (URR) facility, 3D modeling of the NGNP/VHTR configuration and scaling from the TRIGA test environment to the anticipated VHTR operating conditions.

The corresponding temperature/neutron field map reconstruction techniques and optimization of in-core detector positioning to minimize uncertainties will also be performed. The advantages of real-time in-core monitoring will be illustrated.

4.2. Background

4.2.1. VHTR In-Core Environment

The very high temperature reactor (VHTR) is considered one of the possible designs for the next generation of nuclear reactors. The proposed Next Generation Nuclear Plant (NGNP) will be a full-sized demonstration VHTR. The development of instrumentation that can function in the unique environment inside the reactor was identified as a principal technical risk to the NGNP.[1]

Table 1. Normal operating conditions of a VHTR

Temperature	VHTR In-Core Environment
Coolant Inlet temperature	490° to 600°C for prismatic cores, 350°C for pebble bed cores
Coolant Outlet temperature	900° to 950°C
Max fuel temperature	1250°C to 1400°C
Coolant pressure	7 MPa for prismatic cores, 9 MPa for pebble bed cores
Peak neutron fluence*	1.7E20 – 1.67E21 [n/cm^2] over 1 year

*The peak neutron fluence is the expected fast fluence (E>0.1 MeV) for reactor internals which receive the most dose, namely the fuel and the inner reflector.

Instrumentation is needed to measure temperatures, neutron fluence, and the coolant flow rate. The high temperatures present in a VHTR during normal operation make it a challenging environment for sensors. Developing sensors that can that can withstand the temperatures present at the core outlet for an acceptable period of time will be a challenge.[2]

Sensors that are capable of measuring the high-temperature coolant flow will also need to be developed. Being able to accurately measure coolant flow is especially important a graphite block prismatic gas-cooled reactor where radiation-induced graphite deformations would block coolant channels.

Finally, sensors are needed that can measure the neutron flux in the reactor. The in-core flux is not significantly harsher than what is found in conventional reactors, but could pose a challenge as the radiation measuring instrumentation must be able to withstand the harsh temperature environment as well. Table 1 summarizes the normal operating conditions of a VHTR.[3,4,5]

In the proposed designs for the NGNP, the core is cooled by high-pressure helium. Reactor instrumentation must be able to withstand these high pressures (shown in Table 1).

Additionally, any impurities in the coolant, as those summarized in Table 2, could raise material compatibility issues with instrumentation.[6,7,8]

Table 2. Impurities in historical gas-cooled reactors*

Reactor	H_2	H_2O	CO_2	CO	CH_4	N_2	O_2
Dragon	2	0.1	<0.04	1.2	0.3	0.3	N/A
Peach Bottom	*10*	*~0.5*	*<0.5*	*0.5*	*1.0*	*0.5*	*N/A*
AVR	30	3	10	10	-	-	N/A
Ft. St. Vrain	2-7	<1	0.5-3	1-10	0.1-0.8	N/A	N/A
HTTR	*<3.0*	*<0.2*	*<0.6*	*<3.0*	*<0.5*	*0.2*	*<0.04*

*Italicized values are in ppmv, while the rest of values are in pressure units (Pa).

The sensors could also be affected by the graphite dust that is expected to be present. Graphite dust is primarily an issue in pebble bed type reactors. A test size pebble bed reactor core is projected to contain about 10-50 kg of dust. Dust in prismatic core would be at least an order of magnitude less and would be deposited unevenly around the core.[6,9]

Of final concern are anticipated transients and accident conditions. In-core instrumentation would not be expected to survive accident conditions, but they are nonetheless presented for completion. Temperature is the primary attribute of concern during accident conditions.

In most accident conditions, fuel temperatures are not expected to exceed 1600°C.[4,10,11] Of additional concern would be the depressurization and air-ingress accident. This would result in a drop to atmospheric pressure and complications as a result of air entering the core.

4.2.2. Candidate Sensors for VHTR In-Core Flux and Temperature

There are several sensor types which can be used in the VHTR core. The high-temperature and high-radiation environment present significant challenges to sensor design and operational reliability characteristics.

The desire to use the sensors inside the VHTR core also places restrictions on their size. The primary candidates for in-core neutron detection are fission chambers, self-powered neutron detectors (SPNDs), and fiber optic sensors.

In-core fission chambers have been developed for use in French fast breeder reactors. In core fission chambers have primarily been used during startup and shutdown, when counting rates

are too low to use detectors under the vessel. They have also been used during core loading to closely monitor reactivity.

Fitting the necessary electronics into a package small enough to be used inside the core can be difficult; however, all engineering challenges for the use of in-core fission chambers in sodium fast reactors have effectively been solved, but such reactors only operate at about 600° C. In-core fission chambers are also used in the HTTR, but, once again, the temperatures do not exceed about 600° C.[12,13]

Self-powered neutron detectors are advantageous because of their simpler electronics. Generally speaking, fission chambers are more accurate and sensitive than SPNDs. The advantages of SPNDs are their reliability, robustness, small mass, small size, and small power requirements.

Work has been done regarding the feasibility of using SiC SPNDs gas turbine-modular helium reactors. Research found that such detectors could not survive the 850°C coolant temperatures or the fast fluence present in the core.

To mitigate these problems, the sensors must be placed in the central reflector, where the temperature is lower and the neutron spectrum is softer.[14,15]

The final candidate for potential use in in-core neutron measurements is a fiber optic based sensor. The use of fiber optic sensors for neutron flux measurements has not been proven to the extent of other the other detectors, namely SPNDs and fission chambers.

Initial research has shown that such fiber optic sensors could measure gamma flux as well as thermal, epithermal, and fast neutron fluence, and operate at temperatures up to 720° C. These sensors are currently capable of providing neutron and gamma measurements once every 18 seconds.[16,17]

The primary candidates for temperature detection are specialty thermocouples and fiber optic sensors. Thermocouples exist that are capable of operating at temperatures above 1000° C. The HTTR uses N-type thermocouples (NIcrosil-Nisil) to measure coolant temperatures of 1100° C.

Fiber optic sensors also exist which can be used as distributed temperature sensors. Initial research has proven the use of such sensors to measure temperatures up to 850° C with a spatial resolution of 1 cm.

The distributed nature of the sensor provides a significant advantage over the point reading that is generated by a thermocouple; however more research is needed to develop fiber optic sensors that could operate at the temperatures found inside a VHTR core.[18,19,20] The expected neutron/gamma fluences between operating cycles and the neutron energy spectrum are of prime interest.

The fiber optics, within a reactor system, will nominally be held at constant temperature, reducing the likelihood that thermal cycling will be a failure mode of the fiber optic. It is expected, then, that the total fluence will be the limiting condition of fiber lifetime in the reactor.

4.2.3. Fiber Optic Temperature/Neutron/Gamma Mapping for VHTRs

Luna Innovations has previously demonstrated the key technical elements required to develop a highly distributed fiber optic temperature, neutron fluence, and gamma flux mapping system for the VHTR environment.

Key elements shown in previous tests include:

- Fiber survivability in very high temperatures (>1000°C),
- Fiber survivability in high-radiation environments ($2x10^{19}$ n/cm^2 and 87 GRad),
- Distributed temperature measurement using the Rayleigh backscatter technique,
- Measurement of neutron fluence using single point optical sensors.

While previous tests successfully demonstrated fiber performance under each condition independently, limited combined environment testing has been conducted.

Sensors require longer duration testing at combined high temperature, high radiation conditions with real-time distributed measurement of neutron fluence to be qualified for VHTR service.

Standard optical fiber degrades rapidly at temperatures above 800°C. Specialty fibers and coatings that exhibit orders of magnitude improvement in useful fiber life relative to standard fiber at temperatures exceeding 1000°C have been developed and demonstrated for distributed temperature measurements with operational temperatures up to 1100°C.

Standard optical fiber has also been shown to darken, or brown, in the presence of relatively low gamma fields. Survivability of specialty fibers and low reflectivity fiber Bragg gratings (FBG) in very high neutron and gamma fields has been demonstrated using the novel Luna Innovations fiber optic sensor system. Low reflectivity (5%) gratings were exposed to $2x10^{19}$ n/cm^2 (>1 MeV) and $8.7x10^{10}$ Rad over a 60-day test. The FBGs were still functional at this dose level and showed excellent signal to noise ratios.

Typical FBG sensors are difficult to fabricate in fibers that have robust coatings necessary for high-temperature environments. Luna Innovations has developed capability that enables highly distributed temperature measurement using the intrinsic Rayleigh backscatter (RBS) signature that is present in all optical fiber. This approach has been demonstrated using metal-coated fiber (i.e. gold, nickel, or other coatings currently being investigated) to obtain temperature measurements at 1 mm intervals along the fiber at temperatures up to 850°C, and in high-radiation environments; long-duration testing of the fibers under combined high temperature/high radiation environments has not been completed to date. The result of continued development of FBG sensors that take advantage of RBS will be robust, environmentally tailored sensors available at greatly reduced cost.

Experimental observations of FBG sensor performance indicate a predictable sensitivity to neutron and gamma radiation. Using passive, non-scintillating, optical transducers previously developed, point sensors have been used to measure both neutron fluence and gamma flux in real-time.

This work indicates that contributions from neutron energies in the thermal, epi-thermal, and fast bands can be discerned. Initial neutron fluence monitors have shown an error of only 5% at a total fluence of $4.5x10^{17}$ n/cm^2.

Accuracy can be further improved by correcting for gamma cross-sensitivity. The current work will demonstrate distributed neutron and gamma sensing capability.

4.2.4. References

1. "Next Generation Nuclear Plant Pre-Conceptual Design Report." INL/EXT-07-12967, Idaho National Laboratory, Next Generation Nuclear Plant Project. November 2007 (2007).

2. "Design Features and Technology Uncertainties for the Next Generation Nuclear Plant." Independent Technology Review Group. INEEL/EXT-04-01816. Idaho National Engineering and Environmental Laboratory. June 2004 (2004).

3. MacDonald, Philip. "Next Generation Nuclear Plant A Very High Temperature Gas-cooled Reactor", Idaho National Engineering and Environmental Laboratory. Advanced Reactor, Fuel Cycle, and Energy Products Workshop for Universities, March 4-5 2004 (2004).

4. Baccaglini, Guido, et al. " Very High Temperature Reactor Survey of Materials Research and Development Needs to Support Early Deployment." INEEL/EXT-03-00141. Idaho National Engineering and Environmental Laboratory, January 2006 (2006).

5. Windes, W., Burchell, T., Bratton, R. "Graphite Technology Development Plan". INL/EXT-07-13165, Idaho National Laboratory, September 2007 (2007).

6. Kissane, M.P., "A review of radionuclide behavior in the primary system of a very-high-temperature reactor." *Nuclear Engineering and Design*, **239**, 12, Flexible Conversion Fast Reactors Special Section with Regular Papers, December 2009, pp. 3076-3091 (2009).

7. C. Cabet, F. Rouillard. "Corrosion of high temperature metallic materials in VHTR." *Journal of Nuclear Materials*, **392**, 2, July 2009, pp. 235-242 (2009).

8. C. Cabet, et al. "High temperature reactivity of two chromium-containing alloys in impure helium." *Journal of Nuclear Materials*, **375**, 2, April 2008, pp. 173-184 (2008).

9. Ball, S.J., Fisher, S.E,. "Next Generation Nuclear Plant Phenomena Identification and Ranking Tables." NUREG/CR-6944, ORNL/TM-2007/147, Office of Nuclear Regulatory Research. March 2008 (2008).

10. Vilim, R.B., Feldman, E.E, Pointer, W.D., Wei, T.Y.C. "Generation IV Nuclear Energy System Initiative, Initial VHTR Accident Scenario Classification: Models and Data." ANL-GenIV-057. Argonne National Laboratory, Nuclear Engineering Division. September 2005 (2005).

11. Ball, S, "Sensitivity studies of modular high-temperature gas-cooled reactor postulated accidents." Nuclear Engineering and Design, **236**, 5-6, March 2006, pp. 454-462 (2006).

12. G. Bignan, J.C Guyard, C. Blandin, H. Petitcolas, "Direct experimental tests and comparisons between sub-miniature fission chambers and SPND for fixed in-core instrumentation of LWR," in: *OECD Proceedings of a Specialist Meeting Mito-shi*, Japan, NEA, October 1996 (1996).

13. J-P. Trapp, S. Haan, L. Martin, J-L. Perrin, M. Tixier. "High Temperature Fission Chambers: State-of-the-Art," in: *OECD Proceedings of a Specialist Meeting Mito-shi*, Japan, NEA, October 1996 (1996).

14. B. Khorsandi, et al. “Monte Carlo Modeling of Count Rates and Defects in a Silicon Carbide Detector Neutron Monitor System.” Nuclear Technology, **159**, August 2007, pp. 208-220 (2007).

15. M. Reisi Fard. “The Development of a High Count Rate Neutron Flux Monitoring Channel Using Silicon Carbide Semiconductor Radiation Detectors.” Diss. Ohio State University, 2006 (2006).

16. B. Dickerson, et al. “Fiber Optic Sensors for Neutron Fluence Measurement in Thermal, Epi-Thermal, and Fast Energy Bands.” Transactions of the American Nuclear Society, **99**, 2008, pp. 79-80 (2008).

17. B. Dickerson, J. Farmer, J. French, M. Palmer, R. Fielder. “Fiber optic sensors measuring gamma flux and neutron fluence.” Transactions of the American Nuclear Society, **99**, 2008, pp. 289-290 (2008).

18. K. Saito, H. Sawahata, F. Homma, M. Kondo, T. Mizushima. “Instrumentation and control system design.” *Nuclear Engineering and Design*, **233**, 2004, pp. 125-133 (2004).

19. F. Jensen, E. Takada, M. Nakazawa, H. Takahashi, T. Iguchi. “Development of a Distributed Monitoring System For Temperature and Coolant Leakage.” in: *OECD Proceedings of a Specialist Meeting Mito-shi*, Japan, NEA, October 1996 (1996).

20. A. Sang, D. Gifford, B. Dickerson, B. Fielder, M. Froggatt. “One Centimeter Spatial Resolution Temperature Measurements in a Nuclear Reactor using Rayleigh Scatter in Optical Fiber.” *IEEE Sensors Journal*, **8**, 7, July 2008, pp. 1375-1380 (2008).

5. High Fidelity Modeling Approach

5.1. 3D VHTR/NGNP Configuration Model

To create advanced nuclear energy systems it is desirable to have a high fidelity modeling-based design development that relies on simulating features of the entire life cycle of the system before actual physical prototyping - from concept development to detailed design, prototyping, and safety analysis. A 3D whole-core exact-geometry model of a VHTR hexagonal-block configuration with a detailed component representation has been developed and implemented for calculations with MCNP/MCNPX and Serpent.[1] Earlier benchmark studies validated applicability of the modeling approach to correctly represent design features and performance characteristics of HTRs.[2,3]

The model is based on the NGNP pre-conceptual design features. Figure 1 illustrates details of this model. The model color scheme demonstrates the ability to quantify physics characteristics while varying properties per block. The model allows tracking environments in fuel and coolant channels. The sequence is being implemented as MatLab shell that will later be transformed into a stand-alone auxiliary module.[2] The applied modeling approach and tools have been validated in previous efforts.

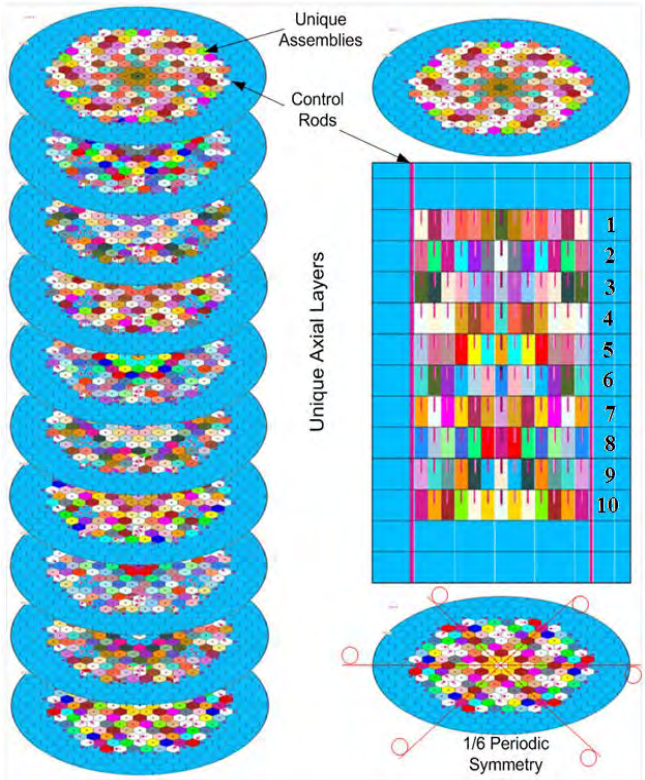

Fig. 1. Reference VHTR model with fuel and coolant channel neutron field tracking.

High Fidelity Modeling Approach

To capture and visualize performance characteristics, the detailed 3D maps are being produced at each block location as shown in Fig. 1 for a sample configuration. These maps allow for tracking of the HTR core loading patterns, in-core sensor responses, control schemes, fluence distributions, power peaking, and etc.

A sample fluence map is shown in Fig. 2. Color and size of each dot correspond to variations in values of performance characteristics.

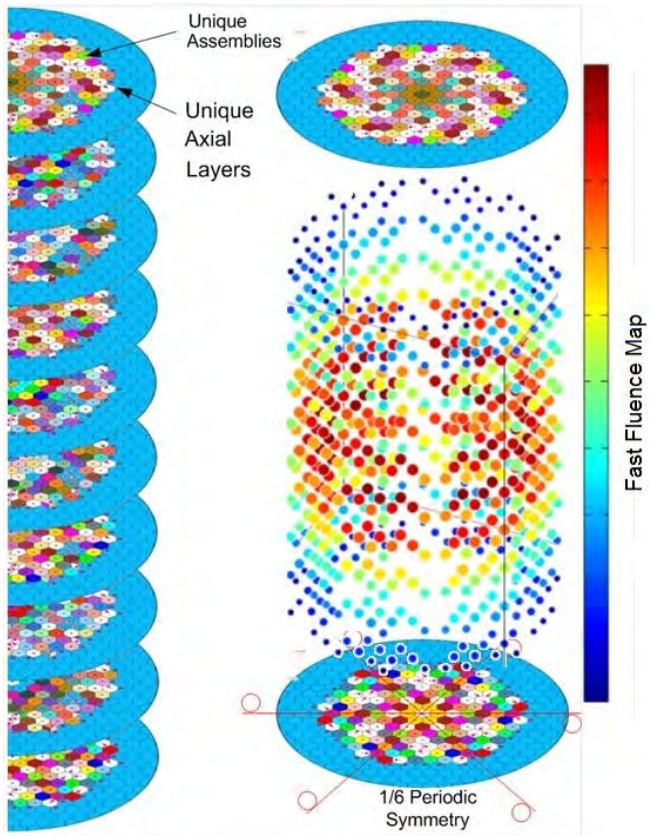

Fig. 2. High fidelity VHTR modeling for 3D mapping – sample VHTR fast fluence map.

Figure 3 provides an example of the developed 3D high fidelity approach to identify, track and visualize power hot spots in a HTR core during its lifetime. In this case, a hot spot range has been selected so that not only the true max power peaking location can be identified and visualized but also values in some proximity to the maximum.

Simulations of the reactor operation over 12 years reveal 3D migration of the hot spot locations within the HTR core (per block). From the perspective of tracking irradiation histories per block, these migration effects are important to identify blocks approaching their lifecycle limits due to radiation damage effects.

Based on the 3D performance maps for HTRs it is possible to determine safety characteristics, sensor locations, as well as optimize control and monitoring strategies. The optimization

objectives could include requirements to minimize numbers of needed in-core sensors, sensor locations, identify optimum control scenarios to maximize operational time and fuel utilization efficiency and others. These 3D maps also vary as a function of fuel type. The HTR cores fueled with LEU-, Th- and TRU-compositions exhibit different power production distributions within their respective core configurations.

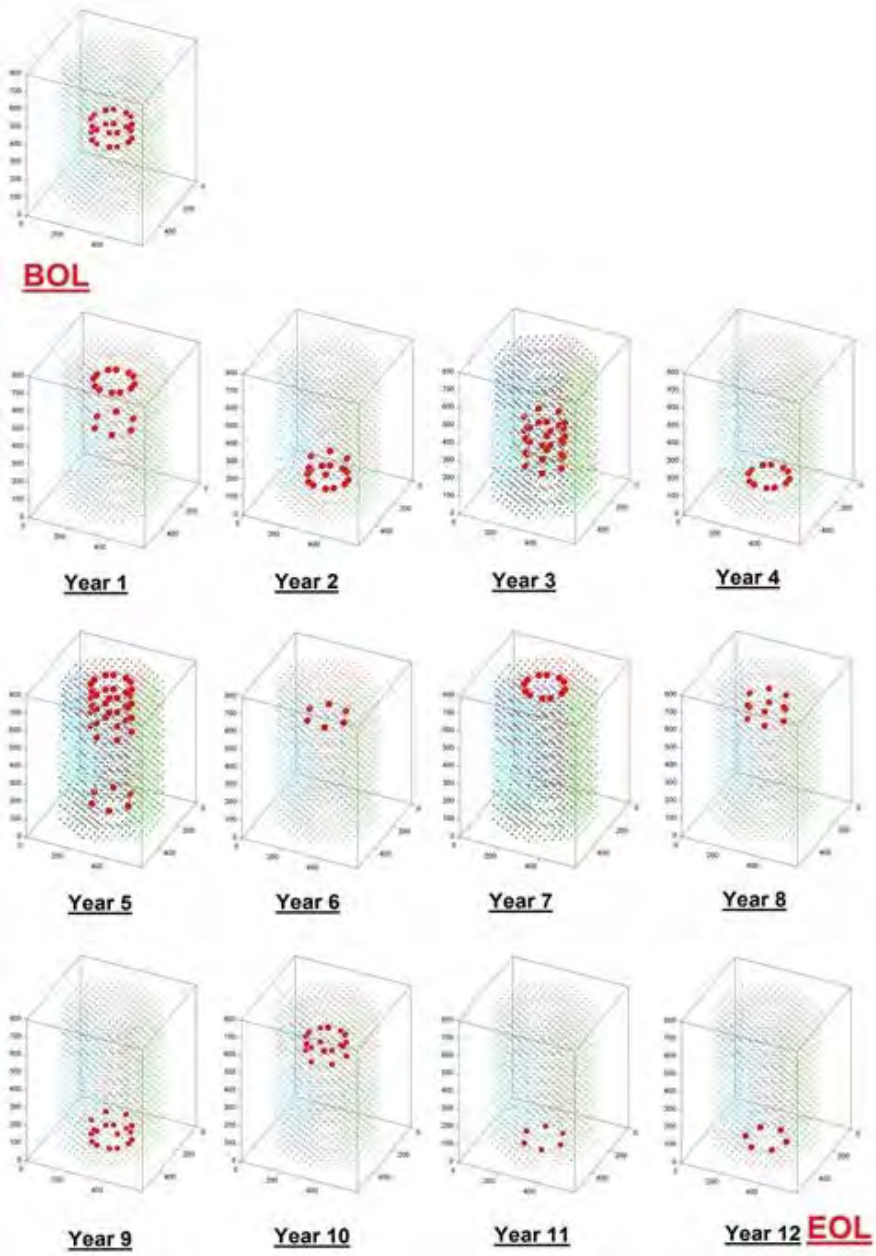

Fig. 3. In-core hot spot identification and evolution during the VHTR operation lifetime.

5.2. Image Reconstruction Applied to 3D Flux Data

5.2.1. Test Problems

A reference flux distribution was generated with a 3D mesh tally. The dimensions of the mesh tally are given in Table 1. A finer mesh tally was also generated with MCNP and applied within the project.

Table 1. Mesh Tally Data for a Reference Flux Distribution

Mesh Tally Parameter	x	y	z
Total number of bins	200	200	24
Mesh cell dimensions [cm]	3	3	46.25

In both 2D and 3D test problems, random and grid placed sensors were considered. Since it is assumed that the fiber optic sensors will span the full length of the core, a grid or random sensor arrangement was generated for a single xy slice, then this arrangement was used for all axial levels of the core.

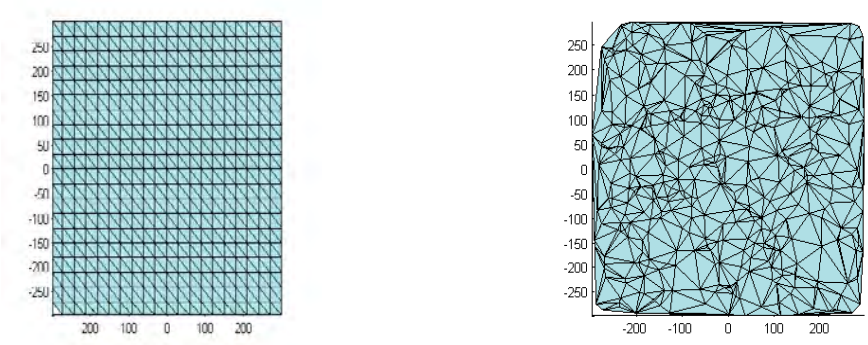

(a) Sample 2D (xy)-slices of the interpolation mesh for the grid and random cases.

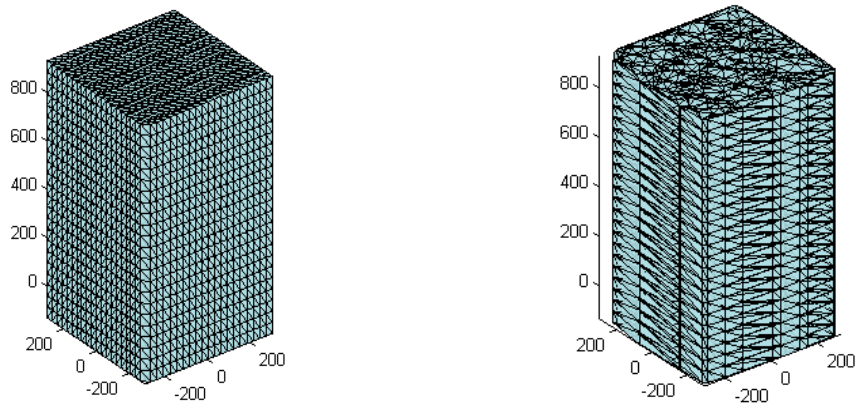

(b) Sample 3D meshes for the grid (left) and random (right) cases.

Fig. 1. 2D meshes and their extrusions into 3D meshes representing the whole core

Since the interpolation scheme used was mesh based, the placement process was analogous to generating a 2D mesh for a single xy slice and extruding it into a 3D mesh over the whole core. Figure 1 illustrates this point. Sensors are located on the vertices of the mesh. The meshes were generated in Matlab by Delaunay triangulation.

5.2.2. Performance of the Applied Reconstruction Methods in the Test Problems

Many of the figures of merit used to assess the accuracy of the reconstruction methods are the same for 2D and 3D cases. Since the overall goal of the flux reconstruction is to pinpoint hot spot location, the primary figure of merit considered was the error in the predicted hotspot location.

This was quantified using an L-2 norm:

$$norm\ of\ \ error\ in\ hot\ spot\ location = \left\| \vec{h}_{reconstructed} - \vec{h}_{actual} \right\|_2 ,$$

where $\vec{h}$ is a vector that contains the (x, y, z) coordinates of the hot spot from either the reconstructed data or the reference data. The norm of the error in the hotspot location is equivalent to the geometric distance between the true hotspot and the predicted hotspot.

This error measure is plotted in Fig. 2 for grid and random sensor configurations.

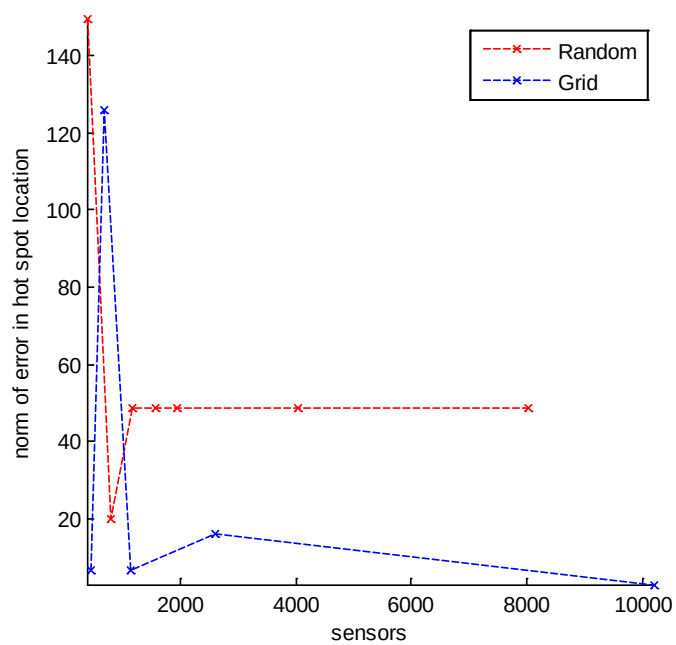

Fig. 2. Norms of the error in the hotspot location as a function of number of sensors positioned in the grid and random configurations.

The results indicate that randomly positioning the sensors does not work in 3D, at least with this reconstruction algorithm. The issue with random sensor positioning is that the random sensor placement results in a deformed interpolation mesh.

Notably, the grid reconstruction algorithm performs very similar to its 2D counterpart.

The error in the reconstructed flux magnitude at the hotspot location from the reference data set is shown in Fig. 3.

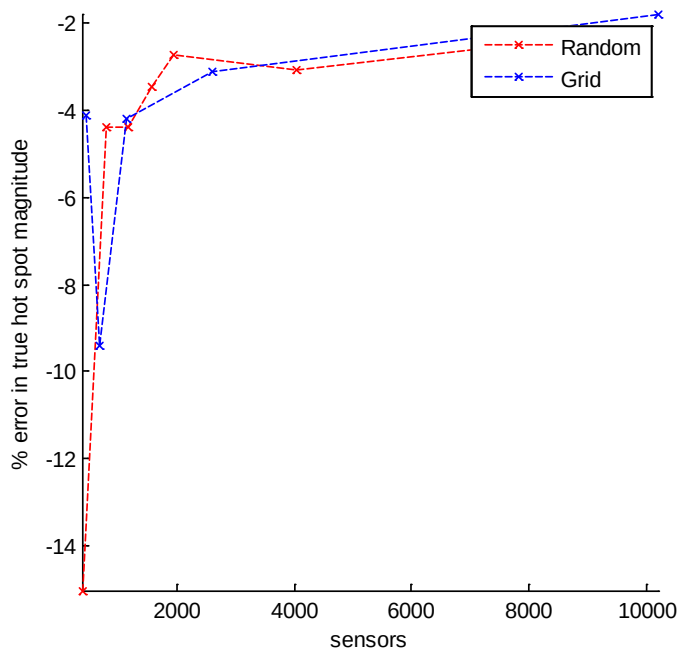

Fig. 3. Error in the reconstructed flux magnitude at the hotspot location from the reference data set as a function of number of sensors positioned in the grid and random configurations.

In general the reconstruction algorithms underestimated the flux at the true hotspot location.

However, the results show that regardless of where they predict the hotpot location, the flux magnitude at the true hotspot location is only off by a few percent.

The norm of the reconstruction residual is shown in Fig. 4. The reconstruction residual is defined as:

$$reconstruction\ residual = \left| \hat{A}_{reconstructed} - \hat{A}_{reference} \right|,$$

where $\hat{A}$ is a 3D array containing the flux at each (x,y,z) point of the mesh. Figure 4 shows the norm of this residual as a function of sensor count for several different sensor configurations.

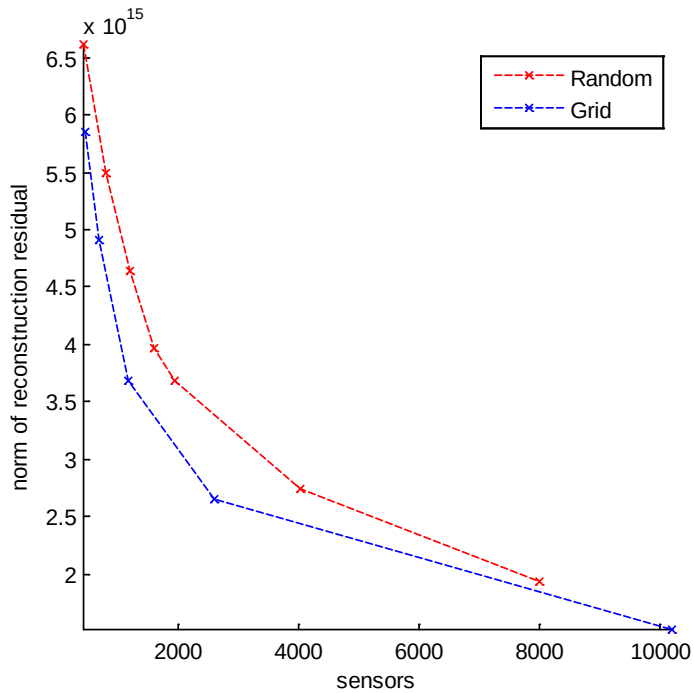

Fig. 4. The norm of the reconstruction residual as a function of sensor count for different sensor configurations.

The relative error in the reconstruction flux is also used as a figure of merit. This error is defined as:

$$relative\ error = \left| \frac{\hat{A}_{reconstructed} - \hat{A}_{reference}}{\hat{A}_{reconstructed}} \right|,$$

where $\hat{A}$ is a 3D array containing the flux at each (x,y,z) point. The relative error is converted into percent error by multiplying by 100%. Figure 5 shows the average of the percent error array as a function of sensor count. The corresponding median percent error is shown in Fig. 6.

The grid sampling using 1155 sensors performs sufficiently well to predict the steady state hotspots in the core; however, there is a room for improvement and development and application of more advanced interpolation methods.

For example, the standard Matlab's 3D data interpolation function, *TriScatteredInterp*, only supports linear interpolation. The 2D test case analyzed previously employed cubic interpolation, but the Matlab function used to do this does not work on 3D arrays. Further investigation into the accuracy lost by doing linear interpolation is warranted. Development of more advanced interpolation methods for predictive signal data analysis and reconstruction towards early detection, management, and mitigation of hot spots is needed.

High Fidelity Modeling Approach

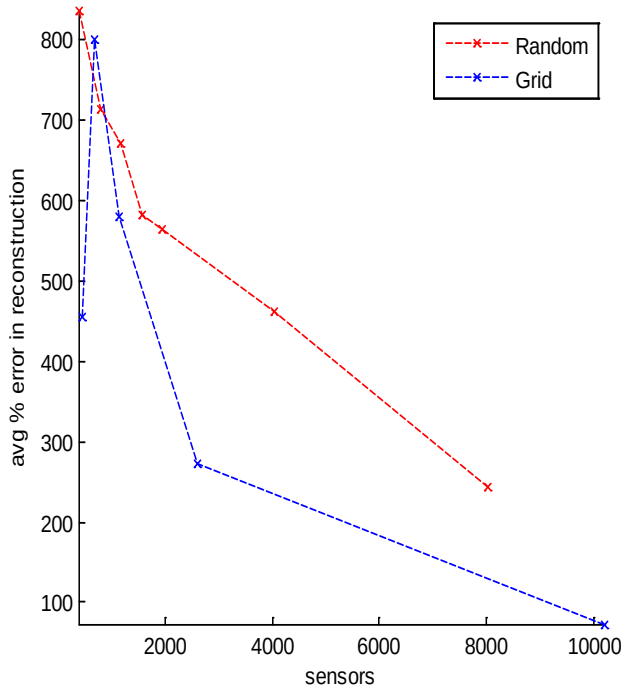

Fig. 5. Average % error in reconstruction as a function of sensor count.

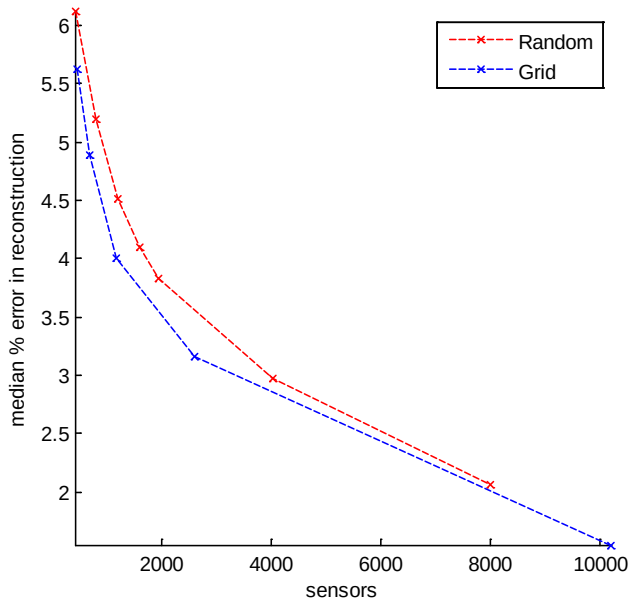

Fig. 6. Median % error in reconstruction as a function of sensor count.

Reconstruction methods for data reconstruction in real time are of paramount importance during reactor transients.

Figure 7 compares an xy slice of the reconstruction domain to the same slice of the original data set. While the hotspot is predicted accurately, the reader may notice some reconstruction artifacts present in the image.

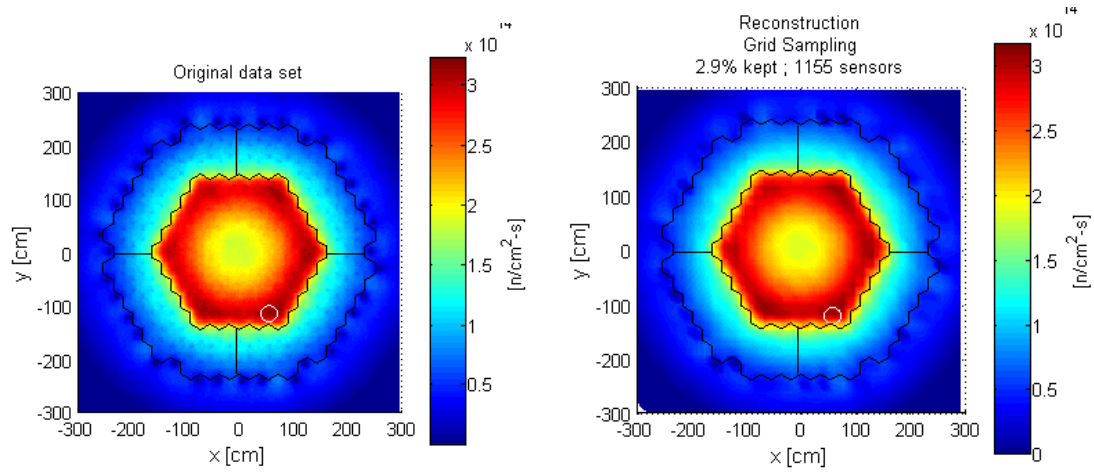

Fig. 7. Comparison of the reconstructed flux (right) and the reference set (left).

Figure 8 shows the relative error in the same xy slice as in Figure 7. The reader should recognize that the color scale axis is truncated at 1 for visualization clarity purposes. The maximum relative error present in the reconstruction is significantly larger than 1.

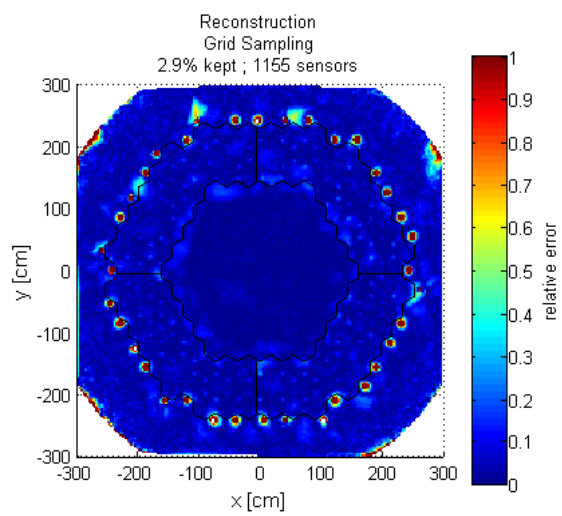

Fig. 8. The relative error present in the reconstruction in the same xy slice as in Figure 7.

5.3. Application of 3D Flux Reconstruction by Interpolation to Fine-Mesh Flux Data

5.3.1. Test Problems

MCNP was used to generate a reference beginning-of-life (BOL) flux distribution in the 650 MWth VHTR. 500 million particles were run during the active cycles to ensure that the mesh tally was resolved properly.

The dimensions of the mesh tally are given in Table 1.

Table 1. Mesh Tally Data for a Reference Flux Distribution

Mesh Tally Parameter	x	y	z
Total number of bins	256	256	128
Mesh cell dimensions [cm]	2.34	2.34	8.67

It was assumed the sensors are sensitive to thermal flux (E < 1E-6 MeV). Therefore, all flux reconstruction efforts presented in this section concern the reconstruction of thermal flux.

The thermal flux distributions generated by MCNP are shown below in Fig. 1.

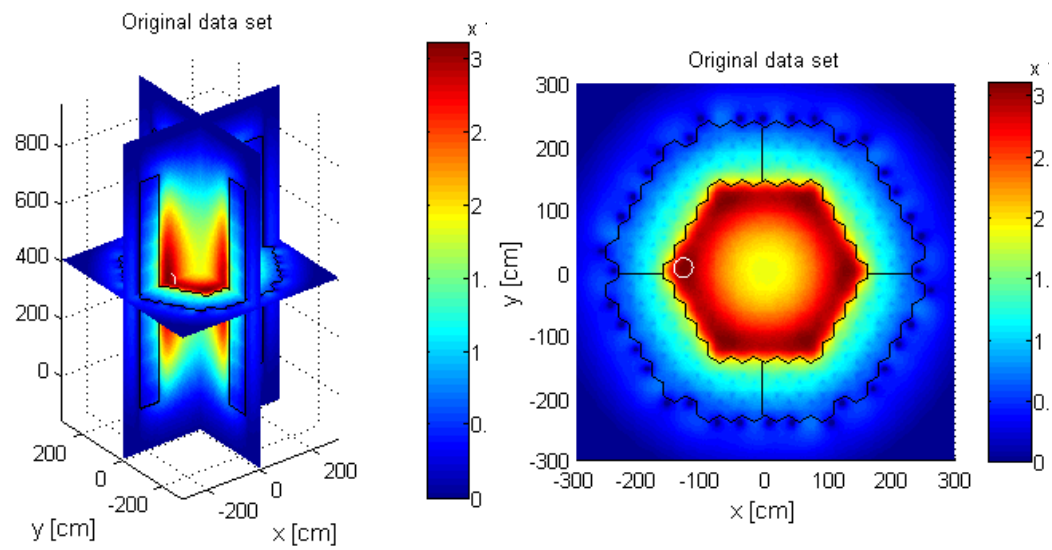

Fig. 1. Reference flux distributions generated with MCNP. The hot spot is identified with a circled area.

5.3.2. Sensor Arrangement

The sensor arrangement in each block is illustrated in Fig. 2.

The pitch was adjusted in such a way that that sensors were placed in the fuel rods lying on the red lines shown in Fig. 3.

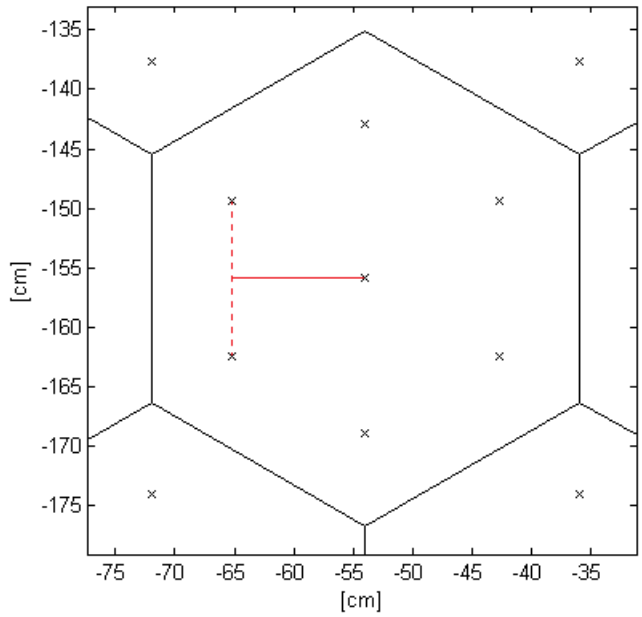

Fig. 2. General sensor layout used in each fuel block. The pitch of the sensor array, which is shown with a solid red line, is a variable.

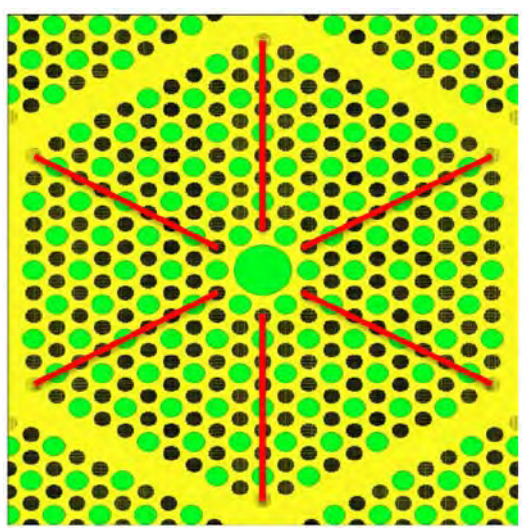

Fig. 3. Sensor array locations within each fuel block.

The pitches considered are given in Table 2. The pitch of 0 means that the block contains a single sensor located at the center. To be clear, the 0 pitch case consisted of 211 sensors, while all other cases used 1477 sensors. The significant difference between the sensor counts may make the 0 pitch case more favorable than the others even though it does not perform as well.

Table 2. Pitch Values in the Block Sensor Lattice

Pitch [cm]
0.000000
3.255563
6.511125
8.138907
11.39447
13.02225

Sensors were placed in all blocks of the inner reflector, all blocks of the active core, and the first ring of the outer reflector.

5.3.3. Reconstruction Results

The results of the reconstruction are shown in Fig. 4 through 6. The error metrics used to gauge the performance of the reconstruction algorithm will be briefly outlined first. The first error metric considered is the norm of the error in hot spot location:

$$norm\ of\ \ error\ in\ hot\ spot\ location = \left\| \vec{h}_{reconstructed} - \vec{h}_{actual} \right\|_2 ,$$

where $\vec{h}$ is a vector that contains the (x, y, z) coordinates of the hot spot from either the reconstructed data or the reference data.

This is equivalent to the distance, in [cm], between the true hot spot and the predicted hot spot. The hot spot is defined as the point in the reactor with the largest value of thermal flux.

The second error metric considered was the norm of the reconstruction residual. The reconstruction residual is defined as:

$$reconstruction\ residual = \left| \hat{\mathrm{A}}_{reconstructed} - \hat{\mathrm{A}}_{reference} \right| ,$$

where $\hat{\mathrm{A}}$ is a 3D array containing the flux at each (x,y,z) point of the mesh.

The final two error metrics are the average and median of the relative error between the reconstruction and the reference result:

$$relative\ error = \left| \frac{\hat{\mathrm{A}}_{reconstructed} - \hat{\mathrm{A}}_{reference}}{\hat{\mathrm{A}}_{reconstructed}} \right| ,$$

where $\hat{\mathrm{A}}$ is a 3D array containing the flux at each (x,y,z) point.

The final error metric considered is the percent error in true hot spot magnitude, defined in terms of flux values:

$$percent\ error\ in\ true\ hot\ spot\ magnitude = \frac{\phi_{reconstructed}(\vec{r}) - \phi_{reference}(\vec{r})}{\phi_{reconstructed}(\vec{r})},$$

where $\vec{r}$ is the location of the hot spot in the reference calculation.

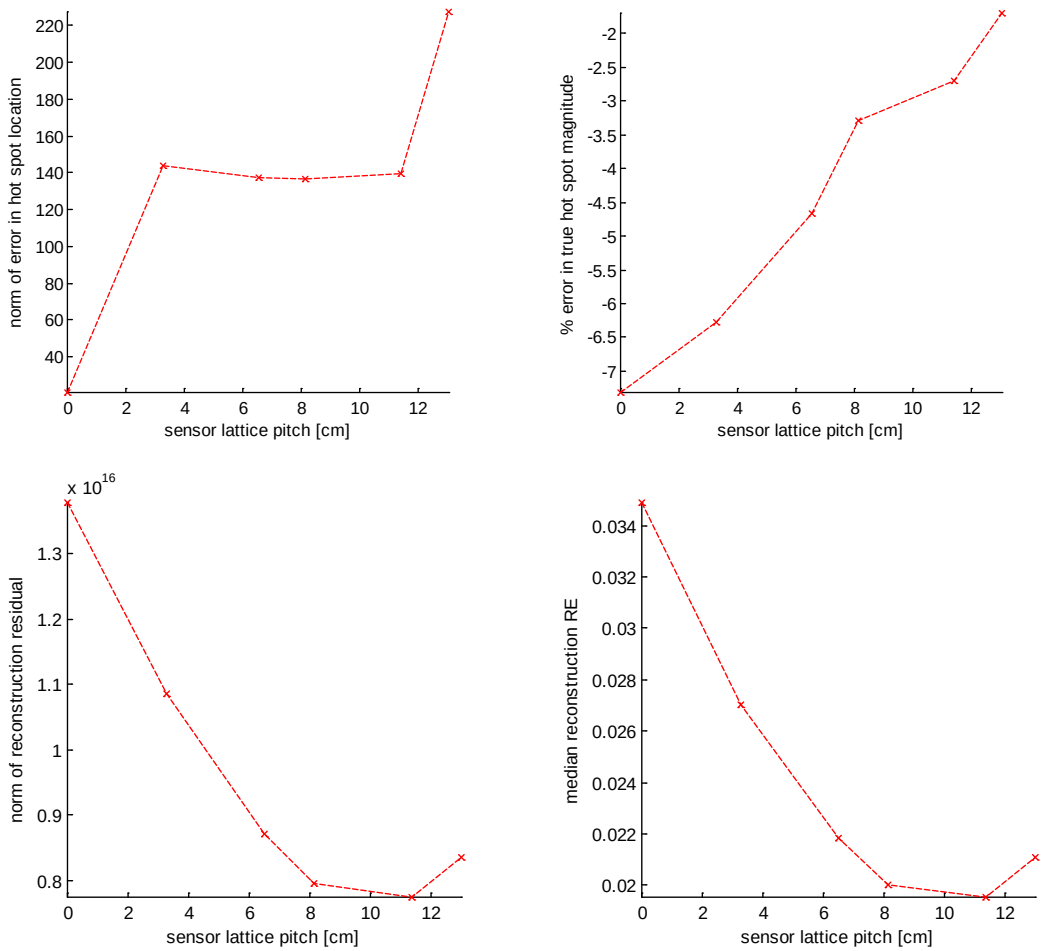

Fig. 4. Results of the reconstruction as a function of sensor lattice pitch.

Only the zero pitch sensor arrangement accurately predicts the location of the hotspot. On the other hand, the zero pitch sensor arrangement performs the worst in all other error metrics, including percent error in hotspot magnitude.

Figure 5 compares the zero pitch reconstruction to the the 11.34 cm pitch reconstruction.

The 11.34 cm pitch was chosen because it performed well in the reconstruction residual and reconstruction relative error metrics.

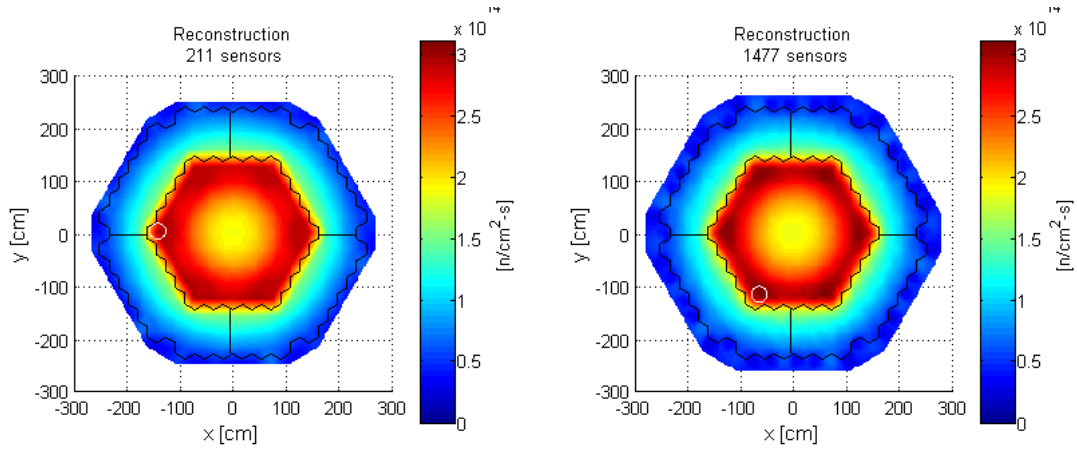

Fig. 5. Side-by-side comparison of the reconstructions generated by the zero pitch (left) and 11.34 cm pitch (right) sensor arrangements. The plots show the xy plane of each algorithms' predicted hot spot.

5.3.4. Sensor failures

Interpolatory reconstruction methods do not work well when sensors fail as illustrated in Fig. 6. To handle sensor failures, it is proposed to solve a neutron transport problem but only in the regions where sensors have failed.

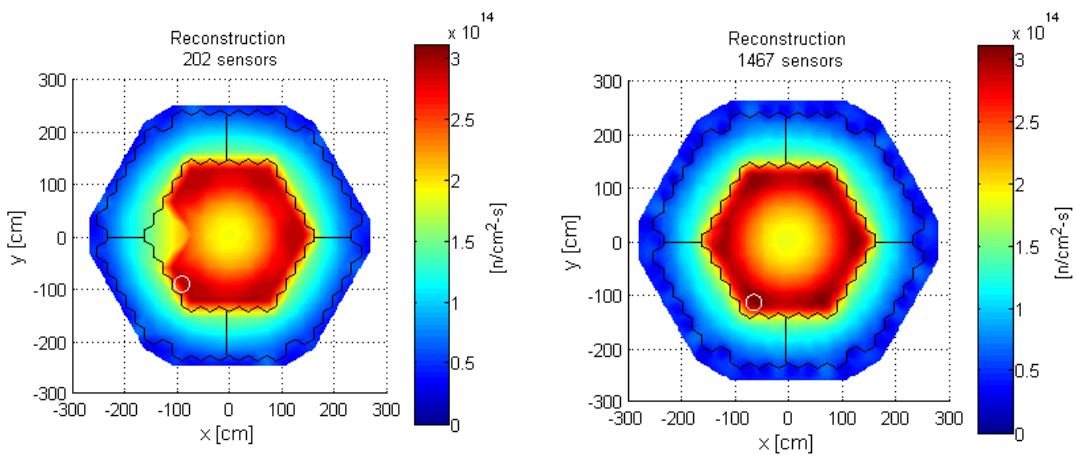

Fig. 6. The effect of sensor failure on flux reconstruction, 10 sensors closest to the true hot spot assumed to have failed. The zero pitch sensor arrangement is shown on the left, while the 11.34 cm pitch arrangement is shown on the right. The predicted hot spots are circled in each plot.

5.4. Emulation of VHTR Conditions in TRIGA

Emulation of the VHTR conditions requires three criteria to be met: the neutron energy spectra, operational temperatures, and the environment of the TRIGA test (including radiation fields, mechanical characteristics, etc.) and the VHTR conditions must closely match or be scalable from TRIGA to VHTR

At the experimental proof-of-performance stage of the project, the Texas A&M University's TRIGA (Training, Research, Isotope Production, and General Atomics) Mark I research reactor with a nominal operational power of 1MW is being utilized to emulate operating conditions in VHTRs.

Because this is a light water reactor operating at much lower operational temperatures than VHTRs, a specialized test device is required to emulate the VHTR high temperature conditions. The sensor test assembly is planned to be irradiated to fluence levels of $2x10^{19}$ n/cm^2 or higher and operate at 1000°C. This will provide the basis of supporting the use of the fiber optics within a reactor environment. A high temperature test furnace has been developed to achieve this goal.[4]

The furnace design is an adaptation of the original General Atomics furnace developed in 1970s for HTR fuel testing in TRIGA reactors. The overall TRIGA setup configuration of the experiments is shown in Fig. 1.

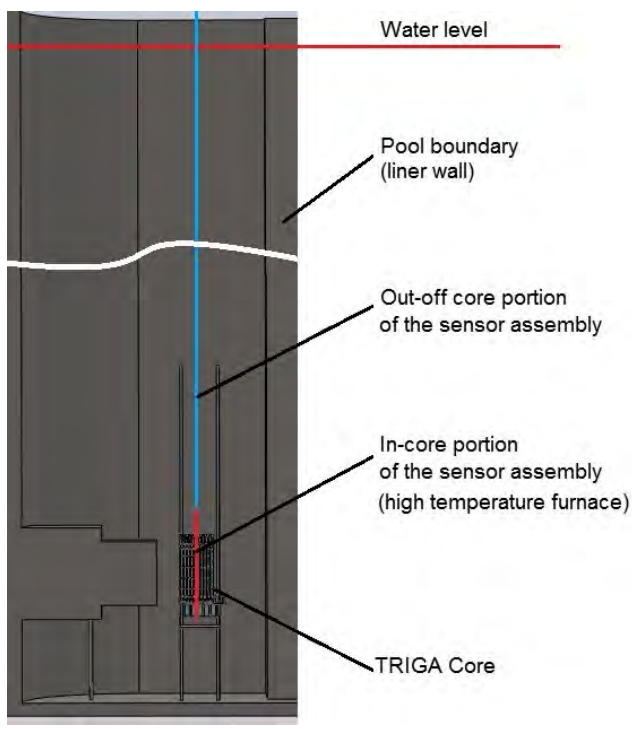

Fig. 1. TRIGA-based high temperature testing assembly.

High Fidelity Modeling Approach

There are significant space constraints on developing experiments within the reactor core, such that a larger furnace that could be used to harden the thermal spectrum becomes unfeasible. Using an external beam port for this purpose is also impractical due to the low neutron fluence and mechanical difficulties of operating the beam port for long irradiation periods. Placing preferential absorbers to focus the desired spectrum reduces the fluence rate such that the required fluence levels will not be achievable within a single year timeframe. Thus, the neutronics environment of VHTRs will require scaling and equivalence analysis to relate experimental results to the VHTR operating conditions.

The high temperature furnace will be inserted into a designated location of the TRIGA core. Figure 1 shows the overall layout of the furnace assembly including the in-core portion of the sensor assembly tube (void tube) and neighboring fuel elements.

The furnace will spend approximately 218 days in the TRIGA reactor core. Although the TRIGA does not operate continuously (24/7), the furnace will be on and data will be collected from the fibers when the reactor is in operation.

This means that the power will be varied over the course of data acquisition, and that the fibers will be subjected to significant thermal cycling that would not be present under normal operating conditions if installed in a VHTR. This cycling could lead to early failure of the fibers that may not be seen without the cycling. Details of the complex irradiation schedule will be accounted for at the scaling stage of the data post-processing when TRIGA results will be related to VHTR conditions.

Some of the design challenges include: operation at 1000°C without inducing incipient boiling; temperature of the coolant adjacent to the furnace assembly must be maintained below the Technical Specification's Limiting Safety System Setting (525°C), and design compliance to the 10 CFR Part 50.59.

Figure 2 shows cross-sectional view of the overall layout of the developed high temperature furnace assembly. There are four major components.

- The graphite heater provides the thermal heat required to attain 1000°C.
- The addition of two concentric niobium thermal shields minimizes the needs for active heat removal systems.
- These shields are supported within aluminum housing to provide a pressure boundary for vacuum conditions.
- The assembly is contained within another tube used for displacing the water in the TRIGA experimental location.

Additionally, this outer tube is pressurized above the hydrostatic pressure of the surrounding water to prevent water leakage into the furnace assembly.

High fidelity computational continuum mechanics (CCM) simulations of the furnace assembly performance characteristics are the basis for the selected design parameters. Initial sizing constraints were based on geometrical restriction within the reactor lattice and shield size and number were determined with 1D heater transfer calculations.

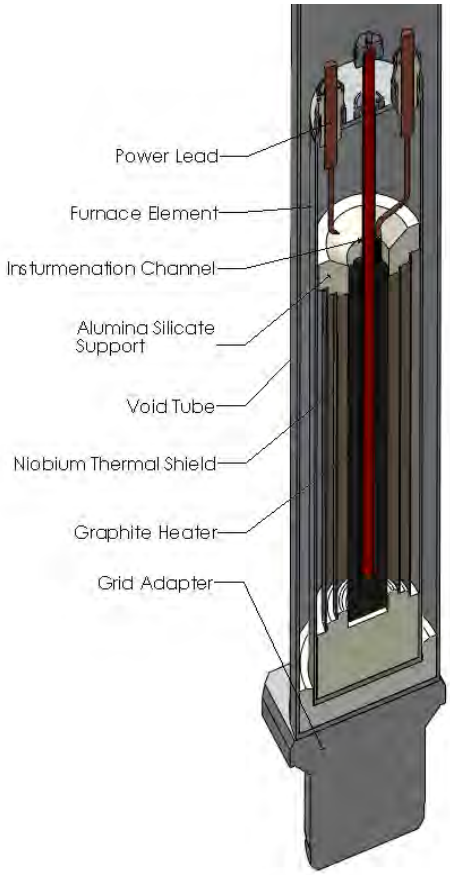

Fig. 2. High temperature furnace assembly emulating VHTR conditions for advanced sensor testing in TRIGA reactors.

The high temperature furnace assembly has been designed based on the results of high fidelity simulations using STAR-CCM+ and MCNP.[1,5] MCNPX was also used for simulating the heating in the thermal shields induced niobium neutron capture reaction as well as reactivity insertions due to flooding of the experiment. The resulting heating from the inner and outer concentric shields were used directly in the thermal modeling.

Figure 3 provides the results of the furnace thermal performance simulations with STAR-CCM+. As can be seen, the design is capable attaining high temperatures at the sensor location while restricting outside temperatures to near ambient levels. The high temperature region is completely shielded from the TRIGA in-core environment and does not result in elevated temperatures outside of the furnace assembly. The model includes ohmic heating of the graphite and copper power leads as well as capture heating in the niobium thermal shields. These are included as field functions in the simulation. Convective cooling was determined using a sub-channel code, taking advantage of the lattice configuration, to reduce the computational requirements. Thus, it has been demonstrated computationally that the developed test assembly design can attain the desired 1000°C-levels at the sensor location without causing an increase in temperature levels outside of the furnace assembly void tube.

High Fidelity Modeling Approach

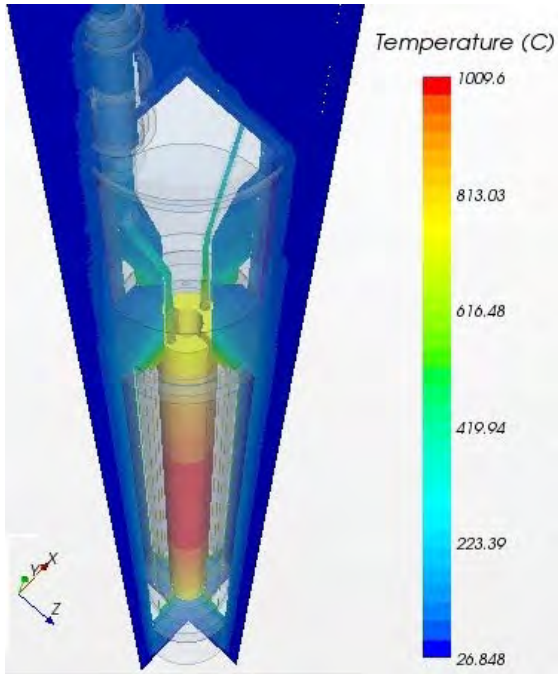

Fig. 3. Thermal performance of the high temperature furnace simulated with STAR-CCM+.

Although high temperatures are attainable, the neutronics conditions of VHTR cores are more difficult to emulate in the TRIGA reactor core because of the inherent physics features. The TRIGA Mark I fuel design uses a zirconium hydride metal lattice which places moderator directly in the fuel. Zirconium hydride comprises 70% of the fuel meat mass, diminishing the fast spectrum.

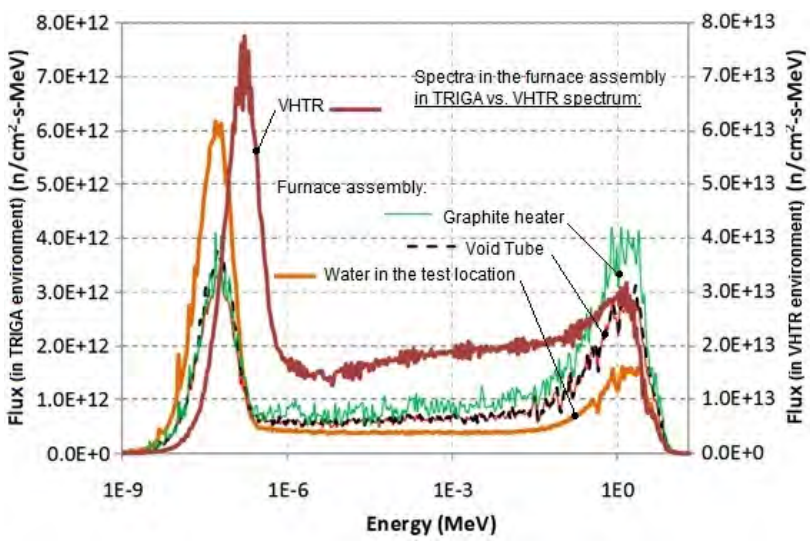

Fig. 4. Neutron energy distributions in the TRIGA test location and in the VHTR core.

Figure 4 shows the resulting differences between the neutron spectra in the TRIGA core and the VHTR spectrum. The high temperature furnace provides the required temperature conditions. The neutronics conditions of VHTRs are much more difficult to emulate because of the inherent physics features of TRIGA reactors. The TRIGA Mark I fuel design uses a zirconium hydride metal lattice which places moderator directly in the fuel.

Figure 5 shows the local heater-to-VHTR flux ratios. None of the energy regions yields flux ratios equal to unity, although the intermediate energy range exhibits the least variation between spectral conditions in these two reactors.

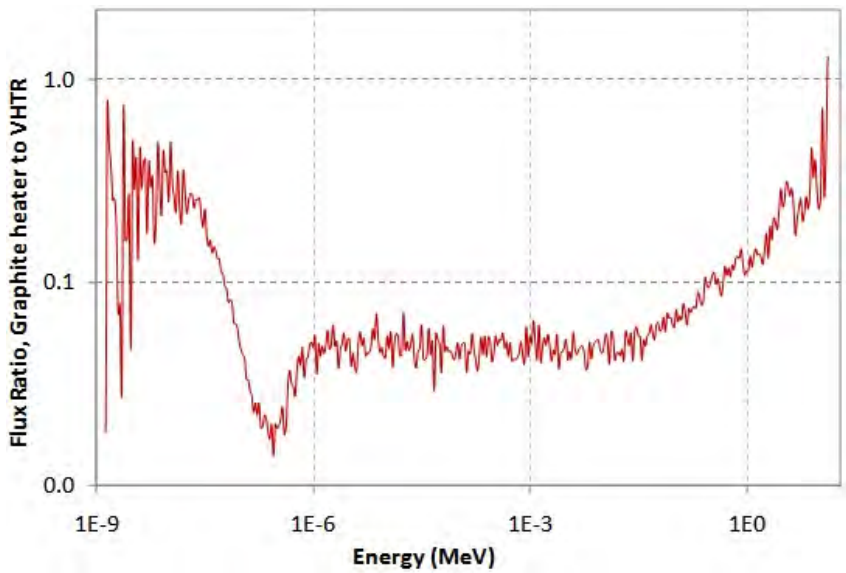

Fig. 5. Scaling and potential spectrum tailoring needs to relate TRIGA test results to VHTR in-core conditions.

Such ratio sets based on flux, fluence and reaction rate calculations will have to be used to determine performance levels that would be equivalent to the VHTR core environment from the corresponding values obtained in the experiments with the high temperature furnace installed in the TRIGA reactor core.

The observed differences between neutronics conditions in TRIGA and VHTR cores will require further scaling and equivalency studies to establish relationships between experimental data and anticipated performance characteristics.

The furnace is an enclosed system, so the operating temperatures and pressure of the TRIGA are irrelevant to a comparison. The neutron flux determines the reaction rates within the fiber optic and is shown in Fig. 6. Figure 6 shows the normalized neutron spectrum for the VHTR averaged coolant channel, the in-core fiber optic location in E2 of the TRIGA, and the averaged TRIGA fuel spectra generated with MCNP5. The relative difference between the VHTR and fiber optic normalized distributions is shown, with a maximum at the trailing edge of the thermal Maxwellian of the VHTR neutron spectrum. A flat relative difference indicates that the distributions are shaped similarly. The fiber optic spectra are quite noisy, due to low numerical sampling in the fiber optic volume; however, the shape is very telling of a low fast-to-thermal

ratio. This is quite far from the expected VHTR distribution and may be cause for poor comparison overall.

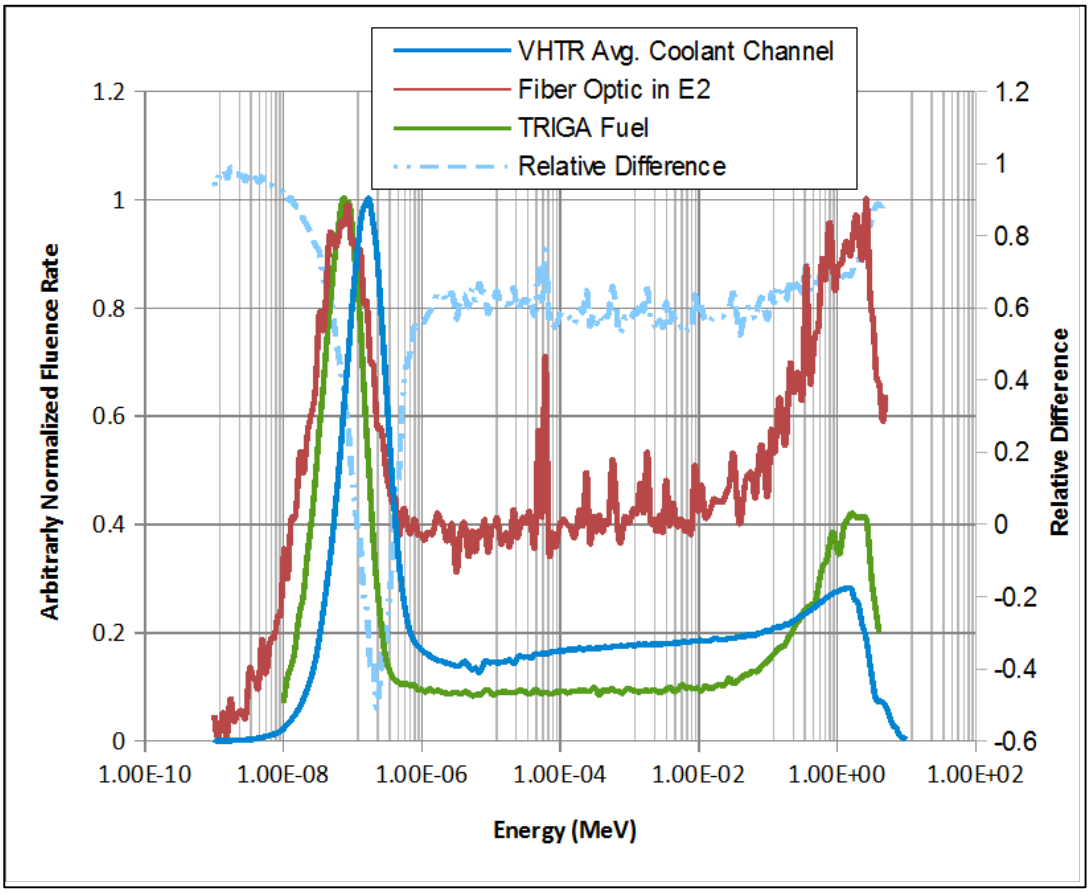

Fig. 6. Comparison of the expected VHTR neutron spectrum and TRIGA neutron spectrum with the relative difference between fiber optic and VHTR on the secondary axis.

5.5. Safety Evaluations and Validation Program

The design basis for this experimental device is the possibility of water ingress and subsequent steam rupture. Due to the proximity of the furnace to the fuel, roughly 0.4 in, this event could result in fuel cladding damage.

To prevent this incident, various measures were taken: a double enclosure of 0.065 in Al-6061 T6 tubing is used and the outer enclosure is pressurized to 400 kPa (the hydrostatic pressure is about 200kPa) with UHP helium.

Additionally, material usage and temperatures are limited on the basis of reducing the thermal storage within the furnace. Temperatures are limited on the basis that there is a perfect amount of water, such that it all completely absorbs all the thermal energy and converts to steam, the

volume required at the failure pressure is equal to open volume of the furnace. This includes the partial pressure of helium.

This leads to the assumption that the graphite heater shuts off. There are pressure switches on the furnace to assure proper performance.

5.5.1. Thermal Conditions

Validation efforts of neutronics and thermal simulations were completed following operational tests of equipment and with experimental data from the TRIGA reactor. These included validation efforts of radiation modeling and fluence measurements.

The first series of validations were completed for radiation modeling of the graphite heaters. Each heater was constructed to allow for power lead contacts with a variable current power supply and placed in vacuum of 10^{-4} torr.

Figure 1 shows the mesh of the graphite heater. Mesh refinement studies concluded this mesh would be suitable.

Fig. 1. Polyhedral computational mesh for the graphite heater to be used in STAR-CCM+ radiation simulations compared to the actual graphite heater.

A distributed fiber optic test system will be used to provide data for validating the thermal modeling.

Using an Optical Backscatter Reflectometer (OBR), the distributed temperature within the high temperature test device can be measured.

The OBR is capable of measuring temperature every 0.5 cm down the length of an attached optical fiber up to temperatures of 850°C with a 0.1°C resolution.

Fiber survivability has been shown above 1000°C.

Table 1 outlines the primary results of the validation efforts. The largest errors resulted in determination of the heat flux from the graphite.

This is attributed to lack of modeling of the thermocouple contacts and from contact resistances of the supports for the graphite heater and power leads.

Table 1. Comparison of STAR-CCM+ Values to Experimental Values.

Current (amps)	Surface Temp (ºC)	Measured Temp (ºC)	Heat Flux (W/m^2)	Power Error	Temp. Error
3.50	39.74	37.7825	82.44	-0.0944	0.0063
4.50	47.17	46.4325	134.83	-0.0919	0.0023
6.00	60.22	57.8975	236.13	-0.0948	0.0070
8.00	79.77	78.4425	411.73	-0.0981	0.0038
10.00	100.47	100.6	632.5	-0.0948	-0.0003
12.00	121.55	121.18	898.15	-0.0862	0.0009
13.50	137.32	135.4875	1126.97	-0.0849	0.0045
15.00	152.95	150.53	1381.29	-0.0876	0.0057
17.00	173.46	169.1375	1760.26	-0.0896	0.0098
18.50	188.55	182.6175	2074.49	-0.0887	0.0130
20.00	202.72	194.7725	2399.59	-0.0936	0.0170
21.25	215.48	205.822	2717.25	-0.0875	0.0202
23.00	232.1	220.4275	3170.96	-0.0799	0.0237
24.50	246.03	232.18	3587.32	-0.0800	0.0274
26.00	259.68	243.9025	4028.76	-0.0760	0.0305
6.00	60.22	59.5475	236.13	-0.0948	0.0020
10.00	100.47	101.23	632.5	-0.0897	-0.0020
17.00	173.46	171.2675	1760.26	-0.0865	0.0049
26.00	259.68	246.9625	4028.76	-0.0907	0.0245
28.00	277.42	262.15	4656.07	-0.0943	0.0285
30.00	294.68	276.7925	5327.23	-0.0959	0.0325
32.00	311.48	290.3725	6041.94	-0.0959	0.0375
34.00	327.84	303.8825	6800.1	-0.0849	0.0415
36.00	343.81	317.1455	7601.9	-0.0842	0.0452
39.00	367.08	338.59	8887.66	-0.0755	0.0466
41.00	382.2	348.185	9801.78	0.0196	0.0548
44.00	404.39	365.8425	11262.82	0.0531	0.0603
46.00	418.92	376.8275	12300.6	-0.0011	0.0648
47.50	429.72	385.5925	13144.9	-0.0172	0.0670

The reflection of radiation from the surface of the vacuum chamber was also neglected, but the surface temperature of the chamber and the environmental temperature of the model were equivalent in all simulations.

Additionally, during the process of heating the graphite, system resistivity was determined with a multimeter and applied to the model as shown in Fig. 2. Inconsistent coupling between the leads and power supply required experimental validation of values applied in models for each heater that was tested.

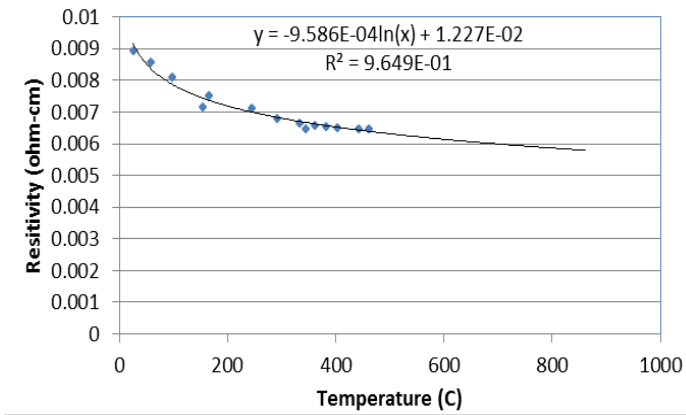

Fig. 2. Resistivity as a function of average graphite temperature.

Validation efforts continued following the completion of the furnace fabrication. The efforts included bench top testing of the furnace in an open pool environment. The parameters that are compared with are: furnace, void tube, and heater surface temperatures. Pressure tests were conducted to ensure weld quality and vacuum capability.

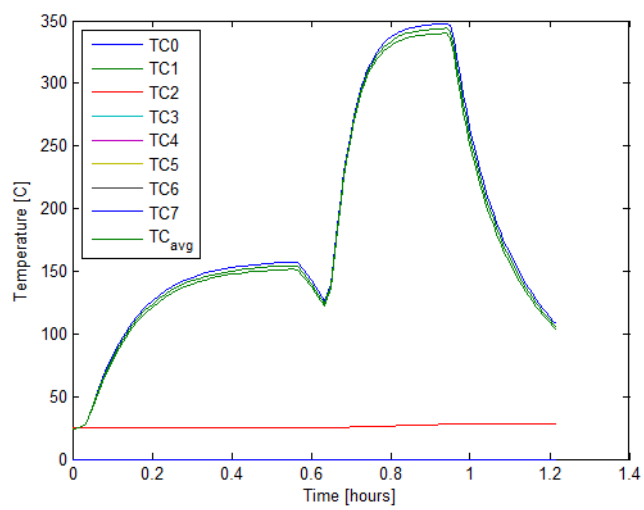

Fig. 3. Sample temperature transient.

5.5.2. Heater Stress Testing

The controller for the furnace will be operated with LabView. This allows for control of the power supply, either manually or automatically, given a desired temperature for any given thermocouple input. Various thermal stress/transient tests to demonstrate heater fabrication were completed. These showed satisfactory cementing of thermocouples and power leads.

Heater stress testing has been successful for the most severe of possible transients, although cooling transients were limited in scope. Figure 3 illustrates transient temperature fluctuations. Maximum temperature condition did not fail during steam rupture evaluations.

5.5.3. Physical Tests

Spatial continuous instrumentation technologies have been under development in recent years to measure temperatures along a specific direction. Unlike other measurement systems that measure at finite locations, fiber optic technology allows for such continuous measurements.

Figure 4 illustrates continuous measurements via the distributed fiberoptics test system. This distributed fiber optic test system is used to provide data for validating the thermal modeling. Using an Optical Backscatter Reflectometer (OBR), the distributed temperature profile within the high temperature test device can be measured. The OBR is capable of measuring temperatures every 0.5 cm down the length of an attached optical fiber up to temperatures of 850°C with a 0.1°C resolution. Fiber survivability has been shown above 1000°C.

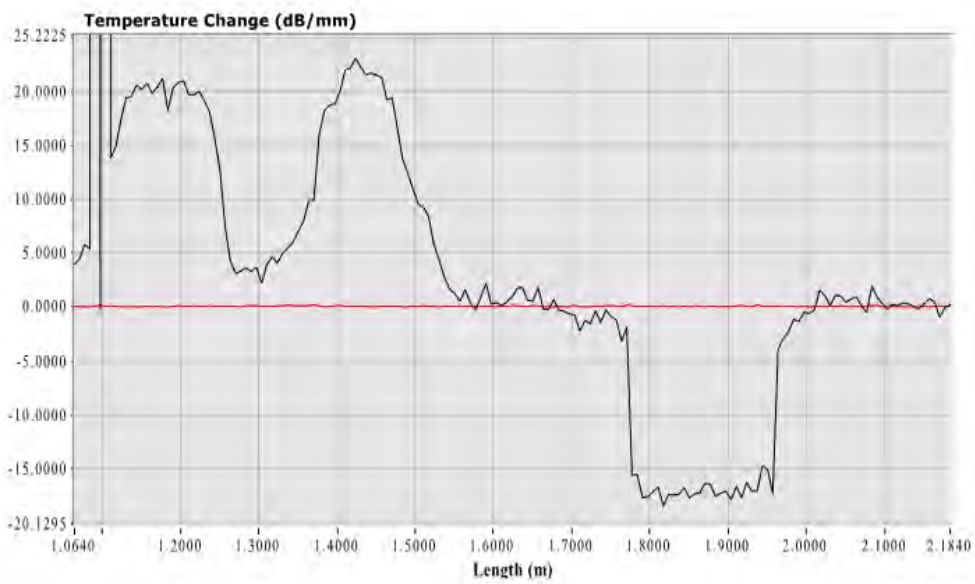

Fig. 4. Continuous temperature measurement showing heated and cooled regions.

Inherently, any material structure will expand during temperature changes within the material. Fiber optic measurements take advantage of this phenomenon by using spectral backscatter analysis to determine the strain induced within the fiber as a result of this expansion. It is then known, that any geometry change in the fiber will induce a change in the strain in the fiber optic.

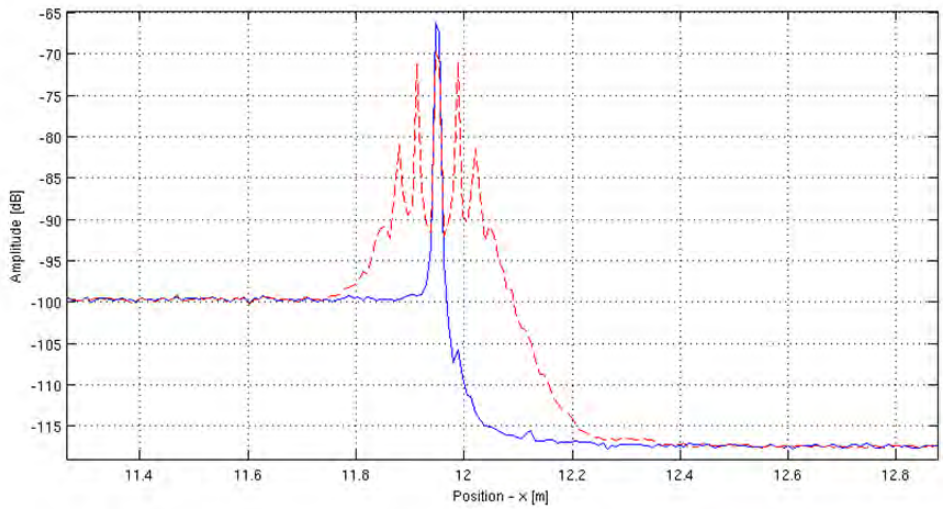

(a) Vibration effect on the return losses at the fiber end.

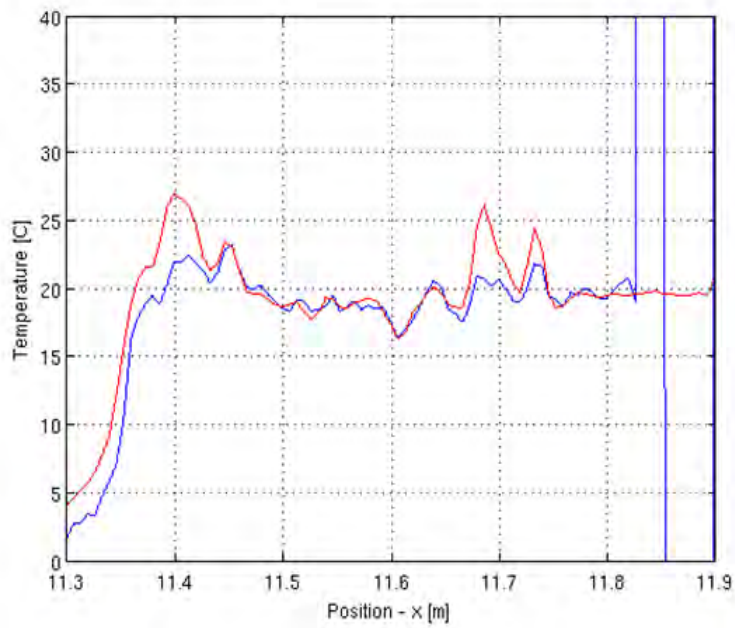

(b) Vibration effect on the temperature distribution measurement.

Fig. 5. Sample fiberoptics performance effects due to vibrations.

It was investigated whether this greatly affects the measurement accuracy and to what extent the vibrations might affect coupling joints. It was shown that the measurement was particularly affected by certain vibrations, those specific in the “fan” range, and the magnitude of those vibrations induced further error.

The fiberoptics sensors are expected to be capable to reliably operate within the reactor vessel internals. The most desirable placement locations of interests are within the core itself. Emerging fiberoptics performance issues in these environments need to be evaluated and quantified.

Under nominal, steady-state conditions, there is a significant amount of coolant flowing through coolant channels and assemblies. There are massive 10MW pumps. These and other system features will contribute to mechanical vibrations.

With the measurement systems distributed throughout the reactor, all these vibrations can be expected to impact the fiberoptics systems.

It is the objective of this study to determine, based on the operating conditions of the TRIGA facility and other supporting equipment, on whether vibration-induced measurement errors can be expected, tolerated, or even avoided.

The effects of various components, present during the tests, are examined. These components are the turbo and scroll pump, computer, and power supply.

The computer and power supply do have a fan and it is suspected that these are enough to alter the measurements. Figure 5 illustrates effects due to vibrations on the return losses and temperature distributions.

5.5.4. Radiation Model Validation

The radiation model was developed consistently with the furnace testing program to assure availability of experimental data for validation. Simplifications included assumptions of constant emissivity values of 0.98 and omissions of the stands, TCs (thermocouples) and their contact points.

Radiative heat transfer boundary conditions were implemented assuming the following two conditions:

- the heater power level is equal to the heat flux, and
- the surface temperature determines the heat flux.

All of the applied thermo physical properties are from the STAR-CCM+ Model.

5.6. Conclusions

Results of the high fidelity simulations indicate that the furnace assembly should be capable of emulating VHTR temperature conditions in TRIGA experiments. The furnace allows the sensor location to reach 1000°C-levels while being completely shielded from the TRIGA core environment. Calculations indicate that no active heat removal systems (i.e. via flowing gas) will be required to maintain temperatures below the TRIGA limiting safety system setting (525°C) at the outer surface of the furnace void tube. While the VHTR temperature environments can be emulated directly with TRIGA experiments using the high temperature furnace assembly, the neutronics conditions will require further scaling and equivalency analysis of the experimental results of the TRIGA core to the expected VHTR operational conditions.

5.7. References

1. J.S. Hendricks, G.W. McKinney, J.W. Durkee, J.P. Finch, M.L. Fensin, M.R. James, et al., MCNPX, Version 2.6.0, Los Alamos National Laboratory Report LA-UR-08-2216, 2008.

2. P. V. Tsvetkov, "Coupled Hybrid Monte Carlo - Deterministic Analysis of VHTR Configurations with Advanced Actinide Fuels," *Proc. ICAPP'06*, pp. 1984 - 1990 (2006).

3. D. E. Ames II, P. V. Tsvetkov, "Benchmark Efforts to Support Studies of Advanced VHTRs," *Proc. 4th Intern. Conf. HTRs*, HTR2008-58206, ASME (2008).

4. E. E. Anderson, S. Langer, N. L. Baldwin and F. E. Vanslager, "An In-Core Furnace for the High-Temperature Irradiation Testing of Reactor Fuels," *Nucl. Techn.*, **11**, pp. 259-265 (1971).

5. Star-CCM+ v5.06.007, distributed by CD-adapco Group, Inc., Melville, NY.

6. Distributed Fiberoptics-Based Measurement System

6.1. Distributed Fiberoptic Characterization of In-Core Nuclear Radiation Fields

6.1.1. Introduction

Luna Innovations Incorporated teamed with Texas A&M University (TAMU) to develop, implement, and test a novel method of characterizing neutron flux distributions, gamma flux distributions and temperature profiles within the core of research reactors.

Since we have entered the beginning of the nuclear Renaissance period, leaders from the nuclear industry have been developing novel reactor designs to achieve modular construction economy, higher fuel utilization, higher electrical generation efficiency, intrinsically passive safety features, barriers to nuclear proliferation, and sometimes elevated reactor temperatures.

One of the goals in modern reactor designs is to achieve a uniform fission rate across all reactor fuel elements in order to avoid the necessity of replacing large sections of fuel when only a few fuel elements have reached their maximum service life.

If a nuclear reactor exhibits wide variations in local fission rate, reactor operators must reduce the average power level considerably in order to prevent any individual fuel element from exceeding its maximum rated fission rate, as illustrated in Fig. 1.

Fig. 1. Uniformity of fission rate profiles and efficiency of fuel utilization.

Uncompensated local hot spots can lead to premature fuel cladding failures, and contaminations of coolant water.

Furthermore, the novel fiber optic sensing technology described here may someday help developers of new reactor designs and fuel assemblies to test their computational evaluations against detailed experiments in prototypic reactor conditions.

6.1.2. Background

Years ago, Luna demonstrated the ability to make distributed fiber optic temperature measurements using its patented optical backscatter reflectometer (OBR) technology, even within the core of a research nuclear reactor.

Further analysis of data from reactor tests also suggested that changes in optical fiber properties that were detectable using Luna's OBR could be used to characterize other radiation field parameters besides temperature distributions.

While comparing performance characteristics of different fibers in nuclear reactors, Luna noted that single-mode optical fiber with a pure silica core was significantly less sensitive to radiation, but still functioned as a distributed temperature sensor.

Recently, Fujikura developed a fluorine doped single mode fiber with even lower radiation induced loss than pure silica core optical fiber. In future distributed radiation probes, this fiber could serve as the leads and as the temperature sensing fiber.

As part of this project, Luna and TAMU proposed to develop novel distributed fiber-optic probes to characterize neutron fluence, gamma flux, and temperature profiles within a nuclear reactor. The concept was to use high GeO content fibers to characterize gamma flux, high boron content fiber to characterize thermal neutron fluences, and pure silica core fiber to measure temperature distributions.

By positioning all three fibers together in the same environment, the cross sensitivities of each fiber to the other parameters of the radiation field could be characterized to yield a well-compensated fiber optic probe of local fission rates.

6.1.3. Distributed Fiberoptic Probe Development

INO made a boron doped preform with 5% B_2O_3 in the core; the preform was drawn into custom single mode optical fiber by Fiberguide to achieve the desired numerical aperture (NA=0.07). Fibercore supplied the single mode optical fiber with high germania content in the core (17% GeO) as an off-the-shelf product (SMKFOO-4.2/125).

The B-doped fiber was designed to be a neutron sensing fiber and the Ge-doped fiber was designed to be a gamma flux sensing fiber.

Pure silica core single mode optical fiber was purchased from OFS and used as the temperature sensing fiber and as the fiber optic leads for the radiation sensing fibers.

The complete fiber optic distributed radiation field monitoring assembly included four main sections along its length, as shown in Fig. 2.

From Luna's Optical Backscatter Reflectometer (OBR 4400) fiber optic sensor interrogation system, the optical fibers were gathered in a flexible sheath up to the reactor pool; then the fibers were sealed in a flexible corrugated stainless steel tube through the reactor coolant water.

Once inside the submerged dry-well of TAMU's in-core heater the optical fibers were again gathered in a braided silica sheath up to the straight probe section.

The fiber leads and radiation sensing fibers were also each individually protected by braided silica sheaths in all sections except the last straight probe.

At the end of the pure silica core leads, a 2 m long section of sensing fiber was spliced to each pure silica core optical fiber lead, so that 1.4 m of each sensing fiber was in a flexible fiberglass sheath and 0.6 m of each sensing fiber was inside the straight probe.

Distributed Fiberoptics-Based Measurement System

Within the straight probe, one fiber of each of the 3 separate sensing types was inserted into the 0.5 mm diameter holes of a 1.8 mm diameter 4-bore quartz tube, ~0.5 m long, leaving one bore empty. There were a total of 8 of these 4-bore tubes housing 8x3=24 sensing fibers in all.

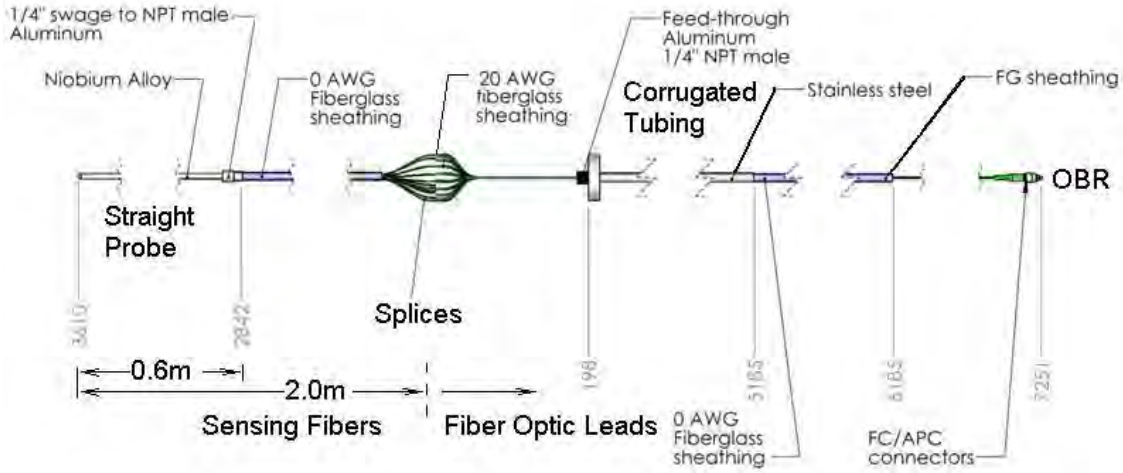

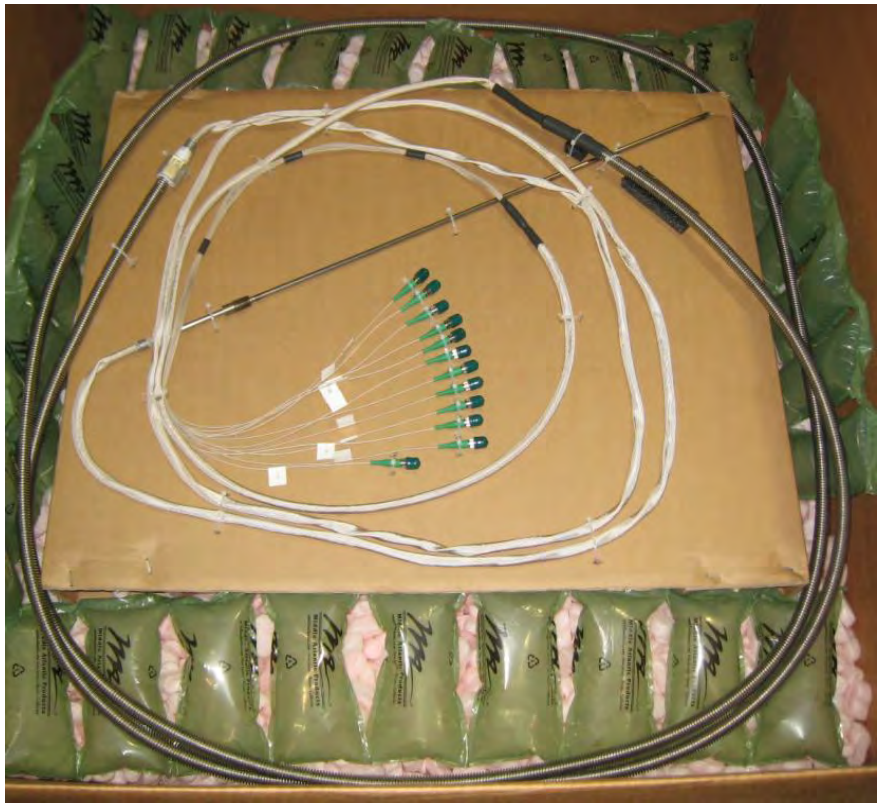

Fig. 2. Construction of fiber optic distributed radiation probe - section diagram (ABOVE) and photo (LEFT) with a close-up of the sensing fibers within 4-bore quartz tubes (RIGHT).

6.1.4. Data Processing Software

To facilitate extracting the effects of radiation on each of the sensing fibers during reactor testing, Luna developed a simple software interface as illustrated in Fig. 3. The purpose of the FiberRadiation software is to compare the data from 4 OBR scans (i.e. a temperature reference, a temperature measurement scan, a radiation sensor signal reference, and a radiation sensor measurement scan) in order to calculate the radiation induced change in the backscattered signal amplitude as a function of position along a single fiber.

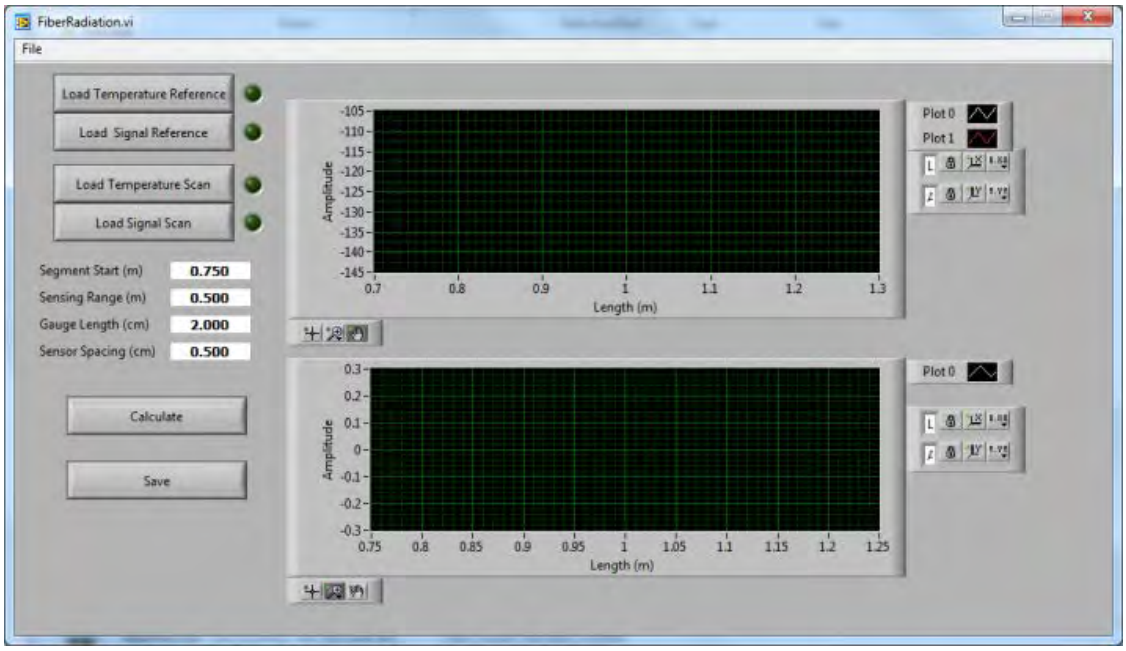

Fig. 3. FiberRadiation software interface developed by Luna.

The user is prompted by text buttons to load a temperature reference (at a known isothermal temperature before heat or radiation is applied) and to load a signal reference (again before the beginning of a given reactor run). As each raw OBR data file is loaded, it is plotted in the upper graph. Then the user is prompted to load a temperature scan (from a temperature sensing pure silica fiber) and a signal scan (from either a B-doped or Ge-doped fiber). Changes in temperature generate changes in the apparent optical path length to each position as a result of the thermo-optic effect. Therefore, in order to compare backscattered amplitudes between the same actual positions, Luna's software corrects for the measured temperature shifts along the fibers.

Basically, higher temperatures make the fiber path elongate, and the temperature compensation is used to "pull back" the position of the measurement scan so the software can compare it to the correct positions on the reference scan. Without this temperature correction, the calculated change in backscattered amplitude after reactor radiation (Δ amplitude) may exhibit unwanted bias or artifacts. From the experimental hardware layout, the user already knows the positions along the fiber corresponding to the reactor mid-plane, the reactor top and bottom, the beginning and end of the straight probe, and the heated region. The user can adjust the segment start position for comparative analysis, and the extent of the sensing range of positions to be analyzed.

The gauge length refers to the distance over which to average backscatter amplitudes, while the sensor spacing refers to the desired distance between averaged output data points. When the user pushes the calculate button, the program first calculates the temperature distribution in order to make a minor adjustment in the apparent positions of the signal scan along the radiation sensing fiber. Using the thermally corrected positions, the program then calculates the change in the backscattered amplitude profile compared to the signal reference scan, and plots this amplitude difference in the lower graph. The user can then save the output as a compact text file, which can be imported by other programs for analysis of trends.

6.1.5. Demonstration

The preliminary pre-radiation testing results for Ge-doped fibers by TAMU are shown in Fig. 4. These data confirm that Ge-doped fibers have the properties that would support robust distributed radiation measurements in the in-core heater. Those desirable properties include elevated uniform backscatter levels and low bend sensitivity.

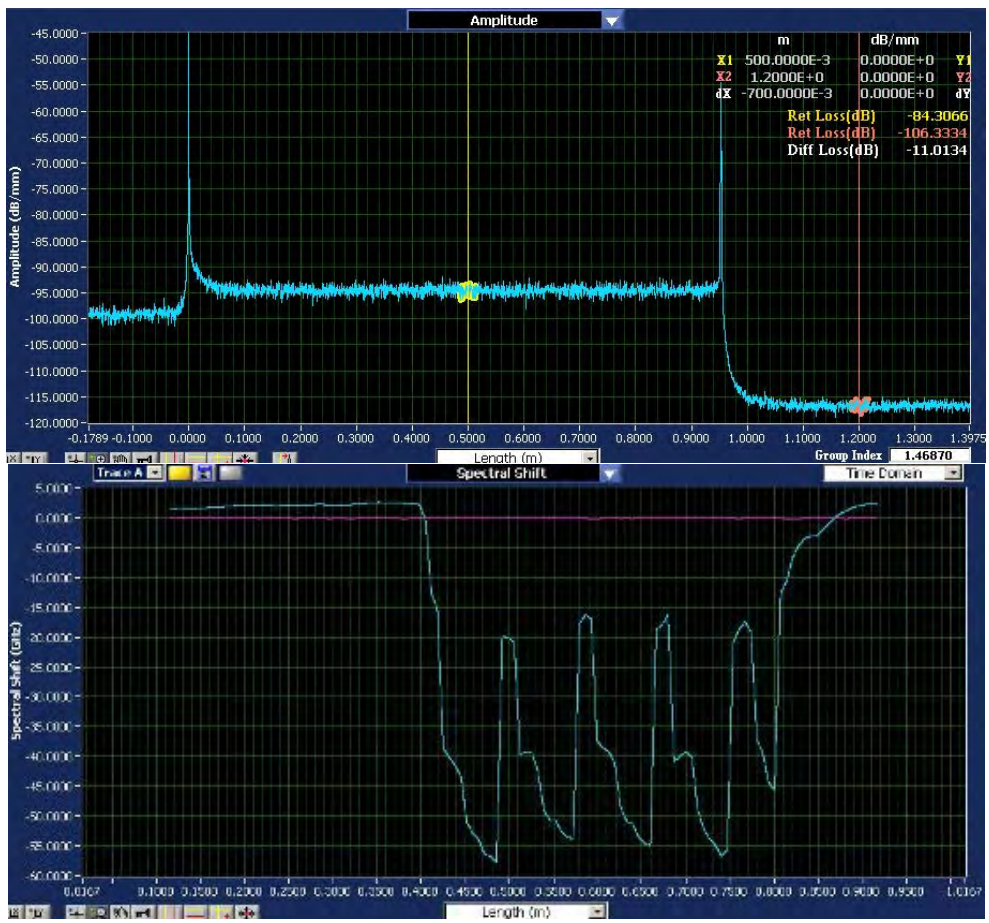

Fig. 4. Ge-doped gamma sensing fiber exhibited a high uniform backscattered signal level despite several 1 inch diameter coils near the yellow highlighted region (ABOVE). The spectral shift pattern repeats around each 1 inch diameter coil as expected (BELOW).

The pre-radiation testing of the B-doped fibers reveals potential problems in Fig. 5. These challenges could potentially hinder effective distributed radiation monitoring.

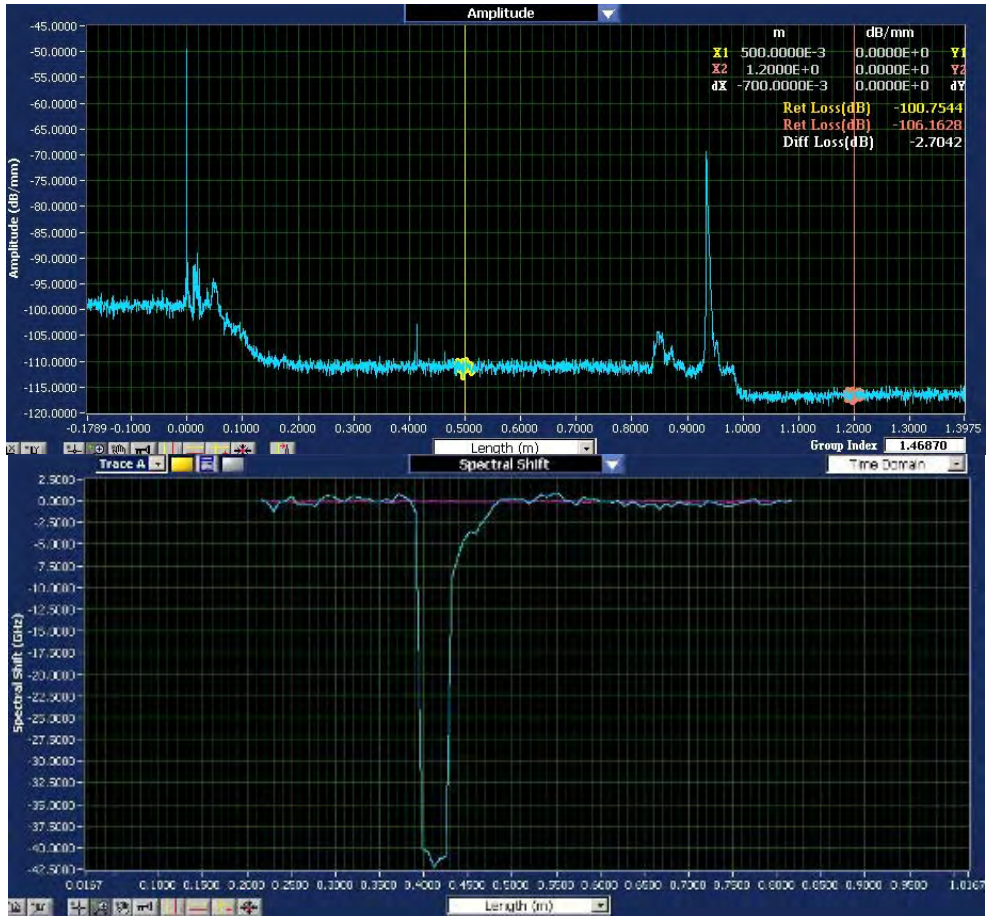

Fig. 5. The low-NA, B-doped neutron sensing fiber is weakly guiding and has a corresponding low scatter level (ABOVE). Even so, as long as the fiber remained straight, it produced the expected local spectral shift in a region locally heated to 60 °C (BELLOW).

The upper plot in Fig. 5 demonstrates a dramatic reduction in backscatter within the B-doped fiber. This is mostly due to the weakly-guiding, low-NA core. It is promising, however, that the spectral shift along the heated section behaved as expected in the lower plot in Fig. 5.

Most concerning is the additional features surrounding the reflection peaks at the beginning and end of the B-doped fiber section. The cause of these artifacts is yet unclear, but similar behavior has been seen in the presence of even gradual bends in Fig. 6.

In the presence of even gradual bends, the low-NA inherently creates a low tolerance to bend-loss. The source and behavior of these features are planned to be investigated in the future research efforts.

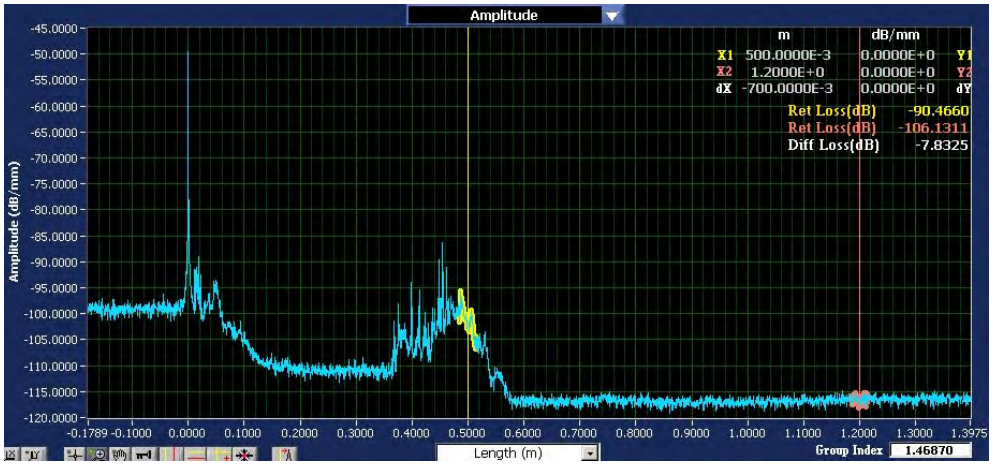

Fig. 6. OBR trace of B-doped neutron sensing fiber was very sensitive to bends with several 6 inch diameter coils beginning near position 0.35m.

Additional reactor data acquired under the recommended settings within the experimental configuration should provide a useful proof-of-concept for the behavior of the distributed radiation sensing probe, at least for the GeO-doped gamma sensing fibers. To obtain useful data from the B-doped fiber in future experiments, it will be beneficial for the sensing fiber to remain straight over the entire length, from the splice to the termination. Alternatively, custom B-F co-doped single mode fiber may provide better light guiding that is less sensitive to bends. Thus, it may form a more rugged neutron sensing fiber system.

6.2. Preliminary Design of the Test Probe Housing

Figure 1 illustrates a feasible configuration for the test probe housing. The top and bottom close-ups of the sensor locations show where either 3 of 4 quartz four bore tubes will hold the 3 different kinds of sensing fibers near each other. The lower Swagelok fitting is for attachment to the test housing, the upper Swagelok is for attachment to the lead out tubing. The niobium tube will be sealed at the distal end (not shown).

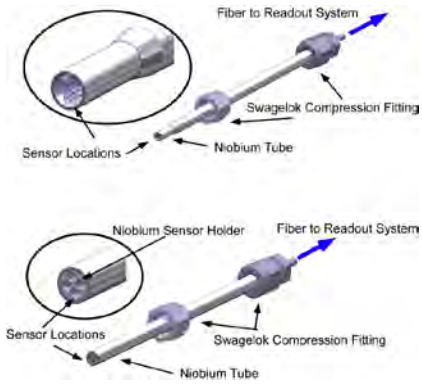

Fig. 1. Preliminary design of the test probe housing.

6.3. Fiberoptics Probe Design for Distributed Measurements

Luna has developed the sensor hardware design to support distributed measurements in the project. The probe design is shown in Fig. 1. The fiber optic probe was designed to provide access and protection for several different sensing fiber types that can be used to monitor the radiation profile of the test reactor at Texas A&M University.

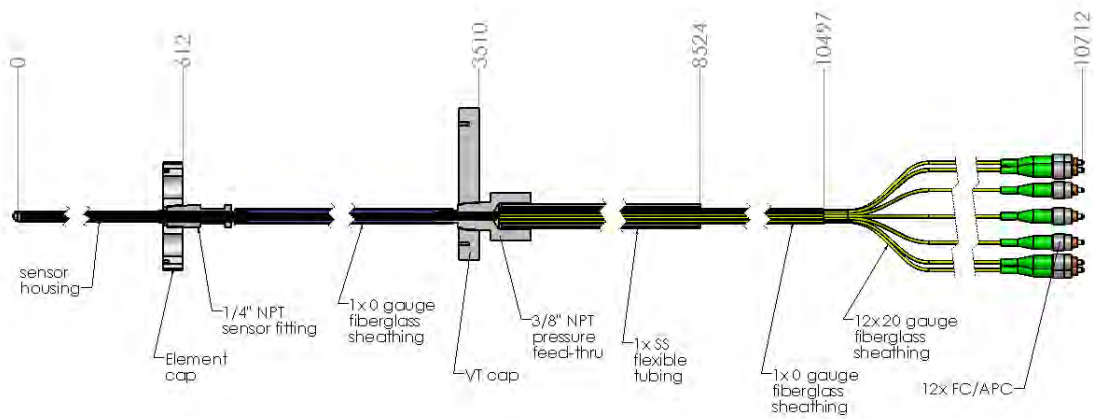

Fig. 1. Design drawing of the distributed fiber optic probe (dimensions in mm unless shown otherwise).

The design for the probe consists of several sections: the lead, high pressure, and vacuum areas. Luna finalized and delivered the fiberoptics probes needed for distributed measurements.

The Lead Out section connects the interrogating optical instruments with the optical fiber sued for sensing. At TAMU, this section goes through the pool surrounding the reactor. The lead section consists of twelve radiation resistant optical fibers housed in 20AWG fiberglass sheathing. These are then bundled in 0AWG fiberglass sheathing.

To protect the optical fibers from the reactor pool, the bundle is housed in a corrugated stainless steel tube; this allows flexibility while preventing water ingress. The lead section passes through a 3/8'' NPT aluminum fiber optic feed through. This will be tested up to 100 PSI for safety.

Each of the twelve fibers is sheathed in a small fiberglass sleeve which gives protection and limits tangling of the optical fiber. The bundle of sheathed optical fiber is placed in a larger sheath which protects the fibers from the corrugated tubing and allowed for controlled lead management. FC/APC connectors are used to provide a low reflectance optical transition to the interrogating instruments.

The pressure transition section was designed provide a fiber optic feed through that can withstand 800 kPa of pressure and transition the fiber to the sensing region. The aluminum pressure feed through is shown in Fig. 2. The left side of Fig. 2 attaches to the corrugated stainless steel tube. Since this is located in water, the galvanic response is minimized between the aluminum and the stainless steel by an epoxy barrier (MS 907).

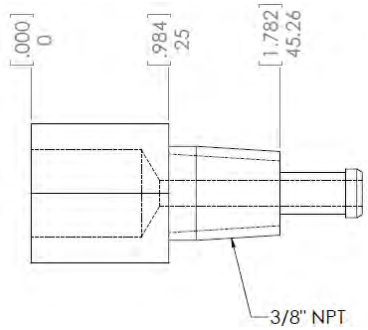

Fig. 2. Aluminum fiber optic pressure feed through.

The optical fiber is fed though the center of the feedthrough and epoxied in place with MS 907. The fiber is then transitioned into small fiber optic sheaths and bundled together in a larger sheath; the larger sheath is the main strain element in the transition section so as not to break the optical fibers. This large sheath is held on the aluminum feed through (right side of Fig. 2) with aluminum wire and MS 907.

A longer length of optical fiber was designed then the actually distance between the void tube cap used in the TAMU facility and element cap, this allows for more routing options, and minimizes the chance of accidental breakage. After transitioning the void, the fibers enter the lower feed through. The larger fiberglass sheath is attached with MS 907 and a wire wrap. The lower feed through, shown in Fig. 3, is made of Niobium so that it can be welded to the protective niobium sheath of the sensing portion.

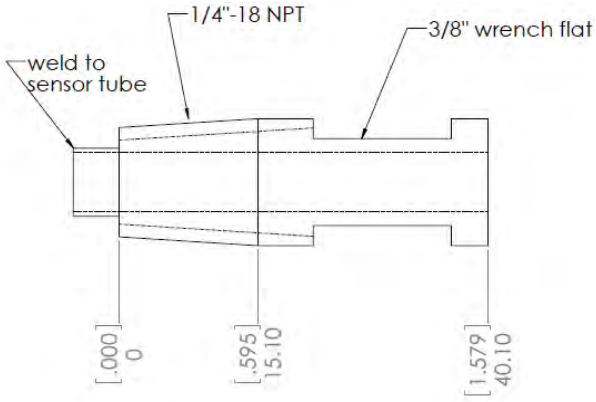

Fig. 3: Lower niobium fiber optic feed through.

The ¼ NPT size was chosen to fit through the pressure feed through hole in the void tube cap so that the probe would be in one piece instead of two. Niobium was used for its ductility properties at high temperatures in a reactor environment.

The high pressure section follows the leaded section after the feed through. The twelve optical fibers are bundled into four 20AWG fiberglass sheaths and the set of four is bundled in a 0AWg fiberglass sheath.

At 3.5 meters of optical fiber in this section allows TAMU to be flexible in positioning the probe and can be used for different configurations.

The bundle of optical fibers enters a niobium tube that has a welded niobium 1/4''NPT thread and is held in place with Miller-Stevens 907. Next is the vacuum section, this consists of the niobium tubes and the sensors.

The four bundles of three optical leads are housed in side of the niobium tube and transition to the sensing fibers at the top of four 4-bore quarts tubes. The niobium tube has been welded closed to provide a vacuum barrier for the sensors.

Figure 4 shows the probe's extent and identifies its functional three regions:

- Lead out region,
- Pressure transition region, and
- Sensing region.

Each area was designed to handle their respective harsh environments, they will be exposed to. For redundancy the probe consists of four sets of three sensing fibers for a total of twelve available sensors.

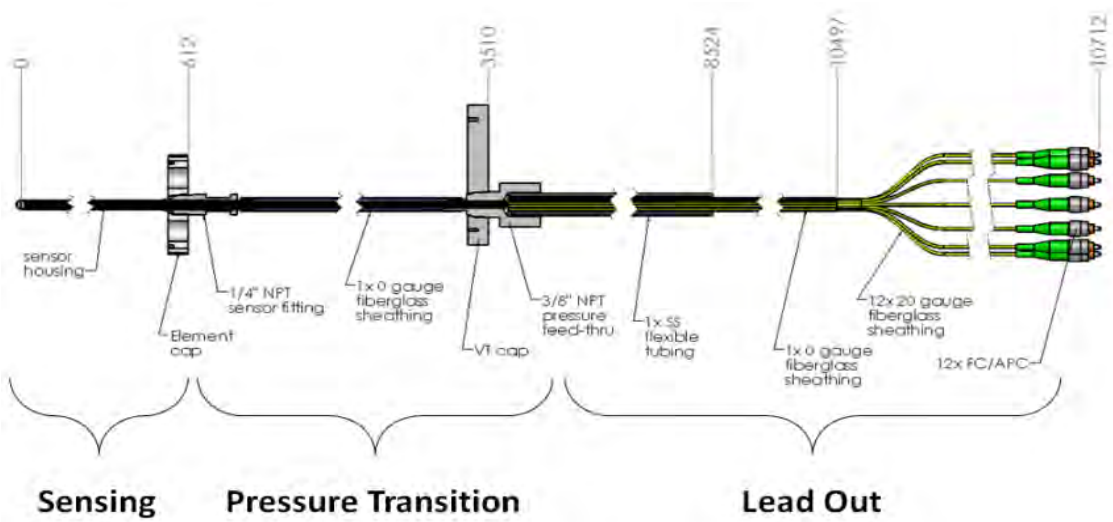

Fig. 4. Distributed fiber optic probe structure (dimensions in mm unless shown otherwise).

The sensing portion consists of several elements:

- The outer sheath,
- Inner quartz ferrules, and
- The sensing fiber.

The sensing fibers consist of a single temperature, neutron fluence, and gamma flux sensing fiber each ~60.8m in length.

Each fiber has been stripped of the protective coating due to the coatings behavior in high temperature and radiation environments.

The lead fibers were spliced to 0.6m of sensing fibers.

Quartz capillary tubes protect the splice from any additional stress and the quartz ferrules the fiber are housed in.

The inner quartz ferrules are 4 fused silica four bore and house the sensing fibers. The fibers are arranged in the bores to provide adequate coverage of the redundant sensing fibers.

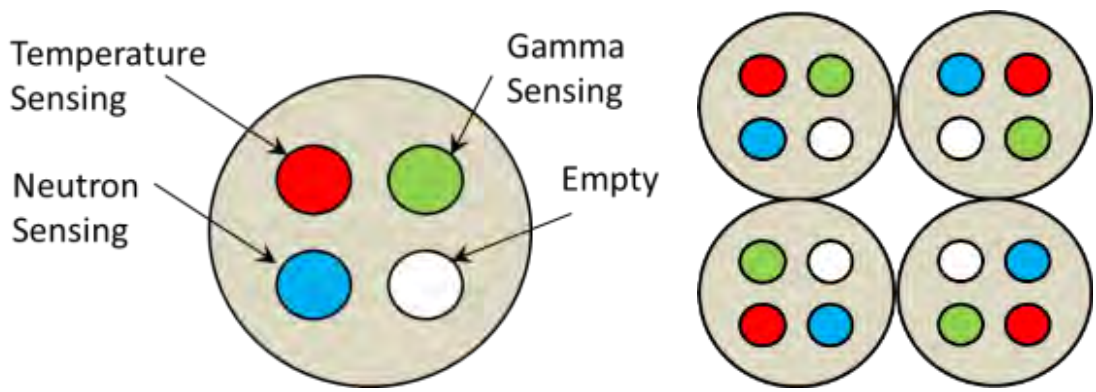

(a) (b)

Fig. 5. (a) Location of the optical fiber in a single quartz 4-bore, (b) location of the quartz 4-bores in the niobium tube.

This stripping however makes fabrication difficult as it increases the possibility of breakage.

The fibers have been terminated to allow distributed monitoring close to the tip of the quartz 4-bore so that the scatter of the end reflection was minimized.

The fibers are arranged in the bores to provide adequate coverage of the redundant sensing fibers.

The 4 quartz 4-bores are held in place with ceramic wool to provide slight vibration protection.

Figure 5 shows the locations of the fibers and 4 bores inside the niobium tube.

Ceramic wool surrounds the bundle of quartz ferrules to provide cushioning between the quartz and the niobium sheath.

The ceramic wool is at the tip of the niobium sheath as well.

The niobium sheath is welded to the niobium feed through and weld at the bottom to provide a pressure barrier to the vacuum inside the element tube.

6.4. Fiberoptics Performance Monitoring

Luna provided a report to TAMU on several optical fiber health problems that could be seen in the optical sensing fiber. This report provides examples for health monitoring while in-situ at TAMU. These problems include: a break, a crush, and a splice.

Examples of this are shown in Fig. 1.

These results and conclusions are incorporated into the independent fiberoptics performance assessment report.

The report outlines expected limitations, potential solutions and further anticipated technology improvements as well as viability evaluations of fiberoptics uses for in-core instrumentation applications.

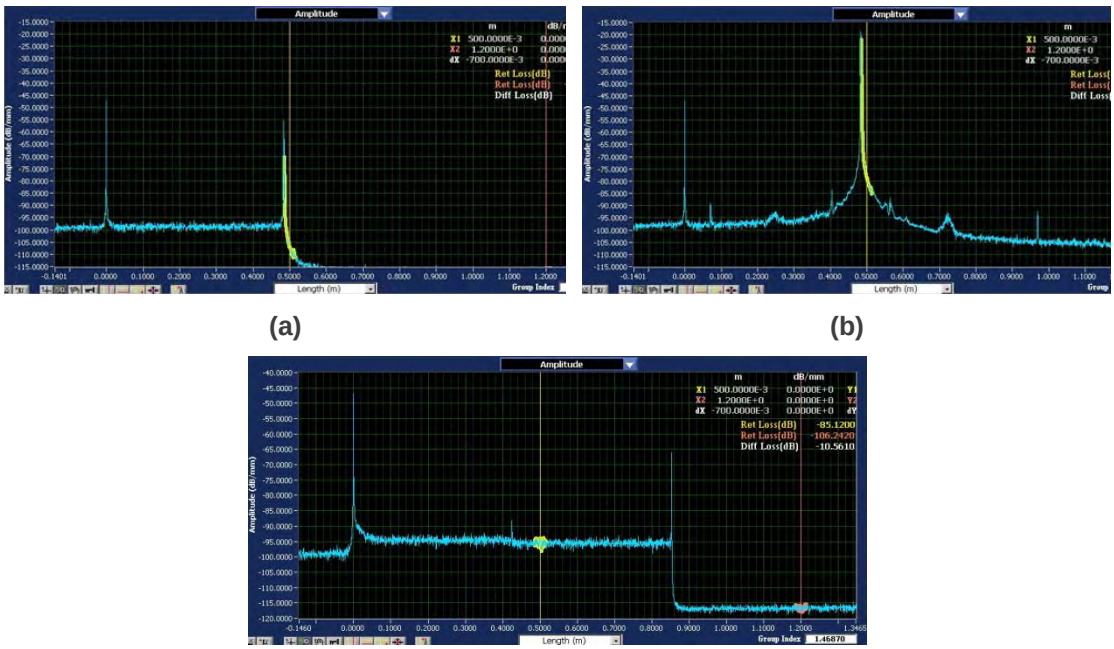

(a) (b)

(c)

Fig. 1. (a) A brake in the Temperature sensing fiber. (b) A crush in the temperature fiber. (c) A splice in a temperature sensing fiber.

6.5. Fiberoptics Data Processing

6.5.1. Data Acquisition Software

An auxiliary software package was developed to extract the neutron fluence and gamma flux information from the radiation sensitive fibers.

Simulated fiber data sets were used to develop the algorithms for the sensing fibers used at Texas A&M University.

Figure 1 shows a screenshot of the simulated data and the corresponding radiation signal.

In Fig. 1:

- The top graph shows the reference and signal data gathered using an OBR.
- A clear radiation signal is seen at a length of 14 meters in lower graph showing the calculated radiation effect.

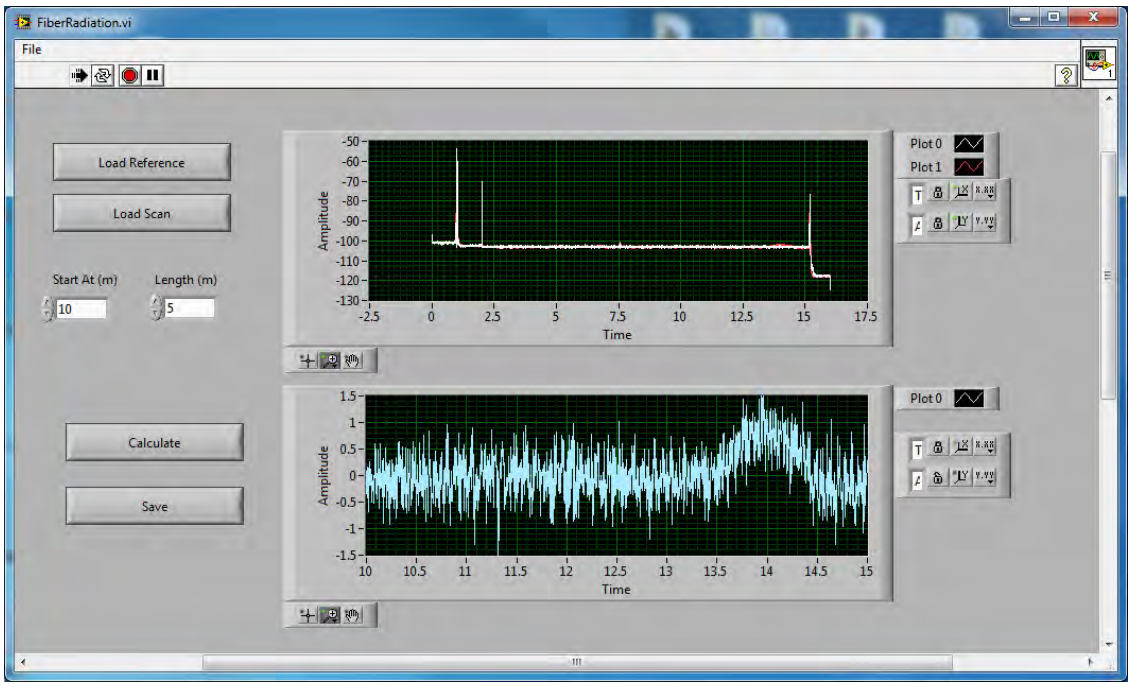

Fig. 1. Screenshot of the fiber radiation software processing using simulated data.

6.5.2. Temperature Correction

Luna developed the algorithms necessary to compensate for the temperature induced changes to irradiated fibers within the fiber optic probe.

Using the temperature fiber's Rayleigh backscatter, temperature shifts at points along the length can be used with the corresponding signals from the gamma flux and neutron fluence fibers.

The temperature correction improves the radiation calculation by reducing temperature induced shift in the Rayleigh backscatter.

The temperature correction algorithm was incorporated into the data acquisition software.

The algorithm increases the signal to noise ratio of the radiation measurement.

Simulated data sets from the three fiber types were used to test the software.

Figure 2 shows the user interface features of the temperature correction functionality of the data acquisition software.

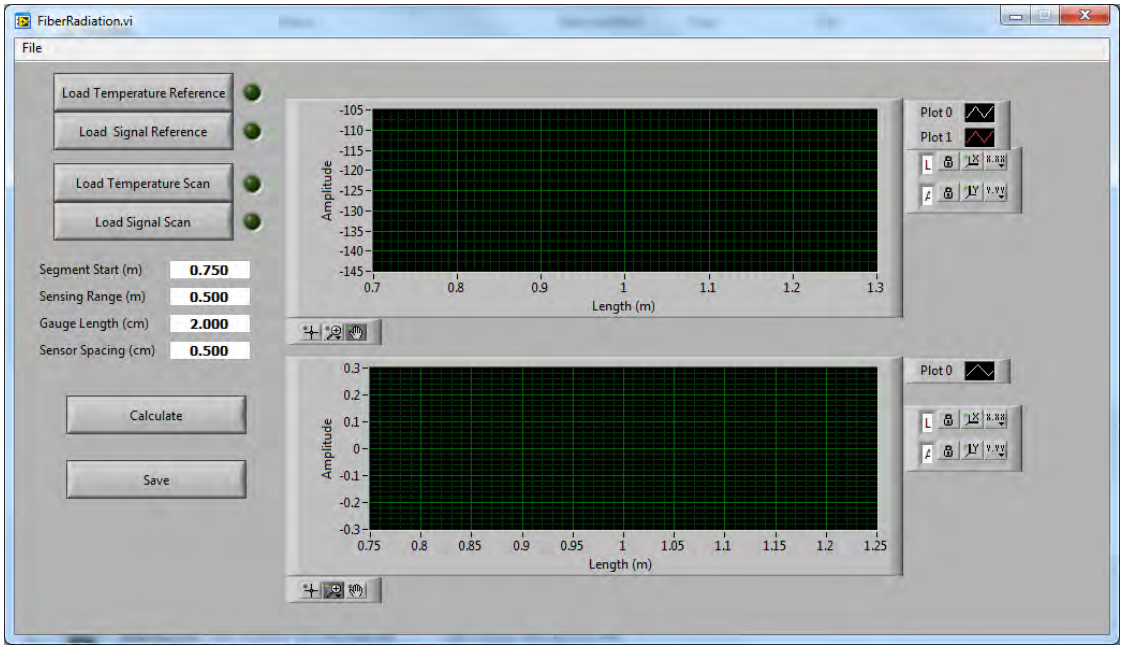

Fig. 2. Temperature correction functionality in the data acquisition software interface.

The user can select the reference files for the temperature and the radiation fibers. Once the references are set, the measurement scan can be loaded and a radiation calculation can be found. The user also can control the location and length of the measurement, as well as spacing and sampling. This process improves the signal quality and manages the memory needed for the calculation.

Luna used simulated data to develop the software for interrogation of the probe. The software simulates both the temperature and radiation induced changes to the backscatter location and levels.

Figure 3 shows the simulation software with a simulated return signal from a distributed temperature sensing fiber and a radiation sensing fiber. The top three graphs in Fig. 3 show the simulated reference, measurement, and calculated temperatures from the simulated temperature sensing fiber. The bottom three graphs represent the simulated radiation reference, measurement, and calculated radiation profile. The bottom right graph shows both the calculated radiation profile before correction (red) and after correction (white). This showed a simulated 4 dB improvement to the precision of the measurement. Additional simulated factors such as low power signal, temperature mismatch, and temperature signal integrity are to be accounted to improve the algorithm robustness as well as provide bounds on the accuracy of the measurement.

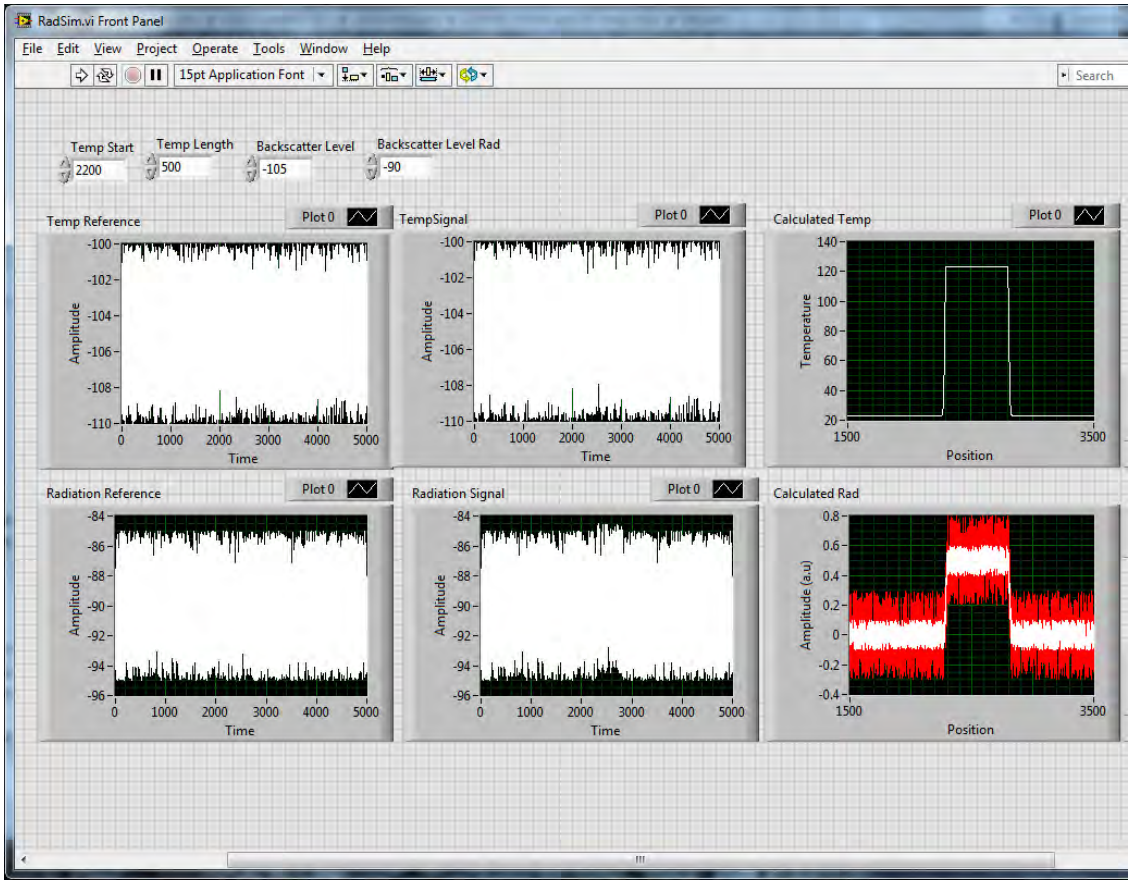

Fig. 3. Temperature correction software with a simulated return signal from a distributed temperature sensing fiber and a radiation sensing fiber.

6.6. Fiberoptics Sensor Hardware Manufacturing

Luna has delivered several sensing fibers and provided Texas A&M sensing lengths as the needs developed. Luna finalized the design, manufactured, and delivered two sensing probes. Figure 1 shows the four quartz ferrules ready to be put in the niobium fixture.

Building of the second probe has progressed quickly learning from the first probe delivered to TAMU. Better termination and more robust fabrication were done for the second probe to lower any variability and ensure safe transport of the distributed sensing probe. The four ferrules are affixed in the niobium then set the fibers in the pressure fitting. Setting the fibers in the aluminum pressure fitting first caused to sensing fibers to break during manufacturing stages for the first probe. Once this is in place, the probe was tested up to the 800 kPa and held to monitor any leakage through the pressure fitting.

Scans were taken at the end of the probe manufacturing process and compared to the initial scan. These scans were shared with the TAMU team for base-line readings.

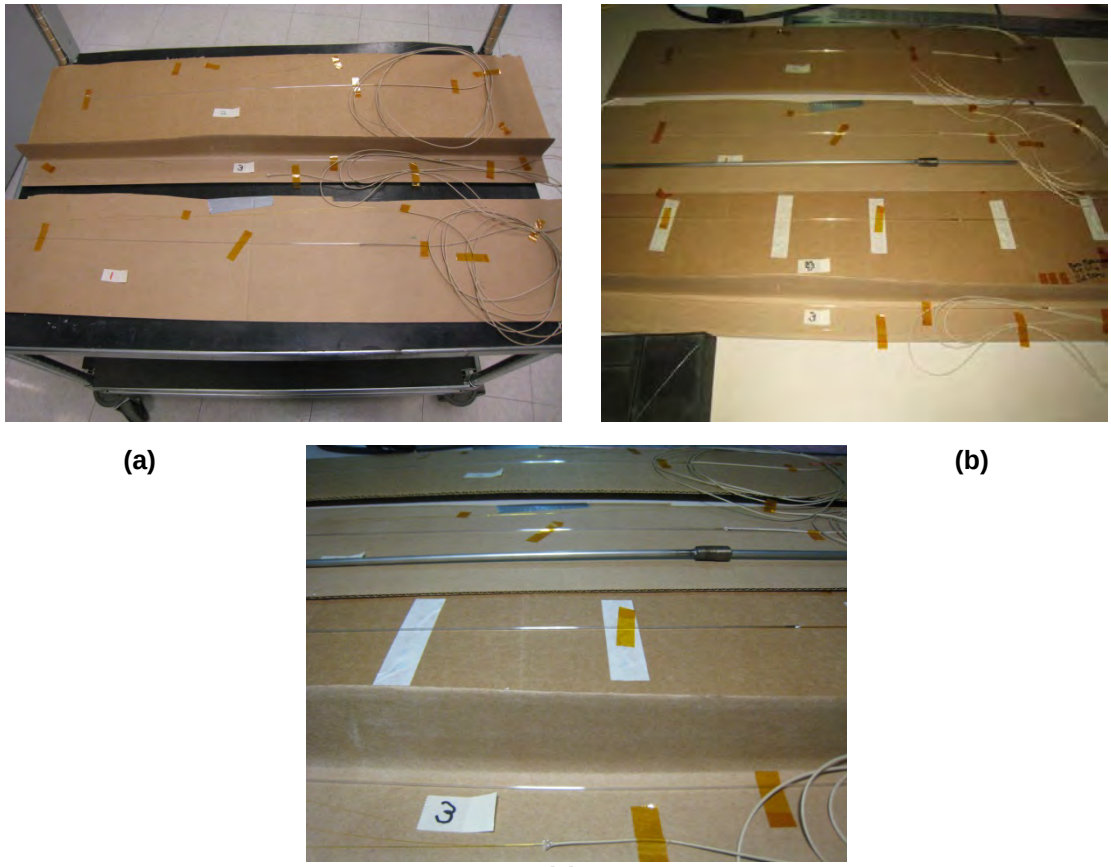

(a) (b) (c)

Fig. 1. (a) Three of the fully populated four- bore quartz ferrules. (b) The four-bores with the niobium tube. (c) Close up of the ferrules and niobium tube.

The first step done in building the probe was stripping the coating off of each fiber. Chemical stripping methods were used to prevent mechanical degradation of the optical fiber. The acrylate coating was removed with an acetone bath for several hours. The polyimide coating was removed after a short period of time in a hot sulfuric bath.

The fibers were spliced to a short interrogation lead and cut to length. After being cut, the optical fibers were then terminated at the distal end to minimize any reflections.

The neutron sensing fiber was cut long to maintain the 0.6m sensing length due to the increased scatter profile at the splice that can be used to sense neutron fluence.

Figures 2 through 4 show the fiber terminations used and their effects on signal processing and sensing performance. In Fig. 4, the splice is seen near the red cursor and the evident intensity loss at that location. This is due to the fusion process depleting the sensing fiber's dopant. The loss of dopant in that area limits the sensing over the depletion zone. The length of the neutron sensing fibers was increased to put the depletion zone outside of the 0.6m sensing length in the probe. After termination the fibers were fed into the quartz four bore ferrules. The bore size was

chosen so that the splice capillary protecting the splice location would slide through. Figure 5 shows the quartz ferulle and the lead side of the sensing fibers.

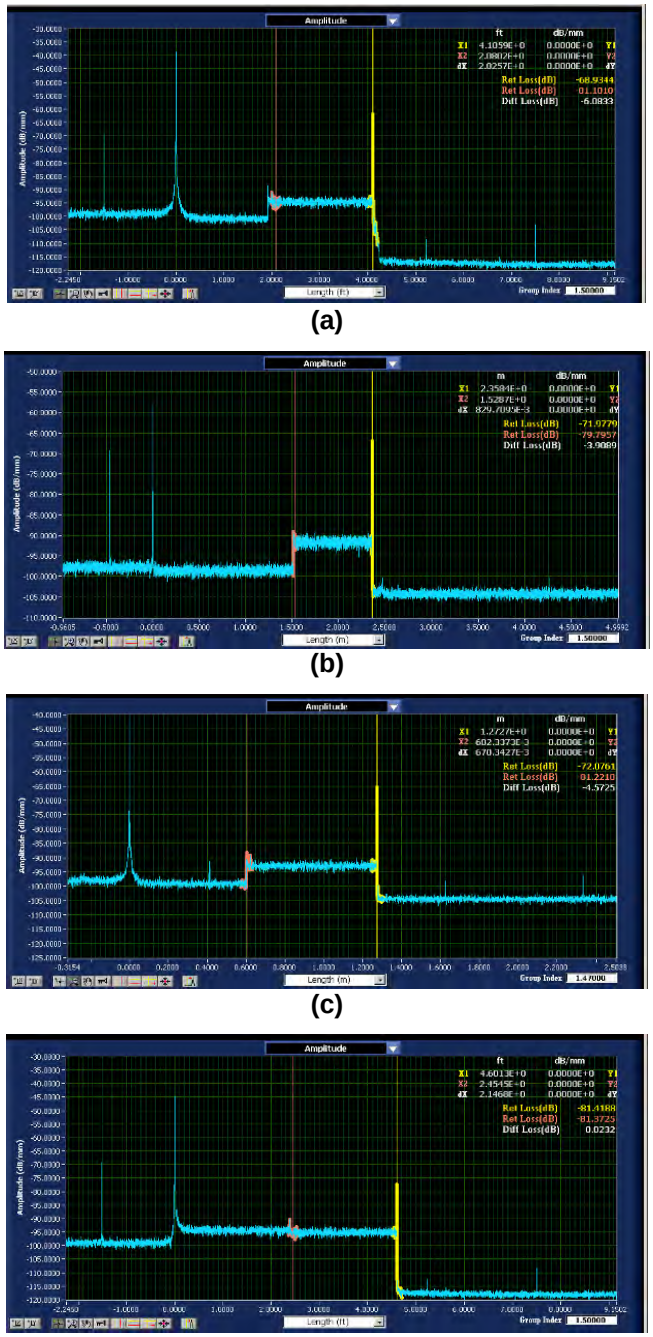

Fig. 2. Gamma sensing optical fiber terminations.

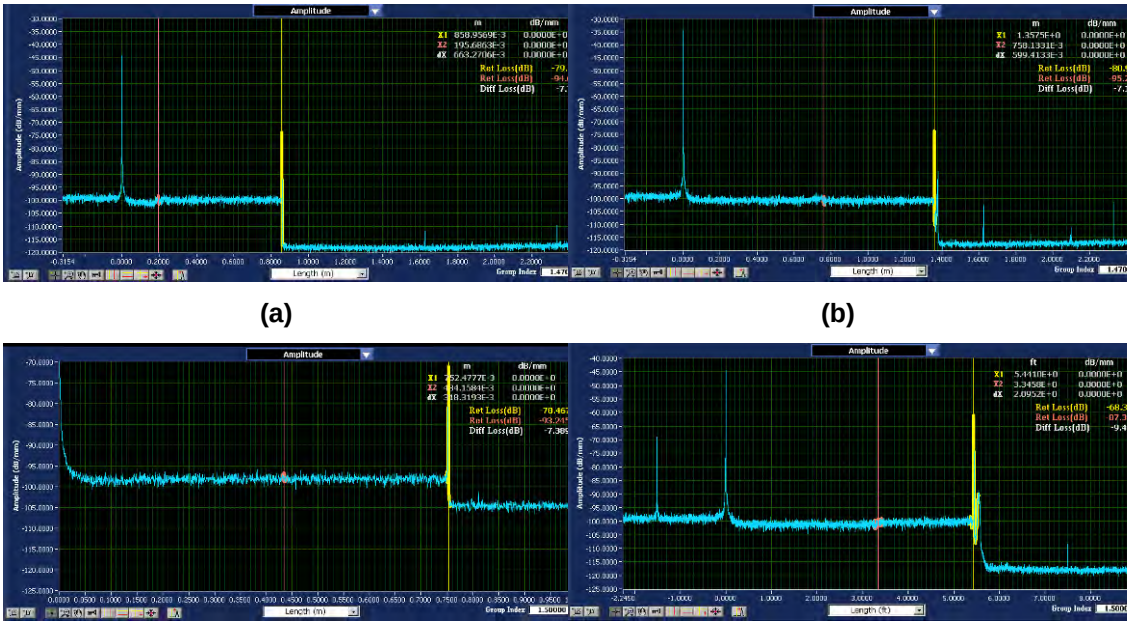

Fig. 3. Temperature sensing optical fiber termination.

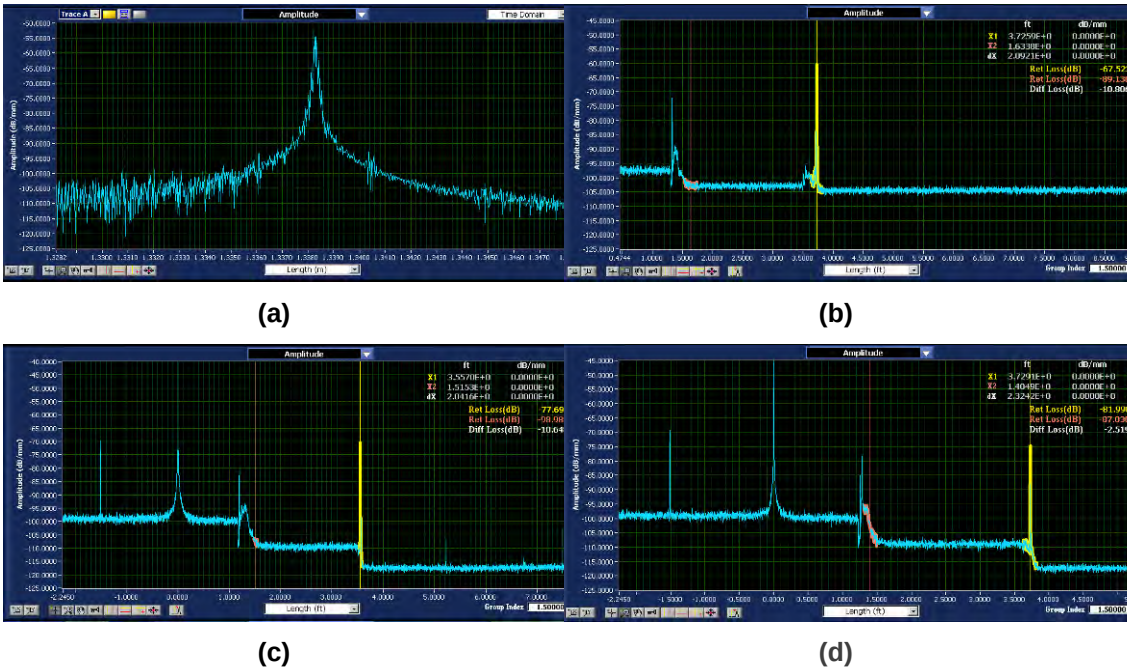

Fig. 4. Neutron sensing optical fiber termination, (a) is zoomed in on one of the terminated tips.

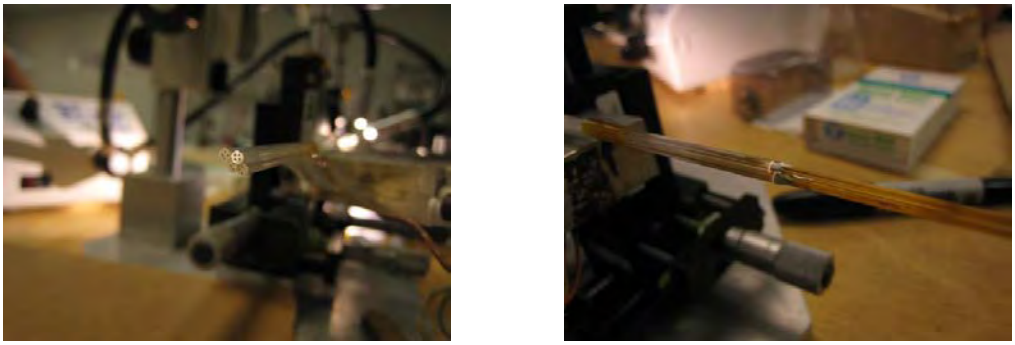

(a) (b)

Fig. 5. (a) Distal end of the quartz capillaries, (b) lead side with sensing optical fibers.

The capillaries were held in place with MS-907. Once the four capillaries were fully populated they were slid into the weld niobium tube. The tube is shown in Fig. 6.

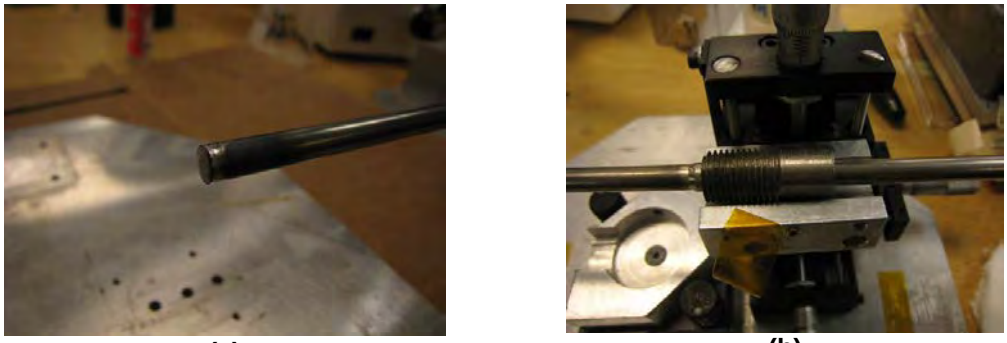

(a) (b)

Fig. 6. (a) Welded niobium tip, (b) welded niobium 1/4 NPT fitting.

The sensing portion was then spliced to the pressure transition portion of the Distributed fiber optic probe. The fibers were then potted into the aluminum pressure fitting with MS-907.

Figure 7 shows the fibers before potting.

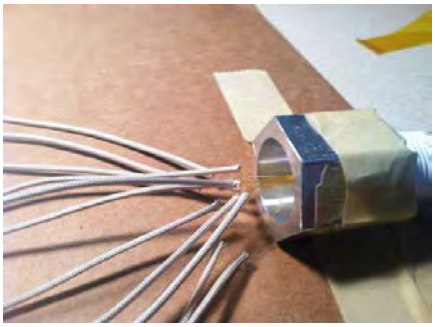

Fig. 7. Fibers through the pressure fitting before potting.

After the 907 was cured the probe was pressure tested in an aluminum pressure tube designed for high pressurization shown in Fig. 8.

Fig. 8. Pressure testing tube.

The pressure was slowly brought up to 800 kPa and held for 20 minutes to see if there was any drift in pressure. Leak detection liquid was used to see if there were any pressure leaks, none were found and pressure held.

The fiber bundle was then place in the large fiberglass sheath and then drawn through the corrugated stainless steel tube.

The corrugated tube was then epoxied to the pressure fitting to provide a strain point as well as minimize the galvanic response between the stainless steel and the aluminum fitting.

The optical fibers were checked again at this point and three of the twelve sensors had failed at the pressure fitting. The three broken sensors were two Gamma and one Neutron sensing fibers. The probe was then boxed and shipped to TAMU.

6.7. Fiberoptics Sensor Hardware Testing

6.7.1. Preface

The testing of the fiber probes was performed as a quality assurance test. Having the data obtained by Luna Incorporated as reference, it was then possible to determine the broken fibers from the healthy one. A total of three testing series were performed on each component of the fiber probes.

6.7.2. Introduction

Luna Incorporated, before shipping the fiber probes, conducted an analysis on each fiber optic sensor for each probe.

They concluded:

- The first fiberoptics probe (FP-1) had some damaged fiber sensors (two gamma and one neutron) and
- The second fiberoptics probe (FP-2) was fabricated properly and all fibers were functioning to their specifications.

The probes were stored differently for shipment purposes.

As a result, the first probe ended up outside of the massive shipping box and the other remains stored within its packaging safely.

Each of the probes carries 12 fibers (4 neutrons, 4 temperature and 4 gammas). FP-2 was considered to be the final product in terms of quality of the prototype concept.

The testing configurations were conserved throughout the testing and were at a resolution small enough to provide rapid measurements and large enough to reduce the noise in the testing.

These configurations were as follows:

- Center wavelength: 1550.50 nm
- Wavelength Range: 10.52 nm
- Gain: 6dB (decibel)
- Spatial Resolution: 0.100 mm
- Integration width: 0.010 m
- Shift resolution: 0.010 cm

The Optical Backscatter Reflectometer (OBR) optical system was aligned and calibrated prior to testing to avoid any indiscriminate errors.

6.7.3. Reference Data

The reference data were obtained by Luna Incorporated. These were used as a reference in comparisons with TAMU results. The numbering system was made in accordance to the probes numbering as determined by Luna end-product markings.

Figure 1 shows the return loss profile of the temperature fiber. The sensing location starts roughly at 10.9 m.

The transition from the lead-on fiber optics to sensing for the temperature fiber is smooth, suggesting that there is no splice and therefore fiber optic failure is not expected to occur due to mechanical problems within temperature sensing fiber optics.

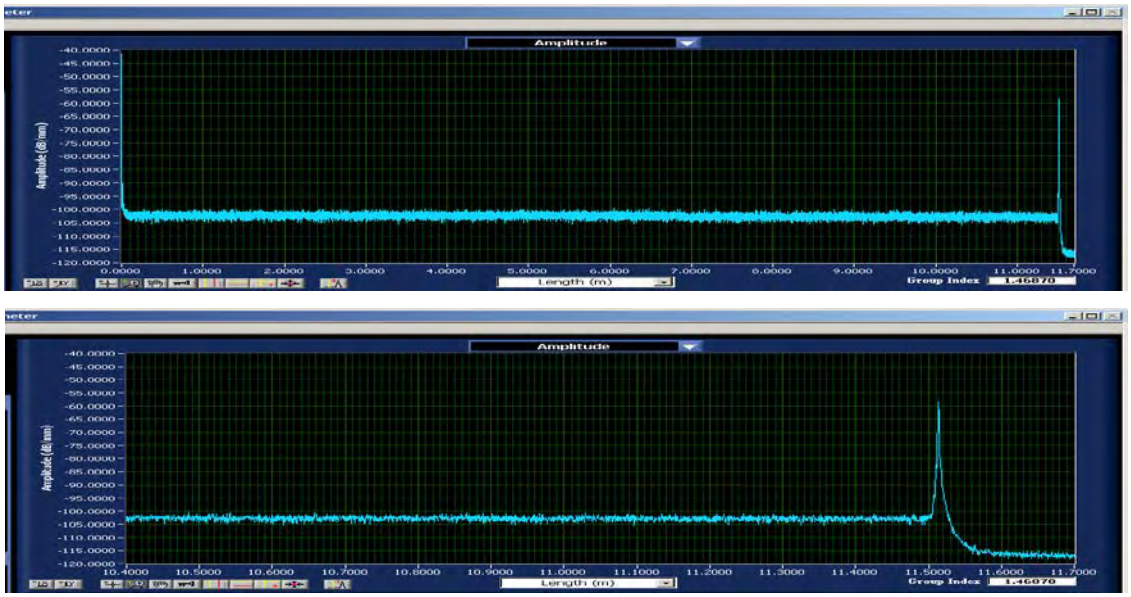

Fig. 1. Temperature 1 (1T).

Figure 2 shows the transition for the lead-on to the gamma sensing portion. This demonstrates a higher return-loss plateau than in the temperature fiber, which is a fairly distinguishing feature.

Fig. 2. Gamma 2 (2G).

Figure 3 shows the features for the neutron sensing fiber. The splice location can be seen clearly at 10.75 m with a smaller return loss for the sensing portion of the fiber.

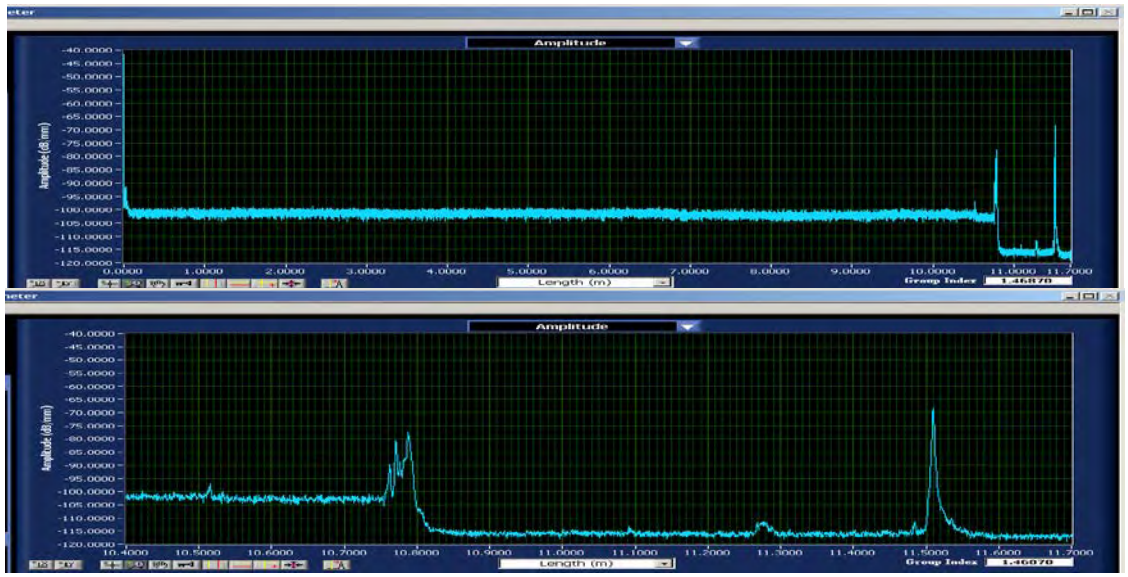

Fig. 3. Neutron 3 (3N).

Upon analyzing the data obtained by Luna, the transition from pressure transition to sensing is very particular for the three fiber types:

- **For neutron**,
  the transition is done through a shift or decrease of amplitude, from ~ -100.000 dB/min to ~ -110.000db/min. Although significant noises are observable, the transition is observable, a reason good enough to conclude that the neutron fiber is working.
- **For gamma**,
  the transition is done smoothly with an increase of amplitude f from ~ -100.000 dB/min to ~ -90.000db/min. Compared to neutrons, no noise is observed throughout the transition. So far as a shift of amplitude is observed presenting that the sensing section of the probe, it can be concluded that the gamma fibers are working.
- As for the **temperature fiber**,
  no transition is observed since the fiber runs all the way. Therefore, observing any change would be a sign of dysfunction.

6.7.4. Obtained Data and Analysis

FP-1: FIBER PROBE 1. The measured data were obtained and marked as follows: 12N – healthy neutron fiber, 11T – healthy temperature fiber, 10G – healthy gamma fiber, 9N – healthy neutron fiber, 8T – healthy temperature fiber, 7G – healthy gamma fiber, 6N – broken neutron fiber, 5T – healthy temperature fiber, 4G – broken gamma fiber, 3N – healthy neutron fiber, 2T – healthy temperature fiber, 1G – broken gamma fiber. Figure 4 provides an overview of these measured sensor profiles:

- **12N (Healthy Fiber).**
  This neutron fiber is in preferred working condition. All the characteristics of a working neutron fiber are present, more importantly the change and decrease of

amplitude and the peak presenting the transition from the pressure transition and the sensing part.

- **11T (Healthy Fiber).**
  No loss is observed throughout the fiber. This temperature fiber is in preferred working condition.

- **10G (Healthy Fiber).**
  This gamma fiber is in preferred working condition. An increase of amplitude introduced by a peak presenting the transition from pressure transition and sensing section is observed. Unlike the reference gamma fiber, there is a questionable peak observed between the lead out and sensing section. More importantly, so far as the sensing section of the fiber is detectable, it can be concluded that this fiber is healthy.

- **9N (Healthy fiber).**
  Fiber neutron -9 is in preferred working condition since it presents all the characteristics of a working neutron fiber, presented by Luna.

- **8T (Healthy Fiber).**
  This fiber is healthy and does not present any loss.

- **7G (Healthy Fiber).**
  This gamma fiber is in preferred working condition as directed by Luna Incorporated.

- **6N (Broken Fiber).**
  This neutron fiber is broken. It behaves like a temperature fiber and present a damaged sensing section.

- **5T (Healthy Fiber).**
  This temperature fiber is in preferred working condition as directed by Luna Incorporated.

- **4G (Broken Fiber).**
  This gamma fiber is broken. Despite the presence of the splice following the OBR connection, presenting the beginning of sensing section, no increase of amplitude is present, a sign of a broken fiber. This fiber will therefore be of no use to the DOE project.

- **3N (Healthy Fiber).**
  This neutron fiber is in preferred working condition as directed by Luna Incorporated.

- **2T (Healthy Fiber).**
  This temperature fiber is in healthy condition despite the presence of a questionable splice between the lead out connection (from the OBR to the probe) and the end of the probe.

- **1G (Broken Fiber).**
  This gamma fiber is broken and would be of no use. First of all, this fiber is shorter than suppose to, 11.5m instead of 8m, and secondly, it doesn't present any change in amplitude presenting the beginning of the sensing section.

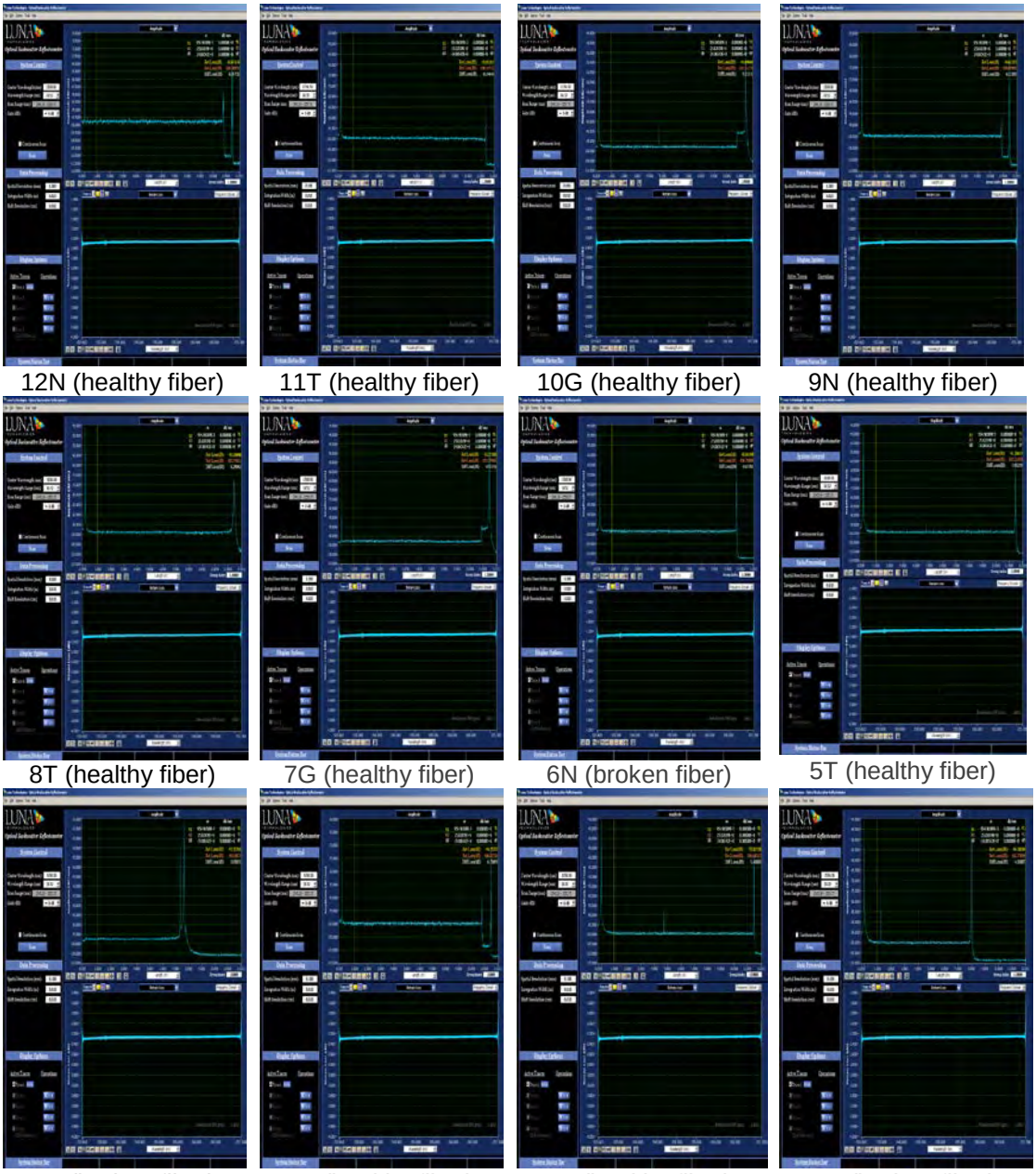

Fig. 4. Fiberoptics sensor profiles of FP1.

FP-2: FIBER PROBE 2. The measured data were obtained and marked as follows: 7T – healthy temperature fiber, 8G – healthy gamma fiber, 9N – broken neutron fiber, 10T – healthy temperature fiber, 11G – healthy gamma fiber, 12N – healthy neutron fiber, 1T – healthy temperature fiber, 2G – healthy gamma fiber, 3N – healthy neutron fiber, 4T – healthy temperature fiber, 5G – healthy gamma fiber, 6N – broken neutron fiber.

Figure 5 provides an overview of these measured sensor profiles:

- **7T (Healthy Fiber).**
  This temperature fiber is in healthy in accordance to the direction of Luna Incorporated.
- **8G (Healthy Fiber).**
  This gamma fiber is in preferred working condition as directed by Luna Incorporated.
- **9N (Broken Fiber).**
  This neutron fiber is broken. It behaves like a temperature fiber and present a damaged sensing section
- **10T (Healthy Fiber).**
  This temperature fiber is in preferred working condition as directed by Luna Incorporated.
- **11G (Healthy Fiber).**
  This gamma fiber is in preferred working condition as directed by Luna Incorporated.
- **12N (Healthy Fiber).**
  This neutron fiber is in preferred working condition as directed by Luna Incorporated.
- **1T (Healthy Fiber).**
  This temperature fiber is in preferred working condition as directed by Luna Incorporated.
- **2G (Healthy Fiber).**
  This gamma fiber is in preferred working condition as directed by Luna Incorporated.
- **3N (Healthy Fiber).**
  This neutron fiber is in preferred working condition as directed by Luna Incorporated.
- **4T (Healthy Fiber).**
  This temperature fiber is in preferred working condition as directed by Luna Incorporated.
- **5G (Healthy Fiber).**
  This gamma fiber is in preferred working condition as directed by Luna Incorporated.
- **6N (Broken Fiber).**
  This neutron fiber is broken.

It is important to note that the reference data set was obtained from Luna Incorporated when testing the Fiber probe 2. They were all assumed to be in preferred working condition, but unfortunately two neutron fibers were perceived as damaged and not in working condition. They are neutron 6 and neutron 9. Luna presented these fibers as characteristic of neutron fibers but upon testing them, it was concluded that they were both behaving as temperature fibers; no decrease in amplitude presenting the transition from the pressure transition to the sensing section of the probe. The most likely explanation for the discrepancy is the damage during delivery despite all efforts and precautions made and built into the probe packaging.

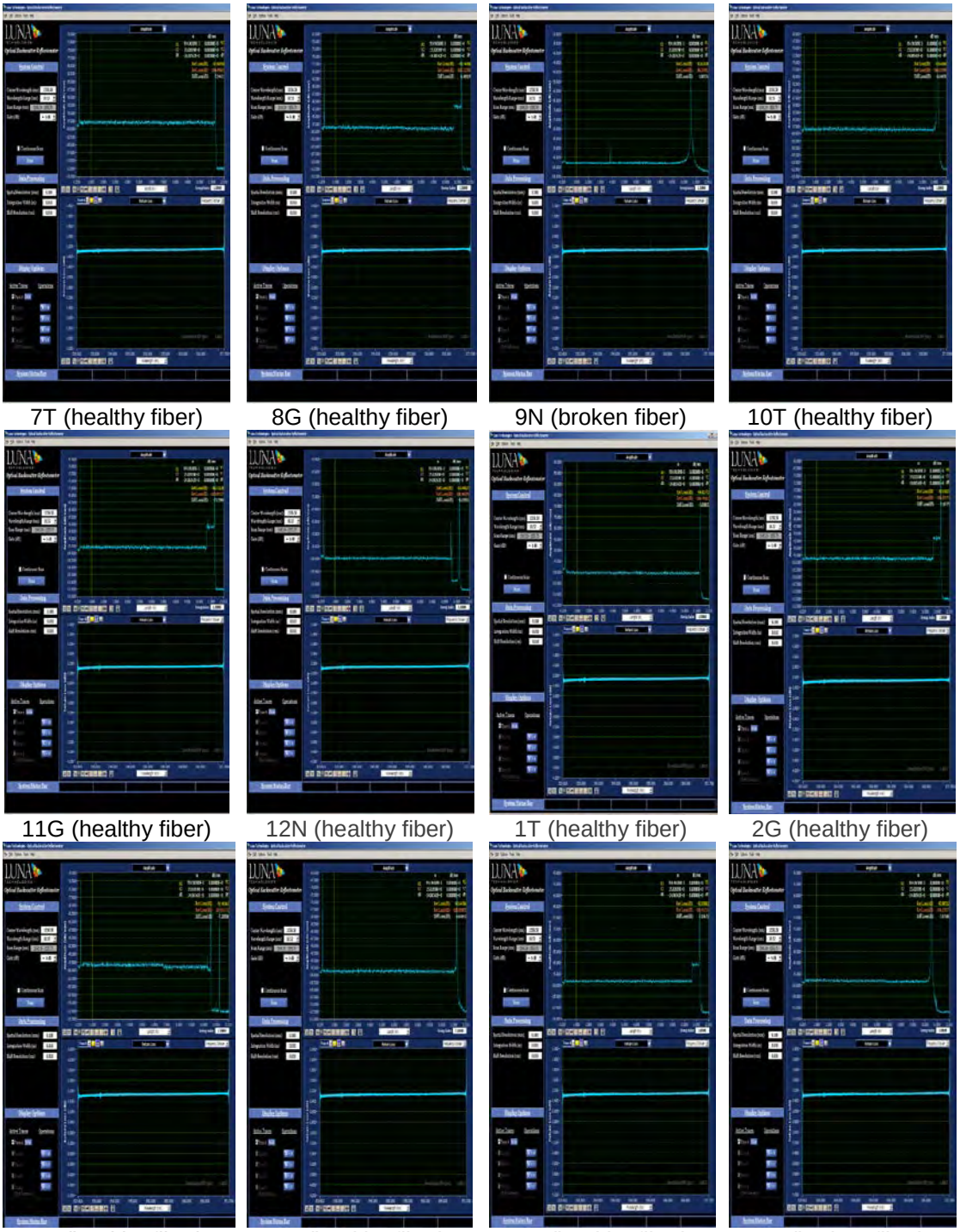

Fig. 5. Fiberoptics sensor profiles of FP2.

The Fiber probe 1 data set was as determined by Luna Incorporated. Following their testing, 3 fibers were determined faulty and broken, 2 gammas and 1 neutron, which is exactly what was determined upon TAMU testing; the broken fibers are gamma 1, gamma 4 and neutron 6.

These evaluations of fiber sensor response profiles in the probes 1 and 2 served as the quality assurance basis in the project as well as the fiber sensor characterization basis. Table 1 summarizes the reported findings from performance studies. Although several fibers were determined as damaged and not available for use, the remaining fibers are of expected operational conditions and will be capable to carry the probe functionality in the project experimental program. Extremely challenging manufacturing and delivery of the probes have led to unintended damage of some of the sensors. The project serves as an important first step in determining needed manufacturing and delivery procedures for potential follow-on efforts by TAMU and Luna. Independent fiber sensor characterization procedures and tests by Luna and TAMU assure minimized error during the production process and delivery.

Table 1. Functional State Evaluation Summary of Fiber Probe 1 and fiber Probe 2

Probe	Sensor	Healthy	Faulty or Broken
FP1	gamma -1		X
	temperature - 2	X	
	neutron - 3	X	
	gamma - 4		X
	temperature - 5	X	
	neutron - 6		X
	gamma - 7	X	
	temperature - 8	X	
	neutron - 9	X	
	gamma - 10	X	
	temperature - 11	X	
	neutron - 12	X	
FP2	temperature - 1	X	
	gamma - 2	X	
	neutron - 3	X	
	temperature - 4	X	
	gamma - 5	X	
	neutron - 6		X
	temperature - 7	X	
	gamma - 8	X	
	neutron - 9		X
	temperature -10	X	
	gamma -11	X	
	neutron - 12	X	

6.7.5. Conclusions

There are two gamma fibers and one neutron fiber that are not working properly in FP-1. This corresponds with previous Luna testing results conducted during the fabrication process. There are two neutrons fibers that are not working properly in FP-2. This deviates from the Luna testing, so likely these fibers did not survive the transportation.

These evaluations of fiber sensor response profiles in the probes 1 and 2 served as the quality assurance basis in the project as well as the fiber sensor characterization basis. Table 1 summarizes the reported findings from performance studies.

Although several fibers were determined as damaged and not available for use, the remaining fibers are of expected operational conditions and will be capable to carry the probe functionality in the project experimental program.

6.8. Vibration Testing

6.8.1. Summary

The spatially continuous instrumentation technology has been developed in recent years to provide a unique capability to measure continuous 1D temperature distributions. Unlike traditional measurement approaches for a finite location, fiberoptics-based instrumentation approaches allow acquiring unidirectional continuous 1D temperature data.

Inherently, any material structure will expand during temperature changes within its components. Fiberoptics-based measurements take advantage of this phenomenon by using spectral backscatter analysis to determine the strain induced within a fiber as a result of such an expansion. Consequently, any geometrical changes in fibers will induce corresponding strain changes in the fiberoptics-based instrumentation system.

As part of the studies performed within the framework of this project, it was investigated whether this behavior has a potential to significantly affect the measurement accuracy and, furthermore, to what extent the vibrations might affect coupling joints. It was demonstrated that certain vibrations will impact the measurements.

6.8.2. Introduction

The spatially continuous instrumentation technology has been developed in recent years to provide a unique capability to measure continuous 1D temperature distributions.

Unlike traditional measurement approaches for a finite location, fiberoptics-based instrumentation approaches allow acquiring unidirectional continuous 1D temperature data.

Inherently, any material structure will expand during temperature changes within its components. Fiberoptics-based measurements take advantage of this phenomenon by using spectral backscatter analysis to determine the strain induced within a fiber as a result of such an expansion.

Consequently, any geometrical changes in fibers will induce corresponding strain changes in the fiberoptics-based instrumentation system.

The vibration effects on measurement accuracy levels were seen to be a significant factor in previous testing efforts for fiberoptics-based instrumentation systems.

The expected operational environment for the fiberoptics sensors is within the reactor core. Under nominal, steady-state conditions, there are numerous components and phenomena contributing to in-core vibration effects, namely:

- coolant flowing through coolant channels and assemblies,
- massive 10MW pumps,
- overall geometry and features of the primary system,
- internal surface conditions,
- inlet and outlet conditions,
- other.

With the measurement systems distributed throughout the reactor, all these vibrations can be expected to impact the fiberoptics-based systems.

The objective of the present analysis is to determine, based on the operating conditions of the Nuclear Science Center TRIGA facility and other support equipment, whether vibration measurement errors can be expected, tolerated, or even avoided.

6.8.3. Vibration Effects on Fiberoptics Temperature Measurements

The effects of various components, which are present in the experimental setup of the high temperature test system to assess fiberoptics performance emulating VHTR-conditions in the TRIGA reactor core, are examined.

These components are:

- turbo and scroll pumps,
- computer, and
- power supply.

The computer and power supply have fans and it is assumed that their operation is enough to perturb the data measured with fiberoptics sensors.

The present vibration testing efforts are focused on temperature sensing fivers due to streamlined options for testing and validation. It is expected that vibration-induced effects in fiberoptics sensors should be common for all types of fibers.

The 10 m temperature sensing fiber was chosen to facilitate flexibility in arranging the geometry. There are two segments of 1 m regular optical fiber, which would bring the total length of the fiberoptics to 12 m. The system includes 2 couplers, one of which is used in the vibration testing. The fiberoptics sensor was not attached to anything that might cause internal stresses during the temperature variation, except to retain its bundled geometry.

The temperature measurements were monitored while saving the data. The based measurements were taken in the ice, so that temperature rise of the bath would not affect the measurements. The tests were commenced after a waiting period to ensure all the water had evaporated from the fiber.

Additional data were taken to quantify return losses at the points of interest. For example, during the vibration testing on the coupler, the return loss at the coupler was monitored - the fiber measurement area was not, until that area is tested.

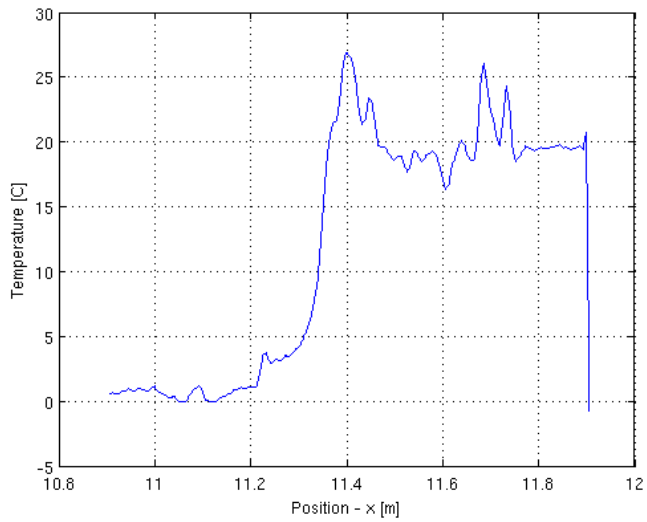

Fig. 1. Control measurements illustrating temperature variations and the maximum temperature difference of 26ºC.

Care was also taken to ensure that there were no bends of less than 4" radius. All couplings were cleaned. The system was calibrated according to the OBR manual. The calibration was further checked with subsequent scans prior to the tests.

There were several groups of vibration tests:

- With temperature change (the fiberoptics sensors settled in an ice bath, then removed), the fiberoptics sensor was introduced to vibrations from the scroll pump, and then, subsequently, from the turbo and scroll pumps, and then from the power supply.

  This group of tests illustrates signal noise levels and measurement differences based on the actual temperature measurement data and the resulting accuracy changes.

- With temperature change, the fiberoptics sensor was introduced to vibrations from the scroll pump, then, subsequently, from the turbo and scroll pumps, and then from the power supply.

  This group of tests illustrates signal noise levels and measurement differences based on the controlled vibration test.

The system setting were - he gain was set to 12 dB, and the wavelength range was set to the maximum setting of 42 nm.

Since the fiberoptics sensor was coiled in the ice bath, some portions were closer to the surface than others. It is not expected that a completely uniform temperature would be achieved.

With the first scan, Figure 1 shows the maximum difference of 26°C from zero to room temperature. This agrees to the independent room temperature measurement of 26.1^{o}C.

Scroll Pump

The scroll pump is inherently the main source of vibration in the entire experimental setup. The vibrations are of a fairly low frequency, about 20 Hz or so. The pump sits in the rig and is not supported in any way other than with gravity.

Figure 2 illustrates the effects of vibrations in the actual signal distribution. There are apparent, well-defined, fluctuations at 2 m, which corresponds to the coupler location, and at the end of the fiber.

The blue line in Fig. 2 indicates the control back scatter signal without any vibration effects.

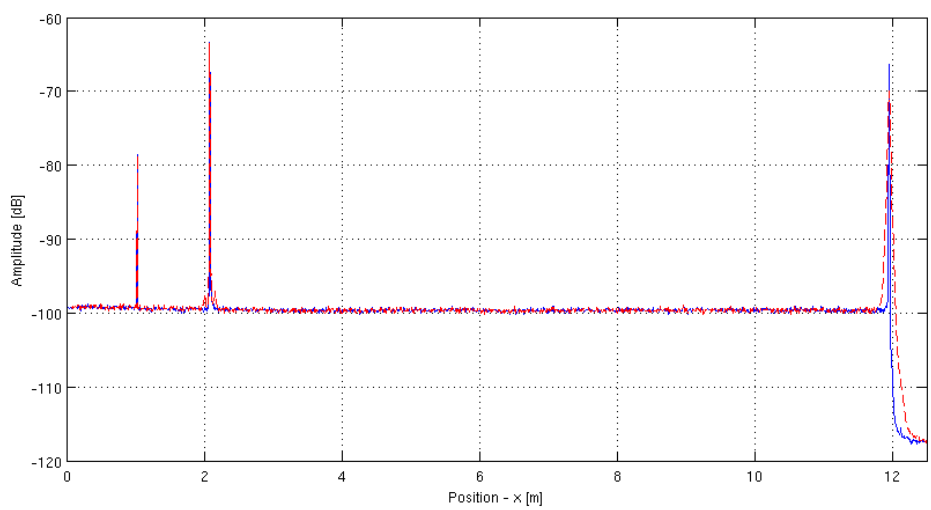

Fig. 2. Back scatter signal with the scroll pump in operation.

Figure 3 zooms in on the coupler location. There is a waveform distribution in the signal. This feature is likely to be induced because of reflection effects and signal losses as the coupled fibers misalign as a result of vibrations.

One might question, since the fiberoptics coupler was completely isolated from the vibration sources, how this might have occurred. The vibration source was turned off and multiple scans were performed to verify that this source was causing the coupler to alter the signal.

It was determined to do just that, and the possible reason for this occurrence is likely from propagating vibration perturbations through the fiberoptics sensor itself. The fiberoptics sensor is made of a glass material. Although there will be some dampening in the sensor core material,

cladding, and surrounding environment, it is possible that vibrations would be capable to reach the coupler through the sensor.

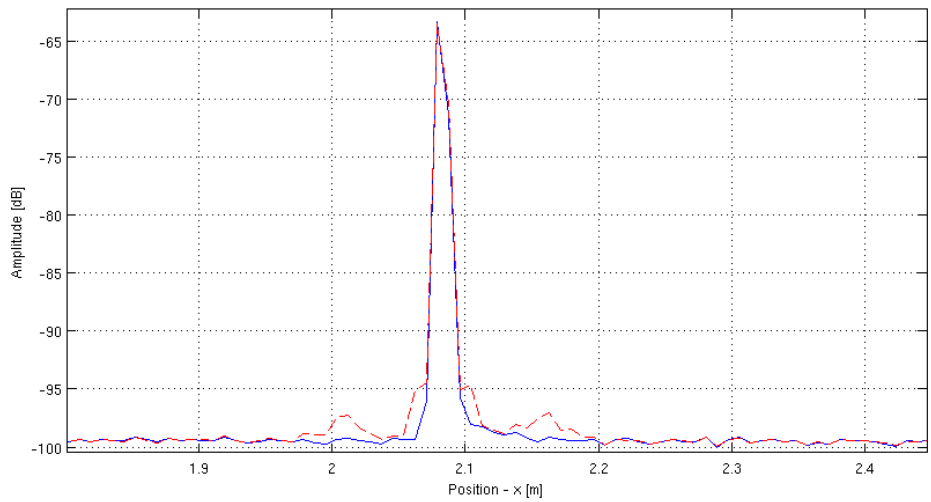

Fig. 3. Scroll pump back scattering signal in the coupler location at 2 meters.

Figure 4 shows a broadening effect in the signal at the fiberoptics sensor end. Because of oscillations in the fiber, one might except that rapid strain changes induce back scatter return losses at the end-location, inducing significant signal depletion.

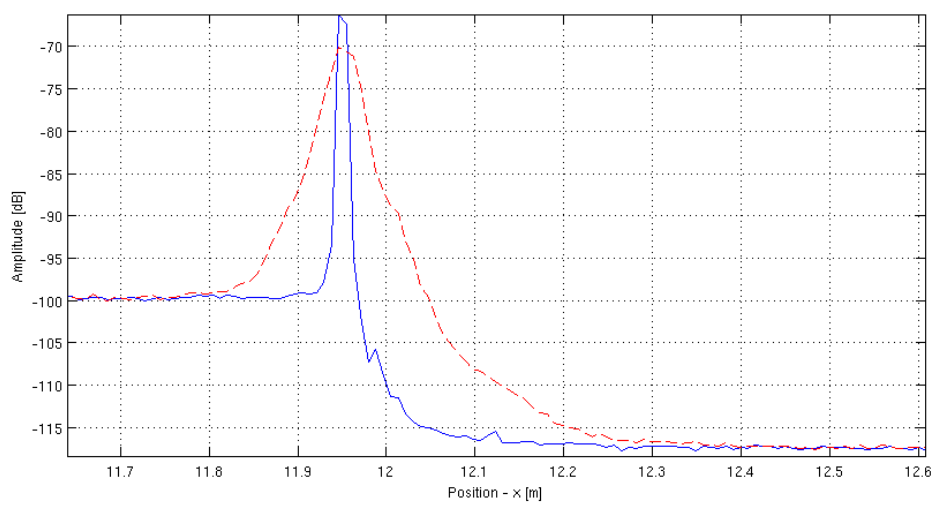

Fig. 4. Scroll pump back scattering signal in the fiberoptics sensor end location.

Figure 5 illustrates significant perturbations in temperature measurements at the tail end of the fiberoptics sensor due to scroll pump induced vibrations. This is most likely due to the fact that the end of the fiber was not secured and allowed to vibrate leading to signal oscillations.

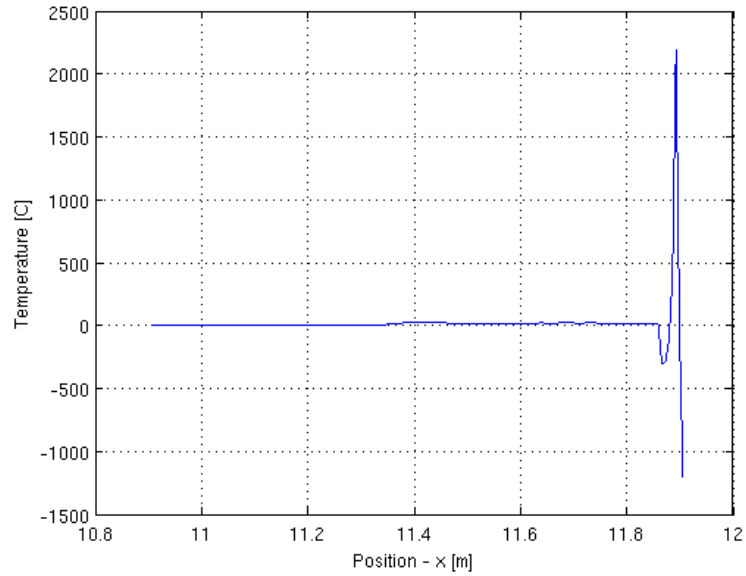

Fig. 5. Perturbations in temperature measurements due to scroll pump vibrations.

Figure 6 shows the control temperature measurement in red and the test measurement in blue. As can be seen, there are only small variations in values between control temperature and test temperature measurements. Thus, it can be concluded that low-level mechanical vibrations are not expected to alter the measured quantities significantly. Most of the observed variations fall likely within the expected ranges of measurement deviations.

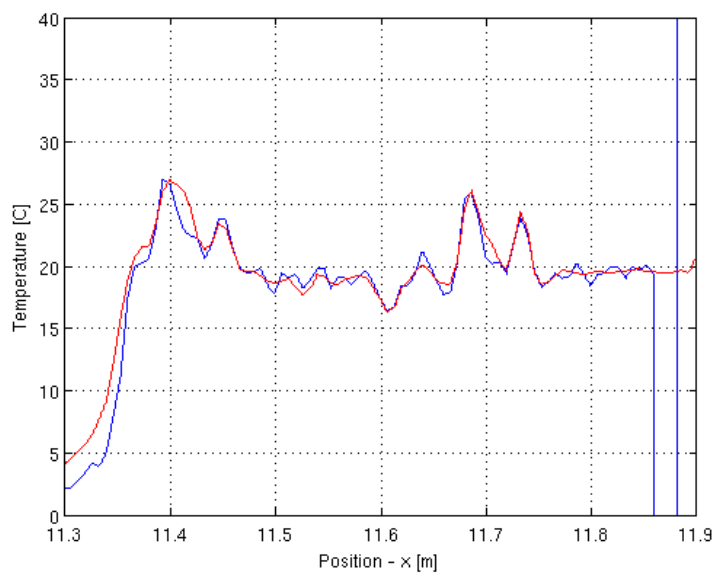

Fig. 6. Control temperature measurements (red) vs. test temperature measurements (blue) with scroll pump vibration effects included.

Scroll Pump and Turbo Pump

The scroll and turbo pump are not able to be isolated as sources of vibration noise effects and measurement accuracy losses. The reason for this is that the scroll pump must keep a sufficiently low vacuum level at the turbo pump exhaust to maintain the proper pressure drop across the turbo pump.

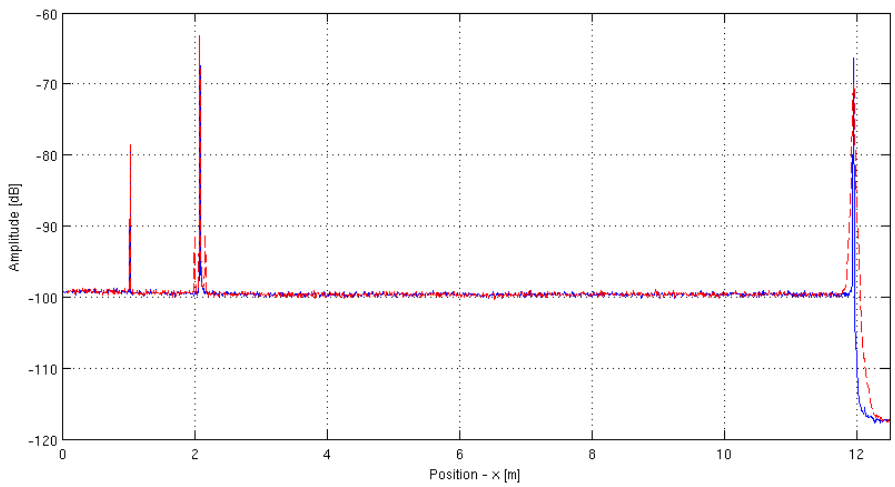

Fig. 7. Back scatter signal with the scroll pump and turbo pump in operation.

In addition to the scroll pump, the turbo pump adds a much higher frequency vibration. Furthermore, there are two high CFM fans that are used to cool the motors. With these, it is likely that the effects might be even greater. However, it might also be the case that the higher frequency operation does not degrade the fiberoptics measurements. It has to be noted that the turbo pump requires vibration isolation.

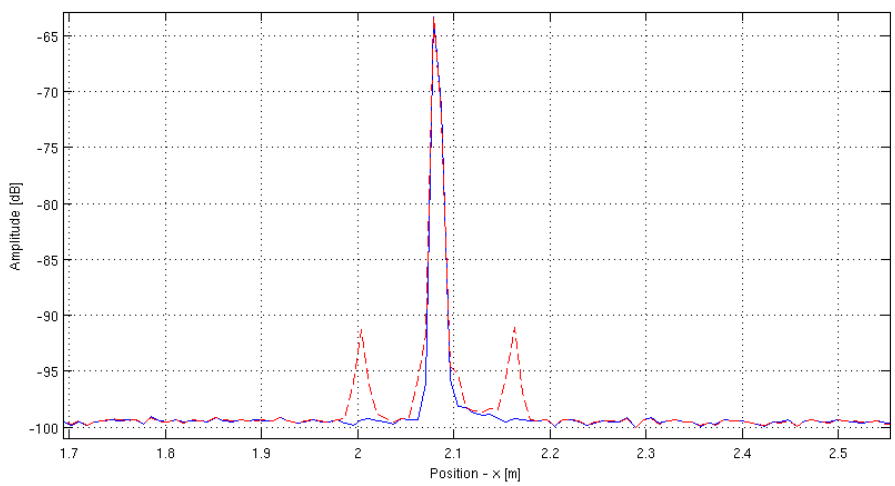

Fig. 8. Back scatter signal in the coupler location at 2 meters with the scroll pump and turbo pump in operation.

Figure 7 shows the signal with both the scroll pump and turbo pump in operation. The signal effects are very similar to the test with just the scroll pump in operation (see Fig. 2). The blue line in Fig. 7 indicates the control back scatter signal without any vibration effects.

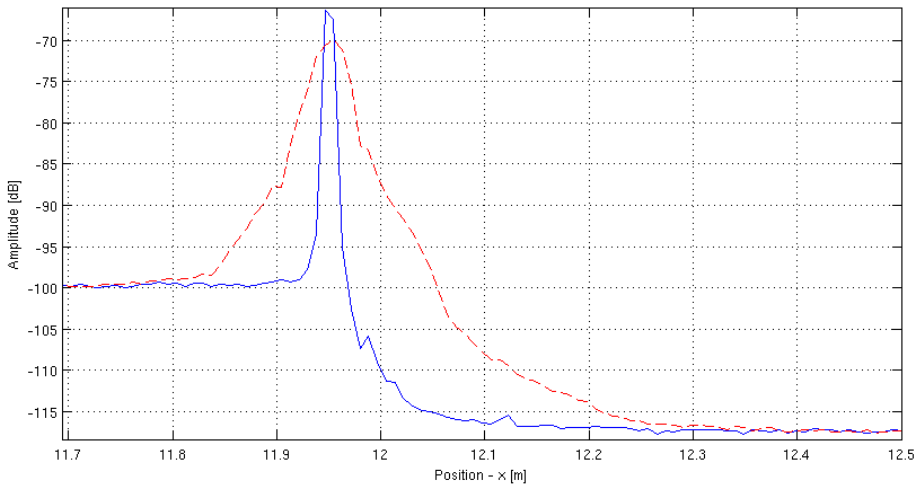

Fig. 9. Back scatter signal in the fiberoptics sensor end location with the scroll pump and turbo pump in operation.

Figure 8 shows the same type of coupler interference as shown in Fig. 3. However, perturbations are visibly larger.

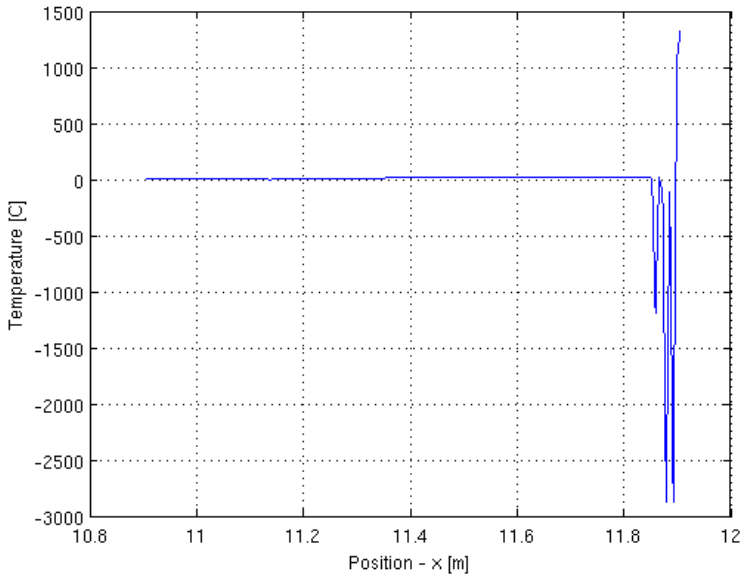

Fig. 10. Perturbations in temperature measurements due to scroll pump and turbo pump.

Similarly, Fig. 9 shows the same type of fiberoptics signal interference in the sensor end location as the one shown in Fig. 4. However, the perturbations are observed to be more significant in Fig. 9.

Figure 10 shows the full temperature measurement. The same peaking that persisted in the previous measurement, as shown in Fig. 5, is evident but with more complex fluctuation profiles.

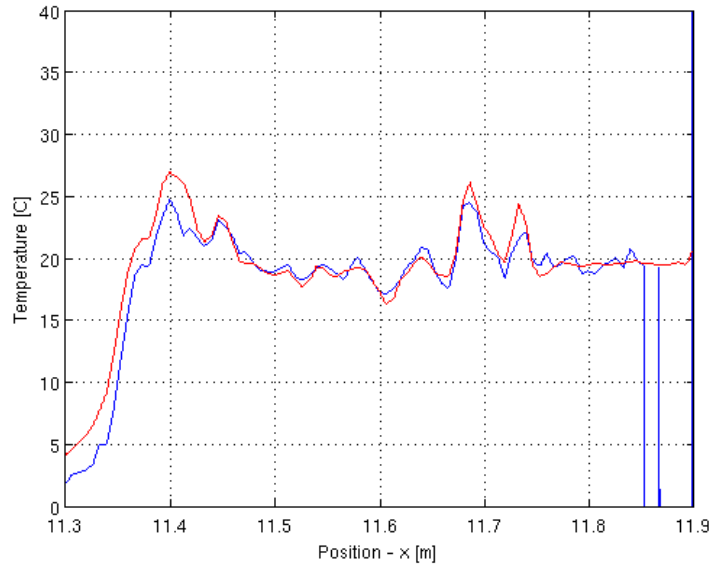

Fig. 11. Control temperature measurements (red) vs. test temperature measurements (blue) with scroll pump and turbo pump vibration effects included.

The same issues from the scroll pump persist with this portion of the test; however, the measurement seems to lose some accuracy by under predicting the temperature with the added higher frequency vibrations, as shown in Fig. 11.

If the bounds of the measurement are contained in Fig. 11, then the temperature profile can be assumed. However, the profile would have to be interpolated between these points and could lead to some fidelity loss.

Power Supply

The power supply is a source of a significant amount of vibration-induced fluctuations. There are two fans within the power supply. These fans increase their flow rate to keep the power supply cool during operation. To assess the resulting effects, test measurements were taken from idle to operation at 30 amps.

Figure 12 shows the back scatter signal under idle power supply conditions. There were no noticeable vibration-induced perturbations at the coupler location. This suggests that either the dampening along the fiber was sufficient, or the magnitude of added vibration induced fluctuations was not sufficient to cause perturbations at the coupler location. The blue line in Fig. 12 indicates the control back scatter signal without any vibration effects.

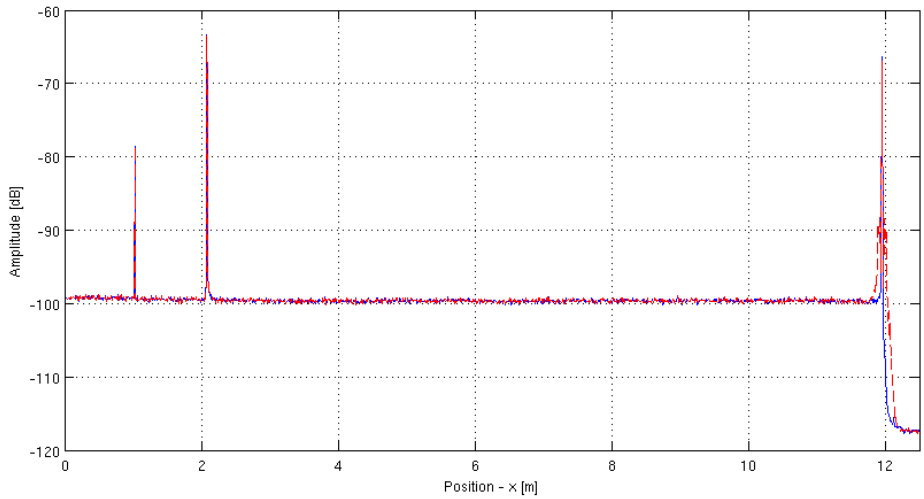

Fig. 12. Back scatter signal under idle power supply conditions.

Figure 13 shows significant signal changes in the sensor end location. The temperature measurement with the power supply in its idle conditions is shown in Fig. 14.

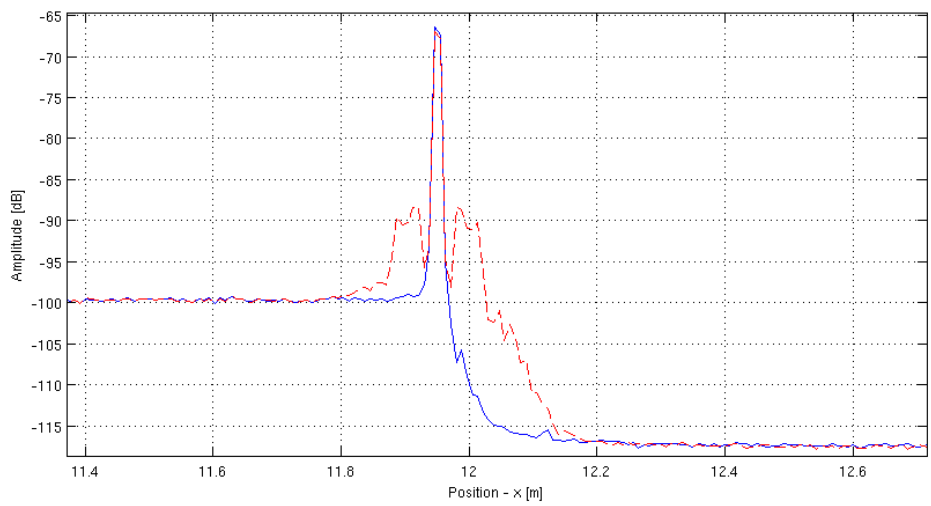

Fig. 13. Back scatter signal in the fiberoptics sensor end location under idle power supply conditions.

The signal perturbations of Fig. 13 translate into a deviation in the temperature measurement as illustrated in Fig. 14. The signal perturbations have noticeably different profiles deviating from the analogous profiles induced by operating pumps as shown in Fig. 4 and 9, for scroll pump only and scroll pump and turbo pump operating together, respectively. However, the corresponding temperature measurement fluctuation appears more limited compare to the variations shown in Fig. 5 and 10.

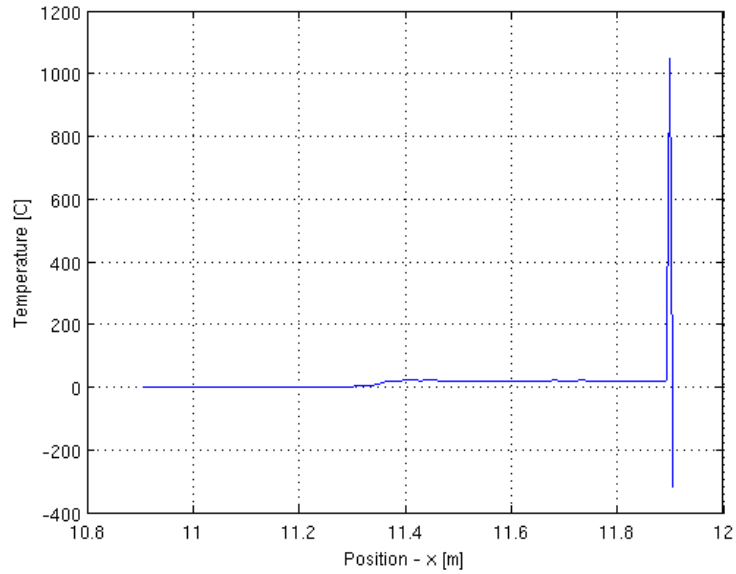

Fig. 14. Perturbations in temperature measurements under idle power supply conditions.

Figures 15 shows the control temperature measurement in red and the test measurement in blue under idle power supply conditions. Compare to the corresponding Fig. 6 and 11 for pump-induced perturbations, the idle power supply seems to be adding larger variations between control temperature and test temperature measurements in certain regions while providing no visible impact in other regions.

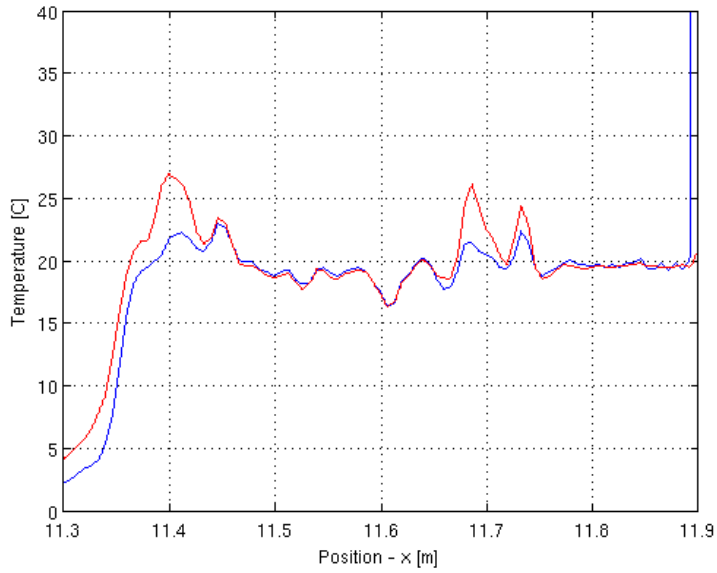

Fig. 15. Control temperature measurements (red) vs. test temperature measurements (blue) under idle power supply conditions.

Figures 16, 17, 18, and 19 show back scatter signal fluctuations and temperature profiles for the operating power supply test. Figures 16 and 17 signal perturbation signatures while Figs. 18 and 19 provide corresponding temperature measurement perturbation signatures for the operating power supply at 30 amps.

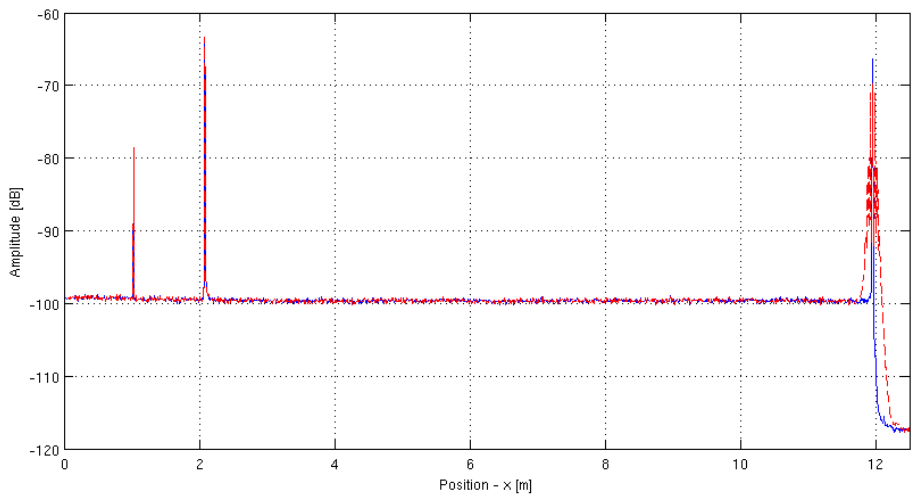

Fig. 16. Back scatter signal under operating power supply conditions.

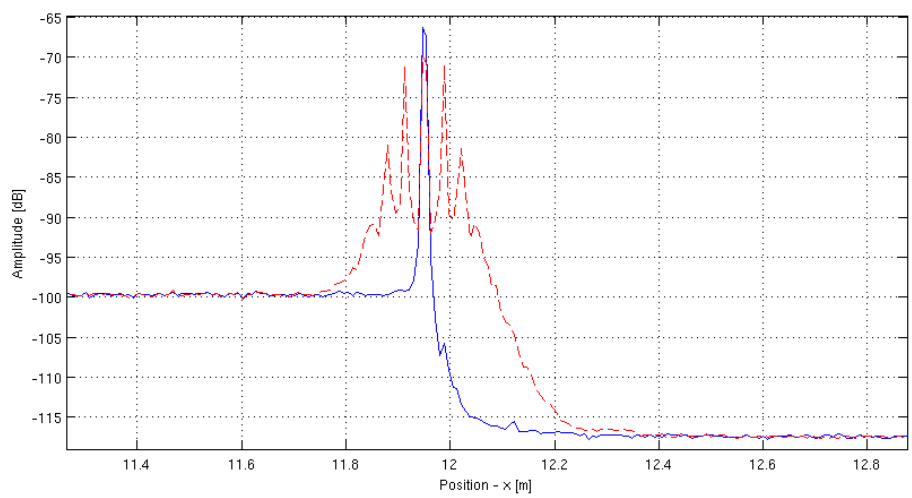

Fig. 17. Back scatter signal in the fiberoptics sensor end location under operating power supply conditions.

Clearly, back scatter signal profiles under working power supply conditions differ from the idle power supply signatures as well as from the pump signatures. The temperature fluctuations exhibit stronger perturbations over the entire range of variations. However, the trend of under predicting the temperature measurements remains.

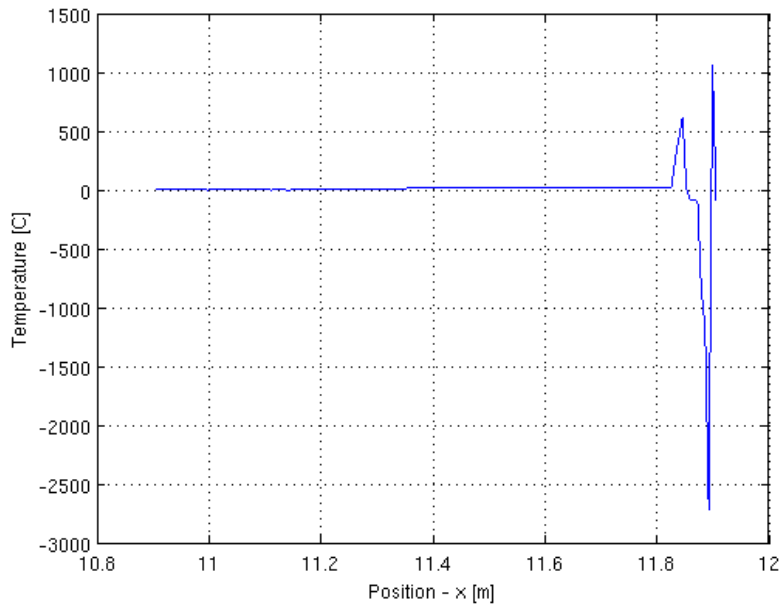

Fig. 18. Perturbations in temperature measurements under operating power supply conditions.

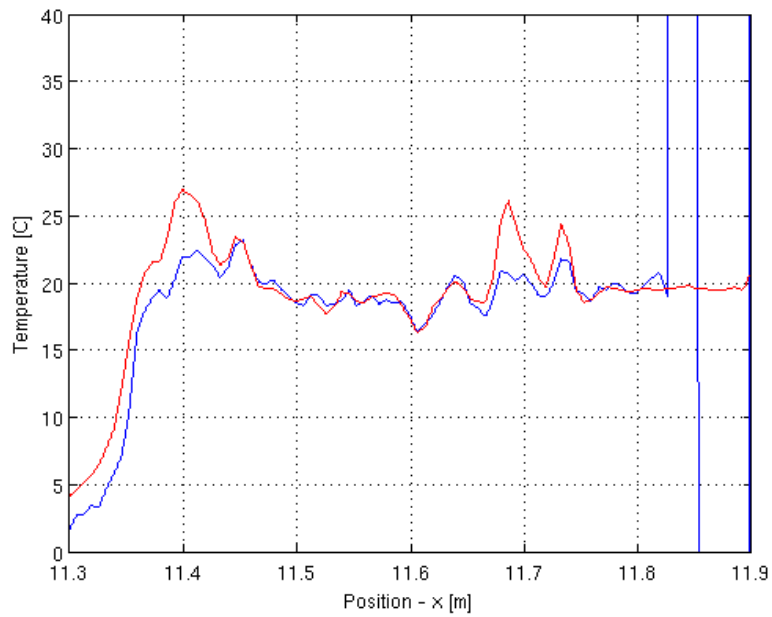

Fig. 19. Control temperature measurements (red) vs. test temperature measurements (blue) under operating power supply conditions.

6.8.4. Conclusions

In the discussed series of experiments, a range of vibration-induced effects on temperature measurements via fiberoptics sensors was demonstrated.

The experimental systems used in the vibration testing were those that would be applicable, not to the fiberoptics instrumentation in a reactor environment, but those that would be present during the experimental studies of the fiberoptics sensors in the present project.

The analysis based on the performed experimental studies led to the following conclusions and recommendations:

- It was determined that the power supply, which is used to power the graphite heater of the high temperature test assembly in the present project, does contribute to the temperature measurement errors via induced perturbations from operational vibrations.

  The pumps contributed only small fluctuations to the measurements.

- It was determined that there is an insignificant difference whether the fiber or the coupler is being subjected to vibrations and their corresponding physical effects.

- It was discovered that vibration phenomena do propagate through the fiber; therefore, vibration isolation of all points of contact is desirable.

7. High Temperature Test Assembly

7.1. Experimental Approach

The experimental approach for testing the fiberoptics for VHTR operating conditions is to irradiate the fiberoptics in an enclosed and inert furnace within the Nuclear Science Center (NSC) TRIGA reactor. A neutron fluence greater than 10^{20} n/cm^2 is desired for the irradiation. This magnitude would provide the support required for understanding the feasibility of the fiberoptics within a reactor environment.

Consequently, many typical irradiation locations at the NSC TRIGA reactor facility are relatively low flux, so a new in-pile irradiation location was analyzed and approved by the Reactor Safety Board. The in-pile furnace, therefore, is required to be significantly robust to prevent fuel damage. An appropriate design was developed and approved by the Reactor Safety Board, and tested.

A new experimental authorization was developed with an internal review at the NSC following the bench top testing. Irradiation began on March 12th and ended on June 4th with 471.99 hours of operation.

This amounts to an approximate thermal fluence of 1.0×10^{19} +/- 7.7×10^{17} n/cm^2. The flux that provides this number was determined experimentally using Au/Al flux foils for a particular core configuration (samples in various positions will affect the flux).

7.2. Description of the System

The in-core furnace was designed with the TRIGA King furnace developed by GA in 1970s as inspiration. This furnace design, unlike the King furnace, employs passive cooling for simplicity. The furnace was originally designed for 1000°C operation, but oxidation of the thermal shields, despite Helium purging attempts, restricted operation to 500°C. The furnace operational conditions differ from the VHTR as shown in Table 1.

Table 1. High Temperature Test Assembly (Furnace) vs. VHTR Operating Conditions

Characteristics	NGNP VHTR	Furnace
Average Temperature [^{o}C]	745	500
Coolant	He	He
Pressure [psia]	1032	35
Operation [months]	18-24	-
Average coolant flux [n/cm^2/s]	5e13	6e12

It is not known if the pressure will make a difference in regard to fiber degradation except in the case of driving diffusion of contaminants into the fiber core. The temperature difference is significant, and with VHTR peak coolant temperatures of 1000oC there is room for further study at various temperatures. It can, however, be argued that a lower temperature provides a more conservative estimate on fiberoptic survivability since the radiation damage annealing effect would be less pronounced at low temperatures.

The high temperature test assembly (=furnace) consists of the furnace element, void tube, and the supporting pressurization system. The system layout is shown in Fig. 1. The furnace structure is the structure that houses the graphite heating element, thermal shields, and fiber optic testing probe. The void tube houses the furnace structure. The supporting pressurization system functions to relieve pressure in the void tube during accidents and maintain a 300 kPa pressure boundary, with helium, to prevent leakage of water into the void tube. The helium, being inert, also acts to prevent conversion of the graphite to carbon monoxide at the temperatures expected during operation.

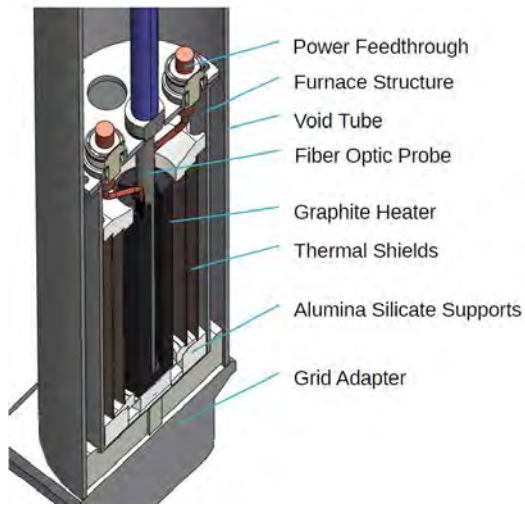

Fig. 1. SolidWorks cut-away view of the high temperature test assembly.

The system sits in the reactor core grid plate surrounded by fuel elements on two sides. The heating element is 43.0 cm in length as to heat the fiber optic probe over the length of the active fuel region of the core. The cooling of the heater is primarily through radiative heating when at operational temperature, so the design takes advantage of the use of thermal shields. The heater is powered by a 5kW, 85 amp power supply with a LabView interface that monitors instrumentation components and controls the power supply to maintain safe operating conditions.

7.3. Conceptual Design

The conceptual furnace design has been developed into a high temperature test assembly design using the STAR-CCM+ thermal models. These models include an evaluation of the 3D temperature profiles, furnace failure pressures, and an evaluation of steam rupture possibilities. The STAR-CCM+ thermal model is complete and agrees with analytical solutions.

The objective is to capitalize on free convection cooling. Thermal analysis results indicate that forced convective cooling will not be required. The capability may be implemented in the design by including the necessary gas feed through and gas flow distributor plate (inside the furnace housing) should the need for additional cooling capability become apparent in bench top testing of the test furnace. Inclusion of these components at the fabrication stage is relatively simple

compared to adding the components after the furnace is built. Material considerations, in regard to radiation embrittlement and creep, have been evaluated and determined to pose no hazard to the safety of the reactor and its support staff.

A void tube design was chosen to provide double encapsulation and to better accommodate the various feed throughs, extra instrumentation, and containment. This design will allow sufficient surface area for connections to be made, ensuring sufficient structural integrity of the closeout flange on the top of the device.

Alternate irradiation positions have been evaluated on a neutron fluence and safety basis, focusing on D7 and E2 locations as shown in Fig. 1. The original proposal called for a furnace the size of a fuel element in the D3 reactor grid location; however, after analysis and reactor safety review, the E2 location was chosen. This position would minimize the impact to reactor operations (D3 is a commonly used experimental location) and therefore provide longer irradiation times since it would not have to be moved. Additionally, the safety argument was enhanced since the E2 location has a very low reactivity worth (1-3 cents of reactivity depending on reactor configuration) with a minimum drop in flux to neighboring fuel (evident by no change in control rod worth).

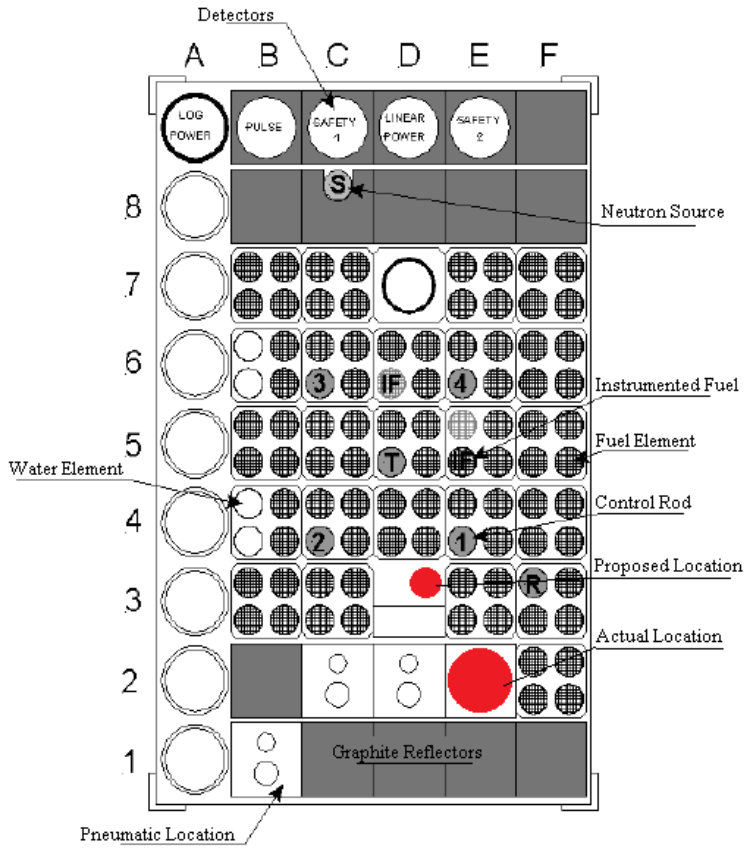

Fig. 1. Reactor core configuration showing the position proposed and the final, Reactor Safety Board – approved position.

A detailed safety analysis report has been produced. This report includes engineered safety considerations and systems for the overall furnace design, instrumentation and controls, nominal and off-nominal pressure and flow characterization, temperature limitations, material selection, and reactivity insertion affects associated with the test furnace. The TRIGA environment has been characterized. The core 3D fluxes, fission power densities and heating power maps have been produced. Out-of-core validation experiments have been conducted to confirm results of the performed predictive simulation results and validate the design decisions. All fabrication activities were performed at Texas A&M Nuclear Science Center Reactor Facility

7.4. Component Fabrication

Fabrication of the furnace and its components took the majority of the project time. In general, the original design had very few modifications to fully realize a complete, working furnace. These will be discussed in further detail in the following sections.

Primarily, the modifications were to the cap design for the furnace element and the void tube, and to the internal structure of the furnace element. The original alumina silicate support design was rejected on the basis of thermal stresses due to firing in the kiln and the top support piece was later determined to not be necessary in the final fabrication, so it was removed.

The fabrication efforts for all parts, excluding the alumina silicate support pieces, thermal shields, and graphite heaters, were completed at the Nuclear Science Center.

The furnace was drawn in SolidWorks to streamline anticipated modifications and design iterations in the fabrication process. The fiber optic probe was fabricated by Luna Innovations.

7.4.1. Furnace Structure

The furnace element was the first portion of the furnace fabricated. This is the main component of the furnace and was originally designed for vacuum conditions. However, considering the time constraints on completing the fabrication, it has been determined to simply operate the furnace structure in the ambient condition of the void tube.

The furnace element, in the context of the discussion, consists of five components. These are the cap, structure, graphite heating element, thermal shields, and alumina silicate supports. All of the aluminum used was purchased from Tri-State Aluminum.

Cap

The cap is the component that seals the furnace element. It has five penetrations for the thermocouples, the fiber optic probe, two power feedthroughs, and a vacuum feedthrough that now acts to equilibrate the furnace element and void tube pressure.

The cap is bolted on to the furnace element via eight 4-40 bolts that compress a lead gasket to complete the seal. Figure 1 shows the cap during the initial fabrication stage.

The cap is machined out of a piece of 1/2” plate 6061-T6 aluminum. The mount for the furnace element was fabricated at the same time to ensure that the bolts lined up exactly. A grove is then machined into the furnace cap that allows for the lead gasket to be made.

Fig. 1. During and post fabrication of the furnace cap and the mount.

Figure 2 shows the gasket during fabrication and after compression. The gasket is made by first heating up the furnace cap with an acetylene torch until the cap is hot enough to melt lead on contact. Care must be taken not to melt the cap or power lead braze. The lead (Pb) is then melted into the grove until the grove is filled and the lead forms a continuously solid bead. The lead is then allowed to cool slowly by setting it aside until it is at room temperature.

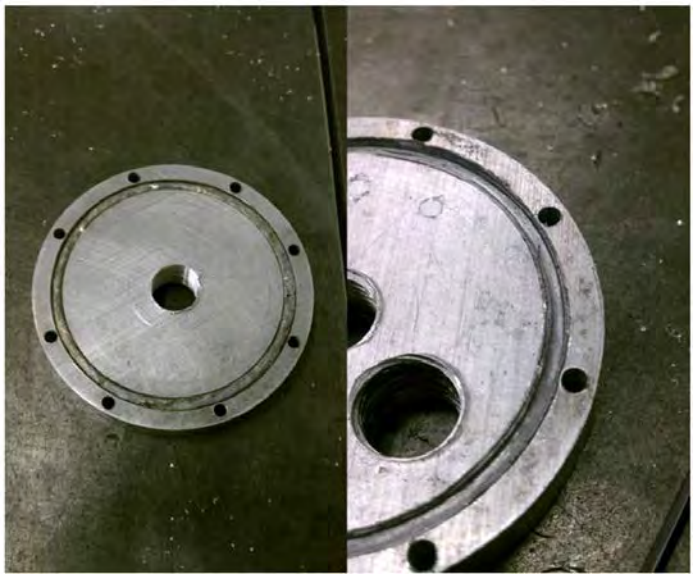

Fig. 2. The furnace structure cap gasket before sealing (left) and after sealing (right).

The power-lead feedthroughs were a bit more challenging, since the feedthrough is supported with 316 stainless steel. The original attempt at joining the steel and aluminum cap was met with failure. This first attempt was to taper a thread onto the feedthrough and then thread this into the cap. The machining of the feedthrough simply destroyed it in the process. There was little else that could be done, so an effort to seal the feedthrough with alumiweld braze was attempted. This proved to be very successful, though quite difficult. There is a very narrow range in temperature were the bonding agent in alumiweld actually adheres to steel and aluminum. The power feedthrough brazed to the furnace cap is shown in Fig. 3. The selection of the power lead and power wires were determined by the amperage limitations of copper. The voltage drop is negligible for this configuration.

Fig. 3. The furnace cap with the power leads brazed into position.

The power leads have to be modified to allow for connecting the power wires and graphite heater. The design of this is fairly simple. Copper stock is cut into rectangular prism blocks. The lead/graphite contact is made by tapping a 1/4" hole for the power lead and using the band saw to make a grove for the molybdenum connector. The block is then rounded to minimize the material and prevent contact with the furnace wall then brazed to the power lead. Following this, the power lead itself is heated and bent to allow for the molybdenum connectors to fit snugly into the copper blocks. These are then brazed together using silver solder as shown in Fig. 4. This appears to be a very robust connection and the contact resistance is small enough that no difference with an ohmmeter is detected.

Fig. 4. Power lead/molybdenum contacts prior to (left) and after (right) brazing.

The power wire/lead block is made in a similar fashion, but the wires have a cross-threaded bolt-hold to allow for a bolt to compress the wire in place as shown in Fig. 5. This keeps the wire in position and helps improve the contact. It is not brazed so that removal is possible. The power leads are also bent inward slightly to reduce potential contact with the void tube.

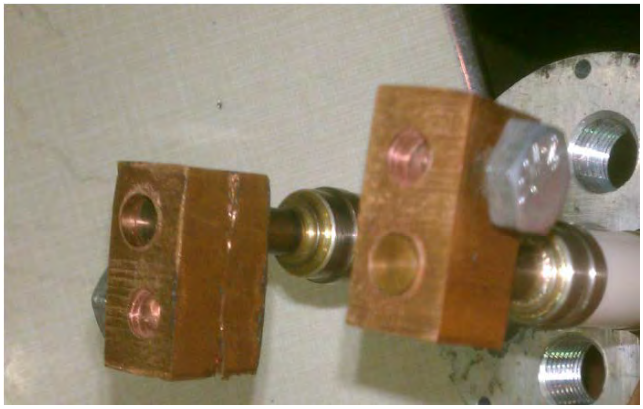

Fig. 5. Power wire/lead contact prior to brazing and rounding of edges.

Figure 6 shows the cap and top internals of the furnace in their completed state. The thermocouple connections and wires take a considerable amount of space, so the alumina silicate spacer had to be dropped from the design. This was an oversight in the initial process, but it actually works out well by removing more mass from the furnace and therefore minimizing the potential thermal storage. The impact of enhancing radiative heat transfer from the graphite is very small.

Fig. 6. The top internals of the furnace.

Structure

The structure is fabricated from a tube of aluminum and is sealed on the bottom by welding a piece onto the tube as shown in Fig. 7. The weld was performed by the NSC machine shop foreman. The furnace cap mount is welded to the tube and then tapped for the 4-40 bolts. The initial welding was done by spot welding, but this turned out to fail under the stresses of bolting the cap on. A continuous weld had to be implemented to ensure the mount would not fail. The open lip is then machined flat to ensure a good seal with the cap.

Fig. 7. The furnace structure with welded mount (left) and bottom (right).

Graphite Heating Element

Figure 8 shows the graphite heating elements. They were designed by TAMU and fabricated by Poco Graphite using AXZ-5QM graphite.

Fig. 8. Receipt and inspection of the graphite heaters.

Table 1 shows the design tolerances (nominal) and the actual geometrical parameters of the heaters as determined upon receipt. Table 1 confirms compliance of the fabricated heaters with the required design specifications.

Table 1. Geometrical Characteristics of the Fabricated Heaters vs. Nominal Design Data

Geometry	Heater 1	Heater 2	Heater 3	Nominal
Length (cm)	43.1	43.1	43.1	43.0
Diameter (cm)	1.982	1.975	1.965	2.0
Thickness (cm)	0.492	0.498	0.496	0.5
Gap (cm)	0.189	0.189	0.193	-
Bore (cm)	0.190	0.183	0.188	-

The molybdenum power leads were threaded into the graphite heater, after tapping with a #3-48 tap, and epoxied in place with a metallic adhesive, Durabond 950 from Cotronics. This was done to enhance the thermal resistance between the molybdenum lead and graphite heater. Molybdenum is used for the power leads since it has a very high melting temperature. The integrity of this was tested through by introducing very high heat and cooling rates on the graphite heater as illustrated in Fig. 9. No cracking of the adhesive was observed.

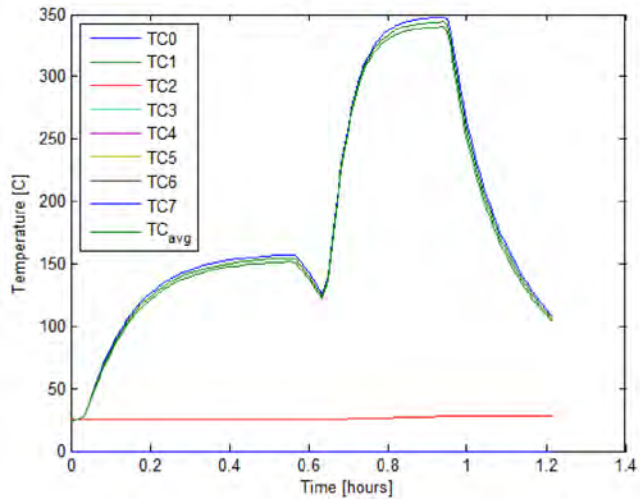

Fig. 9. Thermal stress testing of graphite heaters in the vacuum chamber.

The attachment of thermocouples to the graphite, for monitoring the graphite temperature during operation, is of exceptional importance from safety and operational standpoints. The method to attach the thermocouple was to use a ceramic adhesive, Resbond 920 from Cotronics, to attach high-temperature, Nextel sheathed, k-type thermocouples, from Omega Engineering, directly to the graphite. Figure 10 shows the thermocouple-heater configuration resulted from the process. Concerns of contact with the graphite are neglected since the thermocouples are of grounded variety. After thermal stress testing this method was determined to be satisfactory. Various techniques for applying the adhesive and shaping the thermocouple bead were tried. The final technique uses a pair of needle-nose pliers, the bead is bent down so that the thermocouple can be positions against the graphite without any loss of contact.

Fig. 10. Thermocouple attached to the graphite heater with the lead wire to hold the thermocouple into position without contaminating the graphite.

One issue was neglected during the design phase - possible contact of the fiber optic probe with the graphite. Such a contact could potentially cause shorting to the furnace structure through the probe. Two potential methods are available to avoid this. One method is to use an alumina-woven sleeve around the probe prior to insertion into the graphite. The sleeve was purchased but not used and is reserved as a backup if failure due to contact ever occurs. The current implemented method uses the alumina-oxide adhesive.

Thermal Shields

Thermal shields are of importance to the design since radiative heat transfer will be dominant at the operational temperatures of the furnace. These thermal shields reduce the wall temperatures of the furnace element and the total heat flux required to maintain the required temperatures. This reduction in heat flux reduces the power requirements of the furnace and therefore the likelihood and impact of an accident.

The original design concept used molybdenum thermal shields since they have been used in previous high temperature TRIGA-based furnaces.[1] However, due to design constraints, this material was not available. Consequently, another refractory metal was used - niobium. Niobium was selected for its superior characteristics over other potential candidates. The commercial provider of these shields was Admat Inc. The thermal shields, though originally accepted by the company, proved to be exceptionally difficult to fabricate. After four months of attempts (original purchase was February 2011 and receipt in late August 2011), the design constraints were relaxed to allow for a slightly thicker wall thickness from 0.02 in to 0.0315 in. Table 2 summarizes the actual characteristics of fabricated thermal shields vs. the design specifications.

Table 2. Thermal Shield Characteristics as Fabricated vs. Nominal Design Data

(Nominal design data are given in parenthesis)

Thermal Shield Characteristics	Inner Shield		Outer Shield	
	Fabricated	Nominal as Designed	Fabricated	Nominal as Designed
Outer Diameter (in)	1.34	1.331	1.777	1.772
Inner Diameter (in)	1.254	-	1.6945	-
Height (in)	16.25	16.298	17.125	17.128
Thickness (in)	0.036	0.0315	0.037	0.0315
Mass (g)	297	-	422	-

Polishing of the thermal shields was attempted using a mechanical abrasive polish. A pad holder was designed and built to attach to a drill to polish the inside of the tube. No noticeable change in the reflectivity was observed in the visual appearance of the shield and the polishing step was abandoned. The reflectivity of niobium, however, is already fairly high.

Alumina Silicate Supports

The alumina silicate supports are for retaining the geometry in the furnace element and to provide an electrical and thermal buffer between the graphite, thermal shields, and aluminum walls. Only the bottom support is actually used in the built furnace element, since it provides all of the support required. The mass of thermocouple wire above and around the graphite heater, which was

neglected during design, is significant enough to provide the support needed for the thermal shields. These supports were manufactured by Cotronics and upon arrival their dimensions were verified within accepted tolerances. The supports went through a few design changes to ensure they did not crack during firing. The supports, contain the following design features: holes to allow for gaseous discharge to prevent a pressure differential from collapsing the thermal shields, height differences to support the thermal shields and graphite heater in a concurrent geometry, penetrations for the thermocouples and fiber optic probe, and encasing of the bottom of the probe to minimize radiative cooling to the aluminum wall.

7.4.2. Void Tube

The void tube exists as the secondary but important safety barrier for the furnace. It is fabricated with a dedicated grid adapter for insertion into the reactor grid plate. The furnace has the required feedthroughs for maintaining pressure and providing the furnace with power and instrumentation. The tube is a 12 ft. piece of Al 6061-T6 with a 3.0 in. outer diameter and 0.065 in. wall thickness.

Cap

The void tube cap was made using the same methods as those developed for the furnace cap. Because the space was less limiting, larger dimensions and more bolts were used to ensure complete enclosure. Lead is still used for the gasket and is made in the same manner. The only difference is in the fabrication of the power-lead feedthrough. Figure 11 shows the assembled void tube cap with feedthroughs.

Fig. 11. Void tube cap with power lead (left) and fiber optic feedthroughs (right).

The process for making the feedthrough was to coat the power cable with an exceptional amount of JB-weld and to insert it into a threaded 1/2” pipe. JB-weld was chosen since this is often used at the NSC for coating the thread of valve fittings on experimental long tubes. The flux at these threads on the long tubes is higher than the void tube cap and they last 2+ years.

Grid Adapter

The grid adapter is a fairly important piece of the void tube. It is the support piece of the entire furnace for proper positioning into the reactor. It also contains several pounds of lead to neutralize the buoyancy force. The weld must be able to support the lead weight and be as helium-tight as possible. The weld must be of the highest possible quality.

The grid adapter weld is happened to be the portion of the fabrication process in which the largest delay occurred due to the complexity and importance of the resulting structural strength and integrity.

The grid adapter itself went through some minor design changes. These changes were:

- to accommodate better welding surfaces between the void tube and grid adapter,
- to increase the length of the adapter,
- to increase the volume for lead, and
- to maintain straight geometry of the void tube and grid adapter.

The first grid adapter was fabricated as a two-part design with a 2.25" tube welded to the bottom to contain a mass of lead. This tube extended the grid adapter from the bottom of the grid mount by an extra 18 inches. This length is limited because there is a safety plate in the reactor support structure. Since this is merely an extension, the weld did not have to be helium-tight. The grid adapter was a sealed unit in itself. The welding of this grid adapter to the void tube resulted in thermal stresses of the tube that were released via subsequent cracks as illustrated in Fig. 12. The radial stress crack was 3 in. above the weld. The grid adapter was cut out and the tube shortened to remove the crack. Welding was attempted again in more controlled environments with pre-heating and thermal blankets to reduce cooling rates. However, cracking induced by thermal stresses was then introduced into the grid adapter itself as shown in Fig. 12.

Fig. 12. Thermal stress cracking (left) in the void tube and in the grid plug (right) from suspected rapid cooling due to heat sinking with lead and high thermal conductivity of aluminum.

To address and resolve the thermal stress issues, two grid adapters were fabricated and six welding attempts were made. The fabrication method was changed completely. The second grid adapter was machined to contain two segments for lead to avoid weld in the grid adapter. This was done to address concerns that thermal stresses, which might not be apparent during visual inspections, would cause the tube segment to break off while already installed into the position in the reactor core. The top portion of the lead was inserted, as a plug, after welding to the tube was complete. This reduced the thermal storage and heat sink of the grid adapter by removing much of the lead mass that would be pre-heated during welding. The final welding attempt was performed via 5 passes. This configuration finally passed the pressure test. Figure 13 shows the final grid adapter design as fabricated.

Fig. 13. Final grid adapter design prior to welding to the void tube.

The weld was checked with pressurized CO_2 at 50 psi and leaks visualized with a bubble solution. Once the grid adapter passed this check, the void tube was moved into the confinement building for helium pressure checks in the reactor pool. Figure 14 shows the successful weld that passed the CO_2-leak test.

Fig. 14. The completed weld that passed pressure testing with CO_2.

7.4.3. Pressurization System

The pressure system provides both venting and pressurization capabilities for the furnace. The pressure system comprises of three main parts:

- pressure supply,
- relief to the central exhaust, and
- the bridge-side supply.

The three-part configuration is driven by the isolation capabilities for maintenance as discussed in the Safety Analysis Report. The tubing from the void tube to the bridge-side supply is 20 feet. There is a bend and steel hose fitting in the tube, roughly 4 feet about the void tube, to prevent radiation streaming to the surface. The fiber optics, power leads, and thermocouples are zip-tied to this semi-ridge pipe for support and to prevent wires from interfering with reactor operations.

Pressure Supply

The pressure supply is the portion of the system that contains the helium cylinder with a maximum capacity of 2200 psi with a single-stage mechanical regulator, as shown in Fig. 15. This requires that the pressure setting on the discharge side of the regulator must be checked daily as the supply side changes.

Fig. 15. Supply cylinder and regulator.

This portion of the system includes a check valve to prevent gas reversal during pressure transients. The check valve actuator protects the rubber hose from heated gases. Figure 16 shows the check valve location in the system.

Relief System

The relief system includes two spring-loaded relief valves and one power-operated solenoid valve that is fail closed. The system configuration is shown in Fig. 16. This is a non-safe condition, but it is to prevent the discharge of helium to the central exhaust. Due to this configuration, two additional spring-loaded safety valves were added.

The relief settings for these valves are 45, 50, and 65 psig for the solenoid and spring-loaded valves, respectively. These settings were checked prior to installation.

The activation of the solenoid was checked after installation by applying pressure to the system and slowing increasing the regulator set point.

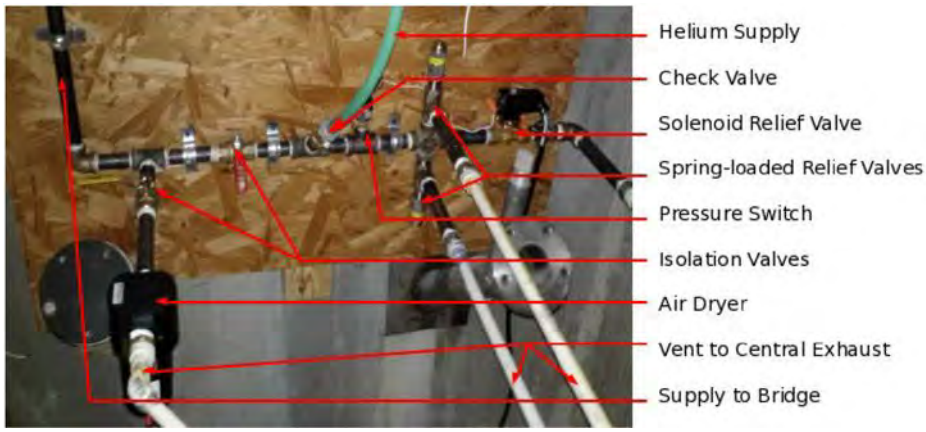

Fig. 16. Configuration and components of the pressure system.

An air dryer is included and used to determine if there is moisture in the system. This check is performed by venting the system and checking the dryer. The dryer uses sudden expansion, which condenses and collects the water from the helium flow.

Bridge-side Supply

The bridge-side supply consists of the feed line to the void tube, a pressure transducer, a pressure switch for the power supply safety, and various coupling elements for quickly disconnecting portions of the system.

The pressure transducer reads the system pressure for LabView, which records all of the data streams.

7.5. Acceptance Testing

The chronological overview of the performed acceptance testing procedures is presented in this section. The discussion includes measurements, their explanations, and corrective measures (as applicable) taken to ensure compliance with the requirements of the safety analysis

All measurements were performed outside of the reactor core but in the reactor pool water. The results from the fiber optics are plotted to reveal key features. It should be noted that data scans were taken regularly at most steady-state temperatures.

January 10, 2013

Upon completing the fabrication, the resistances between the power-leads and void tube were measured. These measurements are needed to ensure that the fiber optic probe, which is

traveling through the graphite heater and is grounded with the aluminum structures, is not drawing any current from the heater.

The heater-probe electrical connection may potentially fail the probe itself and would also reduce the operational temperatures of the furnace for a given current load.

This concern was alleviated by insulating the probe via alumina paste inside the heater. The resistance was measured to be 53 kohm at room temperature.

The resistance between the thermocouples and the heater is not of importance since they are of grounded type.

All connection were verified to have sustained themselves during fabrication.

January 11, 2013

The furnace operation began on January 11, 2013. All TC measurements were verified to be in equilibrium with the reactor pool water, which was measured to be 26°C. The heater TCs measured between 27.1 and 27.2 ^{o}C. The element measured between 27.6 and 28.3^{o}C.

The preliminary checks were completed. The resistance across the heater is measured to be 1.1 ohm. The helium supply is a brand new bottle at 2250 psi and the regulator set to 45psi. The pressure transducer was not reading properly and was recalibrated by reducing the pressure and then increasing it again to generate a linear curve.

The pressure switch responses were verified by increasing the pressure until the relay was activated (at 25 psi) and continued until the relay deactivated (at 60 psi). This ensures that the power supply will shut off if pressure is lost and if pressure exceeds the solenoid relief setting, which was also verified.

Since the relay setting was higher than the solenoid, the solenoid was unplugged so that it did not relieve the pressure.

These venting/pressurization cycles are used to purge the system of as much oxygen as possible.

Initial fiber scans were completed. The fiber 1G and 4G appeared not to be functioning properly, which agree with the receipt specification of the fiber optic probe, which is currently installed in the furnace, as discussed in this report.

The furnace was brought up to 100°C to determine heat functionality and to provide an operational baseline of resistance changes for the entire assembly. The external TCs began behaving strangely, such that they would decrease with temperature rise. This behavior is documented in Fig. 1.

It was suspected that this behavior was caused by EMF interference, potential grounding, or wiring issues. The EMF concerns were discounted when the 208V 3-phase wiring was moved far from the TCs and no noticeable effect was observed. It was later discovered (on January 27th, 2013), that these issues were the result of flipping the +/- of the wiring in the connections.

Despite of the lack of external temperature measurements, it was decided to operate up to 250°C, which was considered safe, to gather more data prior to dismantling the furnace to

increase the baseline for further testing. The surface of the void tube was closely monitored to ensure that there was no nucleate boiling, which would indicate that the surface was exceeding 120°C.

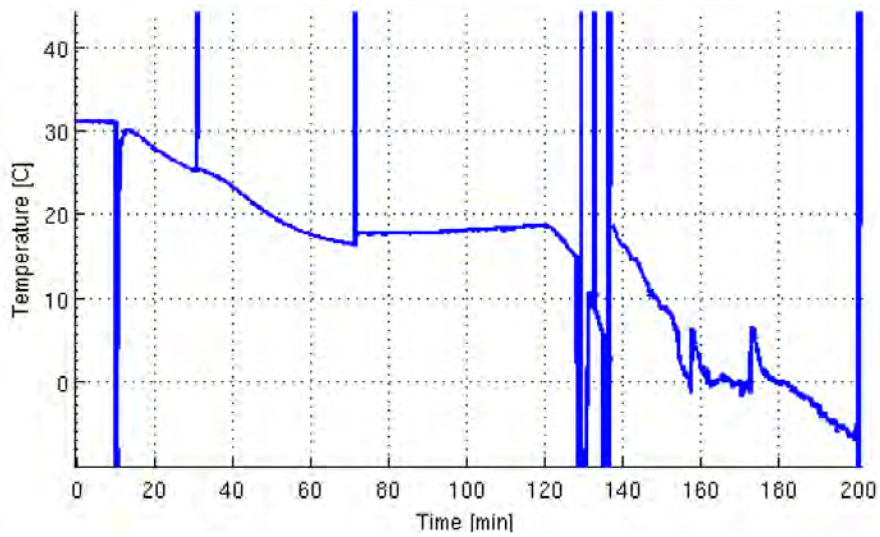

(a) External surface temperature of the furnace

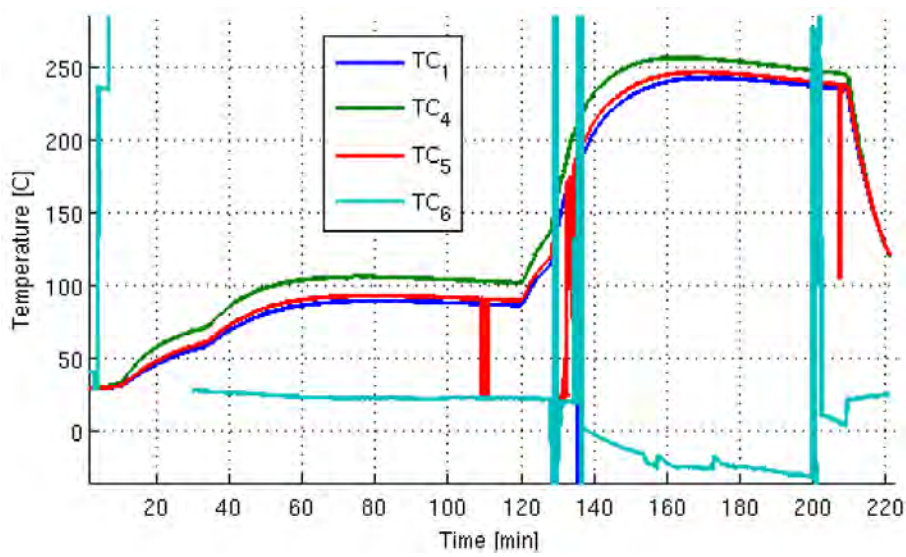

(b) Furnace heater (TC 1, 4, and 5) and the external surface (TC 6) temperatures

Fig. 1. Temperatures in the high temperature test assembly during the acceptance testing on January 11, 2013.

In Fig. 1, the spikes in the temperature profile are due to the faulty connections. These are the result of the opening of the circuit and LabView reporting ~1500°C for these moments.

The decrease in temperature during the constant current moments can be noticed from the data in Table 1. This is the result of the changing resistivity as the material is coming to thermal equilibrium and the change in power due to the dependence of resistance in Joule heating. The TC resistances are measured for TC 2, 3, and 8 as 15, 12, and 9 ohms respectively.

Table 1. Operational Data for January 11, 2013

Time	Current	Voltage	Resistance (ohm)	Average Temperature (°C)	
				Heater	Surface
1845	0	0.00	-	29.63	31.07
1854	2	2.28	0.88	31.74	30.98
1913	6	3.27	1.83	62.35	27.02
1957	9	3.73	2.41	96.00	20.96
2131	25	5.05	4.95	248.65	-

January 12, 2013

The main helium was at 1900 psi. All of the venting from the previous day was considered to be the primary source of helium loss and no major leaks were found via bubble solution checks of threaded components.

Calibrated pressure sensor information was properly implemented into the LabView.

The leakage rate, tested by isolating the main supply, was determined to be 0.17 kPa per second in the pressure system, not the main supply bottle. This was later discovered (March 18, 2013) to be primarily the result of diffusion through the oxygen hose used for the supply and was then replaced by a polythene tubing. Leakage continued until the low-pressure switch turned off the power supply relay, to actively check the safety system. This occurred at 175 kPa or 25.4 psi.

This test included a thermal stressing test and further testing of the TCs. It was noticed that 10.5 amps was a threshold for the functionality of TCs 1 and 6. Above the threshold, those two TCs simply failed to measure temperature levels. However, once the power was reduced, they behaved normally again.

The rate of temperature changes will be limited, but it is desired to know if an immediate shutdown of the furnace will result in a failure of the furnace. To test this effect and outcomes, the furnace was taken up to about 450°C, without external surface temperature monitoring but with nucleate boiling closely monitored, and then the power supply was shut off. Because no nucleation was noticed, the wall temperature remained low.

January 14, 2013

The furnace was removed from the pool and visually inspected. The lead gaskets are all in great shape and all electrical components are functional, except the leads seem to be contacting the void tube. This is likely due to the heat making the copper more malleable and the weight of the copper wires in the tube pushing the feedthroughs outward. They were then bent further in and tapped up with Kapton tape to provide insulation. The copper wire was also shortened by 22 in. to provide the ideal length so only thermal expansion would lead to any pressure to the feedthroughs.

January 17, 2013

The resistance between the void tube and power supply (i.e., the probe grounding to the heater) at room temperature is 53 kohm. The bottle pressure is 1800 psi. The particular purpose of this day is to verify PID controller functionality.

During the startup, issues with TC5 were noticed. Consequently, TC5 was removed from the sampling as illustrated in Fig. 2.

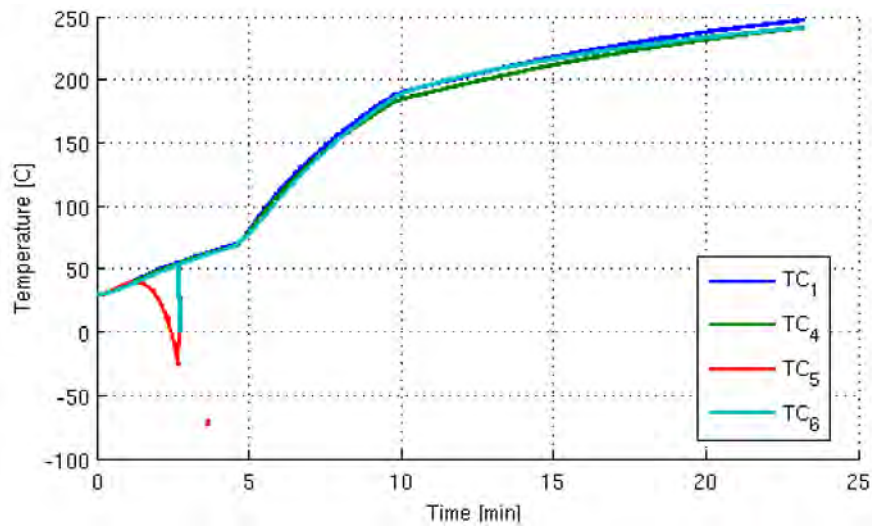

Fig. 2. Furnace heater temperature during the system startup on January 17, 2013.

Figure 3 illustrates the nonphysical reduction in temperature reported by the external TCs (and likely TC5).

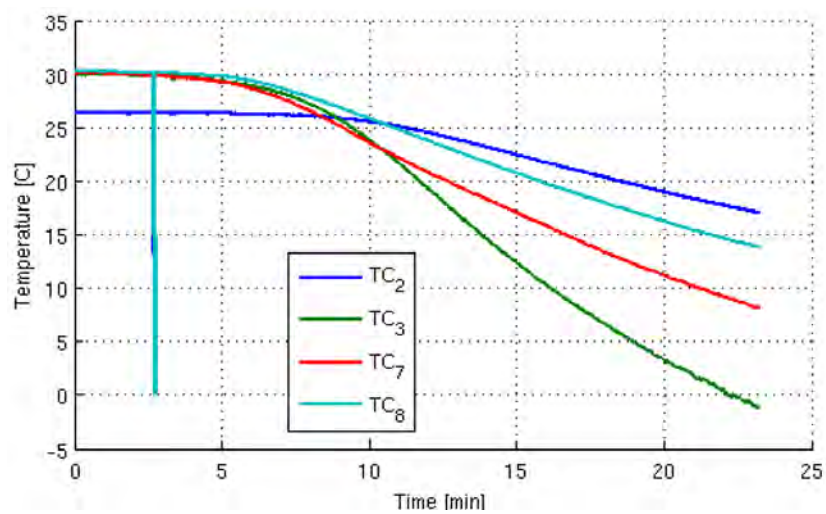

Fig. 3. External surface temperature during the system startup on January 17, 2013.

The power applied during the transients is shown in Fig. 4.

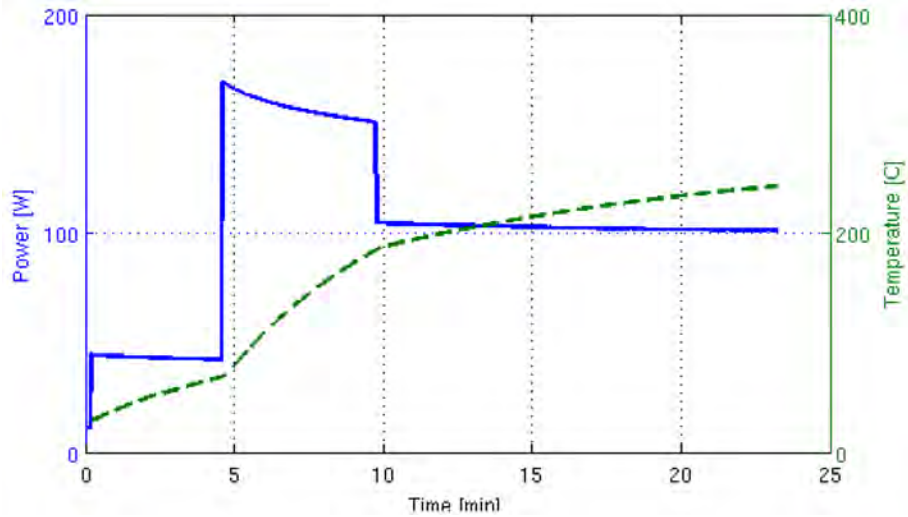

Fig. 4. Power and average heater temperature as a function of time during the system startup on January 17, 2013.

The observed behavior clearly demonstrates the Joule heating being reduced for a constant current with temperature increase.

After temperature stabilized at roughly 250°C, the set point was raised to 300°C, and then to 350°C and the PID controller was allowed to assume control of the power supply.

The procedure is shown in Fig. 5.

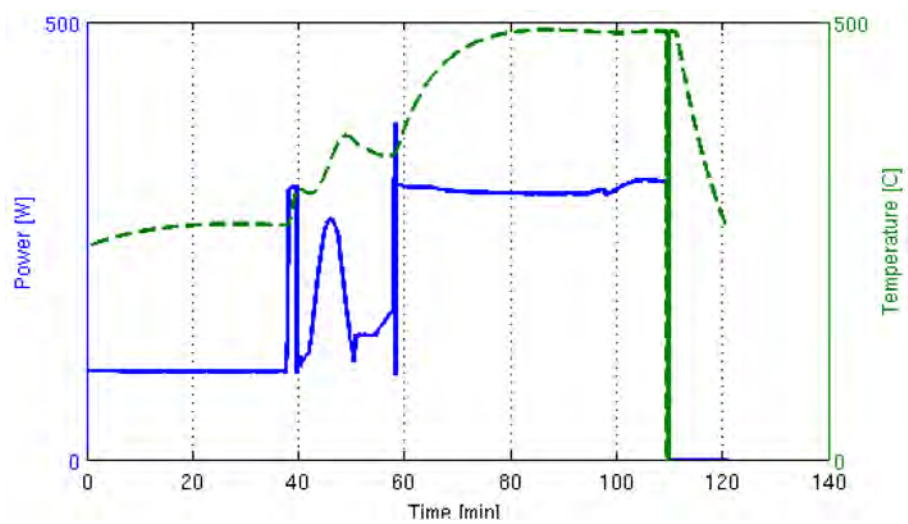

Fig. 5. Power and average heater temperature as a function of time, the PID controller active after the first 40 minutes of the test during the system startup on January 17, 2013.

The PID controller required some optimization to reduce the periodical oscillations and temperature swings.

The final PID parameters are: 1.0, 0.6, 0.0 for the proportional, integral, and differential constants.

The furnace was shutoff following this test for another thermal stress test, since it was planned to be pulled out to fix the TCs.

January 27, 2013

The furnace was removed from the pool and visually inspected. Although no degradation effects were noticed from the shutdown stress test; it is still recommended to slowly cool the furnace during shutdown.

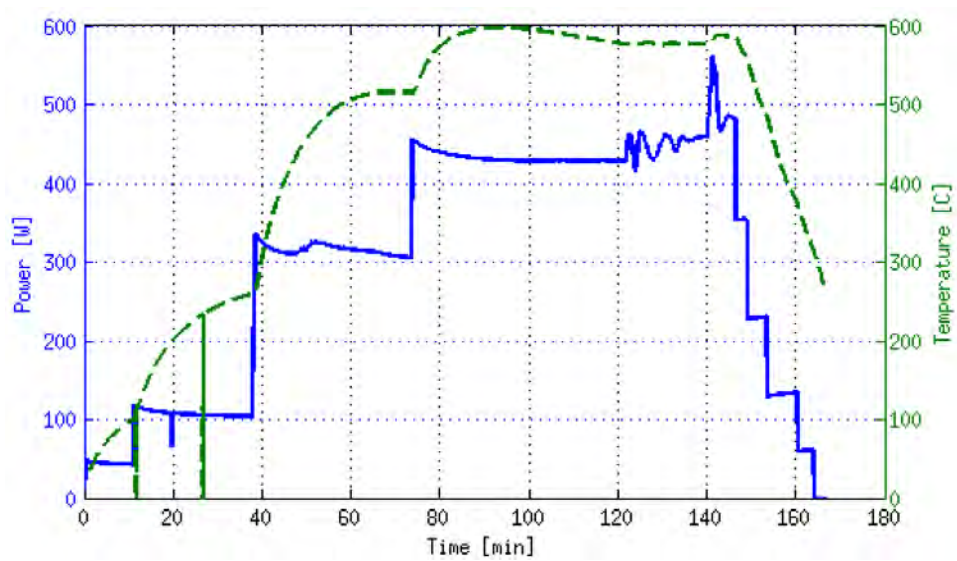

Fig. 6. Power and average heater temperature as a function of time during the system startup on January 27, 2013.

All of the TCs were manually checked with a flame torch to verify their behavior. The response was a measured temperature decrease, so all the connections were dismantled.

It was noticed that those that failed were wired backwards. This would result in the voltage change being polar-reversed and the apparent temperature changes opposite as expected.

Figure 6 shows the power level and the heater temperature for the final day of acceptance testing. Startup and shutdown procedures were performed manually.

The PID controller was tested again and further optimized to reduce the amperage fluctuations.

The PID controller operation is shown in Fig. 7.

After the TC corrections, the external temperatures are behaving properly as illustrated in Fig. 8.

The safety arguments in the SAR restrict operation to a maximum of 180ºC on the surface of the furnace. With this information taken into account, the preceding tests were never in violation of the SAR requirements.

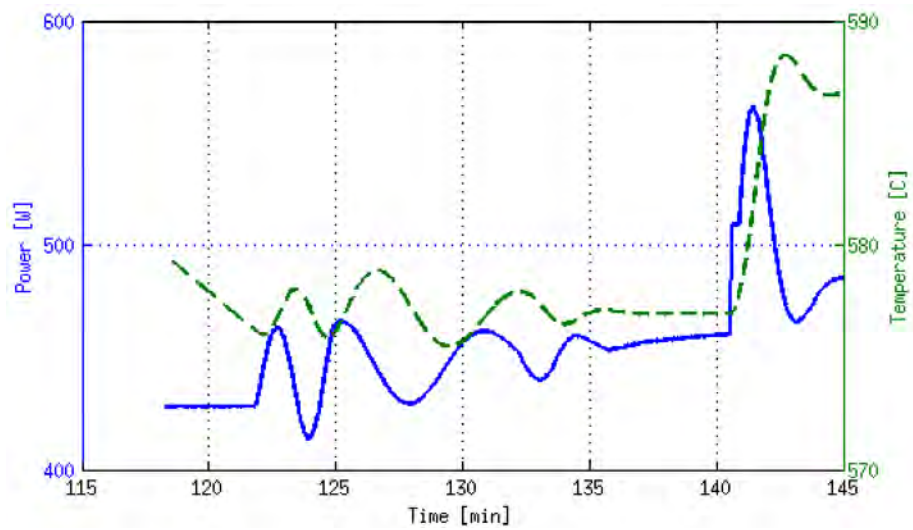

Fig. 7. Power and average heater temperature as a function of time during the PID optimization process for the system on January 27, 2013.

Furthermore, to be noted, this safety requirement only pertains to the in-core operation of the high temperature test assembly. As a result, the maximum operational temperature of the heater is assumed as 600ºC. This is in a fair range for the testing of the fiber optics.

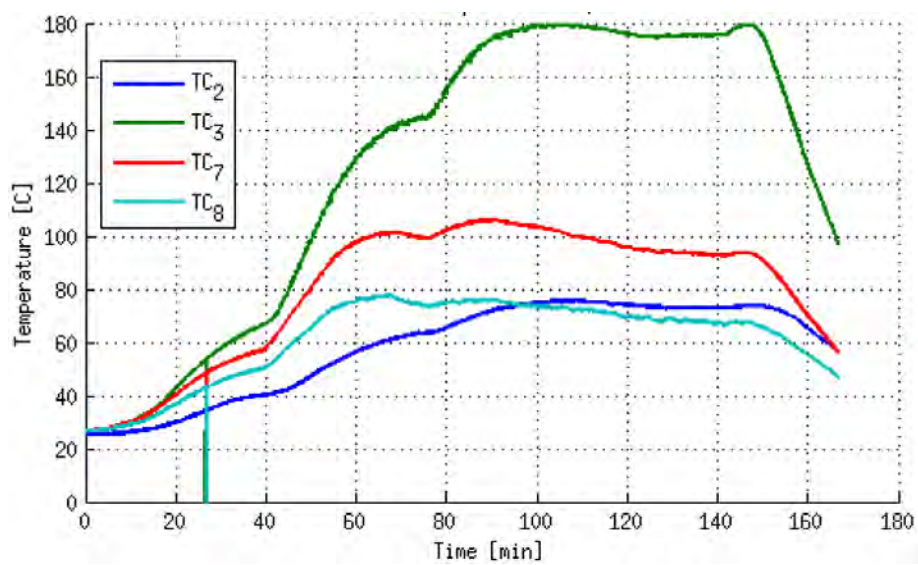

Fig. 8. External surface temperature of the furnace as a function of time following TC adjustments for the system on January 27, 2013.

A comprehensive resistance as a function of temperature is shown in Fig. 9. The resistance change is the result of the overall resistance of the copper and graphite. It follows that thermal transients and the resulting shift to equilibrium causes changes in the resistance.

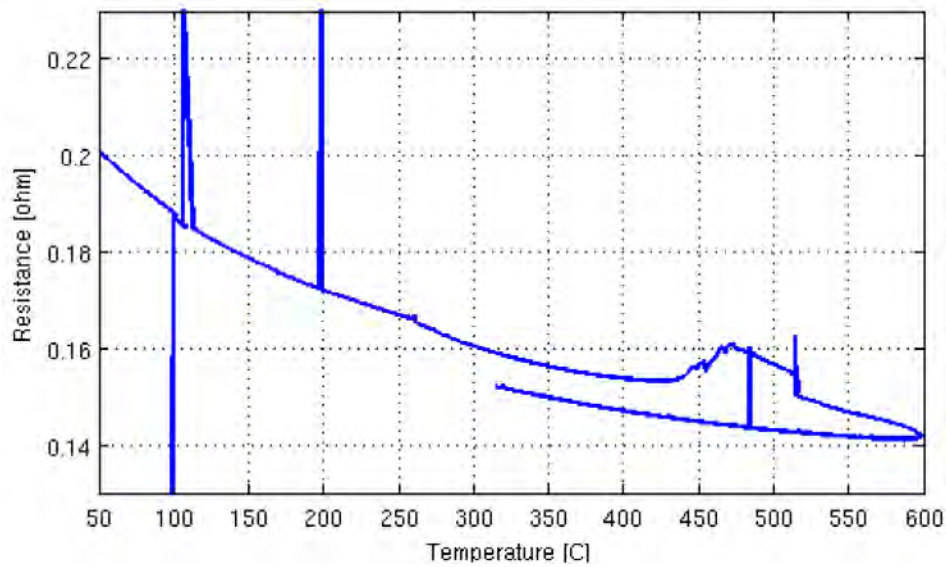

Fig. 9. Resistance as a function of average temperature.

As heat is conducted and radiatively dispersed, other components heat up and cool at different rates. This is of little interest from a safety standpoint, but can potentially lead to large oscillations in the PID control that may not get damped out. This must be monitored during long operational runs.

7.6. Experimental Program

7.6.1. Fiberoptics Probe

The fiberoptics probes were checked for operability when received from Luna. Each probe contains twelve fiberoptics sensors which are held in place via a series of quartz ferrules as discussed in this report. The fibers themselves must be shielded from water, as the hydroxyl attack will degrade the fiber performance to the point of failure. The fiber travels through two penetrations in the void tube and the furnace. These feedthroughs were tested at the designed failure pressure of the respective location. The probe itself sites in the centerline of the graphite heater and extends the entire length of the active fuel meat.

7.6.2. Expected Fiberoptics Behavior

Constraints on operation of measurement systems will vary accordingly to the desired measurement channel and physical conditions. These fiberoptics-based measurement systems are no different, despite their flexibility and size. Various tests were conducted and are documented in this report to determine the usefulness of the fiberoptics within a reactor

configuration from a qualitative standpoint. These tests were vibrations, thermal response, and breakage mode responses.

It has been determined that induced vibrations in the fiberoptics system, specifically at the end and at couplings, would greatly interfere with the signal and therefore result in erroneous measurements. The vibrational sources, which introduce the most error, depend on the scanning parameters of the OBR and the calculation options. The most prominent sources, to be expected, are the power supply, vacuum and reactor pumps, and other mechanical supporting components and structures.

It was also found and verified by Luna that the fibers respond somewhat abnormally in thermal transients. There are structural changes resulting from variations in thermal expansion rates between the fiber core and coating. These changes take a considerable time to come to equilibrium. It appears, though not specifically verified, that after a few thermal cycles, the fiberoptics sensor will begin to lose this delay. It is recommended that fibers are thermally stressed before being put into service. It is not clear if stresses from bending the fiber introduce similar issues.

It was desired to understand the typical modes of failure for the fiberoptics sensors. It is required to understand if and when a fiberoptics sensor fails, whether that failure was a result of mechanical stress (thermal cycling) or from radiation exposure.

7.6.3. Irradiation

The influence of irradiation on the performance of the fiberoptics-based measurement systems was experimentally evaluated. The two relevant characteristics are flux and fluence; the focus is on fluence – time-integrated flux. Due to errors in measurements resulting from vibration sources while at power, the dependence on flux could never be interrogated.

This report discusses the observations and findings on how temperature measurements change with change in fluence as the fiber is irradiated. The lifetime of the fiberoptics sensors, as a function of fluence, is determined for a small set of fibers. The total number of thermal cycles for the fiberoptics probe (all fibers) is twenty seven. A cycle is considered to be from room temperature conditions to operational temperature and is the result of testing, inadvertent shutdowns, and the planned shutdowns during the weekends. It is not directly clear if thermal cyclic stresses are responsible for the failure of the fibers, but some fibers failed almost immediately, likely due to thermal stress on the fiber splice.

The performed experiments demonstrated successful operation of temperature and neutron fiberoptics sensors up to 1x1019 n/cm2; however, all gamma fiberoptics sensors failed. The neutron fiberoptics sensors did not provide experimental data, which were representative of expected neutron distribution, because of high vibration noise levels.

Fiber baseline measurements

The fiber probes were tested prior to installation in the furnace; measurements were compared to those from the post-fabrication tests performed by Luna, the manufacturer of the fiber probes. Following installation into the furnace, while remaining outside of the reactor, further tests were completed and are documented in this report. The tests were required by the Reactor Safety Board to support the program authorization decision. The tests included various temperature transients to ensure reliability of the fiberoptics sensors after thermal stresses, to verify initial

temperature measurements, and to test safety systems. These measurements provide a baseline for going into the neutron and gamma radiation fields and to understand various influences on the measurement system during operation.

For every measurement, there are necessary references. These references are ideally taken at room temperature, so the measurements themselves would represent the temperature/radiation distributions plus room temperature/background radiation levels. For fiberoptics sensors, the distributions in temperature are as expected; however, the magnitude of the fiberoptics-measured values is far greater than the temperature values reported by the thermocouples in direct contact with the heating element. The cause for this discrepancy is not known, but it is suspected that the internal stresses induced in the fiber by the probe, along with miss-matched thermal expansion coefficients, introduce errors into the temperature measurement.

The temperature fiberoptics sensors performed well enough to produce results as illustrated in Fig. 1. The temperature distribution is shown axially along the centerline of the furnace. Thermocouples maintain an average heater temperature of 500°C , with an axial variation of 10-15°C. The observed difference in maximum values is likely the result of internal stresses in the fiberoptics probe due to thermal expansion differences in the quartz and fibers.

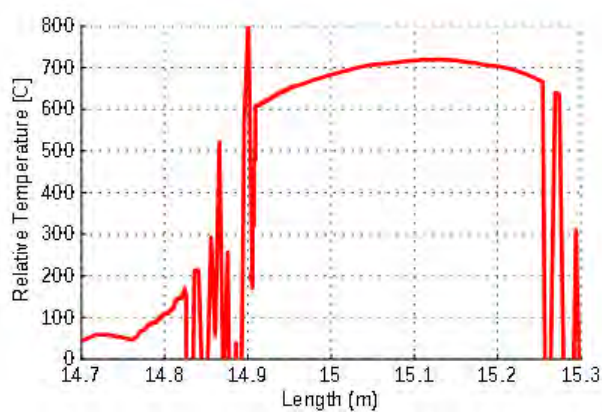

Fig. 1. Temperature distribution within the furnace at 500°C, the reactor is shutdown.

The “spikes” or very sharp gradients in Fig. 1 are the result of noise effects. It has been concluded that the “spike” does not preclude errors in the rest of the measurement but is merely an artifact at that specified spatial location.

Vibration effects

As observed in the earlier testing, vibration phenomena impact the fiberoptics measurements significantly. In order to understand the mechanism and minimize the influence of the vibrations, some troubleshooting actions were performed to isolate the sources. This also provides feedback as to when measurements should and should not be performed, so to enhance the available sets of data for analysis.

Vibration errors were noticed primarily at 1.0 MW operation of the research reactor as shown in Fig. 2. The 0W condition is representative of the reactor being shutdown, though due to decay heat, the power level is never actually 0W.

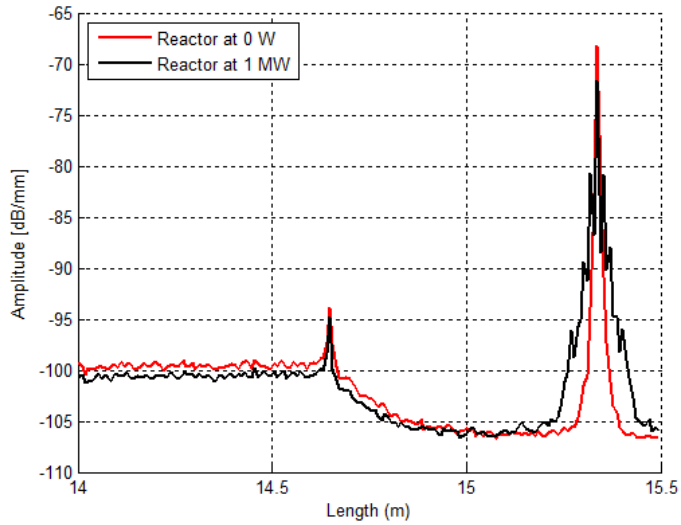

Fig. 2. Return loss of neutron fiber with reactor at two different power levels.

At 1MW, the reactor is operating at its full licensed capacity. Pumps are necessary for reactor operation and perform two functions: cooling and reduce radiation levels above the pool by allowing ^{16}N an opportunity to decay in the pool before reaching the surface. This second pump, called the diffuser, is close to the furnace and in fact pushes water directly down on it. The vibrations were suspected to be the result of the diffuser. However, as Figure 3 shows, this is not entirely the case. With the diffuser off, similar vibrations are observed. It is concluded then, that the vibrational modes of natural circulation are mostly responsible for these errors.

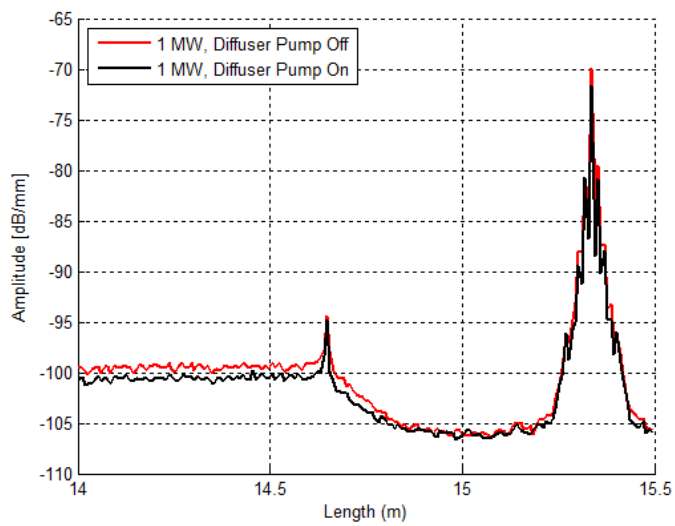

Fig. 3. Return loss of neutron fiber with the reactor at 1.0MW with diffuser pump in the on and off configurations.

Thus, for measurements to be without vibration, they must be taken with the reactor in a shutdown condition. It was also noticed that control rod movements introduced noise into the measurement, so care was taken to take measurements before the reactor was started up in the morning.

Fiber degradation with irradiation

As already discussed, the radiation fibers did not exhibit characteristics that could be correlated to the neutron fluence level or distribution that would be expected. The issue has not been resolved, so such measurements will be neglected in this report. It is likely that the result is due to high vibration noise. However, this vibration is due to natural circulation of the reactor and with the reactor shutdown (little-to-no vibration noise), there is still no apparent measurement data to be evaluated. Thus, the focus is on the return loss along the fiber as this provides indications of the fiber survivability, but it does not provide any data characterizing the actual performance of the sensors to measure various characteristics. Fluence-return loss dependencies were investigated as well.

The fiberoptics sensors are inherently sensitive to influences that change the characteristics of light propagation in the fibers, so it is expected that temperature, flux, and any time response associated with the two would result in measurement changes. An attempt to determine the flux sensitivity of measuring fiberoptics sensors is difficult due to vibration noise effects as a result of the reactor being at power.

Table 1. Fibers Tested and Their Survivability

Fiber Optic	Final Condition	Reason	Comment
Gamma 1	Failed	DOA	
Temperature 2	Failed	Unknown	Failed immediately at startup.
Neutron 3	Survived		
Gamma 4	Failed	DOA	
Temperature 5	Survived		
Neutron 6	Failed	DOA	
Gamma 7	Failed	Irradiation	Failed at 4.5e18 n/cm^2 fluence.
Temperature 8	Survived		
Neutron 9	Survived		
Gamma 10	Failed	Irradiation	Failed at 5.8e18 n/cm^2 fluence.
Temperature 11	Failed	Unknown	Failed immediately at startup.
Neutron 12	Survived		

Table 1 shows the results of the fiber optic survivability testing. There were only two fibers, both gamma sensitive, which failed as a result of the irradiation. The other two gamma fibers were dead on arrival (DOA). All of the neutron and temperature fibers, which were not DOA or failed immediately, survived the entire irradiation and thermal stressing cycles. It is likely that fibers failing immediately, only temperature fibers, were the result of thermal stresses during the initial heating of the furnace. Only seven of the twelve available fibers provided any results. These low numbers can be improved with increased quality of fabrication, since this was the first fiber probe of this type manufactured. The degradation of the fiberoptics sensors can be represented by a few experimental examples. The gamma and temperature fibers provide the best representation of what would be expected with irradiation.

1. Temperature-sensing fibers

The temperature fibers show particular trends during irradiation as the material properties change. Figure 4 shows the temperature measurements, with the furnace heater at an average temperature of 500°C and referenced to the non-irradiated scans, for the first 30 days (4.4e18 n/cm^2) of irradiation.

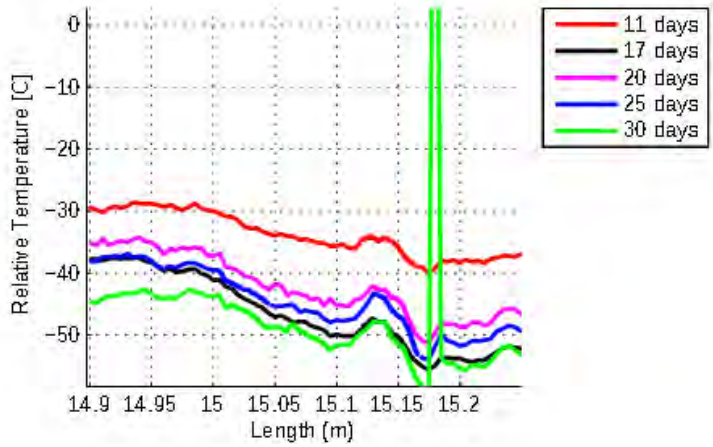

Fig. 4. Relative measurement drift of the temperature fiberoptics sensor during irradiation, referenced to the initial scan.

The scans suggest that irradiation damage relaxes the strain in the fiber, which then settles to a band of relative temperatures around -40oC to -50°C (the spike during the 30 day measurement is a noise artifact). The effect of irradiation is evident at 17 days (2.4e18 n/cm^2), then changes in measurement errors are no longer evident until about 40 days (5.6e12 n/cm^2) of irradiation, as illustrated in Fig. 5.

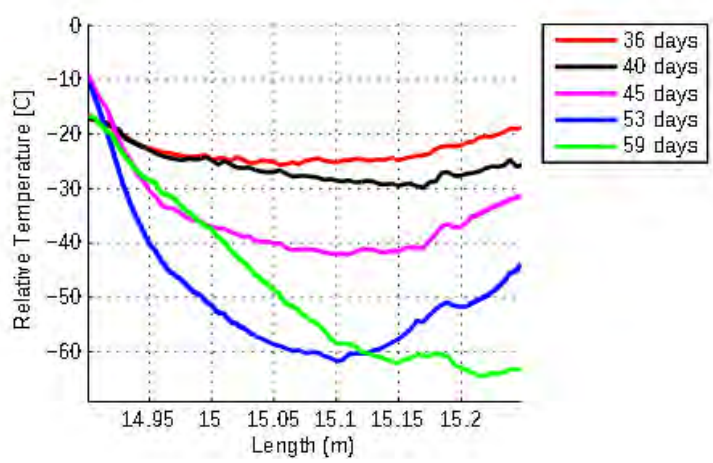

Fig. 5. Relative measurement drift of the temperature fiberoptics sensor during irradiation, referenced to the 30 day scan.

In Fig. 5, the reference scan is the 30 day scan. This is to provide a comparison with the seemingly equilibrium condition. However, beyond 40 days the trend in the measurements appears to continue, shifting the resulting measurements further in the same direction.

The axial flux distribution is not known. Consequently, the fluence data at each spatial location is not available. However, the effect of irradiation looks largely proportional to the flux distribution that would be expected (cosine shape).

Figure 6 illustrates that there are no discernible effects of fluence levels on the return loss of the fiber. In Fig. 6, the initial fiber return loss within just a few days of irradiation is compared to the final irradiation of the fiber. There is just a minimal increase in the overall return loss as would be expected from the results already shown. The temperature fiberoptics sensors seem to become radiation hardened. It is very possible that this effect can be software corrected and managed when enough understanding of the behavior becomes available through future studies.

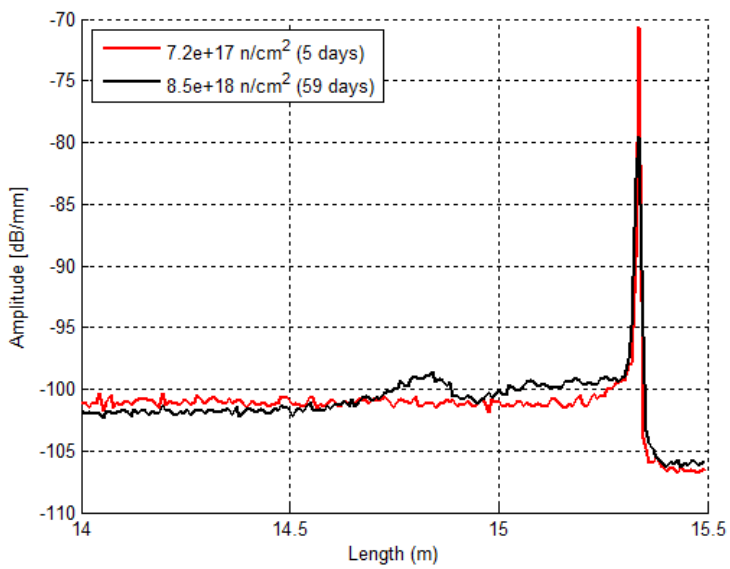

Fig. 6. Return losses in the temperature fiber as a function of distance for two fluence levels.

2. Gamma-radiation-sensing fibers

As shown in Table 1, two gamma fibers (Gamma 1 and Gamma 4) failed during fabrication and transport to Texas A&M University. However, two other gamma fibers (Gamma 7 and Gamma 10) remained functional and were used in the present analysis.

In Fig. 7, the return loss of the gamma fibers is shown during its irradiation. This shows a clear degradation in the measurement with time. Because the gamma fluence level is not known, the neutron fluence values are shown. The return loss is essentially unaffected up to 2.3e18 n/cm^2 with a short peak appearing at roughly 15.2 m. This peak is consistent with the following scan, showing a possible defect or sensitivity to the gamma/neutron fluence in the material.

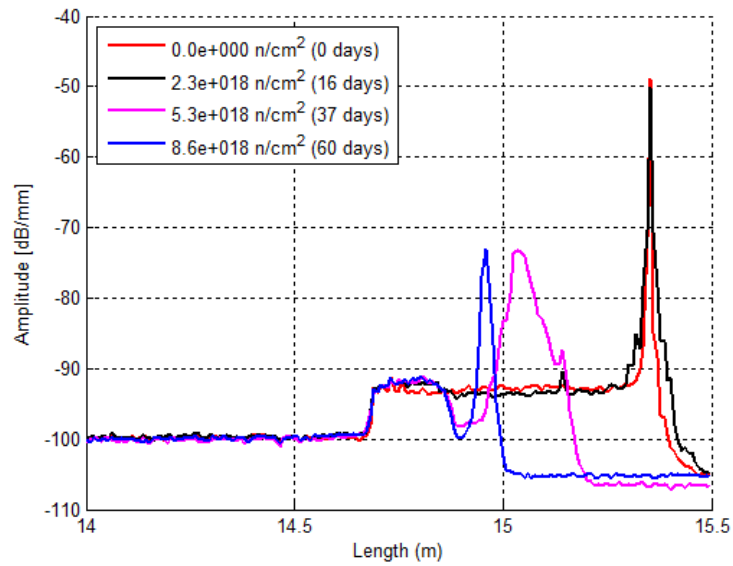

Fig. 7. First gamma fiber return loss as a function of distance from the OBR measurement device for various neutron fluences.

In Fig. 8, a more detailed "time-lapse" of the gamma fiber is shown. Two peaks grow with the fluence until ultimate fiber failure at 5.8e18 n/cm^2. These failure points do not track with the expected axial gamma flux.

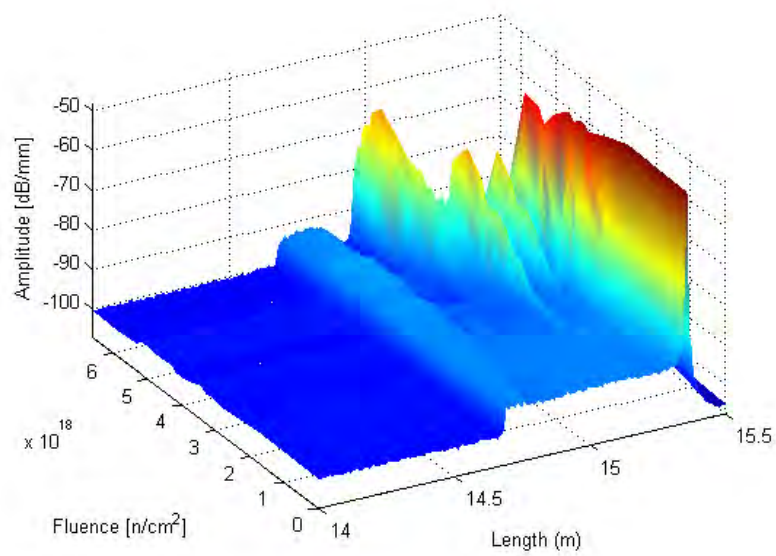

Fig. 8. First gamma fiber return loss as a function of neutron fluence and distance.

It is expected, given the uniform axial shielding characteristics of the furnace and fuel, that the gamma flux would track the neutron flux spatial distribution quite closely. This suggests the failure should appear more uniform than isolated at particular locations.

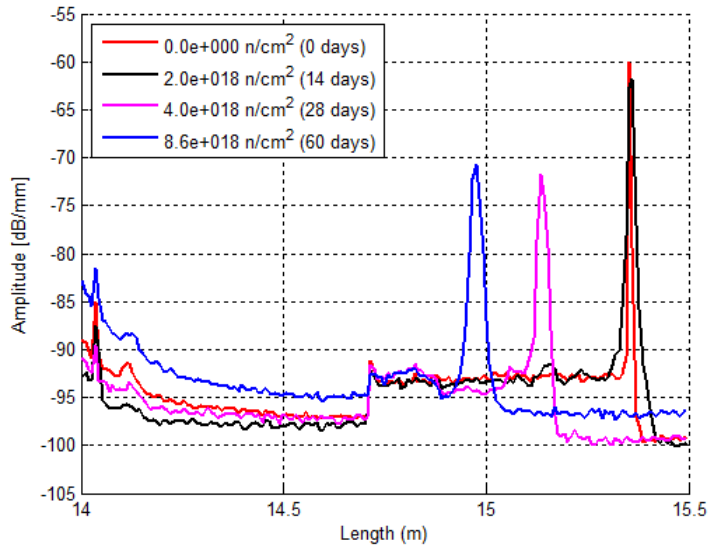

Fig. 9. Second gamma fiber return loss as a function of distance for various neutron fluences.

The observed behavior might be indicative of the gamma flux distribution non-uniformities, might suggest presence of gamma-sensitive impurities in the fiber limiting their lifetime, or might be indicative of developing mechanical stresses due to swelling.

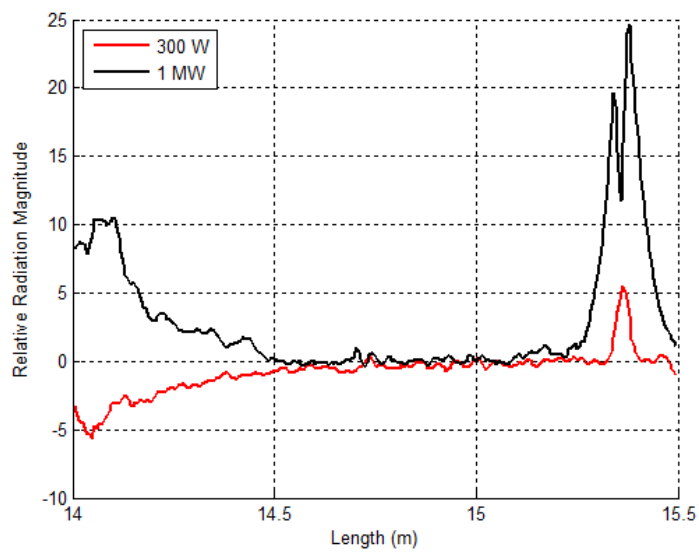

Fig. 10. First gamma fiber radiation measurement as a function of distance at different reactor power levels.

Notably, the onsets of the failure events for both gamma fibers appear in the same spatial location as illustrated in Fig. 9 (see Fig. 7 for the first fiber behavior).

Because the lifetimes of these two fibers are somewhat similar, the mechanism for their failure is likely to be the same as well. It is suspected, though not confirmed, that the likely failure mode is due to the fiber swelling. The following induced stress at ferrule interfaces might have damaged fiber cores.

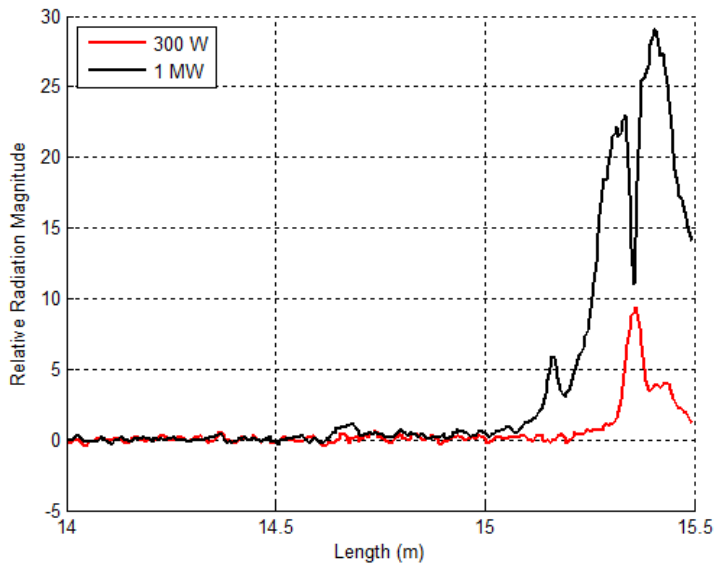

Fig. 11. Second gamma fiber radiation measurement as a function of distance at different reactor power levels.

The gamma fiber measurements take advantage of an additional software package, as discussed in this report, provided by Luna, to perform the calculations to determine the gamma fluxes. The difference between the reactor operation at 300W and 1MW is shown in Fig. 10. This corresponds to two different gamma flux levels. The region of interest is between 14.7 and 15.35 meters in Fig. 10. Both of these scans are referenced to a 0W scan showing no evidence of a flux dependence since the expected distribution is not evident above noise.

The peak broadening at roughly 15.35 meters (the end of the fiber) is the result of vibrations. The effects at between 14.0 and 14.5 meters are the result of a poor splice, which is not a concern in the other gamma fiber. Figure 11 does not show these effects for the second gamma fiber. Notably, the peak at roughly 15.2 m, as shown in Fig. 7, is also picking up in this measurement as illustrated in Fig. 9 and Fig. 11.

3. Neutron-sensing fibers

Figure 12 demonstrates that the neutron-sensing fibers appear to be much more radiation tolerant in the reactor environment than the gamma fibers. Across all of the neutron fibers, there are only small changes in the return losses during the entire irradiation period.

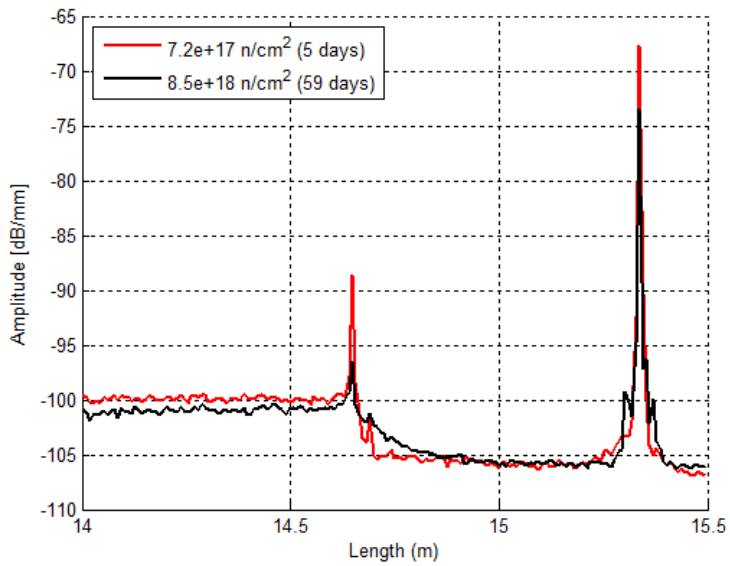

Fig. 12. Neutron fiber return loss as a function of distance for two fluence levels.

The calculations for neutron fibers are performed using the same specialized software package as for the gamma fibers. A comparison between reactor operation outcomes at 0W and 1MW is shown in Fig. 13.

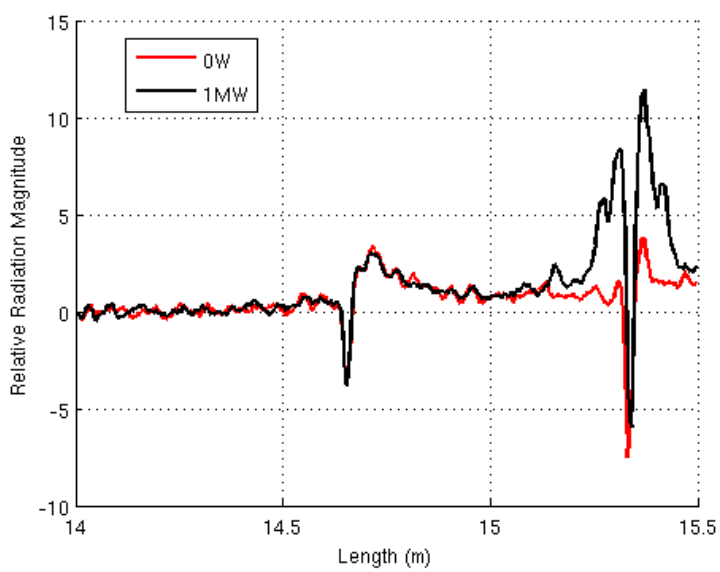

Fig. 13. Neutron fiber measurement as a function of distance at different reactor power levels.

Similar to the previous scans, the noise resulting from vibration-induced phenomena dominates any meaningful signal. Figure 14 suggests that there does not seem to be any observable effects due to fluence levels.

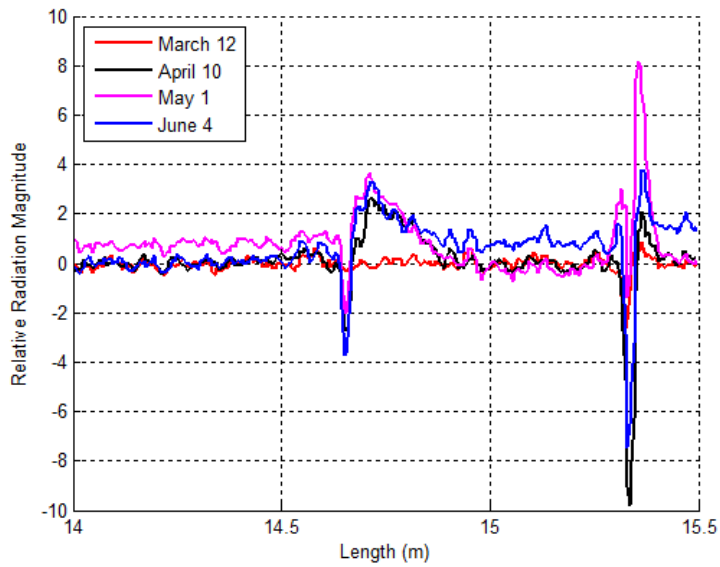

Fig. 14. Neutron fiber measurements for four different days as a function of distance at a reactor power level of 0W.

It is evident from the presented analysis that the gamma fibers are more sensitive to the changes resulting from the radiation exposure in a mixed gamma and neutrons radiation field compare to the neutron fibers. The temperature fibers actually appeared to trend more with radiation exposure than either of the radiation sensitive fibers.

All of the available gamma sensing fibers failed, either as a result of mechanical agitation or due to the influence of the mixed-field radiation exposure. The neutron and temperature fibers, which not initially failed, survived the irradiation in the reactor environment at an average temperature of 500°C.

7.7. Conclusions

It is conclusive that the furnace has been built to meet its performance specifications and operated as expected to meet project objectives. There are some minor operational issues identified which did not impact the safety of the system – namely, automatic startup and shutdown. The safety systems have been tested and performed to their design specifications.

With the delays in procurement and fabrication difficulties, the total irradiation of the fiber optics covered the span of 3 months. Another probe, with twelve more fiber optics has yet to be irradiated, preventing a good sample of data to develop an empirical model on fiber optic survivability. There were seven fibers that were irradiated: two temperature, three neutron, and two gamma fibers. The fibers of the first probe were all irradiated to a neutron fluence of 1.0×10^{19} +/- 7.7×10^{17} n/cm^2 at a nominal 500°C. Both of the gamma fibers failed at 4.5×10^{18} and 5.8×10^{18}n/cm^2, respectively, likely as a result of fiber-ferrule interaction due to fiber swelling as evident by identical failure modes at identical spatial locations.

Neutron and temperature sensing fiber optics showed significantly improved radiation resistance over the gamma fibers, but without a control at ambient temperature, it is difficult to understand the influence of high temperature irradiation on the annealing properties of the fiber optics.

Vibration and other noise sources prevented the validation of neutron and gamma fiber techniques and temperature measurements via the fiber optics were not equivalent to calibrated thermocouple readings. The spatial distributions of the temperature measurements seem to be correct, compared to modeling results, but their magnitude was too great. It is suspected the deviations are the result of internal stresses from mechanical stresses within the probe.

Although fundamental feasibility and potential applications for fiberoptics sensors have been established, the technology, by far, is not ready for near-term practical in-core implementations. The noted challenges include excessive dependencies of sensing system performance characteristics on vibrations due to thermo-mechanical core characteristics, resulting noise effects, internal fiberoptics material effects and their interpretation by the fiberoptics data acquisition and processing, and overall inherent dependencies of fiberoptics sensing technologies on accompanying software components to recover and interpret measured performance characteristics, and frequent calibration needs for the system to operate meaningfully.

These observations strongly suggest the need for further research efforts to systematically resolve these challenges, thus allowing taking a full advantage of the existing fiberoptics and distributed sensing capabilities for next generation in-core instrumentation solutions for current LWRs as well as SMRs and advanced reactor systems.

7.8. References

1. E. E. Anderson, S. Langer, N. L. Baldwin, F. E. Vanslager, “An In-Core Furnace for the High Temperature Irradiation Testing of Reactor Fuels,” *Nucl. Tech.*, **11**, pp. 259-265. 1971. Gulf General Atomic Company.

8. Sensor Networks and Data Processing Algorithms for Future Nuclear Systems

8.1. Introduction

8.1.1. Characterization of In-Core Conditions

Advanced sensor networks and data processing algorithms are needed for future generation nuclear reactors and energy systems. In many cases, detector systems designed for current generation LWRs cannot survive in advanced reactors. Reactor safety margins for these advanced systems must account for uncertainty in reactor operating conditions. Accurate on-line flux reconstruction would significantly reduce the uncertainty present in the core-wide fission distribution and allow for safer reactor operation.

This work will focused on flux reconstruction techniques for the very high temperature reactor (VHTR), one of several next-generation designs supported by the Generation IV International Forum (GIF). The VHTR is an advanced gas-cooled high temperature reactor (HTR). HTRs are attractive because their outlet temperature allows for high-efficiency energy conversion cycles. Additionally, HTRs could be used to supply process heat for industrial applications.

Gas-cooled graphite-moderated reactors have long been a subject of research and application within the nuclear engineering community. The first HTR test reactors came online in the late 1960s. The first was built in Winfrith, and brought to power in 1966. It was a 20 megawatt design built by the Organization for Economic Co-operation and Development High Temperature Reactor Project (DRAGON). In May of 1967, the General Atomic designed Peach Bottom reactor was brought to full power for the first time. The final first-gen HTR test reactor was the German built AVR pebble-bed design that came online in February 1968. [27] Work on HTRs continued and the first full-size commercial HTR, Fort Saint Vrain, came online in 1977. Throughout its operational life, Fort Saint Vrain had many problems with various non-nuclear components. It was shutdown in 1992.

Interest in HTRs originated, and continues to this day, due to the flexibility of the design. The gas coolant has little effect on the neutronic behavior, decoupling neutronics from thermal-hydraulics and giving nuclear engineers more freedom when designing them. HTRs have been built that accept Uranium and Thorium based fuels. HTRs have been proposed to burn weapons-grade plutonium and actinides present in spent LWR fuel. HTRs can also accept a variety of fuel forms; however, all modern designs use TRISO particles or some variant thereof. TRISO particles are known for their ability to contain fission products during normal operation and accident conditions.

In recent years, the United States has been researching such reactor designs through the Next Generation Nuclear Plant (NGNP) project. The NGNP project was led by the Idaho National Laboratory (INL) and considered designs proposed by major reactor vendors Westinghouse, Areva, and General Atomics. All designs were thermal reactors moderated by graphite and cooled by helium. Both pebble bed and prismatic block designs were proposed, but the shuttering of South Africa's pebble bed reactor project led to increased focus on the prismatic block design. The NGNP project considered both 350 MWth and 600 MWth designs. [3]

The INL identified the development of instrumentation that can function inside the reactor as a principal risk to the NGNP project. [2]

Table 1 summarizes typical operating conditions inside a HTR. Designing sensors that can withstand prolonged exposure to the outlet temperature while in a harsh neutron and gamma radiation field is an engineering challenge. Reaching a 1000 °C outlet temperature is a long term goal of the VHTR. In addition to the high temperatures and radiation field, the sensors must be able to withstand the graphite dust in the reactor. Estimating the total amount and distribution of the dust in HTRs is a research area. [5]

Table 1. Normal Operating Conditions in a HTR

(The fast fluence is taken to be all neutrons about 0.1 MeV. [26,4,40])

Reactor Characteristic	Performance Domain
Coolant inlet temperature	490° - 600° C
Coolant outlet temperature	700° - 950° C
Coolant pressure	7 – 8 MPa
Peak fast neutron fluence	1.7×10^{20} – 1.67×10^{21} n/cm^2

8.1.2. Potential In-Core Neutron Sensors

The primary candidates for HTR in-core neutron detectors are fission chambers, self-powered neutron detectors, and fiber optic sensors.

Fission chambers have successfully been used as in-core neutron detectors in a variety of reactors.

For example, in-core fission chambers were developed for use in fast breeder reactors where they were used during startup and shutdown when counting rates are too low to use detectors under the reactor vessel. They were also used during core loading to closely monitor reactivity. Fitting the necessary electronics into a package small enough to be used inside the core was difficult; however, all engineering challenges for the use of in-core fission chambers in sodium fast reactors were solved. Sodium fast reactors operate at about 600° C. [7, 33]

Fission chambers were also chosen for the wide range power monitor in Japan's High Temperature Test Reactor (HTTR). Placed at the top of the permanent reflector, they were exposed to 600° C during reactor operation. [29]

Further research and development is needed to develop fission chambers capable of withstanding the design operating temperatures of the VHTR.

Self-powered neutron detectors (SPNDs) are desirable because of their simple electronics, reliability, robustness, small size, and small power requirements. SPNDs are frequently used for in-core instrumentation in PWRs. Advanced SPNDs capable of withstanding HTR in-core conditions are a subject of research. One such study for silicon carbide SPNDs determined that they could not survive the temperature and fast fluence present in the active core region and recommended that they be placed in the inner reflector instead. [21, 17]

Fiber optic sensors are another candidate for in-core neutron flux detectors; however, they are also the most unproven. Using fibers for in-core temperature sensors has been an area of

research for some time, and challenges still remain. One common problem cited is degradation of performance as a result of radiation-induced darkening. Recent research by Luna Technologies has shown that fiber optic sensors are capable of measuring gamma flux as well as thermal and fast neutron fluence. [14, 13] Further research by Luna showed that the fibers could be used as distributed neutron sensors.

This work focused on the fiber optic distributed neutron sensors developed by Luna Technologies. We believe that the risk in developing a reconstruction algorithm for a yet unproven sensor system is justified by the increase in information that distributed sensors would bring. Quantifying the benefits of distributed neutron sensors will encourage others to fully develop them.

8.1.3. Objectives

The two main tasks of this effort were

- to use a reference VHTR model to quantify the operational characteristics of the reactor and
- to develop an algorithm capable of reconstructing the neutron flux from in-core sensors.

The chief purpose of the VHTR simulations was to generate detailed in-core neutron flux distributions to test the flux reconstruction algorithm.

A flux reconstruction algorithm was sought that

(1) did not rely on a neutron diffusion or transport model of the core,

(2) accurately reconstructed the core-wide neutron flux using a reasonable number of sensors, and

(3) was robust against signal noise and sensor failure.

An algorithm that did not rely on a diffusion or transport model of the core was desired because of the difficulty in generating a model that is both accurate over the entire core lifetime and computationally inexpensive.

8.2. VHTR System Model

8.2.1. Introduction

The VHTR design used in this work was based on the three ring 600 MWth prismatic-block NGNP design (see Table 1 below) developed by Idaho National Laboratory. [25, 2]

The VHTR is a graphite-moderated, helium-cooled reactor. The principal building block of the reactor is a graphite hexagonal prism. These prismatic blocks are stacked together to form the core. Graphite is used as the primary structural material, neutron moderator, and neutron reflector. Enriched uranium is used as fuel. The VHTR is designed to be passively safe. In order to reach this goal, the active core is annular in shape. The graphite inner reflector provides a large heat sink capable of absorbing heat generated by the fuel during accident conditions.

The annular active core region is made of graphite blocks that contain fuel rods, burnable poison rods, and coolant channels. Fuel rods are made of TRISO particles suspended in a graphite matrix.

TRISO particles are capable of containing fission products during normal operation and accident conditions. Helium was chosen as the working fluid in the primary loop because it is chemically inert.

Table 1 summarizes the principal design parameters of the reference VHTR system used in the project as a baseline design to evaluate in-core conditions.[25,2]

Table 1. VHTR System Parameters

Design Parameters	Performance Domain
Power	600 [MWth]
Fuel	UO2
Moderator	Graphite
Coolant	Helium
Coolant pressure	7.12 [MPa]
Core inlet temperature	490 [°C]
Core outlet temperature	1000 [°C]
Core diameter	7 [m]
Core height	10.7055 [m]

8.2.2. Applied Codes and Models

Simulation Tools

In order to develop and test a flux reconstruction algorithm, detailed in-core flux distributions for a VHTR were generated. The neutron transport code MCNP5 was chosen as the primary computational tool for this project. MCNP5 uses the Monte Carlo method to find the solution of the transport equation. Instead of numerically discretizing the integro-differential neutron transport equation, Monte Carlo methods seek to model the neutron transport process explicitly. A pseudo-random number sequence along with proper sampling techniques are used to model individual neutron histories.

The fundamental mode is found by repeatedly simulating batches of neutrons. Each batch starts off as a collection of fission sites (the fission sites for the first iteration are a guess). A predetermined number of neutrons are generated at these fission sites and their energies sampled from a fission spectrum. These neutrons are transported until they are absorbed or leak out of the system. If any of the absorptions result in a fission, the fission site is stored for use in the next batch.

This process is equivalent to power iteration, and so power iteration convergence theory from deterministic transport is relevant. [23] The chief advantage of the Monte Carlo method is that the transport process is simulated without significant spatial, angular, or energy discretization. Geometry can be modeled exactly provided an accurate algorithm exists to track the neutron's position inside the system. Nuclear interactions can be sampled using a continuous energy spectrum. The chief disadvantage of Monte Carlo methods is their poor rate of convergence. All quantities of interest must be extracted from a finite number of neutrons histories.

Monte Carlo codes are advantageous for HTR analysis because they can explicitly model the so-called double-heterogeneity that arises due to the TRISO particles. Virtually all nuclear power reactors have one level of heterogeneity in their design -- a heterogeneous lattice of fuel, coolant, and moderator. In VHTRs, the fuel is a heterogeneous mixture of TRISO particles and graphite. This double heterogeneity has a quantifiable effect on resonance absorption because, while the TRISO kernels are physically very small, they are several mean free paths long to neutron's whose energies lie in fuel cross-section resonances. [35]

The ability of MCNP5 to exactly model the full core was used to avoid the assembly homogenization process that occurs during traditional deterministic full core calculations. In a three ring annular core, two of the three rings are adjacent to the reflector. The long neutron mean free path in graphite causes the neutron energy spectrum in the blocks to be affected by the adjacent reflector blocks. Researchers have successfully used conventional homogenization techniques to generate accurate results for BOL cores; however, modeling fuel depletion accurately is difficult. Neutron flux gradients in the fuel assemblies next to the reflector cause them to deplete unevenly. [12] This phenomena cannot be captured with traditional infinite lattice depletion runs.

The core burnup calculations were performed using VESTA. VESTA is a coupling interface between MCNP5 and ORIGEN. VESTA automatically sets up 43,000 group spectrum tallies in every material marked for depletion. This spectrum is then used to determine the reaction rates in each. This data is passed to ORIGEN which depletes each material separately. VESTA then receives the depleted materials from ORIGEN and passes them back to MCNP5 for use in the next time step. [18, 10, 31]

Core Geometry Preliminaries

The VHTR core was built from hexagonal prism graphite blocks. Two different types of blocks made up the core: reflector blocks and fuel blocks. Right hexagonal prisms and hexagonal lattices were used throughout the design of the VHTR. A right hexagonal prism is fully defined by its height and half-pitch. The half-pitch is defined as a line that starts at a hexagon's center and intersects of one of its side's at a right angle. A collection of regular hexagons arranged face-to-face forms a hexagonal lattice. A hexagonal lattice is fully defined by its half-pitch. Figure 1 depicts a hexagonal prism and a hexagonal array. The half-pitch is shown with a red line, while height is shown with a blue line.

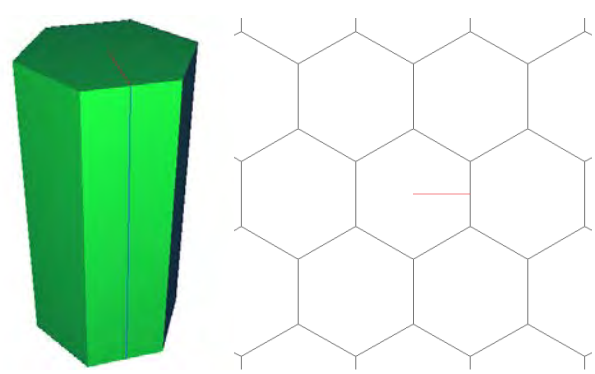

Fig. 1. A hexagonal prism (left) and a hexagonal lattice (right).

Reflector Block Geometry

A reflector block is a hexagonal prism made of solid graphite; however, some reflector blocks are modified to contain coolant channels, control rod holes, and reserve shutdown channels. The reserve shutdown channels are the same size as the control rod holes and will not be redefined in the following tables. Figure 2 shows the four different permutations of the reflector block design. Reflector blocks directly above and below the active core contain coolant channels.

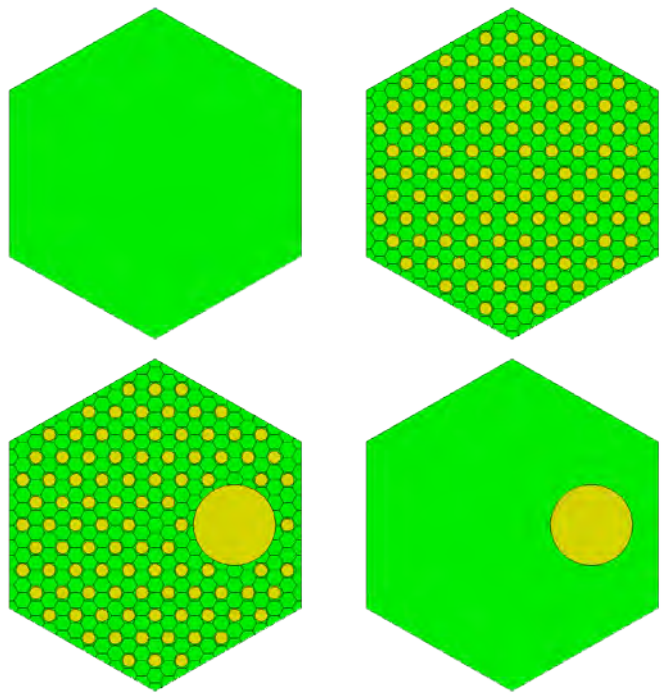

Fig. 2. The four variations of reflector blocks found in the core.

Table 2 summarizes the geometric and material properties of the reflector blocks. In the table, the control rod location is expressed as the distance from the block center as measured along the half-pitch line shown in Fig. 1.

Table 2. Reflector Block Parameters

Reflector Block Parameters	Reference Design Data
Block height	79.3 [cm]
Block half-pitch	18 [cm]
Graphite density	1.72 [g/cm^3]
Coolant channel height	79.3 [cm]
Coolant channel radius	0.79375 [cm]
Coolant channel lattice half-pitch	0.9398 [cm]
Control rod (CR) hole height	79.3 [cm]
CR hole radius	5.05 [cm]
CR hole center	9.75614 [cm]

Fuel Block Geometry

A fuel block is a graphite hexagonal prism with coolant channels, fuel pins, and burnable poison pins arranged inside the block in a hexagonal lattice. The fuel and burnable poison pins are shorter in height than the fuel block.

Graphite plugs are used to fully enclose the rods inside the fuel block. Additionally, each fuel block has a handling hole drilled half-way through the center of each block. The handling hole is used by the fuel reloading machine to move the fuel blocks during fuel shuffling and reloading.

A fuel block layout is shown in Fig. 3.

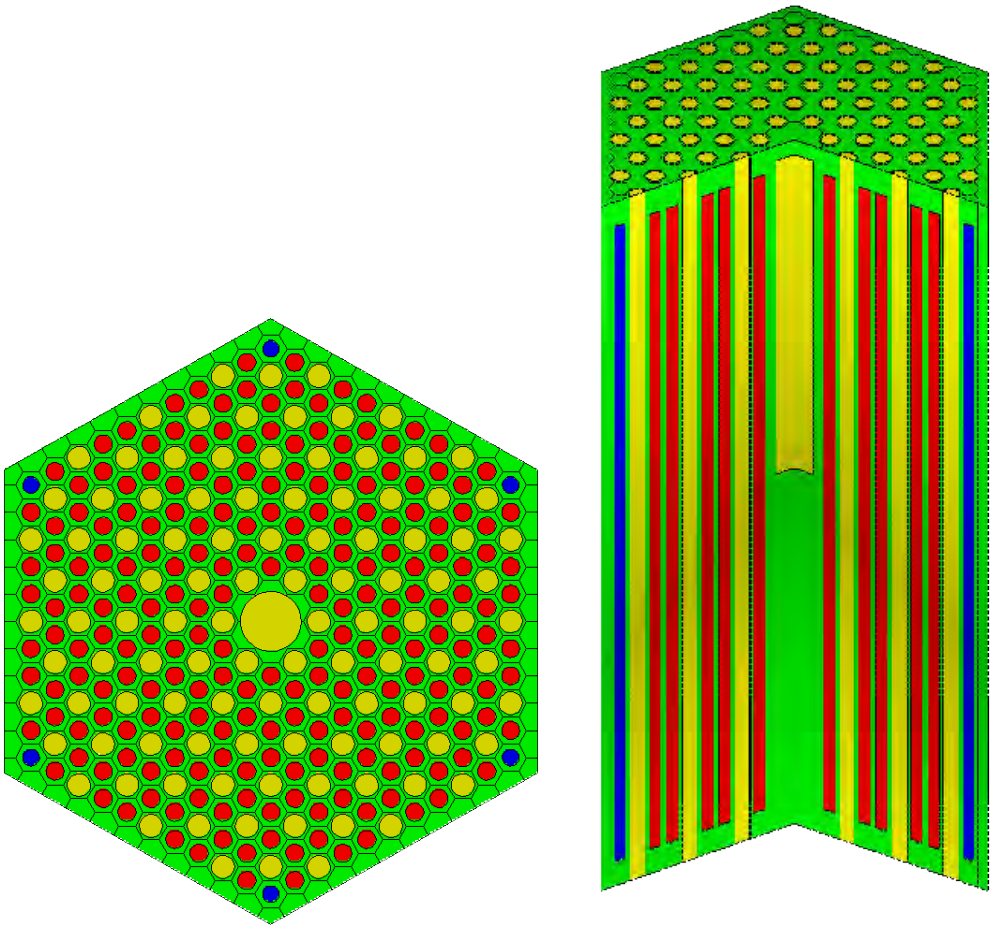

Fig. 3. Cross section (left) and cut-out (right) views VHTR fuel block.

Graphite is shown in green, fuel rods are shown in red, coolant channels are shown in yellow, and burnable poison pins are shown in blue.

Table 3 summarizes the geometric and material properties of the fuel blocks.

Table 3. Fuel Block Parameters

Fuel Block Parameters	Reference Design Data
Block height	73.9 [cm]
Block half-pitch	18 [cm]
Graphite density	1.72 [g/cm^3]
Fuel rod	
Height	73.95 [cm]
Radius	0.6223 [cm]
Coolant channel	
Height	79.3 [cm]
Radius	0.79375 [cm]
Burnable poison	
Height	73.95 [cm]
Radius	0.5715 [cm]
Handling hole	
Height	36.54 [cm]
Radius	2.0638 [cm]
Shutdown channel	
Height	79.3 [cm]
Radius	5.05 [cm]
Center	9.75614 [cm]

Fuel Rods

The exact geometry of each TRISO particle was modeled explicitly. The TRISO particles were modeled as five concentric spheres. The innermost sphere, called the kernel, contained uranium oxide.

A porous carbon buffer layer surrounded the kernel to accommodate any swelling or deformation of the irradiated kernel. The two pyrolytic carbon layers and silicon carbide layer are present to contain fission products.

Table 4 summarizes the geometric and materials properties of the TRISO particles.

Table 4. TRISO Particle Parameters

TRISO Structure	Material	Outer Radius [μm]	Atom Density
Fuel Kernel	UO_2	300	7.2451E-02
Carbon Buffer	C	400	5.7308E-02
First PyC Layer	C	440	9.4160E-02
SiC Layer	SiC	475	9.6152E-02
Second PyC Layer	C	515	9.74E-02

Fuel rods consist of TRISO particles suspended inside a graphite matrix. In reality, the particles are scattered stochastically throughout the matrix during the manufacturing process. In the model, the TRISO particles are arranged in a rectangular lattice as shown in Fig. 4. The lattice pitch was chosen such that the packing fraction was satisfied and no TRISO particles where truncated. A packing fraction of 25 volume % was used.

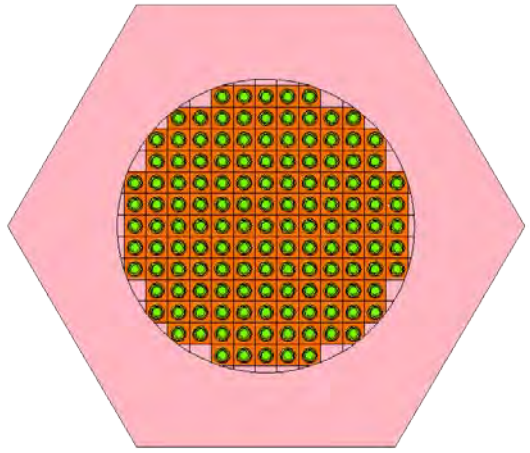

Fig. 4. TRISO lattice inside a fuel pin.

Burnable Poison Pins

The burnable poison pins were made of boron carbide particles interspersed in a graphite matrix. Like the fuel pins, the burnable poison particles were modeled as a regular rectangular lattice.

The boron kernel enrichment and kernel size are parameters that can be varied on a per-block basis to flatten the power profile and control reactivity. Nominal BP particle dimensions are shown in Table 5.

Table 5. Burnable Poison Particle Parameters

Structure	Material	Outer Radius [μm]	Density [g/cm^3]
Kernel	B_4C	100	2.47
Carbon Buffer	C	118	1.0
PyC Layer	C	440	1.87
Matrix	C	-	1.72

Control Rods

The control rods are made of B4C particles interspersed in an annular graphite compact and clad with Incoloy-800.

The composition of Incoloy-800 was taken from PNNL's Compendium of Material Compositions report. [28]

The kernel size, B-10 enrichment, and packing fraction of the B4C particles can be varied to produce a control rod of the desired reactivity worth. In this work, the dimensions of the B_4C particles are identical to those used in the burnable poison pins.

The control rods span the entire length of the reactor when fully inserted. The control rod design parameters are summarized in Table 6.

A cross section of the control rod is shown in Fig. 5.

Table 6. Control Rod Parameters

Control Rod Parameters	Reference Design Data
Cladding inner diameter	2.513 [cm]
B4C compact inner diameter	2.64 [cm]
B4C compact outer diameter	4.13 [cm]
Cladding outer diameter	4.257 [cm]
Cladding	
Material	Incoloy-800
Density	7.94 [g/cm^3]
Compact	
Packing fraction	40 [vol. %]
B-10 enrichment	90 [wt. %]

Core Arrangement

Fuel and reflector blocks are stacked in a hexagonal lattice to form the reactor core. The blocks are stacked 14 levels high. The bottom two levels form the lower reflector, levels 3-12 contain the active core, and levels 13-14 form the upper reflector. All blocks in the top level, level 14, are only 39.65 centimeters high.

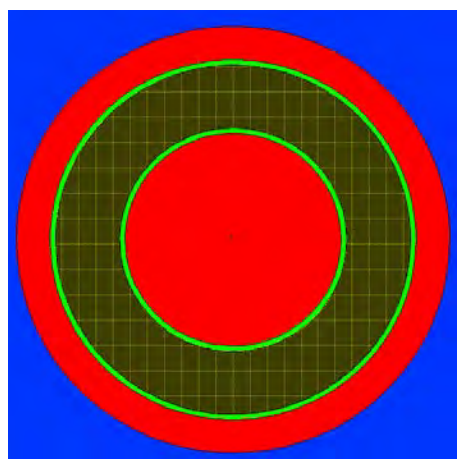

Fig. 5. Control rod.

Figure 6 shows a simplified cross section of an axial level that contains the active core. Fuel rods, coolant channels, and burnable poison pins are not pictured. Instead, the fuel blocks are shaded with a solid color. Handling holes, control rod channels, and reserve shutdown channels can be seen.

The control rod channels are located in the outer reflector and the inner-most ring of the active core. The remaining penetrations are reserve shutdown channels.

While the core exhibits 1/6th periodic symmetry, the full core was modeled within MCNP to make simulating non-symmetric neutron flux distributions possible. While not explored in this work, non-symmetric distributions could arise from skewed control rod insertions. The full core model was used to generate reference neutron flux maps.

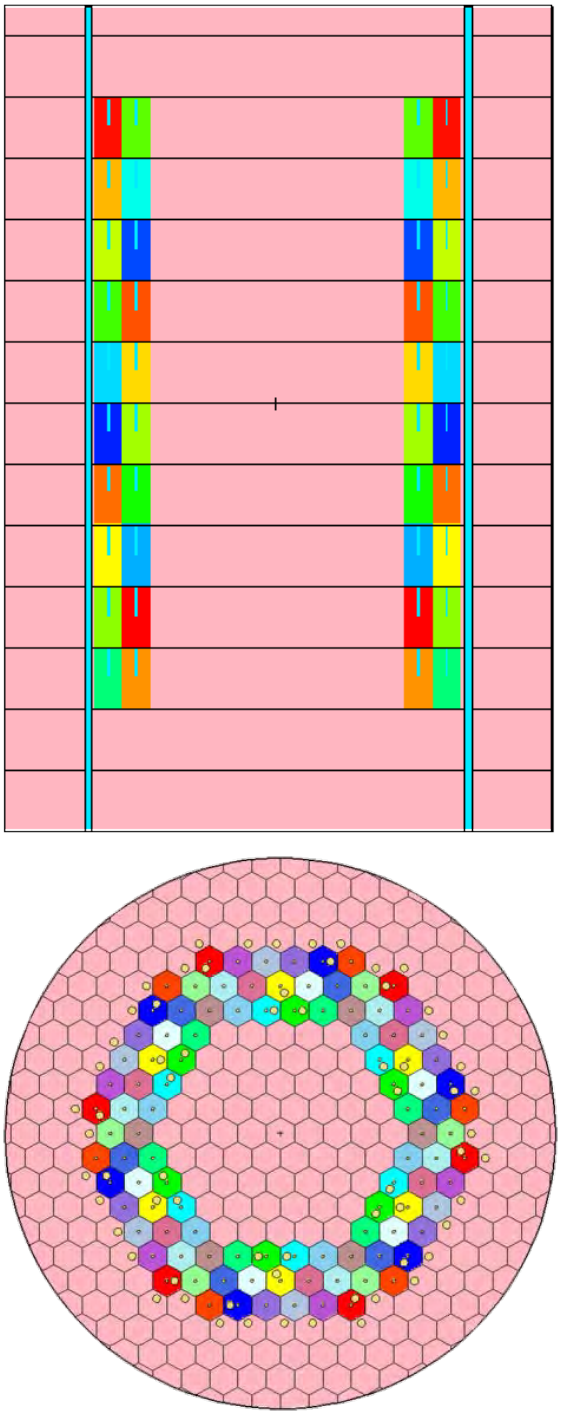

Fig. 6. VHTR core.

Burnup Model

In order to simplify burnup analysis, the core was loaded with fresh fuel only, control rods were left fully withdrawn, and the burnable poison pins were replaced with graphite. Fuel block shuffling was not considered.

A 1/6th symmetric model was utilized for the burnup calculation to improve power iteration's convergence to the fundamental mode. Periodic symmetry is the true symmetry present in the problem, but MCNP5 did not supply a straightforward way to generate periodic symmetry in this geometry.

Mirror symmetry was used instead as an engineering approximation to reality. Figure 7 shows the one-sixth core model. Reflecting surfaces are shown in red.

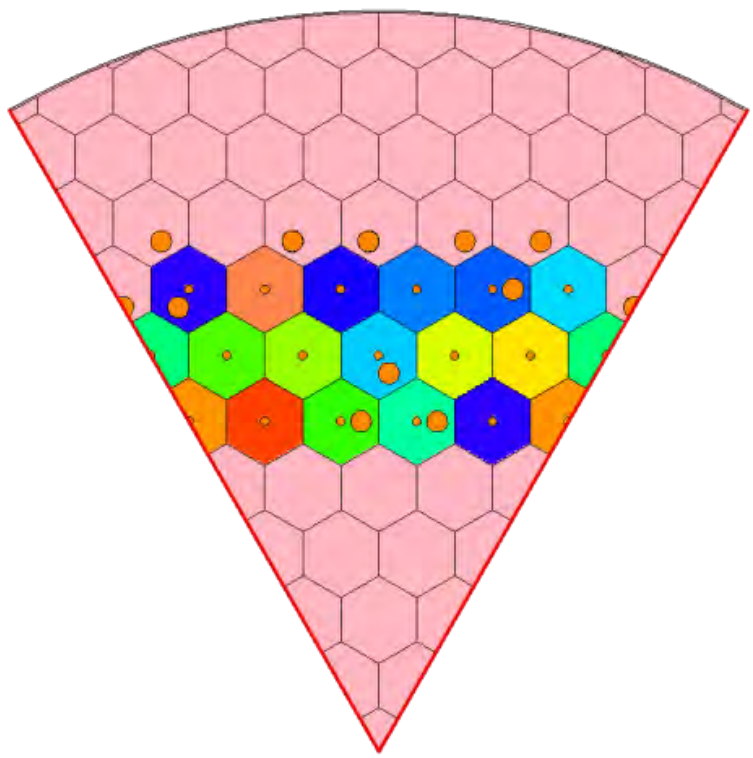

Fig. 7. One-sixth of the VHTR core model.

8.2.3. Performance Analysis

Burnup Results

Figure 8 shows k_{eff} (effective multiplication factor) as a function of time. The omission of burnable poisons led to significant excess reactivity. The initial drop in reactivity was due to fission products such as Xe-135 reaching their equilibrium concentrations. After the initial drop, k_{eff} decreased linearly and the core went subcritical between 489 and 508 days.

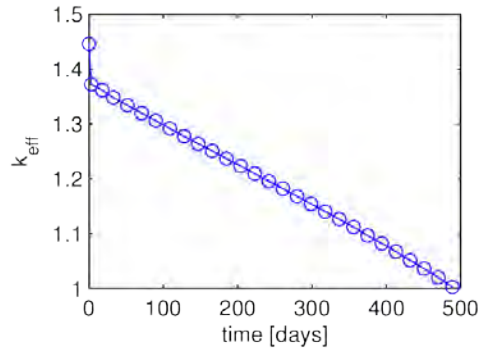

Fig. 8. Effective multiplication factor as a function of time.

The neutron flux peaking factor as a function of time is shown in Fig. 9. The peaking factor starts out at 1.44 and decreases as the core is depleted.

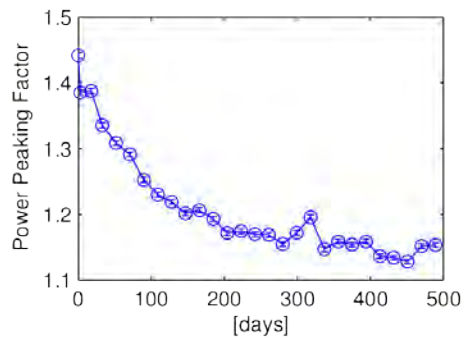

Fig. 9. Neutron flux peaking factor as a function of time.

This work was particularly concerned with the location in the core where neutron flux was at a maximum. The location of the hot spot was a complex function of time. Figure 10 shows how the neutron flux hot spot moved up and down the core as a function of time.

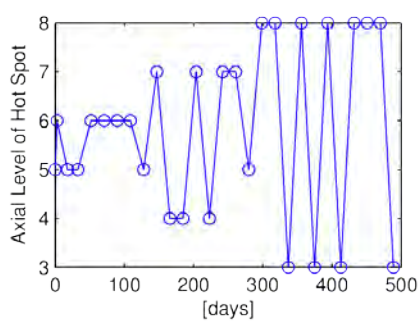

Fig. 10. Axial level of neutron flux hot spot as a function of time.

This complex behavior shows the need for a robust sensor network capable of providing sufficient information to reconstruct the in-core flux distribution.

After the burnup runs were completed, neutron flux mesh tallies were taken to create the detailed neutron flux distributions at each time step. These tallies spanned the entire core with a 200 by 200 by 24 mesh and were used as reference flux distributions for the flux reconstruction algorithms. The mesh had a fine x and y discretization to capture the complex flux distribution arising from the fuel pin lattice. The z discretization was relaxed in order to reduce the runtime necessary to converge the flux tallies in each mesh cell. The dimensions of a single mesh cell are given in Table 7.

Table 7. Dimensions of a Single Mesh Cell

3D Cell	Dimensions
Δx	3 [cm]
Δy	3 [cm]
Δz	46.23 [cm]

Figure 11 shows the thermal flux distribution in the reactor at several different times during operation. The slice in the xy plane contains the neutron hotspot.

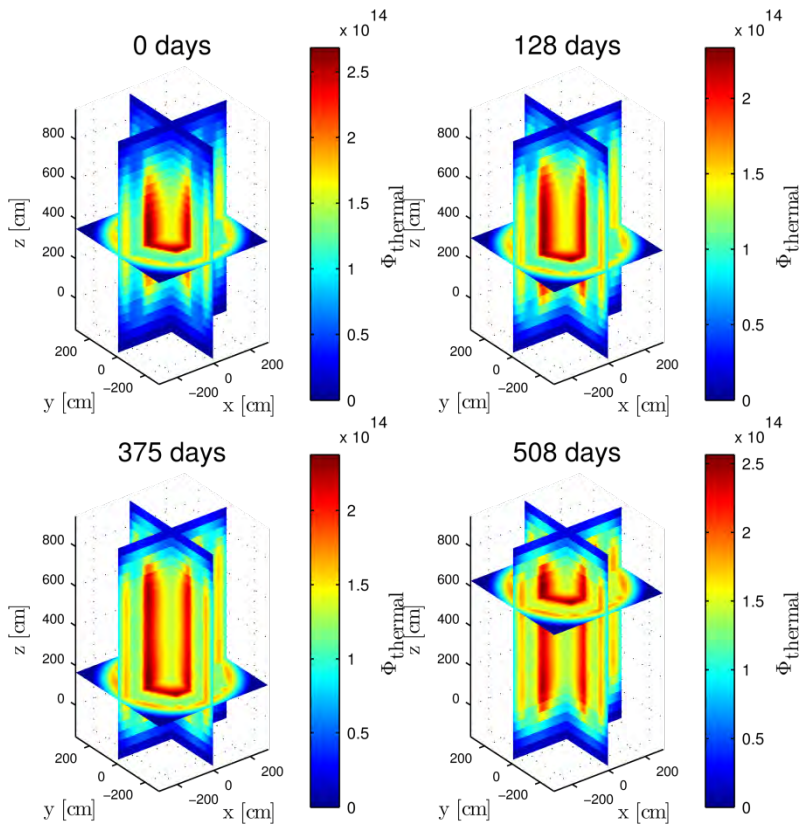

Fig. 11. Snapshots of the thermal neutron flux (incident neutron energies of E<1E-6 MeV) taken at several time points during operation.

In order to illustrate the fidelity missing from the coarse z discretization, several mesh tallies with a 256 by 256 by 128 mesh were run. Figures 12 and 13 show these tallies at the beginning-of-life and end-of-life, respectively. The finer z discretization allows the thermal flux peaks between fuel blocks to be resolved. No other new characteristics are observed.

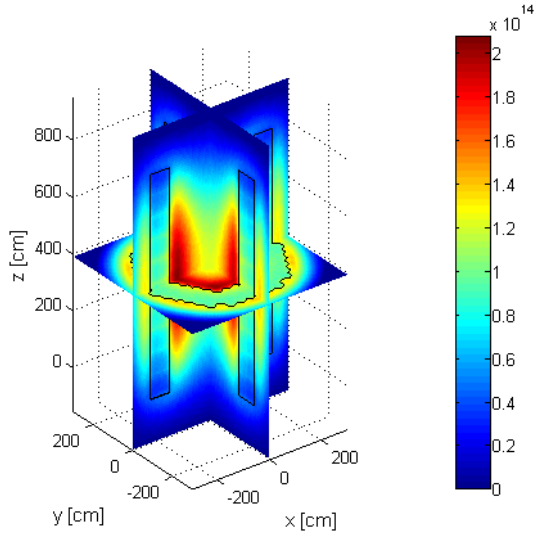

Fig. 12. Thermal neutron flux (incident neutron energies of E<1E-6 MeV) distribution for the VHTR core taken at BOL.

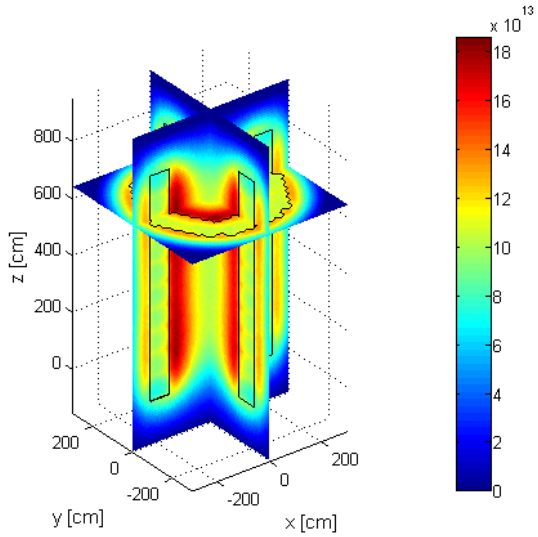

Fig. 13. Thermal neutron flux (incident neutron energies of E<1E-6 MeV) distribution for the VHTR core taken at EOL.

Effects of control rods and burnable poisons

As stated previously, the goal of the MCNP calculations was to generate data representative of the thermal flux distribution in an operating VHTR. While the intent was for the results to be as realistic as possible, a large approximation was made by not considering in-core control material.

The decision to use an uncontrolled core was based on the difficulty of calculating appropriate burnable poison loading. Finding a configuration of burnable poisons and control rods that keeps the core critical for the duration of its lifetime is a complicated problem that must be solved with an optimization algorithm. The long runtime of a single depletion simulation makes optimization algorithms which rely on repetitive simulations unfeasible. Additionally, the 3D nature of the fuel and burnable poison loading in the VHTR makes these types of calculations more difficult than their counterparts for LWRs.

In a k-eigenvalue problem, the reactor is brought to a steady-state configuration by changing the number of neutrons released during fission. As long as k_{eff} is close to unity, this has little effect on the reactor; however, as k_{eff} moves away from unity the neutron spectrum will change.[6] In the present simulation, this effect was largest at BOL when k_{eff} was the highest. In order to investigate the overall effects on the system, a BOL core with control rods inserted and a uniform burnable poison loading was run and flux tallies were taken. This controlled core had a k_{eff} of 1.00338. The purpose of this core loading was to provide the insight as to how much control rods and burnable poisons would affect the in-core neutron flux distribution and neutron spectrum. The thermal flux maps for this core configuration are shown in Fig. 14.

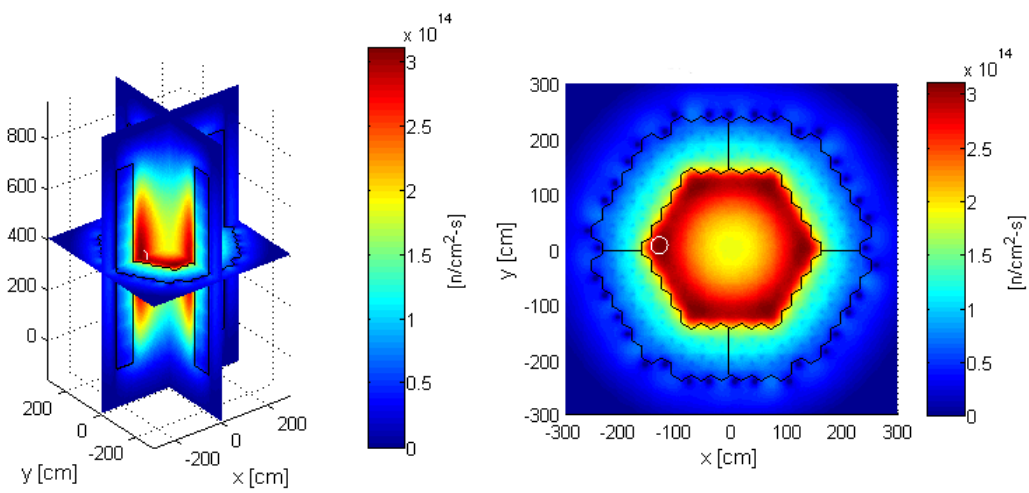

Fig. 14. Thermal neutron flux (incident neutron energies of E<1E-6 MeV) in the controlled reference VHTR core taken at BOL.

The control rods and burnable poison pins cause local depressions in the thermal flux. Figure 15 compares the neutron spectrum of the controlled and uncontrolled cores. The thermal flux peak in the uncontrolled system is considerably higher than in the controlled system.

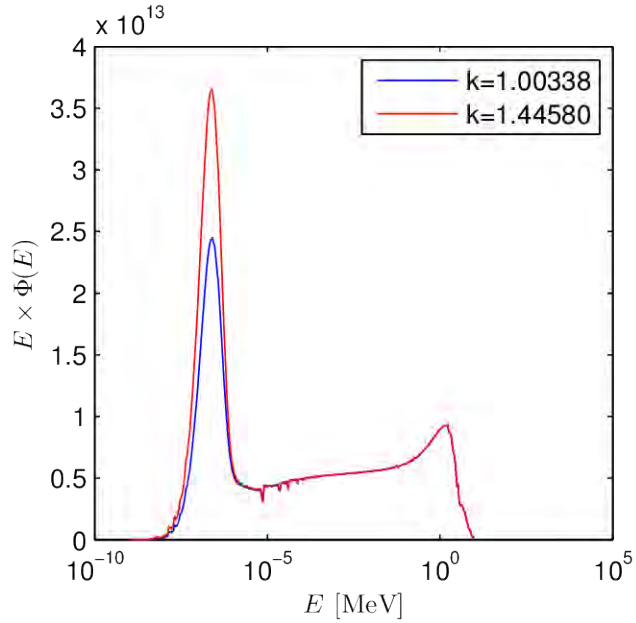

Fig. 15. Comparison of neutron spectra in controlled and uncontrolled VHTR cores.

8.3. Flux Reconstruction Theory

8.3.1. Overview

Since detectors cannot survive in the hottest locations of the core, existing flux reconstruction techniques for HTRs rely on out-of-core detectors for continuous on-line monitoring. Flux reconstruction from ex-core data is the most challenging as these detectors are usually placed outside the reactor pressure vessel.

Only fast neutrons born in periphery fuel assemblies are able to penetrate the vessel, downcomers, and any shielding material and reach the detectors. [11]

In order to address the lack of information on the interior of the core, previous researchers employed harmonic expansion techniques. The fundamental mode and several higher order harmonics are calculated for a few reference core configurations.

The ex-core sensor readings are then used to determine the expansion coefficients for the harmonics. This technique was proposed in literature for both LWRs and HTRs. [37, 24]

There are multiple algorithms developed for LWR flux reconstruction from in-core sensors. Combustion Engineering developed a flux reconstruction method called CECOR to accompany SPNDs in their reactors. Only about a quarter of the assemblies in a core were instrumented. Fine-mesh multigroup diffusion calculations were used to calculate coupling coefficients which related the power in instrumented assemblies to the power in adjacent, uninstrumented assemblies. [34,32]

Over the years, researchers have proposed other algorithms which take different approaches to mathematically resolve the differences between detector readings and flux values predicted by neutron diffusion codes. [20,38,22,36]

While more information about the flux distribution can be extracted from in-core sensors, they are not without their downsides. In-core sensors must be able to survive in the harsh environment core. Adverse conditions may include high temperature, high pressure, high gamma fluence, high neutron fluence, and material compatibility concerns with other in-core materials.

This work focusses on in-core flux reconstruction algorithms in order to synergize with advanced sensors capable of withstanding in-core environments. [19] Furthermore, the focus was on methods that did not require the construction and solution of a diffusion model of the reactor core.

8.3.2. Interpolation-based Methods

The conceptually simplest flux reconstruction methods are those based on pure interpolation. An algorithm that could linearly interpolate on an unstructured grid was used in order to accommodate any possible sensor configuration. Using this method, a tetrahedral mesh is constructed whose vertices correspond to locations where the neutron flux is measured by a sensor. Mathematical methods were then used to linearly interpolate the neutron flux across the reactor core.

2D Barycentric coordinates

Definition. Barycentric coordinates are commonly used with triangles and tetrahedra in computational geometry. They are also known as area coordinates.

Barycentric coordinates relate a point's Cartesian coordinates to the Cartesian coordinates of the enclosing triangle's vertices:

$$\vec{r}_p = \lambda_1 \vec{r}_1 + \lambda_2 \vec{r}_2 + \lambda_3 \vec{r}_3 ,$$

where $\vec{r}_1$, $\vec{r}_2$, $\vec{r}_3$ are the Cartesian coordinates of the three vertices, and λ_1, λ_2, and λ_3 are the barycentric coordinates of the point located at $\vec{r}_p$.

Geometrically, barycentric coordinates can be calculated from the areas:

$$\lambda_1 = \frac{area(p23)}{area(123)},$$

$$\lambda_2 = \frac{area(p31)}{area(123)},$$

$$\lambda_3 = \frac{area(p12)}{area(123)},$$

as shown in Fig. 1.

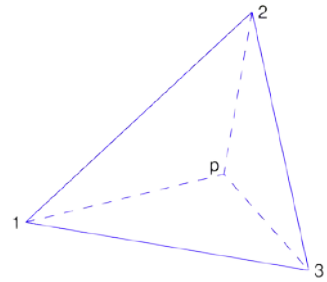

Fig. 1. Barycentric coordinates in 2D.

From this definition, it is clear that barycentric coordinates are a partition of unity. Therefore λ_3 can be expressed in terms of λ_1 and λ_2:

$$\lambda_1 + \lambda_2 + \lambda_3 = 1,$$
$$\lambda_3 = 1 - \lambda_1 - \lambda_2.$$

Barycentric coordinates yield useful information even when the point lies outside the "enclosing" triangle. When p lies inside this triangle, all areas are positive; however, when p lies outside this triangle at least one coordinate will be negative. Using the notation given in Fig. 2, λ_1 will be negative when p lies outside side 1, λ_2 will be negative when p lies outside side 2, and so on.

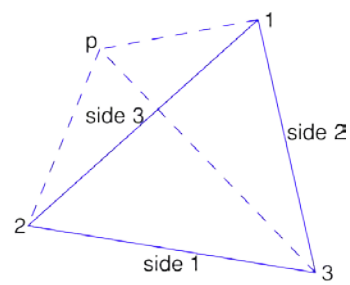

Fig. 2. Triangle side numbering convention.

These relationships hold for tetrahedra as well. As will be shown later, this behavior can be exploited to help determine what mesh simplex a point lies inside.

Converting between barycentric and Cartesian coordinates

In order to derive the relationship between barycentric and Cartesian coordinates, let's expand

$$\vec{r}_p = \lambda_1 \vec{r}_1 + \lambda_2 \vec{r}_2 + \lambda_3 \vec{r}_3,$$

into two separate equations for x and y:

$$x = \lambda_1 x_1 + \lambda_2 x_2 + \lambda_3 x_3,$$

$$y = \lambda_1 y_1 + \lambda_2 y_2 + \lambda_3 y_3.$$

Eliminating λ_3 using $\lambda_3 = 1 - \lambda_1 - \lambda_2$ yields:

$$x = \lambda_1 x_1 + \lambda_2 x_2 + (1 - \lambda_1 - \lambda_2) x_3,$$

$$y = \lambda_1 y_1 + \lambda_2 y_2 + (1 - \lambda_1 - \lambda_2) y_3.$$

Rearranging:

$$\lambda_1 (x_1 - x_3) + \lambda_2 (x_2 - x_3) = x - x_3,$$

$$\lambda_1 (y_1 - y_3) + \lambda_2 (y_2 - y_3) = y - y_3.$$

These equations can be expressed in a matrix form:

$$\hat{T} \vec{\lambda}^* = \vec{r}_p - \vec{r}_3,$$

where:

$$\hat{T} = \begin{bmatrix} x_1 - x_3 & x_2 - x_3 \\ y_1 - y_3 & y_2 - y_3 \end{bmatrix},$$

$$\vec{\lambda}^* = \begin{pmatrix} \lambda_1 \\ \lambda_2 \end{pmatrix}, \text{ and}$$

$$\vec{r}_p = \begin{pmatrix} x \\ y \end{pmatrix}.$$

This relationship shows that in order to calculate the barycentric coordinates of a point, a 2x2 system must be solved.

Once $\vec{\lambda}^*$ is found, λ_3 can be found as

$$\lambda_3 = 1 - \lambda_1 - \lambda_2$$

and the full $\vec{\lambda}$ vector can be assembled. Barycentric coordinates linearly interpolate between the vertices of the triangle, so using them for linear interpolation is straightforward:

$$f(\vec{r}_p) = \lambda_1 f(\vec{r}_1) + \lambda_2 f(\vec{r}_2) + \lambda_3 f(\vec{r}_3).$$

3D Barycentric coordinates

Barycentric coordinates also work for tetrahedral:

$$\vec{r}_p = \lambda_1 \vec{r}_1 + \lambda_2 \vec{r}_2 + \lambda_3 \vec{r}_3 + \lambda_4 \vec{r}_4 .$$

Once again, the λ's form a partition of unity and λ_4 can be expressed in terms of the others:

$$\lambda_4 = 1 - \lambda_1 - \lambda_2 - \lambda_3 .$$

The relationship between barycentric and Cartesian coordinates can be derived by following the same procedure as in the 2D case:

$$\hat{T}\vec{\lambda}^* = \vec{r}_p - \vec{r}_4 ,$$

where:

$$\hat{T} = \begin{bmatrix} x_1 - x_4 & x_2 - x_4 & x_3 - x_4 \\ y_1 - y_4 & y_2 - y_4 & y_3 - y_4 \\ z_1 - z_4 & z_2 - z_4 & z_3 - z_4 \end{bmatrix},$$

$$\vec{\lambda}^* = \begin{pmatrix} \lambda_1 \\ \lambda_2 \\ \lambda_3 \end{pmatrix}, \text{ and}$$

$$\vec{r}_p = \begin{pmatrix} x \\ y \\ z \end{pmatrix}.$$

Interpolating on a Mesh

The goal of this work is to reconstruct the in-core flux distribution given flux measurements at discrete points. This is done through interpolation on a mesh. A mesh is constructed via Delaunay triangulation using the locations of the flux measurements as vertices. Recalling $f(\vec{r}_p) = \lambda_1 f(\vec{r}_1) + \lambda_2 f(\vec{r}_2) + \lambda_3 f(\vec{r}_3)$, the value of a function on a point inside of a simplex can be expressed as a weighted sum of the function values at the simplex's vertices. The appropriate weights are the point's barycentric coordinates. This weighted-sum operation is compactly expressed by the dot product:

$$f(\vec{r}_p) = \vec{\lambda}^e \cdot \vec{F}^e ,$$

where $\vec{\lambda}^e$ are the point's barycentric coordinates relative to the enclosing simplex and $\vec{F}^e$ are the function values at the enclosing simplex's vertices. This can be expanded to illustrate the connection between $\vec{r}_p$ and $\vec{\lambda}^e$:

$$f(\vec{r}_p) = \hat{B}\vec{r}_p \cdot \vec{F}^e ,$$

where $\hat{B}$ is an operator mapping $\vec{r}_p$ to $\vec{\lambda}^e$. In 3D, this is accomplished by solving for $\vec{\lambda}^*$ using $\hat{T}\vec{\lambda}^* = \vec{r}_p - \vec{r}_4$ and then finding λ_4 using $\lambda_4 = 1 - \lambda_1 - \lambda_2 - \lambda_3$.

Let $\hat{M}$ be a matrix containing the Cartesian coordinates of each vertex and $\hat{C}$ be a matrix containing the vertices of each simplex. Together, these two matrices define the mesh.

Additionally, let $\vec{F}$ be a vector containing the values of the flux at each vertex and $\vec{P}$ be a matrix whose rows contain the Cartesian coordinates of every point where the flux is to be interpolated.

Given this notation, the steps to interpolate the flux are as follows:

1. Choose a point p with Cartesian coordinates $\vec{r}_p$. This corresponds to a row of the $\vec{P}$ matrix,
2. Find which simplex p lies inside,
3. Use $f(\vec{r}_p) = \hat{B}\vec{r}_p \cdot \vec{F}^e$ to find the value of the flux at p.

The point in the simplex algorithm

A mesh-walking algorithm was used to locate which simplex a point lies inside. A mesh-walking algorithm was chosen because it is straightforward to implement and because the algorithm starts with an initial guess. Intelligent initial guesses reduce the work the algorithm needs in order to find the enclosing simplex.

Mesh-walking algorithms require information describing how the simplexes of the mesh are connected. Let $\hat{N}$ be the matrix with this information. Row i of $\hat{N}$ contains the information which simplexes are adjacent to simplex i. The steps for the point in simplex algorithm are as follows:

1. Construct $\hat{N}$ from $\hat{C}$. This involves searching $\hat{C}$ to find which simplexes share vertices. This is an expensive operation, but it only has to be performed once per mesh.
2. Choose an initial guess for the enclosing simplex.
3. Calculate the point's barycentric coordinates with respect to current enclosing simplex guess. If all coordinates are positive, the point lies inside that simplex and the algorithm terminates.
4. If one or more of the barycentric coordinates are negative, the point lies outside the current simplex. If λ_c is negative, the current simplex guess is set to neighbor x. If multiple coordinates are negative, any of the negative coordinates can be used to determine the step direction.
5. Repeat steps 3 and 4 until the enclosing simplex is found.

8.3.3. POD-Based Methods

Overview

The proper orthogonal decomposition is a data analysis tool that can be used to create low-dimensional representations of high-dimensional data. POD has been used in a variety of fields including image compression, signal processing, turbulence analysis, and design optimization.

In this work the focus of the application is on its use with time-series data. Given an ensemble of time-series data, POD can be used to create spatial modes, sometimes called empirical eigenfunctions, which can be used to reconstruct the data.

More specifically, POD represents the data as weighted sum of the spatial modes[9]:

$$\phi(\vec{x},t) = \sum_{k=1}^{M} a_k(t)\psi_k(\vec{x}),$$

where $\phi(\vec{x},t)$ is the scalar flux, $a_k(t)$ is the modal coefficient for the k th mode, and $\psi_k(\vec{x})$ is the k th spatial mode.

For a given dataset, there are many decompositions that fit the form given by this weighted sum for $\phi(\vec{x},t)$; however, the POD modes are found by singular value decomposition.

Singular Value Decomposition (SVD)

Consider a data set with m spatial locations whose values are known at N different times. This data set is stored in the $N \times m$ matrix $\hat{\mathrm{A}}$.

The singular value decomposition (SVD) of $\hat{\mathrm{A}}$ is given by:

$$\hat{\mathrm{A}} = \hat{U}\hat{\Sigma}\hat{V}^T,$$

where $\hat{U}$ is the $N \times N$ orthogonal matrix, $\hat{\Sigma}$ is the $N \times m$ matrix whose only non-zero elements lie on its diagonal, and $\hat{V}$ is the $m \times m$ orthogonal matrix. The nonzero elements of $\hat{\Sigma}$ are called the singular values of $\hat{\mathrm{A}}$. The SVD of $\hat{\mathrm{A}}$ is unique, that is to say there is only one decomposition for $\hat{\mathrm{A}}$ that fits the form given by $\hat{\mathrm{A}} = \hat{U}\hat{\Sigma}\hat{V}^T$.

The singular values are always positive and arranged in order of decreasing magnitude, with the largest singular value found in the first row of $\hat{\Sigma}$. The POD modes are the columns of $\hat{V}$. The SVD is connected to low-rank least-squares approximations of $\hat{\mathrm{A}}$.

In particular, a low rank reconstruction of $\hat{\mathrm{A}}$ can be constructed using the following formula:

$$\hat{\mathrm{A}}_k = \hat{U}_k\hat{\Sigma}_k\hat{V}_k^T,$$

where $\hat{A}_k$ is the k th rank reconstruction of $\hat{A}$, $\hat{U}_k$ is a matrix containing the first k columns of $\hat{U}$, $\hat{\Sigma}_k$ is the leading principal k by k minor of $\hat{\Sigma}$, and $\hat{V}_k$ is a matrix containing the first k columns of $\hat{V}$.

The power of the SVD comes from the guaranteed optimality of this low-rank reconstruction. For all k, $\hat{A}_k$ will be the best k-rank reconstruction that can be achieved in the Froebenius norm and the 2-norm.

From this it is concluded that the columns of $\hat{V}$, the POD modes, are an efficient basis to use for data reconstruction; however, there are no mathematical guarantees about its ability to reconstruct data not present in $\hat{A}$.

Gappy Reconstruction

Recall that the matrix $\hat{A}$ includes the all data sets at all times. In practice, a sensor array will only measure a small subset of the data at all times. The goal of the reconstruction algorithm is to take this small subset of information and reconstruct the full neutron flux field.

Previous researchers have called this gappy reconstruction, because the sensor array creates a field of information with gaps where there is no data. In the following paragraphs, the gappy reconstruction procedure is described. This procedure was originally developed by Everson and Sirovich. Later, Willcox applied the method to a variety of engineering problems. [16,8,39]

Let $\hat{\Phi}$ be an $m \times 1$ matrix that contains the scalar flux at all locations at a given moment in time. Let $\hat{N}$ be a matrix that is that same size as $\hat{\Phi}$ and contains 1 at sensor locations and 0 elsewhere. Let $(\hat{a}, \hat{b})$ mean pointwise multiplication between two matrices. Pointwise multiplication of $\hat{N}$ with $\hat{\Phi}$ creates a new matrix with flux values at sensor locations and zeros everywhere else.

Finally, define the gappy inner product,

$$(\hat{a}, \hat{b})_N = \left[(\hat{N}, \hat{a})(\hat{N}, \hat{b}) \right],$$

and the gappy norm:

$$\|\hat{a}\|_N^2 = (\hat{a}, \hat{a})_N .$$

Given a set of gappy data, $\hat{\Gamma} = (\hat{N}, \hat{\Phi})$, the goal is to find the reconstructed field, $\tilde{\Gamma}$ from the POD basis,

$$g \approx \sum_{k=1}^{M} a_k \psi_k .$$

Clearly, $\tilde{\Gamma}$ should reproduce the non-zero entries in $\hat{\Gamma}$ as close as possible. This is accomplished by minimizing the following gappy norm:

$$\left\| \hat{\Gamma} - \tilde{\Gamma} \right\|_{\mathrm{N}}^{2} .$$

In order to find a_k, $\left\| \hat{\Gamma} - \tilde{\Gamma} \right\|_{\mathrm{N}}^{2}$ is differentiated with respect to each a_k. This results in the following system of equations:

$$\hat{\mathrm{M}}\vec{a} = \vec{f} ,$$

where $\mathrm{M}_{i,j} = (\vec{\psi}^{i}, \vec{\psi}^{j})_{\mathrm{N}}$ and $\vec{f} = (\hat{\Gamma}, \vec{\psi}^{j})_{\mathrm{N}}$. The relationship $\hat{\mathrm{M}}\vec{a} = \vec{f}$ is solved for $\vec{a}$, and $\tilde{\Gamma}$ is formed it. Lastly, the missing entries in the gappy data set $\hat{\Gamma}$ are filled in using the corresponding entries in $\tilde{\Gamma}$. This concludes the gappy reconstruction process.

8.4. Flux Reconstruction Implementation and Performance

8.4.1. Introduction

As shown previously, the core hotspot migrates significantly during operation. It is necessary to have a flux reconstruction algorithm that can accurately characterize the core at all points during reactor lifetime. The Monte Carlo depletion run provided flux distributions at twenty-nine different times during the reactor's lifetime. A flux reconstruction algorithm must be able to accurately reconstruct the neutron flux at all twenty-nine times. The steps used to simulate the reconstruction process are given below as follows:

1. Retrieve data for time step i, store in the $m \times n \times o$ matrix, $\hat{\Phi}_i$.
2. Mask $\hat{\Phi}_i$ to show non-zero values only at sensor locations.
3. Generate $\tilde{\Phi}_i$, the reconstructed neutron flux. $\tilde{\Phi}_i$ is the same size as the original unmasked version of $\hat{\Phi}_i$.
4. Compare $\tilde{\Phi}_i$ to the original unmasked version of $\hat{\Phi}_i$.
5. Repeat steps 1-4 for all twenty-nine time steps.

Before presenting the results, the figures of merit (FOMs) used to gauge the performance of the reconstruction algorithm need to be developed. Many of the error metrics are focused on accurate reconstruction of the neutron flux hotspot; however, a few more general metrics are included for completeness – norm of an error in the hot spot location, reconstruction residual, relative error, percent error in the flux, error in the hot spot location coordinates.

The first error metric considered is the norm of the error in the hot spot location:

$$\text{norm of an error in the hot spot location} = \left\| \hat{\mathrm{H}}_{reconstructed} - \hat{\mathrm{H}}_{actual} \right\|_2 ,$$

where $\hat{\mathrm{H}}$ is a matrix that contains the Cartesian coordinates of the hot spot from either the reconstructed data or the reference data. This is equivalent to the distance between the true hot spot and the predicted hot spot. The hot spot is defined as the point in the reactor with the largest value of thermal flux.

The second error metric considered was the norm of the reconstruction residual. The reconstruction residual is defined as:

$$\text{reconstruction residual} = \left| \hat{\mathrm{A}}_{reconstructed} - \hat{\mathrm{A}}_{reference} \right| ,$$

where $\hat{\mathrm{A}}$ is a three dimensional array containing the flux at each point.

The next two error metrics are the average and median of the relative error between the reconstruction and reference flux distribution:

$$\text{relative error} = \frac{\left| \hat{\mathrm{A}}_{reconstructed} - \hat{\mathrm{A}}_{reference} \right|}{\hat{\mathrm{A}}_{reference}} .$$

The final error metrics considered are

- the percent error in the true hot spot magnitude:

$$\%\ \text{error in } \phi(\vec{x}_{hot}) = \frac{\phi_{reconstructed}(\vec{x}_{hot}) - \phi_{reference}(\vec{x}_{hot})}{\phi_{reference}(\vec{x}_{hot})} \times 100\% ,$$

  where $\vec{x}_{hot}$ is the location of the hot spot in the reference calculation.

- the error in the z coordinate of the predicted hot spot:

$$\text{error in the hot spot } z \text{ coordinate} = z_{true} - z_{predicted} ,$$

  where z_{true} and $z_{predicted}$ are the z coordinates of the true and predicted hot spot, respectively. This error metric is useful as it indicates whether or not the axial level of the hot spot is predicted correctly.

Because time-series data is being analyzed, it was often useful to average the FOMs over time in order to create compact data that was easier to visualize. For FOMs that could be either positive or negative, the absolute value was taken before the average to ensure error cancellation did not make a FOM look more attractive than it actually was. Finally, any of these FOMs can be evaluated over the whole core or only the active core region.

8.4.2. Interpolation

Single block sensor arrangements

The single-block sensor arrangement used to test the interpolation-based reconstruction algorithm is shown in Fig. 1. This sensor arrangement was placed in the first ring of the outer reflector, all blocks of the active core, and all blocks of the inner reflector.

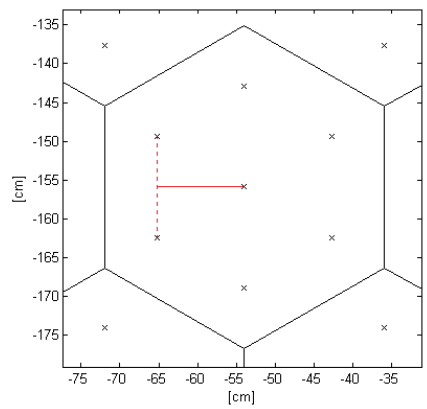

Fig. 1. Sensor layout used in each block.

In order to accommodate the fiber at the center of each block, a narrow hole would need to be drilled through the bottom half of each fuel block. This hole would only need to be wide enough to fit a fiber optic cable and is not expected to affect the structural integrity of the fuel block or significantly influence the bypass flow paths of the helium coolant; however, the hole would have to be sized properly to account for any graphite swelling. Placement of the other six sensors would only be possible by displacing fuel rods. Placing sensors in coolant channels is not recommended. Clear coolant channels are critical to safe reactor operation and putting any instruments in them would have safety ramifications especially if, for example, the sensors broke off and became lodged in the core.

The six different sensor arrangements considered are given in Table 1. Arrangement A contains only one fiber sensor at the center of the block. Arrangements B through F contain seven sensors in each block as shown in Fig. 1.

Table 1. Block Sensor Lattice Pitches

Arrangement	Pitch [cm]
A	0.0
B	3.255563
C	6.511125
D	8.138907
E	11.39447
F	13.02225

The pitch of the array, which is shown with a solid red line in Fig. 1, is different for each sensor arrangement. In total, arrangement A consists of 211 sensors, while all of the other arrangements

used 1477 sensors. The significant difference in sensor count, coupled with the need to remove fuel pins to accommodate the other arrangements, gives arrangement A significant advantage over the others. Figure 2 shows the FOMs relevant to hot spot reconstruction as a function of sensor lattice pitch values in the identified single-block sensor arrangements (see Table 1).

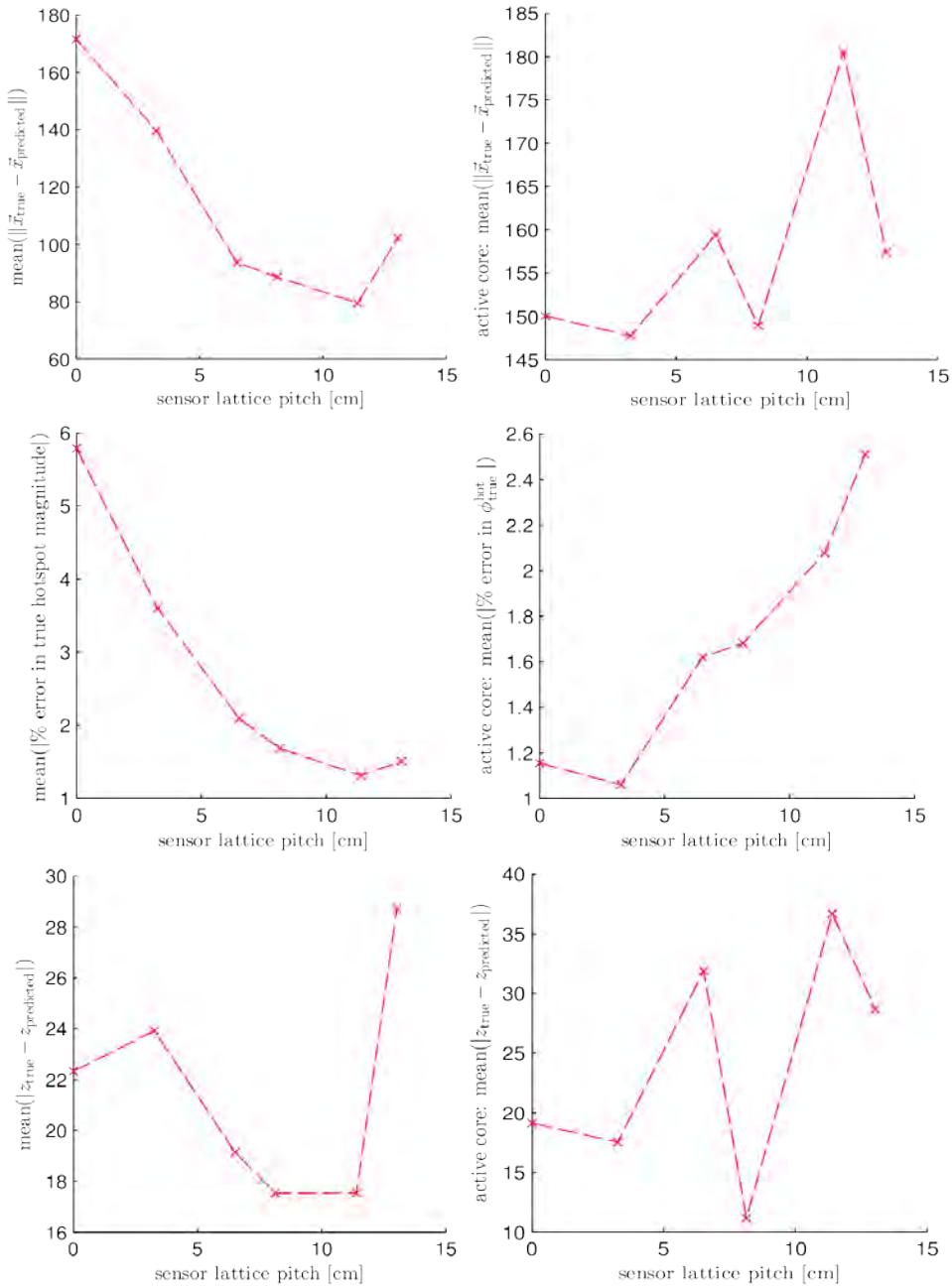

Fig. 2. Hotspot error metrics for interpolation reconstruction algorithm.

Arrangement E predicts the location and magnitude of the core-wide hot spot the best, but performs poorly in these same error metrics when only the active core hot spot is considered.

There is no a clear winner for the active core hot spot FOMs; however, arrangement A performs reasonably well in all and, as mentioned before, consists of significantly fewer sensors.

Effects of noise and sensor failure in interpolation algorithm

The accuracy and effectiveness of the reconstruction algorithm was tested when Gaussian noise was present in the sensor data. Scaled Gaussian noise was added to the sensor data using the following equation:

$$\hat{\Phi}_i = \hat{\Phi}_i + s \times \hat{G} ,$$

where s is the maximum value found in the full unmasked $\hat{\Phi}_i$ matrix and $\hat{G}$ is the matrix of zero mean Gaussian random numbers.

The standard deviation of the random numbers in $\hat{G}$ was varied during the analysis.

Figure 3 shows that the overall quality of the reconstruction, as measured by the average point-wise relative error, decreases linearly as the noise level increases.

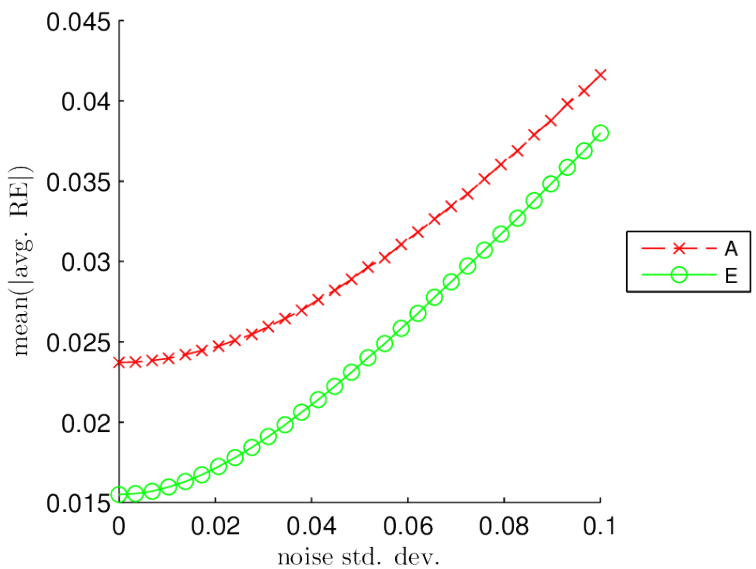

Fig. 3. Relative reconstruction error of the interpolation-based algorithm in the presence of noise.

Figure 4 shows the noise effects on the hot spot reconstruction. The ability of the reconstruction algorithm to accurately predict the location of the hot spot decreases rapidly as noise is added to the system. The FOM least affected by noise is the magnitude of the core-wide true hotspot. The core-wide hotspot lies in the inner reflector during all time steps.

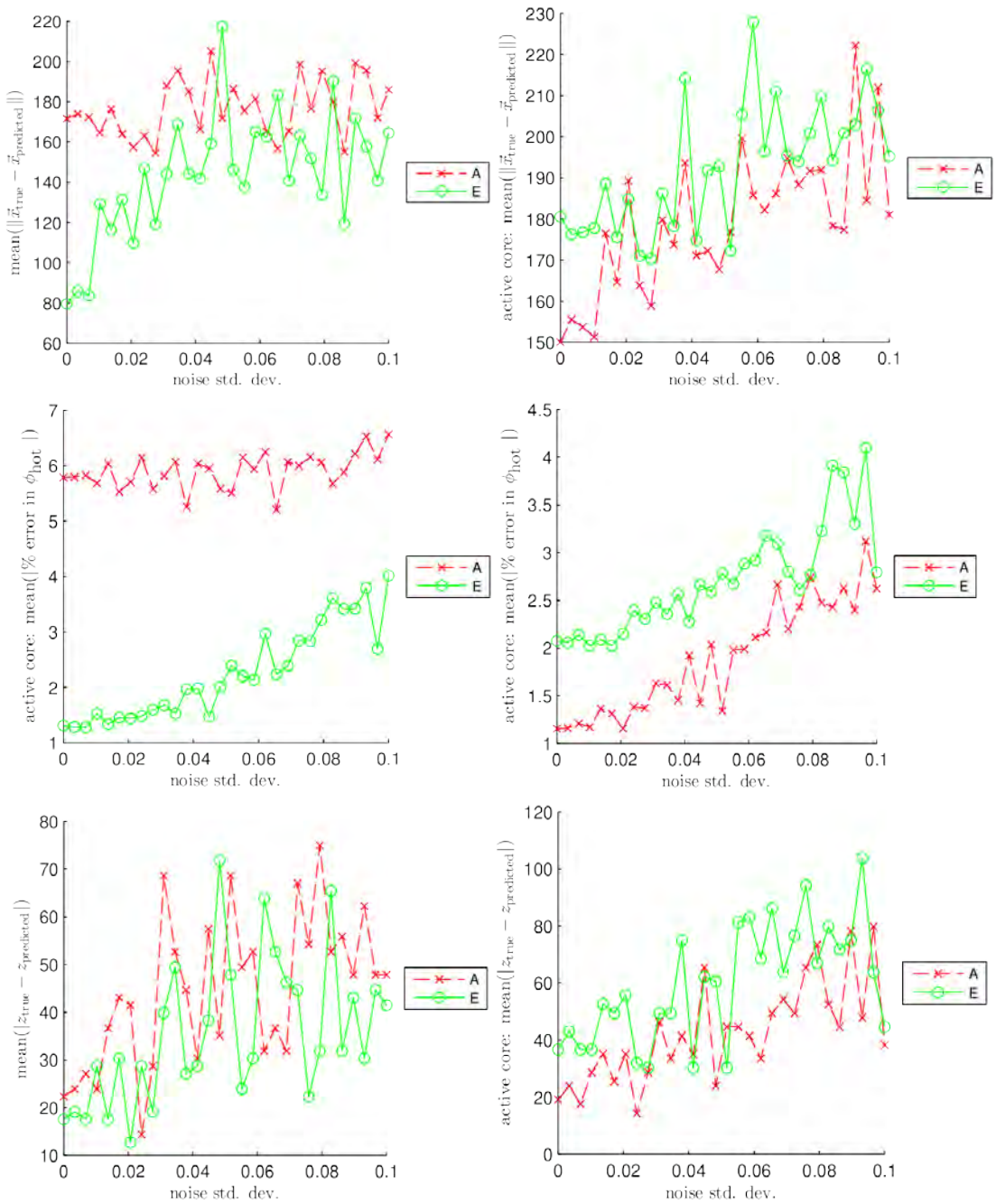

Fig. 4. Hotspot related FOMs for the interpolation-based reconstruction algorithm in the presence of noise.

8.4.3. POD

Effects of POD basis on reconstruction

In order to test the POD-based reconstruction algorithm, the flux data from the twenty-nine time steps, also referred to as snapshots, were assembled into a matrix. The SVD was taken to find the orthogonal set of modes to use for the flux reconstruction.

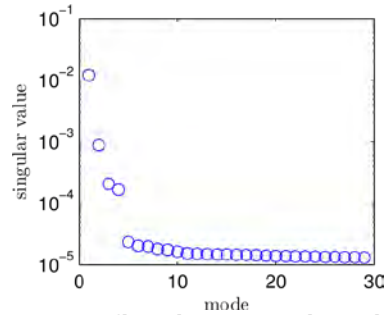

Fig. 5. Singular values of the neutron flux data snapshots (29 time steps).

Figure 5 shows the singular values of the data. The change in the slope near the fifth singular value suggests that there may be a noise floor in the data. [9]

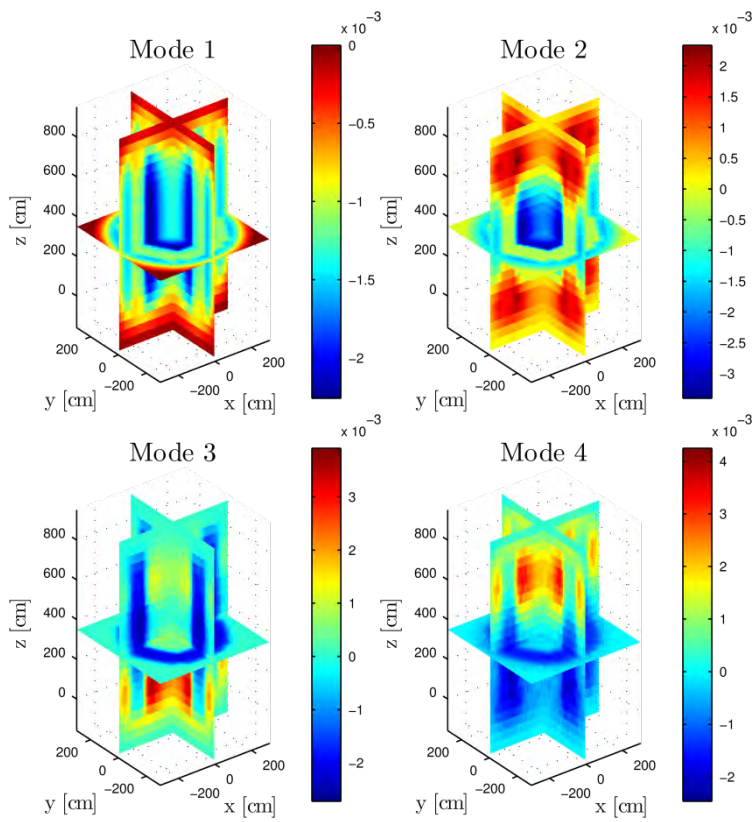

Fig. 6. POD modes 1 through 4.

Indeed, since a Monte Carlo method was used to generate the data, statistical noise was expected to be present. Figure 6 shows the first four modes. These modes correspond to the four largest singular values, and contain most of the information in the dataset.

Figure 7 shows modes 5 through 8. Their lack of any recognizable structure is in agreement with the hypothesis that there is a noise floor in the data.

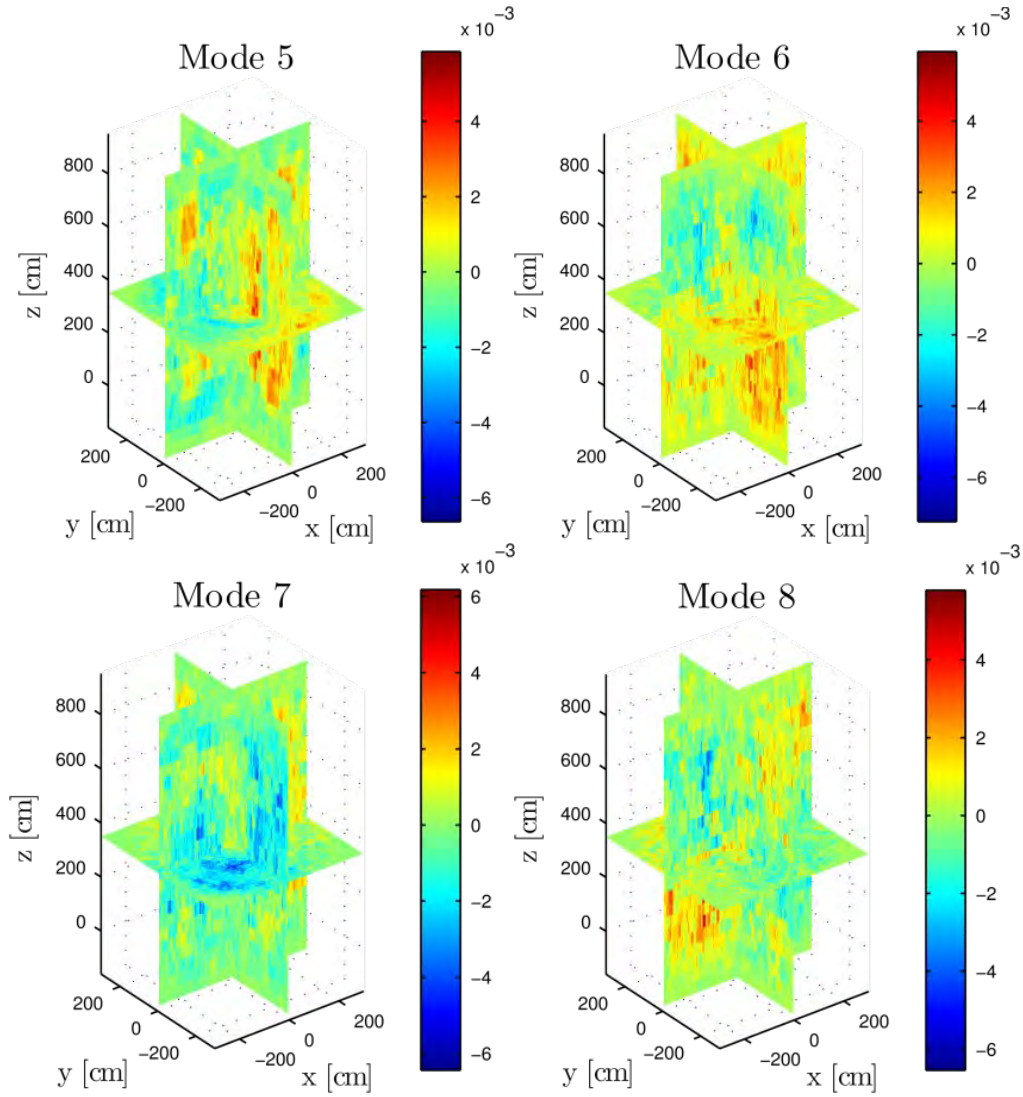

Fig. 7. POD modes 5 through 8.

In order to get a baseline for the performance of the POD method, the sensor arrangement A (see Table 1) was run for all time steps and the number of modes used in the reconstruction was varied from 3 to 29.

Figure 8 shows that the average relative error stays below 0.015 for all time steps when four or more modes are used in the reconstruction process. This is a significant improvement over the interpolation based method.

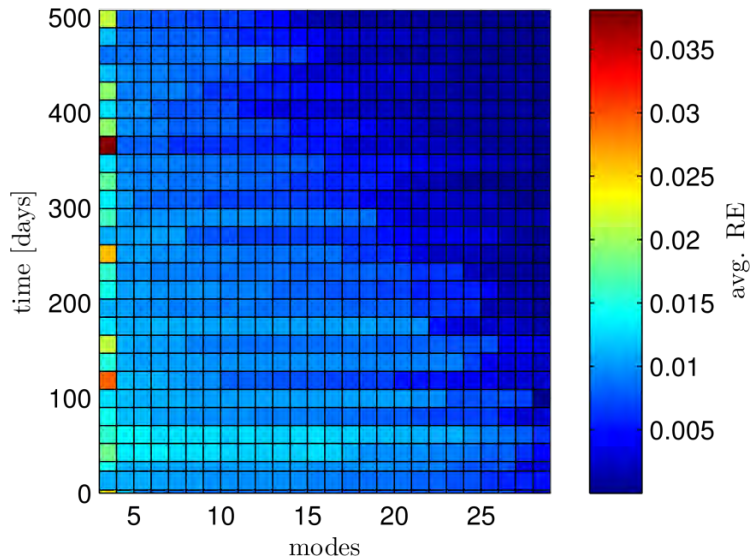

Fig. 8. Average relative reconstruction error for the POD algorithm.

Figure 9 shows several error metrics related to the hot spot prediction. Both the global hot spot and active core region hot spot are considered.

While the error in the true hot spot magnitude is kept small, predicting the location is difficult and is only achieved reliably when a large number of modes are used in the reconstruction.

With that in mind, the figure shows that the error in the z coordinate of the predicted hot spot location is often small, meaning that the reconstruction algorithm can at least predict the axial level of the hotspot.

Nonetheless, a few unexpected spikes in the z coordinate error can be seen even when the 3 mode reconstruction results are ignored.

As mentioned in the theory section, there are mathematical guarantees to the optimality of POD at reproducing the data that the modes were generated from. In reality, the flux distribution in the core at a given time will not exactly match any of the simulation-generated snapshots.

In order to simulate this, only the odd-numbered snapshots were used to generate the POD basis. The resulting basis was then used to reconstruct data for all times.

Figure 10 shows the relative reconstruction error when only the odd-numbered snapshots were used to generate the POD basis.

The average relative reconstruction errors are smallest for the time steps used to generate the basis; however, the reconstruction errors on the remaining time steps were still at an acceptable value.

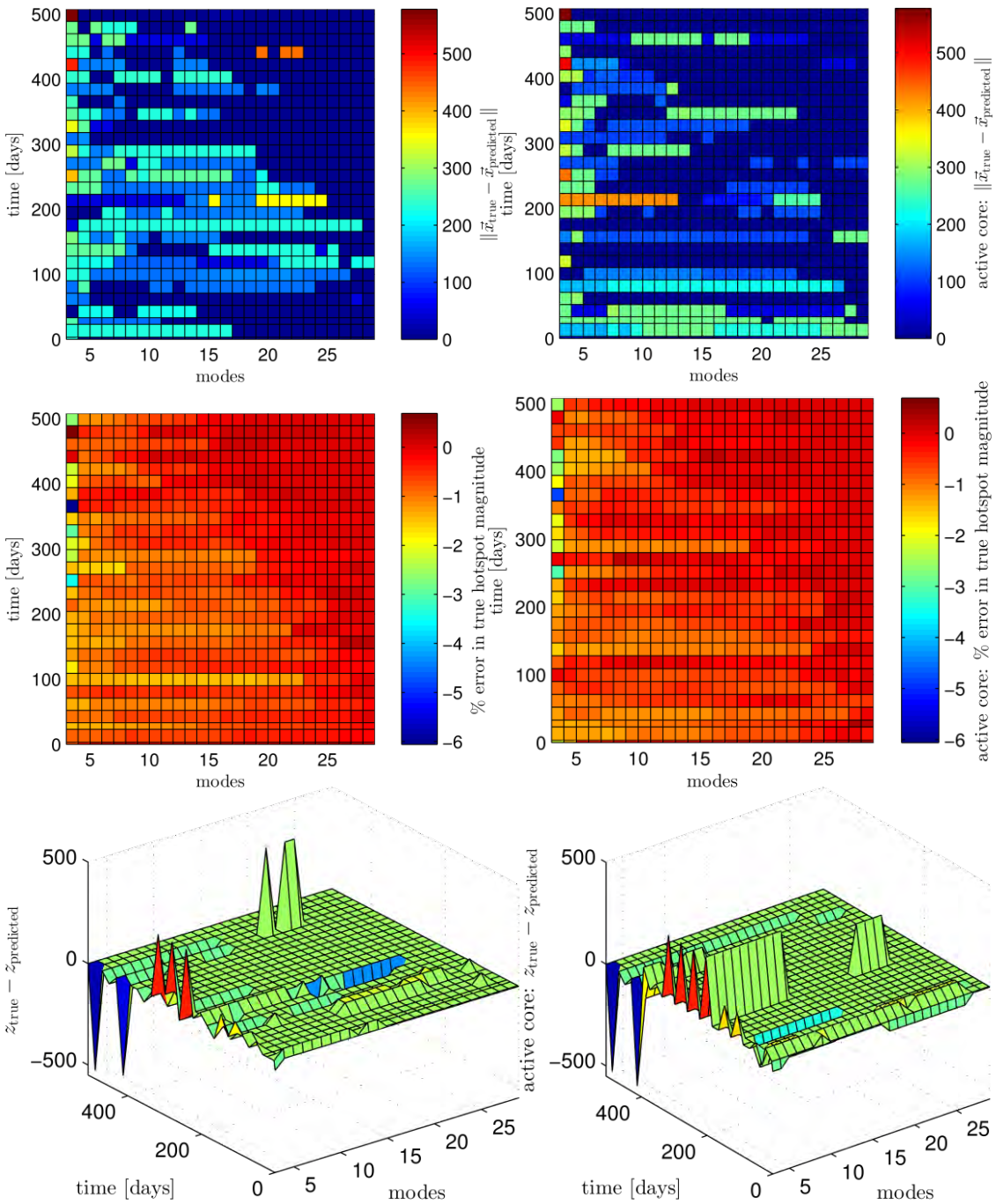

Fig. 9. POD reconstruction for sensor arrangement A using all snapshots.

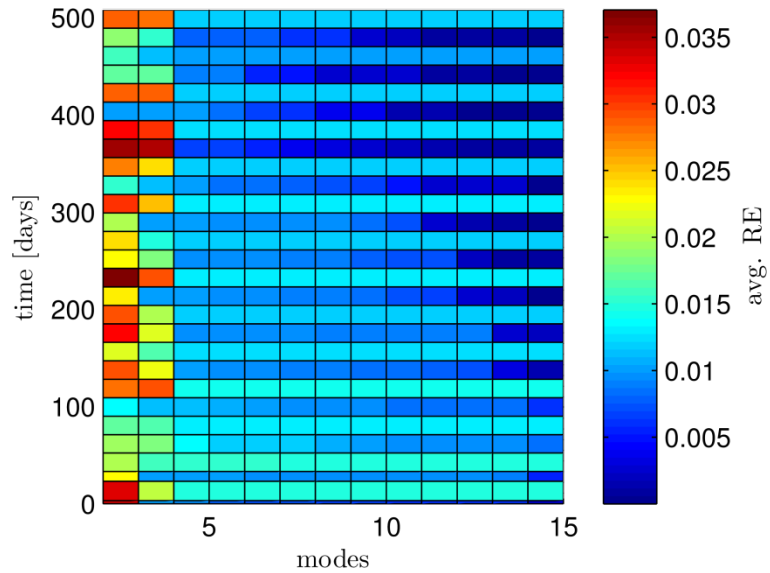

Fig. 10. Average relative reconstruction error for the POD algorithm when only odd-numbered snapshots are used to generate the basis.

Figure 4.11 shows the figures of merit related to the hot spot reconstruction. The core-wide hot spot and active core hot spot magnitude are both reproduced well.

Additionally, the z coordinate of the core-wide hot spot is reconstructed with minimal error provided at least 4 modes are used in the reconstruction process.

The z coordinate of the active core hot spot is only reproduced accurately when a large number of POD modes is utilized.

Effects of sensor locations

With the success of the zero-pitch arrangement A (see Table 1), several other sensor arrangements were considered with the POD method. The new sensor arrangements contained too few sensors to be effective in the interpolation-based reconstruction algorithm.

Figure 12 shows the new sensor arrangements. Arrangement 1 is identical to arrangement A.

Figure 13 shows the average relative reconstruction error for each sensor arrangement at each time step.

All cases were run using all modes (15) from the POD basis generated from the odd-numbered snapshots.

Except for a few troublesome time steps, all sensor arrangements perform similarly. In order to facilitate comparison of the different sensor arrangements, the time averaged error metrics are shown in Fig. 14.

It is interesting to note that, while arrangement 1 contains the most sensors, it does not always perform the best.

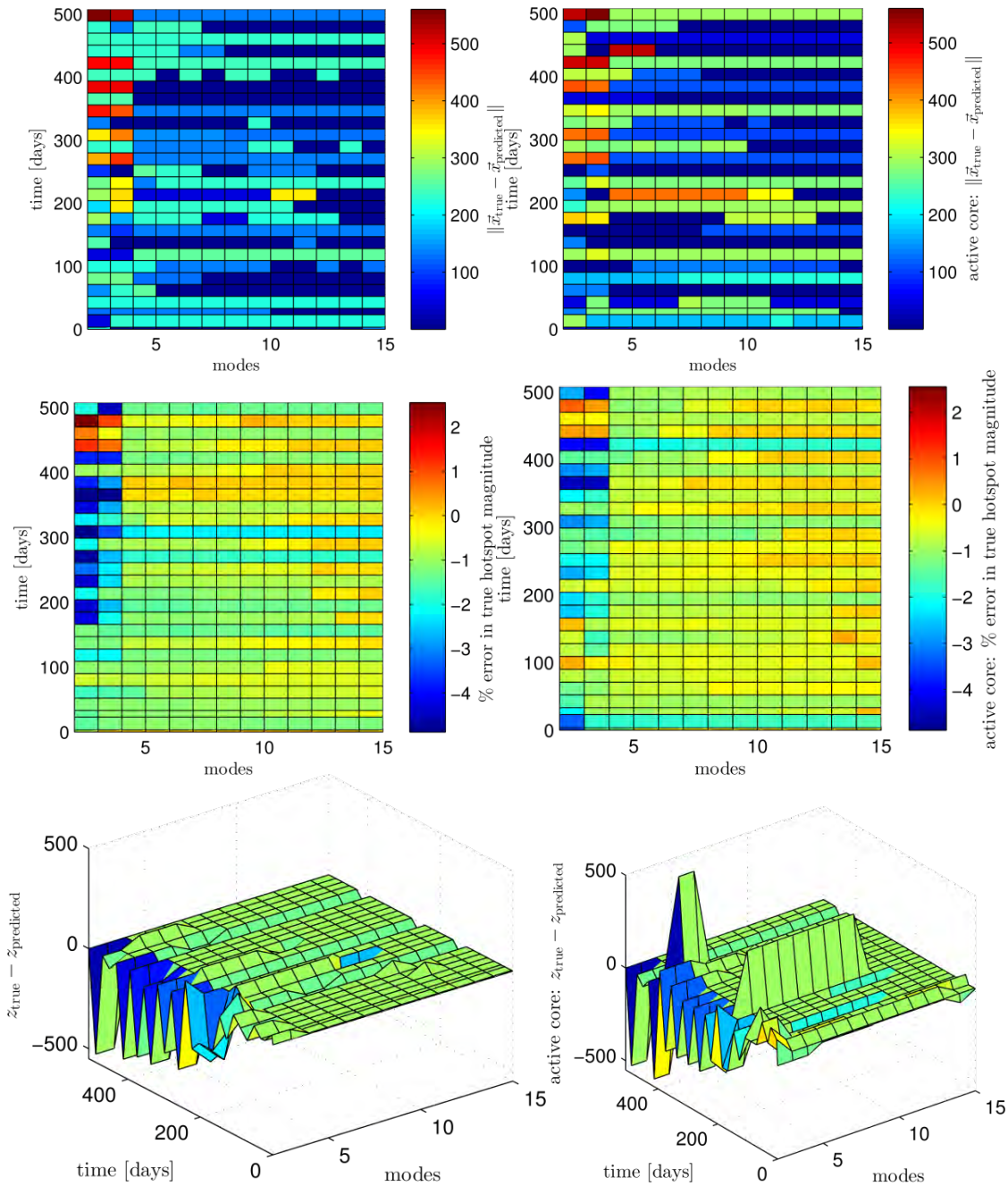

Fig. 11. Hotspot error metrics for the POD method when only odd-numbered snapshots are used to generate the basis.

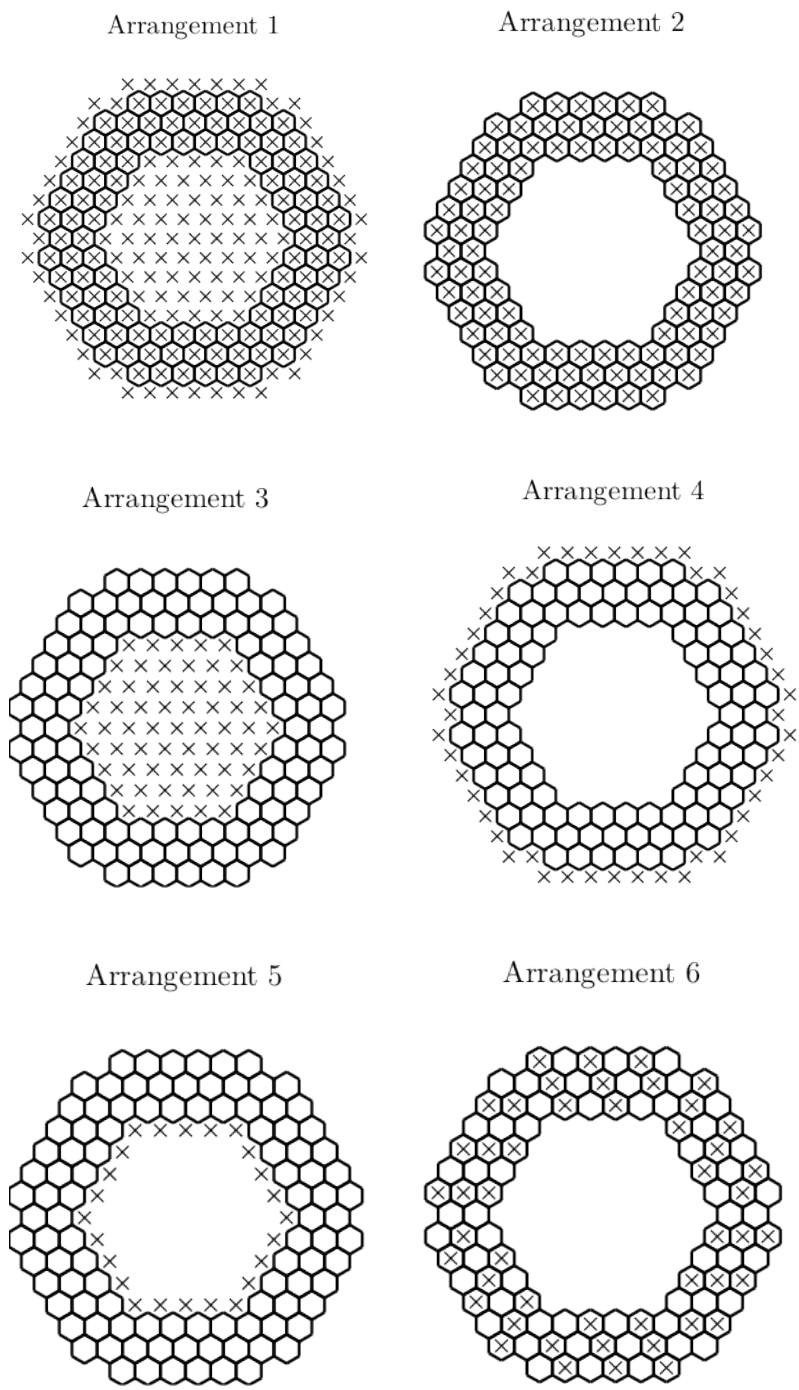

Fig. 12. Six different sensor arrangements used with the POD method, instrumented blocks are marked with an 'X'.

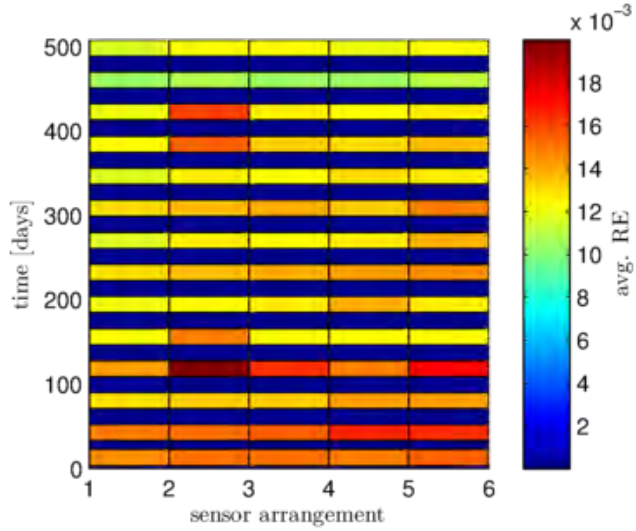

Fig. 13. Average relative reconstruction error for each of the six sensor arrangements using POD-based algorithm.

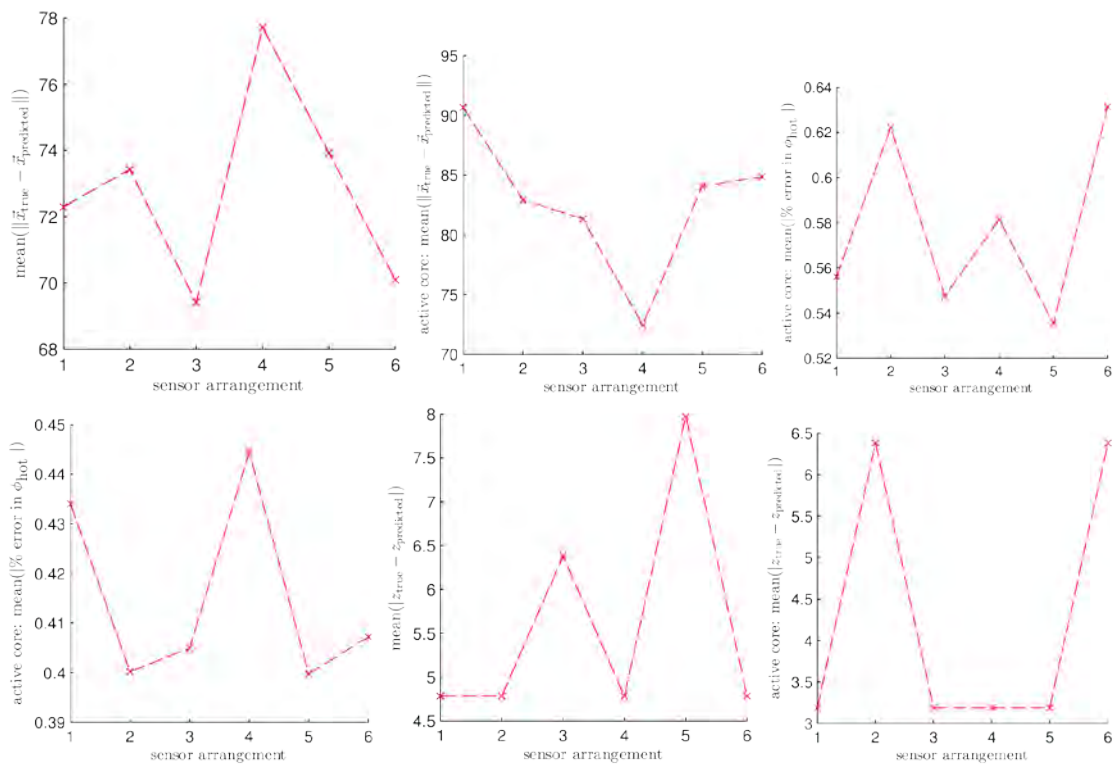

Fig. 14. Hotspot related FOMs for different sensor configurations using the POD method.

Effects of noise and sensor failure

Noise was introduced into the sensor readings in the same manner as before. The effect of noise on the POD-based reconstruction schemes has been studied by previous researchers who found that in such circumstances low-rank reconstructions out-performed their high rank counterparts.

In order test this, the reconstruction algorithm was run using 4, 10, and 15 modes. All cases used sensor arrangement 5 (see Fig. 12).

Figure 15 shows that as the noise level in the sensor readings increases, the 4 mode reconstruction does indeed outperform the 10 and 15 mode reconstructions in the reconstruction relative error FOM.

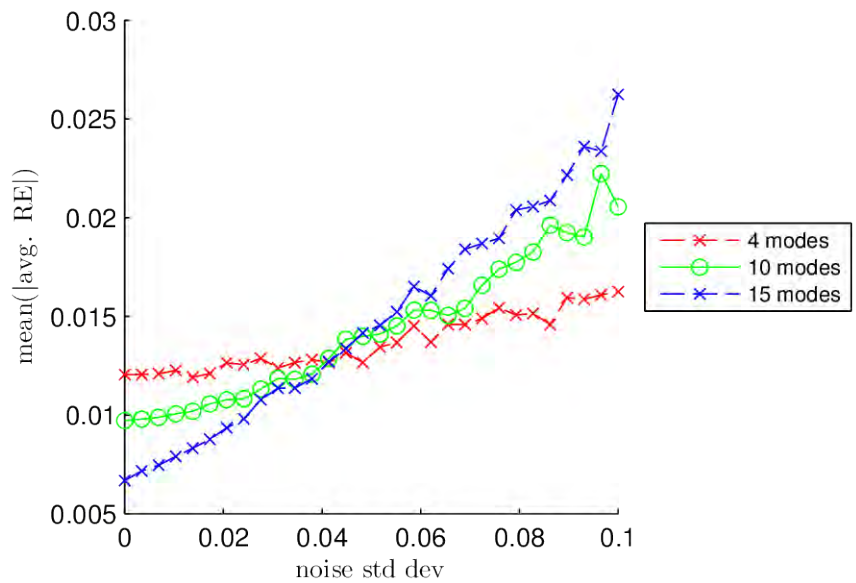

Fig. 15. Average relative reconstruction error as a function of signal noise for the POD-based reconstruction.

Figure 16 shows that the 4-mode reconstruction is no longer superior when the hot spot related FOMs are considered. Instead, all methods perform similarly.

Overall, the POD-based method performs well, and it is conclusively better than the interpolation-based method, in the reconstruction relative error and percent error in true hotspot magnitude FOMs.

Figure 17 shows a more detailed view of the POD algorithm's performance in predicting the z coordinate of the hotspot. Except for a few spikes, the error is modest for the lower levels of noise, but degrades to unacceptable levels as the noise amount increases.

Sensor failures were modeled by deterministically failing the closest sensors to the core-wide hot spot. The reconstruction algorithm was run testing the effects of failing up to 5 sensors for each of the 6 sensor arrangements (see Fig. 12).

All cases used all modes from the POD basis generated from the odd-numbered snapshots.

Figure 18 shows the hot spot FOMs for all cases. Sensor failure has the largest effect on arrangements 4 and 5; however, these two arrangements had the fewest sensors to begin with.

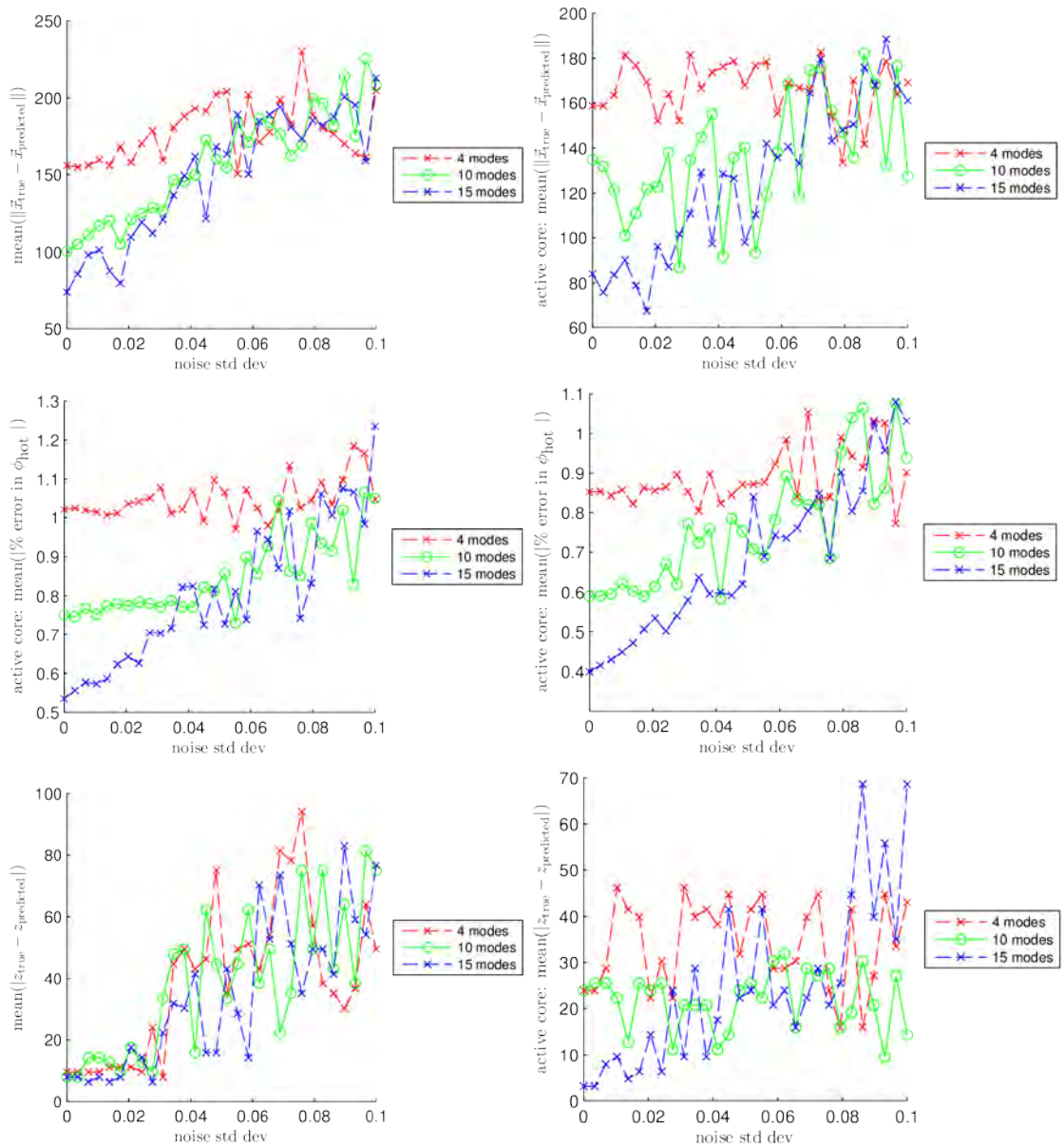

Fig. 16. Hotspot FOMs for the POD reconstruction in the presence of noise.

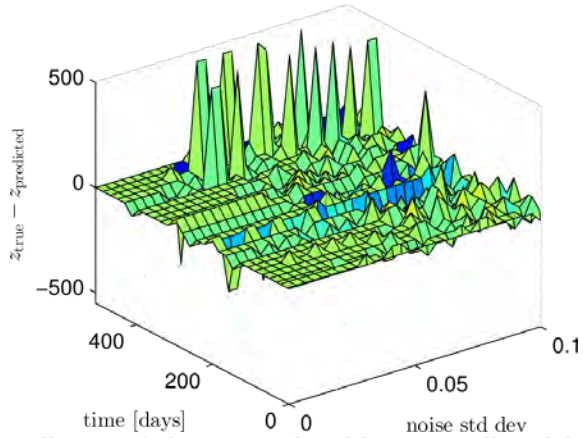

Fig. 17. Error in *z*-coordinate of the POD algorithm's predicted hotspot location when signal is noisy.

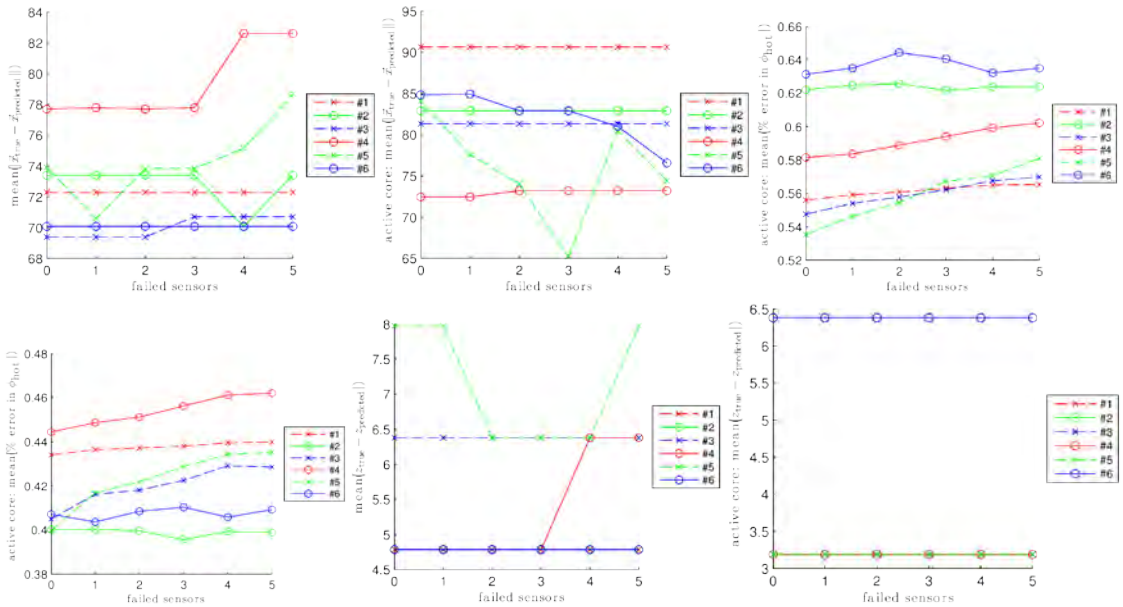

Fig. 18. Hotspot related FOMs for the POD algorithm when sensors fail.

8.5. Conclusions

The MCNP model was used to generate full core flux distributions that were representative of HTRs. The burnup results showed how the neutron hot spot migrates around the reactor during operation, illustrating the need for a sensor system capable of tracking this phenomenon during operation.

Predicting the exact location of the core-wide and active core hotspots was a difficult task. Due to the 1/6th symmetry of the core about the z axis, there should have been six spots, all of which lay in the same xy plane that had same maximum flux value. In reality, physical processes would introduce random fluctuations that remove the perfect symmetry in the flux distribution.

In this work, the stochastic nature of the transport solution introduced a small noise floor into the data. After noise was added to the data, these 6 hotspots were very close in magnitude and it was difficult for a reconstruction algorithm to single out which location had the largest neutron flux. Recognizing this, the focus was primarily on predicting the z coordinate of the hot spot and the magnitude of the true hot spot.

Two flux reconstruction algorithms were developed and tested:

- Linear interpolation, and
- Proper orthogonal decomposition (POD).

Neither algorithm relied on a neutron diffusion or transport model of the core.

The interpolation-based algorithm is conceptually straightforward and performs well provided enough sensors are placed in the core. It is doubtful that it would be economically feasible to remove fuel pins from the core just to insert more sensors. Thus, only the zero-pitch arrangement is potentially viable. In this configuration, 211 sensors were assumed. As illustrated in Fig. 1, this sensor configuration predicts the magnitude of the core-wide true hotspot poorly (-6% error on average), but predicts z coordinate well. It performs better when the active core hotspot is considered. The main disadvantage of the interpolation-based algorithm is that it is not robust against signal noise or sensor failure. Any amount of noise in the signal directly translates to degraded performance and the algorithm has no way to compensate for sensor failure.

The POD-based reconstruction method is recommended over the interpolation-based method because it yields more accurate reconstructions with fewer sensors. The POD-based method was able to reconstruct the in-core flux with 24 sensors more accurately than the interpolation-based algorithm could with 211 sensors. The POD method was also better at handling signal noise and sensor failure. Signal noise did cause the reconstruction to degrade, but the quality of the reconstruction degraded slower than the interpolation-based method. The chief disadvantage of the POD-based method is that its behavior is not as predictable as the interpolation-based method. The snapshots fed into the algorithm must span the operating conditions experienced by the reactor. Furthermore, the number of POD modes used in the reconstruction has a large effect on the accuracy. In this work, it was computationally feasible to use all of the modes during the reconstruction. However, if hundreds or thousands of snapshots are used to generate the POD basis, this would no longer be true. Figure 2 summarizes the considered sensor arrangements for the POD-based reconstructions.

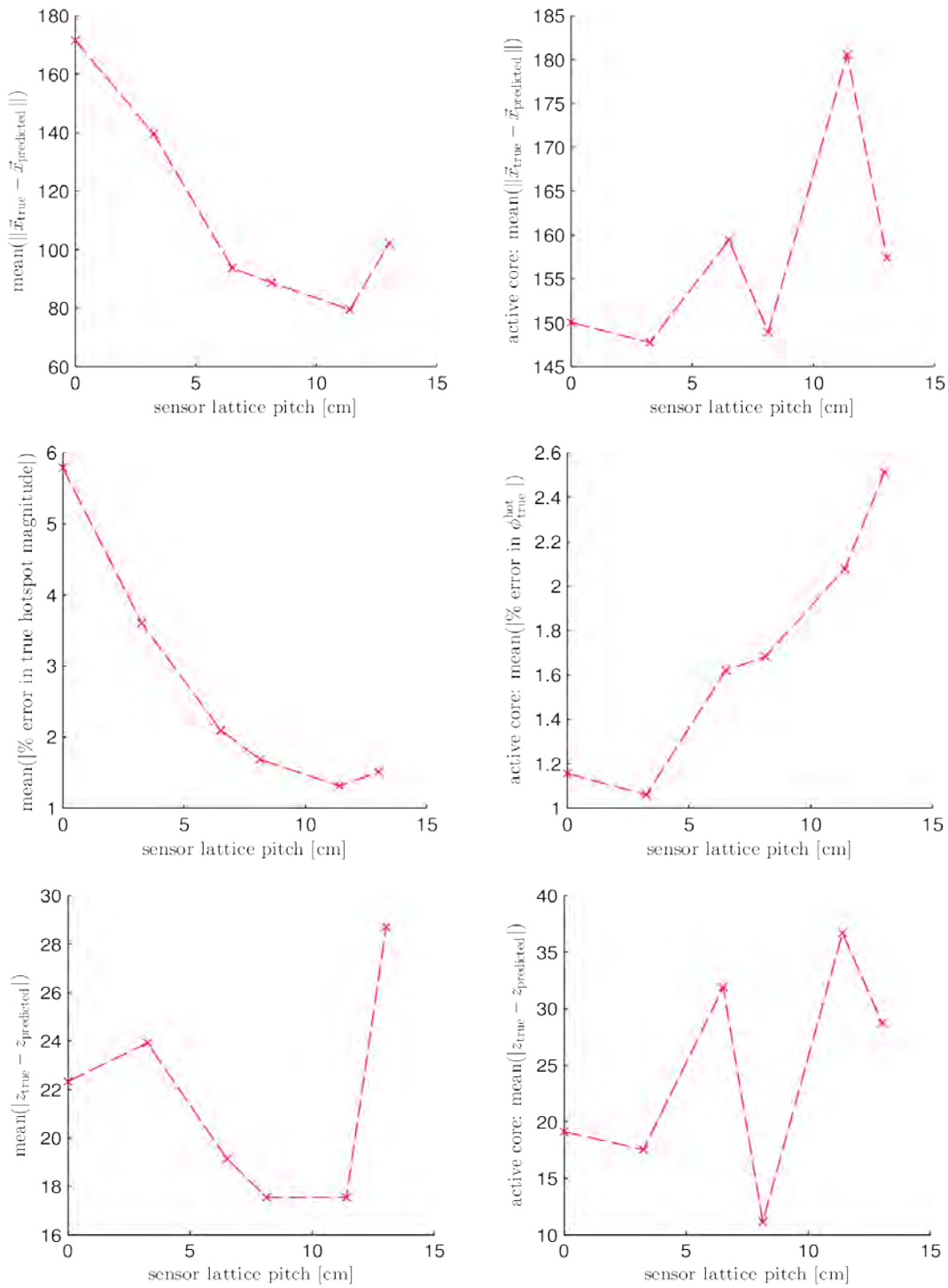

Fig. 1. Hotspot error metrics for the interpolation reconstruction algorithm.

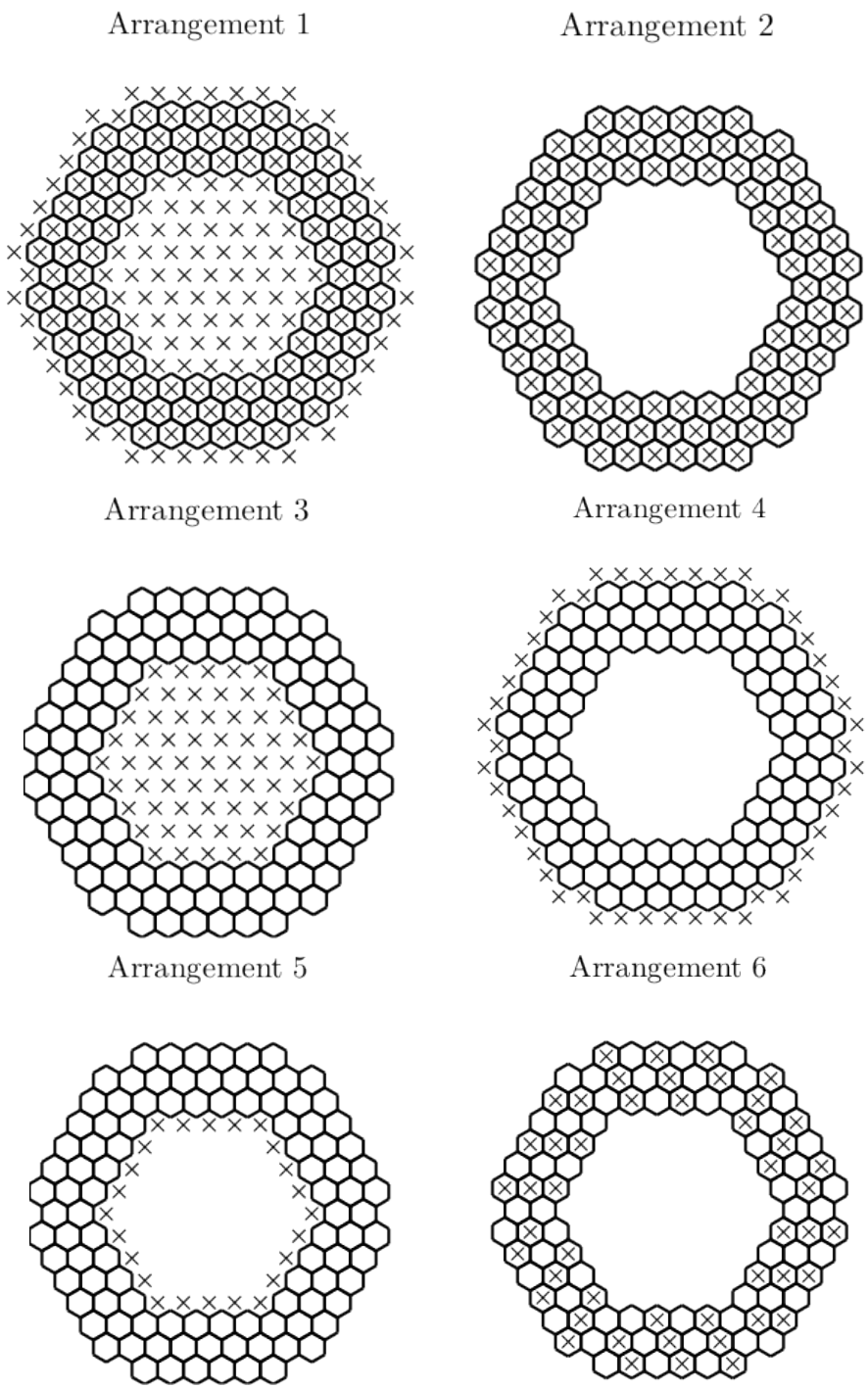

Fig. 2. Six different sensor arrangements used with the POD method, instrumented blocks are marked with an 'X'.

8.6. References

1. A Technology Roadmap for Generation IV Nuclear Systems. [Online; accessed 9-November-2012]

2. "Next Generation Nuclear Plant Pre-Conceptual Design Report." INL/EXT-07-12967, Idaho National Laboratory, November 2007.

3. "Assessment of High Temperature Gas-Cooled Reactor (HTGR) Capital and Operating Costs.

4. G. Baccalgini, "Very High Temperature Reactor Survey of Materials Research and Development Needs to Support Early Deployment." INEEL/EXT-03-00141, Idaho National Engineering and Environmental Laboratory, 2006.

5. S.J. Ball and S.E. Fisher, "Next Generation Nuclear Plant Phenomena Identification and Ranking Tables." NUREG/CR-6944, United States Regulator Commission, 2008.

6. G. I. Bell and S. Glasstone. *Nuclear Reactor Theory*. Robert E. Krieger Publishing Company, 1970.

7. G. Bignam, J. C. Guyard, C. Blandin, and H. Petitcolas, "Direct Experimental Tests and Comparisons Between Sub-Miniature Fission Chambers and SPND for Fixed In-Core Instrumentation of LWR." In *OECD Proceedings of a Specialist Meeting*. OECD, 1996.

8. T. Bui-Thanh, M. Damodaran, and K. Willcox, "Aerodynamic Reconstruction and Inverse Design Using Proper Orthogonal Decomposition." *AIAA Journal*, **42**(8):1505-1516, 2004.

9. A. Chatterjee, "An Introduction to the Proper Orthogonal Decomposition." *Current Science*, **78**(7):808-817, 2000.

10. A. G. Croff, "ORIGEN2 – A Revised and Updated Version of the Oak Ridge Isotope Generation and Depletion Code." ORNL-5621, Oak Ridge National Laboratory, 1980.

11. M. W. Crump and J. C. Lee, "Calculation of Spatial Weighting Functions For Ex-Core Neutron Detectors." *Nuclear Technology*, **41**:87-96, 1978.

12. V. M. Descotes, "Reactor Physics of a Deep-Burner Prismatic Core for VHTR." Master's Thesis, Ecole Polytechnique de Montreal, 2011.

13. B. Dickerson, J. Farmer, J. French, M. Palmer, and R. Fielder, "Fiber Optic Sensors Measuring Flux and Neutron Fluence." *Transactions of the American Nuclear Society*, **99**:289-290, 2008.

14. B. Dickerson, J. French, B. Chang, and R. Fielder, "Fiber Optic Sensors for Neutron Fluence Measurements in Thermal, Epi-Thermal, and Fast Energy Bands." *Transactions of the American Nuclear Society*, **99**:79-80, 2008.

15. J. J. Duderstadt and W. R. Martin, *Transport Theory*, John Wiley and Sons, 1979.

16. R. Everson and L. Sirovich, ”Karhunen-Loeve Procedure for Gappy Data,” *Journal of the Optical Society of America*, **12**(8):1657-1664, 1995.

17. M. R. Fard. *The Development of a High Count Rate Neutron Flux Monitoring Channel Using Silicon Carbide Semiconductor Radiation Detectors*, PhD Thesis, Ohio State University, 2006.

18. W. Haeck, “VESTA User’s Manual,” DSU/SEC/T/2008-331, Institut De Radioprotection et de Surete Nucleaire, 2009.

19. H. M. Hashemian and W. C. Bean, “Sensors for Next-Generation Nuclear Plants: Fiber-Optic and Wireless,” *Nuclear Science and Engineering*, **169**:262-278, 2011.

20. C. F. Karlson, “Continuous Advancements in In-Core Power Distribution Measurement Methods Using SIMULATE-3 and CECOR 3.4,” *Nuclear Science and Engineering*, **121**:57-66, 1995.

21. B. Khorsandi, “Monte Carlo Modeling of Count Rates and Defects in a Silicon Carbide Detector Neutron Monitor System,” *Nuclear Technology*, **159**:208-220, 2007.

22. K. Lee and C. H. Kim, “The Least-Squares Method for Three-Dimensional Core Power Distribution Monitoring in Pressurized Water Reactors,” *Nuclear Science and Engineering*, **143**:268:280, 2003.

23. E. E. Lewis and W. F. Miller, *Computational Methods of Neutron Transport*, American Nuclear Society, 1993.

24. F. Li, J. Guo, D. Wang, J. Wei, J. Zhang, and C. Hao, “The Possibility to Online Reconstruct the HTR In-Core Power Distribution,” *PHYSOR 2010 – Advances in Reactor Physics to Power the Nuclear Renaissance*, 2010.

25. P. MacDonald, “NGNP Preliminary Point Design – Results of the Initial Neutronics and Thermal-Hydraulics Assessments,” INEEL/EXT-03-00870, Idaho National Engineering and Environmental Laboratory, 2003.

26. P. MacDonald, “Next Generation Nuclear Plant: A Very High Temperature Gas-Cooled Reactor,” *Advanced Reactor Fuel Cycle and Energy Products Workshop for Universities*. Idaho National Engineering and Environmental Laboratory, March 2004.

27. L. Massimo, *Physics of High-Temperature Reactors*, Pergamon Press, 1975.

28. R. J. McConn, C. J. Gesh, R. T. Pagh, R. A. Rucker, and R. G. Williams, “Compendium of Material Composition Data for Radiation Transport Modeling,” PNNL-15870, Pacific Northwest National Laboratory, 2011.

29. K. Saito, H. Sawahata, F. Homma, M. Kondo, and T. Mizushima, “Instrumentation and Control System Design,” *Nuclear Engineering and Design*, **233**:125-133, 2004.

30. J. Spanier and E. M. Gelbard, *Monte Carlo Principles and Neutron Transport Problems*, Dover, 2008.

31. X-5 Monte Carlo Team, "MCNP – A General N-Particle Transport Code, Version 5, Volume I: Overview and Theory," LA-UR-03-1987, Los Alamos National Laboratory, 2003.

32. W. B. Terney, J. L. Biffer, C. O. Dechand, A. Jonsson, and R. M. Verluis, "The C-E CECOR Fixed In-Core Detector Analysis System," *Transactions of the America Nuclear Society*, **44**:542-543, 1983.

33. J. Trapp, S. Haan, L. Martin, J. Perrin, and M. Tixier, "Higher Temperature Fission Chambers: State-of-the-Art," *OECD Proceedings of a Specialist Meeting*, NEA, 1996.

34. R. M. Versluis, "C-E In-Core Instrumentation – Functions and Performance," *IEEE Transactions on Nuclear Science*, **31**:761-765, 1984.

35. J. C. Lee and W. R. Martin, "An Advanced Neutronic Analysis Toolkit with Inline Monte Carlo Capability for VHTR Analysis," DE-FC07-06ID14745, University of Michigan, 2009.

36. C. Wang, H. Wu, L. Cao, and P. Yang, "On-Line Reconstruction of In-Core Power Distribution by Harmonics Expansion Method," *Nuclear Engineering and Design*, **241**:3042-3050, 2011.

37. Y. Wang, F. Li, and S. Han, "On-Line Monitoring the Incore Power Distribution by Using Ex-Core Ion-Chambers," *Nuclear Engineering and Design*, **225**:315-316, 2003.

38. R. J. Webb and J. C. Brittingham, "Comparison of the CECOR Algorithm to Langrange Multiplier Method to Estimate Reactor Power Distributions," *Nuclear Technology*, **132**:206-213, 2000.

39. K. Willcox, "Unsteady Flow Sensing and Estimation Via the Gappy Proper Orthogonal Decomposition." *Computers and Fluids*, **35**:208-226, 2006.

40. W. Windes, T. Burchell, and R. Bratton, "Graphite Technology Development Plan," INL/EXT-07-13165, Idaho National Laboratory, 2007.

High Temperature Test Assembly emulating operating conditions of HTRs in TRIGA

9. Conclusions

Robust 3D in-core monitoring technologies are essential for next generation nuclear power systems. If available, they would be capable to provide real time information about reactor conditions assuring its safety and reliability.

Given the harsh environments of high temperature reactors, new in-core instrumentation has to be developed. Existing approaches may fail prematurely in VHTRs. The challenge is currently mitigated by providing out-of-core monitoring capabilities together with reconstruction of in-core values.

The report discusses efforts to develop suitable advanced in-core instrumentation technologies and corresponding experimental confirmation approaches for their performance in VHTRs via emulation of VHTR in-core conditions in TRIGA reactors. An advanced 3D in-core mapping via a distributed sensor network would be capable of reliable performance in high temperature/high radiation environments for prolonged periods comparable at least to the fuel loading lifecycles of HTRs. The key objectives of the project were:

- to experimentally confirm performance characteristics of distributed fiberoptics sensors networks in HTRs via emulation of VHTR conditions in TRIGA (Training, Research, Isotope Production, General Atomics) reactor cores.
- to develop a 3D in-core reconstruction approach taking advantage of information provided by the distributed fiberoptics sensors networks.

The goal is to predictively identify stressful in-core regions that may lead to hot spots.

9.1. Outcomes of the Experimental Program

This report presented the results and observations obtained in the course of the 3-year program. The gained practical experience with fiberoptics sensors and computational evaluations of distributed sensing networks for reactor in-core applications indicate potential opportunities for future applications, especially in the environments which would be either physically hostile or geometrically challenging for traditional sensing technologies.

Furthermore, as indicated above, distributed sensing allows gathering more robust data during reactor operation which is essential not only for predictive safety monitoring but also for competitive reliability and economics. The project was focused on NGNP/VHTR environments but the analyzed fiberoptics sensing and 3D in-core monitoring via distributed sensing are of paramount value for LWRs, emerging SMRs and all advanced nuclear reactors.

With the delays in procurement and fabrication difficulties, the total irradiation of the fiber optics covered the span of 3 months. Another probe, with twelve more fiber optics has yet to be irradiated, preventing a good sample of data to develop an empirical model on fiber optic survivability. There were seven fibers that were irradiated: two temperature, three neutron, and two gamma fibers. The fibers of the first probe were all irradiated to a neutron fluence of 1.0×10^{19} +/- 7.7×10^{17} n/cm^2 at a nominal 500°C. Both of the gamma fibers failed at 4.5×10^{18} and 5.8×10^{18}n/cm^2, respectively, likely as a result of fiber-ferrule interaction due to fiber swelling as

evident by identical failure modes at identical spatial locations. Neutron and temperature sensing fiber optics showed significantly improved radiation resistance over the gamma fibers, but without a control at ambient temperature, it is difficult to understand the influence of high temperature irradiation on the annealing properties of the fiber optics.

Vibration and other noise sources prevented the validation of neutron and gamma fiber techniques and temperature measurements via the fiber optics were not equivalent to calibrated thermocouple readings. The spatial distributions of the temperature measurements seem to be correct, compared to modeling results, but their magnitude was too great. It is suspected the deviations are the result of internal stresses from mechanical stresses within the probe.

Although fundamental feasibility and potential applications for fiberoptics sensors have been established, the technology, by far, is not ready for near-term practical in-core implementations. The noted challenges include excessive dependencies of sensing system performance characteristics on vibrations due to thermo-mechanical core characteristics, resulting noise effects, internal fiberoptics material effects and their interpretation by the fiberoptics data acquisition and processing, and overall inherent dependencies of fiberoptics sensing technologies on accompanying software components to recover and interpret measured performance characteristics, and frequent calibration needs for the system to operate meaningfully.

These observations strongly suggest the need for further research efforts to systematically resolve these challenges, thus allowing taking a full advantage of the existing fiberoptics and distributed sensing capabilities for next generation in-core instrumentation solutions for current LWRs as well as SMRs and advanced reactor systems.

9.2. Fiberoptics Engineering Challenges

There are various challenges that appeared while working with the fiber optics. Possibly the more prominent engineering challenge for fiber optics, beyond radiation hardiness, is the implementation of the fibers in a system without external stress loads due to vibration, thermal changes, or mechanical movement.

The fiber optic has to have a reference scan that is indicative of the initial conditions of the system to get a true reference for any relative changes. The initial reference is required to determine the conditions during operation. Conversely, deviations from 'nominal' operating conditions are as simple as scanning between events and comparing the changes. The operating principle of these fiber optic measurement systems is the following:

- Capture an initial state of conditions, determined by the behavior of light through the fiber.
- Introduce an external stress (through temperature) or change in material characteristics (neutron or gamma flux)
- Scan new state of conditions
- Use software to calculate the strength of the external effect as compared to the initial condition

So, unlike measurement systems that are compared to a ubiquitous reference, like 0°C, the fiber optic measurement references its own initial state. That implies that the reactor must but shut down for a reference scan to determine the operational flux and temperature, or that comparisons made between operating states will, for example, show the flux tilting or formation of hot spots due to CRUD buildup.

The means for determining temperature is through the measurement of stress in the fiber optic, so a reference cannot be performed outside of the system then the fiber installed. This would change the geometry of the fiber optic and therefore change the stress state. A probe device could be used to alleviate this concern, but that would, in part, forfeit the flexibility of the measurement system which is one of the benefits.

Another engineering challenge is the measurement drift resulting from material property changes from radiation fluence and thermal cycling. Temperature measurements drift due to irradiation. Thermal transients affect the long-term characteristics of the fiber optic. It is unclear if these effects can be compensated via software improvements, especially as fabrication and manufacturing techniques are perfected. This thermal cycling also brings up an issue of thermal equilibrium. If the fiber optics are used to perform a time-dependent study on a short time scale (this assumes that many fibers are bundled and scanned sequentially since scans due take some time), the response of the fiber optic will have to be compensated.

While this project demonstrated the survivability of the neutron and temperature fiber optics, it is not conclusive. There is a multitude of further research topics in the development of the measurement systems, materials, and software that is needed for advancing fiberoptics-based sensor technologies to practical reactor instrumentation applications. In particular, further research efforts are required to alleviate some of the concerns associated with the detectors if they are to be realized for the reactor environment and to provide results capable for computational validation and monitoring and control of a reactor system.

These are merely observations and should not be considered as a final and conclusive assertions. There are some foreseeable engineering challenges as this technology is developed further, predominately the time-resolution of scans as the fiber optic establishes equilibrium with the system and reference scan dependence on system variables. These and other challenges are only obstacles requiring more material research and software development.

9.3. Development of the 3D In-core Reconstruction Method

The MCNP model was used to generate full core flux distributions that were representative of HTRs. The burnup results showed how the neutron hot spot migrates around the reactor during operation, illustrating the need for a sensor system capable of tracking this phenomenon during operation.

Two flux reconstruction algorithms were developed and tested: linear interpolation, and Proper Orthogonal Decomposition (POD). Neither algorithm relied on a neutron diffusion or transport model of the core.

The interpolation-based algorithm is conceptually straightforward and performs well provided enough sensors are placed in the core. It is doubtful that it would be economically feasible to remove fuel pins from the core just to insert more sensors. Thus, only the zero-pitch arrangement

is potentially viable. In this configuration, 211 sensors were assumed. This sensor configuration predicts the magnitude of the core-wide true hotspot poorly (-6% error on average), but predicts z coordinate well. It performs better when the active core hotspot is considered. The main disadvantage of the interpolation-based algorithm is that it is not robust against signal noise or sensor failure. Any amount of noise in the signal directly translates to degraded performance and the algorithm has no way to compensate for sensor failure.

The POD-based reconstruction method is recommended over the interpolation-based method because it yields more accurate reconstructions with fewer sensors. The POD-based method was able to reconstruct the in-core flux with 24 sensors more accurately than the interpolation-based algorithm could with 211 sensors. The POD method was also better at handling signal noise and sensor failure. Signal noise did cause the reconstruction to degrade, but the quality of the reconstruction degraded slower than the interpolation-based method. The chief disadvantage of the POD-based method is that its behavior is not as predictable as the interpolation-based method. The snapshots fed into the algorithm must span the operating conditions experienced by the reactor. Furthermore, the number of POD modes used in the reconstruction has a large effect on the accuracy. In this work, it was computationally feasible to use all of the modes during the reconstruction.

10. Publications

- 2011

1. M. P. Johnson*, T. G. Lewis*, P. V. Tsvetkov, “3D High-Fidelity VHTR Modeling for Performance Optimization Simulations: Monitoring and Operation”, *Trans. Amer. Nucl. Soc.*, **104**, pp. 81-82, USA (2011).

2. P. V. Tsvetkov, S. M. Bragg-Sitton, J. M. Johns*, T. G. Lewis III*, A. B. Alajo*, M. P. Johnson*, “Distributed Sensor Networks for Online 3D In-Core Monitoring in VHTR Environments”, *Trans. Amer. Nucl. Soc.*, **104**, pp. 931-933, USA (2011).

3. J. M. Johns*, M. P. Johnson*, P. V. Tsvetkov, S. M. Bragg-Sitton, A. B. Alajo*, “Emulation of VHTR Operating Conditions in TRIGA Reactors”, *Trans. Amer. Nucl. Soc.*, **104**, pp. 78 - 80, USA (2011).

- 2012

4. J. M. Johns*, P. V. Tsvetkov, “Development of TRIGA-Based Experimental Device for Fiber Optics In-Core Instrumentation Testing for VHTRs”, Paper 202, *Proc. ANS Topical Meeting on Advances in Reactor Physics (PHYSOR2012)*, April 15-20, 2012, Knoxville Convention Center, Knoxville, TN USA (2012).

5. P. V. Tsvetkov, S. M. Bragg-Sitton, J. M. Johns*, M. P. Johnson*, “3D In-Core Monitoring in Advanced Reactor Environments”, *Trans. Amer. Nucl. Soc.*, **106**, pp. 626-627, USA (2012).

- 2013

6. J. M. Johns*, M. P. Johnson*, P. V. Tsvetkov, S. M. Bragg-Sitton, “Fiberoptics-Based Sensing for Real-Time 3D In-Core Monitoring in NGNP/VHTR Environments”, *Trans. Amer. Nucl. Soc.*, **109**, pp. 1033-1036, USA (2013).

7. M. P. Johnson*, P. V. Tsvetkov, “3D Mapping and Reconstruction for In-Core Monitoring in Advanced Reactors”, *Trans. Amer. Nucl. Soc.*, **109**, pp. 1120-1122, USA (2013).

“*” designates participating students.

11. Presentations

- 2011

  1. M. P. Johnson*, "3D High-Fidelity VHTR Modeling for Performance Optimization Simulations: Monitoring and Operation", *ANS 2011 Annual Meeting, June 26-30, 2011, Hollywood, FL, the Westin Diplomat Resort and Spa* (2011).

  2. P. V. Tsvetkov, "Distributed Sensor Networks for Online 3D In-Core Monitoring in VHTR Environments", *ANS 2011 Annual Meeting, June 26-30, 2011, Hollywood, FL, the Westin Diplomat Resort and Spa* (2011).

  3. J. M. Johns*, "Emulation of VHTR Operating Conditions in TRIGA Reactors", *ANS 2011 Annual Meeting, June 26-30, 2011, Hollywood, FL, the Westin Diplomat Resort and Spa* (2011).

  4. S. M. Bragg-Sitton, "In-Core Testing of Distributed Fiber Optic Sensors", *TRTR Meeting, September 2011, INL* (2011).

- 2012

  5. J. M. Johns*, "Development of TRIGA-Based Experimental Device for Fiber Optics In-Core Instrumentation Testing for VHTRs", *PHYSOR2012, April 15-20, 2012, Knoxville Convention Center, Knoxville, TN* (2012).

  6. P. V. Tsvetkov, "3D In-Core Monitoring in Advanced Reactor Environments", *ANS 2012 Annual Meeting, June 24-28, 2012, Hyatt Regency Chicago, Chicago, IL* (2012).

- 2013

  7. P. V. Tsvetkov, "Fiberoptics-Based Sensing for Real-Time 3D In-Core Monitoring in NGNP/VHTR Environments", *ANS 2013 Winter Meeting, November 10-14, 2013, Omni Shoreham Hotel, Washington D.C.* (2013).

  8. P. V. Tsvetkov, "3D Mapping and Reconstruction for In-Core Monitoring in Advanced Reactors", *ANS 2013 Winter Meeting, November 10-14, 2013, Omni Shoreham Hotel, Washington D.C.* (2013).

"*" designates participating students.

12. Participating Students

Name	Citizenship	Major	Project Area
Dr. Ayodeji B. Alajo	Nigeria	Post-doctoral researcher, Nuclear Engineering	VHTR/TRIGA model development and scaling analysis tasks.
Eloura Durkee	U.S.	Undergraduate student, Nuclear Engineering	Test article design, fabrication, and NSCR integration, VHTR/TRIGA model development
Hanniel Honang	U.S.	Undergraduate student, Nuclear Engineering	Test article design, fabrication and NSCR integration, assistance in experimental program efforts
Dr. Tom G. Lewis III	U.S.	Post-doctoral researcher, Nuclear Engineering	System and sensor network modeling, mapping and reconstruction, scaling, V&V
Jesse Johns	U.S.	Graduate student, Nuclear Engineering	Test article design, fabrication, and NSCR integration, experimental program
Matthew Johnson	U.S.	Graduate student, Nuclear Engineering	Distributed sensor network mapping and optimization
Sathish Lakshmipathy	India	Graduate student, Nuclear Engineering	VHTR core operation characteristics modeling algorithm development (core shuffling)
Carl Mullins	U.S.	Graduate student, Aerospace Engineering	Test article design, fabrication and NSCR integration, hardware-software interface via Lab View
Eric Myers	U.S.	Health Physics	System diagnostics; neutron and gamma sensor selection and validation of fiber optics; characterization of overall fiber performance

13. Appendix

13.1. Procurement and Fabrication Process

Void Tube, Aluminum Tubing, OD: 3.0", Thick: 0.083", Length: 12'

- Feedthroughs
  - TCs
  - Power, Solid sealing technology, http://www.solidsealing.com/
  - Fiber Optics, Supplied by Luna
  - Helium Flow x2, Swagelok, http://www.swagelok.com/
- Aluminum block for grid plug
- Alumina spacer for furnace element

Furnace Element, Aluminum tubing, OD: 2", Thick: 0.049"

- Feedthroughs
  - TCs
    - Nextel insulation.
    - Conax Buffalo, http://www.conaxbuffalo.com/details.aspx?cid=T6&pid=T623
    - Pave Tech., http://www.pavetechnologyco.com/design/thermo_productindex.html
    - Power, Solid sealing technology, http://www.solidsealing.com/
    - Fiber Optics, Supplied by Luna
  - Helium flow, Swagelok, http://www.swagelok.com/

Niobium Thermal Shields: $1500, Admat, http://www.admatinc.com/

Alumina baffles, Alumina Silicate possesses the properties that would be more fitting.

Piping/Flow Tubing

- Swagelok, http://www.swagelok.com/
- Pressure relief valves, Spring Loaded and Power Operated
- Solenoid valves
- Power relief valves

Wiring and Thermocouples, K type, SLE

Computer Rack

Graphite heaters:

These were ordered from Poco Graphite. They have a plant in Decatur, Texas. Their response was prompt and they were helpful with the material choice of the graphite, which was chosen to be AXZ-5Q. The quoted price was: $2586.00 (all images were taken some time after receipt). All heaters were visually checked.

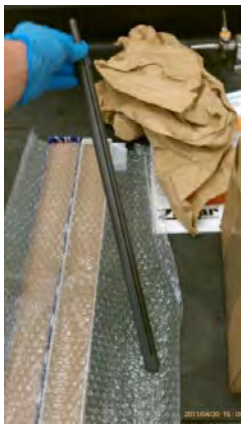

Epoxy/Cement:

These were ordered from Cotronics. Shipment was swift, though the staff were not very helpful with respect to questions about their materials. The packaging was neat and tight. No apparent damage to the box.

13.2. Fiberoptics Testing

Failure modes

There are various failure modes available for the fiber optics. The fibers are inherently fragile, so mishandling them can cause the ends of the fibers to inadvertently brake. Avoiding this as the fibers are being put into place is paramount.

Moreover, the fibers can be subjected to various materials, environmental conditions, and physical constraints that would further induce fiber degradation and failure.

Signs of various failures

How to determine that a fiber is about to fail, and by what mode. For example, water ingress on the coupling reduces the return loss. A signal enhancement is noticed initially.

Mostly, the failures are mechanical, such that they would be induced in or outside of a reactor environment.

Signal interference

Due to the inherent flexibility in the fiber optics, users of the measurement system will most generally attempt to apply the fiber optics in unusual geometries, most generally to reach locations that vintage measurement system would not reach.

Since light generally travels un-impeded in the fibers, users might become complacent in the geometry of which the fiber measurement system is placed.

Therefore, quantification of various degree of bending should be done. When fiber optics are bent, there may be some light loss due to the impinging photon on the surface overcoming the index of refraction.

To conduct these tests, it is suggested that three phases of testing are done.

- First, the fiber would be calibrated normally and put into a relatively "straight" geometry. Then a series of measurements are taken with the fiber bent, as not to enforce curvature changes in the fiber itself, as various point along the measurement path. The resulting changes in the measurements will be noted. This will be repeated for various degrees in the curvature.
- Second, the fiber should be put into highly curved geometries, then calibrated. After straightening out the fiber optic, then measurements are taken. This is to ensure that the calibration point does not impede the measurement accuracy.
- The third phase would be to determine the number of bends, at various degrees that would begin to vary the measurements at the end of a very long fiber.

Bending in the fiber can be read as strain, which can be incorrectly interpreted as temperature difference. If I understand correctly, the fiber calibration should be performed with the fiber in the correct configuration for the final application – e.g. if there will be bends, then we need to calibrate with those bends.

Calibration after installation will be required at standard ambient temperature to provide a baseline for subsequent measurements at elevated temperature.

The suggestion to perform some benchtop testing to determine hysteresis-type effects is good – basically run some tests on straight fiber, curve it to simulate bending that could occur during installation, then straighten it again and repeat the original tests to ensure that the measurements have not changed (within measurement error).

Effects of vibrations

Due to the high velocity of Helium in the VHTR, vibrational effects will be fairly noticeable. The testing of vibrational effects on the measurement integrity and fiber integrity should be completed.

Testing can be conducted through mechanical means; for instance, with a pump or other device attached to the measurement device or measurement location, or through venturi in a flow field (generally used for pressure drop, but can induce eddy controlled eddies).

This can be used to replicate the expected flow oscillations in the VHTR during operating conditions.

Fluence induced measurement error

Naturally, in a reactor environment, the fission rate density (prompt and delay/fission product contributions) imposes the highest contribution to the gamma and neutron fluence; therefore, the effects of activation products can be ignored, such as nitrogen-16 production.

However, shutdown conditions tell another story - though the fluence rate will be significantly smaller.

Inherently, though, over time the measurements will begin to drift. This drifting will need to be quantified and incorporated in the calibration to imposed proper operation and accurate measurement. Since no other distributive system is available, either passive systems, like iron wire or Cd/Au foil analysis, or active systems will need to be used for validation purposes.

There currently are 3mm diameter fission chambers that may be used. They cost $18,000 for 10. These would provide excellent feedback as to the fiber performance.

Temperature effects on gamma/neutron measurements

There might be some alteration in the gamma/neutron measurement as a function of the temperature of the fiber optic. This is inherent to the cross-section of neutrons in a material changing as a result of the nuclei vibrations.

The composition and functionality of these fibers, however, is unknown - so the testing will be done pretty much as a shot in the dark.

Conducting these kinds of tests will be through the use of manually varying furnace temperature. Simply changing the temperature should not change the gamma or neutron

fluence, so, in this regard, we can understand the temperature related effects of the neutron/gamma interactions.

Operational temperature ranges

The upper temperature limit of the fiber optic systems would be important to determine. This would help determine the instrumentation strategy.

Moreover, during severe accidents, it would be important to know that the fiber measurements would not lose their validity if the temperature were to rise significantly.

The furnace can be removed from the reactor to do this test. The temperature limit is set to prevent the total heat storage in the furnace to cause a steam rupture and to prevent creep in the high pressure aluminum structure.

A short test would not be cause for any concern.

Chemical attack reference times

As stated by Luna, water and other alkalis attack the fiber optic and eventually render it useless. Determining, under various temperature conditions, the length of time these fibers are expect to last would be imperative to a safety analysis of their implementation.

For example, water ingress in HTRs that use water-secondary systems would possibly cause degradation very quickly at the expected 488C inlet temperature conditions if the encapsulation were impaired.

Time response

Testing the speed at which data can be reliably obtained is fairly important. Whether transient conditions, albeit slow, can be accurately measured could lead to further validation techniques.

It is our understanding that this may not be possible with a single OBR, but having multiple OBRs to measure at a given periodicity would, perhaps, suffice. This would not be do-able for the current project.

An additional requirement is that the fiber optic reaches equilibrium quickly. Temperature, gamma, and neutron response should be quick to allow for a "snap shot" to be captured. The OBR does its measurement very quickly; however, computation and display of the data is fairly lengthy. The OBR will not be an issue in this. It was determined that the return-to-normal time for the temperature fiber exceeded 15 minutes when the fiber was removed from a cold source.

Spatial Resolution

When producing measurement data for code validation and determining hotspot information, the spatial resolution of the fiber optic is very important. This is the primary capability of the fiber optic, so it is very important to have this feature documented.

Due to the nature of the Raleigh scattering, the phenomena of spatial discretization is actually continuous. Interpreting how to define the spatial resolution then, might be a bit

tricky. According to the OBR manual general resolution is +/- 10um over 30 m, the sensing resolution is +/- 2cm. There is also a "data segment size" of 1.0 mm.

The testing of the spatial properties will be fairly straight forward, except in the case of the neutron fibers. Temperature distributions are easily produced and manipulated. With the proper measurements of the fiber and by applying various gradients, the spatial resolution can be determined.

For the gamma fibers, shielding will need to be used in conjunction with high activity sources. Using the La source against the dry cell may be an option. With the neutron fiber, simply using the core is our only option. There may be some opportunities to use paraffin or cadmium to force spatial changes. Even more so, determining thermal to fast fluence ratios might be possible.

Calibration requirements

This is more important for the temperature fiber; ideally the furnace will not be shutdown - just put into a low power state to prevent unnecessary thermal transients in the furnace. The fiber may, with time, drift due to radiation induced re-structuring in the fiber. This will change the strain parameters, surely, and therefore change the temperature measurement as a result.

The proposed testing would be simply to add fibers during various intervals of the irradiation period. This would introduce fresh, calibrated fibers to compare with the already irradiated fiber optics. Since this would require a complete shutdown of the furnace, the choice of re-calibrating the irradiated fibers will need to be made.

The choice to do this would allow for a new baseline to be established. Additionally, the fibers can be compared at the cold iron condition. Conversely, not allowing for re-calibration allows for comparison at operating temperatures and preserves a fluence history of the calibration of the fibers. This will also introduce a determination of the integrity of an initial calibration over the fiber life-time.

13.3. Acceptance Testing

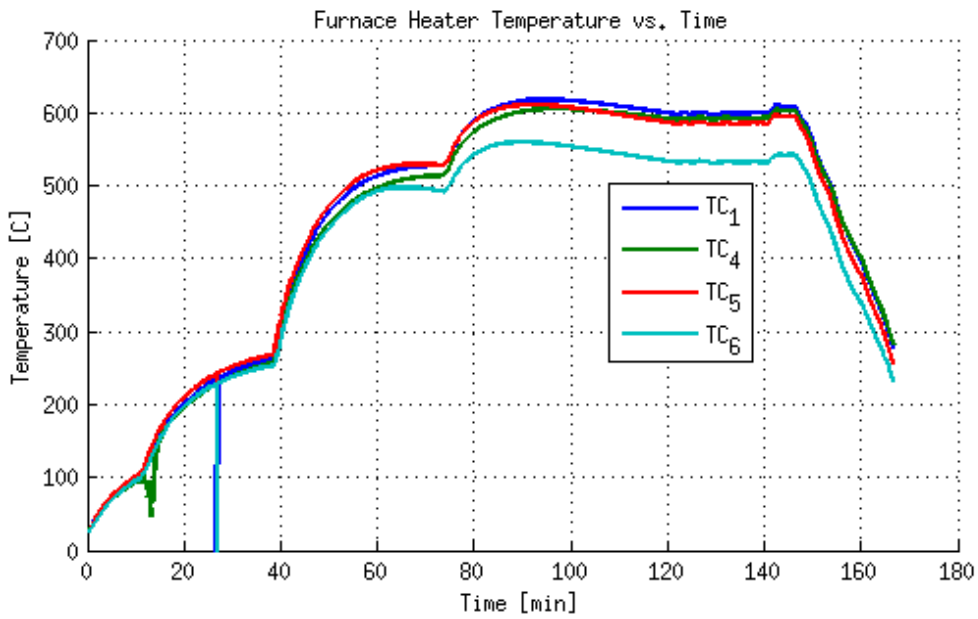

(a) Furnace heater.

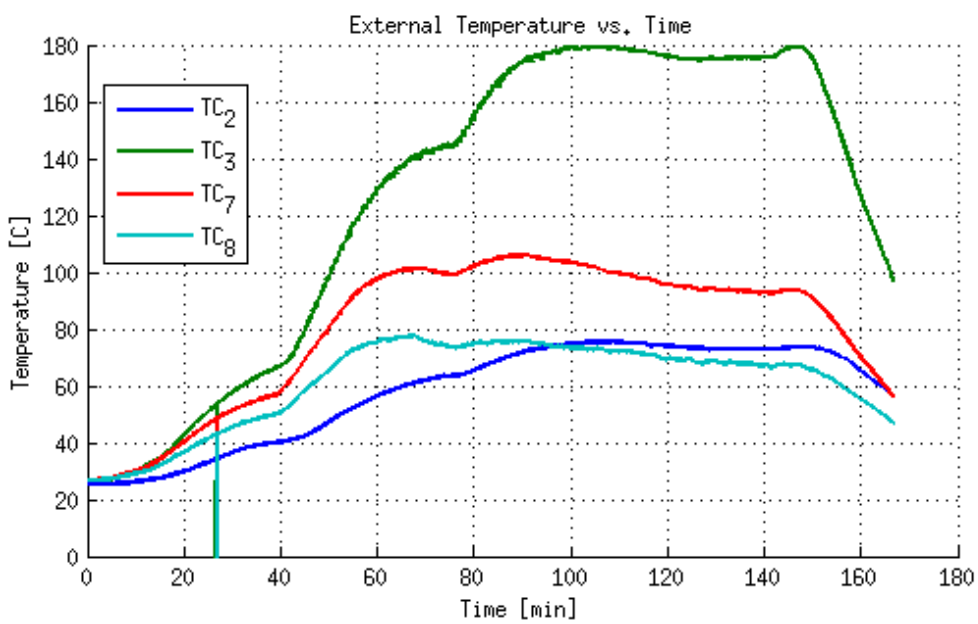

(b) External Temperature.

Fig. 1. Heater and external temperatures.

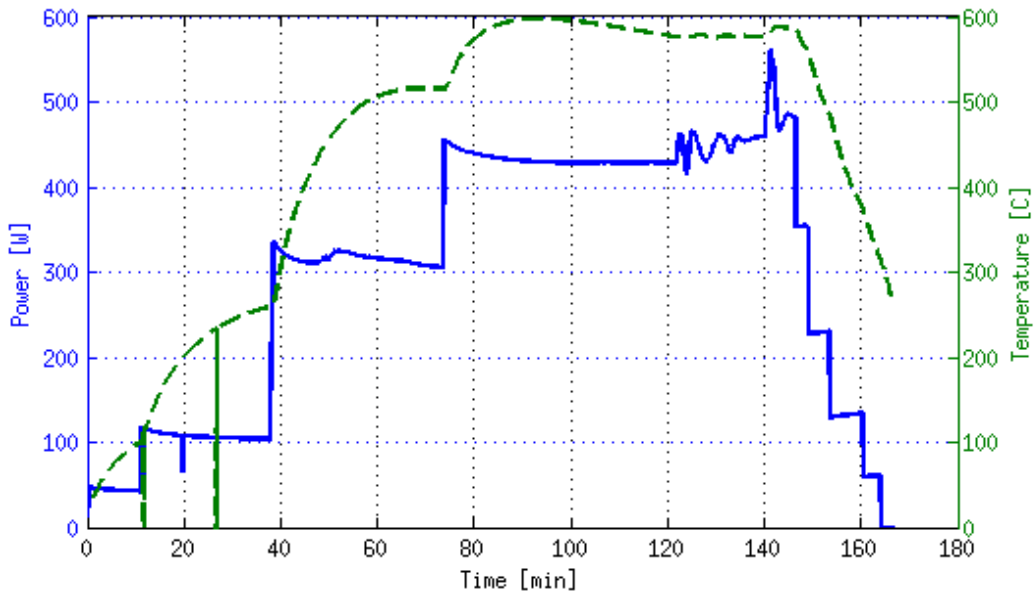

(a) Power-temperature dynamics.

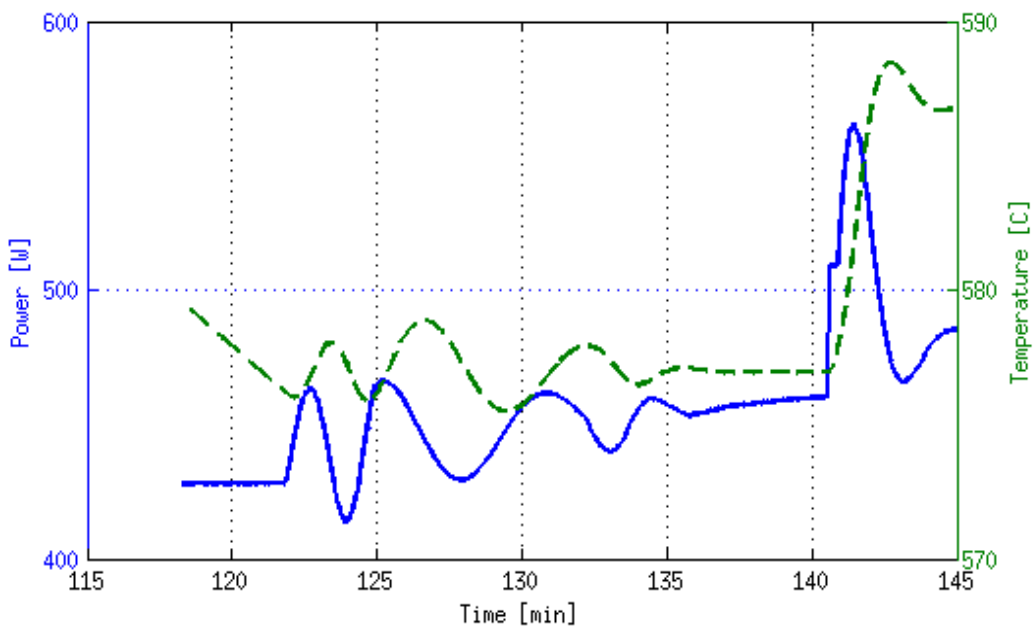

(b) Power-temperature dynamics between 115 min and 145 min.

Fig. 2. Power and engaging PID controller.

13.4. VHTR Control Rod Modeling

13.4.1. Design Details

The design for the control rods was taken from the General Atomics design for the MHTGR.[1,2] The control rods are modeled as an annular graphite matrix containing 40 wt% B4C particles. The control rods are clad with Incoloy-800. The particles properties are given in Table 1.

Table 1 Properties of the B_4C Pellets in VHTR Control Rods

Boron composition	90% B-10, 10% B-11
B4C kernel radius	100 μm
Graphite buffer coating thickness	18 μm
PyC coating thickness	23 μm

Figure 1 provides the VHTR control rod geometry details as modelled in the present evaluations.

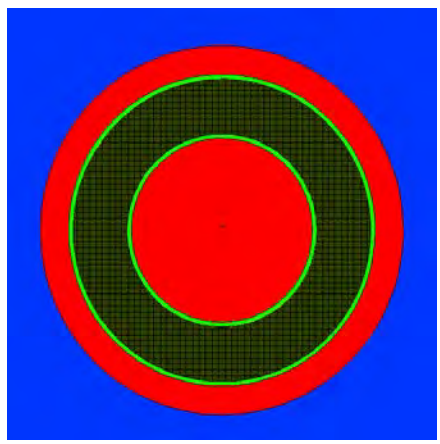

Fig. 1. XY view of the VHTR control rod geometry. The red material is He inside the control rod channel. The blue shows the graphite block material.

The B_4C kernels used in the burnable poison compacts were the same as those in Table 1 except natural boron was used. Determination of the optimal burnable poison loading in the core for a given reloading scheme is a sizable project in and of itself and, as such, it was left outside the scope of the present analysis. This project has considered nominal loadings necessary to yield critical configurations. B_4C particle packing fractions around 3% were found to be sufficient.

13.4.2. References

1. Wright, J.K., Lloyd, W.R. Analysis of Potential Materials for the Control Rod Sleeves of the Next Generation Nuclear Plant. INL/EXT-06-11614 (2006).

2. “Preliminary Prismatic Coupled Neutronics Thermal Fluids Benchmark of the MHTGR-350 MW Core Design”, Draft (December 2010), Idaho National Laboratory (2010).

13.5. Presentations

13.5.1. 3D High-Fidelity VHTR Modeling for Performance Optimization

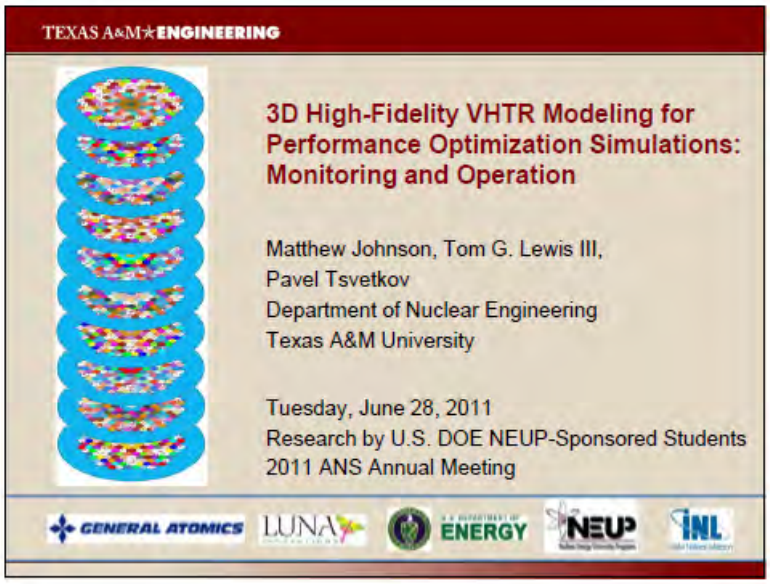

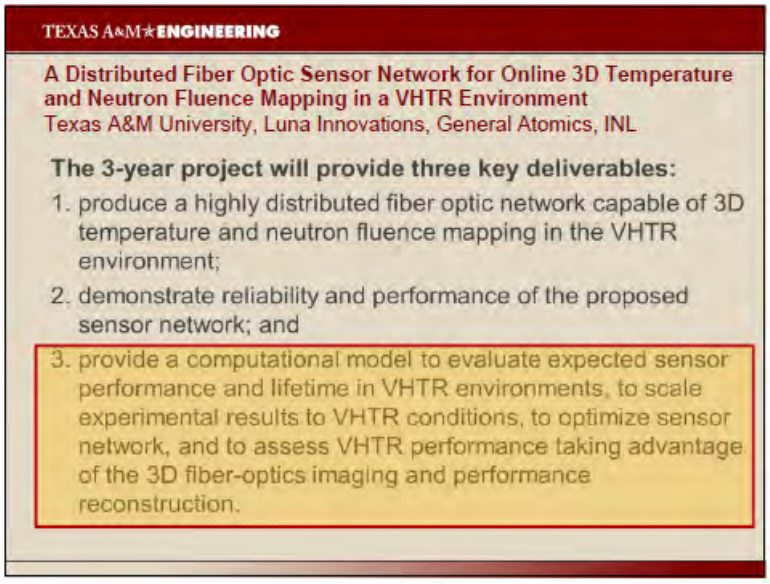

TEXAS A&M ENGINEERING

3D High-Fidelity VHTR Modeling Objectives

- Predict core behavior
- Develop methodologies for 3D flux (and power density) reconstruction
- Predict hotspots and off normal conditions with a limited amount of sensors
- Reconstruction will rely on knowledge of the expected core behavior, hence the current focus on high fidelity modeling

TEXAS A&M ENGINEERING

Benefits

- Predictive evaluation of potential failure modes for in-core components
- Hot spot management asssitance
- Determine the fluence in reflector blocks, especially the replaceable inner reflector
- Assistance in determining lifecycle limits and longevity of in-core components

TEXAS A&M ENGINEERING

Methodology

- Using well tested codes:
  - Current analysis is done in mcnpx 2.6.0 and its built-in coupling to CINDER90
  - Monte Carlo methods are robust for VHTR modeling and reduce challenges associated with geometry and cross sections processing for advanced systems.
  - Pre-processing is automated via scripting. Input files are generated with a Python script, which makes the input easier to manipulate and understand

TEXAS A&M ENGINEERING

High Fidelity MCNP model of NGNP core

- Full core is modeled with 1/6 periodic symmetry in materials. The symmetry in materials is used to reduce the number of burnable regions and therefore memory requirements during fuel depletion runs. The full core is still modeled so, for non-burnup runs, the effects of an uneven control rod insertion can be modeled.
- Detectors are modeled using cell flux tallies. This allows for fluxes to be tallied for each unique fuel block. TMESHes are used to visualize the fundamental mode flux distributions

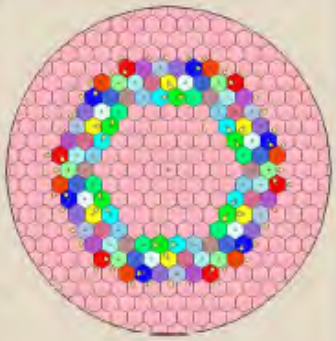

TEXAS A&M ENGINEERING

High Fidelity MCNP model of NGNP core

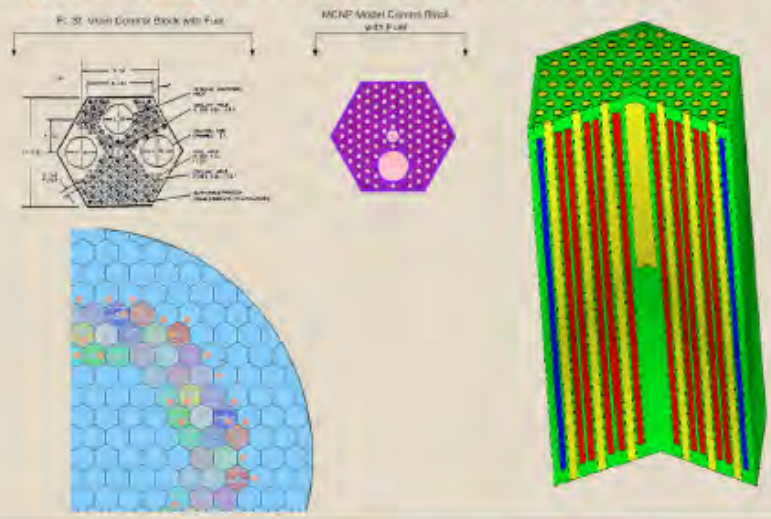

TEXAS A&M ENGINEERING

Phase I Modeling Assumptions/Limitations

- No heat transfer phenomena captured - core is isothermal (provisions can be made to couple to CFD simulations if needed)
- No control rods or burnable poison is used
  - No criticality search performed during burnup steps
- A single material is burned for each fuel block
- TRISO particles truncated at fuel compact edges
- These assumptions will be re-evaluated and relaxed in Year 2 and 3 of the project

TEXAS A&M ENGINEERING

Core lifetime

- k_{eff} results for a representative 3-ring 600 MWth core
  - 15% enriched Uranium fuel
  - 25 vol% packing fraction of TRISO in fuel compacts
  - Kernel radius of 150 μm
- Core lifetime of ~17 months

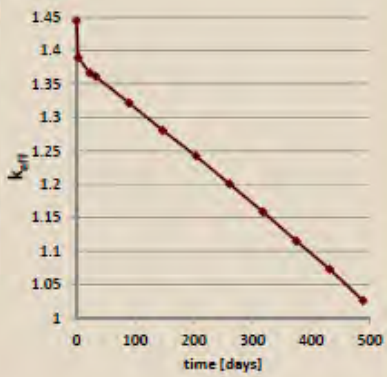

TEXAS A&M ENGINEERING

Hot Spot Migration and Localization with the Core

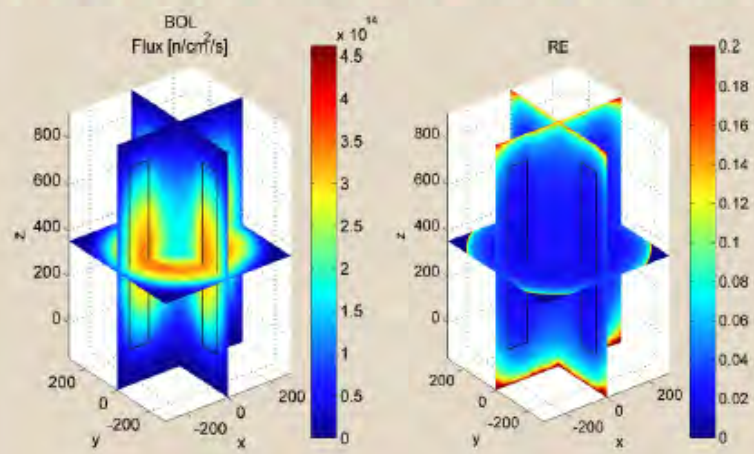

TEXAS A&M ENGINEERING

Peaking Factor Evolution during Operation

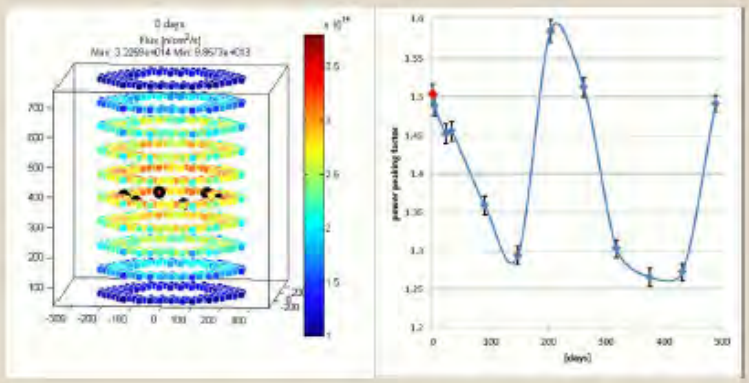

TEXAS A&M ENGINEERING

Single Block Peaking Factors

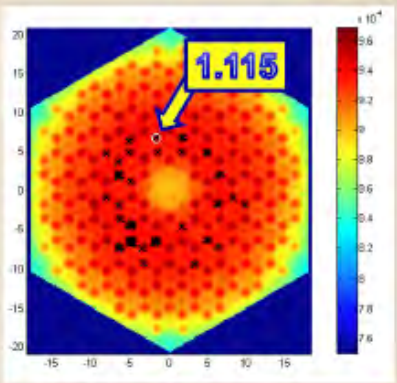

Fast flux hot spot localization
(0.1<E<5 MeV)

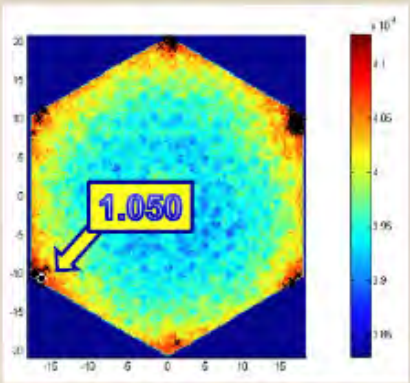

Thermal flux hot spot localization
(0<E<1.0E-5 MeV)

TEXAS A&M ENGINEERING

Time stepping during burnup runs representing reactor operation conditions

- Acknowledged as a source of error, especially given the sometimes abrupt changes in hot spot locations
- Currently computational resources restrict fidelity of kcode intermediate calculations
- Possible solutions: alternative codes (Serpent, MCNP5 + Monteburns or MOCUP); access to faster computational clusters (ex. INL HPC)

TEXAS A&M ENGINEERING

Graphite Fast Fluence in Estimation

- Compared against the GA report
- Fast fluence is defined for E > 0.1 MeV

16.3 Month Fast Fluence [n/cm^2]	
min	6.31E+20
max	1.77E+21
mean	1.30E+21

Max 36 Month Fast Fluence [n/cm^2]	
16 month extrapolated	GA report
3.90E+21	1.7E+21

TEXAS A&M ENGINEERING

Conclusions

- 3D high-fidelity modeling approach is being developed for applications in performance simulations studies targeting monitoring and operational aspects of VHTRs.
- The modeling approach allows for development and applications of in-core 3D performance map reconstruction techniques accounting for novel direct 3D in-core measurement approaches for extreme environments of HTRs.
- Presented sample results showed 3D mapping capabilities of performance characteristics.
- The simulation methodology and reconstruction techniques are being developed for sensor array optimization studies targeting in-core 3D monitoring options.

TEXAS A&M ENGINEERING

Conclusions

Key milestones:

- Development of theoretical approach to estimating neutron fluence distributed along the length of the sensing fiber.
- Test furnace engineering design with reactor safety board approval.
- Fiber optic sensor design and completion of out-of-core laboratory testing.
- Test furnace fabrication, assembly and completion of out-of-core testing.
- Delivery of sensor strings with connectors to university; installation in test furnace.
- Assembly installation in TRIGA and completion of irradiation test matrix.
- 3D VHTR and TRIGA modeling with representation of distributed sensor network elements, performance reconstruction and optimization of the network design.
- Modeling validation using test measurements and scaling to the prototypical VHTR conditions.

13.5.2. Distributed Sensor Networks for Online 3D In-Core Monitoring

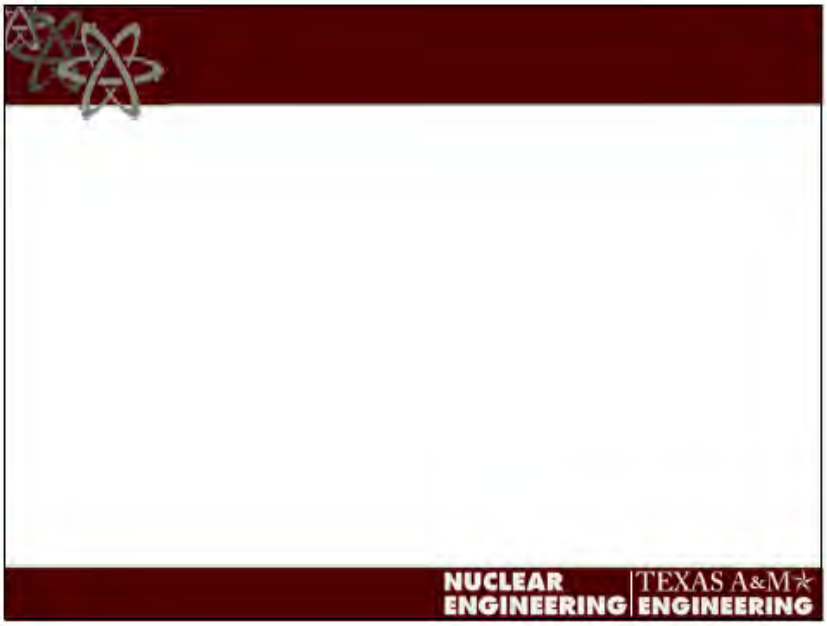

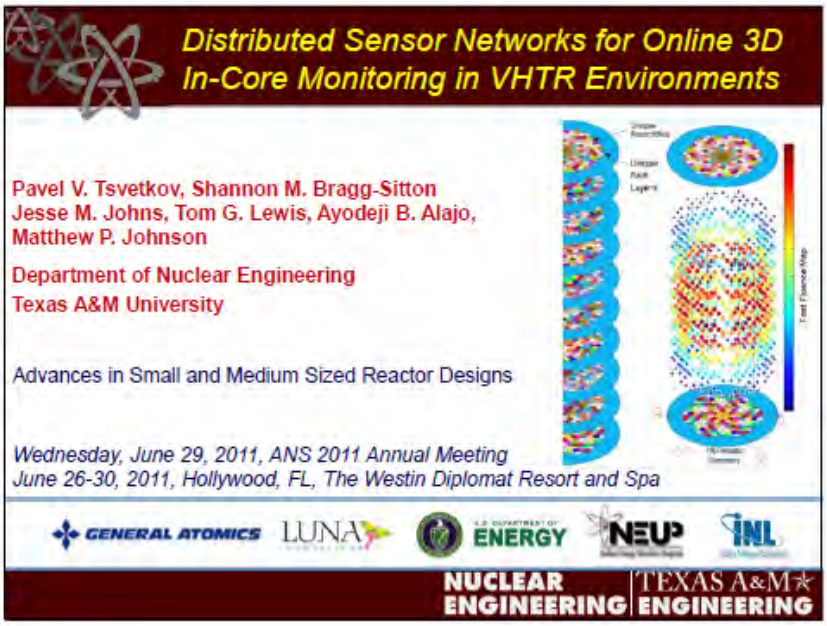

Distributed Sensor Networks for Online 3D In-Core Monitoring in VHTR Environments

- Overview
- High-Fidelity Modeling Approach
- Emulation of VHTR Conditions in TRIGA
- Validation Efforts
- Current Status
- Conclusions

GENERAL ATOMICS LUNA ENERGY NEUP INL

NUCLEAR ENGINEERING

Distributed Sensor Networks for Online 3D In-Core Monitoring in VHTR Environments

Overview

Small and Medium Sized Advanced Reactors
Safety, Reliability, Autonomity, Economics, …

- Robust in-core measurement systems capable to provide characteristic operational information
- Longevity of sensor performance
- Real time operation
- Ability to predict hot spot formation conditions

GENERAL ATOMICS LUNA ENERGY NEUP INL

NUCLEAR ENGINEERING

Distributed Sensor Networks for Online 3D In-Core Monitoring in VHTR Environments

Overview

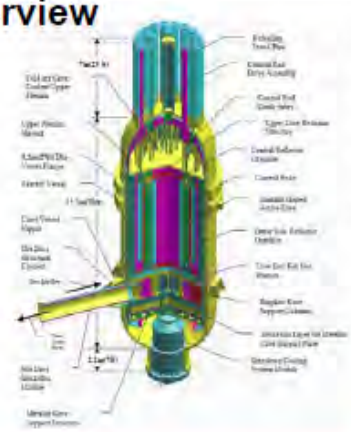

- **In-core monitoring challenge** – reliable long-term operation in extreme high-temperature high-fluence environments
- **Use of fiber optic sensors** – direct in-core 3D monitoring for in-core management (loading, hot spots, temperature and fluence maps)

GENERAL ATOMICS

NUCLEAR ENGINEERING

Distributed Sensor Networks for Online 3D In-Core Monitoring in VHTR Environments

Overview

Collaboration of University, Nat. Lab., Industry

Texas A&M University, Project Lead

Luna Innovations, Primary Industry Partner

General Atomics, Advisor

Idaho National Laboratory, Advisor

GENERAL ATOMICS LUNA ENERGY NEUP INL

NUCLEAR ENGINEERING

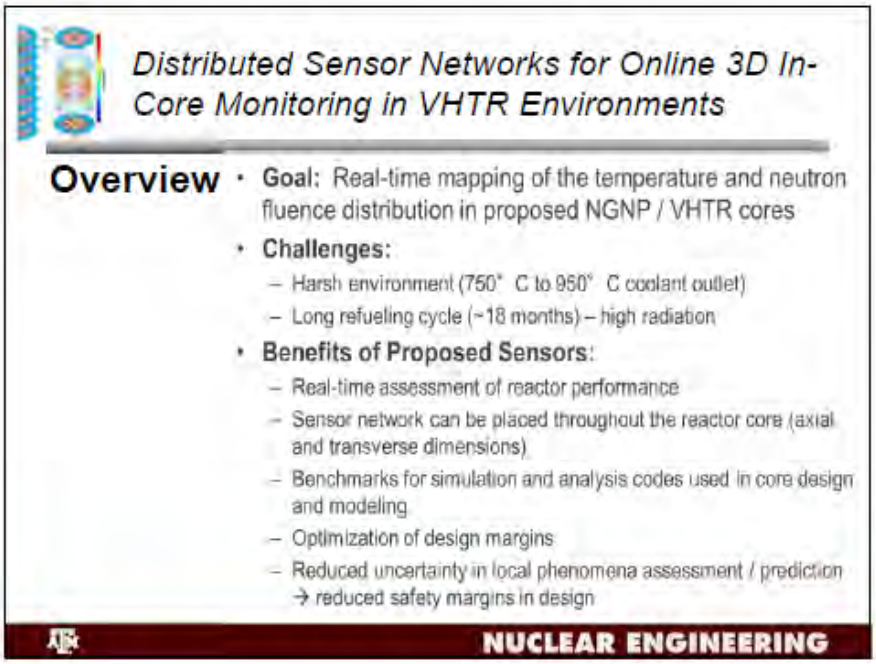
Distributed Sensor Networks for Online 3D In-Core Monitoring in VHTR Environments
Overview
• Goal: Real-time mapping of the temperature and neutron fluence distribution in proposed NGNP / VHTR cores
• Challenges:
– Harsh environment (750° C to 950° C coolant outlet)
– Long refueling cycle (~18 months) – high radiation
• Benefits of Proposed Sensors:
– Real-time assessment of reactor performance
– Sensor network can be placed throughout the reactor core (axial and transverse dimensions)
– Benchmarks for simulation and analysis codes used in core design and modeling
– Optimization of design margins
– Reduced uncertainty in local phenomena assessment / prediction → reduced safety margins in design
NUCLEAR ENGINEERING

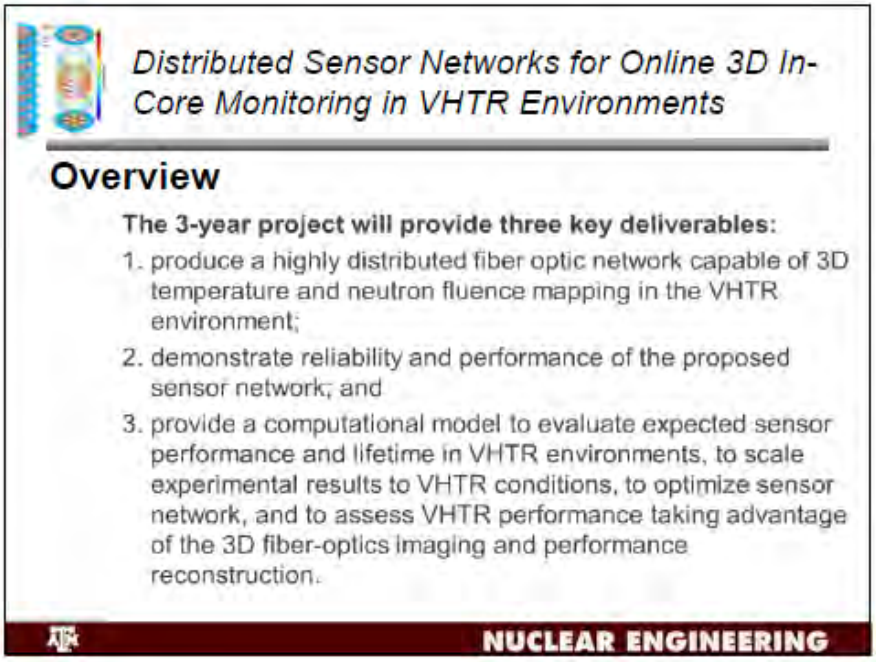
Distributed Sensor Networks for Online 3D In-Core Monitoring in VHTR Environments
Overview
The 3-year project will provide three key deliverables:
1. produce a highly distributed fiber optic network capable of 3D temperature and neutron fluence mapping in the VHTR environment;
2. demonstrate reliability and performance of the proposed sensor network; and
3. provide a computational model to evaluate expected sensor performance and lifetime in VHTR environments, to scale experimental results to VHTR conditions, to optimize sensor network, and to assess VHTR performance taking advantage of the 3D fiber-optics imaging and performance reconstruction.
NUCLEAR ENGINEERING

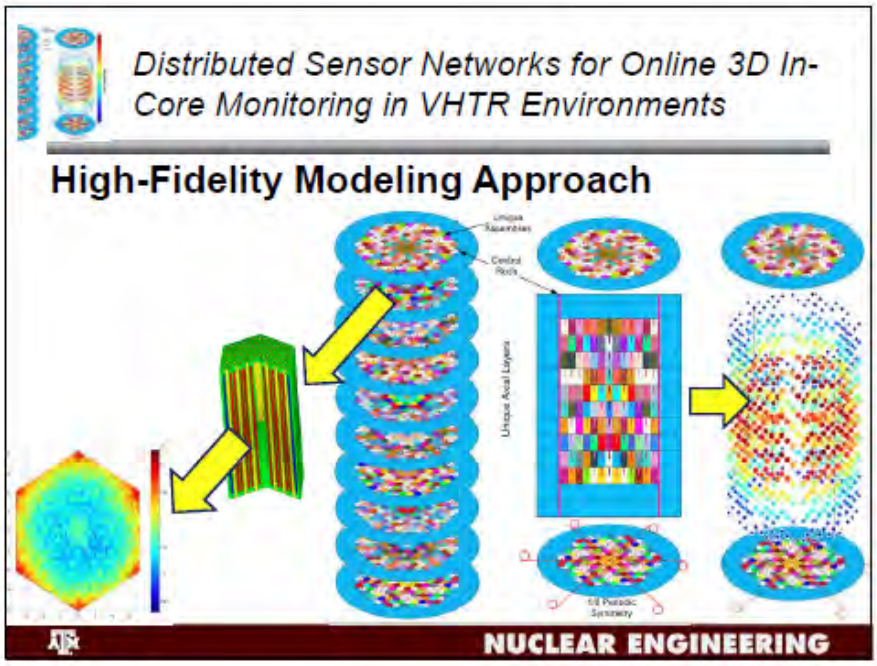
Distributed Sensor Networks for Online 3D In-Core Monitoring in VHTR Environments
High-Fidelity Modeling Approach
NUCLEAR ENGINEERING

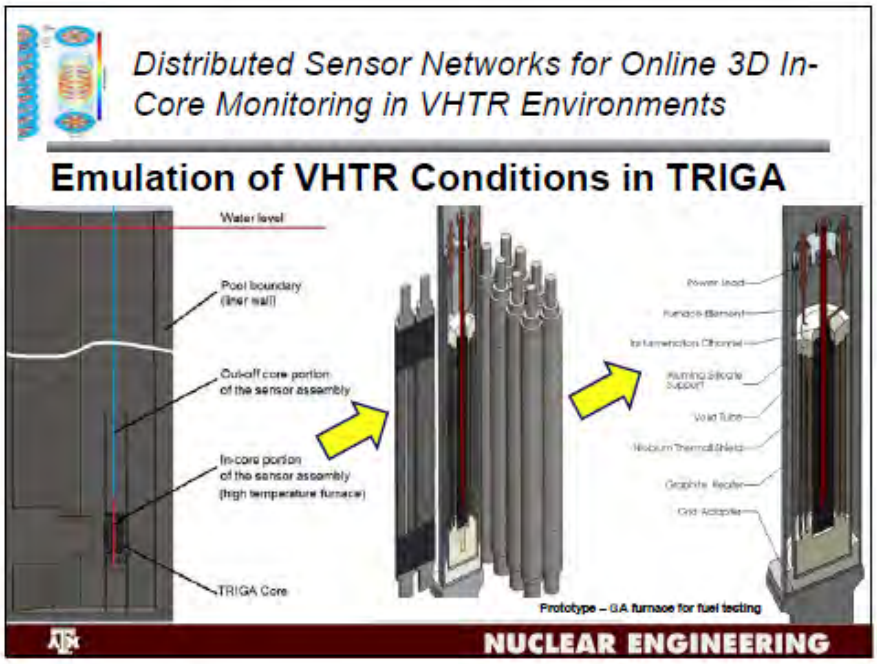
Distributed Sensor Networks for Online 3D In-Core Monitoring in VHTR Environments
Emulation of VHTR Conditions in TRIGA
Water level
Pool boundary (liner wall)
Cutoff core portion of the sensor assembly
In-core portion of the sensor assembly (high temperature furnace)
TRIGA Core
Prototype – GA furnace for fuel testing
NUCLEAR ENGINEERING

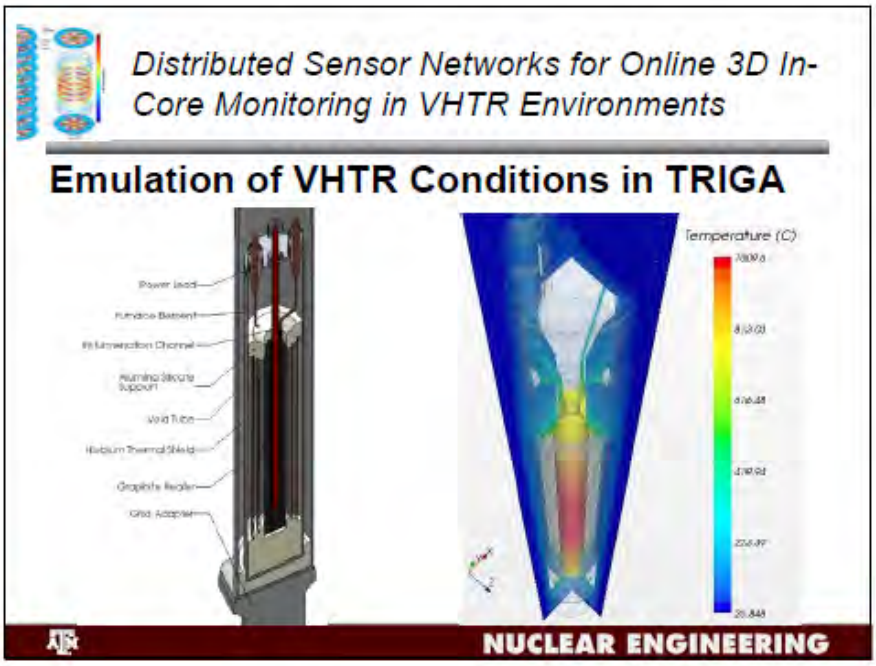
Distributed Sensor Networks for Online 3D In-Core Monitoring in VHTR Environments
Emulation of VHTR Conditions in TRIGA
Temperature (C)
NUCLEAR ENGINEERING

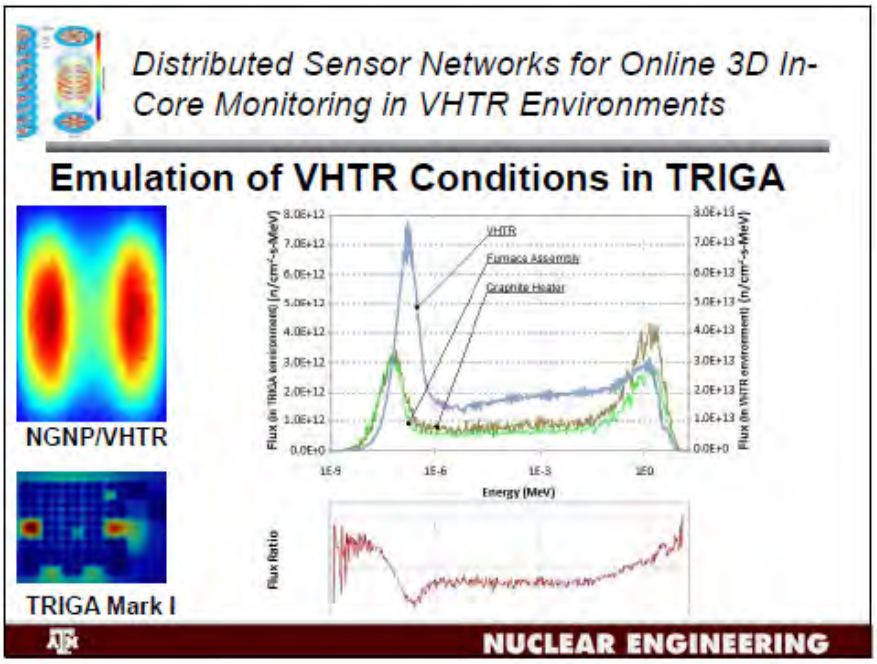
Distributed Sensor Networks for Online 3D In-Core Monitoring in VHTR Environments
Emulation of VHTR Conditions in TRIGA
NGNP/VHTR
TRIGA Mark I
VHTR
Furnace Assembly
Graphite Heater
Energy (MeV)
Flux Ratio
NUCLEAR ENGINEERING

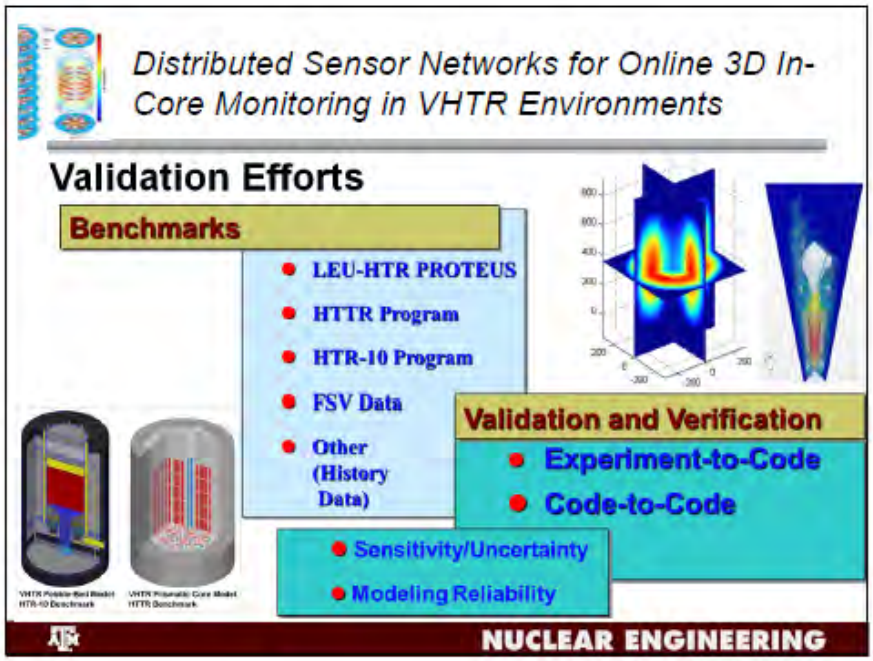
Distributed Sensor Networks for Online 3D In-Core Monitoring in VHTR Environments
Validation Efforts
Benchmarks
LEU-HTR PROTEUS
HTTR Program
HTR-10 Program
FSV Data
Other (History Data)
Validation and Verification
Experiment-to-Code
Code-to-Code
Sensitivity/Uncertainty
Modeling Reliability
NUCLEAR ENGINEERING

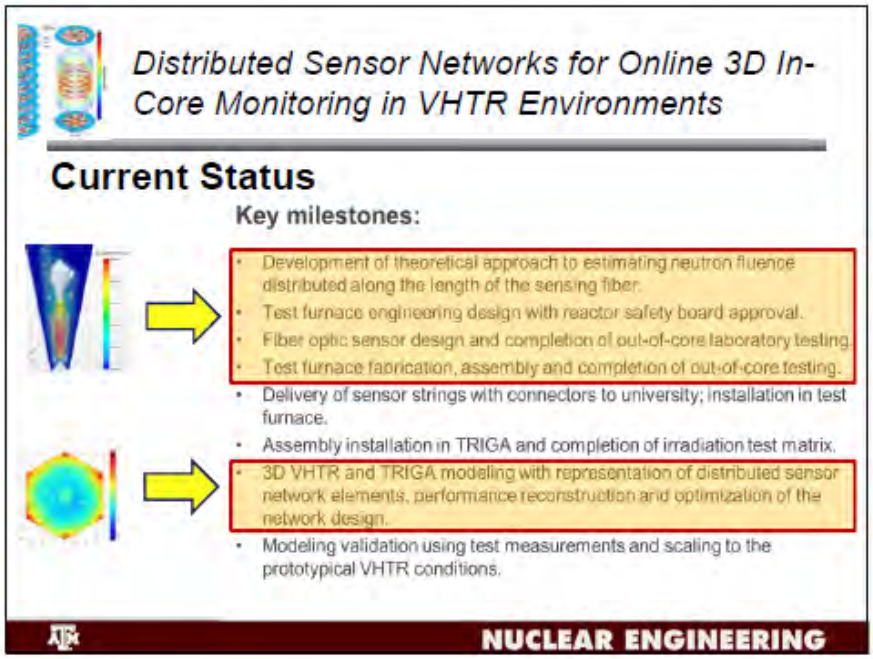
Distributed Sensor Networks for Online 3D In-Core Monitoring in VHTR Environments
Current Status
Key milestones:
Development of theoretical approach to estimating neutron fluence distributed along the length of the sensing fiber.
Test furnace engineering design with reactor safety board approval.
Fiber optic sensor design and completion of out-of-core laboratory testing.
Test furnace fabrication, assembly and completion of out-of-core testing.
Delivery of sensor strings with connectors to university; installation in test furnace.
Assembly installation in TRIGA and completion of irradiation test matrix.
3D VHTR and TRIGA modeling with representation of distributed sensor network elements, performance reconstruction and optimization of the network design.
Modeling validation using test measurements and scaling to the prototypical VHTR conditions.
NUCLEAR ENGINEERING

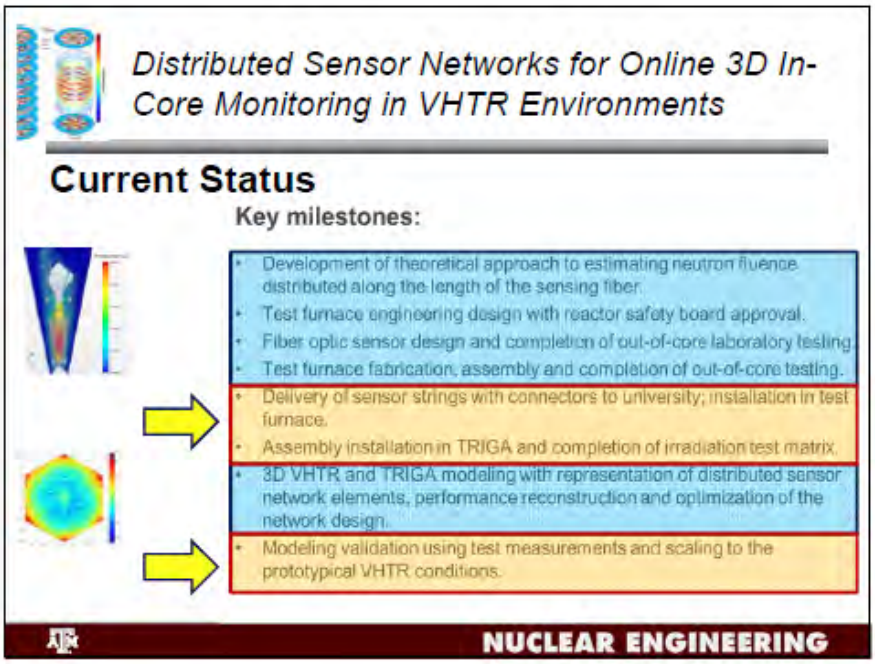
Distributed Sensor Networks for Online 3D In-Core Monitoring in VHTR Environments
Current Status
Key milestones:
Development of theoretical approach to estimating neutron fluence distributed along the length of the sensing fiber.
Test furnace engineering design with reactor safety board approval.
Fiber optic sensor design and completion of out-of-core laboratory testing.
Test furnace fabrication, assembly and completion of out-of-core testing.
Delivery of sensor strings with connectors to university; installation in test furnace.
Assembly installation in TRIGA and completion of irradiation test matrix.
3D VHTR and TRIGA modeling with representation of distributed sensor network elements, performance reconstruction and optimization of the network design.
Modeling validation using test measurements and scaling to the prototypical VHTR conditions.
NUCLEAR ENGINEERING

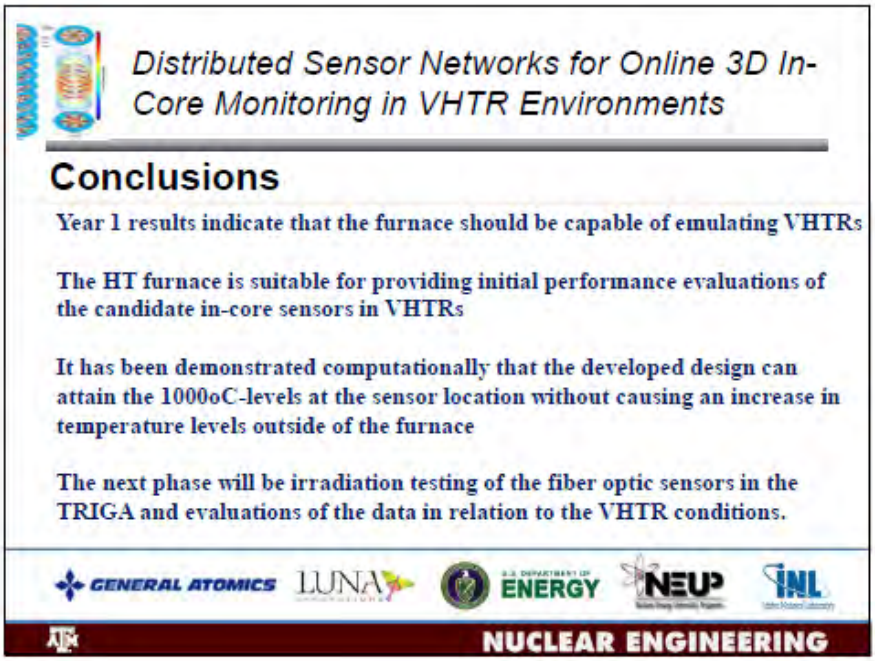
Distributed Sensor Networks for Online 3D In-Core Monitoring in VHTR Environments
Conclusions
Year 1 results indicate that the furnace should be capable of emulating VHTRs
The HT furnace is suitable for providing initial performance evaluations of the candidate in-core sensors in VHTRs
It has been demonstrated computationally that the developed design can attain the 1000oC-levels at the sensor location without causing an increase in temperature levels outside of the furnace
The next phase will be irradiation testing of the fiber optic sensors in the TRIGA and evaluations of the data in relation to the VHTR conditions.
GENERAL ATOMICS
LUNA
ENERGY
NEUP
INL
NUCLEAR ENGINEERING

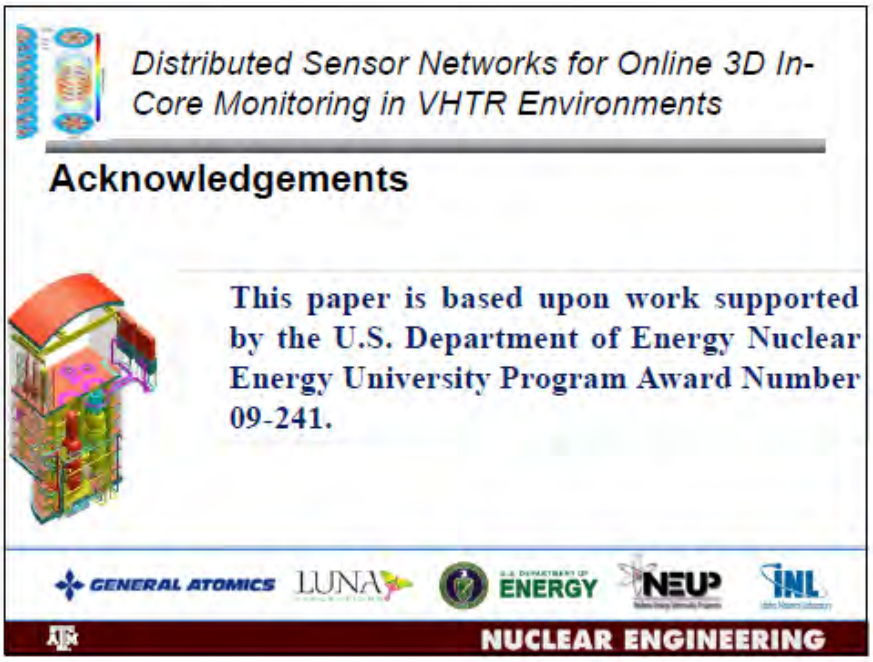
Distributed Sensor Networks for Online 3D In-Core Monitoring in VHTR Environments
Acknowledgements
This paper is based upon work supported by the U.S. Department of Energy Nuclear Energy University Program Award Number 09-241.
GENERAL ATOMICS
LUNA
ENERGY
NEUP
INL
NUCLEAR ENGINEERING

Distributed Sensor Networks for Online 3D In-Core Monitoring in VHTR Environments
QUESTIONS?
GENERAL ATOMICS
LUNA
ENERGY
NEUP
INL
NUCLEAR ENGINEERING
TEXAS A&M ENGINEERING

Distributed Sensor Networks for Online 3D
In-Core Monitoring in VHTR Environments
THANK YOU
GENERAL ATOMICS
LUNA
ENERGY
NEUP
INL
NUCLEAR ENGINEERING
TEXAS A&M ENGINEERING

13.5.3. Emulation of VHTR Operating Conditions in TRIGA Reactors

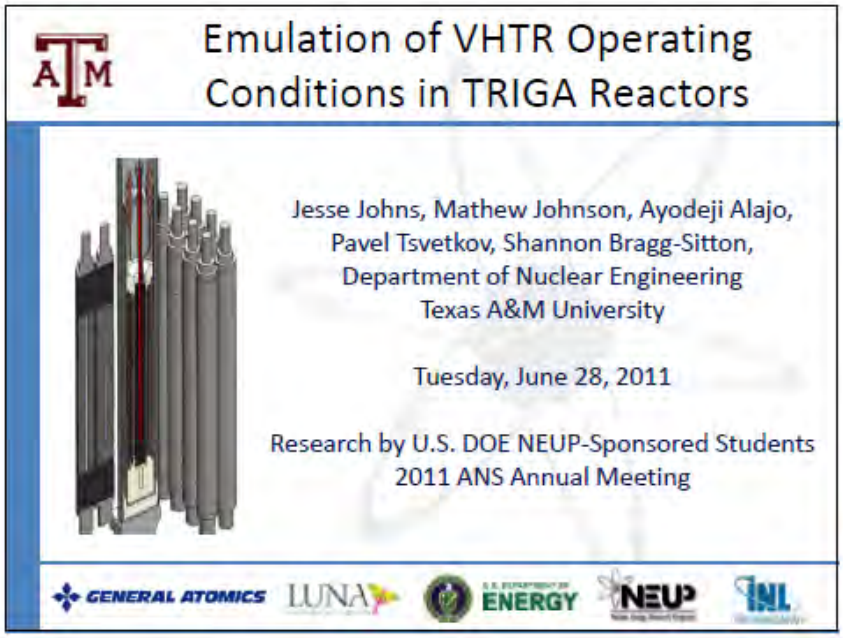

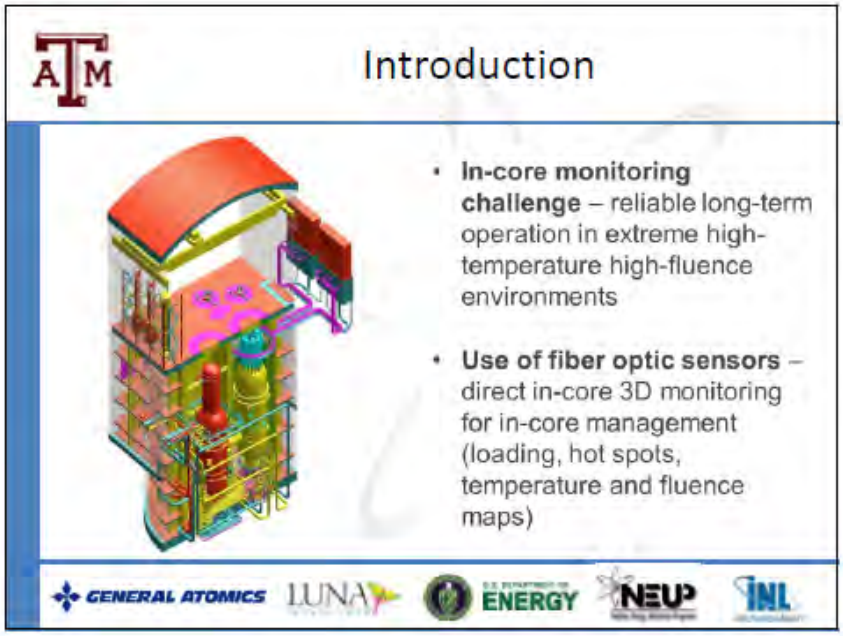

Introduction

A Distributed Fiber Optic Sensor Network for Online 3D Temperature and Neutron Fluence Mapping in a VHTR Environment

Texas A&M University, Project Lead

Luna Innovations, Primary Industry Partner

Advisors:
General Atomics
Idaho National Laboratory

Introduction

- **Goal:** Real-time mapping of the temperature and neutron fluence distribution in proposed NGNP / VHTR cores
- **Challenges:**
  - Harsh environment (750° C to 950° C coolant outlet)
  - Long refueling cycle (~18 months) – high radiation
- **Benefits of Proposed Sensors:**
  - Real-time assessment of reactor performance
  - Sensor network can be placed throughout the reactor core (axial and transverse dimensions)
  - Benchmarks for simulation and analysis codes used in core design and modeling
  - Optimization of design margins
  - Reduced uncertainty in local phenomena assessment / prediction → reduced safety margins in design

Introduction

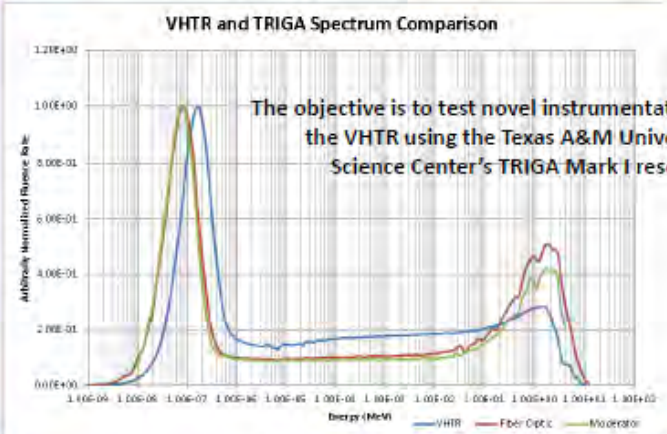

The objective is to test novel instrumentation for use in the VHTR using the Texas A&M University Nuclear Science Center's TRIGA Mark I research reactor.

Introduction

The 3-year project will provide three key deliverables:

1. produce a highly distributed fiber optic network capable of 3D temperature and neutron fluence mapping in the VHTR environment;
2. demonstrate reliability and performance of the proposed sensor network; and
3. provide a computational model to evaluate expected sensor performance and lifetime in VHTR environments, to scale experimental results to VHTR conditions, to optimize sensor network, and to assess VHTR performance taking advantage of the 3D fiber-optics imaging and performance reconstruction.

Distributed Sensing

Fiber optic sensors promise to provide detailed distributed measurements.

- Online hot spots determination and flux mapping
- Continuous code validation becomes possible

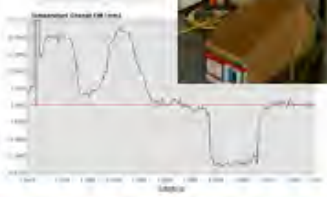

Test fibers in the operating conditions that would be expected in the VHTR.

Challenges

The TRIGA reactor sits in a pool of light water open to the atmosphere.

- Thermal flux ~ peak at .09 eV
- Low temperatures
  - Fuel ~ 390°C
  - Coolant ~ 26°C
- Low fluence rate ~ 4e12 n/cm^2/s
- Safety and experimental limitations
  - Temperature, thermal storage, size, reactivity

Experimental Design

Design an experimental apparatus to emulate the conditions of a VHTR in a TRIGA reactor for advanced instrumentation testing.

- Operate at +1000ºC
- Sustained operation for 1 year, to a neutron fluence of 2e19 n/cm^2
- Accessibility for fiber optics and instrumentation replacement
- Conform to 10 CFR 50.59
  - Required safety criteria for experimental authorization
- Passive cooling – heater in vacuum

Experimental Design

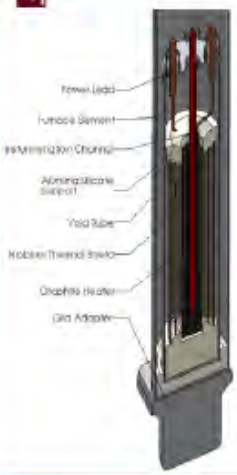

- Extended from an earlier furnace design from the 70's designed by General Atomics for use in the TRIGA Mark I
  - KING TRIGA designed originally to test fuels – Too small for our purposes
  - Required forced cooling and located in a fuel position

Modeling - Neutronics

MCNP5/X 2.6 was used for simulating the TRIGA reactor and simplified furnace model.

- The model includes the latest cross-section data, scattering kernels, and temperature induced broadening.
- Temperature date from NSC-written and validated sub-channel code

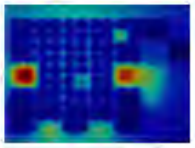

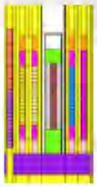

Modeling - Neutronics
Verification & Validation

MCNP model was scaled to matched Au/Cd flux foils data from the D3 core location.

- Nominal scaling was high by ~5.5%
- Fast (epithermal) to thermal flux ratios were comparable to 13.1%

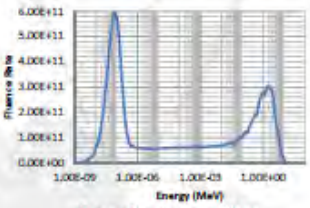

Energy Spectrum in Fiber

Absolute fiber optic irradiation time expected to be roughly 230 days.

Used BOL fuel concentrations. BURN was not suitable due to memory requirements. MCNPX 2.7 will allow for MPI runs.

Modeling – Heat Transfer

Started with 1D Matlab script to begin design iterations.

- Radiative heat transfer
- Free convection correlationships
- Failure criteria
  - Steam production/stress failure
  - Safety factor of 2.75
    - 2.0 required by facility Tech Specs

Still provides maximum operating conditions for safety controllers.

Modeling – Heat Transfer

Computation continuum mechanics software package used to support analysis of fiber optics.

- STAR-CCM+ v6.02, developed by Cd-adapco

Provides extra temperature data to Matlab script for total thermal storage and allows for behavioral study of furnace operation.

Temperature limited to either:

- ~160°C on aluminum housing
- 1138°C averaged operating temperature

Modeling – Heat Transfer
Verification & Validation

Physics model verification done concurrently with furnace model development –

- Conduction
  - Near perfect agreement, even with poor mesh refinement – max error: 1.169% in surface heat flux
- Forced convection (incomplete)
- Radiation
  - Near perfect agreement, even with poor mesh refinement – max error: 0.79% in surface heat flux

Modeling – Heat Transfer
Verification & Validation

- Natural convection (incomplete)
  - Fair agreement with generalized empirical relationships >20% error on local heat transfer coefficients depending on model and mesh refinement
  - V2F non-linear and k-e RAS turbulence models

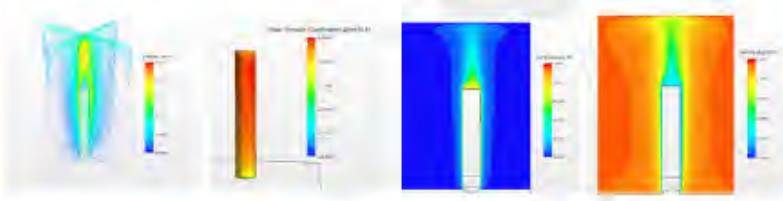

Modeling – Heat Transfer
Verification & Validation

Validation modeling to proceed as procurement process continues, providing validation of fiber optic sensing and STAR-CCM+/Matlab calculations

- Graphite heater in vacuum chamber
  - Instrumented with k-type TCs with Nextel coating
- LabView PID controller to interface with power supply and safety systems

Modeling – Heat Transfer
Verification & Validation

Experiments provide better material information
- Resistivity as a function of power/temperature

Ohmic heating is well approximated with constant volumetric heat generation.

Convection validation to wait for bench top testing of completed furnace.

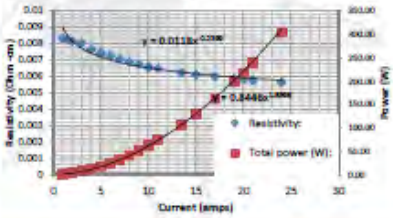

Modeling – Heat Transfer

Radiation Validation

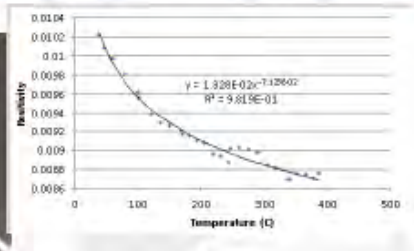

Modeling – Heat Transfer

Radiation Validation

rho = 1.636e-13*T^4 - 3.74e-10*T^3 + 3.221e-7*T^2 - 1.259e-4*T + 2.794e-2 [ohm/m]

Constant Volumetric Heat Generation				
Power Density [W/m^3]	Surface Temp [C]	Relative Error	Heat Flux [W/m^2]	Relative Error
70366.49215	60.2	0.001961241	235.91	-0.095641894
187434.555	100.02	-0.00323201	627.27	-0.097255514
519790.5759	173.02	0.003943364	1751.86	-0.090859548
1195183.246	260.54	0.026104929	4058.63	-0.08398001
1386806.283	278.99	0.031458995	4715.5	-0.082783338
1589528.796	296.71	0.036217423	5411.13	-0.081710635
1802722.513	313.76	0.041502336	6145.18	-0.080470403
2004397.906	328.61	0.042852872	6838.32	-0.079708383
2239162.304	344.62	0.046543638	7645.72	-0.078929651
2593193.717	366.65	0.051027742	8864.21	-0.077927516
2885026.178	383.26	0.056451029	9869.35	-0.077218712
3321884.817	405.99	0.062829376	11374.97	-0.076311202
3607748.691	419.72	0.065990746	12360.73	-0.075796082
3874607.33	431.83	0.070190552	13280.66	-0.07540413

Ohmic Heating				
Current [amps]	Surface Temp [C]	Relative Error	Heat Flux [W/m^2]	Power Error
6	60.22	0.002021356	236.13	-0.094798526
10	100.47	-0.002030023	632.5	-0.089728685
17	173.46	0.004933424	1760.26	-0.086500307
26	259.68	0.024451441	4028.76	-0.090721575
28	277.42	0.02852606	4656.07	-0.094343127
30	294.68	0.032526128	5327.23	-0.095948785
32	311.48	0.037456357	6041.94	-0.095918646
34	327.84	0.041518459	6800.1	-0.084851977
36	343.81	0.045171444	7601.9	-0.084208592
39	367.08	0.051734122	8887.66	-0.075488201
41	382.2	0.071288456	9801.78	0.019600351
44	404.39	0.090458448	11262.82	0.053070318
46	418.92	0.083064355	12300.6	-0.00114669
47.5	429.72	0.081375894	13144.9	-0.017164137

Modeling – Heat Transfer

Maximum radial temperature from 1D script and STAR-CCM+ match within 4.5%.

- Conductive heat flux causes large temperature gradients not accounted for in script.

Provides extra temperature data to Matlab script for more accurate total thermal storage.

More detailed material properties with polynomial fits as a function of temperature.

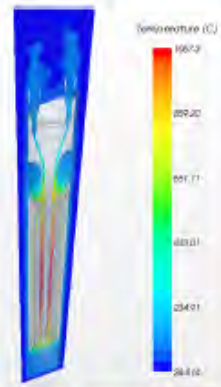

Modeling – Heat Transfer
Simulation

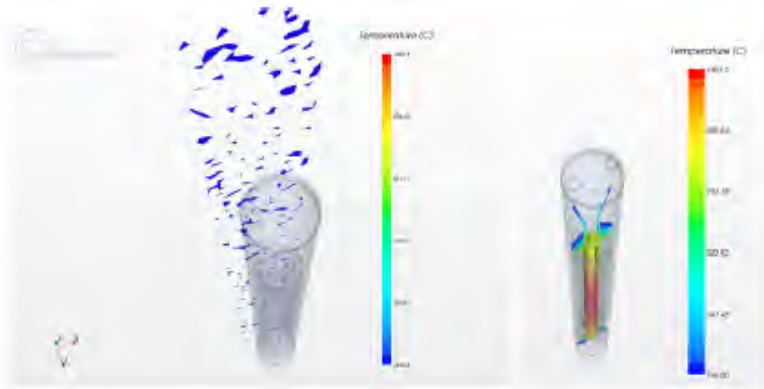

Modeling – Heat Transfer

Maximum radial temperature from 1D script and STAR-CCM+ match within 4.5%.

- Conductive heat flux causes large temperature gradients not accounted for in script.

Provides extra temperature data to Matlab script for more accurate total thermal storage.

More detailed material properties with polynomial fits as a function of temperature.

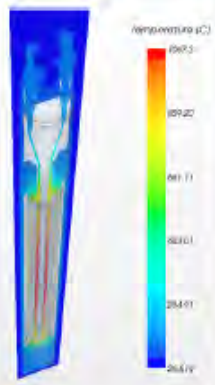

Modeling – Heat Transfer
Simulation

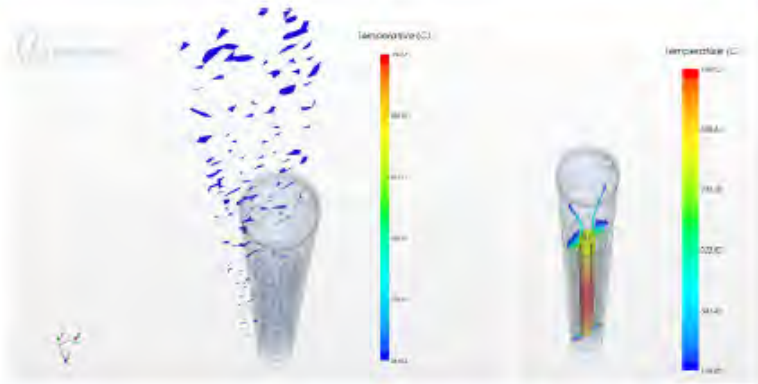

Final Remarks
and Conclusions

Key milestones:

- Development of theoretical approach to estimating neutron fluence distributed along the length of the sensing fiber.
- Test furnace engineering design with reactor safety board approval.
- Fiber optic sensor design and completion of out-of-core laboratory testing.
- Test furnace fabrication, assembly and completion of out-of-core testing.
- Delivery of sensor strings with connectors to university; installation in test furnace.
- Assembly installation in TRIGA and completion of irradiation test matrix.
- 3D VHTR and TRIGA modeling with representation of distributed sensor network elements, performance reconstruction and optimization of the network design.
- Modeling validation using test measurements and scaling to the prototypical VHTR conditions.

Final Remarks
and Conclusions

- Results of the high fidelity simulations indicate that the furnace assembly should be capable of emulating VHTR temperature conditions in TRIGA experiments.
- The furnace allows the sensor location to reach 1000oC-levels while being completely shielded from the TRIGA core environment.
- Successful completion of the work concludes the first phase of the project. The next phase will be to build, test, and verify prior to implementation. These efforts are in progress.

Final Remarks
and Conclusions

Confident that the safety of the NSC reactor core will not be impacted.

Temperature requirements, following bench top tests, may change.

Temperature fiber optic sensors perform, under normal conditions, as expected. Gamma and neutron fibers have not been tested yet.

Acknowledgements

This paper is based upon work supported by the U.S. Department of Energy Nuclear Energy University Program Award Number 09-241.

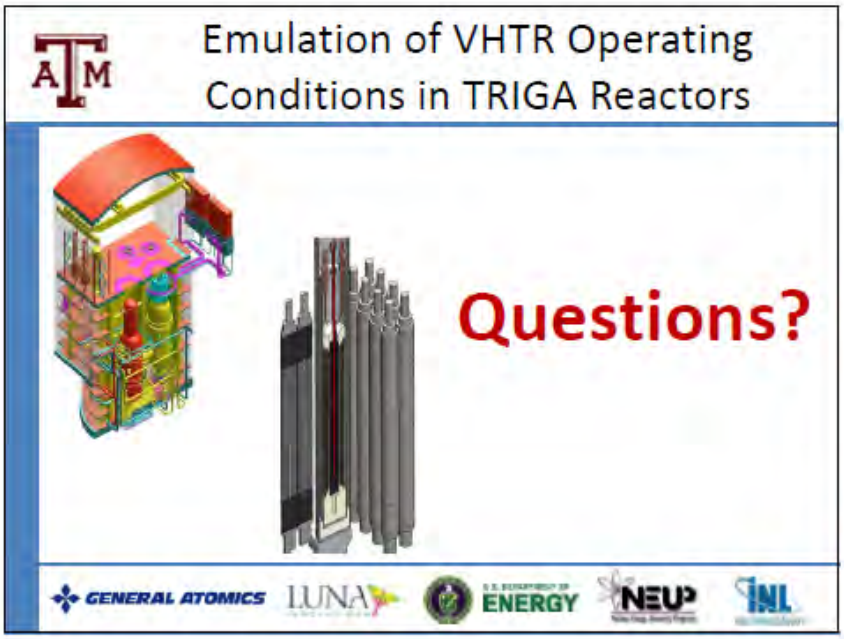
Emulation of VHTR Operating Conditions in TRIGA Reactors
Questions?
GENERAL ATOMICS
LUNA
ENERGY
NEUP
INL

13.5.4. In-Core Testing of Distributed Fiber Optic Sensors

This project is supported by a 2009 Nuclear Energy University Programs award.

TEXAS A&M UNIVERSITY

In-Core Testing of Distributed Fiber Optic Sensors

Co-PIs: Shannon Bragg-Sitton, Pavel Tsvetkov
Graduate Students: Jesse Johns & Matt Johnson
Texas A&M University

Joseph French and Bryan Dickerson,
Luna Innovations, Primary Industry Partner

Project Advisors: General Atomics, Idaho National Laboratory

E-mail: sitton@tamu.edu

Project Scope

TEXAS A&M UNIVERSITY

- **Goal:** Real-time mapping of the temperature, neutron fluence and gamma flux in an operating reactor. (e.g. VHTR)
- **Challenges:**
  - Harsh environment (750°C to 950°C coolant outlet)
  - Long refueling cycle (~18 months) – high radiation
- **Benefits of Proposed Sensors:**
  - Real-time assessment of reactor performance
  - Sensor network can be placed throughout the reactor core (axial and transverse dimensions)
  - Benchmarks for simulation and analysis codes used in core design and modeling
  - Optimization of design margins
  - Reduced uncertainty in local phenomena assessment / prediction → reduced safety margins in design

Sensor Technology

TEXAS A&M UNIVERSITY

Fiber optic sensors will be used to monitor
- Total Neutron Fluence
- Gamma Flux
- Temperature

The OBR measures the Rayleigh Backscatter of the optical fiber

The sensor interrogation uses an Optical Backscatter Reflectometer (OBR™) system

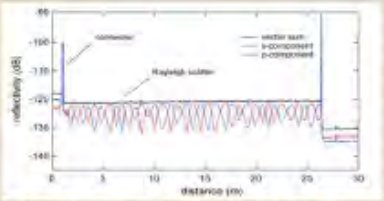

Strain, temp., etc. cause Rayleigh fingerprint to stretch – shift in the mean period between perturbations leads to a shift in optical frequency.

Radiation and Temperature stimuli change the Rayleigh backscatter of the optical fiber

LUNA

Fiber Temperature Performance

TEXAS A&M UNIVERSITY

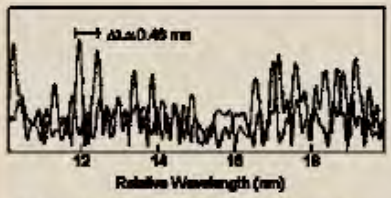

(a)Wavelength spectra along a 5 mm fiber interval for a heated (solid) and unheated (dotted) measurement scan.

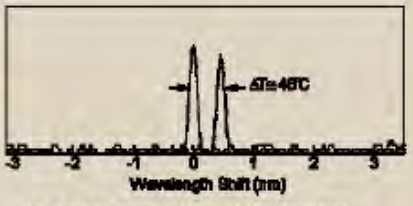

(b) Cross correlation of the heated spectra with reference (unheated) spectrum.

Demonstration of a thermal shift of an optical fiber.

Measurement Approach

TEXAS A&M UNIVERSITY

In a single scan, the *entire* fiber is recorded

How Strain is Measured

Measurement Approach

TEXAS A&M UNIVERSITY

In a single scan, the *entire* fiber is recorded

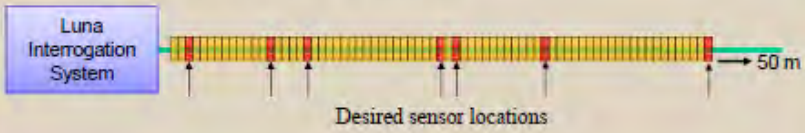

Software settings determine where along the fiber strain is reported

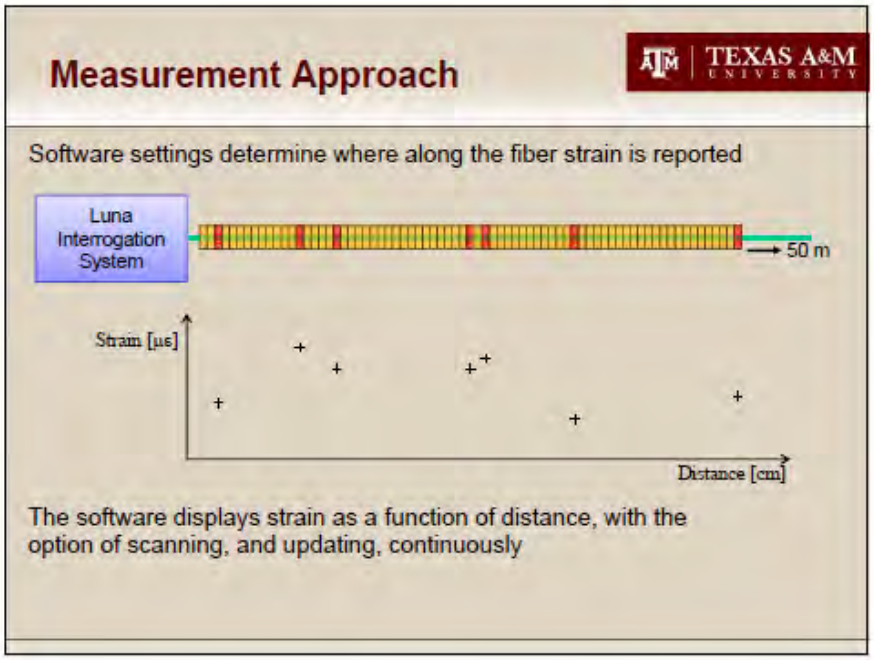
Measurement Approach
TEXAS A&M UNIVERSITY
Software settings determine where along the fiber strain is reported
Luna Interrogation System
50 m
Strain [με]
Distance [cm]
The software displays strain as a function of distance, with the option of scanning, and updating, continuously

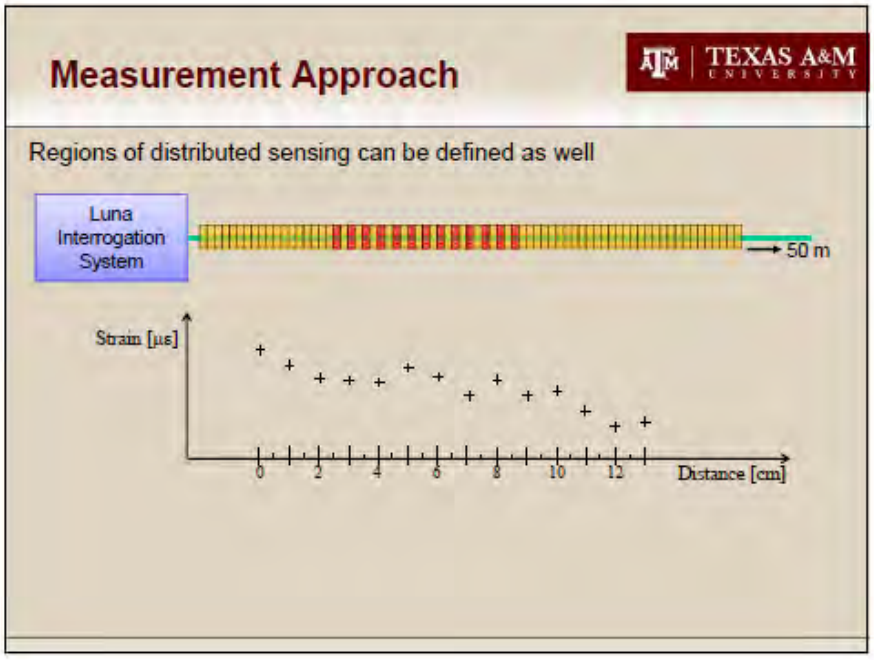
Measurement Approach
TEXAS A&M UNIVERSITY
Regions of distributed sensing can be defined as well
Luna Interrogation System
50 m
Strain [με]
0
2
4
6
8
10
12
Distance [cm]

Measurement Approach

TEXAS A&M UNIVERSITY

Regions of distributed sensing can be defined as well

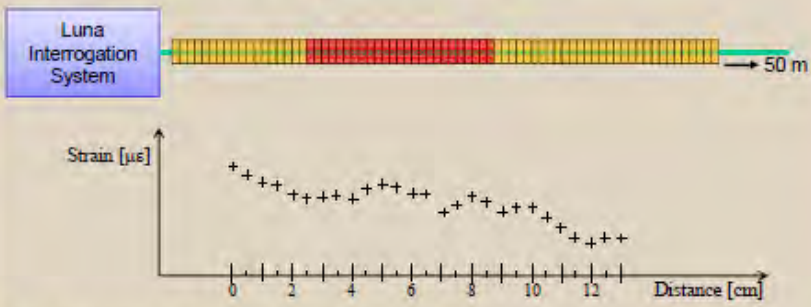

Spatial resolutions as small as 0.5 cm can be defined in software

Measurement Approach – High Definition Sensing

TEXAS A&M UNIVERSITY

Regions of distributed sensing can be defined as well

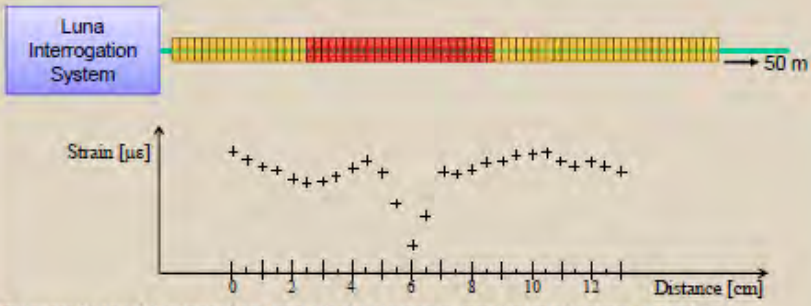

Extremely useful observing how strain changes continuously over a region

Small, localized events can be observed, where larger foil gages would have averaged, and washed out the response

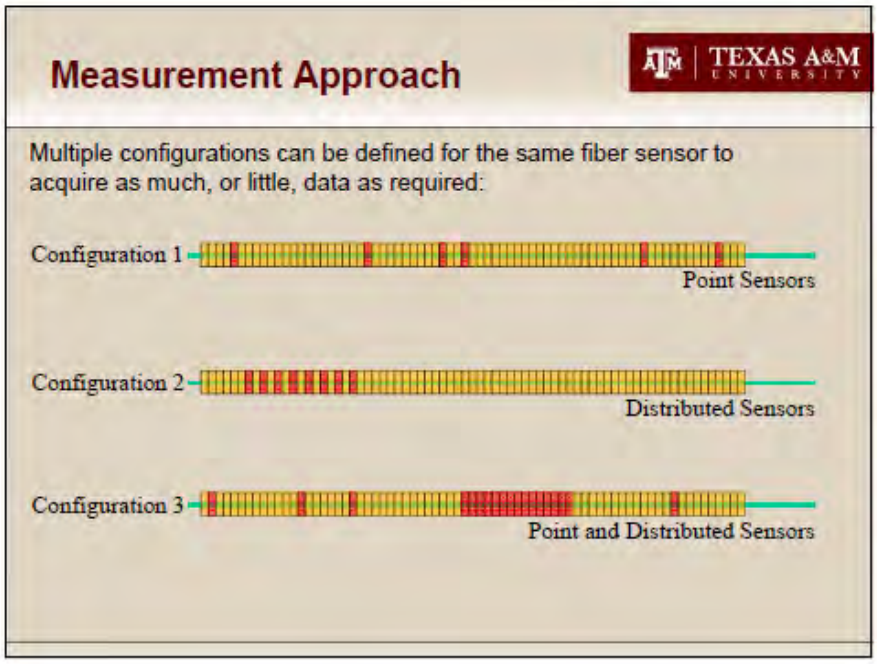
Measurement Approach
TEXAS A&M UNIVERSITY
Multiple configurations can be defined for the same fiber sensor to acquire as much, or little, data as required:
Configuration 1
Point Sensors
Configuration 2
Distributed Sensors
Configuration 3
Point and Distributed Sensors

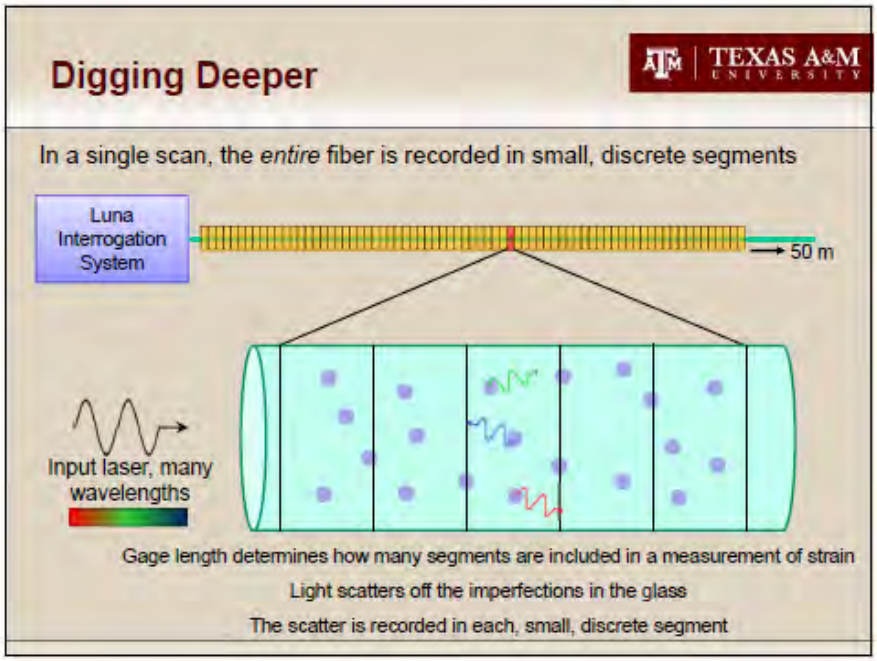
Digging Deeper
TEXAS A&M UNIVERSITY
In a single scan, the *entire* fiber is recorded in small, discrete segments
Luna Interrogation System
50 m
Input laser, many wavelengths
Gage length determines how many segments are included in a measurement of strain
Light scatters off the imperfections in the glass
The scatter is recorded in each, small, discrete segment

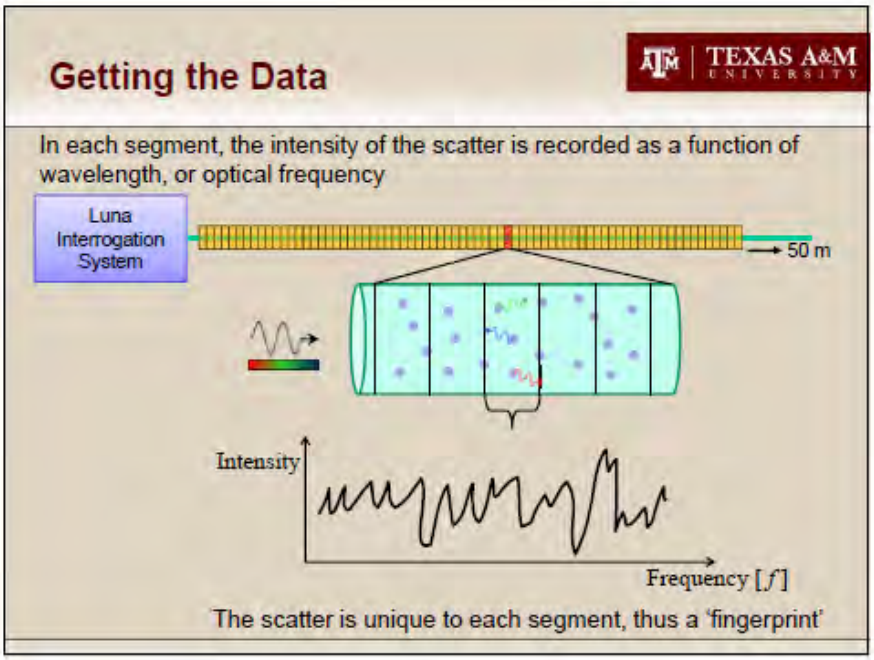
Getting the Data
TEXAS A&M UNIVERSITY
In each segment, the intensity of the scatter is recorded as a function of wavelength, or optical frequency
Luna Interrogation System
50 m
Intensity
Frequency [f]
The scatter is unique to each segment, thus a 'fingerprint'

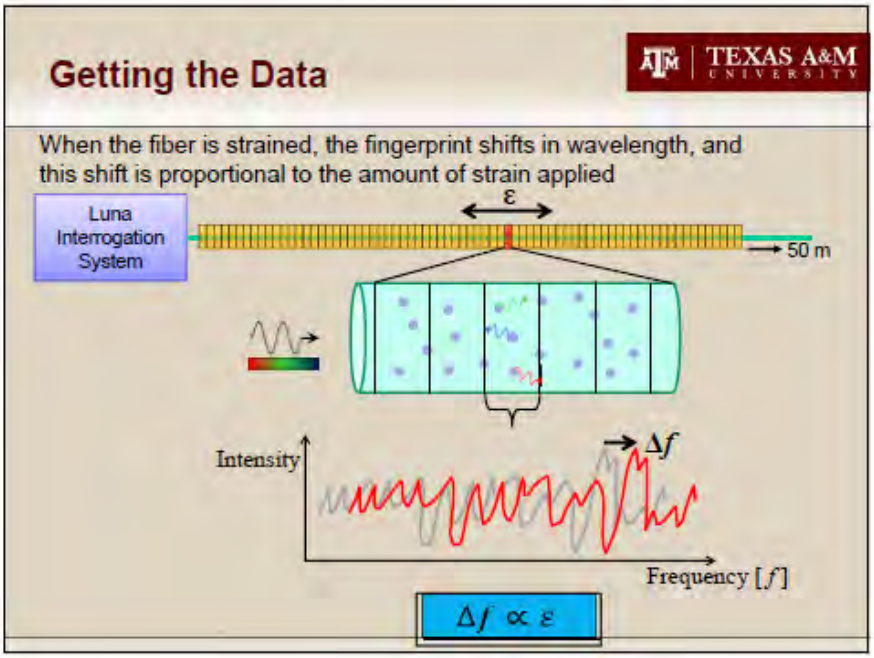
Getting the Data
TEXAS A&M UNIVERSITY
When the fiber is strained, the fingerprint shifts in wavelength, and this shift is proportional to the amount of strain applied
ε
Luna Interrogation System
50 m
Intensity
Δf
Frequency [f]
Δf ∝ ε

Temperature & Radiation Sensing

TEXAS A&M UNIVERSITY

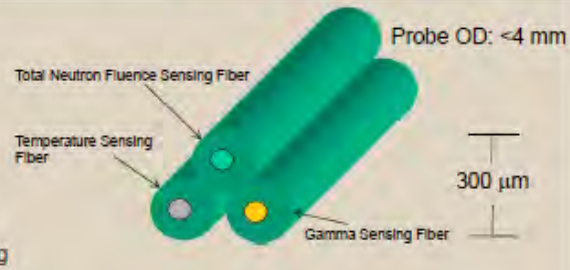

- Three optical fibers:
  - Thermal sensing
  - Gamma flux sensing
  - Neutron fluence

  **Each fiber specifically selected to enhance response sensitivity to individual stimuli

Fiber Type	Relative Sensitivity		
	Thermal	Gamma	Neutron
Temperature Sensing	High	Extremely Low	Low
Gamma Sensing	Low	High	Low
Neutron Sensing	Low	Extremely Low	High

Proposed Sensor Performance

TEXAS A&M UNIVERSITY

Sensitivities

Total Neutron Fluence - TBD

Gamma Flux - TBD

Temperature - ± 1%

Spatial Resolution – 1 cm

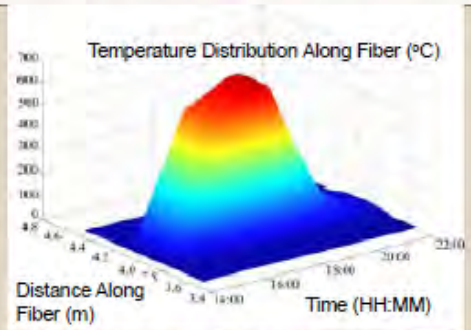

Distributed temperature map produced using a fiber optic temperature sensor and OBR.

Demonstrated Operating Ranges

- Temperature Range up to 800°C with brief excursions to 1050°C
- Total Neutron Fluence levels ~5×10^{19} n/cm^2

Experimental Demonstration

TEXAS A&M UNIVERSITY

- Sensors testing in a relevant environment over a long duration
- Real-time data acquisition
  - Allows assessment of fiber performance, degradation, etc. without removal and visual observation
  - 3-4 fiber bundles inserted into test device (3 fibers per bundle)
    - With available switch, 8 fibers can be monitored with one OBR (higher capacity switches available, or additional OBRs can be used to increase sensor monitoring capability)
    - Mechanical disconnect to switch to other installed fibers if failure occurs
  - Damaged fibers can be removed for analysis and replaced if necessary

Experimental Apparatus

TEXAS A&M UNIVERSITY

- Design an experimental apparatus to emulate VHTR conditions VHTR in a TRIGA reactor (as much as possible)
- Operating environment:
  - Sensor temperature: +1000°C
  - Sustained operation for 1 year
  - Total neutron fluence ≥ 2×10^{19} n/cm^2
- Design guidance:
  - Accessibility for fiber optics and instrumentation replacement
  - Conform to 10 CFR 50.59
    - Required safety criteria for experimental authorization
  - Resistive heating, passive cooling
    - Graphite heater in vacuum
    - Niobium thermal radiation shields

Test Facility – Nuclear Science Center Reactor

TEXAS A&M UNIVERSITY

- TRIGA Mark I reactor design
- 1-MW operating power
- Refueled in 2006, LEU U-ZrH
- Neutron fluence rate:
  - 10^{12} n/cm^2-s to 1.4×10^{13} n/cm^2-s thermal
  - 10^{11} n/cm^2-s epithermal
- Gamma dose (reactor face): ~2×10^7 rad/hr
- Various test positions possible
  - Options limited due to test duration and need to leave some positions open for other test articles

Previous GA King Furnace Design

TEXAS A&M UNIVERSITY

- Licensed for use in TRIGA facilities in early 1970s (NRC licenses R-38 and R-67)
- Designed to aid in analysis of the in-pile behavior of high-temperature gas-cooled reactor fuels
- Allowed fuel samples to be tested in a radiation environment at temperatures up to 1800 °C
- Heating provided by a cylindrical graphite element
- Radiation shields used to drop the temperature from centerline to surface
- Designed to fit a "standard" TRIGA core fuel element position (3.73 cm OD); ~20 cm (8") in length

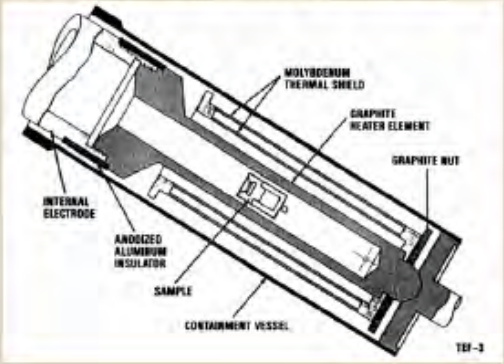

GENERAL ATOMICS

Test Furnace Design

TEXAS A&M UNIVERSITY

- Design basics:
  - Aluminum housing to minimize activation
  - Heating provided by a specially-designed graphite element
  - Refractory metal thermal shields
  - Central instrumentation channel
- Failure criteria:
  - Steam production/stress failure
  - Safety factor of 2.75 (Facility TSR: 2.0)
- Temperature limitations
  - ~160°C on aluminum housing
- Engineering design complete and approved by NSCR Safety Analysis Committee

Graphite Heater Element

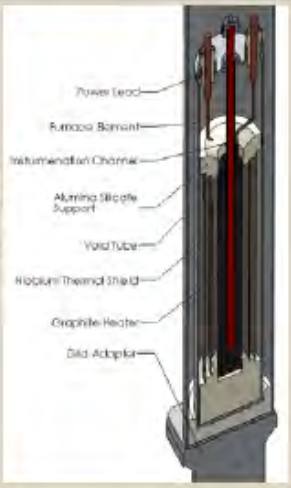

Test Furnace Design

TEXAS A&M UNIVERSITY

- Multi-fiber probe installed at the center of the test furnace
- Fiber optic measurements verified using standard instrumentation in close proximity
  - Thermocouples
  - Activation wires
  - Miniature fission chambers and gamma detectors
- Test furnace position
  - Occupies a full, 4-element grid position
  - Surrounded on three sides by fuel to achieve higher fluence

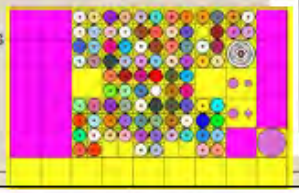

Test Furnace Design

TEXAS A&M UNIVERSITY

- Neutronic modeling of the furnace performed to predict the neutron and gamma fluence rates at the experiment position
  - Maximum possible neutron fluence rate is expected to be 1.72×10^{13} n/cm^2-s over the full neutron energy spectrum (5.74×10^{12} n/cm^2-s below 0.5 eV)

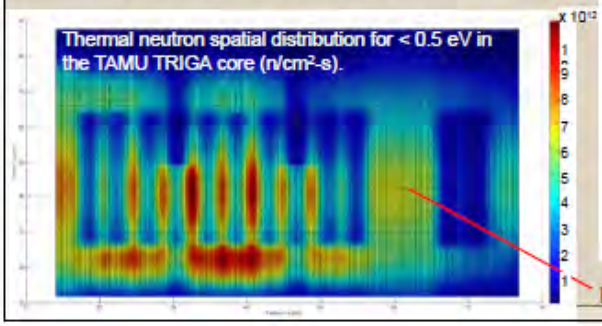

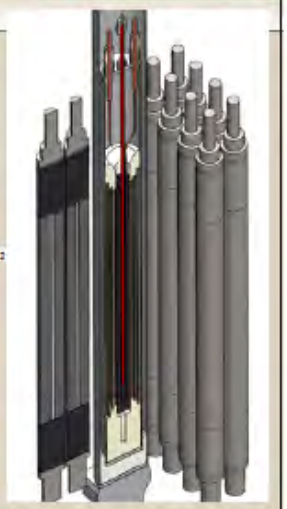

Thermal Modeling: STAR-CCM+

TEXAS A&M UNIVERSITY

- Continuum, multi-physics package selected to produce a highly resolved model of experimental performance for both steady state and transient conditions
- Parameters selected to achieve a maximum of 1000°C at the sensor position while maintaining the safety of the TRIGA reactor core (limiting safety system setting)
- High-fidelity model developed concurrently with an analytical model to facilitate the design process and provide model verification

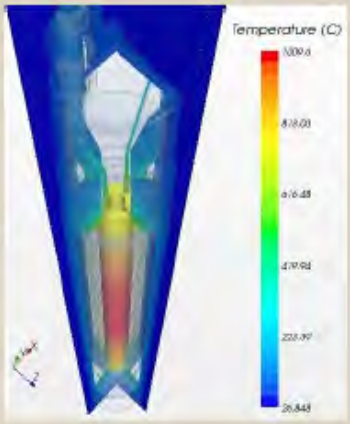

Planned Operating Conditions

TEXAS A&M UNIVERSITY

- Test fixture voided
- Two refractory metal thermal shields minimize heat transfer to the external boundary and neighboring core positions
  - Self-heating in the thermal shields is predicted to not exceed 15 W and 22 W for the inner and outer shields
  - Predicted maximum 10ºC rise in the furnace external temperature
- Heater operating conditions:
  - 348 W
  - Predicted temperatures:
    - 1008ºC at centerline
    - 165ºC at tube surface

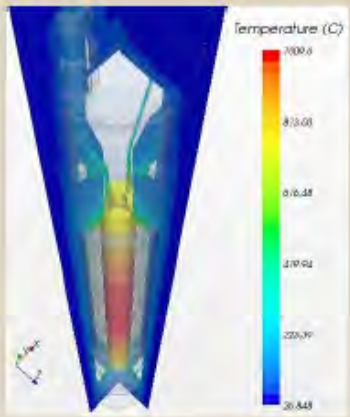

Initial Benchtop Testing

TEXAS A&M UNIVERSITY

- Initial heater element and fiber tests at elevated temperature have been conducted in a vacuum environment to:
  - Verify analytical and STAR-CCM+ models for thermal radiation and conduction
  - Support behavioral studies, including heater element resistivity changes as a function of temperature and curre
  - Support equipment tests, including power supply load and tuning for PID controllers
- In-air testing
  - Vibration sensitivity
  - Effect of large temperature gradients
  - Determination of fiber conductivity

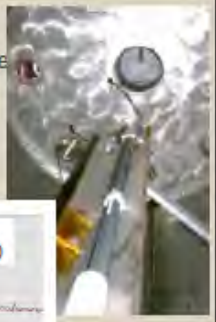

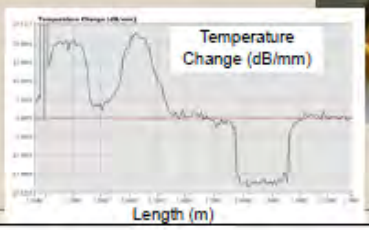

Current Status

TEXAS A&M UNIVERSITY

- Continuation of fiber optic benchtop testing
- All major furnace components received
- Minor components now in shipment
- Furnace assembly and installation ~Nov / Dec 2011

Acknowledgements

TEXAS A&M UNIVERSITY

- Significant credit goes to graduate student Jesse Johns for all his work in the design and analysis of the test furnace.
- This paper is based upon work supported by the U.S. Department of Energy Nuclear Energy University Program Award Number 09-241.

Extra Slides

TEXAS A&M UNIVERSITY

Primary Deliverables

TEXAS A&M UNIVERSITY

The 3-year project will provide three key deliverables:

1. produce a highly distributed fiber optic network capable of 3D temperature and neutron fluence mapping in the VHTR environment;
2. demonstrate reliability and performance of the proposed sensor network; and
3. provide a computational model to evaluate expected sensor performance and lifetime in VHTR environments, to scale experimental results to VHTR conditions, to optimize sensor network, and to assess VHTR performance taking advantage of the 3D fiber-optics imaging and performance reconstruction.

Key Milestones

TEXAS A&M UNIVERSITY

Key milestones necessary to achieve the desired goals include:

- Development of theoretical approach to estimating neutron fluence distributed along the length of the sensing fiber.
- Test furnace engineering design with reactor safety board approval.
- Fiber optic sensor design and completion of out-of-core laboratory testing.
- Test furnace fabrication, assembly and completion of out-of-core testing.
- Delivery of sensor strings with connectors to university; installation in test furnace.
- Assembly installation in TRIGA and completion of irradiation test matrix.
- 3D VHTR and TRIGA modeling with representation of distributed sensor network elements, performance reconstruction and optimization of the network design.
- Modeling validation using test measurements and scaling to the prototypical VHTR conditions.

VHTR vs TRIGA Neutron Spectrum

TEXAS A&M UNIVERSITY

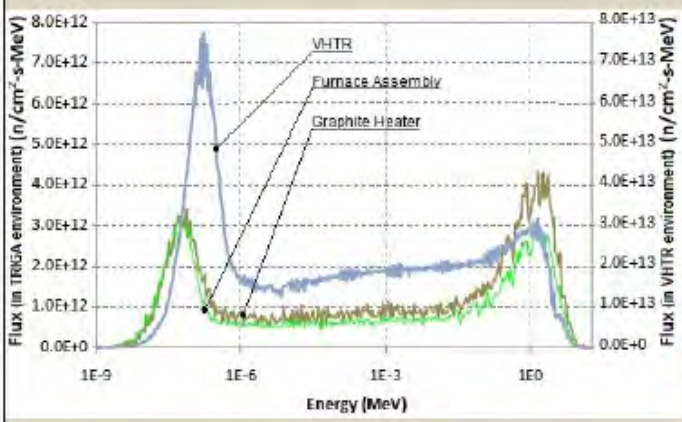

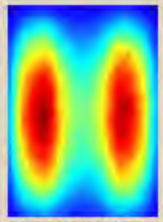

NGNP/VHTR

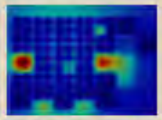

TRIGA Mark I

Spectrum not ideal, but sufficient to provide initial sensor performance characterization.

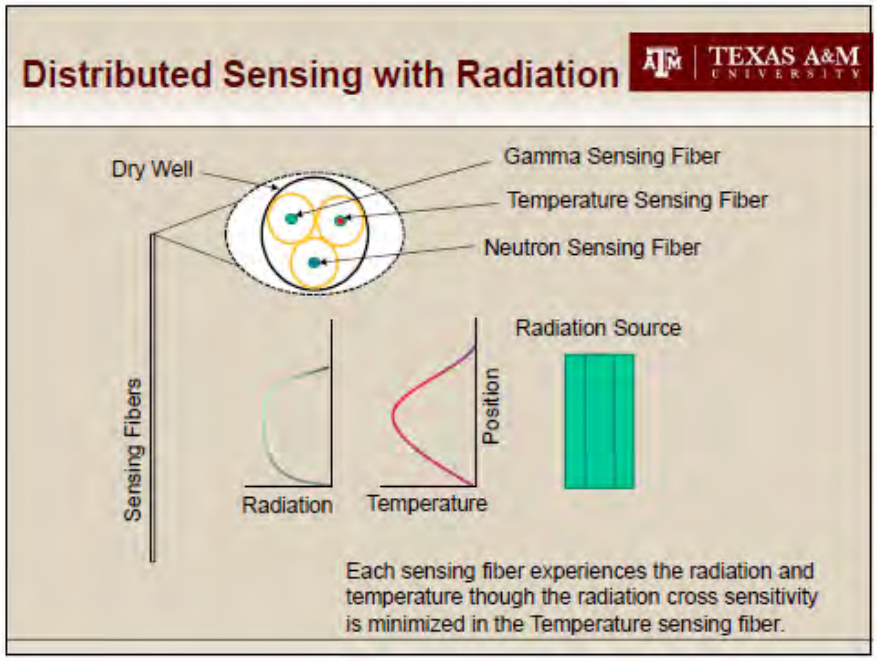
Distributed Sensing with Radiation
TEXAS A&M UNIVERSITY
Dry Well
Gamma Sensing Fiber
Temperature Sensing Fiber
Neutron Sensing Fiber
Radiation Source
Sensing Fibers
Position
Radiation
Temperature
Each sensing fiber experiences the radiation and temperature though the radiation cross sensitivity is minimized in the Temperature sensing fiber.

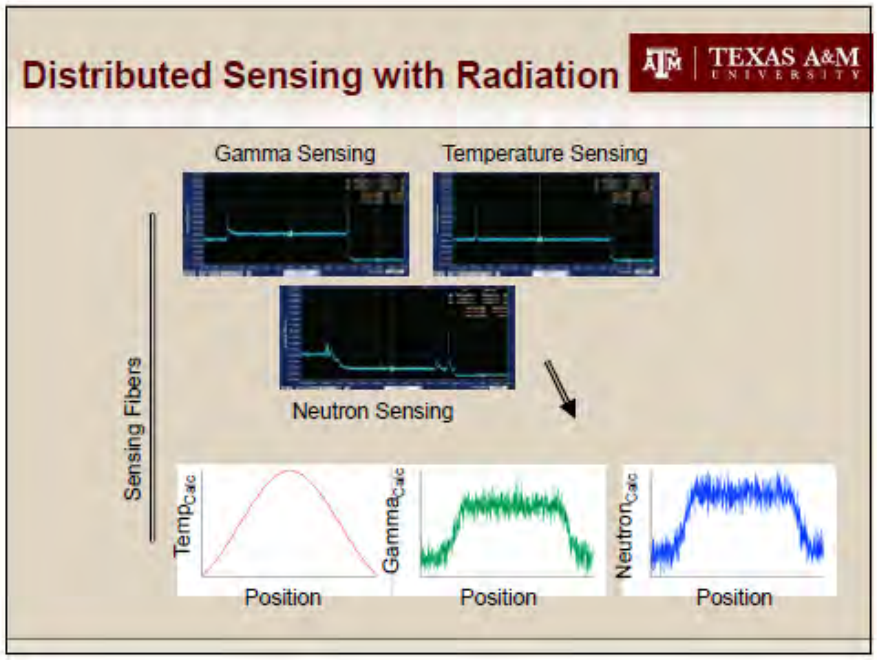
Distributed Sensing with Radiation
TEXAS A&M UNIVERSITY
Gamma Sensing
Temperature Sensing
Neutron Sensing
Sensing Fibers
Temp_Calc
Gamma_Calc
Neutron_Calc
Position
Position
Position

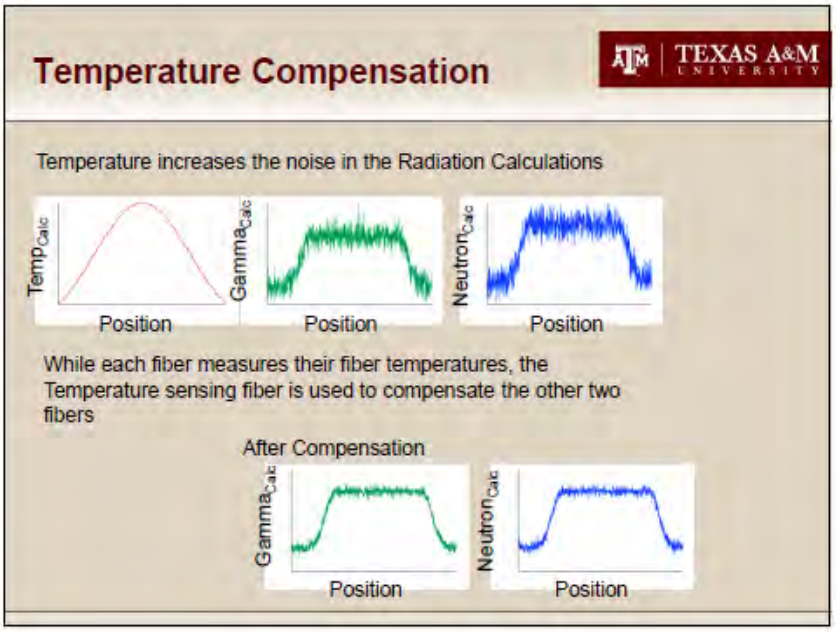
Temperature Compensation
TEXAS A&M UNIVERSITY
Temperature increases the noise in the Radiation Calculations
Temp Calc
Position
Gamma Calc
Position
Neutron Calc
Position
While each fiber measures their fiber temperatures, the Temperature sensing fiber is used to compensate the other two fibers
After Compensation
Gamma Calc
Position
Neutron Calc
Position

13.5.5. TRIGA-Based Experimental Device for Fiber Optics Testing

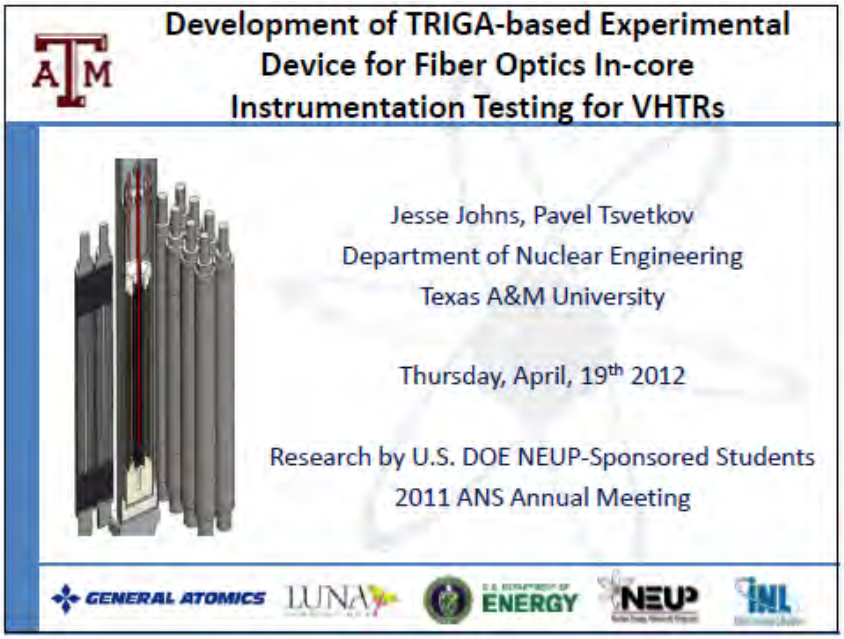

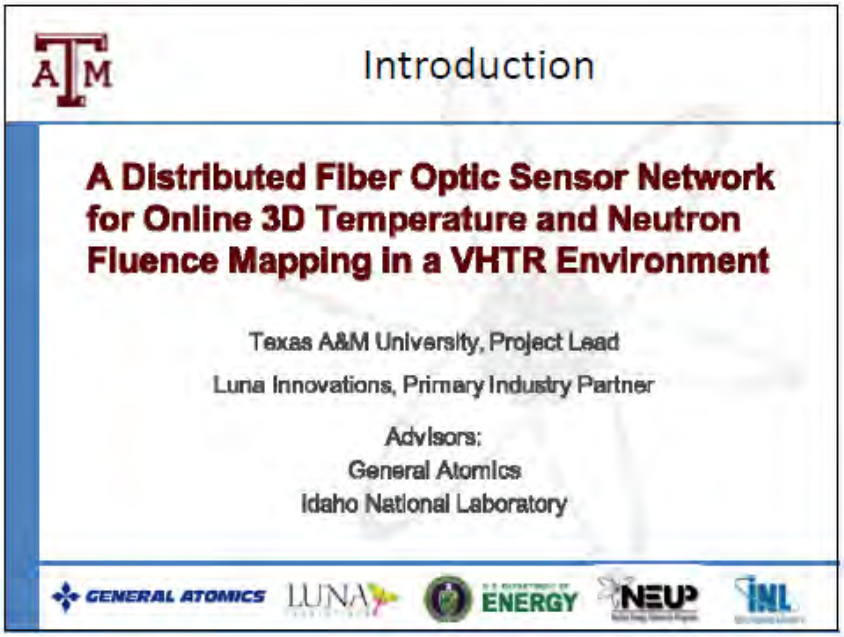

Introduction

- **Goal:** Real-time mapping of the temperature and neutron fluence distribution in proposed NGNP / VHTR cores
- **Challenges:**
  - Harsh environment (750° C to 950° C coolant outlet)
  - Long refueling cycle (~18 months) – high radiation
- **Benefits of Proposed Sensors:**
  - Real-time assessment of reactor performance
  - Sensor network can be placed throughout the reactor core (axial and transverse dimensions)
  - Benchmarks for simulation and analysis codes used in core design and modeling
  - Optimization of design margins
  - Reduced uncertainty in local phenomena assessment / prediction → reduced safety margins in design

Introduction

The 3-year project will provide three key deliverables:

1. produce a highly distributed fiber optic network capable of 3D temperature and neutron fluence mapping in the VHTR environment;
2. demonstrate reliability and performance of the proposed sensor network; and
3. provide a computational model to evaluate expected sensor performance and lifetime in VHTR environments, to scale experimental results to VHTR conditions, to optimize sensor network, and to assess VHTR performance taking advantage of the 3D fiber-optics imaging and performance reconstruction.

Distributed Sensing

Fiber optic sensors promise to provide detailed distributed measurements.

- Online hot spot determination and flux mapping
- Continuous code validation becomes possible

Test fibers in the operating conditions that would be expected in the VHTR.

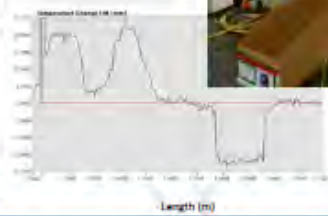

[1] A. K. Sang, M. E. Froggatt, D. K. Grifford, S. T. Kreger, and B. D. Dickerson, "One centimeter spatial resolution temperature measurements in a nuclear reactor using Rayleigh scatter in optical fiber," IEEE Sens. J.8(7), 1375–1380 (2008).

Challenges

The TRIGA reactor sits in a pool of light water open to the atmosphere.

- Thermal flux ~ peak at .09 eV
- Low temperatures
- Low thermal fluence rate: 4e12 $\frac{n}{cm^2 s}$
- Safety and experimental limitations
  - Temperature, thermal storage, size, reactivity

[2] G. Cheymol, H. Long, J. F. Villard, and B. Brichard, *High level gamma and neutron irradiation of silica optical fibers in CEA OSIRIS nuclear reactor*, IEEE Trans. Nucl. Sci.55(4), 2252–2258 (2008)

[3] R.S.Fielder, D.Klemer, K.L.Stinson-Bagby, *High neutron fluence survivability testing of advanced Fiber Bragg Grating sensors*, AIP Conference Proceedings, vol. 699, nº 1, Feb. 2004, pp. 650-657.

Challenges

Energy Spectrum

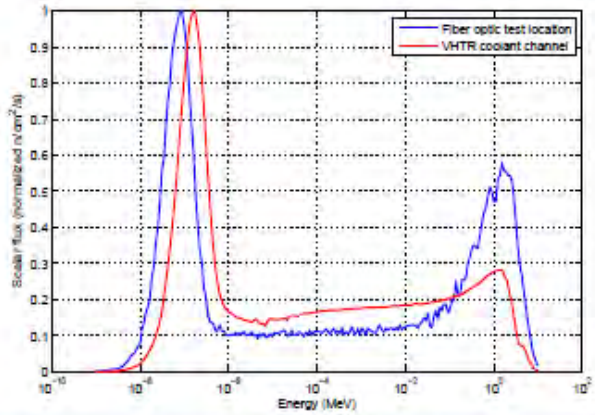

Experimental Design

Design an experimental apparatus to emulate the conditions of a VHTR in a TRIGA reactor for advanced instrumentation testing.

- Operate at ~1000ºC
- Sustained operation for 1 year, to a neutron fluence of 2e19 n/cm^2
- Accessibility for fiber optics and instrumentation replacement
- Conform to 10 CFR 50.59
  - Required safety criteria for experimental authorization
- Passive cooling – heater in vacuum

Experimental Design

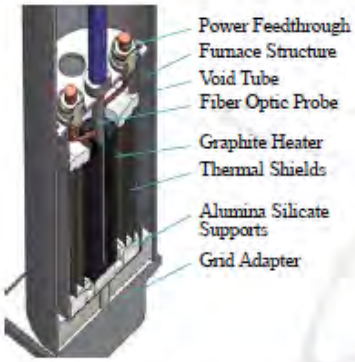

- Extended from an earlier furnace design from the 70's designed by General Atomics for use in the TRIGA Mark I
  - KING TRIGA designed originally to test fuels – Too small for our purposes
  - Required forced cooling and located in a fuel position

Modeling - Neutronics

MCNP5/X 2.6 was used for simulating the TRIGA reactor and simplified furnace model.

- The model includes the latest cross-section data, thermal scattering data, and
- Temperature date from NSC-written and validated sub-channel code

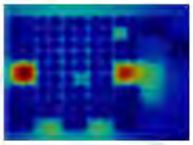

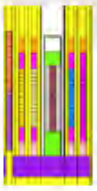

Modeling - Neutronics

Verification & Validation

MCNP model was scaled to matched Au/Cd flux foils data from the D3 core location.

- Nominal scaling was high by ~5.5%
- Fast (epithermal) to thermal flux ratios were comparable to 13.1%

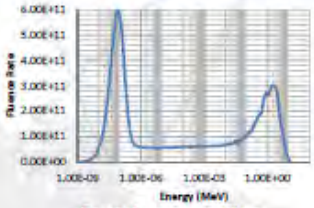

Energy Spectrum in Fiber

Absolute fiber optic irradiation time expected to be roughly 230 days.

Used BOL fuel concentrations.

Modeling – Heat Transfer

Started with 1D Matlab script to begin design iterations.

- Radiative heat transfer
- Free convection correlationships
- Failure criteria
  - Steam production/stress failure
  - Safety factor of 2.75
    - 2.0 required by facility Tech Specs

Still provides maximum operating conditions for safety controllers.

Modeling – Heat Transfer

Computation continuum mechanics software package used to support analysis of fiber optics.

- STAR-CCM+ v6.02, developed by Cd-adapco

Provides extra temperature data to Matlab script for total thermal storage and allows for behavioral study of furnace operation.

Temperature limited to either:

- ~160°C on aluminum housing
- 1138°C averaged operating temperature

Modeling – Heat Transfer
Verification & Validation

Physics model verification done concurrently with furnace model development –

- Conduction
  - Near perfect agreement, even with poor mesh refinement – max error: 1.169% in surface heat flux
- Forced convection (incomplete)
- Radiation
  - Near perfect agreement, even with poor mesh refinement – max error: 0.79% in surface heat flux

Modeling – Heat Transfer
Verification & Validation

Validation modeling to proceed as fabrication is completed

- Graphite heater in vacuum chamber
  - Instrumented with k-type TCs with Nextel coating
- LabView PID controller to interface with power supply and safety systems

Modeling – Heat Transfer
Verification & Validation

Experiments provide better material information

- Resistivity as a function of power/temperature
  Ohmic heating is well approximated with constant volumetric heat generation.

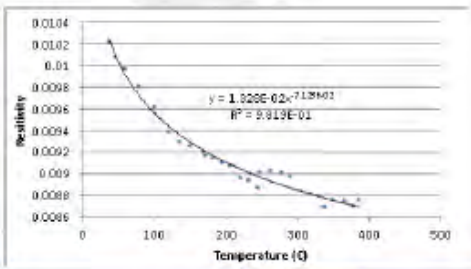

Modeling – Heat Transfer

Radiation Validation

Current (amps)	Measured Temp (°C)	Surface Temp (°C)	Heat Flux (W/m²)	Power Error	Temp Error
3.50	37.79	39.74	82.44	-0.0944	0.0063
6.00	59.55	60.22	236.13	-0.0948	0.0020
10.00	101.23	100.47	632.5	-0.0897	-0.0020
17.00	171.27	173.46	1760.26	-0.0865	0.0049
26.00	246.96	259.68	4028.76	-0.0907	0.0245
30.00	276.79	294.68	5327.23	-0.0959	0.0325
47.50	385.59	429.72	13144.9	-0.0172	0.0670

- Environmental temperature
- Power leads directly modeled without contact resistance
- Thermocouples not included

Modeling – Heat Transfer

Stress Test

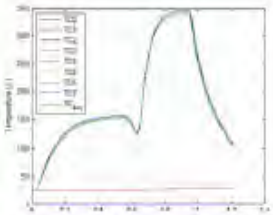

Verify cementing method for power leads and thermocouples.

Verify transient analysis of thermal models.

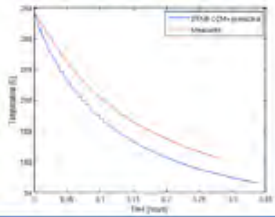

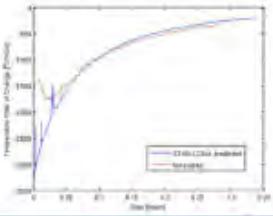

Modeling – Heat Transfer

Gas physics modeled with V2F non-linear eddy viscosity model, with heat transfer coupling.

Surface to surface radiation modeling, with constant emissivity.

Constant volumetric heat generation in heater and thermal shields.

- MCNPX predicts 14.7 and 21.2 W for the inner and outer shields

Power requirements:

- 390W – T_{gh} = 1116C, T_s = 190C
- 348W -- T_{gh} = 1008C, T_s = 165C

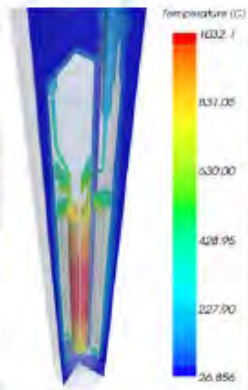

Current Progress

Furnace Fabrication

Poop.

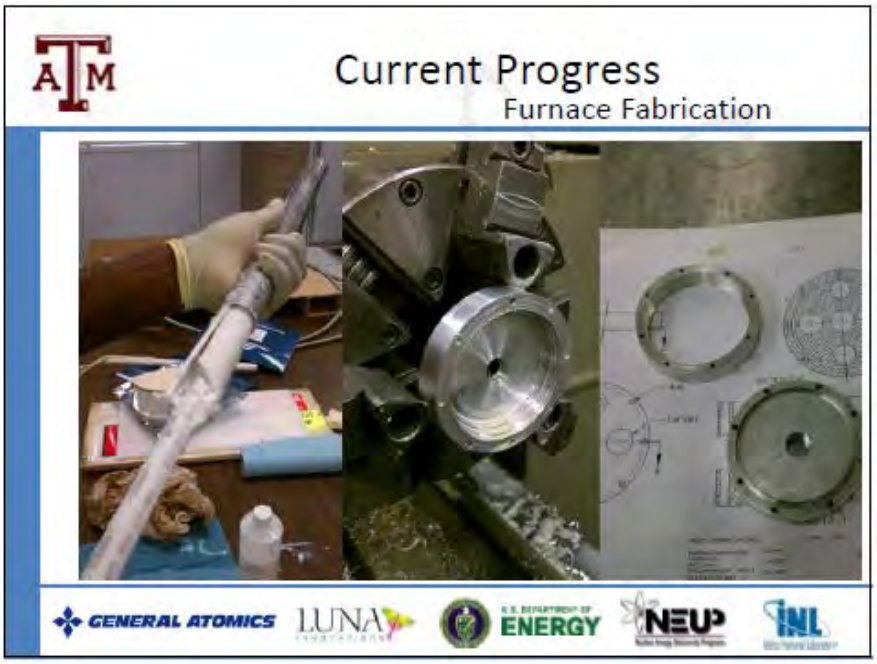
Current Progress
Furnace Fabrication
GENERAL ATOMICS
LUNA
ENERGY
NEUP
INL

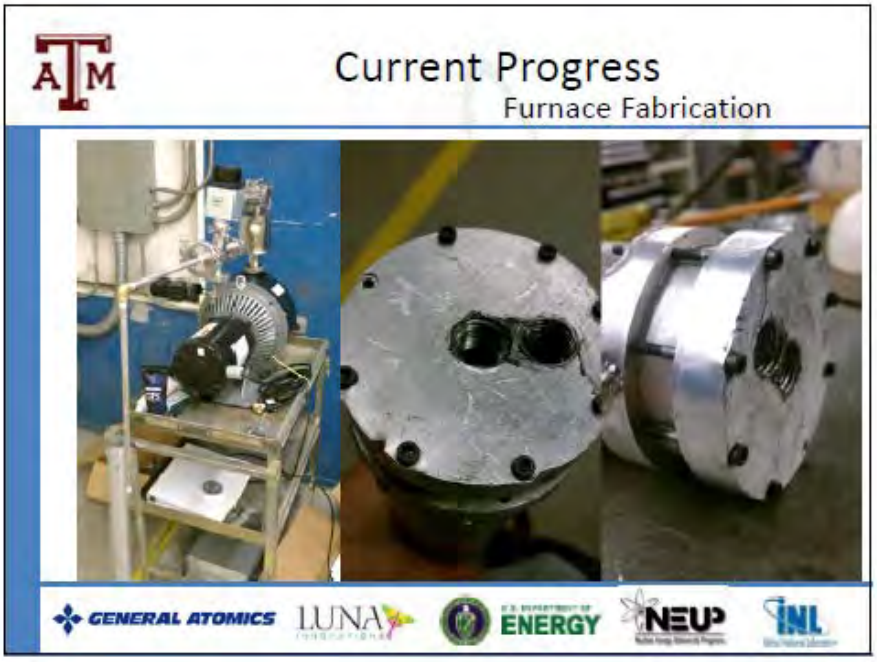
Current Progress
Furnace Fabrication
GENERAL ATOMICS
LUNA
ENERGY
NEUP
INL

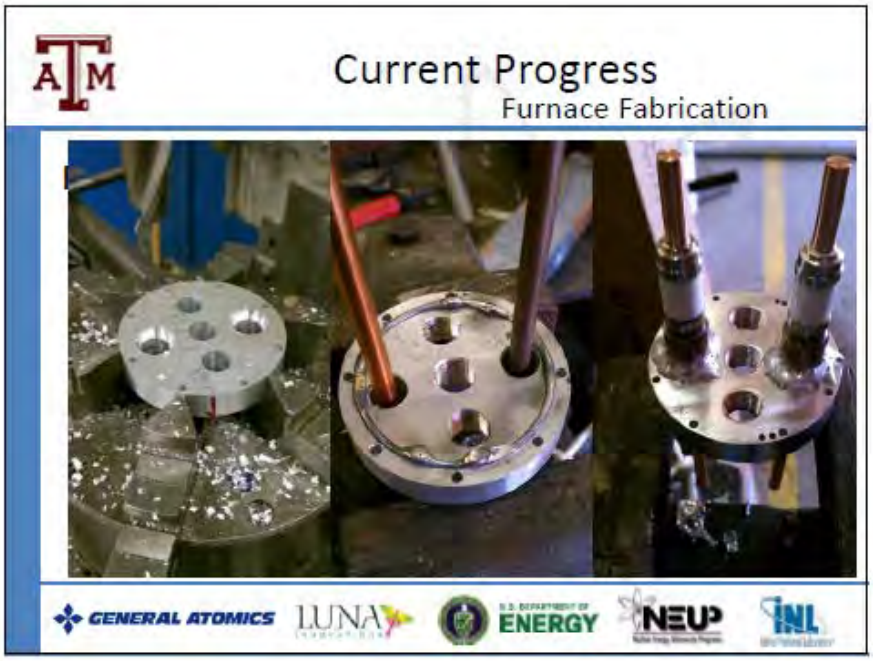
Current Progress
Furnace Fabrication
GENERAL ATOMICS
LUNA
ENERGY
NEUP
INL

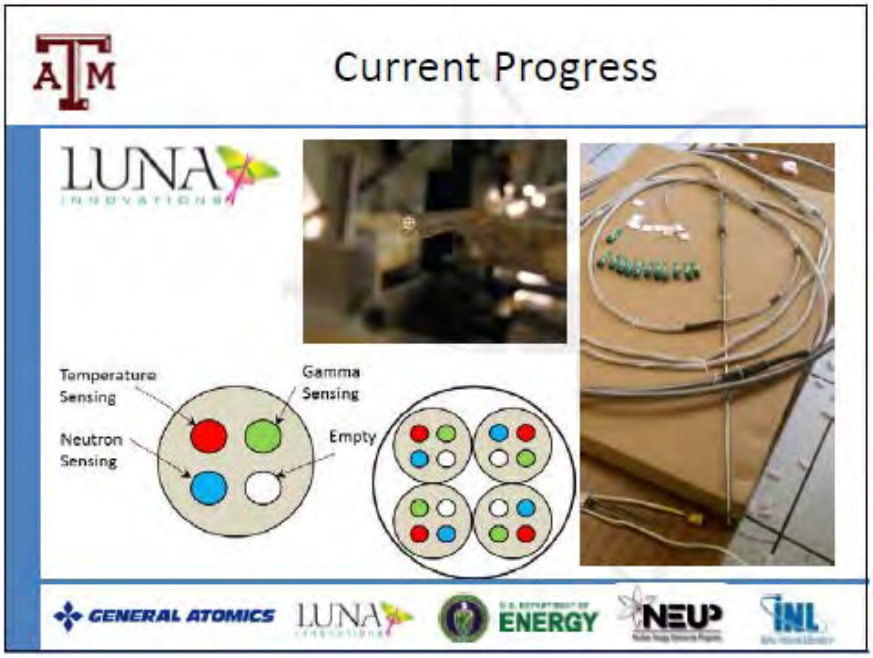
Current Progress
LUNA
Temperature Sensing
Gamma Sensing
Neutron Sensing
Empty
GENERAL ATOMICS
LUNA
ENERGY
NEUP
INL

Current Progress
Pressure Sensor Calibration

Ensure proper safety system response.

Comply with NEUP QA requirements.

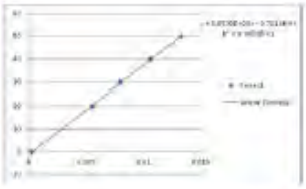

Final Remarks
and Conclusions

Key milestones:

- Development of theoretical approach to estimating neutron fluence distributed along the length of the sensing fiber.
- Test furnace engineering design with reactor safety board approval.
- Fiber optic sensor design and completion of out-of-core laboratory testing.
- Test furnace fabrication, assembly and completion of out-of-core testing.
- Delivery of sensor strings with connectors to university; Installation in test furnace.
- Assembly Installation in TRIGA and completion of irradiation test matrix.
- 3D VHTR and TRIGA modeling with representation of distributed sensor network elements, performance reconstruction and optimization of the network design.
- Modeling validation using test measurements and scaling to the prototypical VHTR conditions.

Final Remarks
and Conclusions

Confident that the safety of the TRIGA reactor core will not be impacted by the experiment.

Temperature requirements, following bench top tests, may change , but operation to 1000°C is expected to be achievable.

Temperature fiber optic sensors perform, under normal conditions, as expected. Gamma and neutron fibers test have not yet been done in depth.

Acknowledgements

This paper is based upon work supported by the U.S. Department of Energy Nuclear Energy University Program Award Number 09-241.

All fabrication was performed at the Texas A&M University Nuclear Science center.

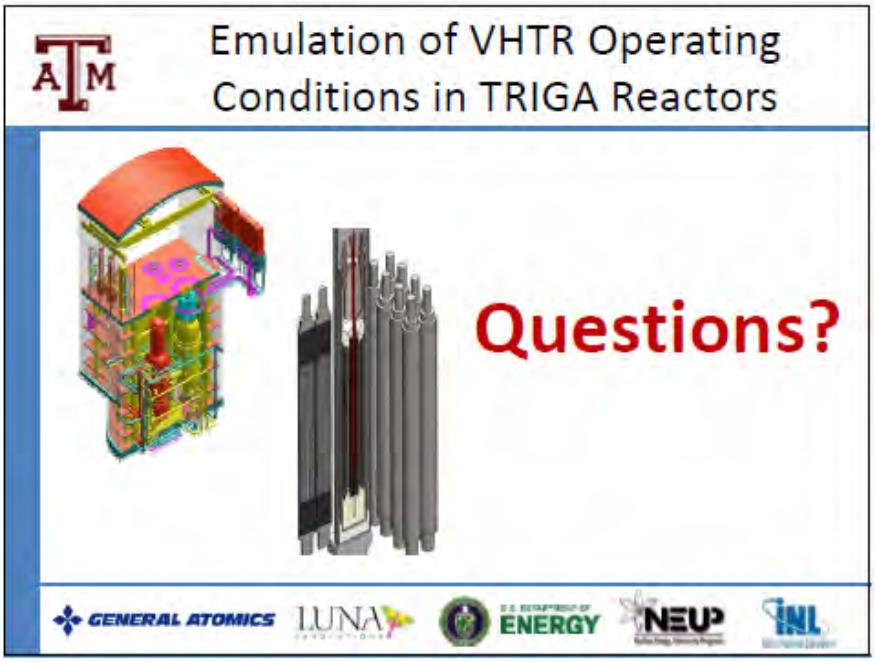
Emulation of VHTR Operating Conditions in TRIGA Reactors
Questions?
GENERAL ATOMICS
LUNA
ENERGY
NEUP
INL

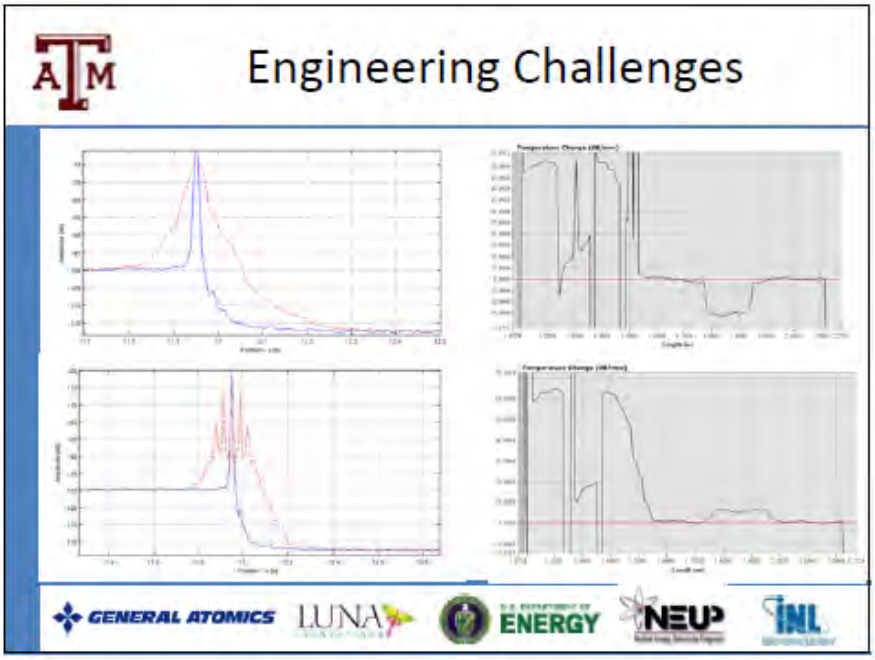
Engineering Challenges
GENERAL ATOMICS
LUNA
ENERGY
NEUP
INL

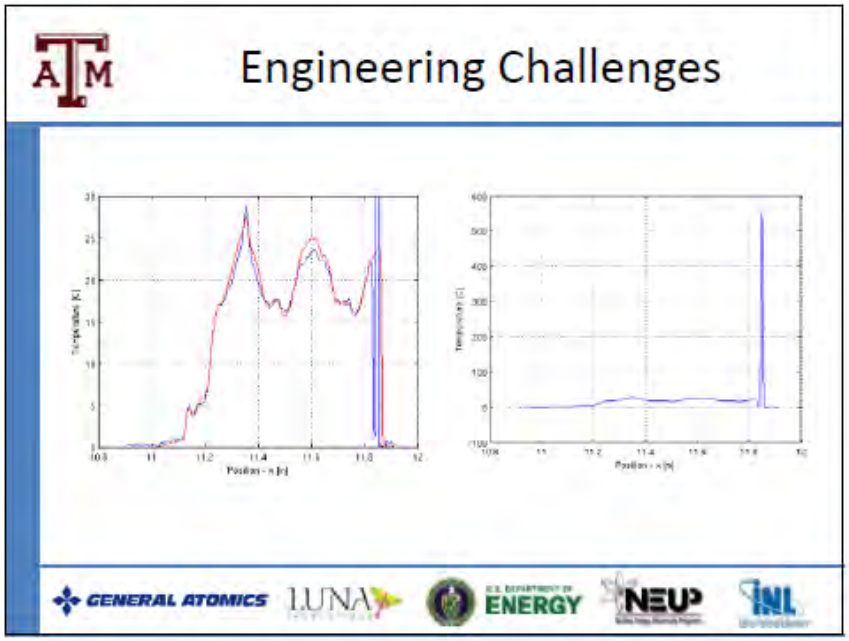
Engineering Challenges
GENERAL ATOMICS
LUNA
ENERGY
NEUP
INL

13.5.6. 3D In-Core Monitoring in Advanced Reactor Environments

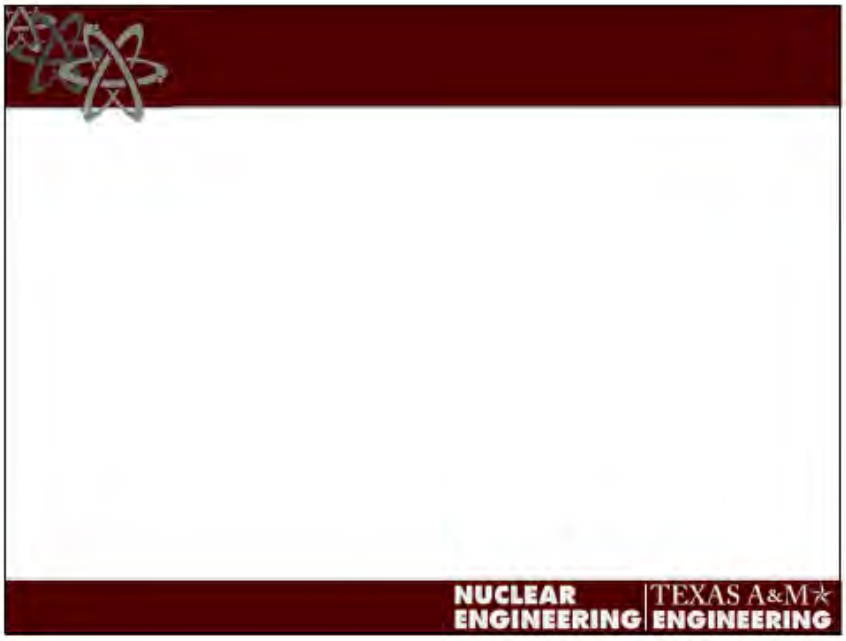

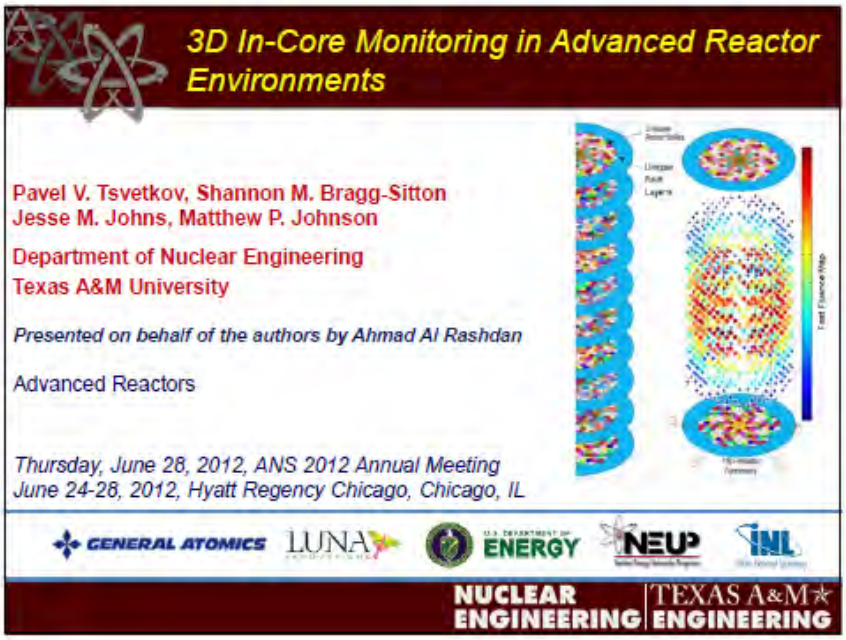

3D In-Core Monitoring in Advanced Reactor Environments

- Overview
- High-Fidelity Modeling Approach
- VHTR Environments in TRIGA
- In-Core Environment Reconstruction
- Current Status
- Conclusions

GENERAL ATOMICS LUNA ENERGY NEUP INL

NUCLEAR ENGINEERING

3D In-Core Monitoring in Advanced Reactor Environments

Overview

Sensors for Advanced Reactors

Safety, Reliability, Autonomity, Economics, …

- Robust in-core measurement systems capable to provide characteristic operational information
- Longevity of sensor performance
- Real time operation
- Ability to predict hot spot formation conditions

GENERAL ATOMICS LUNA ENERGY NEUP INL

NUCLEAR ENGINEERING

3D In-Core Monitoring in Advanced Reactor Environments

Overview

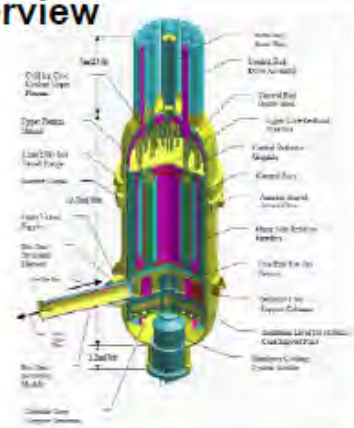

- **In-core monitoring challenge** – reliable long-term operation in extreme high-temperature high-fluence environments
- **Use of fiber optic sensors** – direct in-core 3D monitoring for in-core management (loading, hot spots, temperature and fluence maps)

GENERAL ATOMICS

NUCLEAR ENGINEERING

3D In-Core Monitoring in Advanced Reactor Environments

Overview

Distributed Sensor Networks for Online 3D In-Core Monitoring in VHTR Environments

- Collaboration of University, Nat. Lab., Industry
- **Texas A&M University, Project Lead**
- Luna Innovations, Primary Industry Partner
- General Atomics, Advisor
- Idaho National Laboratory, Advisor

GENERAL ATOMICS LUNA ENERGY NEUP INL

NUCLEAR ENGINEERING

3D In-Core Monitoring in Advanced Reactor Environments

Overview

- **Goal:** Real-time mapping of the temperature and neutron fluence distribution in proposed NGNP / VHTR cores
- **Challenges:**
  - Harsh environment (750° C to 950° C coolant outlet)
  - Long refueling cycle (~18 months) – high radiation
- **Benefits of Proposed Sensors:**
  - Real-time assessment of reactor performance
  - Sensor network can be placed throughout the reactor core (axial and transverse dimensions)
  - Benchmarks for simulation and analysis codes used in core design and modeling
  - Optimization of design margins
  - Reduced uncertainty in local phenomena assessment / prediction → reduced safety margins in design

NUCLEAR ENGINEERING

3D In-Core Monitoring in Advanced Reactor Environments

Overview

The 3-year project will provide three key deliverables:

1. produce a highly distributed fiber optic network capable of 3D temperature and neutron fluence mapping in the VHTR environment;
2. demonstrate reliability and performance of the proposed sensor network; and
3. provide a computational model to evaluate expected sensor performance and lifetime in VHTR environments, to scale experimental results to VHTR conditions, to optimize sensor network, and to assess VHTR performance taking advantage of the 3D fiber-optics imaging and performance reconstruction.

NUCLEAR ENGINEERING

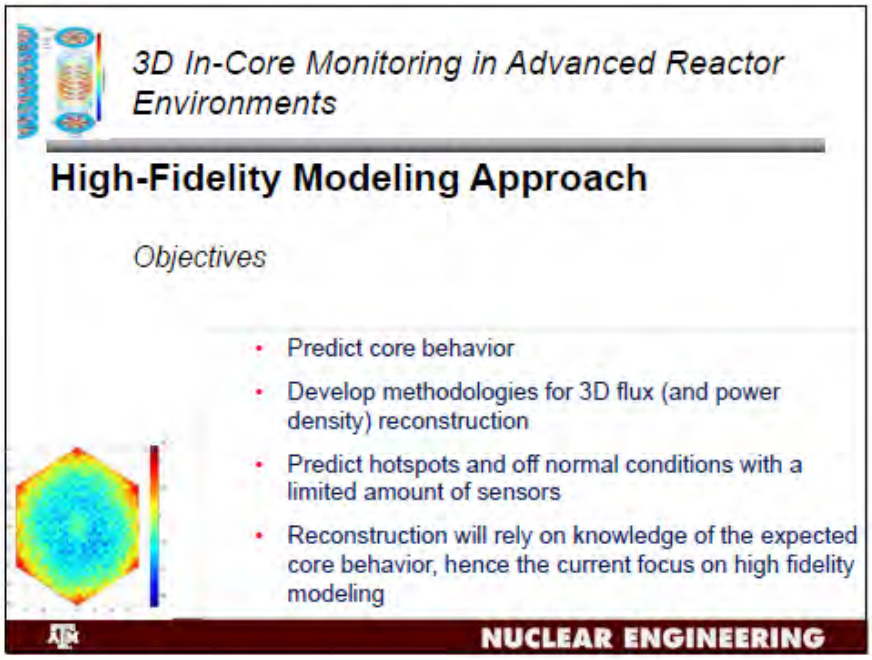
3D In-Core Monitoring in Advanced Reactor Environments
High-Fidelity Modeling Approach
Objectives
Predict core behavior
Develop methodologies for 3D flux (and power density) reconstruction
Predict hotspots and off normal conditions with a limited amount of sensors
Reconstruction will rely on knowledge of the expected core behavior, hence the current focus on high fidelity modeling
NUCLEAR ENGINEERING

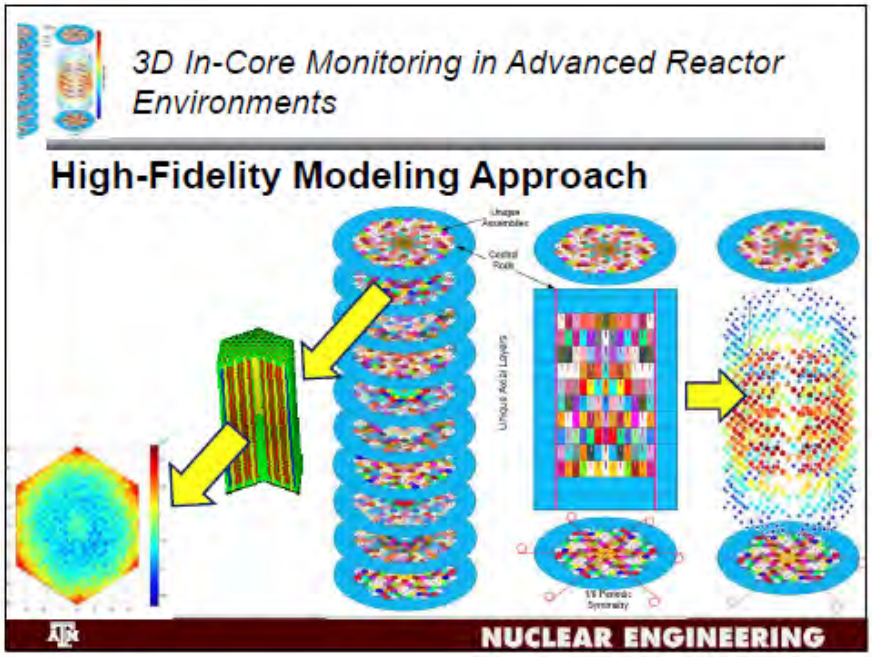
3D In-Core Monitoring in Advanced Reactor Environments
High-Fidelity Modeling Approach
NUCLEAR ENGINEERING

3D In-Core Monitoring in Advanced Reactor Environments

High-Fidelity Modeling Approach

Methodology and Tools

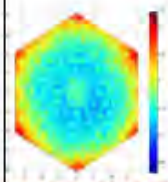

- MCNPX whole core modeling with unique block tracking
- Runtime automation to capture core performance
- Sensor modeling using cell flux tallies
- Sensor grid optimization to maximize predictive capability
- Sensor failure effect evaluations

NUCLEAR ENGINEERING

3D In-Core Monitoring in Advanced Reactor Environments

High-Fidelity Modeling Approach

Hot Spot Migration and Localization with the Core

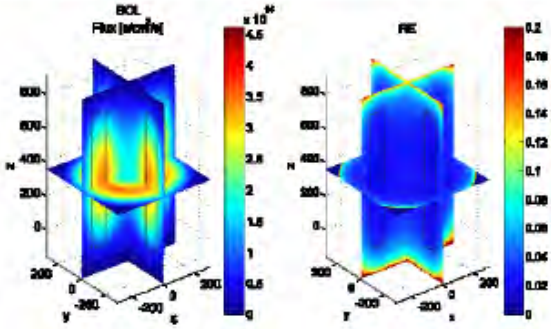

NUCLEAR ENGINEERING

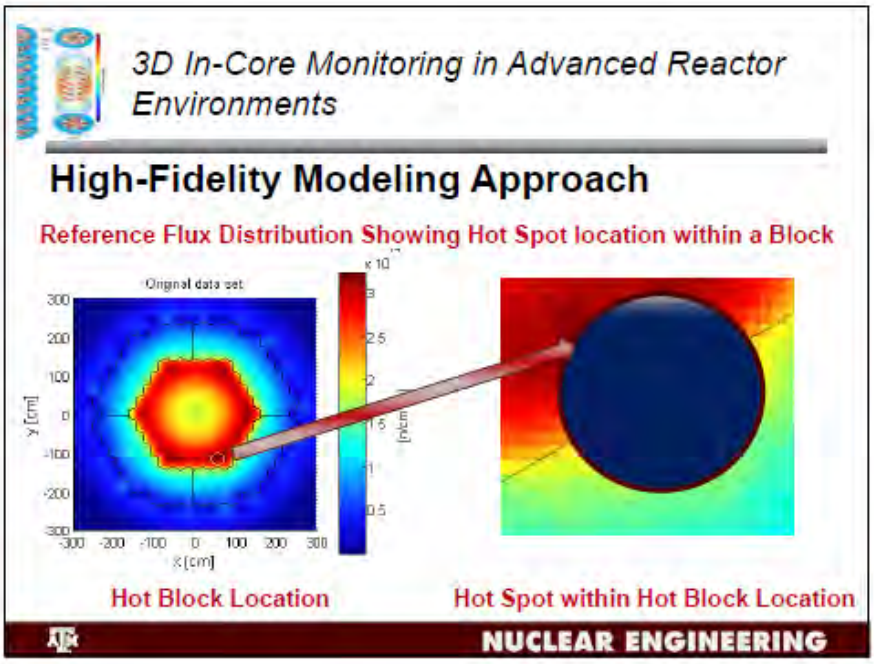
3D In-Core Monitoring in Advanced Reactor Environments
High-Fidelity Modeling Approach
Reference Flux Distribution Showing Hot Spot location within a Block
Original data set
y [cm]
x [cm]
Hot Block Location
Hot Spot within Hot Block Location
NUCLEAR ENGINEERING

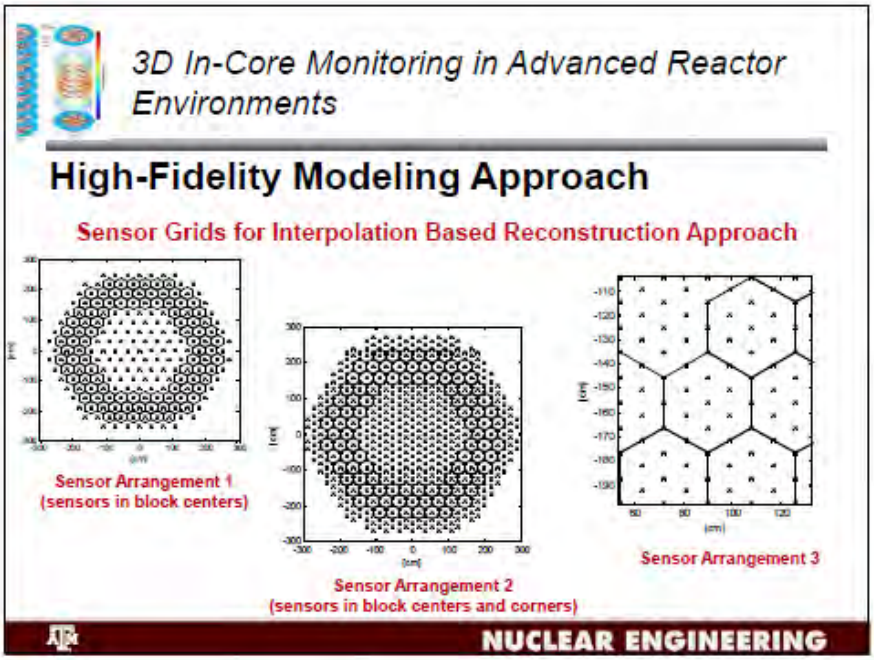
3D In-Core Monitoring in Advanced Reactor Environments
High-Fidelity Modeling Approach
Sensor Grids for Interpolation Based Reconstruction Approach
Sensor Arrangement 1
(sensors in block centers)
Sensor Arrangement 2
(sensors in block centers and corners)
Sensor Arrangement 3
NUCLEAR ENGINEERING

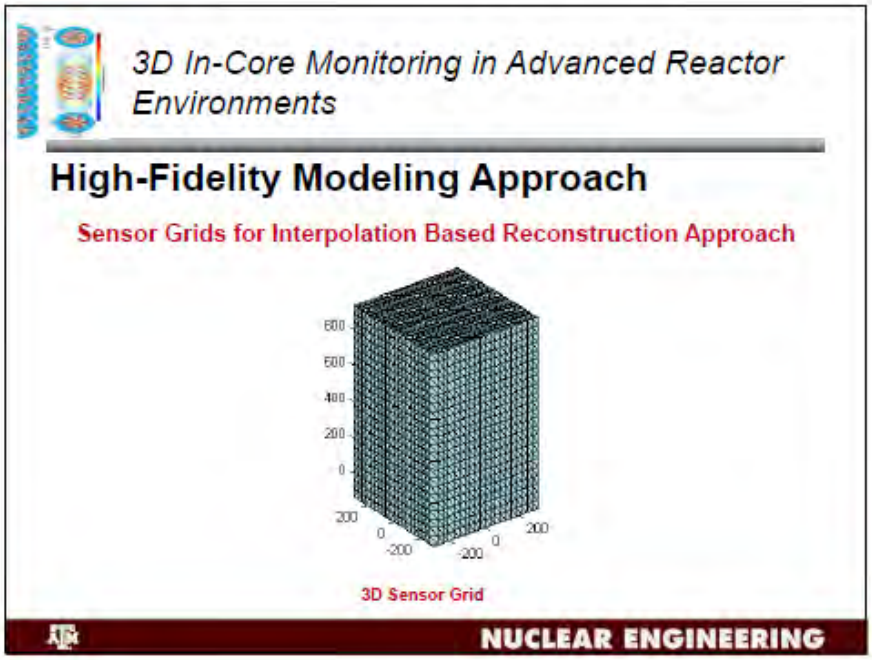
3D In-Core Monitoring in Advanced Reactor Environments
High-Fidelity Modeling Approach
Sensor Grids for Interpolation Based Reconstruction Approach
3D Sensor Grid
NUCLEAR ENGINEERING

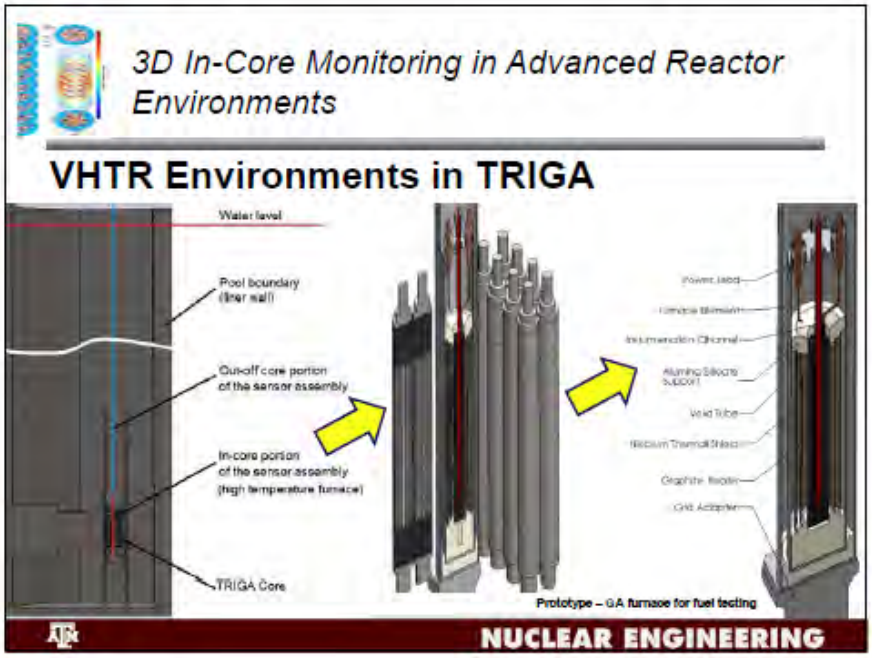
3D In-Core Monitoring in Advanced Reactor Environments
VHTR Environments in TRIGA
Water level
Pool boundary (liner wall)
Out-of core portion of the sensor assembly
In-core portion of the sensor assembly (high temperature furnace)
TRIGA Core
Prototype – GA furnace for fuel testing
NUCLEAR ENGINEERING

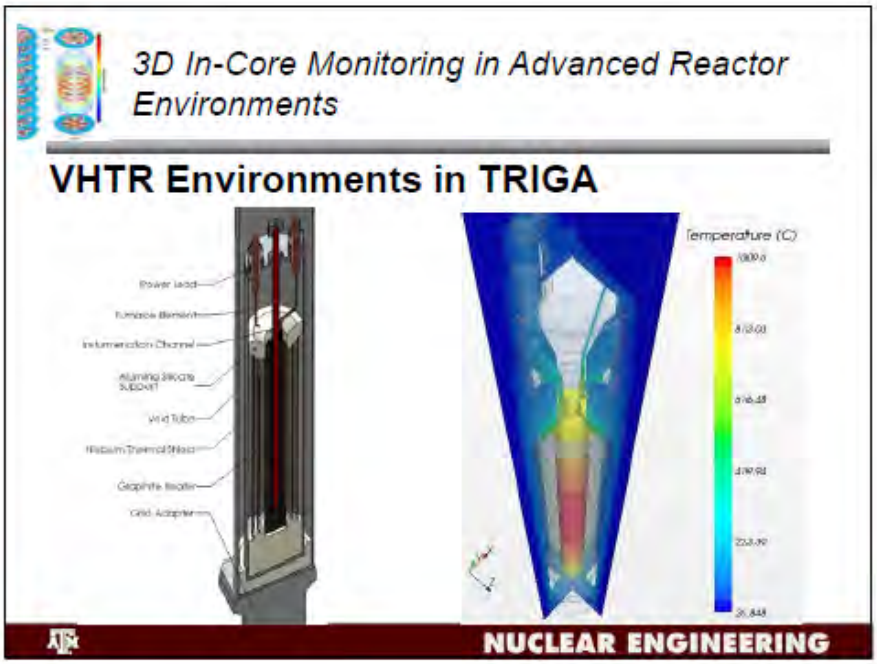
3D In-Core Monitoring in Advanced Reactor Environments
VHTR Environments in TRIGA
Temperature (C)
NUCLEAR ENGINEERING

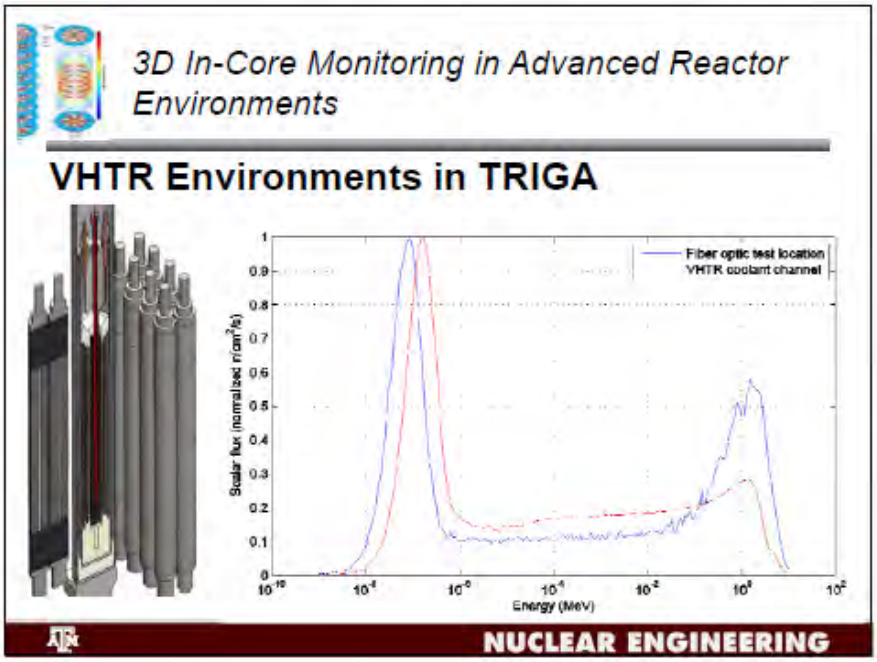
3D In-Core Monitoring in Advanced Reactor Environments
VHTR Environments in TRIGA
Fiber optic test location
VHTR coolant channel
Scalar flux (normalized n/cm²/s)
Energy (MeV)
NUCLEAR ENGINEERING

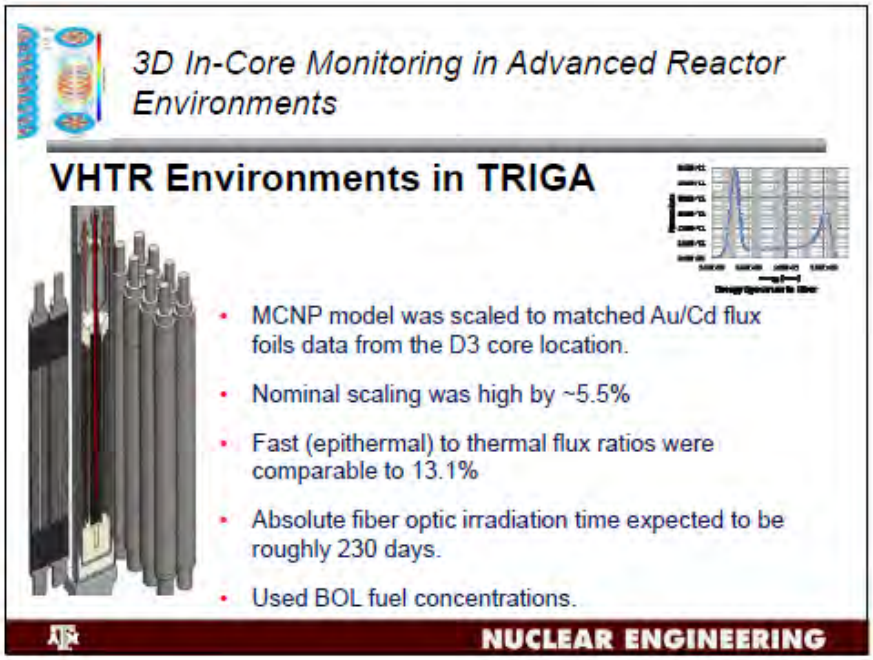
3D In-Core Monitoring in Advanced Reactor Environments
VHTR Environments in TRIGA
MCNP model was scaled to matched Au/Cd flux foils data from the D3 core location.
Nominal scaling was high by ~5.5%
Fast (epithermal) to thermal flux ratios were comparable to 13.1%
Absolute fiber optic irradiation time expected to be roughly 230 days.
Used BOL fuel concentrations.
NUCLEAR ENGINEERING

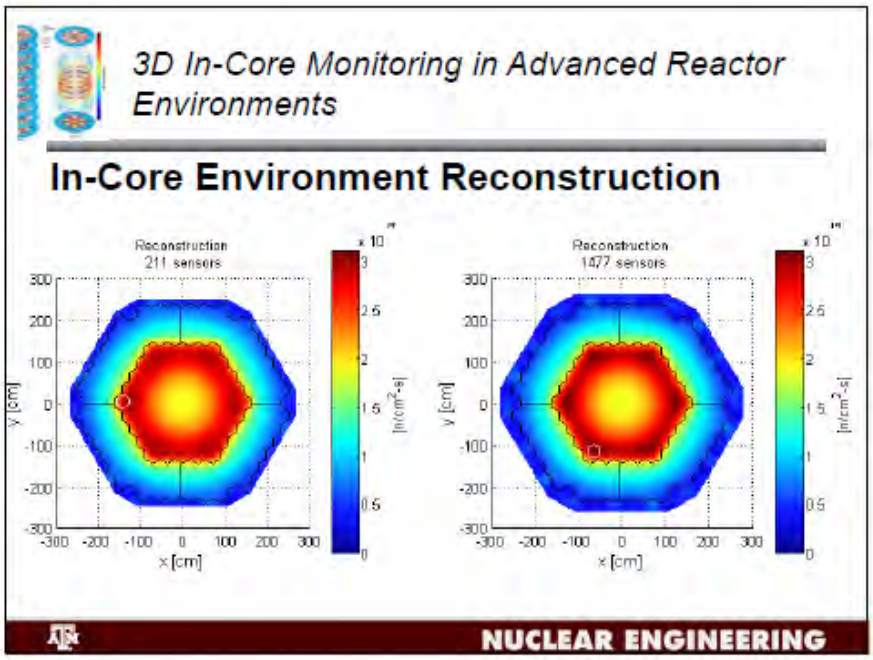
3D In-Core Monitoring in Advanced Reactor Environments
In-Core Environment Reconstruction
Reconstruction
211 sensors
Reconstruction
1477 sensors
y [cm]
x [cm]
[n/cm²-s]
NUCLEAR ENGINEERING

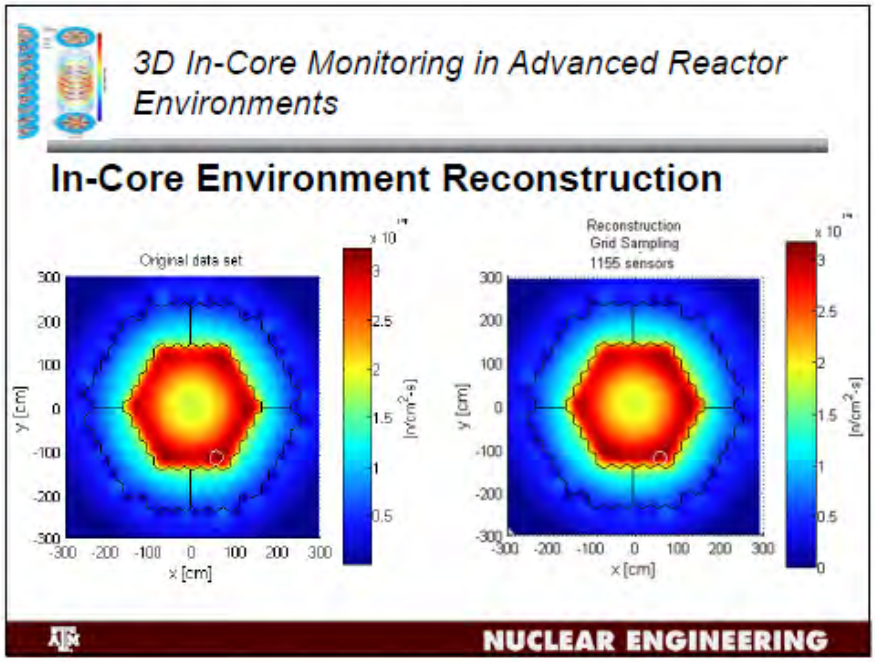
3D In-Core Monitoring in Advanced Reactor Environments
In-Core Environment Reconstruction
Original data set
Reconstruction
Grid Sampling
1155 sensors
x 10^14
y [cm]
x [cm]
[n/cm^2-s]
NUCLEAR ENGINEERING

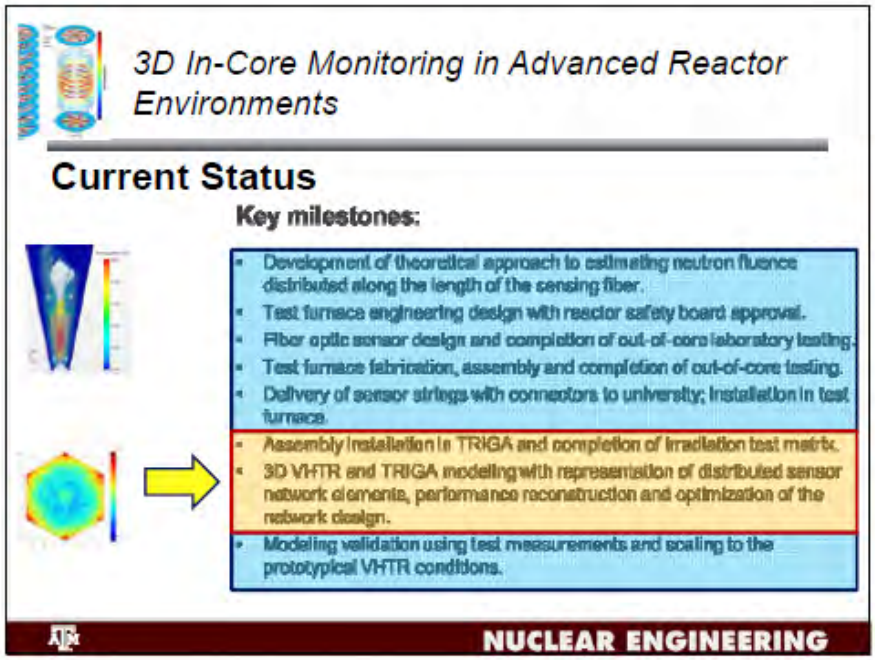
3D In-Core Monitoring in Advanced Reactor Environments
Current Status
Key milestones:
Development of theoretical approach to estimating neutron fluence distributed along the length of the sensing fiber.
Test furnace engineering design with reactor safety board approval.
Fiber optic sensor design and completion of out-of-core laboratory testing.
Test furnace fabrication, assembly and completion of out-of-core testing.
Delivery of sensor strings with connectors to university; installation in test furnace.
Assembly installation in TRIGA and completion of irradiation test matrix.
3D VHTR and TRIGA modeling with representation of distributed sensor network elements, performance reconstruction and optimization of the network design.
Modeling validation using test measurements and scaling to the prototypical VHTR conditions.
NUCLEAR ENGINEERING

3D In-Core Monitoring in Advanced Reactor Environments

Conclusions

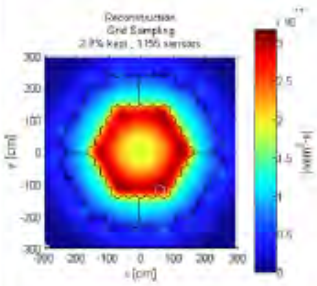

High fidelity simulations indicate that the furnace assembly should be capable of emulating VHTR in TRIGA. The furnace allows the sensor location to reach 1000oC while being completely shielded from the TRIGA.

Calculations indicate that no active heat removal systems will be required to maintain TRIGA safety setting (525oC).

The simulation methodology and reconstruction techniques have been developed for sensor array optimization studies targeting in-core 3D monitoring options.

The grid sampling case using 1155 sensors in a grid pattern is sufficient for hot spot location at standard operating conditions.

The irradiation testing results and final project conclusions will be presented at the ANS annual meeting in 2013, stay turned !

GENERAL ATOMICS LUNA ENERGY NEUP INL

NUCLEAR ENGINEERING

3D In-Core Monitoring in Advanced Reactor Environments

Acknowledgements

This paper is based upon work supported by the U.S. Department of Energy Nuclear Energy University Program Award Number 09-241.

GENERAL ATOMICS LUNA ENERGY NEUP INL

NUCLEAR ENGINEERING

3D In-Core Monitoring in Advanced Reactor Environments
QUESTIONS?
Direct your questions about this effort to
Dr. Tsvetkov (tsvetkov@tamu.edu) and Dr. Bragg-Sitton (sitton@tamu.edu)
GENERAL ATOMICS
LUNA
ENERGY
NEUP
INL
NUCLEAR ENGINEERING
TEXAS A&M ENGINEERING

3D In-Core Monitoring in Advanced Reactor Environments
THANK YOU
GENERAL ATOMICS
LUNA
ENERGY
NEUP
INL
NUCLEAR ENGINEERING
TEXAS A&M ENGINEERING

13.5.7. Fiberoptics-Based Sensing for Real-Time 3D In-Core Monitoring

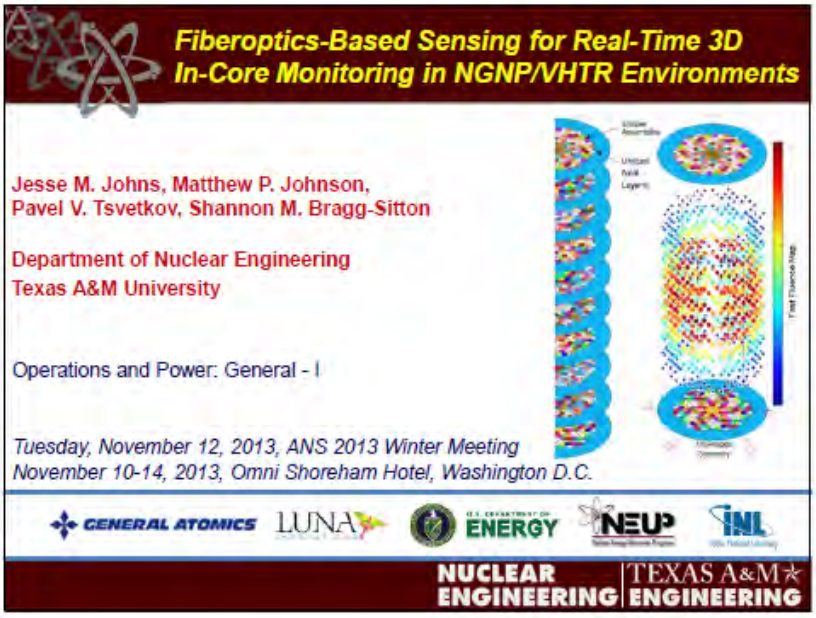

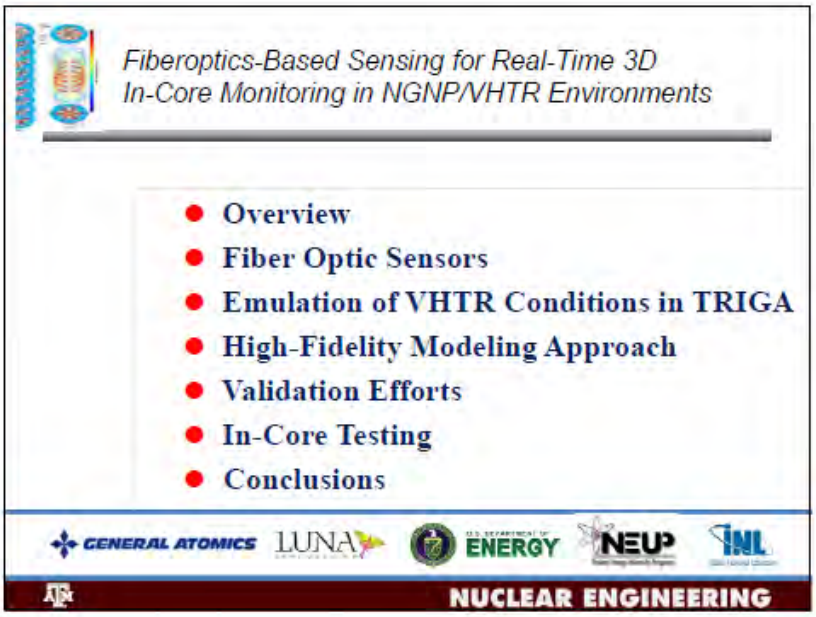

Fiberoptics-Based Sensing for Real-Time 3D In-Core Monitoring in NGNP/VHTR Environments

Overview

Small and Medium Sized Advanced Reactors
Safety, Reliability, Autonomity, Economics, …

- Robust in-core measurement systems capable to provide characteristic operational information
- Longevity of sensor performance
- Real time operation
- Ability to predict hot spot formation conditions

GENERAL ATOMICS LUNA ENERGY NEUP INL

NUCLEAR ENGINEERING

Fiberoptics-Based Sensing for Real-Time 3D In-Core Monitoring in NGNP/VHTR Environments

Overview

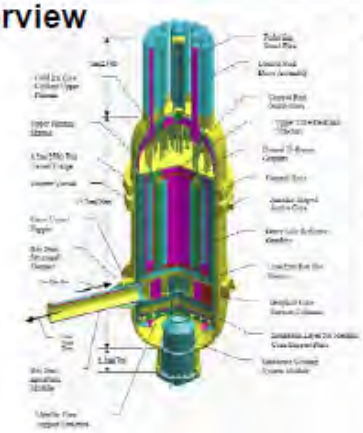

- **In-core monitoring challenge** – reliable long-term operation in extreme high-temperature high-fluence environments
- **Use of fiber optic sensors** – direct in-core 3D monitoring for in-core management (loading, hot spots, temperature and fluence maps)

GENERAL ATOMICS

NUCLEAR ENGINEERING

Fiberoptics-Based Sensing for Real-Time 3D In-Core Monitoring in NGNP/VHTR Environments

Overview

Collaboration of University, Nat. Lab., Industry

Texas A&M University, Project Lead

Luna Innovations, Primary Industry Partner

General Atomics, Advisor

Idaho National Laboratory, Advisor

NUCLEAR ENGINEERING

Fiberoptics-Based Sensing for Real-Time 3D In-Core Monitoring in NGNP/VHTR Environments

Overview

- **Goal:** Real-time mapping of the temperature and neutron fluence distribution in proposed NGNP / VHTR cores
- **Challenges:**
  - Harsh environment (750° C to 950° C coolant outlet)
  - Long refueling cycle (~18 months) – high radiation
- **Benefits of Proposed Sensors:**
  - Real-time assessment of reactor performance
  - Sensor network can be placed throughout the reactor core (axial and transverse dimensions)
  - Benchmarks for simulation and analysis codes used in core design and modeling
  - Optimization of design margins
  - Reduced uncertainty in local phenomena assessment / prediction → reduced safety margins in design

NUCLEAR ENGINEERING

Fiberoptics-Based Sensing for Real-Time 3D In-Core Monitoring in NGNP/VHTR Environments

Overview

The 3-year project will provide three key deliverables:

1. produce a highly distributed fiber optic network capable of 3D temperature and neutron fluence mapping in the VHTR environment;
2. demonstrate reliability and performance of the proposed sensor network; and
3. provide a computational model to evaluate expected sensor performance and lifetime in VHTR environments, to scale experimental results to VHTR conditions, to optimize sensor network, and to assess VHTR performance taking advantage of the 3D fiber-optics imaging and performance reconstruction.

NUCLEAR ENGINEERING

Fiberoptics-Based Sensing for Real-Time 3D In-Core Monitoring in NGNP/VHTR Environments

Fiber optic sensors will be used to monitor
- Total Neutron Fluence
- Gamma Flux
- Temperature

The OBR measures the Rayleigh Backscatter of the optical fiber

The sensor interrogation uses an Optical Backscatter Reflectometer (OBR™) system

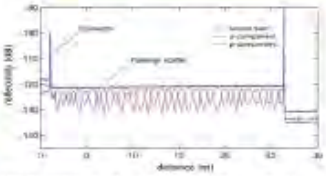

Strain, temp., etc. cause Rayleigh fingerprint to stretch – shift in the mean period between perturbations leads to a shift in optical frequency.

Radiation and Temperature stimuli change the Rayleigh backscatter of the optical fiber

Fiber Optic Sensors

NUCLEAR ENGINEERING

Fiberoptics-Based Sensing for Real-Time 3D In-Core Monitoring in NGNP/VHTR Environments

Fiber Optic Sensors

Fiber optic sensors promise to provide detailed distributed measurements.

- Online hot spots determination and flux mapping
- Continuous code validation becomes possible

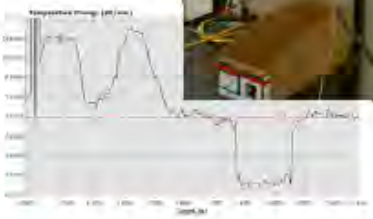

Test fibers in the operating conditions that would be expected in the VHTR.

NUCLEAR ENGINEERING

Fiberoptics-Based Sensing for Real-Time 3D In-Core Monitoring in NGNP/VHTR Environments

Emulation of VHTR Conditions in TRIGA

The TRIGA reactor sits in a pool of light water open to the atmosphere.

- Thermal flux ~ peak at .09 eV
- Low temperatures
  - Fuel ~ 390°C
  - Coolant ~ 26°C
- Low fluence rate ~ 4e12 n/cm^2/s
- Safety and experimental limitations
  - Temperature, thermal storage, size, reactivity

NUCLEAR ENGINEERING

Fiberoptics-Based Sensing for Real-Time 3D In-Core Monitoring in NGNP/VHTR Environments

Emulation of VHTR Conditions in TRIGA

Design an experimental apparatus to emulate the conditions of a VHTR in a TRIGA reactor for advanced instrumentation testing.

- **Operate at +1000°C**
- **Sustained operation for 1 year, to a neutron fluence of 2e19 n/cm²**
- **Accessibility for fiber optics and instrumentation replacement**
- **Conform to 10 CFR 50.59**
  - **Required safety criteria for experimental authorization**
- **Passive cooling – heater in vacuum**

NUCLEAR ENGINEERING

Fiberoptics-Based Sensing for Real-Time 3D In-Core Monitoring in NGNP/VHTR Environments

Emulation of VHTR Conditions in TRIGA

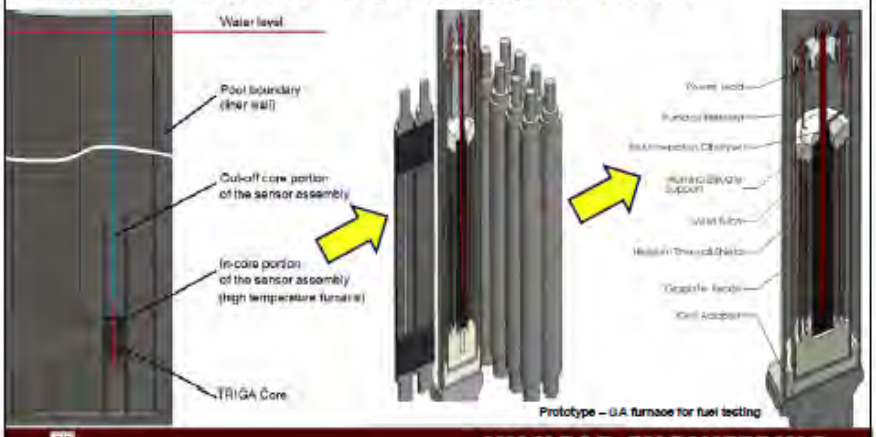

NUCLEAR ENGINEERING

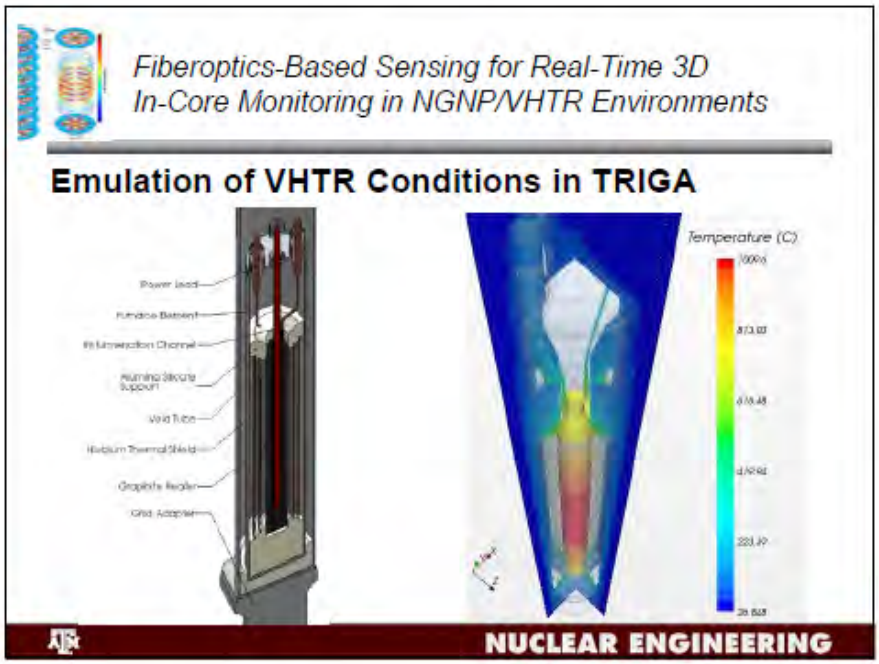
Fiberoptics-Based Sensing for Real-Time 3D
In-Core Monitoring in NGNP/VHTR Environments
Emulation of VHTR Conditions in TRIGA
Temperature (C)
NUCLEAR ENGINEERING

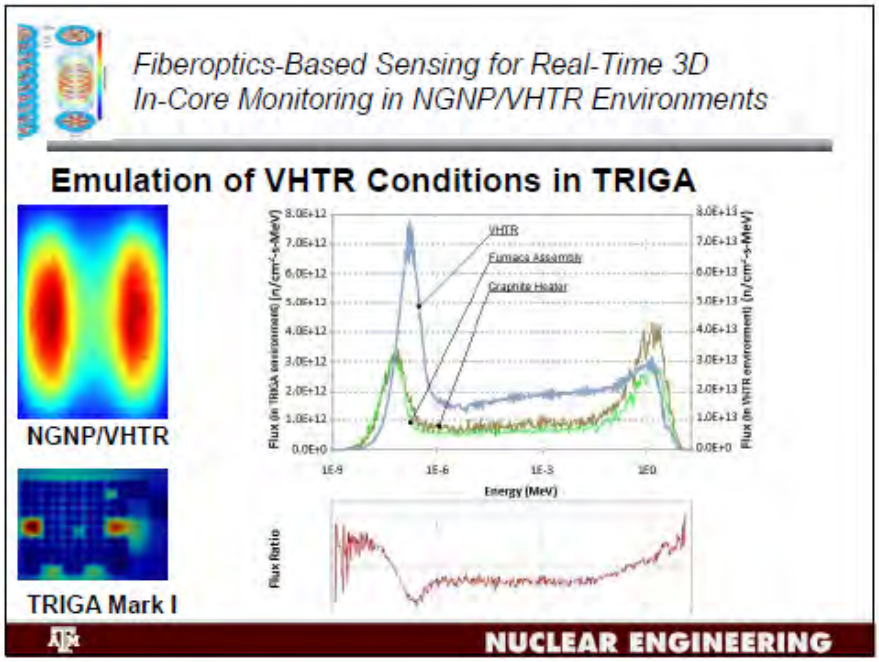
Fiberoptics-Based Sensing for Real-Time 3D
In-Core Monitoring in NGNP/VHTR Environments
Emulation of VHTR Conditions in TRIGA
NGNP/VHTR
TRIGA Mark I
VHTR
Furnace Assembly
Graphite Heater
Energy (MeV)
Flux Ratio
NUCLEAR ENGINEERING

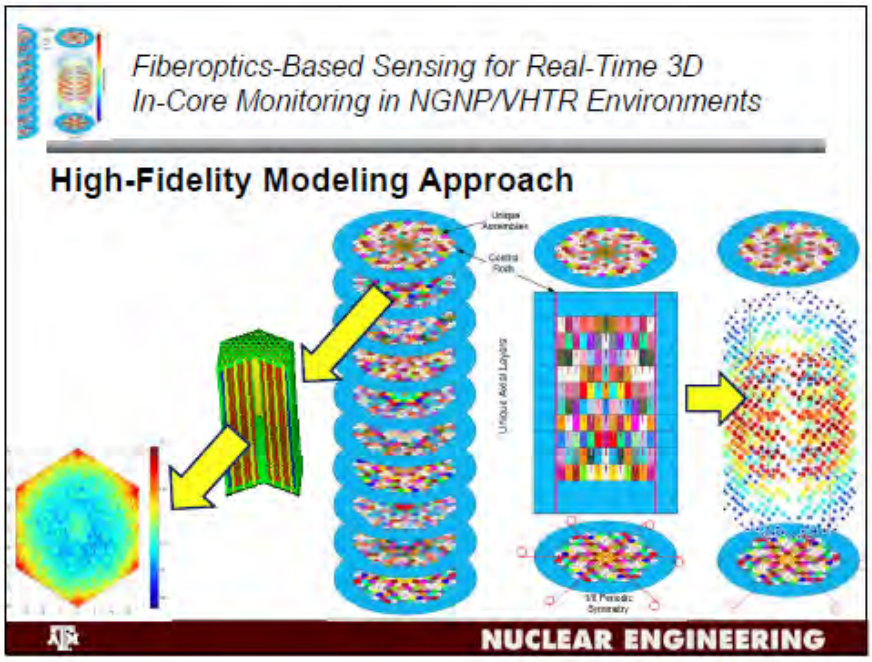
Fiberoptics-Based Sensing for Real-Time 3D
In-Core Monitoring in NGNP/VHTR Environments
High-Fidelity Modeling Approach
NUCLEAR ENGINEERING

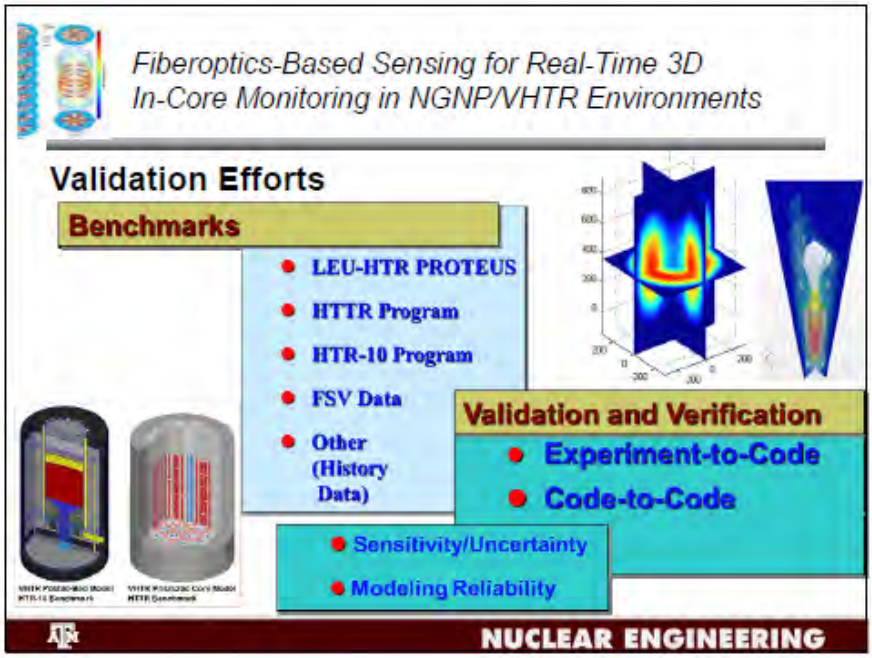
Fiberoptics-Based Sensing for Real-Time 3D
In-Core Monitoring in NGNP/VHTR Environments
Validation Efforts
Benchmarks
LEU-HTR PROTEUS
HTTR Program
HTR-10 Program
FSV Data
Other (History Data)
Validation and Verification
Experiment-to-Code
Code-to-Code
Sensitivity/Uncertainty
Modeling Reliability
NUCLEAR ENGINEERING

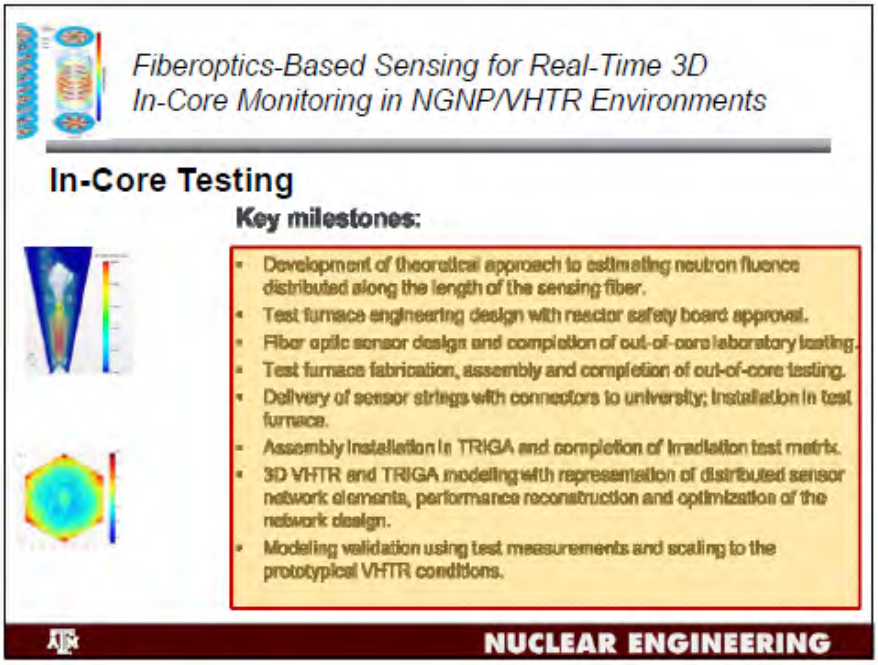
Fiberoptics-Based Sensing for Real-Time 3D
In-Core Monitoring in NGNP/VHTR Environments
In-Core Testing
Key milestones:
Development of theoretical approach to estimating neutron fluence distributed along the length of the sensing fiber.
Test furnace engineering design with reactor safety board approval.
Fiber optic sensor design and completion of out-of-core laboratory testing.
Test furnace fabrication, assembly and completion of out-of-core testing.
Delivery of sensor strings with connectors to university; Installation in test furnace.
Assembly installation in TRIGA and completion of irradiation test matrix.
3D VHTR and TRIGA modeling with representation of distributed sensor network elements, performance reconstruction and optimization of the network design.
Modeling validation using test measurements and scaling to the prototypical VHTR conditions.
NUCLEAR ENGINEERING

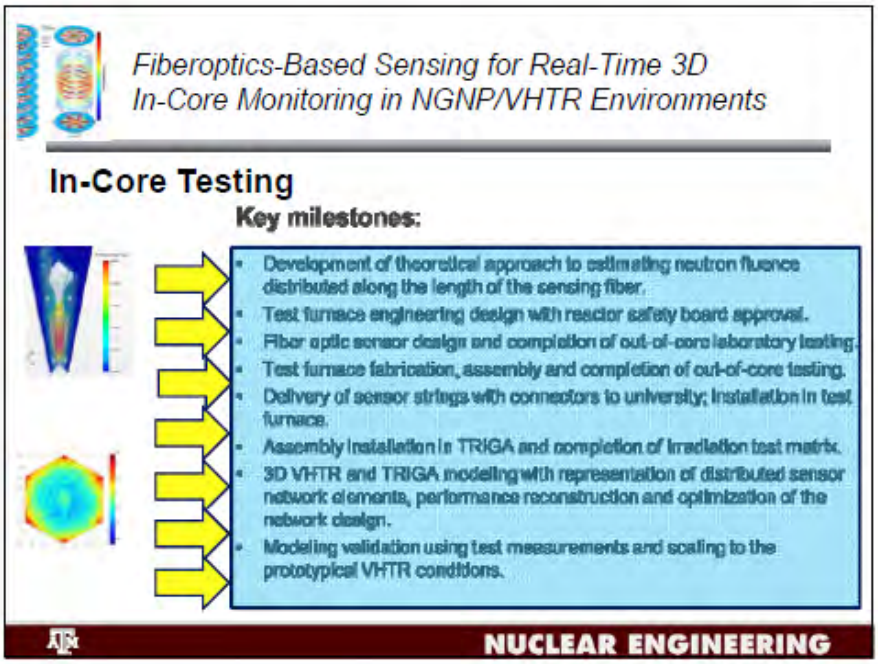
Fiberoptics-Based Sensing for Real-Time 3D
In-Core Monitoring in NGNP/VHTR Environments
In-Core Testing
Key milestones:
Development of theoretical approach to estimating neutron fluence distributed along the length of the sensing fiber.
Test furnace engineering design with reactor safety board approval.
Fiber optic sensor design and completion of out-of-core laboratory testing.
Test furnace fabrication, assembly and completion of out-of-core testing.
Delivery of sensor strings with connectors to university; Installation in test furnace.
Assembly installation in TRIGA and completion of irradiation test matrix.
3D VHTR and TRIGA modeling with representation of distributed sensor network elements, performance reconstruction and optimization of the network design.
Modeling validation using test measurements and scaling to the prototypical VHTR conditions.
NUCLEAR ENGINEERING

Fiberoptics-Based Sensing for Real-Time 3D In-Core Monitoring in NGNP/VHTR Environments

In-Core Testing – High Temperature Furnace

The furnace is capable of an automatic startup triggered by a user input followed by a swap to a auto controller.

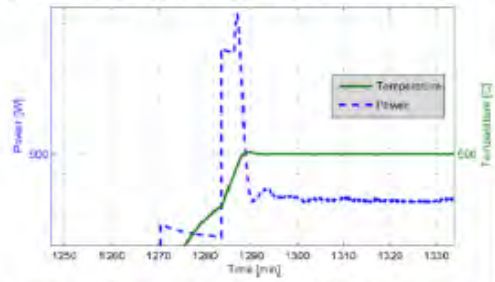

The transition limits the temperature gradient from exceeding 0.2 °C/s and prevents overshoot to less than a degree.

NUCLEAR ENGINEERING

Fiberoptics-Based Sensing for Real-Time 3D In-Core Monitoring in NGNP/VHTR Environments

In-Core Testing – High Temperature Furnace

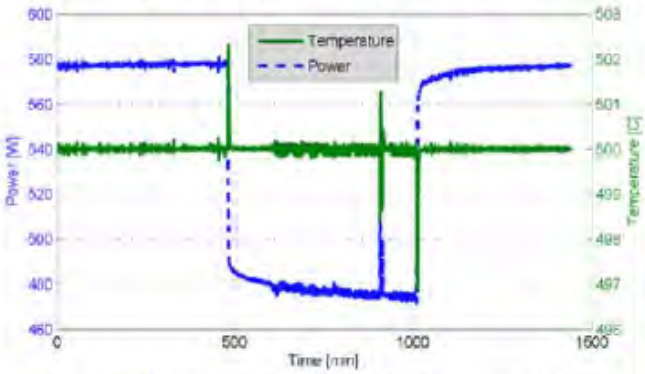

Full day operation of the high temperature furnace

NUCLEAR ENGINEERING

Fiberoptics-Based Sensing for Real-Time 3D In-Core Monitoring in NGNP/VHTR Environments

In-Core Testing – Fiberoptics vs. STAR-CCM+

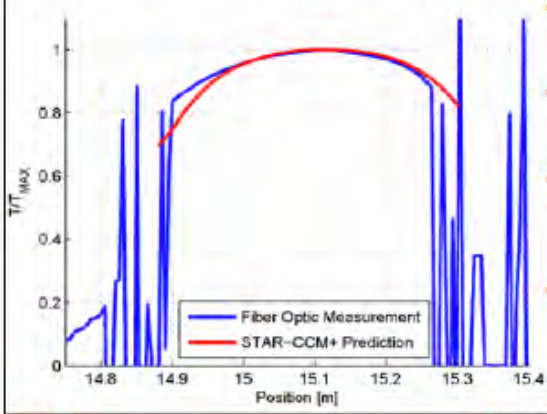

- Largest discrepancies are at the axial ends of the graphite due to model assumptions
- Measurements were affected by vibrations due to natural circulation cooling
- The shape of the temperature distribution does match closely model predictions
- Absolute values were affected by material effects and their interpretation by the fiberoptics data acquisition software.

NUCLEAR ENGINEERING

Fiberoptics-Based Sensing for Real-Time 3D In-Core Monitoring in NGNP/VHTR Environments

In-Core Testing – Fiberoptics Lifetime

- 12 sensors were available for irradiation within the probe (4 of each type – temperature, gamma, neutrons)
- 2 temperature sensors failed initial thermal stressing at startup
- 2 gamma sensors failed as a result of 3-month irradiation (at the 5.8e18 n/cm^2 fluence reached)
  The failure is likely due to material swelling
- Both types of failures occurred with the same characteristics of increased return loss

NUCLEAR ENGINEERING

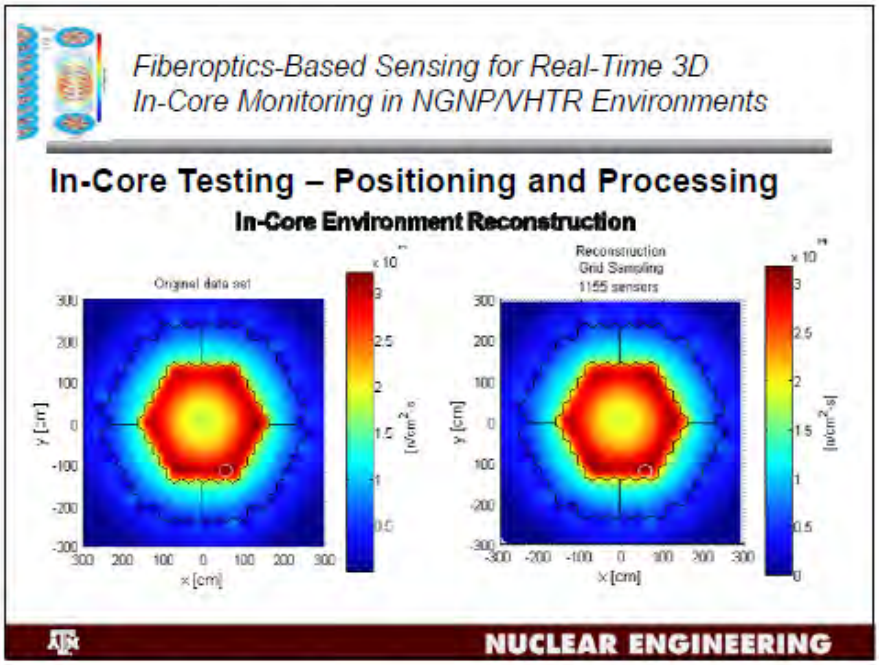
Fiberoptics-Based Sensing for Real-Time 3D
In-Core Monitoring in NGNP/VHTR Environments
In-Core Testing – Positioning and Processing
In-Core Environment Reconstruction
Original data set
Reconstruction
Grid Sampling
1155 sensors
x [cm]
y [cm]
NUCLEAR ENGINEERING

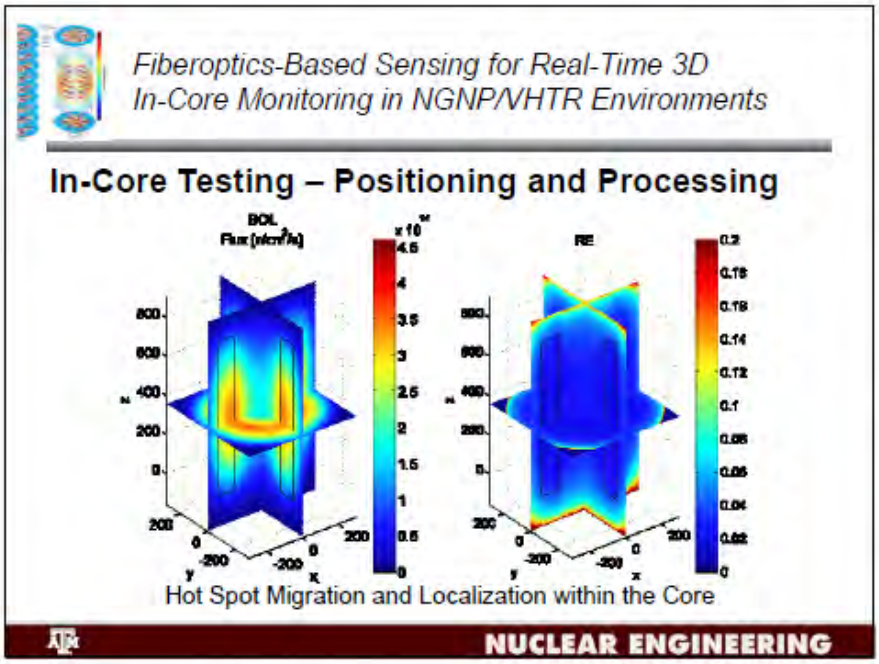
Fiberoptics-Based Sensing for Real-Time 3D
In-Core Monitoring in NGNP/VHTR Environments
In-Core Testing – Positioning and Processing
BOL
RE
Hot Spot Migration and Localization within the Core
NUCLEAR ENGINEERING

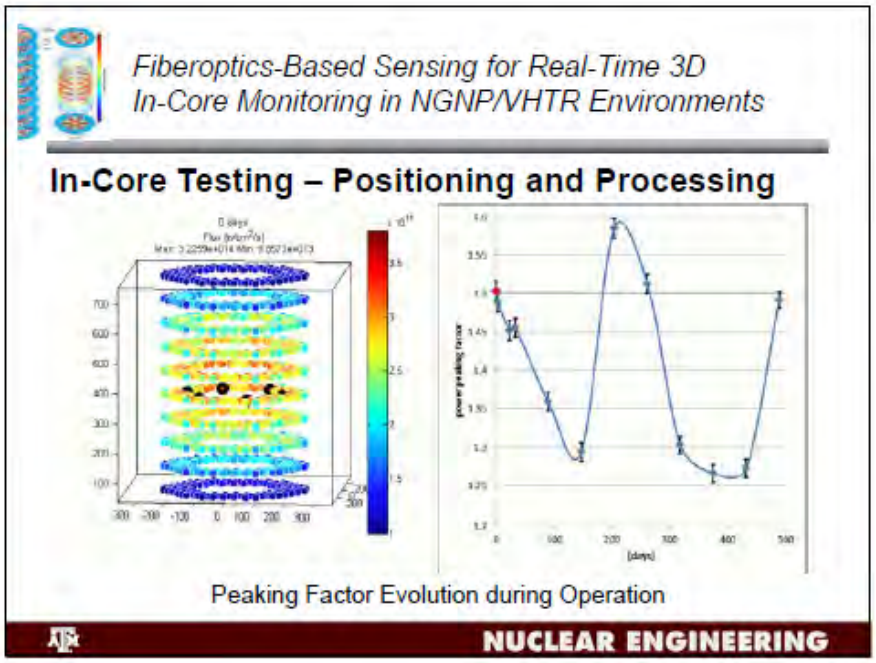
Fiberoptics-Based Sensing for Real-Time 3D
In-Core Monitoring in NGNP/VHTR Environments
In-Core Testing – Positioning and Processing
Peaking Factor Evolution during Operation
NUCLEAR ENGINEERING

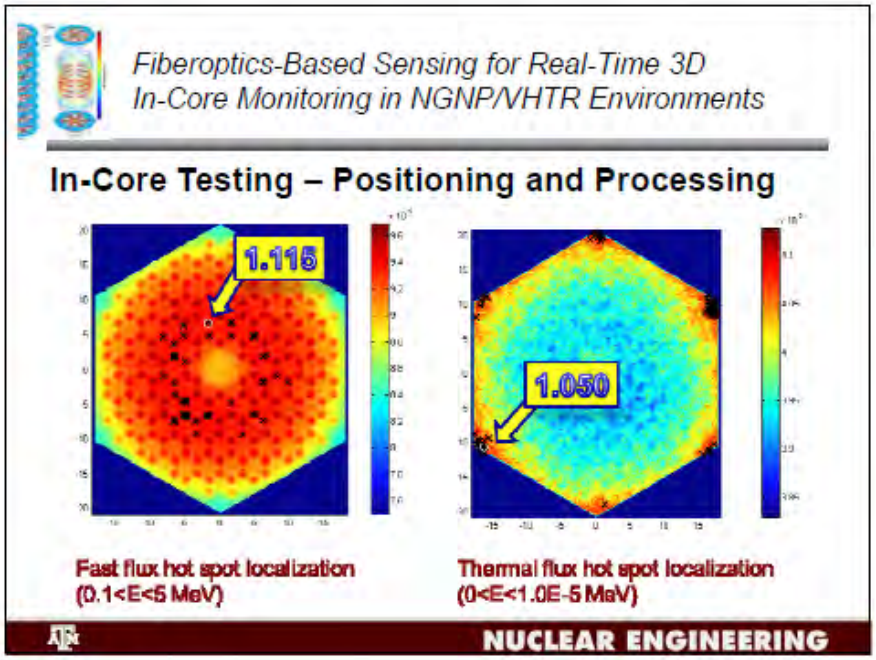
Fiberoptics-Based Sensing for Real-Time 3D
In-Core Monitoring in NGNP/VHTR Environments
In-Core Testing – Positioning and Processing
1.115
1.050
Fast flux hot spot localization
(0.1<E<5 MeV)
Thermal flux hot spot localization
(0<E<1.0E-5 MeV)
NUCLEAR ENGINEERING

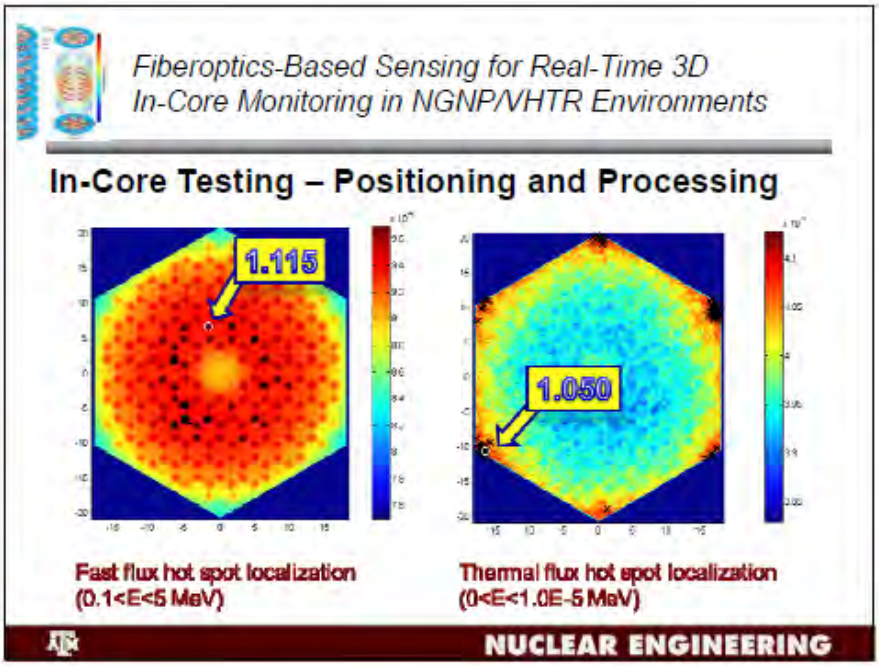
Fiberoptics-Based Sensing for Real-Time 3D
In-Core Monitoring in NGNP/VHTR Environments
In-Core Testing – Positioning and Processing
1.115
1.050
Fast flux hot spot localization
(0.1<E<5 MeV)
Thermal flux hot spot localization
(0<E<1.0E-5 MeV)
NUCLEAR ENGINEERING

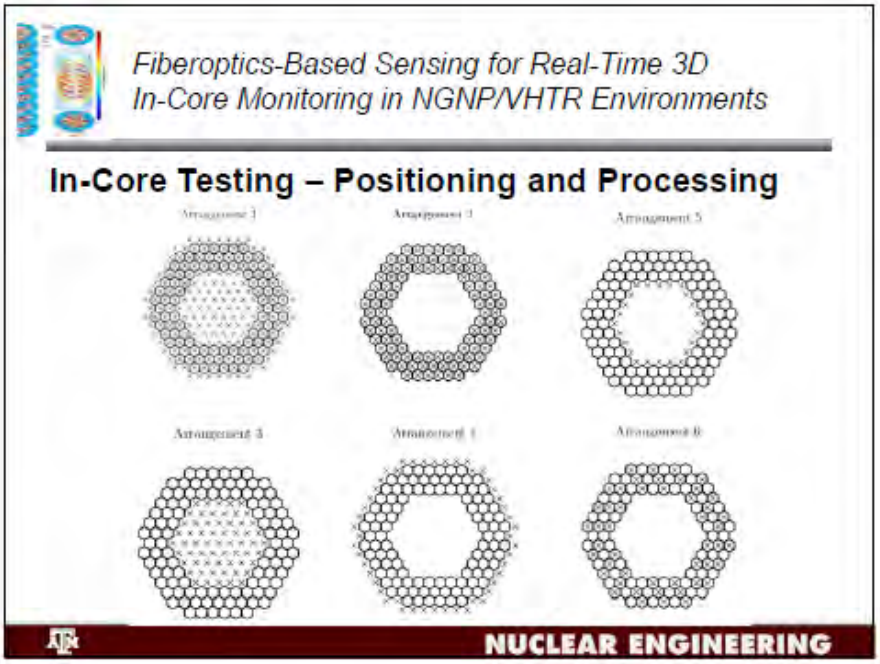
Fiberoptics-Based Sensing for Real-Time 3D
In-Core Monitoring in NGNP/VHTR Environments
In-Core Testing – Positioning and Processing
NUCLEAR ENGINEERING

Fiberoptics-Based Sensing for Real-Time 3D In-Core Monitoring in NGNP/VHTR Environments

In-Core Testing – Positioning and Processing

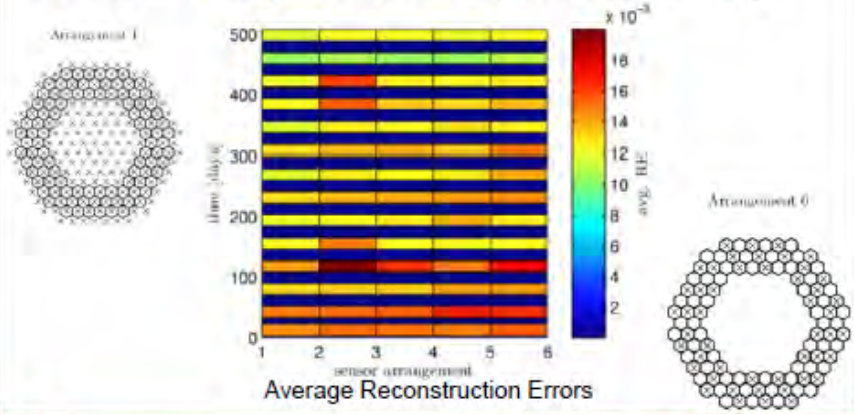

Average Reconstruction Errors

Fiberoptics-Based Sensing for Real-Time 3D In-Core Monitoring in NGNP/VHTR Environments

Conclusions

- The gained experience indicate potential opportunities for future applications, especially in the environments which would be either physically hostile or geometrically challenging for traditional sensing technologies.
- Distributed sensing allows gathering more robust data during reactor operation which is essential not only for predictive safety monitoring but also for competitive reliability and economics.
- The project was focused on NGNP/VHTR but the analyzed fiberoptics sensing and 3D in-core monitoring via distributed sensing are of paramount value for LWRs, emerging SMRs and all advanced reactors.

Fiberoptics-Based Sensing for Real-Time 3D In-Core Monitoring in NGNP/VHTR Environments

Conclusions

The noted challenges include excessive dependencies of sensing system performance characteristics on:

- vibrations due to thermo-mechanical core characteristics,
- noise effects,
- internal fiberoptics material effects,
- accompanying software components to recover and interpret measured performance characteristics,
- frequent calibration needs.

These challenges will have to be resolved in future R&D efforts.

GENERAL ATOMICS LUNA ENERGY NEUP INL

NUCLEAR ENGINEERING

Fiberoptics-Based Sensing for Real-Time 3D In-Core Monitoring in NGNP/VHTR Environments

Acknowledgements

We would like to extend our appreciation to our participating undergraduate students, Hanniel Honang Ndjomou and Carl Mullins, for the hard work and dedication to the success of the project.

GENERAL ATOMICS LUNA ENERGY NEUP INL

NUCLEAR ENGINEERING

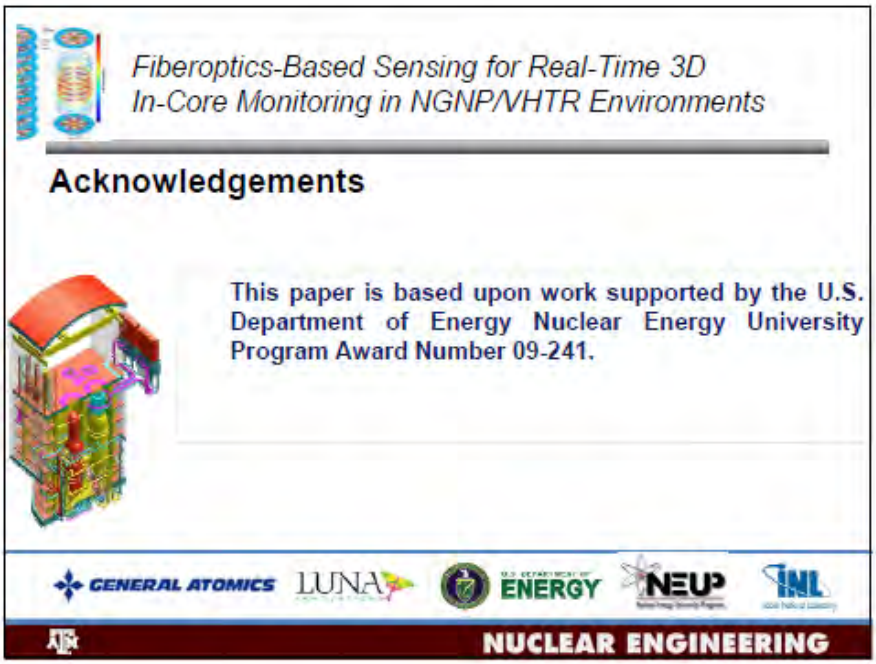
Fiberoptics-Based Sensing for Real-Time 3D
In-Core Monitoring in NGNP/VHTR Environments
Acknowledgements
This paper is based upon work supported by the U.S. Department of Energy Nuclear Energy University Program Award Number 09-241.
GENERAL ATOMICS
LUNA
ENERGY
NEUP
INL
NUCLEAR ENGINEERING

Fiberoptics-Based Sensing for Real-Time 3D
In-Core Monitoring in NGNP/VHTR Environments
QUESTIONS?
GENERAL ATOMICS
LUNA
ENERGY
NEUP
INL
NUCLEAR ENGINEERING
TEXAS A&M ENGINEERING

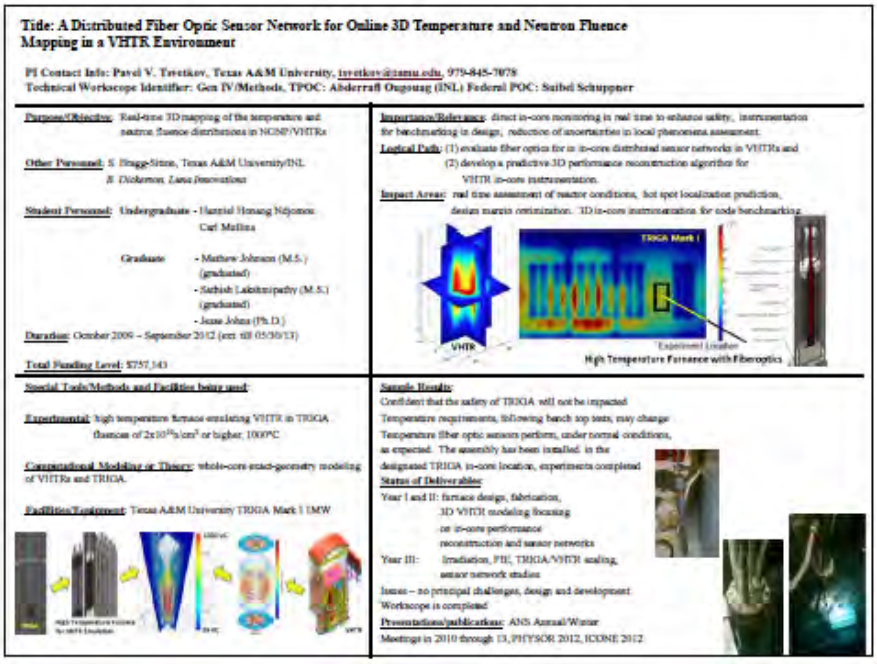

Title: A Distributed Fiber Optic Sensor Network for Online 3D Temperature and Neutron Fluence Mapping in a VHTR Environment

PI Contact Info: Pavel V. Tsvetkov, Texas A&M University, tsvetkov@tamu.edu, 979-845-7078
Technical Workscope Identifier: Gen IV/Methods, TPOC: Abderraft Ougouag (INL) Federal POC: Suibel Schuppner

Purpose/Objective: Real-time 3D mapping of the temperature and neutron fluence distributions in NGNP/VHTRs

Other Personnel: S. Bragg-Sitton, Texas A&M University/INL
B. Dickerson, Luna Innovations

Student Personnel: Undergraduate - Hannial Honang Ndjomou
Carl Mullins

Graduate - Mathew Johnson (M.S.) (graduated)
- Sathish Lakshmipathy (M.S.) (graduated)
- Jesse Johns (Ph.D.)

Duration: October 2009 – September 2012 (ext. till 05/30/13)

Total Funding Level: $757,143

Importance/Relevance: direct in-core monitoring in real time to enhance safety, instrumentation for benchmarking in design, reduction of uncertainties in local phenomena assessment.

Logical Path: (1) evaluate fiber optics for in in-core distributed sensor networks in VHTRs and
(2) develop a predictive 3D performance reconstruction algorithm for VHTR in-core instrumentation.

Impact Areas: real time assessment of reactor conditions, hot spot localization prediction, design margin optimization. 3D in-core instrumentation for code benchmarking

Special Tools/Methods and Facilities being used:

Experimental: high temperature furnace emulating VHTR in TRIGA fluences of $2x10^{13}n/cm^2$ or higher; 1000°C

Computational Modeling or Theory: whole-core exact-geometry modeling of VHTRs and TRIGA.

Facilities/Equipment: Texas A&M University TRIGA Mark I 1MW

Sample Results:
Confident that the safety of TRIGA will not be impacted
Temperature requirements, following bench top tests, may change
Temperature fiber optic sensors perform, under normal conditions, as expected. The assembly has been installed in the designated TRIGA in-core location, experiments completed

Status of Deliverables:
Year I and II: furnace design, fabrication,
3D VHTR modeling focusing on in-core performance reconstruction and sensor networks
Year III: irradiation, PIE, TRIGA/VHTR scaling, sensor network studies

Issues – no principal challenges, design and development
Workscope is completed

Presentations/publications: ANS Annual/Winter Meetings in 2010 through 13, PHYSOR 2012, ICONE 2012

Distributed Sensing

LUNA

Luna's Approach – High Definition Sensing

Regions of distributed sensing can be defined as well

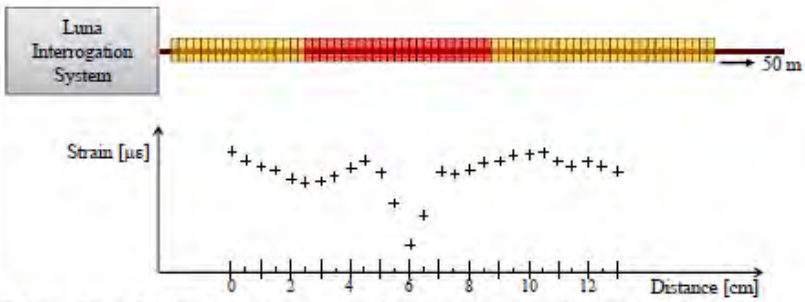

Extremely useful observing how strain changes continuously over a region

Small, localized events can be observed, where larger foil gages would have averaged, and washed out the response

LUNA

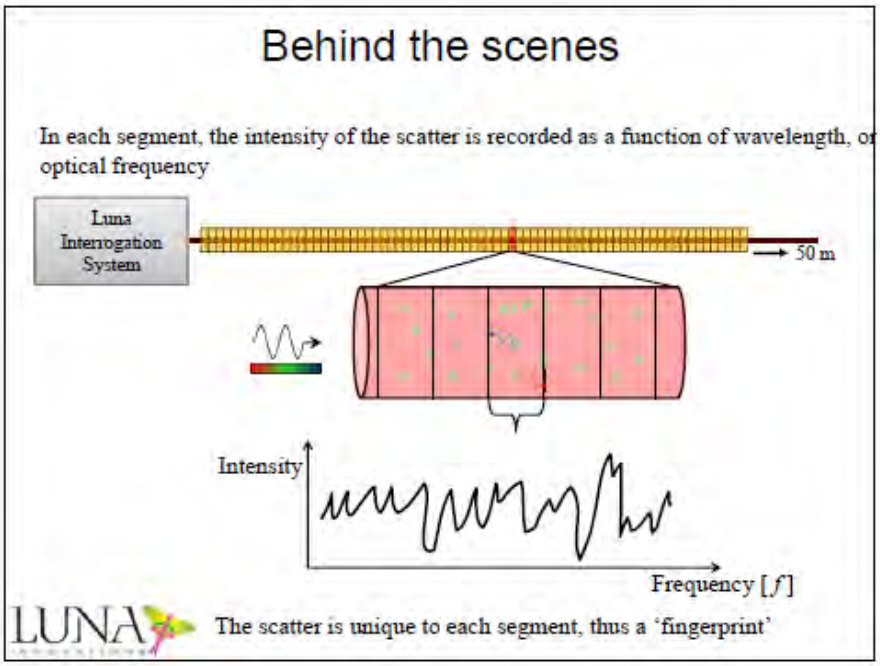
Behind the scenes
In each segment, the intensity of the scatter is recorded as a function of wavelength, or optical frequency
Luna Interrogation System
50 m
Intensity
Frequency [f]
LUNA
The scatter is unique to each segment, thus a 'fingerprint'

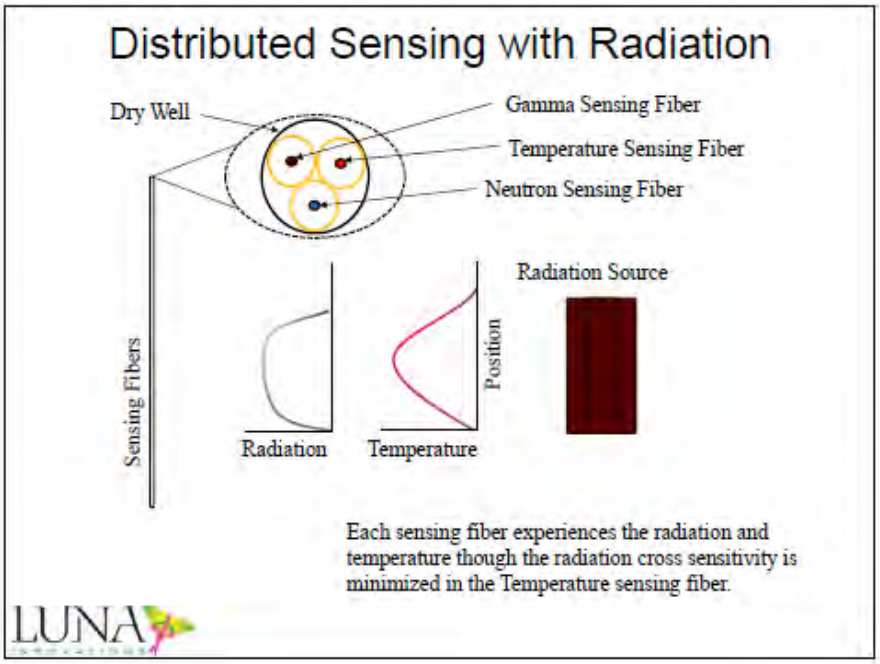
Distributed Sensing with Radiation
Dry Well
Gamma Sensing Fiber
Temperature Sensing Fiber
Neutron Sensing Fiber
Radiation Source
Sensing Fibers
Position
Radiation
Temperature
Each sensing fiber experiences the radiation and temperature though the radiation cross sensitivity is minimized in the Temperature sensing fiber.
LUNA

13.5.8. 3D Mapping and Reconstruction for In-Core Monitoring

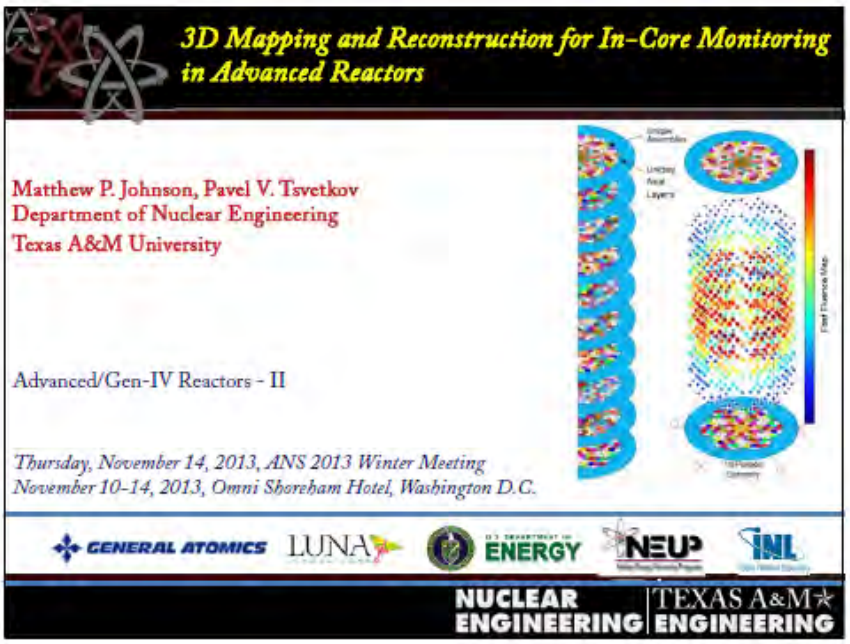

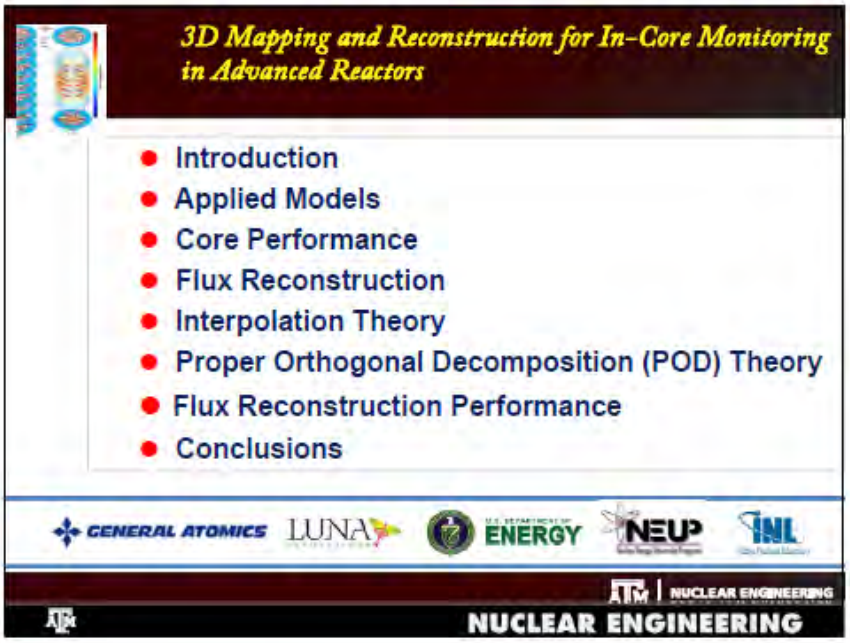

Introduction

HTR background

- Brief history of HTRs
  - DRAGON (1966): 20 MW
  - Peach Bottom (1967)
  - AVR (1967): pebble bed
  - Ft. St. Vrain (1977): full-size power reactor, shut down in 1992
- This work uses three ring VHTR based off of the INL NGNP design
- HTR advantages: flexible in their neutronic design, can be engineered to be intrinsically safe

NUCLEAR ENGINEERING TEXAS A&M UNIVERSITY

Introduction

Need for new sensors

- Potential in-core sensors include
  - Fission chambers
  - Self-powered neutron detectors (SPNDs)
  - Fiber optic sensors
- Current generation fission chambers and SPNDs are not capable of surviving for prolonged periods in the high temperature environment of HTRs
- Fiber optics can survive in high temperatures. They have been used as temperature sensors for some time; however, recently a method for using them as neutron detectors was suggested.
- Fiber optics yield significantly more data than other sensors since they record data along their entire length.

NUCLEAR ENGINEERING TEXAS A&M UNIVERSITY

Applied Models

Core overview

- Prismatic blocks stacked into a cylinder
- Graphite is used as primary structural material
- Active core region is annular
- Graphite inner reflector provides a large heat sink
- Helium selected as a coolant because it is chemically inert
- Electricity generation options: direct Brayton cycle, secondary loop with a Rankine cycle

Power	600 MWth
Fuel	UO_2
Moderator	Graphite
Coolant	Helium
Coolant pressure	7.12 MPa
Core inlet temperature	490 °C
Core outlet temperature	1000 °C
Core diameter	7 m
Core height	10.7 m

NUCLEAR ENGINEERING TEXAS A&M UNIVERSITY

Applied Models

Core Geometry

Fuel Blocks	1020 (170 unique)
Operational Control Rods	36
Startup Control Rods	12
Reserve Shutdown Channels	6
Power	600 MWth
U Enrichment	15 at. %

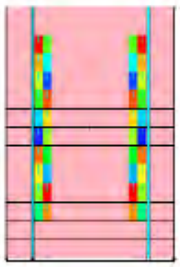

Cross-sectional views of the core. Fuel blocks are color coded according to their burnable material.

NUCLEAR ENGINEERING TEXAS A&M UNIVERSITY

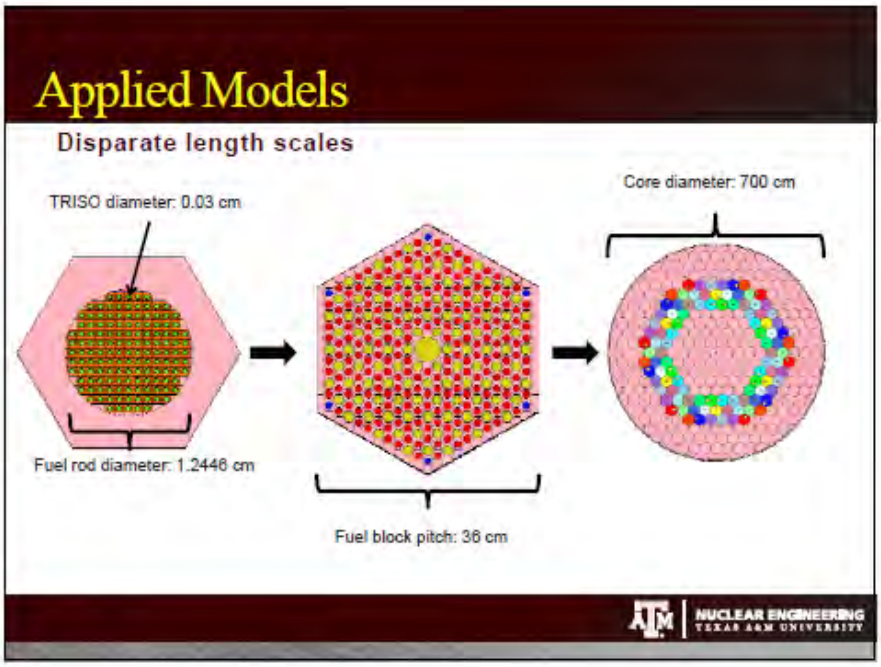
Applied Models
Disparate length scales
TRISO diameter: 0.03 cm
Core diameter: 700 cm
Fuel rod diameter: 1.2446 cm
Fuel block pitch: 36 cm
NUCLEAR ENGINEERING
TEXAS A&M UNIVERSITY

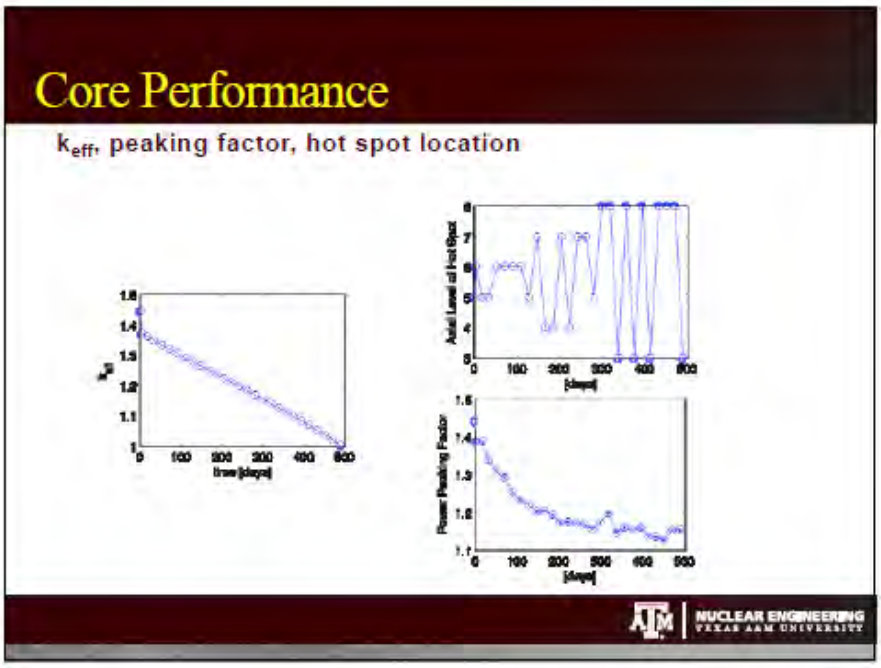
Core Performance
k_{eff}, peaking factor, hot spot location
NUCLEAR ENGINEERING
TEXAS A&M UNIVERSITY

Flux Reconstruction

Problem statement

- Given flux measurements at discrete locations within the reactor, can the full flux distribution to reconstructed?
- Fiber optic sensors run the full length of the core, so measurement in z is continuous

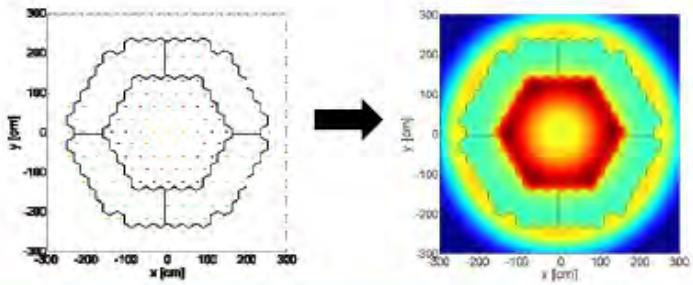

NUCLEAR ENGINEERING
TEXAS A&M UNIVERSITY

Flux Reconstruction

Goals

- Accurate reconstruction of the full-core thermal neutron flux with special emphasis on the location and magnitude of the neutronic hot spot
- norm of error in hot spot location $= \|\vec{x}_{recontructed} - \vec{x}_{actual}\|_2$
- reconstruction residual $= |A_{reconstructed} - A_{actual}|$
- relative error $= \frac{|A_{reconstructed} - A_{actual}|}{A_{actual}}$
- percent error in $\phi(\vec{x}_{hot}) = \frac{\phi_{reconstructed}(\vec{x}_{hot}) - \phi_{actual}(\vec{x}_{hot})}{\phi_{actual}(\vec{x}_{hot})} \times 100$
- error in hot spot z coordinate $= z_{actual} - z_{predicted}$
- Two different algorithms were investigated: interpolation and POD

NUCLEAR ENGINEERING
TEXAS A&M UNIVERSITY

Interpolation Theory

Overview

- Interpolation is the most straightforward method, but how accurate is it?
- Sensor locations will be related to the hexagonal lattice.
- Interpolation on unstructured grids

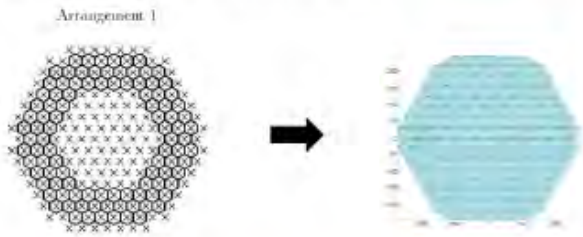

NUCLEAR ENGINEERING
TEXAS A&M UNIVERSITY

Interpolation Theory

Summary

- Construct a mesh whose simplexes are located at the flux measurement locations and interpolate.
- Mesh generation algorithms abound; however, Delaunay triangulations work just fine.
- Barycentric coordinates are commonplace in computational geometry, thus there is plenty of existing software that does the aforementioned calculations. In this work Matlab was used.

NUCLEAR ENGINEERING
TEXAS A&M UNIVERSITY

POD Theory

Proper orthogonal decomposition

- Has connections to image compression*

- In engineering, often used in conjuction with Galerkin projection to form low order models
- **Used to analyze time-series data**

* source: David Amsallem & Charbel Farhat, Stanford University, CME 345 class notes

NUCLEAR ENGINEERING TEXAS A&M UNIVERSITY

POD Theory

Proper orthogonal decomposition

- Given time-series data, POD can be used to represent this data in the following form:

$$\phi(\vec{x},t) = \sum_{k=1}^{M} a_k(t)\psi_k(\vec{x})$$

- The POD modes, ψ_k, sometimes referred to as empirical eigenfunctions, are found with the singular value decomposition. Data from *m* spatial locations at *N* different times are stored in matrix in *Nxm* matrix **A**. Taking the singular value decomposition:

$$A = U\Sigma V^T$$

- *U* is an *NxN* orthogonal matrix, *Σ* is an *Nxm* matrix whose only nonzero elements lie on its diagonal, and *V* is an *mxm* orthogonal matrix.
- The columns of V are used as the POD modes.

NUCLEAR ENGINEERING TEXAS A&M UNIVERSITY

POD Theory

Gappy reconstruction

- Sensors only measure a small subset of the data. How to accurately find all a_k?
- Previous researchers have called this gappy reconstruction
- Let Φ be a vector that contains the scalar flux at all locations in the domain at a moment in time. Let n be a mask vector, the same size as Φ, that contains 1 at sensor locations and 0 elsewhere.
- The data from the sensors is then (n, Φ), where $(\cdot,\cdot)$ represents pointwise multiplication.
- Define the gappy inner product

$$(a, b)_n = [(n, a), (n, b)]$$

- And the gappy norm

$$\|a\|_n^2 = (a, a)_n$$

NUCLEAR ENGINEERING TEXAS A&M UNIVERSITY

POD Theory

Gappy reconstruction

- Given a set of gappy data, $g = (n, \Phi)$, find a reconstructed field, , from the POD basis

$$\tilde{g} \approx \sum_{k=1}^{M} a_k \psi_k$$

- Seek $\tilde{g}$ that minimizes:

$$\|g - \tilde{g}\|_n^2$$

- The above expression is differentiated w.r.t. each a_k to yield the following system of equations

$$Ma = f$$

where $M_{ij} = (\psi^i, \psi^j)_n$ and $f_i = (g, \psi^i)_n$

- Solve for a, calculate $\tilde{g}$, use $\tilde{g}$ to fill in missing entries from g

NUCLEAR ENGINEERING TEXAS A&M UNIVERSITY

Flux Reconstruction Performance

FOMs

Review the FOMs used to quantify reconstruction algorithm performance

- norm of error in hot spot location = $\|\vec{x}_{recontructed} - \vec{x}_{actual}\|_2$
- reconstruction residual = $|A_{reconstructed} - A_{actual}|$
- relative error = $\frac{|A_{reconstructed} - A_{actual}|}{A_{actual}}$
- percent error in $\phi(\vec{x}_{hot})$ = $\frac{\phi_{reconstructed}(\vec{x}_{hot}) - \phi_{actual}(\vec{x}_{hot})}{\phi_{actual}(\vec{x}_{hot})} \times 100$
- error in hot spot z coordinate = $z_{actual} - z_{predicted}$

These FOMs are calculated at each time step. In order to make visualization and comparison easier, they may be averaged over time. For FOMs that may be positive or negative, the absolute value is taken before averaging.

These FOMs can be calculated for the whole core flux or just the flux in the active core region

NUCLEAR ENGINEERING TEXAS A&M UNIVERSITY

Flux Reconstruction Performance

Interpolation

- In order to test the interpolation algorithm, sensors were placed in all blocks of the inner reflector, all blocks of the active core, and one ring of the outer reflector.
- Within each block, six different sensor configurations were considered:

Configuration	Pitch [cm]
A	0.0
B	3.25563
C	6.511125
D	8.138907
E	11.39447
F	13.02225

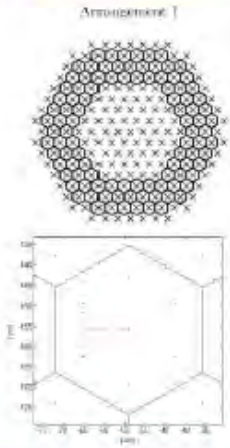

NUCLEAR ENGINEERING TEXAS A&M UNIVERSITY

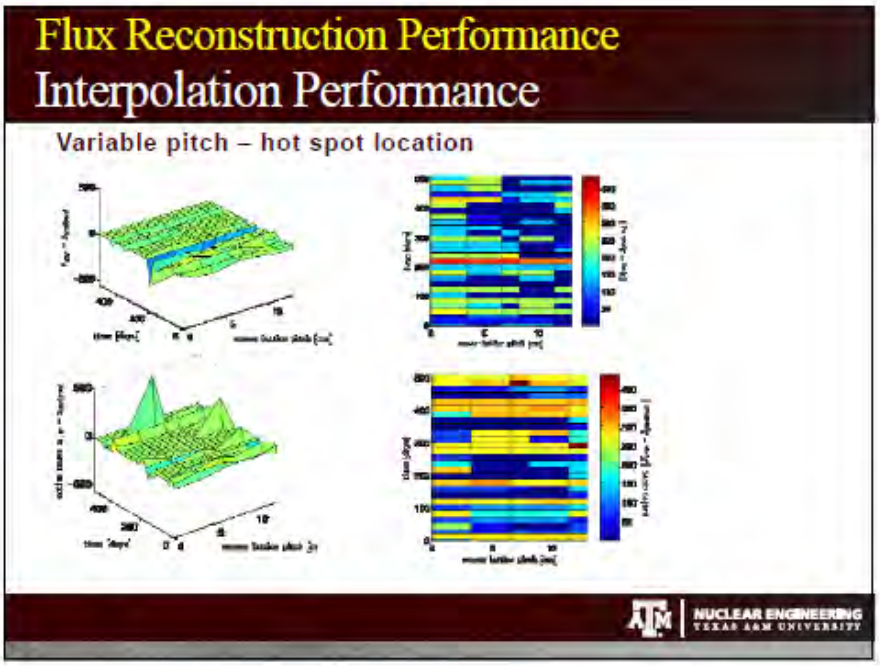
Flux Reconstruction Performance
Interpolation Performance
Variable pitch – hot spot location
NUCLEAR ENGINEERING
TEXAS A&M UNIVERSITY

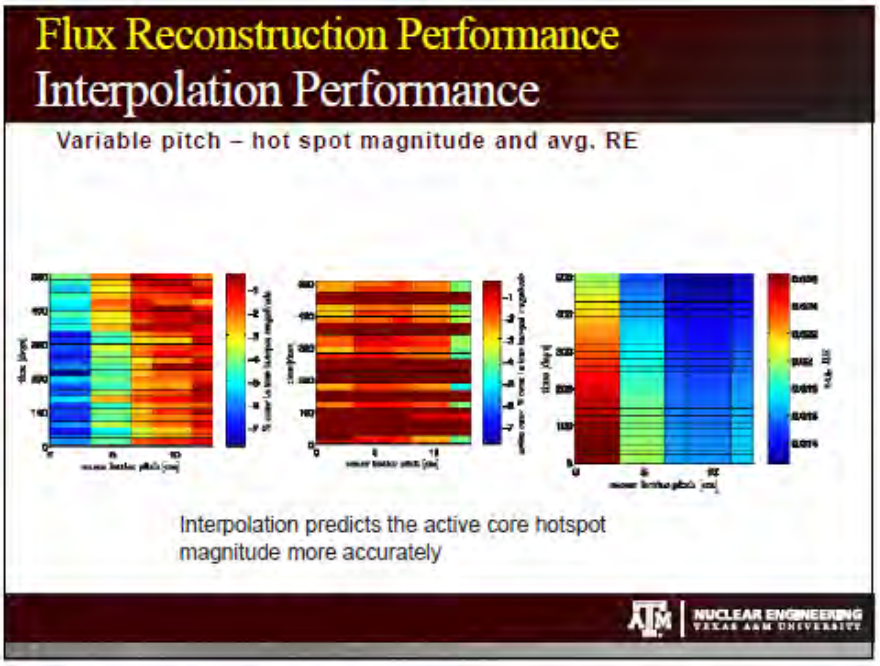
Flux Reconstruction Performance
Interpolation Performance
Variable pitch – hot spot magnitude and avg. RE
Interpolation predicts the active core hotspot
magnitude more accurately
NUCLEAR ENGINEERING
TEXAS A&M UNIVERSITY

Flux Reconstruction Performance
POD Performance

POD modes

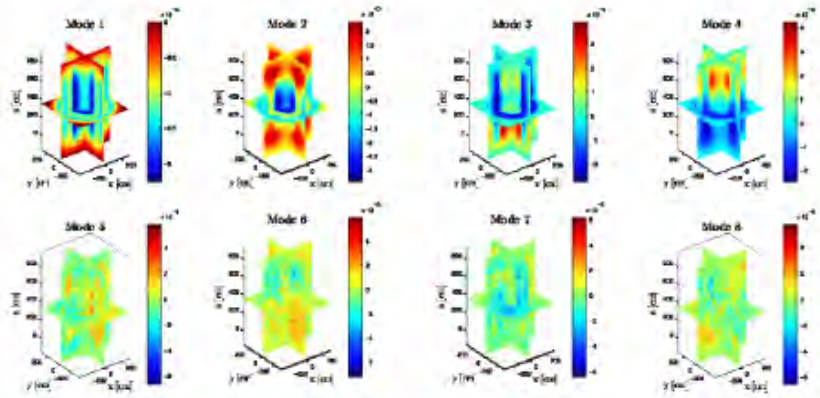

NUCLEAR ENGINEERING
TEXAS A&M UNIVERSITY

Flux Reconstruction Performance
POD Performance

Singular values

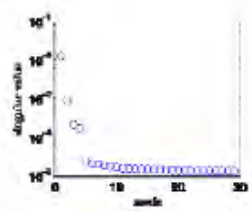

Singular values decrease in magnitude rapidly before leveling off. There is a noise floor in the data due to the Monte Carlo solution method.

NUCLEAR ENGINEERING
TEXAS A&M UNIVERSITY

Flux Reconstruction Performance
POD Performance

Number of modes used in reconstruction

- Vary number of POD modes used during the reconstruction.
- Two cases: all time steps to create the POD basis, half of the time steps used to create the POD basis

$$A = U\Sigma V^T$$

- The second test case is important because in reality, the flux distribution in the reactor will not be an exact match to one of the simulation results

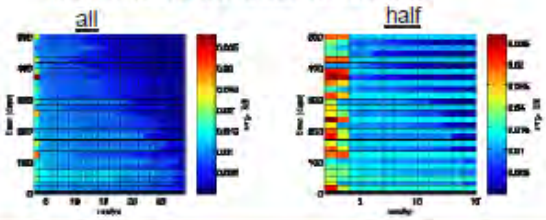

NUCLEAR ENGINEERING
TEXAS A&M UNIVERSITY

Flux Reconstruction Performance
POD Performance

Number of modes used in reconstruction

- As expected, using all modes perfectly reconstructs the data
- In reality, the in core flux distribution will not be a perfect match to one of the snapshots used to generate the POD basis. This is simulated by only using half (every other) snapshot when generating the POD basis.
- Only using half of the modes still outperforms the interpolation based reconstruction, especially in the % error in true hotspot magnitude FOM
  - POD results only compare directly to the interpolation results for the zero-pitch arrangement.
- All remaining POD reconstruction results use the POD basis generated from half the data

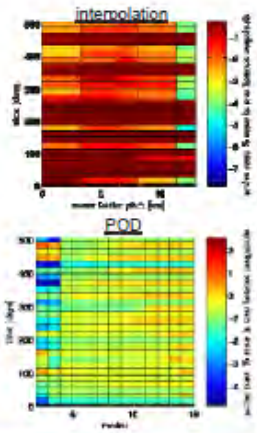

NUCLEAR ENGINEERING
TEXAS A&M UNIVERSITY

Flux Reconstruction Performance
POD Performance

POD different sensor arrangements

- The high accuracy of the POD method using a single sensor at each block center suggests that even fewer sensors could be used

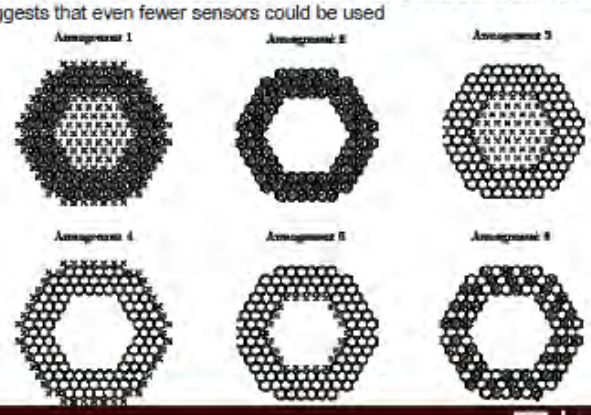

NUCLEAR ENGINEERING
TEXAS A&M UNIVERSITY

Flux Reconstruction Performance
POD Performance

POD different sensor arrangements

- Reconstruction algorithm run using all 15 modes of the half snapshot POD basis
- From the avg. RE FOM, it is clear that all perform similarly. This is in contrast the interpolation algorithm where simply changing the sensor pitch adjusted the average RE by ~1%

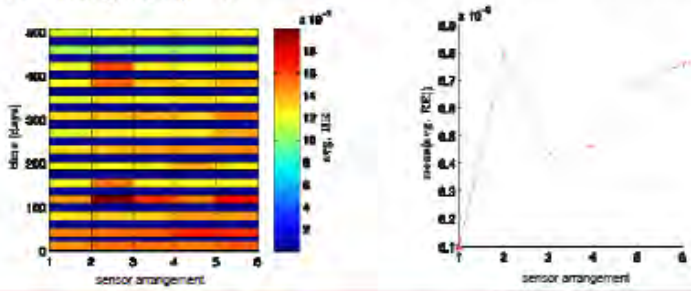

NUCLEAR ENGINEERING
TEXAS A&M UNIVERSITY

Flux Reconstruction Performance
POD Performance

Summary of results for different sensor arrangements

- There isn't a big difference in any of the FOMs
- Once again, the z coordinate of the hot spot is predicted very well, but it's (x,y) coordinates are not.
- Interesting that arrangement 1 does clearly perform better than the others, even though it contains the most instrumented blocks
- While the margins are slim, arrangements 3 and 5 reproduce the true hot spot's magnitude most accurately.

NUCLEAR ENGINEERING TEXAS A&M UNIVERSITY

Flux Reconstruction Performance

Noise and sensor failure

- What happens when there is noise?
- Uniform noise was added to the sensor signals

$$\Phi_{noisy} = \Phi + \alpha .* n .* \pi .* \Phi$$

where " .* " indicates point-wise multiplication, Φ is a mx1 matrix containing the flux measurements, α is a mx1 matrix whose entries individually randomly chosen to be 1 or -1, n is the error to be introduced by the noise, and π is a mx1 matrix of random values between 0 and 1

- Interpolation algorithm was run using sensor arrangement 1 with pitches A and E
- POD algorithm was run using sensor arrangement 5, but with a varying number of modes

NUCLEAR ENGINEERING TEXAS A&M UNIVERSITY

Flux Reconstruction Performance
Noisy Reconstruction

Avg RE

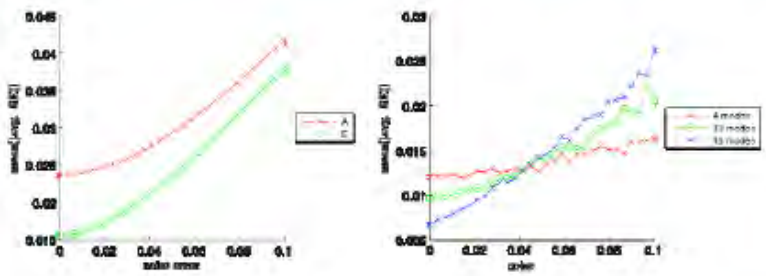

NUCLEAR ENGINEERING
TEXAS A&M UNIVERSITY

Flux Reconstruction Performance
Noisy Reconstruction

Conclusions

- The POD method clearly outperforms the interpolation method in the avg. RE and true hot spot magnitude FOMs
- They perform similarly on the hot spot location error metrics. Small levels of noise (< 3%) have almost no effect on POD reconstruction, but after that threshold reconstruction error increases.
- Regarding the number of POD modes used: reconstructions using fewer modes are less effected by noise, but have initially lower accuracy.

NUCLEAR ENGINEERING
TEXAS A&M UNIVERSITY

Flux Reconstruction Performance

What if sensors fail?

- Sensors were failed deterministically, according to their closeness to the true hot spot location
- Cases were run for POD using all 15 modes from the half snapshot basis
  - All sensor configurations were tested
- Cases for interpolation were not run because interpolation clearly fails as it has no way of filling in the lost data

NUCLEAR ENGINEERING TEXAS A&M UNIVERSITY

Flux Reconstruction Performance
Sensor Failure

Conclusions

- Sensor failure does not have a large effect on the performance of the POD algorithm.
- Sensor arrangements using even few sensors could be considered.

NUCLEAR ENGINEERING TEXAS A&M UNIVERSITY

Summary/Conclusions

- Interpolation and POD were investigated as flux reconstruction techniques because they do not rely on diffusion models
- POD appears to have better performance, although it relies in pre-computed snapshots of the neutron flux. The accuracy of the POD method would degrade rapidly if the reactor flux distribution was significantly different than the snapshots.
- The exact location of the hot spot is hard to predict. Due to core symmetry there should be 6 locations in the core that contain the hot spot. In a real system stochastic phenomena would remove the perfect symmetry in the flux distribution. In a Monte Carlo simulation, the stochastic solution process removes the perfect symmetry.
  - All 6 theoretical hot spots would have the same z coordinate. The reconstruction algorithms are effective at predicting the z coordinate.

NUCLEAR ENGINEERING
TEXAS A&M UNIVERSITY

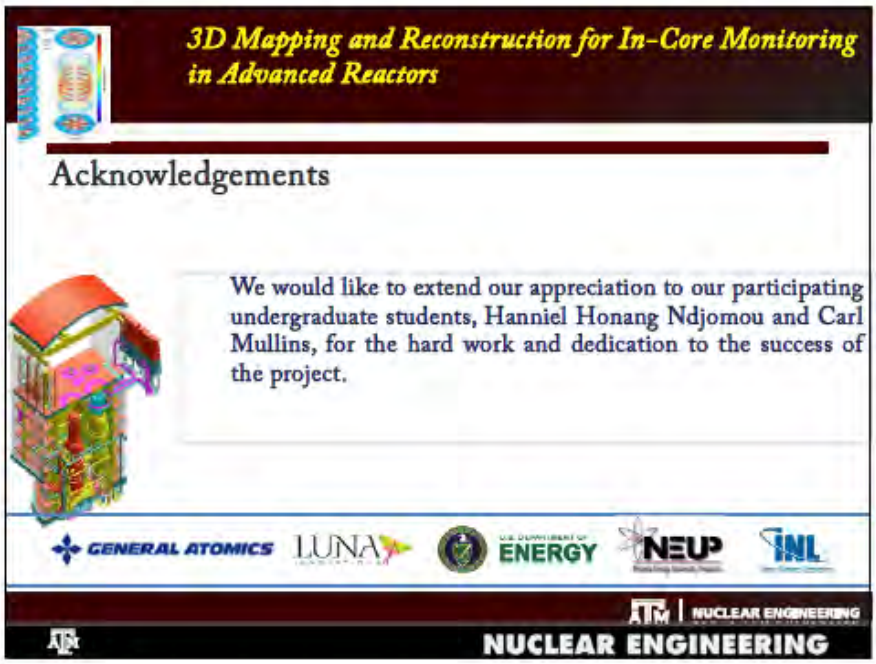

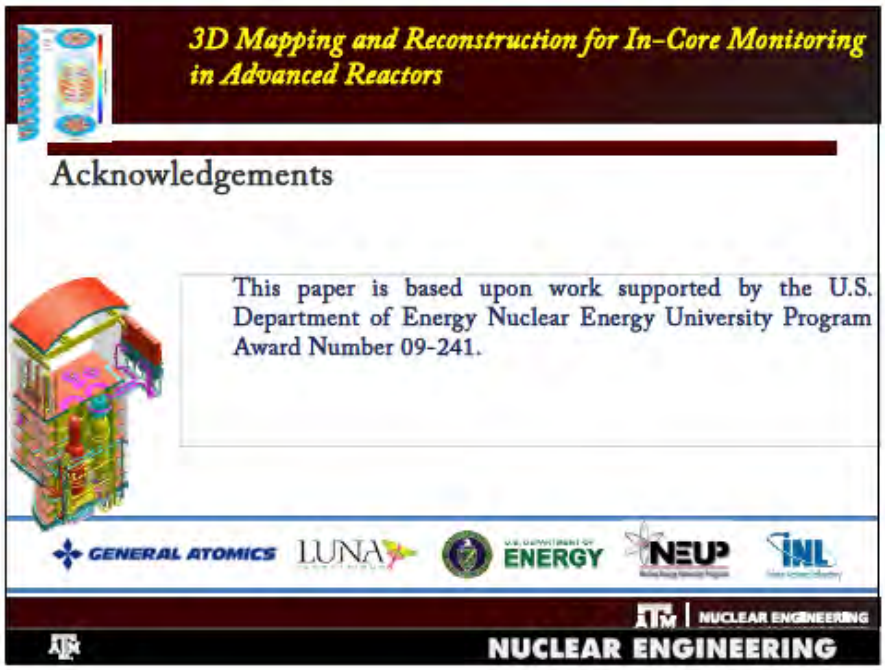
3D Mapping and Reconstruction for In-Core Monitoring in Advanced Reactors
Acknowledgements
This paper is based upon work supported by the U.S. Department of Energy Nuclear Energy University Program Award Number 09-241.
GENERAL ATOMICS
LUNA
ENERGY
NEUP
INL
NUCLEAR ENGINEERING
NUCLEAR ENGINEERING

3D Mapping and Reconstruction for In-Core Monitoring in Advanced Reactors
QUESTIONS?
GENERAL ATOMICS
LUNA
ENERGY
NEUP
INL
NUCLEAR ENGINEERING
TEXAS A&M ENGINEERING

3D Mapping and Reconstruction for In-Core Monitoring in Advanced Reactors
THANK YOU
GENERAL ATOMICS
LUNA
U.S. DEPARTMENT OF ENERGY
NEUP
INL
NUCLEAR ENGINEERING
TEXAS A&M ENGINEERING

13.6. Safety Analysis for In-Core TRIGA Furnace

This analysis was completed by Mr. Jesse M. Johns, graduate student and Ph.D. candidate at Texas A&M University, Department of Nuclear Engineering.

The report was submitted to the Texas A&M University Nuclear Science Center Reactor Safety Board for review in support of the project experimental program.

Following the successful review process, the experimental program was approved, conducted and completed as described in this report.

List of Figures

Figure 1: Schematic of the TRIGA King furnace [7]
Figure 2: A schematic of the nuclear science center reactor core
Figure 3: SolidWorks representation of the furnace design prior to fabrication.
Figure 4: Time to rupture for Al 6061 T6 at 260C as a function of pressure
Figure 5: Over pressure system on the void tube
Figure 6: STAR-CCM+ geometry (left) and numerical mesh (right)
Figure 7: View of graphite heater with thermocouple instrumentation and setup in vacuum chamber.
Figure 8: Resistivity as a function of average graphite temperature
Figure 9: Simulated furnace with expected system temperature distributions.
Figure 10: XY cross-section of MCNP geometry (left) and the XZ cross-sectional view (right)
Figure 11: Neutron energy distribution within peak-flux fiber location within experiment with D1 normalized to fast flux
Figure 12: View of internal of furnace without fiber optic probe
Figure 13: Thermocouple and fiber optics measurement accuracy test (notice ice cup on left)
Figure 14: Temperature distribution as measured by the fiber optic for the experimental test
Figure 15: View of the bike pump connection of the left and pressure transducer on the right
Figure 16: Linear pressure calibration curve for one of three transducers
Figure 17: Cap with final power-lead design, which includes brazing and socket-like inserts
Figure 18: MATLAB plot of temperature recording of thermal stress test
Figure 19: Cross-sectional view of fiber optics probe
Figure 20: View of fiber optic containing ferrules during fabrication stages

List of Tables

Table 1: Tabulated thermophysical data used in calculations
Table 2: Final design parameters of furnace
Table 3: Comparison of some STAR-CCM+ calculated values to experimentally measured values
Table 4: Power (W) generated by each fuel element in the fuel bundles. Red, blue, and gray indicate furnace, water, and graphite locations respectively.
Table 5: Reactivity insertions for various postulated configurations
Table 6: Parameters of GA and TAMU furnace builds, comparing only to what is available for the GA design

1 Introduction

Reactor core monitoring is often plagued by restrictions on instrumentation systems development. The harsh temperature and radiation environment imposes significant engineered material challenges, especially in the proposed Very High Temperature Reactors [1,2]. There are also substantial geometrical limitations on the use of conventional systems. The sheer size of the detector and power/signal cabling requires large penetrations and special constraints for use of those detectors.

Fiber optic instrumentation technologies for reactor environments have recently emerged at the levels of maturity allowing in-core exploratory testing. These can potentially relieve concerns of the radiation and temperature environment and provide the capability to enter, with a very small footprint/cross-section, nearly any geometrical configuration for continuous, distributive detection of neutron, gamma, and temperature measurements [3]. These have already been in use for some time in measuring temperature and strain along a continuous path for other applications. Without going into the details of this form of measurement, it is the objective of this DOE NEUP funded project to test these fiber optics in an environment similar to those found in gas-cooled very high temperature reactors such as those proposed for NGNP [4,5,6]. This requires a high temperature environment with high neutron and gamma radiation fields, in which their usability has already been demonstrated for low temperatures.

Achieving the high temperatures within a reactor environment, namely the Texas A&M University's Nuclear Science Center, requires a heated irradiation device. Therefore, a furnace was designed for use within the TRIGA reactor core for continuous operation at power without impact to the safety of the reactor core, fuel cladding, and the facility personnel.

This safety analysis report provides the safety case and justification for the "Distributed Fiber Optic Sensor Network for Online 3D Temperature and Neutron Fluence Mapping in a VHTR Environment" project. It is proposed to test these fiber optic sensors at 1000°C as they are irradiated in the Nuclear Science Center (NSC) TRIGA reactor. The required neutron and gamma fluences for the testing of the fiber optic are $2*10^{15}$ n/cm^2 and 87 Grad. The NSC reactor has relatively low neutron flux, measured to be between $3*10^{12}$ and $4*10^{13}$ n/cm^2; consequently, the test article must be irradiated for a significant amount of time. The experiment is scheduled to be in operation for an entire year, ideally, from one maintenance period to the next. However, the experiment end in May 2013. For this test, a furnace must be designed to operate in a pool environment for said amount of time and must not affect the integrity of the fuel cladding or phase of the surrounding coolant.

2 Overview

The furnace design concept borrows from the TRIGA King furnace developed by General Atomics, shown in Figure 1, for use in the Mark I TRIGA reactor [7]. This particular furnace is used for irradiation of small fuel samples at high temperature up to 1800°C in a single fuel element location. See Figure 2 for a core schematic. The King furnace requires active cooling systems, supplied by a helium port, and there are no available testing locations or penetrations that are sufficient for fiber optic test species. A new furnace design was developed which accommodates passive cooling through radiative and free-convective heat transfer. In additional, the proposed furnace design employs more spatial availability for irradiation samples. Like the King furnace, there are thermal shields in the proposed design; however, lacking molybdenum availability imposed niobium instead. Table 6 in the Appendix provides a characteristic overview over both furnace concepts.

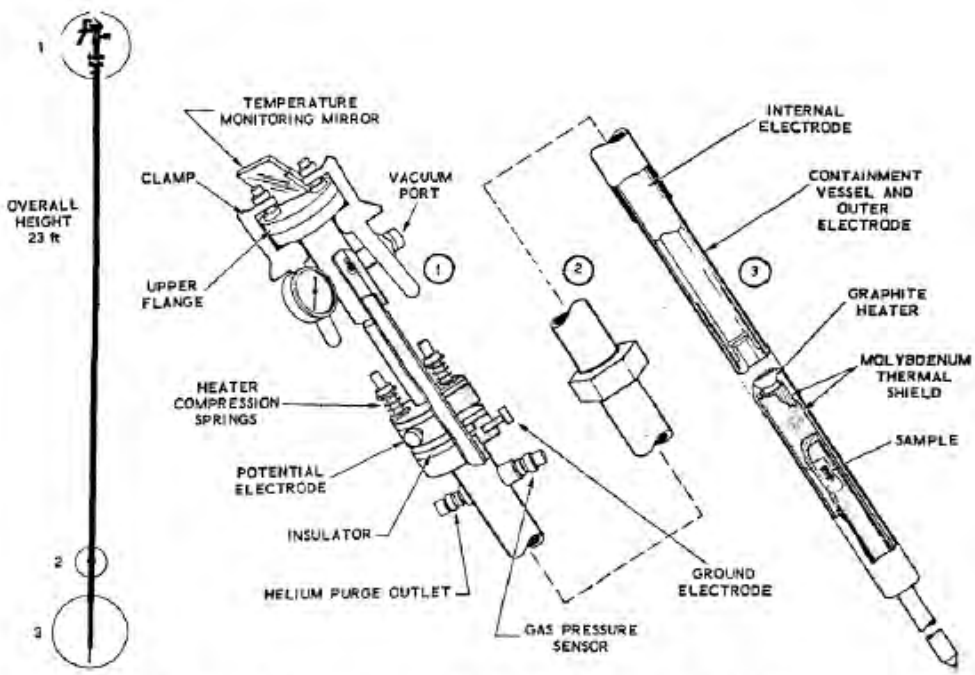

Figure 1: *Schematic of the TRIGA King furnace [7].*

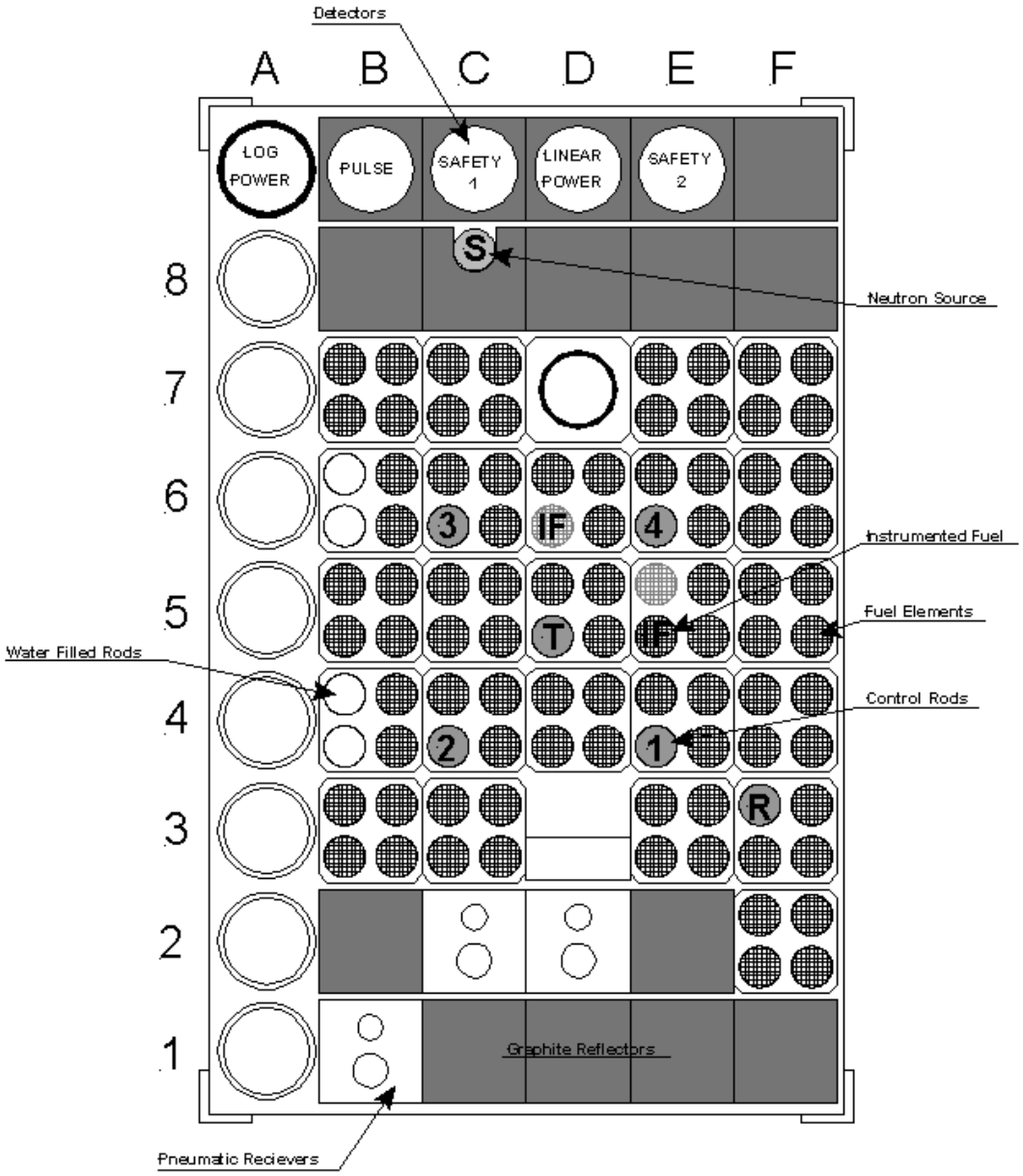

Figure 2: *A schematic of the nuclear science center reactor core.*

Note: Each core location is designated by cluster location (e.g., 5C) and by one of four positions in the cluster. See the following example:

In Figure 3, the furnace assembly is shown. The fiber optic probe, which is constructed by Luna Innovations, is at the radial centerline of the furnace. The probe consists of a 1/4" niobium tube and houses four quartz ferrules for supporting the fiber optics. Each ferrule contains four fiber optic sensors (see Figures 19 & 20 in the Appendix). Surrounding the probe is a custom designed graphite resistive heater fabricated by Poco Graphite. Two molybdenum connections are threaded and epoxied into the graphite with Durabond 950 from Cotronics. These are silver-soldered to 1/4" copper power leads, purchased from Kurt Lesker, providing both structurally and electrically robust contacts. The power leads are "soldered" to the

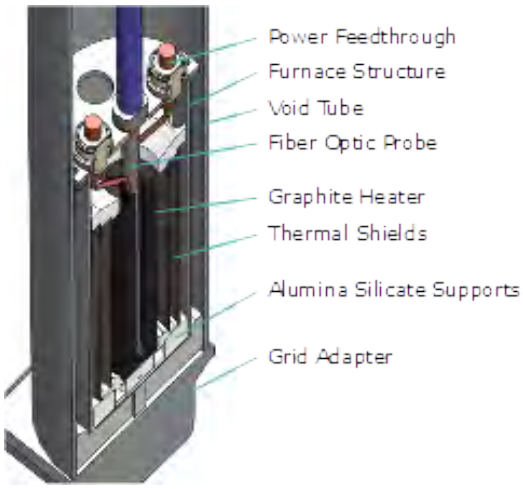

Figure 3: *SolidWorks representation of the furnace design prior to fabrication.*

element cap with Alumiweld, which is widely available. Radially outward from the graphite heater, are two custom niobium thermal shields. These are purchased from Admat and are supported concentrically via an alumina support from Cotronics. Completing the furnace is the vacuum boundary (Furnace Structure) and thermocouple feedthroughs (not shown) fabricated by Conax Buffalo. The furnace element cap is machined and fabricated with a lead gasket groove and the lead gasket is made by melting pure lead into that groove. All sealing surfaces are then smoothed and polished to provide maximum sealing capability.

The void tube completes the whole furnace by providing the pressure boundary against the water and the ultimate boundary against damaging fuel. The diameter of the void tube is limited to a single reactor grid location. Grafoil thread sealant is used exclusively for all threaded connections expected to be within the radiation field. Alumina paste, Resbond 920 from Contronics, is used for connecting thermocouples to the graphite heater. The grid adapter is hollow and filled with lead to bring the entire furnace assembly to a neutrally buoyant condition within the reactor pool.

In Figure 2, the proposed furnace locations are D1 and E2. These locations are determined by various criteria: maintaining the highest possible flux while not affecting reactor operation, experimental locations, and detector response.

The primary design constraints imposed on this system are:

- internal operating temperature of 1000°C
- external operating temperature less than 524°C
- void tube outer diameter for 3.25 in.

The parameters that were determined:

- void tube and furnace structure tube wall thickness
- furnace and void tube height
- graphite heater cross-section and positioning
- thermal shield material, size, and number
- wire gauge

The rest of the design followed simply as a to support the furnace and various safety systems.

3 Engineered Safety Systems

With a system of this nature within a reactor core, there is concern for the safe operation of the reactor. Successfully deploying a high temperature pressure vessel in operation to neighboring reactor fuel can be a daunting task.

In considering the safety margins provided by a larger experimental location, the original concept of using a fuel element location (the approach used by General Atomics with the King TRIGA furnace) was scrapped in favour of a grid location. This increase in available space allows for the implementation of a void tube. The void tube serves several functions. The first is to provide a secondary pressure boundary for the furnace to prevent damage to fuel. Additionally, the void tube displaces water to help bolster a fast neutron flux for a closer comparison to the desired reactor environment of the Very Higher Temperature Reactor (VHTR). Finally and least obvious, the increase in space allows for more instrumentation to be installed for better monitoring of the system.

The void tube is pressurized with helium above the hydrostatic pressure to prevent water leakage into the furnace; the leakage of helium can be used to monitor the integrity of the tube during the irradiation. All of the related safety systems and limits are established to maintain the integrity of the void tube.

3.1 System Limits

System design requires that safety limits are established and adhered to throughout the design process. It is imperative that the safety limits reflect the allowed operational constraints to prevent the failure of the engineered system for probable modes of failure.

3.1.1 Pressure

Limits on the operational pressure and temperature of the furnace are implemented to prevent any lose of integrity to the system. Pressure is limited in both high-pressure and low-pressure states.

The low-pressure limit, of 25 psig, is the hydrostatic pressure at the bottom of the void tube. If pressure drops below 25 pisg, the furnace will automatically shutdown. This low pressure condition is expected if the main helium supply empty, valves are not properly aligned, or leakage is not adequately replenished by the main supply due excessive leakage out through a stuck-open relief valve, or any number of leaking opportunities. As illustrated through the report, prevention water ingress is the primary concern due to potential steam production; however, the introduction of air also an issue because of the reaction with graphite to form carbon monoxide. Consequently, this will degrade the graphite heater performance. All gases are exhausted to the central exhaust, so carbon monoxide is not a biological issue.

The failure pressure of the void tube is calculated to be 545 psig (with a safety factor of 3.5); however, due to the many fitting limitations on the over-pressure system, the relief pressure is set to 55 psig. There are various relief valves implemented to preclude reaching this pressure, see the later section on this. The high-pressure relief condition is expected to be reached during startup conditions of the furnace, changes in environmental temperature, or if there is vaporization within the void tube. If pressure is unable to be maintained, a pressure setting of 65 psig for automatically shutting down the furnace has been implemented.

Automatic shutdown of the furnace can not be ensured by digital control systems, so pressure switches are implemented on the void tube pressure side that at capable of opening a relay on the 3-phase power to the power supply. The relay is normally open and power to the replay is supplied through a series circuit with the pressure switches. This ensures that any one off-condition will cause furnace to shutdown.

3.1.2 Temperature

Currently, without a fabricated furnace to verify modeling, there are three temperature limitations implemented. The first of these is the peak graphite heater temperature, which is measured by thermocouples installed directly on the resistive heater. The other three limitations are of minor safety concern: the furnace wall temperature, and the element cap temperature.

The graphite temperature indicates the operating temperature of the furnace and therefore the total thermal storage of the system. While 1000°C operation is the design limit, operation of the graphite at 1252°C would indicate that the thermal storage in all structures would be great enough to cause a water-steam rupture of the void tube, see later section for more details. Due to possible modeling errors due to various unknown contact resistances, emissivities, etc., the limitation is set to 1152°C to provide sufficient protection for the system and allow for heat temperature over-shoot.

The furnace wall temperature limitation is in place as a results of potential thermal creep in the structural material used for the furnace – Aluminum 6061-T6. This limitation is 50% of the absolute melting temperature, which is imposed since the void tube and furnace will have a pressure differential of 1 atm and 3 atm, respectively. The melting temperature is 587.8°C which corresponds to a creep limit at 430°C. This limitation is fairly arbitrary since thermal and radiation induced creep limitations are somewhat application specific rules of thumb. Reference 8 indicates, with some extrapolation, that the failure time at 1MPa pressure differential and 260°C will result in a creep rupture in 1.37e6 hours or 57083 days, see Figure 4. This extrapolated failure time is an exponential fit. Therefore, It is expected that this will not be a realizable failure mode. Favorably, irradiation effects on Al-6061 will improve the stress resistance characteristics [9].

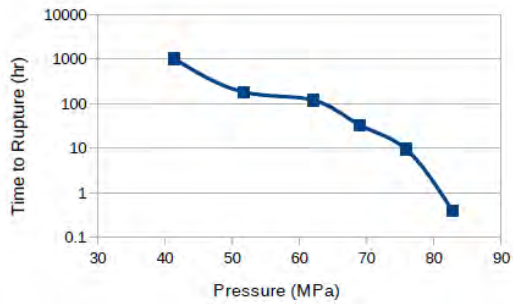

Figure 4: *Time to rupture for Al 6061 T6 at 260C as a function of pressure.*

The furnace cap temperature limitation is applied to protect the fiber optic probe. The probe feedthrough has a limitation of 150°C. The lead gasket melting temperature is roughly 327°C, so this is not a limiting condition. It is not expected that the cap will reach 150°C.

All of the temperature limitations are enforced by the LabView digital controller, which monitors the temperature and input current. When a signal for any high temperature alarm is encountered, the controller will forcefully scale down the output current of the power supply.

3.2 Overpressure System

A system for providing higher-than-hydrostatic pressure has been designed and implemented for the void tube to prevent water leakage. As indicated previously, this system's purpose is to monitor the void tube integrity and to prevent rupture of the furnace by making water ingress impossible due to the pressure differential. This system vents to the building central exhaust to allow for radiological monitoring via the facility air monitors. The pressure is maintained by a single-stage mechanical regulator with a high-purity helium supply. There are three pressure relief mechanisms: a power-operated solenoid relief valve that is wired with a pressure switch that activates at 50psig and two spring-loaded relief valves from Swagelok that are set at 55 psig and 65 psig.

Figure 5 shows the over pressure system as designed and built at the NSC. It features three main components: the main supply, void tube, and pressure relief to the central exhaust. The main supply has a single-stage mechanical regulator (VR1) that maintains the pressure in the line. There are various isolation valves for maintenance on the void tube and system itself (VMV1-4). There is a power-operated solenoid (VSV1) that is actuated by a pressure switch (VPS3). This is set to open at 350 kPa, ideally for relieving pressure during thermal transients of the furnace. There are two spring-loaded relief valves (VSRV1/2) that open at higher pressures for evacuating the system during large pressure transients and to provide a passive means of pressure relief were the solenoid to fail. There is a manual relief valve that was an air dryer for relieving the system for maintenance. The air dryer (not shown) provides moisture monitoring of the over-pressurization system. Quick disconnects (VQC1/2) at the bridge-side allows operators the capability to easily

disconnect the system to move the reactor bridge and to allow for the removal of the furnace. A procedure for this is provided, see the later section.

Ideally, pressure will be on the system throughout the weekend to ensure that there is no water leakage.

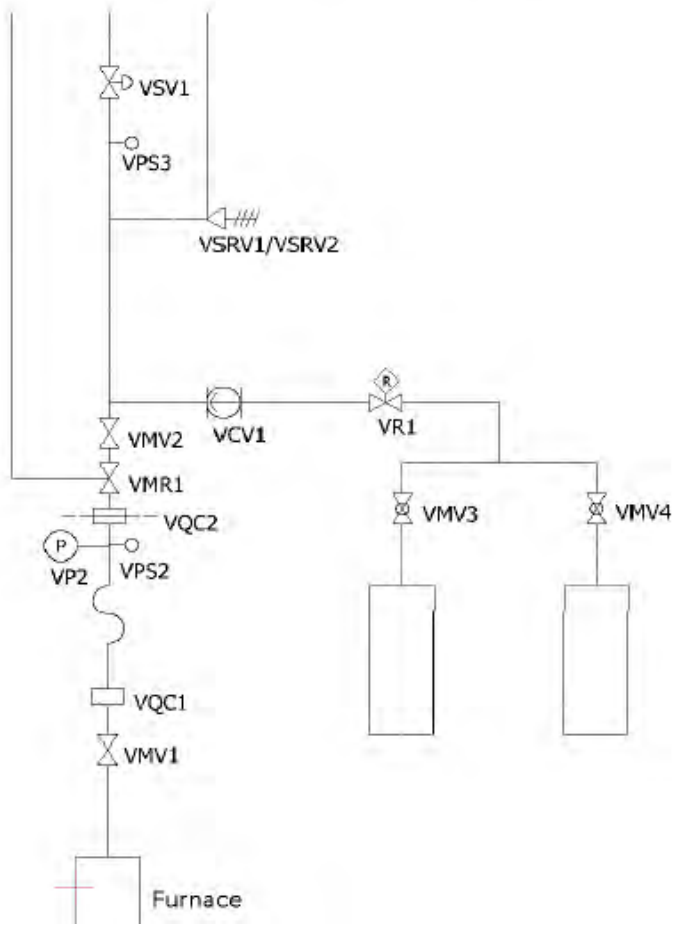

Figure 5: *Over pressure system on the void tube.*

4 Modeling and Analysis

The design of the furnace went through separate phases. These phases included scripted thermal analysis using MATLAB scripts and final modeling with STAR-CCM+ [10] and MCNP [11]. MATLAB provided solutions to the number of thermal shields required given input parameters of tube dimensions (from available stock) and temperature limitations from above calculations. This is performed as a single dimension calculation. The STAR-CCM+ model provided a final 3D representation of the temperature distributions and verification of analytical calculations with MATLAB (and vice versa). Finally, MCNP provided capture heating terms within the niobium thermal shields implemented in the STAR-CCM+ model and determined the expected irradiation times and reactivity insertions.

4.1 Thermal Analysis

The initial thermal analysis was performed with analytical treatments. This provides instant feedback in the analysis and design phase and provides for many of the design needs based on system constraints. The worst-case condition of operation for the furnace is expected, from a safety standpoint, to be steady-state operation at 1MW as compared to reactor pulsing. This is due to higher heat generation in neighboring fuel. With this higher heat flux out of the fuel pin, the coolant temperature is higher than seen in a pulse and the reduction of cooling due to voiding has a much more significant impact. Fluences rates do not affect the furnace in any safety calculations; only the total fluence will determine material degradation and a pulse does not contribute significantly to the total fluence.

Thermophysical data, shown in Table 1, come from a variety of sources, including various radiative heat transfer handbooks that are approximations. The following table summarizes the data used, with typical SI units used.

Here are a few important observations on the data summarized in the table below. Aluminum has a high thermal expansion compared to the other materials used in the furnace design. This results in non-uniform expansion of the furnace-internals during operation and has be compensated by allowing for designing components that are only radially supported, like the alumina silicate supports, so they move freely in the axial direction. Tolerances on the fabricated pieces are such that there is radial room to expand without contacting structural components.

Table 1: *Tabulated thermophysical data used in calculations.*

	Material			
Property	Al 6061-T6	Niobium	Alumina Silicate	Graphite
Thermal Conductivity	167	53.7	1.082	70
Specific Heat Capacity	903	264	880	707.95
Density	2702	8570	1922	1660
Expansion Coefficient	14	4.06	3.24	4.2
Emissivity	0.18	0.14	0.35	0.98
Yield Stress	276			
Resistivity (ohm-cm)				0.0187

A sensitivity study was *not* performed to determine the accuracy needs of these data; however, if bench-top tests conclude there are issues in the design – this analysis will be performed to determine which thermophysical properties need to be examined more closely.

4.1.1 Governing Equations

This section covers the model and methods used in the thermal analysis. These are an iterative set of solvers that determine the temperature distributions, failure pressure of the void tube and furnace for a given wall thickness, and the required amperage for ohmic heating of the graphite heater to maintain the proper heat flux.

4.1.1.1 Determining Temperature Distributions

Simple single-dimensional relationships are used for determining the temperature distributions within the furnace and void tube.

The following assumptions are made within these calculations:

- furnace is in perfect vacuum
- thermophysical properties remain constant
- emissivity is not a function of wavelength (gray radiative boundary)
- surface temperature of furnace structure must remain below 150°C

The last assumption was made to account for an incomplete understand of the heat transfer between the furnace and void tube. Empirical natural convection relationships were used originally, but the results varied significantly among the different models so, this 150°C temperature limit was applied as a conservatism and to reduce any thermal creep issues that might arise.

An initial estimate of the thermal power of the heater is made and is used to determine the surface temperature of the heater and internal temperature of the first thermal shield:

$$Q_h = \frac{\sigma A_h (T_h^4 - T_{si}^4)}{\frac{1-\epsilon_h}{\epsilon_h A_h} + \frac{1-\epsilon_s}{\epsilon_s A_{si}}}$$

where subscript *h* indicates the heater and *si* is the inner portion of the shield. This is repeated for each thermal shield to the aluminum furnace surface. The conductive heat is solved through each shield with:

$$T_{so} = T_{si} - \frac{Q \ln(\frac{r_o}{r_i})}{2\pi H k}$$

were subscript *i* is the inner surface and *o* is the outer surface. Iteratively, then the thermal power and temperatures are solved and forced to a self-consistent solution. The iterations end when the heat flux out of the aluminum wall is equal to the heat flux out of the graphite heater such that:

$$\frac{\left|q_{graphite\,surface} - q_{aluminium\,wall}\right|}{q_{graphite\,surface}} < 10^{-5}$$

4.1.1.2 Determining System Pressure Limits

The failure pressure calculation imposes a few assumptions:

- thin-walled pressure vessel
- constant thermophysical properties
- water properties (from IAPWS IF-97) at limiting pressure

Given the geometrical constraints on the furnace, the limiting pressure can be determined with a safety factor:

$$\sigma_t = \frac{\sigma_y}{SF}$$

$$P_{fail} = \frac{\sigma_t t}{r_i} + P_{ext}$$

It is assumed that the perfect mass of water is introduced into the system such that the all of the thermal energy (from operational temperature to room temperature) in the system converts all of the water into steam. If the volume of the steam, at the limiting pressure, is greater than the volume of the void tube, then rupture is expected to occur.

4.1.1.3 Determining Operational Power

The furnace operation depends on a resistive graphite heater. This heater requires an input current to maintain the joule heating to maintain temperatures to a sufficient level for the experiment. A power supply with 60 amp capability is available. This current limitation is the design specification for the sizing of the graphite heater. The current calculation is as follows:

$$R = \frac{\rho L}{A_{xs}}$$

where A_{xs} is the cross-sectional area of the heater. Heater power, which is known from the thermal calculations, is determined by:

$$Q_h = i^2 R$$

And by manipulating terms, the current requirement is:

$$i=\sqrt{Q_h R}$$

and if the current is above the 60 amp limitation, the cross-sectional area of the heater is reduced.

4.1.2 Initial Design Calculations

A scoping analysis was preformed using an automated MATLAB script. The process of optimization was performed to determine the ideal OD of thermal shields within the furnace among the other design aspects previously discussed. This is performed in an iterative fashion for all of the geometrical design criteria, which must satisfy the safety criteria. If the safety criteria is not met after the optimization, then various set parameters are changed. These are: number of thermal shields, masses of materials, and the thickness of aluminum wall.

The final design configuration is show in Table 2.

Table 2: *Final design parameters of furnace.*

Parameter	Value
Nominal Operating Tempera	1000
Maximum Operating Temper	1253
Thermal Power (W)	236
Overpressure in VT (kPa)	300
Height of VT (in)	144
OD of VT (in)	3
Thickness of VT (in)	0.065
Height of FE (in)	19
OD of FE(in)	2.25
Thickness of FE (in)	0.065
Number of thermal shields	2
Thickness of thermal shields	0.0254

4.1.3 Continuum Mechanics Model

A three dimension, high-fidelity computational continuum mechanics simulation was completed to enhance the understand of the expected furnace performance. The software used is Cd-adapco's STAR-CCM+ [10] which fully integrates CAD development, meshing, and physics modeling with coupled systems.

4.1.3.1 Model Setup

The geometry for the system, after being determined via MATLAB, is modeled in SolidWorks. There are inherently two models: a model for the CFD analysis and

another for the design drawings. The CFD geometry includes many feature implications. This is because computational models for thermal and fluid analysis are not currently capable of modeling every intricate detail with moderate computational resources. In fact, it is often advantageous to alter physical geometry via chamfers in the computational domain to ease meshing requirements and help satisfy continuity requirements between cells with only a minor reduction in accuracy. Otherwise, false numerical diffusion propagating from sharp corners could potentially result in very wrong results by diffusing, improperly, scalars indefinitely through the solution. Additionally, in the CFD geometry, there are many features that are specifically unrelated to the solution and other features that can be removed as a conservatism and save of meshing requirements.

Ohmic heating is used as a user defined field function within the power leads and graphite heater. Here the resistivity is treated as a function of temperature as determined by results from validation experiments (see later section). Thermophysical data for all solid-state materials is assumed constant and helium data is polynomial fitted from NIST data at 300 kPa (the operational pressure of the void tube). The $v^2 - f$ turbulence model is used with the SIMPLE algorithm for pressure and velocity iterations. This turbulence model has been shown to perform better than other turbulence models to predict heat transfer into the fluid, due to better surface modeling. This model uses a non-linear eddy viscosity approach, which does increase the memory requirements by introducing one more equation [12]. A constant heat transfer coefficient is used on the surface of the void tube as determined by the NSC's sub-channel code for neighboring fuel elements [13]. Radiation heat removal was determined using a view-factor calculation with constant, gray-body emissivities for all surfaces. Due to the size of the copper power leads, there is some potential for error due to massive memory requirements of the ray-tracing tracking routine, however, the impact of heat transfer in the copper to affect the temperatures within the furnace is minimal.

4.1.3.2 Computational Domain

The mesh within STAR-CCM+, see Figure 6, is limited by 16GB of memory. Much care was taken to reduce the cell skewness in fluid volumes to less than 85 degrees. This ensures that the convective and diffusive terms are represented accurately by the control volumes. In the solid volumes, the cell skewness is less important, so the mesh resolution is reduced as much as possible while maintaining the CAD surfaces to allow for conformal interfaces. This is to ensure conservation of diffusive terms over the interface.

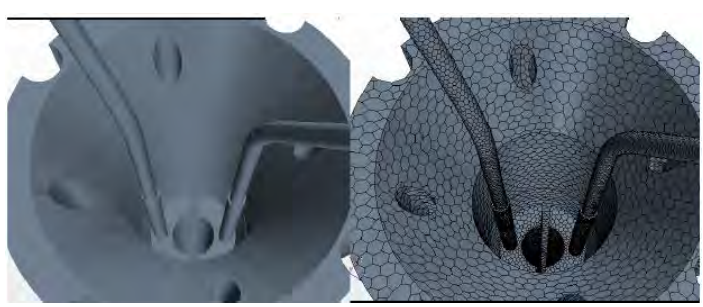

Figure 6: *STAR-CCM+ geometry (left) and numerical mesh (right).*

4.1.3.3 Convergence Study

A convergence study was not performed because computational resources were not available while maintaining minimum y^+ requirements for the turbulence model. Symmetry conditions could not be used due to the unsteady nature of a problem with natural circulation. This would naturally reduce memory cost significantly. It is uncertain if the solution is mesh independent; however, experimental validation was conducted using the same meshing parameters as the model. These showed excellent agreement, so it is assumed this model is meshed properly.

4.1.3.4 Physics Verifications and Validation

Verification studies have been completed to ensure the proper modeling of this complex system. STAR-CCM+ does improve the efficiency of human interaction with the computational model; however, due to the inherent integration of the numerical mesh, physics, and numerical schemes, a proper verification study must be completed individually for each physics phenomenon to ensure proper inputs. This verification study was performed on the conduction and convection portions of the model. A validation on radiative heat transfer was performed given the available test set up and data needs for the modeling itself. Radiation modeling is a little more complex than conduction and convection; this is a result of ray tracking overlays on top of the mesh.

Many numerical and physics model constraints were determined on a trail-and-error basis. This includes stability requirements, like the Courant number, and voxel splitting for the radiative modeling. There are very often many case-by-case specific parameters, which can not be easily determined a priori simply due to how the physics models couple with each other.

Further, a validation of the entire system's performance will be completed during the benchtop testing of the experimental device upon completion of fabrication. Comparisons and possible correction to the modeling will be completed to ensure proper operational parameters. The possible corrections will be correcting for: the geometry if any design changes are implemented during fabrication and applying contact resistances where applicable.

4.1.3.4.1 Conduction

A verification case was developed for the conduction models. These models were used to verify conduction calculations as well as to determine the meshing requirements required by finite volume methods to properly solve diffusion problems. In this, the stability is analyzed by convergence and speed of convergence. Compared to an analytical solution, the result is compared and the minimum mesh requirement is noted for the case that satisfies these constraints.

With a plate-type geometry, the thermal conductivity of the materials were altered to various extremes: insulator to conductor. This was to stress the numerical solvers and optimize meshing schemes. The geometry also has a simple resistive temperature network, so the numerical solutions can be compared with the analytical. It turns out that Courant number must be less than unity for a stable solution and a coarse mesh happens to be sufficiently better than a fine mesh for convergence. The coarsest mesh resulting in an accuracy of less than 1.5% for the computed heat flux was three elements in thickness, and the convergence with a Courant number of 0.02 was 5 iterations.

4.1.3.4.2 Convection/Turbulence

This sections remains largely incomplete since it is an on-going research topic itself. However, much like in the previous section, determination of solver requirements is the key understanding gained. The manual [10] primarily is referenced for this section as the validation cases were completed with this data.

Using a vertical cylinder with natural circulation, the meshing requirements for a mesh-independent solution were close to those used in the furnace model. The resulting heat flux from Nusselt number relationships, however, was not properly determined with the selected turbulence modeling coming the closest. This is not proper for comparison because the flow in the cylinder was not fully developed in the flow direction. This was not performed because the velocity gradient in the flow direction will exist in the furnace model. It is imperative that solution stability exists for all points in the flow., and this is the main purpose of the study.

4.1.3.4.3 Radiation

A validation case that analyzed experimental data from heater testing was conducted during the initial fabrication stages and during off-gasing and cooking of the resistive heaters.

The first series of thermal validations were completed to model radiative heat transfer from the graphite heaters. Each heater was constructed with the power-leads connected to the variable current power supply, and each heater was operated with a vacuum of 10^{-4} torr, see Figure 7. Four of the high-temperature, k-type thermocouples are attached directly of the graphite to measure the average surface temperature.

Additionally, graphite resistivity was determined with a multimeter during the experiment. This results in a resistivity as a function of temperature and is applied to the STAR-CCM+ model as shown in Figure 8. Many experiments were needed to determine the resistivity, properly, because of inconsistencies in the contacts between the graphite heater and power supply. This results in different voltage drops for many of the experiments. If the resistance is substantially higher than the average, these data are removed. The reason to support this choice is that the thermal expansion in a loose contact will enhance contact more than in a already tight contact. This will result in a different shape to the curve.

Figure 7: *View of graphite heater with thermocouple instrumentation and setup in vacuum chamber*

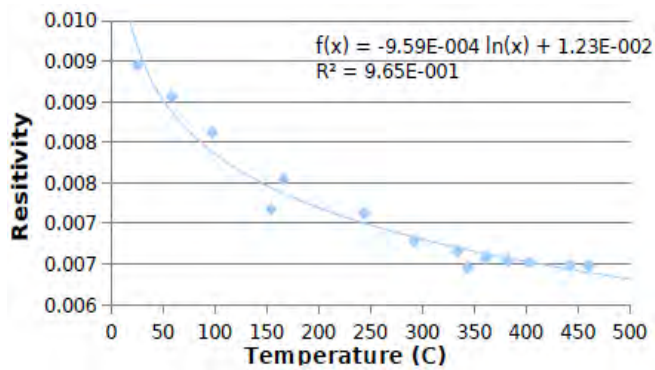

Figure 8: *Resistivity as a function of average graphite temperature.*

Table 3 outlines the primary results of the radiation validation efforts. The largest errors resulted in determination of the heat flux from the graphite. This is attributed from the lack of modeling of the thermocouple contacts and from contact resistances of the supports for the graphite heater and power leads. Also, noting that the surface heat flux was determined with the Stefan-Boltzmann law. The reflection of radiation from the surface of the vacuum chamber was also neglected, but the surface temperature of the chamber and the environmental temperature of the model were equivalent in all simulations. Overall, the model agrees fairly well to experimental data and overall, the models over-predict the surface temperatures.

Table 3: *Comparison of some STAR-CCM+ calculated values to experimentally measured values.*

Current [amps]	Measured Temp [C]	Surface Temp [C]	Relative Error	Heat Flux [W/ m2]	Power Error
3.5	37.7825	39.74	0.0063	82.44	-0.0944
8	78.4425	79.77	0.0038	411.73	-0.0981
10	100.6	100.47	-0.0003	632.5	-0.0948
20	194.7725	202.72	0.0170	2399.59	-0.0936
26	246.9625	259.68	0.0245	4028.76	-0.0907
30	276.7925	294.68	0.0325	5327.23	-0.0959
41	348.185	382.2	0.0713	9801.78	0.0196
46	376.8275	418.92	0.0831	12300.6	-0.0011

4.1.3.5 Results

The results from the final STAR-CCM+ simulation, displayed in Figure 9, were in agreement to the MATLAB calculations. This means that peak temperatures were close to the expected values from the analytical calculations. The average material temperatures from these results were fed into a final failure calculation in MATLAB. With the results of these calculations, the furnace mass was minimized as according to previous safety discussions.

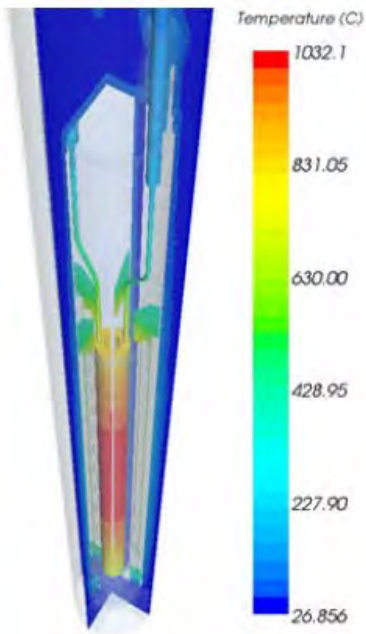

Figure 9: *Simulated furnace with expected system temperature distributions.*

Naturally, it is a bit over-zealous to produce STAR-CCM+ model for such a device, but axial and radial temperature distributions are now obtainable. This provides a computational comparison for fiber optic measurements for validation and verification tests during operation within the furnace.

4.1.4 Local Fuel Cooling Impact

An analysis of the impact of the cooling of the fuel in close proximity to the furnace was conducted. There are two causes for concern that might introduce reduced cooling for the neighboring fuel. These are: steam generation or helium from a possible weld breakage reducing liquid volume in the coolant channel. Both of these incidents can likely reduce the surface cooling such that inner fuel temperature increases about the LSSS.

However, it is important, prior to this discussion to note the following:

- The neighboring fuel elements operate between 4666W and 9679 W (see Table 4).
- The furnace is expected to operate with a power less than 600W.
- The peak fuel element power is 17.6kW.
- The highest neighboring fuel element is also neighbored by a large water hole.

The analysis of the cooling impact analysis is completed with qualitative arguments, since methods for a detailed analytical treatment are not readily available.

Table 4: *Power (W) generated by each fuel element in the fuel bundles. Red, blue, and gray indicate furnace, water, and graphite locations respectively.*

	2		4	
D	0	0	0	0
	0	0	0	0
E	0	0	9679	10558
	0	0	6962	9098
F	4666	5126	6101	0
	3771	4581	5924	7783

With the heater operating at 2.5% of the neighboring fuel power, it is unexpected that steam production to occur in any capacity. This means that any steam produced will condense immediately in the sub-cooled water of the coolant channel, since departure of nucleation is not observed in the core at operation. In fact, the SAR states that the DNBR is 2.42 for the peak fuel element in the core, which is surrounded by fuel operating at similar power. This provides a substantial margin against steam production.

The only possible issue is due to helium leakage, which could potentially reduce cooling on the fuel surface. There are two preventative measures in place. One is the reduced mass flow capabilities of the helium supply, which is 1/10th of the calculated mass flow rate in the sub-channel. Additionally, the top of the void tube is designed to fail before the bottom. Due to the asymmetry of the fuel location and experiment, two-phase cooling calculations are difficult and unreliable. If leakage poses an issue, another location (possibly the D1 position) can be considered.

4.1.4.1 Further Discussion

The void tube is design to have the lowest pressure retention at the cap where the feedthroughs come through the void tube. This helps ensure that a rupture occurs outside of the fueled region and the fore all gaseous leakage will not impact the core. With the sudden depressurization, the furnace will instantly shutdown (ensured pressure switches that control power to the power supply). This provides that power is not being supplied to the heater during such an event, reducing the potential for further steam production.

The void tube is welded to the grid adapter that holds and positions the furnace in place. The weld is a possible location for failure, especially after many months of irradiation and maintaining its integrity is crucial since the grid adapter if filled with lead used to neutralize the buoyancy of the entire furnace assembly. The welding process will be conducted with great care to minimize any negative impact of thermal stresses and heat treatment.

4.1.5 Thermal Analysis Conclusions

It is expected that the furnace will not perform in such a way as to unfavorably affect the fuel integrity. The operational power is considerably less that than of the neighboring fuel elements and the furnace has a much lager OD. This results in a surface heat flux reduction to 1.1% of the furnace compared to the fuel element.

The calculations and modeling were completed by redundant means, using analytical and numerical calculations. These vary from experimentally derived heat transfer correlations to turbulence modeling. The heat transfer correlations have been validated by core power and temperature measurements via the NSC-developed sub-channel code. Modeling capabilities and design configurations were also experimentally validated for the furnace itself. Benchtop validation is awaiting completion of the furnace.

It is, therefore, under the best judgment of the author that the furnace is fully capable of safe operation within the reactor core.

4.2 Neutronic Analysis

The neutronic analysis was performed to assess the performance of the furnace within the NSC reactor. The NSC model was originally developed by Dr. Hsu and has been heavily updated and corrected by the author. This model contains only a few material and geometric assumptions. This are further detailed in the input deck itself.

4.2.1 Overview

The code used for the calculation is MCNPX v2.7.0 [13] with ENDF BVII.0 data libraries and beginning-of-life (BOL) fuel constituents, see Figure 10 for the

geometrical representation. This NSC reactor core model has been validated to experimental data with very good agreement. This furnace model determines the expected spatial and energy dependent fluence rates in the fiber optic, radiation induced heating in the thermal shields, and core-reactivity effects due to flooding.

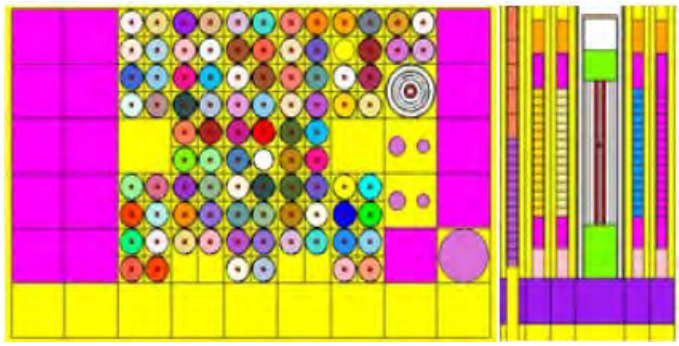

Figure 10: *XY cross-section of MCNP geometry (left) and the XZ cross-sectional view (right).*

The above figure shows the primary experimental location in the E2 position (see Figure 2 and 10). It is also possible to insert the furnace into the D1 position, as a safest-bet, so an analysis is also completed for this position.

4.2.2 Verification and Scaling

Neutronic models were validated by neutron fluence measurements for current in-core experimental locations with the use of gold flux foils. Flux foil measurements are completed regularly at the NSC to facilitate calculation of radioisotope production for sample irradiation and these measurements were compared to the MCNP5 model with good agreement and with maximum errors of 11.35% in the fast-to-thermal flux ratios. Scaling for the thermal flux was performed and therefore the fast flux is under-represented. Inherently, the model over-predicts thermalization and therefore also over-predicts control rod-heights. There is only a minor effect on the axial flux distributions within the fiber optic.

4.2.3 Fluence Requirements

The fiber optics, defined by the experimental proposal, are required to be irradiated to a neutron fluence of 2e19 n/cm² which will require about 335 days of absolute irradiation. This irradiation time assumes that the reactor operates continuously with a capacity factor of 19.5 percent. This is determined by the total MW hours generated by the reactors versus what could potentially be generated with constant operation.

The fluence rate (see Figure 11), as calculated by MCNPX, in the E2 position averages about 1.78e13 n/cm²/s with a thermal flux of 4.13e11 n/cm²/s. This "average" is the average of calculations performed with the following configurations:

- No experiment in D3 with the core away from the thermal column
- No experiment in D3 with the core against the thermal column
- An experiment in D3 with the core away from the thermal column
- An experiment in D3 with the core against the thermal column

This expected fluence rate has not be experimentally validated with flux foils. Such a measurement is planned, but may not be completed prior to inserting the furnace in the core, simply due to core reconfiguration efforts.

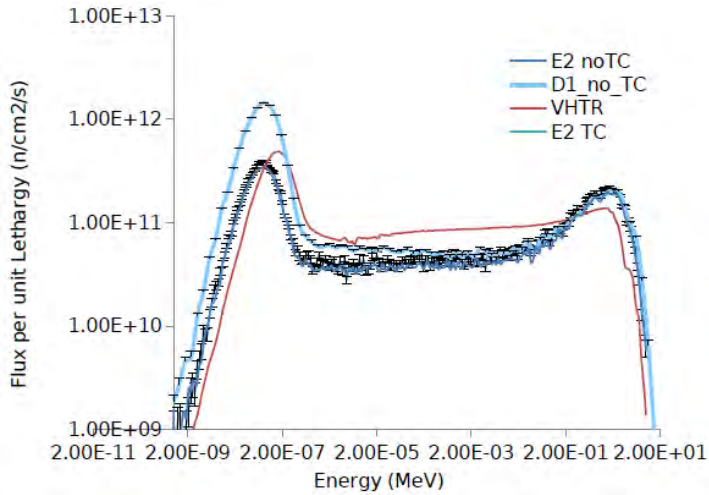

Figure 11: *Neutron energy distribution within peak-flux fiber location within experiment with D1 normalized to fast flux.*

It is noticed, not unsurprisingly, that the thermal flux is considerably higher when the fast flux of the D1 position result scaled to that of the E2 position. This would preclude that the D1 position is more favourable for the experimental location from a spectral argument. The thermal flux magnitudes are comparable for all cases.

4.2.4 Reactivity Insertion

It is required to evaluate the reactivity worth of an experiment to determine if it must be secured or not. This threshold is 30 cents (as per Tech Specs Section 14.3.6.1 and normalized to $\beta=0.0073$). Additionally, various scenarios of water ingress are possible depending on the reactor position and the portion of the furnace that floods, see Table 5. The highest expected reactivity insertion is calculated to be less than $0.07.

These calculations were performed with the MCNPX model. All sections of open volume within the furnace were filled with water. For this case, the core configuration was changed to include operation against and away from the thermal column and with the D3 location either filled with water or voided by an empty long tube. These two sets of configurations were performed with the control rods at the

same height, so the TC configuration will be slightly over-predicted. These configurations were chosen based on their impact on the spatial neutron distribution. The thermal column creates a significant tilt in the spatial flux, heavily biased towards the east side of the core. The D3 location is essentially a water hole with significant thermalization potential. It is interesting to note that the flux tilt actually depreciates the reactivity worth of the proposed experimental location.

Table 5: *Reactivity insertions for various postulated configurations.*

	D3		noD3	
TC	0.00029	dk/k	0.00045	dk/k
	0.040845	$	0.06338	$
noTC	0.00024	dk/k	0.00049	dk/k
	0.033803	$	0.069014	$

4.2.5 Niobium Capture Heating

Only one concern was voiced during the preliminary reactor safety board review. This concern was in regard to determining and accounting for the niobium neutron capture heating in the thermal shields. The implication of having a heat generation term withing the thermal shield is reducing the effectiveness of the shield, thereby increasing the heat radiative heat transfer radially outward. This will result in the following: increased power demand of the heater, increased temperature of the furnace supporting structures, and an increase in the total storage of the furnace. So, if the internal heating of the niobium thermal shields has not accounted for, the current rating of the power leads will be under-determined and the safety calculation would be less conservative than it currently is.

Provided then, that the MCNP code allows for coupled photon and neutron simulations, and using saturated activities for niobium radiative capture, the predicted heat generation terms were determined to be 7.94e5 and 8.73e5 W/m^3 for the inner and outer thermal shields, respectively. These are used with the STAR-CCM+ model to determine the final temperature distribution.

5 Radiological Concerns

Effluence of activated material is likely only to exist during the initial operation of the furnace. This is due to the off-gasing of any binders within the graphite. Initially, the the graphite heaters were taken to 450°C in a vacuum chamber to burn off most of the binders; however, some binders might still exist and other soluble gaseous materials could have permeated into the graphite during storage at the Nuclear Science Center. The initial heat-up of the furnace will be conducted during non-reactor operating hours and outside of the reactor to prevent negative impacts to the facility and personnel. All gaseous products will be evacuated by the over-pressure system to the Central Exhaust system, as discussed in previous sections.

Radiological toxicity during handling is a potential concern. Handling will be necessary for replacing fiber optic probes and other portions of the furnace that might have failed. These would include the furnace cap, graphite heater, and thermocouples – everything else is expected to be resistance enough to the radiation environment to remain operational for one year. This concern is due to the activation of materials used in the furnace. Those materials, like copper and iron, have been minimized to prevent high radiation fields with reasonable decay times.

An activation analysis has not been conducted. The doses will be experimentally determined and handled accordingly via ALARA methodologies. Materials that will impact radiation levels have been minimized and any further reduction will result in a negative safety impact to the furnace.

6 Controllers

The controller for the system is LabView. The LabView code was developed by Carl Mullins and controls the power supply via PID as a function of graphite heater temperature and records all pressure and temperature data. This data is used for analysis of system performance as well as for safety shutdown systems.

LabView will provide some safety for the system, which were discussed in a previous section. The safety loop can be over-ridden manually, in particular, during start ups of the furnace. Manual over-ride has to be turned off for the furnace PID controller to be activated. This provides that the safety loop is active during normal operation. The safety loop includes only logic for the scaling of furnace power based on the heater temperature.

7 Fabrication Process and Controls

The furnace is fabricated at the Nuclear Science Center by the author with the support of the machine shop foreman. All portions of the fabrication were conducted in steps to ensure that no single component was designed inappropriately. Various components were purchased from manufacturers where the experience, materials, and infrastructure were not available.

Figure 12 shows the completed furnace cap with thermocouples and power-leads attached to the graphite heater through their respective feedthroughs.

Figure 12: *View of internal of furnace without fiber optic probe.*

7.1 Quality Assurance Program

The QA program implemented in this project is quite simple. All purchases, processes, and fabrication steps are documented, to include pictures and a discussion of observations. Reputable companies, based on previous experience, were used to the greatest extent possible. All orders received were documented and manufactured pieces were compared to original drawings to ensure conformance to tolerances specified.

7.2 Instrument Calibration

Instrumentation calibration and verification is necessary for data collection and proper safety system performance. Equipment to perform calibrations are not always readily available, so those deficiencies are outlined here.

7.2.1 Temperature

There are two forms of temperature measurement within the furnace: k-type thermocouple and fiber optic. The k-type TCs are used to measure the temperature at various points throughout the furnace and are assumed to be reliable and accurate with error limits of +/- 1.1^{o}C or 0.4%, whichever is great. These TC measurements are used for system performance and safety data. Fiber optic temperature measurements provide continuously distributed measurements through the center of the graphite heater. These measurements require constant calibration with changing environmental conditions and the behaviour of the fiber optics is less known than that of the TCs used. The fiber optics are not used to determine system parameters.

Thermocouple measurements were verified by using an ice bath and by bringing water to a boil. This only provides a 0°C to 100°C reference compared to the 30-1100°C operating range. These thermocouples are required for validating the temperature measurements with the fiber optics. All of the fiber optics to be used in the furnace are tested against a reference TC. Figure 13 shows the experimental set up for fiber optic verification. Calibrations are not conducted, even for fibers that perform poorly, because of the nature of the fiber measurement. Coefficients are required for the conversion from strain to temperature measurements, which are manufacturer specifications on the fiber. Therefore, defects are noted.

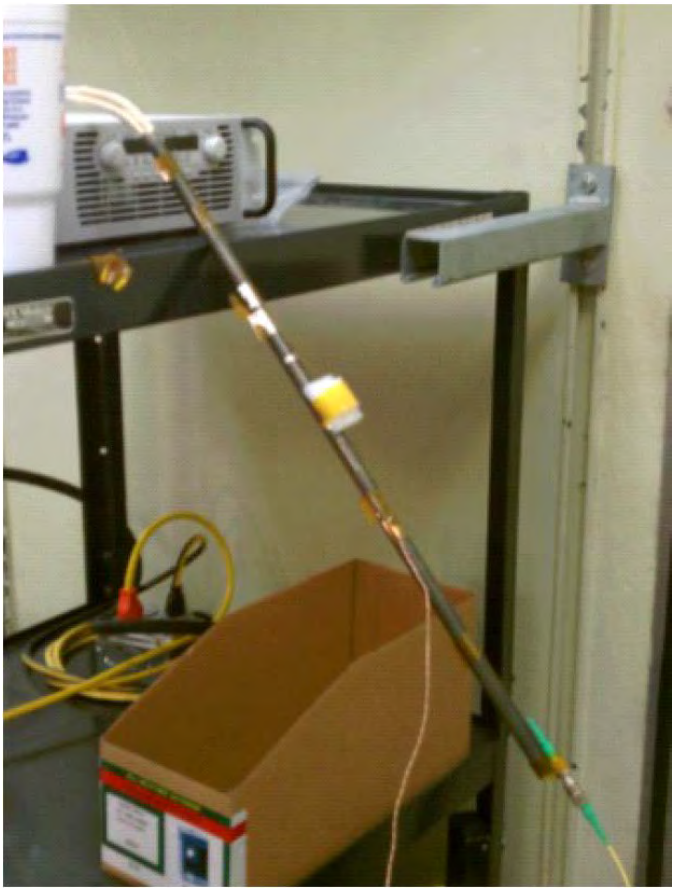

Figure 13: *Thermocouple and fiber optics measurement accuracy test (notice ice cup on left).*

The thermocouples used in the furnace are either Kapton or Nextel insulated. The Nextel insulation is used for thermocouples expected to reach temperatures above 750°C and is therefore used within the furnace element. Outside of the furnace, and within the feedthrough, Kapton is exclusively used. Nexel is a boron-based insulating material that is expected to dissociate with time due to transmutation. Replacement due to thermocouple failures in this regard are expected and redundancy of measurement is included in the design for the graphite heater. Kapton exhibits exceptional radiation tolerance and is likely not to be of any concern.

Performance of the furnace-internal thermocouples for long irradiation periods have not been experimentally verified, but there is supporting evidence that they should function properly. The thermocouples within the instrumented fuel elements of the NSC's reactor core aree k-type and are directly embedded into the fuel. The fluence reached by each thermocouple is orders of magnitude greater than what will be expected in the furnace. Only a few failures have ever occured within the reactor and these failures are often attributed to mechanical failure due to poor handling of the instrument guide tubes. Therefore, it is expected that the k-type thermocouples implemented within the furnace are expected to survive during their service life.

The measurement with the heater at 45°C is shown in Figure 14. The features from left to right are: heater, spacer, heater, and ice bath. This is a representation of the temperature profile of the setup in Figure 13, where the spacer would indicate room temperature and the ice bath would be 0°C (note that these measurements are referenced to isothermal, room-temperature conditions) The fiber measurements, overall, showed very good agreement with the TC readings.

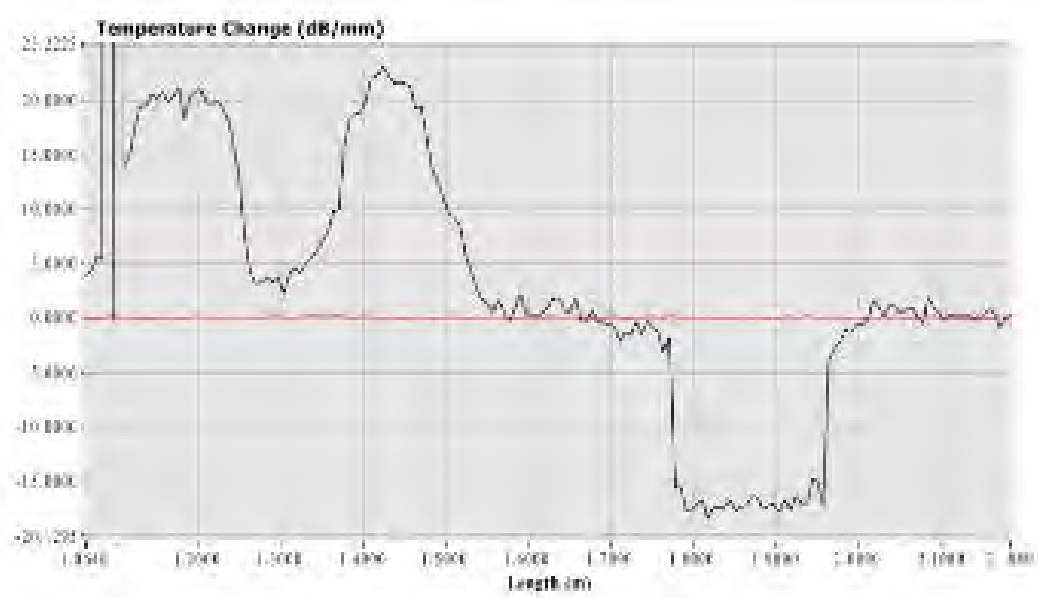

Figure 14: *Temperature distribution as measured by the fiber optic for the experimental test.*

7.2.2 Pressure

Pressure transducers are calibrated with a home-made device with two external pressure gauges (the POOPC – Pre-Operational, On-line Pressure Calibrator). These pressure gages are store-bought, and are not calibrated except by the standards of the manufacturer, which are unknown to the author. The pressure device is a simple PVC pipe with an attached bike pump fitting, see Figure 15. This bike pump is used for pressurizing the device. The resulting voltage output from the pressure transducer is linearly fitted to the pressure gage indications, see Figure 16.

Figure 15: *View of the bike pump connection of the left and pressure transducer on the right.*

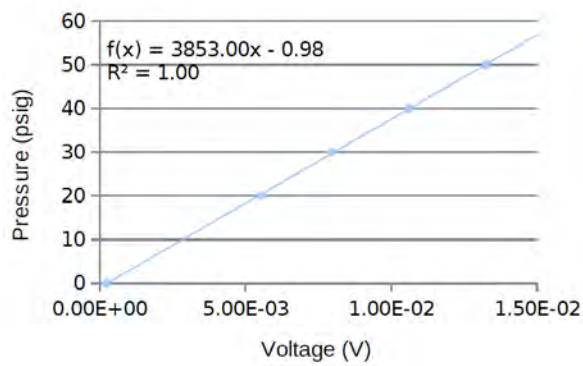

Figure 16: *Linear pressure calibration curve for one of three transducers.*

7.3 Experimental Fabrication Techniques

There are a few experimental techniques developed for this project resulting from a the lack of expertise in the field of building a high-temperature furnace in vacuum conditions. This section outlines these techniques.

7.3.1 Lead Gasket

The use of soft metal gaskets, especially lead, is prevalent in vacuum systems. However, the process of making the lead gasket is not. For this system, the diameter and size of the gasket were far from available – at least cheaply. Therefore, lead gaskets were made simply by heating and melting lead into the gap grove, then after cooling, shaved to a very flat finished.

7.3.2 Power Feedthroughs

The power leads posed a design challenge for the experimental device. The challenge of power transmittance through water and a pressure and vacuum barrier were not fully understood during the initial design phases of the furnace. So a special feedthrough was designed for the void tube and vacuum feedthroughs were purchased for the furnace element.

7.3.2.1 Void Tube

The power feedthrough for the void tube is an aluminum union that is epoxied with an excessive amount of JB-weld. This epoxy is used to build up a pressure boundary between the wire jacket of the power lead and the aluminum union. JB-weld is used in the construction of the fittings on experimental long tubes at the NSC, and has demonstrated itself to be fairly radiation resistant. The fittings on the experimental tubes have very low failure rates. These fittings reach much higher fluences than compared to what is expected at the top of the void tube. It is expected that this feedthrough will perform sufficiently during the irradiation time.

7.3.2.2 Furnace Element

The vacuum grade power feedthroughs for the furnace are not available in any material other than stainless steel. As previously mentioned, the bulk of furnace material is aluminum. This poses a difficult challenge to seal the vacuum feedthrough. A brazing concept was implemented using Alumiweld to bond the furnace cap to the power feedthrough, see Figure 17.

Figure 17: *Cap with final power-lead design, which includes brazing and socket-like inserts.*

This process proved to be very successful in holding a rough vacuum. High vacuum has not been tested; high vacuum is unlikely to be necessary for proper operation of the furnace.

7.4 Materials Selection

The following discussion outlines the material choices and their possible impact in a reactor environment.

7.4.1 Graphite

Graphite selection was performed to ensure high resistivity for ohmic heating and high strength to maintain structural integrity during the course of a year of cyclic stresses. The selected Graphite is AXZ-5Q from Poco.

The radiation resistance of graphite is naturally high if the impurities within the graphite are low. This is due to the negligibly low absorption cross-section of carbon. Graphite is easily machinable, so modifications to the heater can be done on-demand. This includes adding threads for the molybdenum power leads and tapping out a through-hole for the fiber optic probe. The resistive heater selection was not final when the design of the furnace began; however, given the benefits and history of graphite use in reactors, this became a nature and obvious choice.

7.4.2 Aluminum

Aluminum as a structural material was selected on the premise of reducing radiological concerns of removing the furnace from the reactor core for handling. This choice of aluminum significantly limits operational temperatures compared to using steel. The alloy of choice is 6061-T6, which used nearly exclusively by the NSC.

7.4.3 Niobium

Niobium is a refractory metal used for the fiber optics probe (decision for this is unknown – recall Luna fabricated the probes) and the thermal shields. Molybdenum was actually the original selection for the thermal shields, since GA used if in their King TRIGA furnace; however, a manufacturer was not available in the United States for the specifications required on the thermal shields. Niobium is capable of high polish to obtain a low emissivity for use as a radiative thermal shield. It does oxidize very quickly, but this does not affect the surface finish.

7.4.4 Molybdenum

Molybdenum is a refractory metal with an extremely high melting temperature and is used for the power lead connections to the graphite heater. These power leads were already available from prior experiments.

7.4.5 Copper

Copper is an excellent choice for electrical applications. Its wide availability and use makes this an obvious selection.

There are significant activation issues associated with Cu, however, and will lead to significant radiological concerns with handling.

7.4.6 Alumina Silicate

Alumina silicate is used for structural components to support the graphite heater and thermal shields within the furnace. This maintains the geometry for ideal heat transfer and prevents electrical shorting of the graphite heater. The alumina silicate has low thermal and electrical conductivities, which makes it a supreme candidate. . It does, however, possess a significant thermal storage concern; therefore, the mass of alumina silicate is minimized as much as possible.

Upon receipt of the final fabricated pieces, the density was found to be about twice that as expected. The top support was removed from the final design as it was found that only the bottom support was required for properly supporting the furnace components.

7.5 System Testing

Many verifications were conducted to ensure that design constraints and decisions were valid. These tests included: testing of thermocouple attachment techniques, thermal models, epoxy integrity during/after thermal cycling, and heater coating concepts.

7.5.1 Thermal Stress Testing

Much of the furnace fabrication was completed with little to know experience on the understanding of how various connections would behave. The foremost of these are the thermocouple connections to the graphite heater and the alumina paste slugs used for preventing the heater from shorting with itself. Therefore, various thermal transient stress tests were conducted to verify that the thermal stresses do not cause failure to the graphite or induce error in thermocouple readings during large transients.

Such tests were conducted in the vacuum chamber were there are some temperature limitations up to about 415C. Above this, there is significant melting and volatilization of the power lead cladding and no ventilation of off-gassing products.

The testing was conducted by increasing the power load on the graphite heater with large increments, see Figure 18. The first such transient imposed 15 amps on the heater, shut off the power supply allowing it to cool and during the cooling increase power to 45 amps. This causes a very large temperature gradient. After allowing the heater to cool again, the connections and overall integrity was visually checked

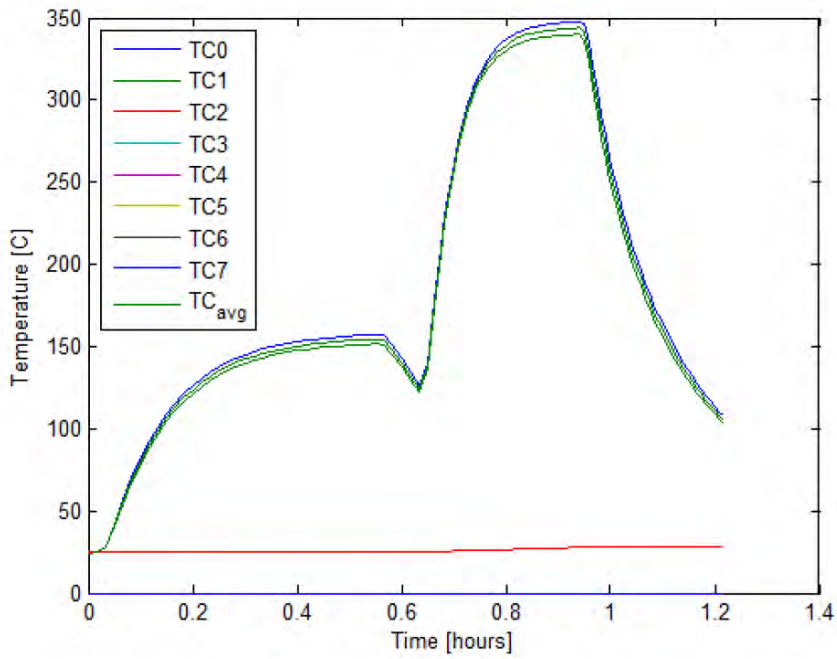

Figure 18: *MATLAB plot of temperature recording of thermal stress test.*

then destructively checked. The connections held on firmly and only minor cracking was noticed in the epoxy on the molybdenum power leads. This is not a concern at all since the leads are threaded into the graphite.

7.5.2 Heater Coating

It was originally proposed to coat the graphite heaters to reduce the emissivity of the surface, therefore reducing the radiative heat transfer from the surface. This would, potentially, reduce the power requirements of the heater and reduce the wall temperatures of the furnace. However, the difficulty of uniformly coating the heater proved to reduce the efficiency of this concept to the point that it added no benefit to the heater. The concept was scrapped.

7.6 Procedures

The only procedure provided is for disconnecting the furnace supporting systems to allow for bridge movement. This include checking the system for isolation prior to venting and then disconnecting power, data, and helium connections. Operations will **not** have the authority to connect the system back to the bridge.

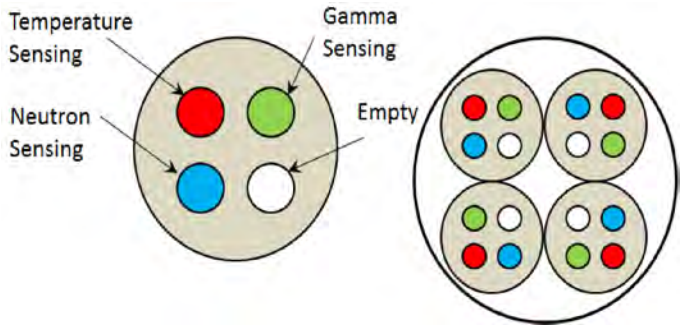

Figure 19: *Cross-sectional view of fiber optics probe.*

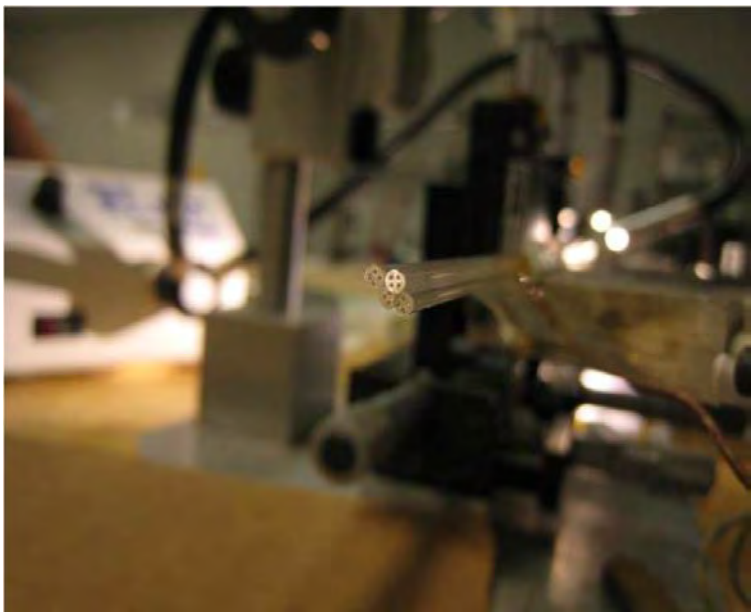

Figure 20: *View of fiber optic containing ferrules during fabrication stages.*

Table 6: *Parameters of GA and TAMU furnace builds, comparing only to what is available for the GA design.*

Parameter	General Atomics	TAMU
Operating Temperature	1800C	1000C
Cooling	Mixed Convection/ Radiation	Free Convection/ Radiation
OD	1.41"	3.25"
Sample Length	<1.0"	18.0"
Cost	>$250,000	<$55,000

8 Finalization of Experiment

The furnace was fabricated and integrated into a single operational unit. A series of bench top tests, organized as a bench top testing program verifying functionality and operation of all safety systems, were conducted following the completion of the furnace fabrication stage.

The bench top testing program included tests of the following systems:

- Gas leakage from the void tube over pressure system. Monitor pressure drop on the supply tank for 24 hours.
- Verify solenoid response for venting the system to Central Exhaust. Throttle regulator to increase and decrease pressure in the system.
- Verify power supply safety shutdown via analog high/low pressure signals.
- Verify power supply safety logic with LabView for pressure related signals.
- Verify power supply shuts off with loss of signal from computer/LabView.
- Verify thermocouple response with initial heating of furnace. Monitor pressure responds normally.
- Verify PID controller response.
- Verify system temperatures at nominal operating conditions.

9 Conclusions and Request for Irradiation

A furnace for in-core, high temperature irradiation of fiber optics has been designed and analyzed to conform with NSC Technical Specifications for in-core reactor experiments.

The furnace safety analysis includes discussion and quantitative evaluations of the system design and design basis considerations

Discussions and evaluations of the fabrication, instrumentation, calibration, control, monitoring, and operation have shown that the furnace design is expected to satisfy safety margins and do so with minimal impact on the facility and operations of the reactor core.

The proposed reconfiguration of the reactor core will not affect operations and is intended to provide a minimal experimental footprint.

Provided that the proceeding calculations hold and there are no problems with the irradiation, test articles, and supporting systems, an irradiation time was requested and granted in the NSC reactor core until late-May of 2013. It is to the best ability of the project experimental team to determine the safe operation range of the developed, designed and manufacured experimental device.

At the time of the present report, the experimental program has been copmleted successfully.

References

1. "Design Features and Technology Uncertainties for the Next Generation Nuclear Plant," Independent Technology Review Group, INEEL/EXT-04-01816, Idaho National

2. K. Saito, H. Sawahata, F. Homma, M. Kondo, T. Mizushima, "HTTR: Instrumentation and Control System Design," *Nucl. Eng. Design,* **233**, pp. 125-133 (2004). Engineering and Environmental Laboratory.

3. B. Dickerson, J. Farmer, J. French, M. Palmer, R. Fielder, *"Fiber Optic Sensors Measuring Gamma Flux and Neutron Fluence," Trans. Amer. Nucl. Soc.,* **99**, pp. 289-290. 2008.

4. "Next Generation Nuclear Plant Pre-Conceptual Design Report," INL/EXT-07-12967, INL. 2007.

5. S. J. Ball, S. E. Fisher, "Next Generation Nuclear Plant Phenomena Identification and Ranking Tables," NUREG/CR-6944, ORNL/TM-2007/147 (2008).

6. 4. K. Saito, H. Sawahata, F. Homma, M. Kondo, T. Mizushima, "HTTR: Instrumentation and Control System Design," *Nucl. Eng. Design*, **233**, pp. 125-133 (2004).

7. E. E. Anderson, S. Langer, N. L. Baldwin, F. E. Vanslager, "An In-Core Furnace for the High Temperature Irradiation Testing of Reactor Fuels." *Nucl. Tench.,* **11**, pp. 259-265. 1971. Gulf General Atomic Company.

8. H. A. Saller, J. A. VanEcho, J. T. Stacy. "Creep-Rupture Properties of 6061-T6 Aluminum Alloy at 450 and 500F." BMI-970. United States Atomic Energy Commision, 1954.

9. D. J. Alexander. "The Effects of Irradiation on the Mechanical Properties of 6061-T651 Aluminum." *Effects of Radiation on Materials: 16th Internation Symposium, ASTM STP 1175.* Oak Ridge National Laboratory.

10. STAR-CCM+ v7.02, distributed by CD-adapco Group, Inc., Melville, NY

11. J. S. Hendricks, G.W. McKinney, J.W. Durkee, J.P. Finch, M.L. Fensin, M.R. James, et al., MCNPX, Version 2.7.0, Los Alamos National Laboratory Report LA-UR-11-02295, 2011.

12. Lien, L. S., Kalitzin, G., Durbin, P. A. 1998 "RANS modeling for compressible and transitional flows", Center for Turbulence Research - Proceedings of the Summer Program 1998

13. J. Johns, W. Reece, "A New Method for Calculating Fuel Temperature in TRIGA Mark I Research Reactors," *ICONE20*, Anaheim, CA, USA, July 30-Aug. 3, 2012.

13.7. Experimental Setup In/By the Pool Wall

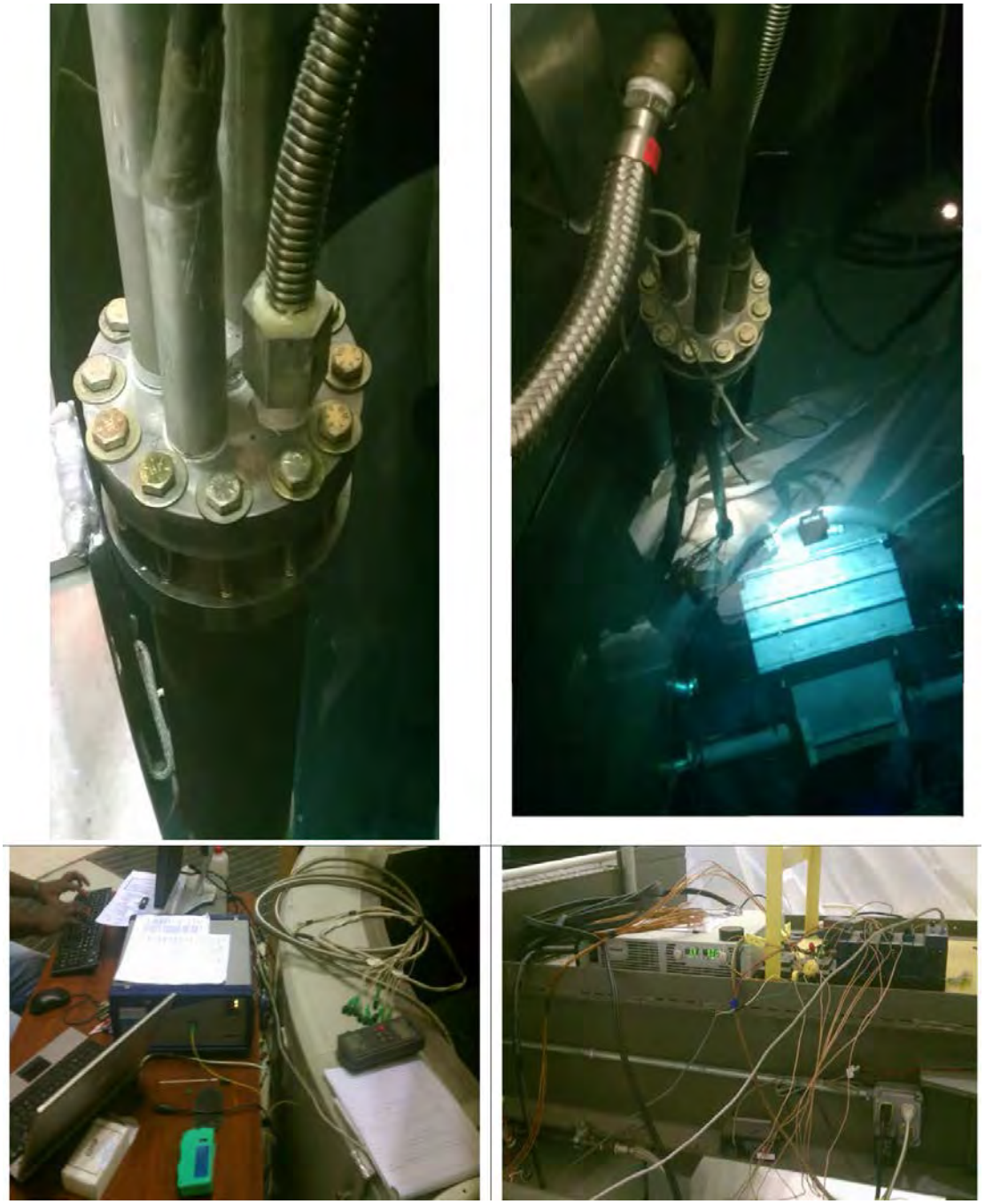

Fig. 1. In/by pool wall hardware.

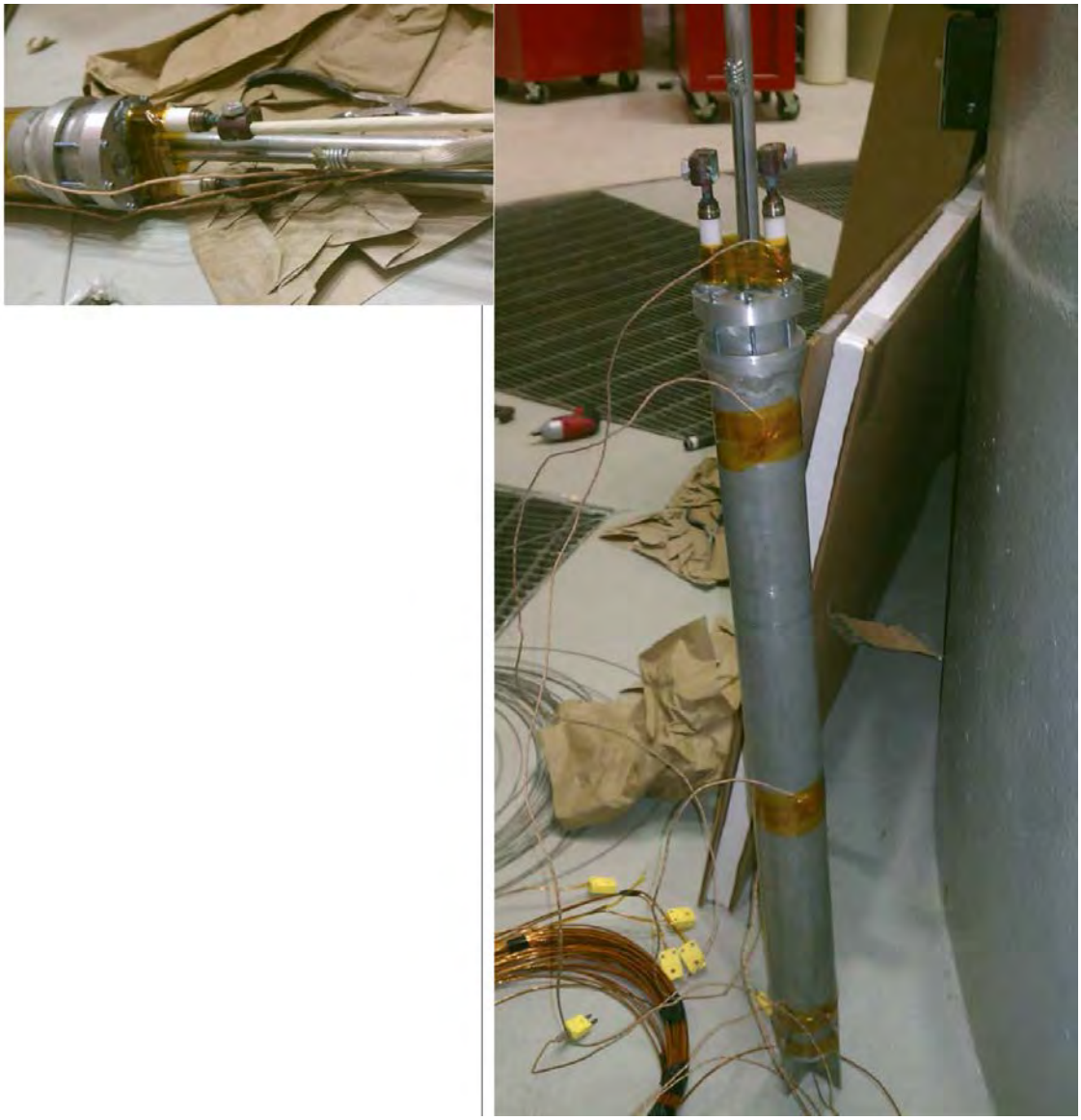

Fig. 2. Final fabrication.

13.8. High Temperature Test Assembly (Furnace) Operation

The experiemntal program was completed by Mr. Jesse M. Johns, graduate student and Ph.D. candidate at Texas A&M University, Department of Nuclear Engineering. Mr. Johns' efforts were asssited by the group of participating undergraduate students, Carl Mullins (Aerospace Engineering) and Hanniel J. N. Honang (Nuclear Engineering), and graduate student, Sathish Lakshmipathy (Nuclear Engineering).

Abstract

This report reflects the installation of the furnace in the reactor. This begins with the core reconfiguration of the E2 grid position to make room for the experiment. The report then discusses the various physics calculations and measurements associated with experiment in the core, including reactivity measurements and neutron/gamma flux distributions. The flux was measured, for the location, with Al/Au flux foils to give a representative flux for calculating the fluence of the fiber optics during irradiation. The fiber optics were tested for their performance at low and high temperature during and prior to reactor operations.

As of this writing, the furnace has accumulated roughly 280 hours of reactor operation since the installation on March 12th, 2013.

I. Introduction

This furnace design is the accumulation of several years of effort, including reactor and mechanical modeling and design. The furnace was designed and fabricated without prior experience in high temperature furnace fabrication techniques. The result is an collection of gained experiences that can be read about in the Fabrication and Acceptance Testing report. The objective of this experiment is to provide an in-pile high-temperature irradiation device for the testing of advanced fiber optic instrument for commercial reactor core measurement of temperature, gamma fluence, and neutron flux distributions.

The fabrication of the furnace finally came to a close in January of 2013 when the benchtop testing was completed satisfactorily with minor changes (see Acceptance Testing document). Predominately, the most significant change is the operational temperature of the furnace itself. The initial desire operation of the device demonstrated that temperature of 1000C would be reachable within safety limits; however, oxidation of the thermal shields has increased the effectiveness of radiative heat transfer. This results in increased power requirements for the heating element and a more shallow temperature gradient across the radial direction of the furnace. The peak operational temperature becomes 500C due to high wall temperatures of 180-195C. Since the gasket integrity is no longer an issue, this is a permissible operational temperature.

Fiber optic performance evaluation is limited following the initial testing phases. The temperature distributive measurements were the only measurements from the fiber optics that behaved reliably, but some conclusions can be made about the radiation sensitive fiber optics.

II. Furnace Operation

Preliminary operational data for the furnace is available in the acceptance testing report; the following discussion will outline the operation of the furnace within the reactor core and the comparisons to modeling attempts during fabrication.

Pressure instrument was not available during the initial phases of testing for the furnace. There were problems with LabView supplying the correct voltage to the transducer resulting in erroneous calibration curves. All pressure-related safety systems for automatic shutdown of the power supply were operable at all times during operation. The lack of measurement prevents the analysis of events, but does not impact the same operation of the system.

Moreover, there are times that data was not recorded as a result of user error.

1. Operation Results

This discussion will begin by analyzing the typical operation of the furnace with an overview of expected performance during normal conditions. The normal operating condition of the furnace are shown in Table 1.

The furnace possess the capability to startup automatically, given a user input, and swap to a PID controller. The PID controller has the following parameters for the proportional, integral, and differential constants: 0.650, 1.800, 0.000, respectively and linearity and beta set to 1.00 and 0.88 respectively. These are manually optimized to perform with the necessary *smoothness* for maintaining temperature without sporadic behavior. Figure 1 shows the transition during the startup to the PID

controller. The transition limits the temperature gradient from exceeding 0.2 C/s and prevents temperature overshoot to less than a degree. This is ideal to ensure the thermocouples, which are attached directly to the graphite heater with an alumina cement, do not shear off as a result of thermal stress gradients between the cement and the heater. Testing during the fabrication phase has demonstrated that the adhesion method for the thermocouples is robust, but this limit is posed nonetheless.

Table 1: Nominal operating parameters.

Parameter	Value	Units
Hydrostatic Pressure	16	psig
Operating Pressure	25-35	psig
Avg. Heater Temperature	500	C
Peak Heater Temperature	520	C

Optimization of the PID controller was conducted during the acceptance testing and improved following operation in the reactor environment. The ability of the PID controller to maintain temperature during reactor transients, since the heat deposition by radiation is significant, is of particular interest. The furnace will operate at a constant temperature throughout the week, so the PID controller is specifically tuned for reactor operation rather than furnace startup.

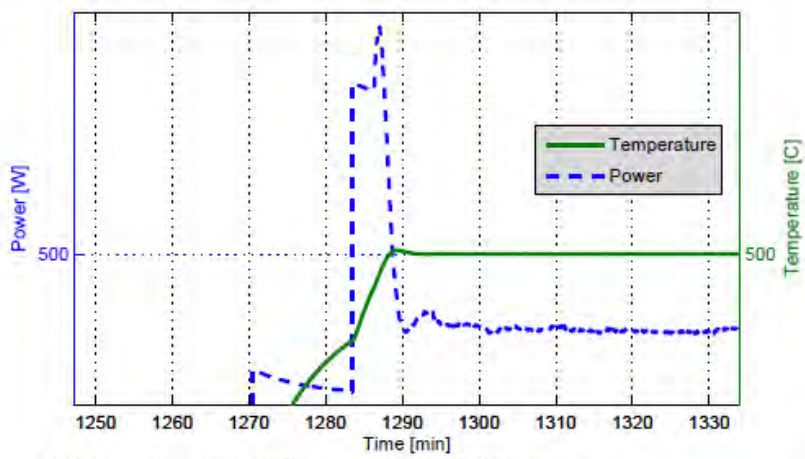

Figure 1: Automatic swap to PID controller by LabView.

During operation, the reactor undergoes various transients of known power. These are normally to accommodate sample movements or experiments and vary between 100 kW and 1 MW. With the PID controller active, the furnace temperature is maintained. This provides a direct comparison between the radiation and ohmic heating. It should be noted, that the radiation-induced heating will be most

significant in the thermal shields, aluminum, and alumina-silicate supports. This suggests that the regions of energy deposition are not the same and therefor not strictly comparable. However, for qualitative discussion, this comparison will provide insight on the modeling importance of the radiation-induced heating. Figure 2 shows the operation of the furnace throughout a day, completely unattended where the depression in power between 500 and 1000 minutes when the reactor operates at 1.0MW.

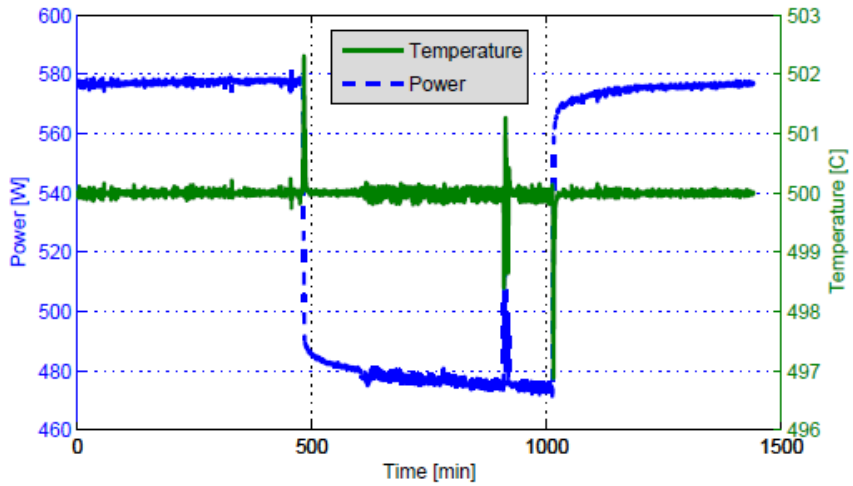

Figure 2: Full day operation of furnace, showing ohmic power and temperature.

It is interesting to note a few features of Figure 2. In particular, the magnitude of power required from the power supply to maintain the required operational temperature when the reactor is or is not operating. The difference is roughly 100W. This result suggests that 100W is deposited into the furnace when the reactor is in its nominal operating power level. Computational modeling suggested that a total of 75W would be deposited in the alumina supports and niobium thermal shields. Overall, this energy deposition is fairly significant - 20% of the total heat deposition. There are also two other features to note but are of lesser importance to the furnace operation. The first feature is the trend after startup (~500 min and see Figure 3) and shutdown (~1000 min) as a result of activation/decay of the furnace and fission product accumulation/decay in the neighboring fuel. The second feature is the temperature drift during reactor transient. The maximum deviation from nominal operation is during shutdown ans is limited to just over 3ºC. This is fairly insignificant from an operational standpoint.

Measurements (see Table 2) suggest that the axial temperature gradient does not change significantly as the operational state of the reactor changes; however, the external temperature magnitude does increase nearly to the operational limit, see Figure 4. Recall the the PID controller maintains the furnace at 500ºC and the bulk of the heat generated from ohmic heating. It is a benefit that the axial distribution of temperature does not change; this provides a great comparison for flux-induced error into the temperature measuring fiber optic.

The external temperature rises by nearly 20C when the reactor is operating at 1MW. While this is not particularly significant, it does raise an interesting question on which contributing factor is most responsible for the effect, from the degradation of the radiation heat transfer to the energy deposition

directly into the furnace materials. These are merely observations and will not be investigated further in this report.

Table 2: Heater and external temperatures of furance operating at 500C with and

Location	Heater Element				External	
TC	1	2	3	4	5	6
0MW	501	506	493	463	178	84.6
1MW	503	507	490	462	196	93

without the reactor operating.

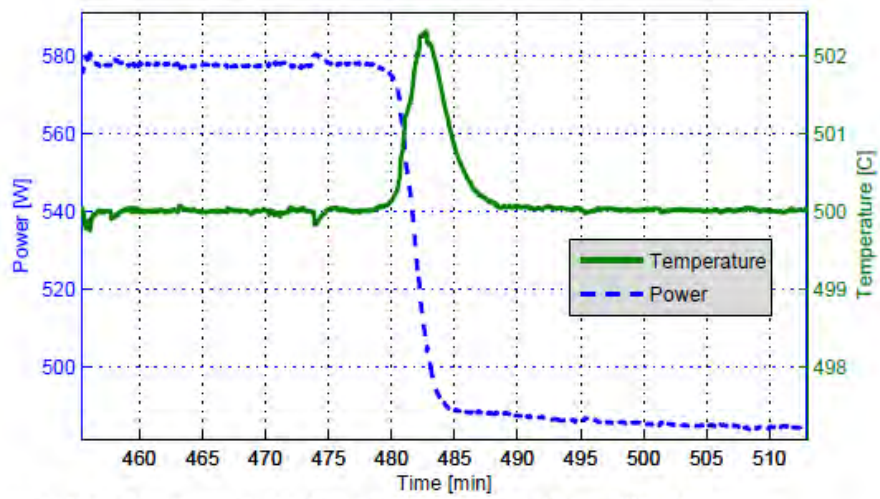

Figure 3: Furnace operation during reactor startup at time = 480 minutes.

The last portion of interest for normal operation, is the furnace startup. The startup is automatically performed by LabView by analyzing the temperature gradient and stepping up the current by 5 amps when the gradient is less than 0.04 C/s, see Figure 5. These parameters were experimentally determined to be the most simple and ideal for the furnace configuration to maintain the desired range on the temperature gradient (between 0.2 and 0.04 C/s). When the furnace reaches 480C, LabView swaps over to the PID controller; swapping at 480C prevents the PID controller, which does not actually have a derivative limit, from exceeding the desire thermal gradient.

There is some leakage expected, since the furnace operates as a pressurized system. Many attempts were made to minimize the leakage as much as possible. With a helium sniffer, leaks were detected and fixed. These fixes include removing unnecessary joints, JB-welding some threaded components, and replacing the helium hose with a flexible polythene tube. The leakage is still an ever present problem that must be accommodated. The daily helium loss from the main supply bottle is roughly 400-500 psi a day, which is significant but manageable. Even with operating the furnace 24 hours a day, the bottle only needs to be changed out every week.

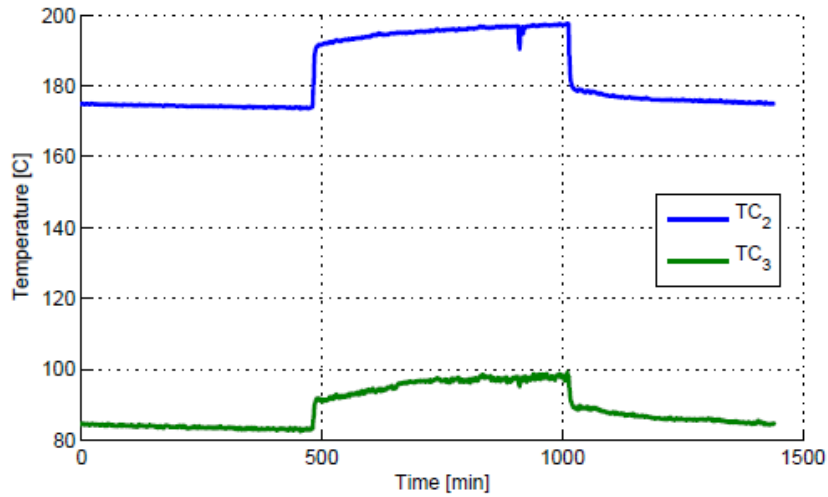

Figure 4: Full day operation of furnace, showing external temperature.

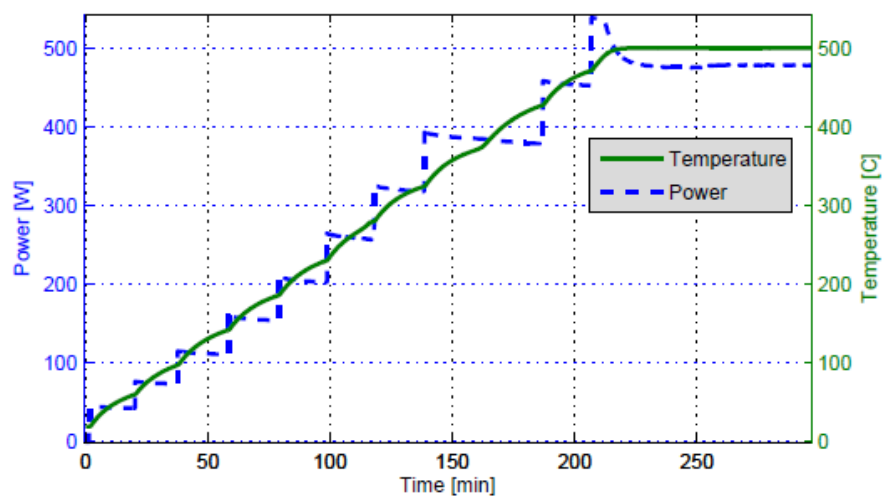

Figure 5: Furnace startup and swap to the PID controller.

The leakage of the void tube while isolated is shown in Figure 6. The average leak rate from this figure is determined to be 0.3 psi/min. This suggests that there is just over an hour of time before the pressure switches will kick off the heater following pressure no longer being maintained[1].

1 The cause of the significant portion of the leak was later determined to be through the power leads.

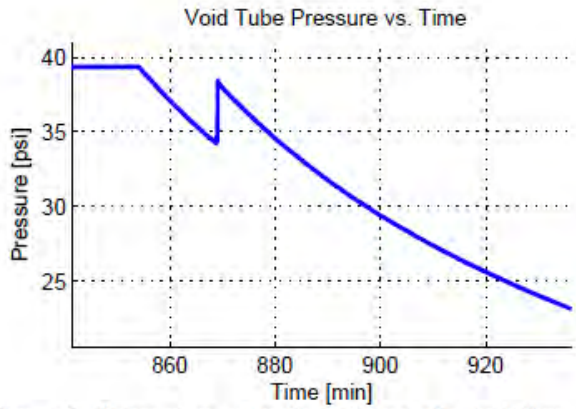

Figure 6: Pressure as a function of time after isolation.

Overall, the furnace operation is stable. The supporting systems and the entire furnace, excluding the fiber optics, is a robust system capable of taking a significant amount of user abuse. It is expected to operate with minimal maintenance needs, requiring only pressure calibration monthly as required by the instrumentation.

During the initial phases of furnace operation, there was a trend between heater temperature and ohmic power. As time continued forward, for a constant current of 60 amps, the heater temperature dropped and the ohmic power increased (see Figure 7). The reason for this is unknown, but it is suspected that the thermal shields have oxidized due to residual oxygen in the furnace. This oxidation would reduce the effectiveness of the thermal shields by increasing the emissivity. This result is that more power is required as the radiative heat removal increases for a given temperature. Moreover, this temperature change results in a change in the internal heater resistivity and therefore the power requirements change. Eventually, this trend stopped; there is no longer a temperature dependence with time, further defending the oxidation hypothesis. There are other possible causes: increase in contact resistance in the copper couplings, spallation of the silver solder on the graphite heater causing a path of lesser resistance (unlikely because deposition moves down the temperature gradient), and current leakage from the heater to the aluminum. Oxidation of the graphite would reduce the cross-sectional area of the heater and increase the overall resistance – this would benefit the heater, so has been ruled out.

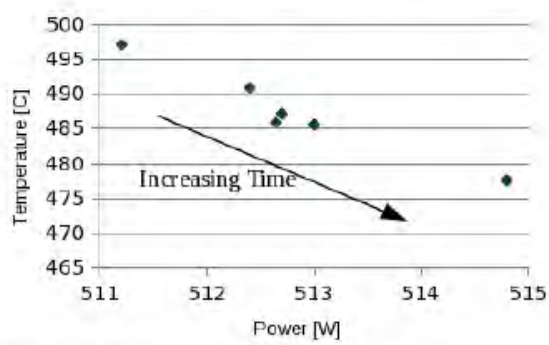

Figure 7: Temperature versus ohmic power.

2. Comparison to Thermal Modeling

The furnace was designed and fabricated with the guidance of analytical and numerical tools. It is necessary to determine just how well those models actually predicted the furnace performance, to what degree they should be used in the future, and where the greatest sensitives might exist. It is also natural to classify the greatest uncertainties in the system and to evaluate how those impact the modeling. However, the STAR-CCM+ modeling was performed for an earlier design of the furnace, so the assumptions are no longer valid for a strict comparison without updating the simulation.

The operational temperature that was calculated, with both MATLAB 1D modeling and STAR-CCM+, was 1000°C with an input current of 65 amps. However, as demonstrated, the actual operational temperature is 500°C, which is likely a result of oxidation of the thermal shields and lack of a vacuum environment for the graphite heater. It is not suspected that the model is poorly represented as validation cases showed that STAR-CCM+ did accurately predict heater temperatures in a controlled vacuum chamber experiment[2]. However, in this case, helium is in contact with the graphite allowing for natural convection cooling in addition with radiative cooling. The design process has been finalized and it is not necessary to repeat the calculations to verify this result.

3. Off-normal Incidents

During the operation of the furnace, there have been a few incidents. These are a result of human error as opposed to device failure such as an inadvertent furnace shutdown by isolating the gas supply. The result of these events, actually, demonstrate the robustness of the furnace and safety systems. These incidents resulted in the rapid cooling of the furnace without any noticeable impact on the thermocouple response following a restart of the furnace.

On April 18th, after swapping out the helium main supply tanks, the system was not properly returned to service[3]. This resulted in a pressure drop (see Figure 8). After approximately 90 minutes, the pressure switch cut power to the relay and automatically shut off the power supply. This resulted in the rapid shutdown of the furnace to protect the reactor for postulated incidents. The rapid lines in the figure are a result of the LabView software failing to communicate with the power supply (it is completely off at this point) and so it freezes when attempting to write data. The curve, however, is noticeable since there are points in the data loop where data is actually written. This bug was corrected following this event.

III. Fiber Optic Performance

This section will briefly discuss the performance of the fiber optics during the initial testing and operation of the furnace within the reactor core. These include temperature, gamma flux, and neutron flux spatial distributions and magnitude. The neutron and gamma flux measurements require a standard for normalization, so the flux foil data will be used. It should be noted that the flux was measured in the E2 position with a long tube without an experiment in the D3 position. This experimental tube is very similar to the furnace, with the exclusion of niobium thermal shields to absorb some neutrons, so this value represents an upper bound on the fluence. Additionally, experiments are normally in the D3 position since this is one of the more prolific experimental location for reactor commercial samples. These samples do absorb neutron, quite significantly, so it is expected

2 See the Safety Analysis report for further details.
3 The procedures were updated with pictures for the valve alignments to help prevent this from occurring again.

this will reduce the flux in the E2 position even further. It is not certain what this magnitude would be.

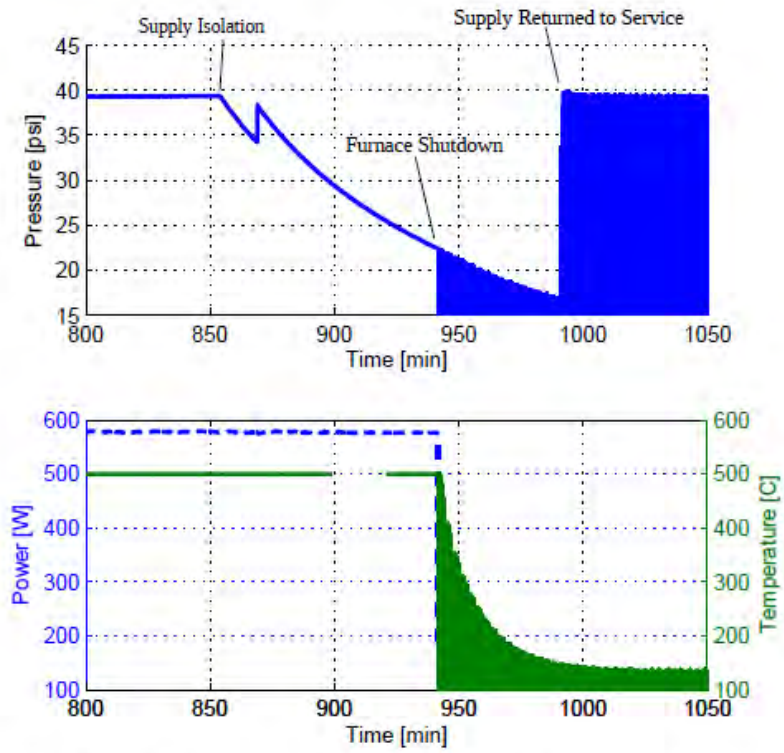

Figure 8: April 18th inadvertent furnace shutdown by isolation of supply gas.

1. Comparison to MCNP and flux foils

The furnace was modeled using MCNP 5.1.5 to determine the ideal location for the experiment and the safety parameters for the experimental location. This includes reactivity worth as a result of flooding/inadvertent removal of the furnace. Additionally, MCNP provided an expected gamma and neutron flux magnitude and spatial distribution that would be expected at the fiber optic. These calculations were validated with Au/Al flux foil measurements in the E2 location with an experimental long-tube. These long-tubes are nearly identical to the furnace in that they are made of aluminum 6061 T6 and displace the same amount of water. The wall thickness, compared to the furnace, is greater by 1/16th of an inch.

The results of the MCNP simulation for reactivity worth is show in Table 3. Experimentally, the reactivity worth was determined to be $0.014 for the case of the reactor away from the thermal column and with an experiment in the D3 location (D3/noTC as per the table). This is a significant difference, but likely a result of using fresh fuel isotopics in the model. This suggests that the flux in the position

is likely over-represented, in other words, the simulation suggests a tighter coupling of the experimental location to the reactor and therefore would predict a high flux magnitude as shown in Figure 9.

Table 3: Reactivity insertions for various postulated configurations.

	D3	noD3
TC	$0.041	$0.063
noTC	$0.034	$0.069

The distribution and expected magnitude for the fiber optics in the E2 position is shown in Figure 9. The expected magnitude is nearly in the center of the fiber and the gradient isn't incredibly steep, so the irradiation should be fairly uniform. The flux foils results, from Table 4, are also plotted and show a similar gradient (slightly shifted) with a smaller magnitude. Note that the flux from MCNP is the total flux and the flux foil measurements are for thermal flux only. The thermal flux calculated for the peak location of the fiber, at a position of 15 cm, is 5.88e12 n/cm^{2}s when using the energy bin of 0.0168 to 0.342 eV. So the agreement for thermal flux is quite good – the eipthermal-to-thermal ratio is off considerably.

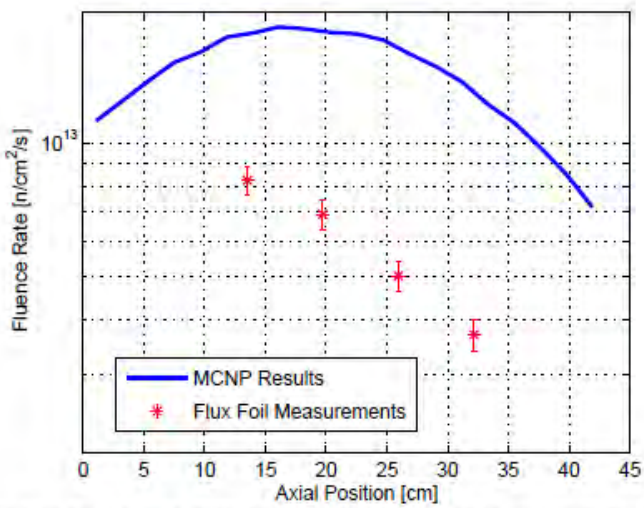

Figure 9: Neutron distribution within fiber optic calculated with MCNP and measured by flux foils.

The Maxwellian corrected flux foil data can be seen in Table 4, showing the results of a 2-hour irradiation in the E2 position of a typical long tube. This does not include an experiment in the D3 position, so it marks the upper bound for non-coupler operation. It is expected that operation against the coupler box will increase the flux in this location due to spatial tilting of the neutron flux.

Can	Height (cm)	Thermal Fluence Rate ϕ ($cm^{-2} * s^{-1}$)	Uncertainty	Epithermal Fluence Rate ϕEPI ($cm^{-2} * s^{-1}$)	Uncertainty
1	32.18	3.69E+12	2.90E+11	2.02E+11	8.18E+09
2	25.76	5.02E+12	4.04E+11	2.83E+11	1.15E+10
3	19.73	6.93E+12	5.31E+11	3.55E+11	1.44E+10
4	13.51	8.26E+12	5.93E+11	3.70E+11	1.50E+10

Table 4: Flux foils measurements of the E2 position of the NSCR.

The axial distribution of the neutron flux is not similar to the distribution of Figure 9; however, this is likely because the long tube does not extend to the bottom of the fuel meat and the fiber optic probe does. In fact, the probe extends beyond the fuel meat in both directions. Noting that 2.4 cm would be the bottom of the fuel meat.

The fiber optic radiation measurements are currently not available. It is believed that the vibrations resulting for reactor operation are responsible for this effect, though measurements are not possible at low power, either. Vibration influences have been isolated: control rod movements, diffuser pump operation, power supply cooling fans, and natural convection, such that each effect was studied by removing the other effects. These results will be discussed in the final report.

2. Comparison to STAR-CCM+

It is possible to make a comparison of the thermal distribution from fiber optic measurements to the spatial gradient from the simulation (see Figure 10). There largest errors will be at the axial ends of the graphite since there are significant assumptions on the contact resistances with the alumina supports. This will affect the heat transfer from these ends a great deal. It was assumed, in the modeling, that there would be about 20% contact (only allowed 20% of the mesh volume to transfer heat between surfaces).

The fiber optic measurement is severely affected by vibrations induced by the natural circulation cooling of the reactor while it is operating. The affected regions are typically at the fiber end (15.25+ meters) and at the feedthrough into the furnace (14.8 – 14.9 meters). It does appear that the vibration-induced noise effects the measurement only locally and that the rest of the measurement is not impacted. Despite this, the shape of the temperature distribution do closely match with the peak being predicted within a centimeter. As expected, the temperature gradients near the edges of the graphite heating element (the end of the STAR-CCM+ data plot corresponds with the end of the graphite heater) are steeper. In the STAR-CCM+ simulation, the peak temperature is 908°C and the fiber optic measures 720.2°C, compared to the thermocouple readings in Table 7 this does not demonstrate good performance for the fiber optics. It is expected that the internal stresses introduced by the inherent fiber optic probe might be the culprit for the poor agreement. The niobium sheath and quartz ferrules will act to stretch the fiber and compress it, and these stresses will appear to the software as if generated by thermal expansion of the fiber optic. This poor performance does not bode well for the fiber optics.

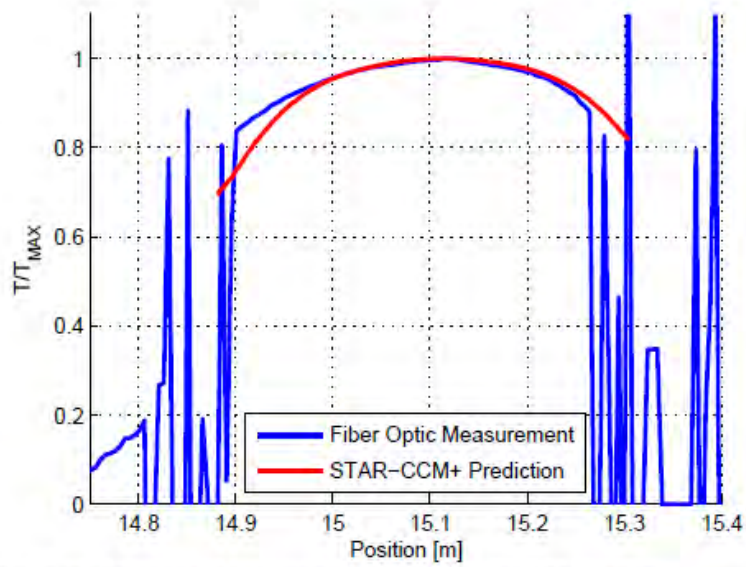

Figure 10: Normalized temperature distribution from fiber optics measurements and the STAR-CCM+ model.

IV. Conclusions

The furnace operation has been smooth and stable and it is expected to maintain operational integrity throughout the next few months with minimal maintenance. The process of installation and data acquisition has occurred without major problems with only minor concerns related to the LabView software. These have been corrected in their entirety as of this writing on the 14th of May. The automatic PID controller works very well with the parameters that were set manually.

Some of the modeling has fallen short, in particular the reactivity worth of the experiment was over estimated. While this was quite a conservative result, the causes are currently unknown. Since the experiment is very well within technical specification limits of the NSCR, further modeling will not be performed. The thermal modeling also feel short, but primarily as a result of containing assumptions in the means of heat transfer that are no longer valid for the experiment. The axial distribution appears to be well predicted.

The radiation detection fibers optics are, from initial investigations, are not functioning properly. This makes spatial measurements difficult to validate, expect with flux foils. These flux foils, however, were determined using a different experimental device. The difference, however, is not excepted to be significant, since the OD of the long-tube and furnace is identical. Therefore displacing the same volume of water.

The temperature fiber optics do produce measurements that are seemingly believable; however, the measured peak and average temperature does not correspond to well to what the installed

thermocouples measure. This is likely do to thermal stresses induced by the fiber optic probe. This performance, however, is not acceptable. The fiber optic performance, up to this point, has been poor.

Appendix

Title: A Distributed Fiber Optic Sensor Network for Online 3D Temperature and Neutron Fluence Mapping in a VHTR Environment

PI Contact Info: Pavel V. Tsvetkov, Texas A&M University, tsvetkov@tamu.edu, 979-845-7078
Technical Workscope Identifier: Gen IV/Methods, TPOC: Abderrafi Ougouag (INL) Federal POC: Suibel Schuppner

NEUP Nuclear Energy University Programs
U.S. Department of Energy

Purpose/Objective: Real-time 3D mapping of the temperature and neutron fluence distributions in NGNP/VHTRs

Other Personnel: S. Bragg-Sitton, Texas A&M University/INL
B. Dickerson, Luna Innovations

Student Personnel: **Undergraduate** - Hanniel Honang Ndjomou
Carl Mullins
Graduate - Mathew Johnson (M.S.) (graduated)
- Sathish Lakshmipathy (M.S.) (graduated)
- Jesse Johns (Ph.D.)

Duration: October 2009 – September 2012 (ext. till 05/30/13)

Total Funding Level: $757,143

Outcome/Result: Gained experience indicate significant potential opportunities for future distributed fiberoptics sensor applications as an integral part of the eactor instrumentation. Distributed sensing allows gathering much more robust data from the reactor.

Importance/Relevance: direct in-core monitoring in real time to enhance safety, instrumentation for benchmarking in design, reduction of uncertainties in local phenomena assessment.

Logical Path: (1) evaluate fiber optics for in in-core distributed sensor networks in VHTRs and
(2) develop a predictive 3D performance reconstruction algorithm for VHTR in-core instrumentation.

Impact Areas: real time assessment of reactor conditions, hot spot localization prediction, design margin optimization, 3D in-core instrumentation for code benchmarking.

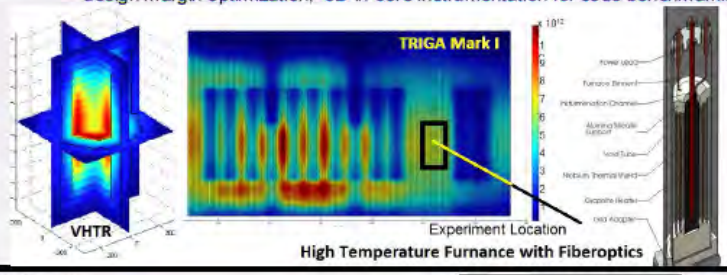

Special Tools/Methods and Facilities being used:

Experimental: high temperature furnace emulating VHTR in TRIGA fluences of $2x10^{19}$n/cm^2 or higher, 1000°C

Computational Modeling or Theory: whole-core exact-geometry modeling of VHTRs and TRIGA using MCNP, Serpent, STAR-CCM+

Facillities/Equipment: Texas A&M University TRIGA Mark I 1MW, Optical Backscatter Reflectometer and Distributed Fiberoptics Probes

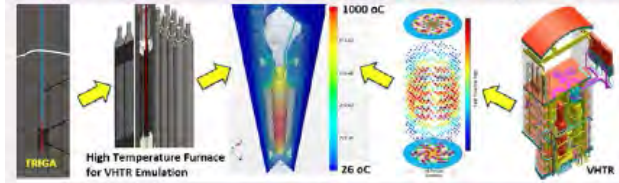

Sample Results:
- The gained practical experience with fiberoptics sensors
- Feasibility and applications have been established
- Temperature fiber optic sensors perform as expected.
- Technology is not ready for near-term use
- The noted challenges include vibrations, noise, material effects, software, calibration…

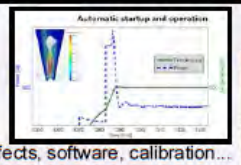

Status of Deliverables:

Year I and II: furnace design, fabrication, 3D VHTR modeling focusing on in-core performance reconstruction and sensor networks

Year III: Irradiation, PIE, TRIGA/VHTR scaling, sensor network studies.

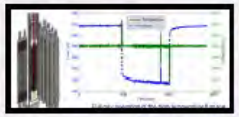

Future R&D needs: vibrations, noise, materials, software, calibration

The project was focused on NGNP/VHTR but the analyzed fiberoptics sensing and 3D in-core monitoring via distributed sensing are of paramount value for LWRs, emerging SMRs and all advanced reactors.

Presentations/publications: ANS Annual/Winter Meetings in 2010 through 13, PHYSOR 2012, ICONE 2012, Journals

Contact Information

Shannon M. Bragg-Sitton
Senior Nuclear Engineer
Fuel Performance and Design
Idaho National Laboratory
P.O. Box 1625 MS 3860
Idaho Falls, ID 83415-3860
Tel 208-526-2367
Fax 208-526-2930
Shannon.Bragg-Sitton@inl.gov

Pavel V. Tsvetkov
Associate Professor
Department of Nuclear Engineering
Texas A&M University
337 Zachry Engineering Center, MS 3133
College Station, TX, 77843-3133
Tel 979-845-7078
Fax 979-845-6443
Tsvetkov@tamu.edu

University Information

Texas A&M University, Department of Nuclear Engineering
337 Zachry Engineering Center, MS3133, College Station, TX, 77843
Tel 979-845-7078
Fax 979-845-6443
http://engineering.tamu.edu/nuclear

NUCLEAR ENGINEERING
TEXAS A&M UNIVERSITY

Page intentionally blank